transactions of the ASME

journal of heat transfer

Published Quarterly by
The American Society of
Mechanical Engineers
Volume 98 • Series C • Number 2
MAY 1976

EDITORIAL STAFF
Editor, **J. J. JAKLITSCH, JR.**
Production Editor,
MARINA EVDOCHENKO
ditorial Prod. Asst., **BARBARA SIGNORELLI**

HEAT TRANSFER DIVISION
Chairman, **R. W. GRAHAM**
Secretary, **A. S. RATHBUN**
Senior Technical Editor, **E. M. SPARROW**
Technical Editor, **B. T. CHAO**
Technical Editor, **D. K. EDWARDS**
Technical Editor, **R. EICHHORN**
Technical Editor, **P. GRIFFITH**
Technical Editor, **R. B. KINNEY**
Technical Editor, **R. SIEGEL**
Technical Editor, **R. L. WEBB**

POLICY BOARD, COMMUNICATIONS
Chairman and Vice-President
S. P. KEZIOS

Members-at-Large
R. E. ABBOTT
I. BERMAN
J. W. HOLL
D. F. WILCOCK

Policy Board Representatives
Basic Engineering, **J. E. FOWLER**
General Engineering, **S. P. ROGACKI**
Industry, **J. E. ORTLOFF**
Power, **A. F. DUZY**
Research, **P. GOLDSTEIN**
Codes and Stds., **P. M. BRISTER**
Nom. Com. Rep.,
J. W. HOLL

Business Staff
345 E. 47th St.
New York, N. Y. 10017
212/752-6800
Mng. Dir., Com., **C. O. SANDERSON**

OFFICERS OF THE ASME
President, **C. L. TUTT, JR.**
Exec. Dir. & Sec'y, **ROGERS B. FINCH**
Treasurer, **J. D. PAULUS**

EDITED and PUBLISHED quarterly at the offices of The American Society of Mechanical Engineers, United Engineering Center, 345 E. 47th St., New York, N. Y. 10017. Cable address, "Mechaneer," New York, Second-class postage paid at New York, N. Y., and at additional mailing offices.

CHANGES OF ADDRESS must be received at Society headquarters seven weeks before they are to be effective. Please send old label and new address.

PRICES: To members, $25.00, annually; to nonmembers, $50.00. Single copies, $15.00 each. Add $1.50 for postage to countries outside the United States and Canada.

STATEMENT from By-Laws. The Society shall not be responsible for statements or opinions advanced in papers or . . . printed in its publications (B 13, Par. 4).

COPYRIGHT © 1976 by the American Society of Mechanical Engineers. Reprints from this publication may be made on conditions that full credit be given the TRANSACTIONS OF THE ASME, SERIES C—JOURNAL OF HEAT TRANSFER, and the author and date of publication stated.

INDEXED by the Engineering Index, Inc.

(Contents continued on page 201)

Downloaded 04 Feb 2011 to 194.85.80.107. Redistribution subject to ASME license or copyright; see http://www.asme.org/terms/Terms_Use.cfm

CONTENTS (CONTINUED)

TECHNICAL NOTES

DISCUSSION

ERRATA

ADDENDUM

An Analysis of Critical Heat Flux in Flow Reversal Transients

R. A. Smith[1]
Research Engineer,
Shell Development Co.,
Houston, Texas.
Assoc. Mem. ASME

F. A. Price[2]
Charles T. Main, Inc.
Boston, Mass.

P. Griffith
Professor, M.I.T.
Mem. ASME

A large inlet break Loss of Coolant Accident in a Pressurized Water Reactor (PWR) would cause the flow through the core to reverse within milliseconds. Currently approved methods of analysis conservatively assume that vapor blanketing of core heat transfer surfaces occurs upon this first reduction to zero flow. A coordinated experimental and analytical study has been conducted to determine when and where the vapor blanketing or Critical Heat Flux (CHF) conditions actually do develop in constant pressure rapid flow reversals. The results indicate that first occurrence of CHF is due not to low coolant velocities, but to flow stagnation in the channel interior with associated rapid channel voiding. Calculations indicate that good cooling should persist over large regions of the core for about 1 s longer than is currently assumed.

1 Introduction

A large inlet break Loss of Coolant Accident (LOCA) in a Pressurized Water Reactor (PWR) would cause the flow through the core to reverse within milliseconds. There exists a dearth of information in the "boiling crisis" or "Critical Heat Flux" (CHF) literature at very low flows, and computations of cladding temperatures approved for licensing purposes now conservatively assume that vapor blanketing of core heat transfer surfaces occurs upon the first reduction to zero flow. The result is that none of the stored thermal energy in the core fuel elements is removed after the reactor goes subcritical, and calculated cladding temperatures climb rapidly toward allowable limits as the energy is redistributed within the fuel elements.

An analysis of Critical Heat Flux in high pressure Freon-113 flow reversal transients has been performed to predict when and where the boiling crisis actually does develop in constant pressure rapid flow reversals. The results indicate that CHF is *not* likely to occur upon the first reduction to zero flow in a PWR accident, but that under some conditions a flow stagnation point could develop shortly after the reversal within the central axial region of the core length. This could lead to rapid voiding and fluid expulsion at a rate that would completely void the core average coolant channels of liquid coolant within 1 or 2 s of the stagnation point inception. Computations indicate that this expulsion and voiding process would be terminated by CHF virtually halting the energy deposition into the coolant as soon as moderately high void fractions and intermediate flowing qualities are achieved. Still the good cooling probably does persist over large regions of the core for about 1 s longer than is currently assumed.

2 Freon-113 Transients

In the reactor LOCA, the precipitous drop in system pressure from 2250 psia (15.5 MPa) is halted within milliseconds of the break by flashing in the upper plenum and/or hot leg piping at about 1500 psia (10.3 MPa). Further pressure blowdown occurs at a much reduced rate. The flow transients that ensue may therefore be approximated as constant system pressure transients. Constant system pressure transient CHF experiments in 200 psia (1.38 MPa) Freon-113 were conducted with the apparatus shown in Fig. 1. Freon-113 at this pressure can be used to simulate water experiments at 1500 psia (10.3 MPa). The heat fluxes and power requirements are then an order of magnitude less in the Freon as predicted by well established Freon-water scaling laws for CHF (2). The test section for these experiments was an electrically heated round tube (with tube wall as a resistive heater) 8 ft (2.44 m) long and 0.435 in. (1.1 cm) in inside diameter. The flow reversal valve had two positions, one for upflow and one for downflow.

Fig. 2 illustrates the kind of flow reversal transients run in the Freon loop. From initially steady upflow conditions, two flow reversals were imposed in the test section. These reversals were separated in time by a specified period of downflow, τ_d. Test section power input was held constant during the transient. For purposes of illustration Fig. 2 shows how the axial coolant enthalpy profile would change following each reversal were the coolant to remain subcooled throughout the experiment.

---

[1] Former Research Assistant, M.I.T.

[2] Former Research Assistant, M.I.T.

Contributed by the Heat Transfer Division for publication in the JOURNAL OF HEAT TRANSFER. Manuscript received by the Heat Transfer Division October 30, 1975. Paper No. 76-HT-TT.

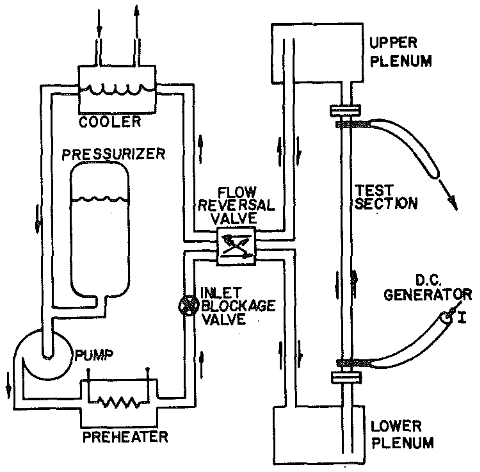

Fig. 1 Schematic of the flow reversal loop

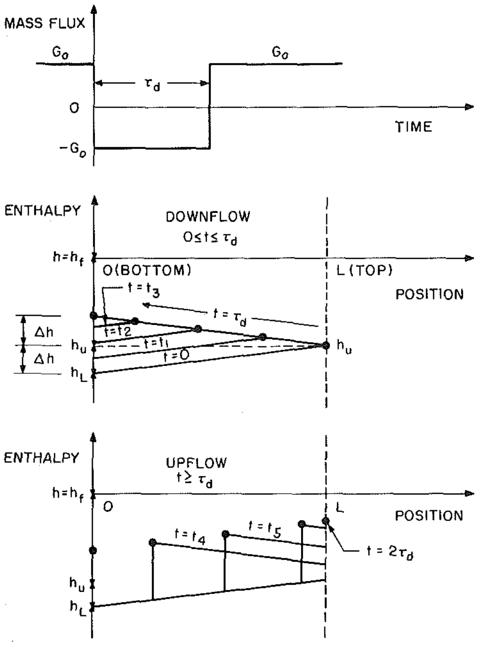

Fig. 2 Simple single phase double reversal transient

If a series of these transients were to be run at successively higher power levels, each with the same initial mass flux, exit plenum pressure, and enthalpy, and each with the same period of downflow, τ_d, one might expect there to result for these experiments a minimum CHF power level above which CHF occurred during the transient and below which it did not.

Fig. 3 shows the minimum CHF boundary determined experimentally in the fashion just described for a range of downflow periods, τ_d. The symbols plotted with the curves relate to analyses of specific documented transients and will be discussed later in the paper. Two curves are shown because two CHF detectors were used: thermal paint on the exterior tube wall, and a thermocouple at the top of the tube electrically insulated from the exterior wall with a mica chip. The thermal paint was selected to indicate occurrence of CHF when the outside wall temperature rose 15–20°F (8–11°C) above its initial steady value with nucleate boiling at the inside surface. Similarly a 20°F (11°C) rise in temperature above this initial value was the criterion for CHF indication with the thermocouple. The paint showed that the minimum CHF always occurred at the top of the tube. This is consistent with Fig. 2 which showed that the peak coolant enthalpy occurs briefly at the top of the tube following the second reversal. The thermal paint is considered the more sensitive detector for "fleeting" CHF since its thermal time response was not hampered by the mica insulation.

3 Transient CHF Analysis

The experiments were performed to provide a benchmark against which a transient CHF analysis, including flow reversals might be compared. The fundamental hypothesis for the analysis was that CHF would occur in the transients at the same instantaneous local fluid conditions at which CHF has been previously observed in steady flow experiments. The basis for this is the notion that there is really no such thing as a steady state CHF. What is steady-state in an Eulerian coordinate system may be highly transient in a Lagrangian coordinate system. Lagrangian transients at the CHF location in steady flow experiments are quite rapid involving the suspension of liquid away from the wall in a rush of vapor. The local fluid conditions at which CHF occurs are not very sensitive to the kind of reactor transients perceived from a Eulerian frame of reference.

For high enough up flow velocities the local conditions at CHF in steady flow experiments in round tubes are well documented in the form of correlations:

$$(q/A)_{\mathrm{CHF}} = f(P, G, D, X) \tag{1}$$

The quality is the flowing quality defined as the vapor mass flow rate divided by the total mass flow rate through the tube. Quality is a useful correlating variable for CHF when CHF is due to excessive vapor flow rate in annular flow causing dryout on the heater surface.

Griffith, Walkush, and Avedisian [3] have proposed, however, that at low flows the CHF mechanism is more like pool boiling CHF and that the channel cross section averaged void fraction should be a better correlating variable than quality. Consider for example a large diameter vertical tube filled with stagnant saturated liquid water in which a small stream of steam bubbles is drifting upward. The quality is 100 percent and the void fraction is near zero. There is sufficient liquid at the walls to support considerable heat flux in nucleate boiling. As a correlating variable, void fraction is more sensitive than quality to the presence or absence of liquid at low flows.

These ideas were adopted as the basis for predicting CHF levels as the flow rate passed from upflow through the low flow range ($|G| \leq 500{,}000$ lbm/hr-ft^2 = 678 kg/m^{2}s) to downflow in the Freon-113 flow reversal transients. Section 3.1 describes the CHF criteria

---

[3] Numbers in brackets designate References at end of paper.

Nomenclature

D = inside diameter
G = mass velocity
h = enthalpy
h_f = enthalpy of saturated liquid
$h_{fg} = (h_g - h_f)$
h_g = enthalpy of saturated vapor

P = pressure
P_0 = initial exit pressure
(q/A) = heat flux
X = quality
X_0 = initial exit quality
τ = time constant

τ_c = reciprocal cutoff frequency
τ_d = duration of downflow

Subscripts

d = downflow
u = upflow

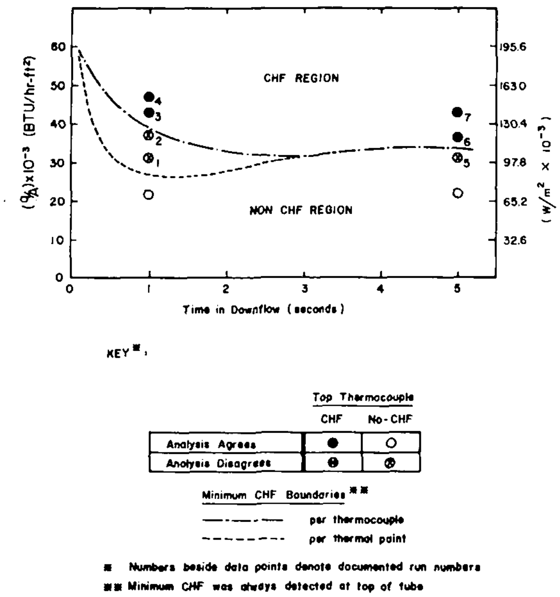

Fig. 3 Summary of the measured and calculated CHF. The thermal paint (bottom line) is considered the better measurement. The calculations appear to be quite satisfactory.

used in conjunction with the instantaneous local fluid conditions calculated from computer simulations of the Freon-113 transients as described in Section 3.2.

3.1 **Critical Heat Flux Criteria.** The CHF criteria developed here were specifically for testing the low flow CHF ideas above in our constant pressure, constant test section power flow reversal experiments. If these ideas were correct CHF would not occur at low void fraction near zero flow during the first flow reversal but later in the transient with higher void fractions and vapor flow rates. A first model to test this hypothesis need not accurately predict CHF levels at low voids and near zero net flow; it need only indicate that CHF levels there are not limiting. Of course, accurate predictions of CHF levels were required at the higher voids and vapor flow rates. This distinction permitted the use of the simple homogeneous two-phase flow model as discussed in the following.

A study of published steam-water CHF data in round tubes and a search through the published steady flow CHF correlations revealed only one correlation with even qualitatively correct behavior in the low flow range. Fig. 4 presents the Bowring [4] CHF correlation for steady upflow in round tubes scaled to 200 psia (1.38 MPa) Freon-113 by the method of Ahmad [2] along with the steady flow 200 psia (1.38 MPa) Freon-113 CHF data of Coeffield [5] and Price [1]. The agreement with data is surprisingly good and must be considered somewhat fortuitous since Bowring's correlation tends to overpredict CHF in water at low flows. The unique feature of this correlation is that it yields a finite and reasonable CHF value even at zero mass flux which is consistent with Griffith's low-flow pool boiling CHF hypothesis.

Fig. 5 shows the relationship between void fraction and CHF at low flows in Freon-113 ($G \leq 500{,}000$ lbm/hr-ft^2 = 678 kg/m^{2}s) as determined by three separate investigations [3, 6, 7] in three different test sections. The CHF values are shown normalized to the pool-boiling CHF value as correlated by Zuber [8]. A comparison [9] between Walkush's curve in Fig. 5 with the Bowring/Ahmad correlation at low flows supported the use of the Bowring/Ahmad equations for all upflow mass velocities down to the countercurrent flow range (valid for $G > 50{,}000$ lbm/hr-ft^2 = 68 kg/m^{2}s).

If these criteria are used with a separated-flow model with vapor drift the flowing quality is undefined in countercurrent flow, and the CHF-void curve should be used directly ($-130{,}000 \leq G \leq 50{,}000$ lbm/hr-ft^2 or $-176 \leq G \leq 68$ kg/m^{2}s). As mentioned above the homogeneous two-phase model was used in this investigation. While the homogeneous model can adequately represent the vapor flow rates in cocurrent flow as required in the Bowring correlation (via G and X), it is known to be inadequate for predicting void fractions at low flows. In accordance with the arguments at the beginning of this section an empirical construct was adopted for representing CHF levels in the narrow countercurrent flow range of mass flux which was traversed very quickly in these experiments. This was simply to enter the Bowring/Ahmad correlation directly with $|G|$ and X from the homogeneous model for all countercurrent flow mass velocities ($-130{,}000 \leq G \leq 50{,}000$ lbm/hr-ft^2 or $-176 \leq G \leq 68$ kg/m^{2}s).

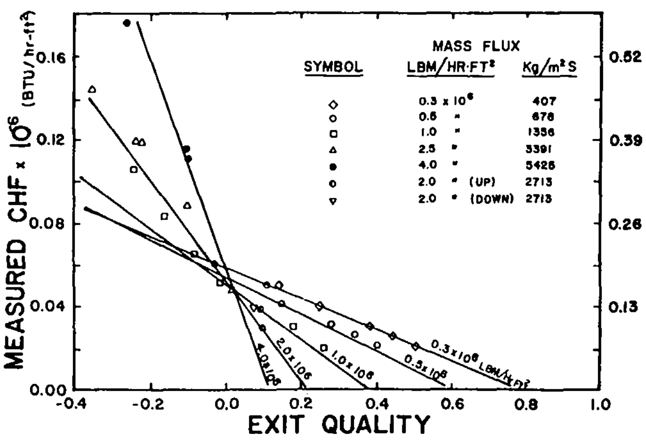

Fig. 4 CHF versus quality for high velocity Freon (reference [1])

In a rapid flow reversal the quality from the homogeneous model remained essentially constant as the countercurrent flow range was traversed. The variations in CHF levels over this range of mass flux were small (~10–20 percent) in the Bowring correlation with the maximum CHF level occurring at G = 0. This behavior was felt to be qualitatively correct since the void fraction would remain essentially constant through the countercurrent flow range in such rapid flow reversals. Successful predictions of time and location of CHF in our experiments are considered to substantiate the low flow CHF hypothesis and to help qualify the models used to predict the higher void, higher vapor flow CHF's. Additional work is required to develop and qualify models for transients in which CHF can be expected to occur in countercurrent flow (such as combined flow stagnation and heat flux excursion transients).

A modification of Worley's procedure [10] was adopted for predicting CHF in downflow using the Bowring/Ahmad upflow correlation. The hypothesis is that flow direction is important only in the low-flow range where void fraction is a useful correlating variable. Accordingly from a given set of downflow conditions (P_d, G_d, D_d, X_d)

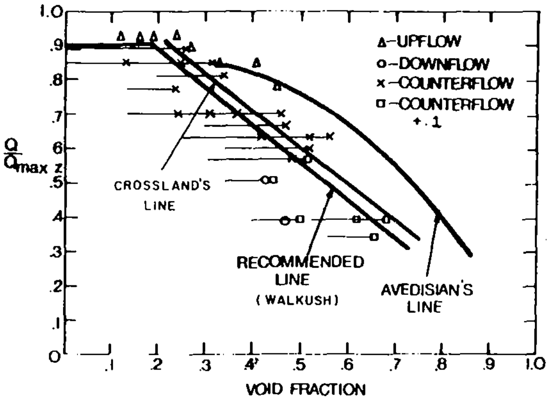

Fig. 5 CHF versus void fraction for low velocity flows (Freon 113) (reference [7])

the CHF may be determined from a corresponding set of upflow conditions giving the same void fraction

$$(q/A)_d^{\mathrm{CHF}} = (q/A)_u^{\mathrm{CHF}} = f(P_d, |G_d|, D_d, X_u)$$

where X_u is the quality that yields the same *void fraction* in upflow as did X_d in downflow. The void-quality relations in upflow and in downflow were obtained from Worley's report. The Bowring/Ahmad correlation was used to predict $(q/A)_{\mathrm{CHF}}$, and this procedure was used for all $G \leq -130{,}000$ lbm/hr-ft^2 = -176 kg/m^{2}s.

3.2 **Transient Local Conditions Model.** The transient one-dimensional fluid conservation equations of mass, momentum, and energy were programmed to permit a digital simulation of the flow transients in the heated test section via the BACTRAC3 computer program [9]. Fundamental features of the model include:

(i) homogeneous equilibrium no-slip two-phase mixture behavior;
(ii) incompressible liquid subcooled fluid behavior;
(iii) transient radial conduction heat transfer in the tube wall;
(iv) plenum-to-plenum pressure drop forced computation.

The pressure drop forced computation feature allowed simulation of transients using measured plenum pressure histories without having to model the loop dynamics outside of the test section and plena.

In our experiments the test section pressure drop was measured via a differential-pressure transducer and by a gage-pressure transducer in each plenum. These signals, along with the enthalpies in each plenum provided the forcing function for the digital simulation and they were recorded along with two outer wall thermocouple signals on FM analog magnetic tape. These signals were subsequently played back through an analog/digital converter and stored as sampled data files on a memory disk accessible by the computer on which the digital simulation was run.

The BACTRAC3 program iteratively updates the local fluid conditions in discrete time steps for each of up to 25 axial stations along the tube length. At the end of each time step the fluid conditions and heat flux into the coolant for every axial station are compared against the CHF local conditions of Section 3.1 to determine if and when CHF occurs at any of the stations. When CHF occurs at a station the transient wall conduction model changes to a low "beyond-CHF" heat transfer coefficient at the inside tube wall surface, and with subsequent time steps the propagation of the effects of this change to the outer wall surface is computed. The wall heat transfer model has no provision for beyond-CHF "rewet" such that once CHF occurs at a station the beyond-CHF heat transfer coefficient is used there until the end of the simulation.

4 Transient CHF Analytical Results

A thermocouple near each end of the tube was selected for comparison against the analysis. The thermocouples were directly attached to the tube wall to improve their time response, but the signals became buried in electrical "noise" such that large first-order low pass filters (τ_c = 1 s) were required in the course of the signal processing to retrieve the recorded information. This of course eliminated the improvement in time response sought by removing the mica chip insulation from between the thermocouple and the wall. Nevertheless the temperature traces were recorded and should be viewed as having been processed through a first-order lag with a 1 s time constant.

4.1 **Simulation Example.** Fig. 6 depicts a typical plena pressure forcing function for a transient (Price's Run No. 4) [1] involving a downflow period of a little over one second. Sharp pressure spikes followed by "ringing" can be seen at the times of flow reversal valve action. The pressure difference across the tube is about 8 psid (55 kg/m^2) in upflow and near zero in downflow. This is all superimposed on a rather rapid 40 psia (0.28 MPa) surge in system pressure followed by a rapid dip and a return to normal. Results of the simulation indicate that this behavior is due to net vapor generation and expansion in the tube followed by a collapse of the voids as they are swept out into the upper plenum which is full of subcooled liquid.

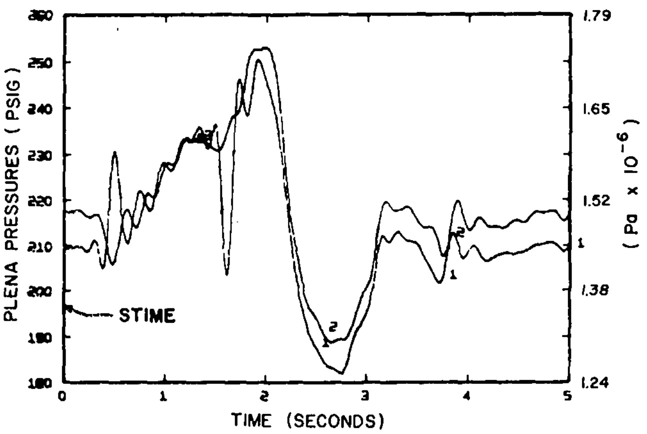

Fig. 6 For this reversal: q/A = 47,250 Btu/hr-ft^2; $X_0 = -0.20$; P_0 = 213 psia; $G = 2.5 \times 10^6$ lbm/hr ft^2; 226°F; Tout = 289°F.

Fig. 7 shows the measured and predicted outside tube wall temperature for this sample run. The solid line curves labeled 1 and 2 are the recorded and filtered thermocouple traces at the bottom and top ends of the tube respectively, while the X's represent the predicted traces for those locations. If the predicted temperature traces were completely accurate the filtered thermocouple curves should appear as first order lag (τ = 1 s) responses to the "X" curves. The calculated first-order lag response to the top thermocouple prediction is shown as a dotted line on this figure. The times for flow reversal valve action are indicated by arrows at the top of the figure.

Focusing first on the top end of the tube (curve 2) a CHF is predicted to occur shortly after the second reversal as the voids are swept out into the upper plenum. The top thermocouple trace does exhibit the expected behavior confirming that a CHF did occur when and where it was predicted.

At the lower tube end the measured and predicted temperature traces differ substantially. This may, however, be explained in a manner consistent with the model by a "fleeting" CHF wherein the wall is rewet shortly after CHF occurs. There was no provision for rewet in this model as mentioned in Section 3.2. In the predicted trace the initial rise in temperatures during downflow was not due to CHF but to the wall at subcooled temperatures being washed by warmer fluid from above. A CHF was predicted to occur in upflow shortly after the second reversal. In the simulation, however, the wall at the bottom thermocouple location was washed within 0.1 s of the time of CHF by fluid from the lower plenum which was ≃60°F (33°C) subcooled.

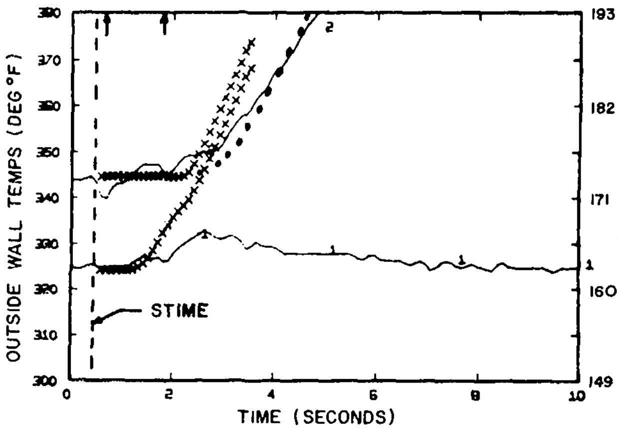

Fig. 7 Temperature-time traces for the lower (1) and upper (2) thermocouples compared to the calculations for BACTRAC 3. There is a time constant of about 1 s on the thermocouples so that the measured ramps should be indexed left about 1 s for comparison with the calculations. The dotted curve with the upper traces shows exactly how a 1 s first order lag would respond to the predicted temperature ramp. The calculations appear quite satisfactory.

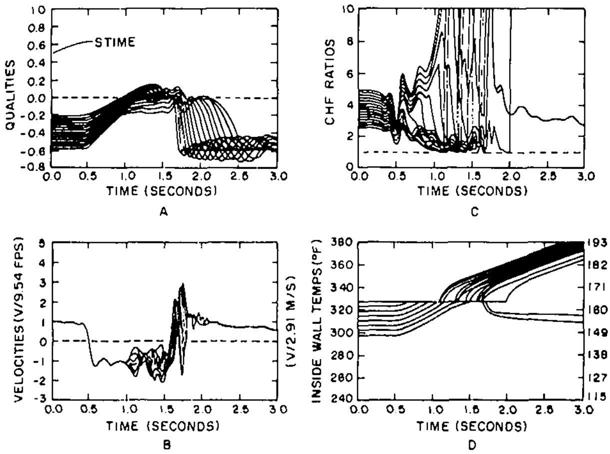

Fig. 8 Details of the BACTRAC3 simulation of this run. The quality increases linearly with length until the flow reversal occurs. Before the reversal occurs the bottom trace is for the bottom control volume, the next trace for the second control volume, and so forth up to the top control volume. It is clear that at 1.5 s much of the tube is in the positive quality region. At the second reversal the quality decreases again, generally to a lower value since there is no provision for rewet in the model once CHF has occurred. The CHF ratio drops to 1 (signaling CHF) at about 1 second and then scoots off the top of the page. It never again recovers. The velocity traces follow the quality traces reaching a large value as voids are swept into the upper plenum at about 1.6 s. The temperature-time traces in the lower right take off at CHF, as can be seen, and never recover.

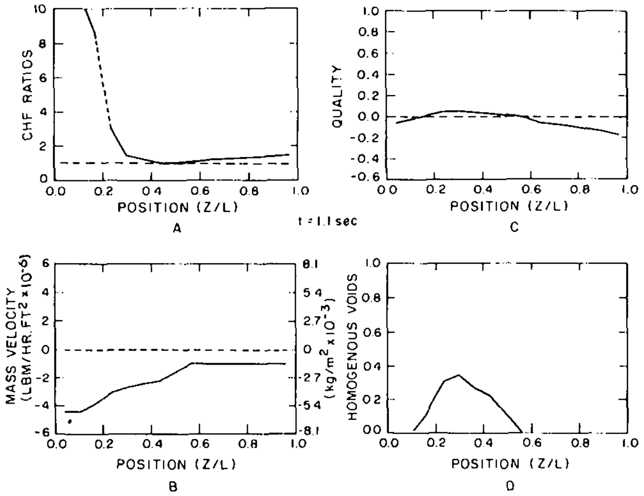

Fig. 9 Details of the CHF ratio, quality, mass velocity and void fraction just before the instant of CHF from the BACTRAC 3 simulation—CHF occurs at the center first for this run

Clearly a rewet would have occurred and the actual wall temperature would have dropped sharply toward the original level. A CHF, therefore, may have occurred as predicted, but the duration of the beyond-CHF condition would have been too short to permit detection by the filtered thermocouple traces.

Detailed output from the simulations were obtained graphically as in Figs. 8 and 9. In each of these plots are displayed the computed quantities for 15 axial stations along the tube length through the duration of the simulation. In this example carrying the simulation for 3 s was sufficient to represent the entire transient of interest.

Fig. 8(*a*) and 8(*b*) are best reviewed together as they portray the behavior of velocities and qualities in the tube. The notion of negative quality was adopted to represent subcooled enthalpies via the relation, $h = h_f + Xh_{fg}$. Fig. 8(*b*) clearly shows the two flow reversals bounding about one second of downflow duration. These velocities were computed via a momentum balance from the input pressure difference across the tube length, and they are here normalized to the initial velocity level. The qualities exhibit the transition from the upflow to the downflow steady profile as in Fig. 2, but notice in Fig. 8(*a*) and 8(*b*) that as positive qualities are developed the coolant velocities become different at the ends of the tube. The efflux of coolant at the bottom is accelerated and the inward flux at the top is decelerated, thus making room for the vapor being generated in the central portion of the tube length. This tendency toward flow stagnation and two-phase expansion was found to be an inherent feature of flow reversal transients in a heated channel as the enthalpy maximum in the central region of the tube length first exceeds the enthalpy of saturated liquid and begins net vapor generation.

Fig. 8(*c*) and 8(*d*) depict the margin to CHF at each station as well as the inside tube wall surface temperature response to CHF when the CHF does occur. Margin to CHF is expressed as the Critical Heat Flux Ratio (CHFR) which is

$$\text{CHFR} = (q/A)_{\text{CHF}}/(q/A)_{\text{ACTUAL}}$$

where $(q/A)_{\text{CHF}}$ is determined for the existing local instantaneous fluid conditions by the CHF criteria of Section 3.1. Of course no CHF is predicted to occur as long as CHFR > 1.0. The critical value CHFR = 1.0 is dotted in Fig. 8(*c*) which clearly shows the minimum CHFR as a function of time in the transient. When CHF occurred at a particular axial station the computer plotter terminated that trace in Fig. 8(*c*) with a vertical line.

Fig. 8(*b*) and 8(*d*) show that shortly after the two-phase expansion process began the CHF condition first occurred and spread over all but the bottom two axial stations in about 1 s.

Fig. 9 shows the conditions in the tube just prior to the first occurrence of CHF. Fig. 9(*c*) shows that the peak quality in the center of the tube has crossed over into the realm of positive qualities, leading to an expanding void fraction as depicted in Fig. 9(*d*). That this void is expanding is confirmed by the mass flux into the tube at the top being less than the mass flux out at the bottom as shown in Fig. 9(*b*). Fig. 9(*a*) shows that the minimum CHFR occurs in the central voided region, and it also shows an unusually large CHFR at the botton end of the tube. This is due to the tube wall being suddenly washed with warmer fluid in downflow from above and the resultant very low heat fluxes into the coolant from the wall.

4.2 **Summary of Data Comparison.** The proof-test selected for the model was the ability to predict the minimum CHF boundary curves of CHF versus τ_d for the experiments as was depicted in Fig. 3. Recall that each point along the minimum CHF boundary curve represents a series of tests at successively higher power levels each having the same initial exit conditions and the same τ_d. To permit such a comparison Price reran and recorded two such series for τ_d = 1 s and τ_d = 5 s, respectively. A total of seven fully documented transients were involved, and all nominally began with the initial steady state conditions of:

$$P_0 = 200 \text{ psia } (1.38 \text{ MPa})$$

$$G = 2.5 \times 10^6 \text{ lbm/hr-ft}^2 \ (3390 \text{ kg/m}^2\text{s})$$

$$X_0 = -0.15$$

Since the minimum CHF occurred briefly at the top end of the tube as the voids were swept out following the second flow reversal, the question was focused on predicted versus experimentally detected occurrence of CHF at the top thermocouple location.

Fig. 3 presents the results of both of the test series on the CHF versus τ_d coordinates. Each of the numbered symbols represents the results of a simulation like that reviewed in the previous section. The two unnumbered non-CHF points represent simulations using plena pressures forcing functions from Runs 1 and 5, respectively, but with the reduced heat flux values indicated. A study of Fig. 3 reveals that for the τ_d = 1 s series the analytical model agrees with the more sensitive thermal paint indication of the level of minimum CHF. The filtered signals from the directly attached thermocouple agreed with the unfiltered indications from the mica chip insulated thermocouple. For the $\tau_d = 5$ s series the minimum CHF was predicted to be somewhat lower than any of the experimental indications. This may have been due to failure of paint and thermocouples to detect the most fleeting CHF's. On balance it is concluded that the model quite adequately represents the level of minimum CHF in the transients. For the four documented transients that yielded both measured and predicted CHF's the time of CHF at the top thermocouple was predicted within 0.25 s of the experimental indications. The tube wall heat-up transients at the tube bottom obscured the time of CHF in the lower wall thermocouple traces. Good agreement was obtained at the tube bottom, however, on the level or occurrence of CHF except for two very short duration CHF transients—one of which was discussed here in Fig. 7.

5 Conclusions

Flow reversal transients are of particular interest in the Critical Heat Flux technology because (1) in passing through zero flow the channel experiences conditions that are difficult to represent in steady-state experiments, and (2) flow reversals in a heated channel lead to an enthalpy maximum in the interior of the channel. This can lead to fluid expulsion and rapid channel voiding upon inception of net vapor generation. Based on the experiments and analyses discussed previously, the following conclusions are drawn:

1 Critical Heat Flux in flow reversal transients can be predicted using steady-state CHF correlations. Previous investigators have demonstrated success with such an approach for other transients, and this study supports extending the validity of this conclusion to transients involving flow reversals and stagnation. Pressure decay transients were not studied here, but there is no a priori reason why these same correlations should not work for them if accurate predictions of transient nonequilibrium local conditions of void fraction and vapor flow rate were available.

2 At low flow and low void fractions the heat flux limited (pool boiling CHF) mechanism governs, and the allowable heat flux under these conditions is far greater than operating reactor heat flux levels. CHF did not occur upon first reduction to zero flow in these experiments nor is it likely to occur under similar flow conditions in a Pressurized Water Reactor large inlet-break Loss of Coolant Accident.

3 Based on the tendency toward fluid expulsion and channel voiding in flow reversal transients it is hypothesized here that the worst Pressurized Water Reactor LOCA break location from the standpoint of time to CHF is one which produces a flow stagnation in the core. For such a case in the Freon experiments computations indicated that even if CHF were delayed the unchecked energy deposition into the coolant would cause 100 percent local channel voiding in less than 1 s. Comparable computations for 1500 psia (10.3 MPa) water with typical reactor full power core average heat fluxes gave channel voiding times between 1 and 2 s. This provides an estimate for an upper limit in the time delay for CHF during which efficient boiling heat transfer may be presumed to persist over large regions of the core. The calculated voiding time for peak heat flux locations was a few tenths of a second. As a basis for interpretation a calculation was made [9] for a typical PWR fuel element operating at a heat flux of 540,000 Btu/hr-ft^2 (1,760,400 W/m^2) which indicated that a 1 s delay in CHF after reactor scram lowers the peak beyond CHF cladding temperature by 200°F (111°C) from that with no CHF delay.

Acknowledgments

Funding for the work reported herein was provided entirely by the Electric Power Research Institute (EPRI) of Palo Alto, California.

References

1 Price, F. A., "Transient Critical Heat Flux During Flow Reversal," SM thesis, Department of Mechanical Engineering, M.I.T., 1975.

2 Ahmad, S. Y., "Fluid to Fluid Modeling of Critical Heat Flux: A Compensated Distortion Model," AECL 3663, 1971.

3 Griffith, Peter, Avedisian, C. T., and Walkush, J. P., "Counter Flow Critical Heat Flux" AIChE Paper No. 25, presented at National Heat Transfer Conference, San Francisco, Aug. 1975.

4 Bowring, R. W., "A Simple But Accurate Round Tube, Uniform Heat Flux Dryout Correlation Over the Pressure Range 0.7–17 MN/m^2 (100–2500 psia)," AEEW-R789, 1972.

5 Coeffield, R. D., et al., "A Subcooled DNB Investigation of Freon 113 and Its Similarity to Subcooled Water DNB Data," *Nuclear Engineering and Design II*, 1969, pp. 143–153.

6 Avedisian, C. T., and Griffith, P., "Critical Heat Flux in Countercurrent Flow," Department of Mechanical Engineering, M.I.T. Report No. 80629-84, Feb. 1974.

7 Walkush, J. P., and Griffith, P., "Counterflow Critical Heat Flux Related to Reactor Transient Analysis," EPRI 292-2, Interim Report, Jan. 1975.

8 Zuber, N., "Hydrodynamic Aspects of Boiling Heat Transfer," AEC Report No. AECU-4439, 1959.

9 Smith, R., "Critical Heat Flux in Flow Reversal Transients," ScD thesis, Department of Mechanical Engineering, M.I.T., 1975.

10 Worley, L. C., and Griffith, P., "Downflow Void Fraction, Pressure Drop and Critical Heat Flux," Department of Mechanical Engineering, M.I.T., Report No. 80620-83, 1973.

M. R. Özgü
Homer Research Laboratories,
Bethlehem Steel Corp.,
Bethlehem, Pa.
Assoc. Mem. ASME

J. C. Chen
Professor,
Department of Mechanical Engineering
and Mechanics,
Lehigh University,
Bethlehem, Pa.
Mem. ASME

Local Film Thickness During Transient Voiding of a Liquid-Filled Channel

Using a recently developed method, measurements were obtained of local film thicknesses during transient voiding of a liquid-filled channel. The liquid film remaining on the channel walls was found to vary in thickness over a range of 0.015–0.15 times channel diameter. In a Lagrangian coordinate system, the film thickness at a fixed distance from the head of the void was found to increase with increasing void acceleration. In an Eulerian system, the film thickness at a fixed location on the channel wall was found to decrease with increasing acceleration, when measured at the same time after passage of the head of the void. In all cases, film thickness monotonically decreased with increasing distance from the head of the void. Complete film breakage (dryout) was not observed in these experiments. These experimental measurements of local film thicknesses during transient voiding conditions are pertinent to thermal analyses for reactor safety studies.

Introduction

A subject of major concern for the safety of nuclear reactors is coolant expulsion in the reactor core in the event of either flow reduction or power excursion. It has been established that coolant expulsion is caused by accelerating growth of a single vapor or gas bubble in the coolant channel. It is also known that a thin liquid film is left on the walls of the coolant channel during the expulsion process [1–4].[1] The existence of this residual film is particularly significant for two main reasons. First, due to the large vapor-liquid interface of the film, additional vapor generation and, hence, the void growth rate is governed by evaporation from this residual liquid film. Second, evaporation of the film provides a cooling mechanism for the channel walls (fuel elements). Hence, the presence of this residual liquid film directly affects possible excess overheating of fuel elements. The lifetime of this residual film, which is a function of its thickness, is therefore of paramount importance.

The physics of steady-state voiding and film deposition is fairly well understood [5–10]. However, only limited information is available on the more realistic case of transient voiding where phase velocities vary with time. Kottowski [11] attempted to measure residual film thicknesses using a forced convection loop operating with potassium and sodium as the test fluids. Film thicknesses were estimated from measured times required to reach dry-out. Transient and local details could not be obtained from these experiments. Fauske, Grolmes, and Ford [12–14], studied vapor growth in freon- and water-filled tubes. By photographic observations of the movement of the bubble and of the free liquid interface above the liquid slug, they estimated residual film thickness by mass balance, assuming no liquid drainage. Again, local variations of the film with position along the channel were not reported. In a second study, Kottowski [15] did obtain measurements of the local film thickness for gas void growth in liquid-metal filled pipes. Film thicknesses were reported for different pipe diameters, expulsion velocities, and accelerations.

The objective of this investigation was to obtain direct measurement of film thicknesses during transient voiding. In particular it was desired to obtain data on the time varying local film thicknesses for various voiding velocities and accelerations.

Theoretical Considerations

With the notation shown in Fig. 1, the dynamic voiding process can be expressed in terms of the following integral momentum equation for the indicated control volume:

$$\int_v \frac{\partial}{\partial t}(\rho_L V_L)dv + \int_\sigma V_f \rho_L V_f \cdot n d\sigma = \Sigma F \quad (1)$$

where, if shear is neglected

$$\Sigma F \simeq (p - p_{\text{atm}})A - \rho_L A L g \quad (2)$$

Equation (1) can be solved analytically for the following two special cases:

(*a*) **Plug flow; $\delta = 0$.** For this case,

---

[1] Numbers in brackets designate References at end of paper.

Contributed by the Heat Transfer Division and presented at the Winter Annual Meeting, Houston, Texas, November 30–December 5, 1975, of THE AMERICAN SOCIETY OF MECHANICAL ENGINEERS. Revised manuscript received by the Heat Transfer Division March 15, 1976. Paper No. 75-WA/HT-27.

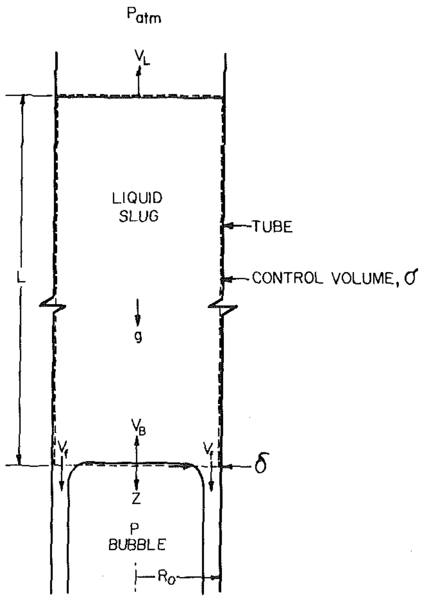

Fig. 1 Schematic of bubble and liquid slug

$$\int_\sigma V_f \rho_L V_f \cdot n d\sigma = 0, \qquad V_L = V_B$$

The solution is

$$\frac{\partial V_L}{\partial t} = \frac{(p - p_{\text{atm}})}{L\rho_L} - g \tag{3}$$

(*b*) **Steady state; Taylor bubble; $\delta \neq 0$.** The classical potential flow solution for this case [6] is

$$V_B = 0.464\sqrt{gR_0} \tag{4}$$

The equation for the associated film thickness is

$$\frac{\delta}{R_0} - \frac{1}{2}\left(\frac{\delta}{R_0}\right)^2 = 0.165\left(\frac{z}{R_0}\right)^{-1/2} \tag{5}$$

Equation (5) gives accurate δ values only for $z/R_0 < 1.0$. For $1.0 \leq z/R_0 \leq 10.0$ the results of equation (5) must be multiplied by 1.5 to get correct film thicknesses [17].

For the general case of transient voiding with finite film around the void, the momentum flow out of the control volume associated with the film is

$$M = \int_\sigma V_f \rho_L V_f \cdot n d\sigma = \int_{r=R_0-\delta}^{R_0} 2\pi r V_f^2 \rho_L dr \neq 0$$

Thus, knowledge of both the film thickness δ and flow velocity V_f within the film is required to solve for the transient voiding dynamics. To the authors' knowledge this information is not currently available. The experimental results presented in this study represent a first step toward the solution of this general problem.

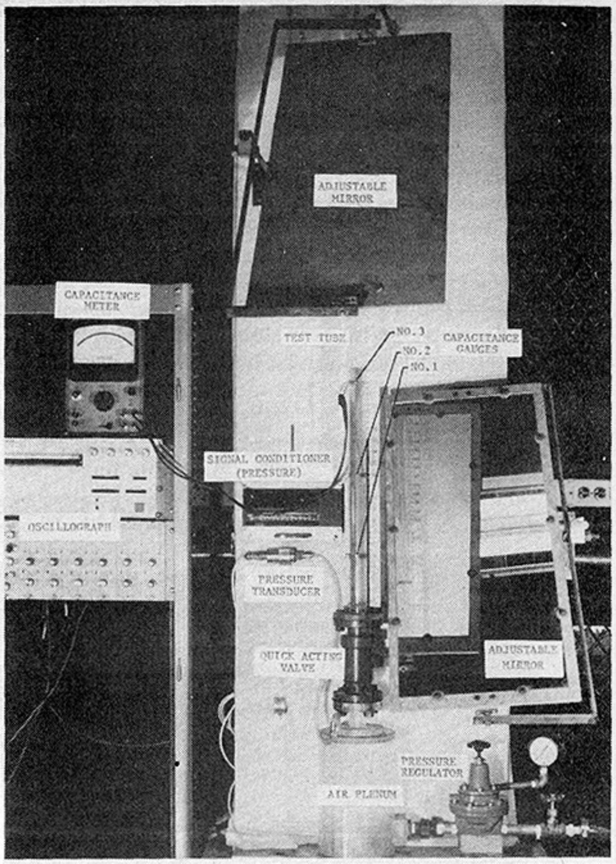

Fig. 2 Experimental facility

Experimental Program

The experiments were carried out in a 2.54 cm ID × 135 cm long acrylic tube. The facility, as shown in Fig. 2, consisted of an air supply line, pressure regulator, air plenum, and the test section. Adjustable mirrors were positioned to aid in the photographic recording of the expulsion phenomenon. Fig. 3 shows details of the test section, which was mounted vertically above the air plenum. A quick-acting valve separated the test section from the air plenum as indicated. The test section was equipped with four capacitance gages mounted at the elevations indicated in Fig. 3. These gages utilized a newly developed

Nomenclature

A = pipe cross-sectional area
a = bubble acceleration
D_i = test tube diameter
g = gravitational acceleration
L = liquid slug height
M = momentum flow out of liquid slug
n = unit vector along normal to surface
p = air plenum pressure
p_{atm} = atmospheric pressure
Δp_i = net initial bubble driving head, = $p - p_{\text{atm}}$ − [initial liquid head]
R_0 = test tube radius
t = time after start of transient
t_1 = time when bubble nose reaches capacitance gage No. 1
$t^* = t - t_1$
V_1 = velocity of bubble nose when at station No. 1
V_B = bubble velocity
V_f = flow velocity within film
V_L = liquid slug velocity
X_B = distance between bubble nose and valve seat
X_w = water free surface displacement
X_1, X_2, X_3 = distance between bubble nose and capacitance gages No. 1, 2, and 3, respectively
z = axial position below bubble nose
δ = local film thickness
δ_{avg} = average film thickness
ρ_L = liquid density
σ = control volume surface
υ = volume

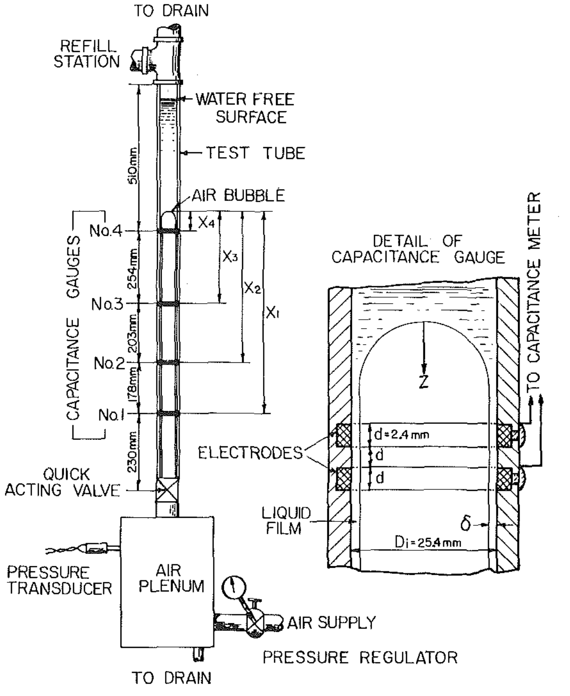

Fig. 3 Details of test tube and capacitance gage

technique for measurement of local film thicknesses [16]. Signals from the gages were measured by a 1 MHz capacitance bridge and recorded on a fast response oscillograph.

In the experiments, the test section was filled with colored water to a height of 63.5 cm above the seat of the quick acting valve, prior to each run. The pressure in the air plenum was then adjusted to a selected value. This plenum pressure was continuously measured and recorded. The voiding transient was then initiated by completely opening the quick-acting valve connecting the test tube to the air plenum. A 16 mm camera, operated at 64 frames per s, was used to record the growth of the air void and the associated liquid expulsion. The exit of the test tube was kept at atmospheric pressure in all tests.

By selection of the air pressure in the plenum (above atmospheric pressure) various expulsion velocities and accelerations were obtained. Four different expulsion cases, corresponding to plenum gage pressures of 8.5, 10.3, 13.7, and 20.6 kPa, were investigated. This resulted in velocities and accelerations up to 6 m/s and 8 g's, respectively. The conditions of these four expulsion cases are summarized in Table 1.

Film thickness measurements were obtained at each of the three lower capacitance stations throughout the expulsion history for each of the four test cases. A typical oscillograph record of the capacitance gage signal is shown in Fig. 4. The signal gives a clear indication of the passage of the expanding bubble and permits direct measurement of the residual film thickness on the channel wall.

Results and Discussion

(a) Voiding Dynamics. As noted previously, four different cases with various air plenum pressures were investigated. In each case the plenum pressure was set at some value greater than atmospheric pressure plus the static head of the initial liquid column. This pressure excess, providing the driving head for bubble growth and liquid expulsion, was Δp_i = 2.2, 3.9, 7.4, and 14.2 kPa, for the four cases. It should be noted that the net driving head increases from these initial values in the course of each expulsion due to decreasing liquid column length as liquid is left behind in the form of a residual film on the channel wall around the expanding bubble. It is this increase in net driving head that causes increased acceleration in the flow as expulsion progresses.

Fig. 5 shows the displacement of bubble interface (bubble head) with increasing time for each of the four cases. The displacement distance, normalized with respect to the tube radius, was measured from the valve seat, as obtained from movie records. Times were measured from the instant of initial fluid movement. As expected, the results in Fig. 5 show that increasing initial driving head (Δp_i) resulted in faster interface movement, i.e., faster expulsion. The curves shown in Fig. 5 represent polynomial fits to the displacement data. The bars indicate the reproducibility as found in several repeated runs. The time varying velocities and accelerations for each case were obtained from the first and second derivatives of these curves, respectively. Fig. 6 shows similar data for the displacement of the liquid column free surface for each corresponding case. Again, the curves represent polynomial fits to the displacement data.

Figs. 7 and 8 show the variations in bubble interface velocity and acceleration with time for each of the four cases. In these two figures time was measured from the instant when the bubble interface reached the lowest film thickness measuring station. For each case this instant of time (t_1) is indicated on Fig. 5. The solid curves represent the experimentally determined velocities and accelerations. For comparison the corresponding velocities and accelerations predicted by the plug flow approximation (equation (3)) are shown by the dashed curves. It is obvious that the plug flow approximation is inadequate, indicating that film effects are significant. It is seen from Fig. 7 that the experimentally determined velocity of the bubble in-

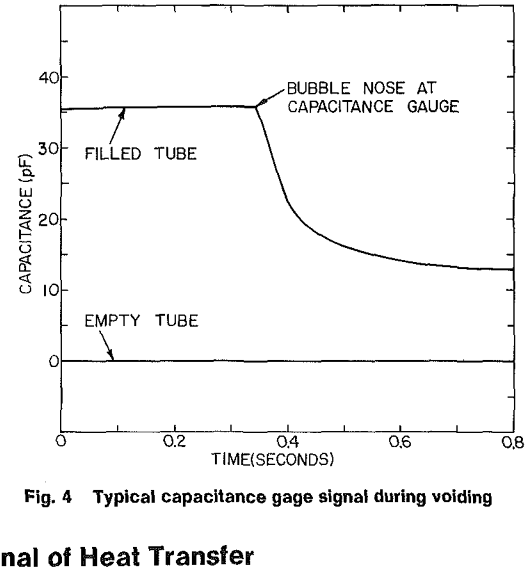

Fig. 4 Typical capacitance gage signal during voiding

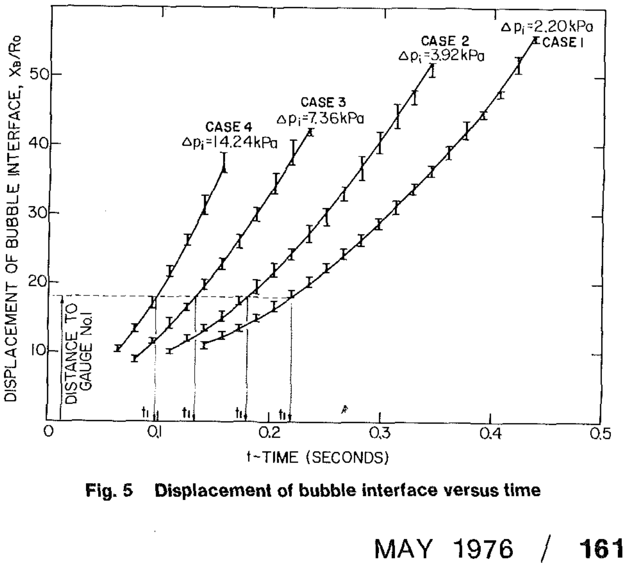

Fig. 5 Displacement of bubble interface versus time

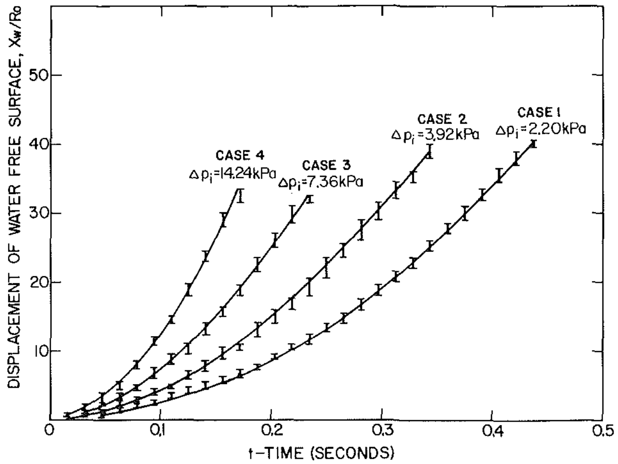

Fig. 6 Displacement of water free surface versus time

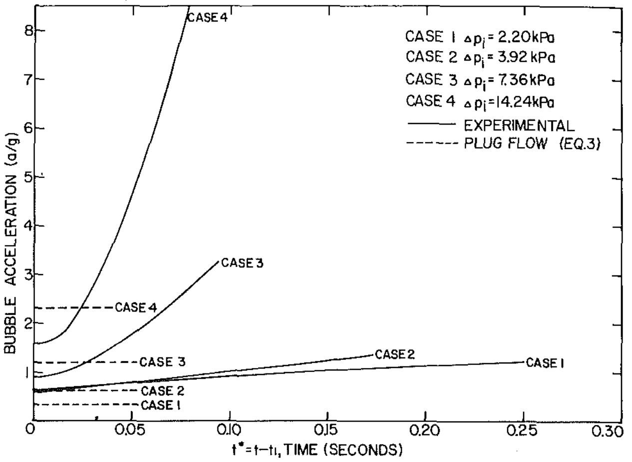

Fig. 8 Bubble acceleration versus time

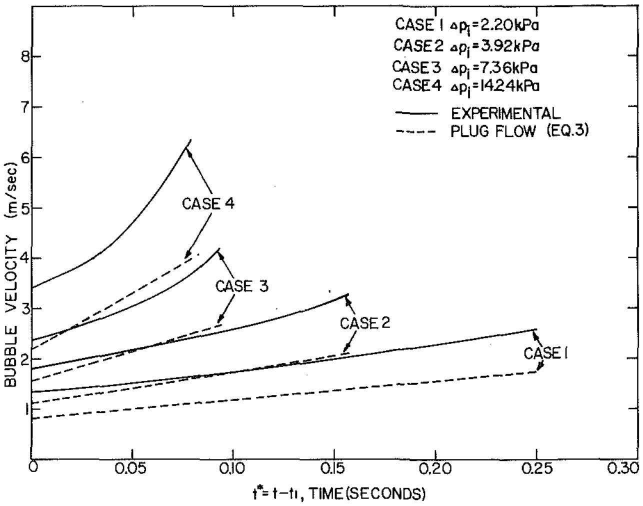

Fig. 7 Bubble velocity versus time

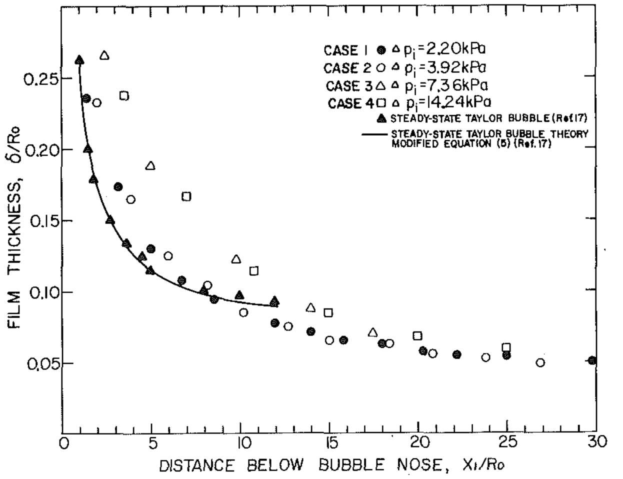

Fig. 9 Film thickness measured at station No. 1 versus distance X_1 below bubble nose

terface increased with time for all four cases. As noted previously, this was caused by the increasing net driving head as expulsion progressed. As is seen in Fig. 8, the actual acceleration obtained in each case was positive and increased with increasing time.

(b) Film Thicknesses. The film thickness results are presented subsequently in the Eulerian and Lagrangian frames of reference in order to aid interpretation of the complex interaction of velocity and acceleration effects. A misleading impression may be obtained by careless examination of just one frame of reference. For example, as pointed out later, film thickness appears to increase with increasing expulsion rate in the Lagrangian system, whereas in the Eulerian system film thickness appears to decrease with increasing expulsion rate.

The film thicknesses measured at the three capacitance gage stations are shown in Figs. 9–11. Axial locations of the three stations are indicated in Fig. 3. The data in these figures represent the Eulerian record obtained at a specific probe station as the bubble head passes the probe and proceeds downstream away from the station. Thus, for each case, the film thickness is plotted as a function of distance below the bubble nose, X_1, X_2, X_3, corresponding to measurements obtained at the three stations. The precision of the film thickness measurements was estimated to be approximately 0.05 mm in the range of measurements made, corresponding to 8 percent of the minimum film thickness. The results indicated in these figures clearly show that the liquid film deposited on the channel wall does not remain static, since the local film thickness changes as the expulsion progresses. While it is obvious that net flow must have occurred in the residual liquid film, these data alone do not indicate whether net flow occurs downward due to gravitational drainage or upward due to air drag. It should be noted, however, that for all cases the film measured at all three probe stations underwent continued thinning as the expulsion progressed, reaching asymptotic value at $X/R_0 > 30.0$. Since these tests were carried out under adiabatic conditions this film thinning cannot be attributed to liquid evaporation.

In Figs. 9–11 experimental results and the corresponding theoretical equation from [17] for the steady-state case of Taylor bubbles are also plotted for comparison. Comparing the different cases, the local film thickness at a given distance below the bubble nose is seen to increase consistently with increasing expulsion velocity and acceleration. At sufficiently large distances below the head of the bubble, the liquid film thickness becomes essentially independent of expulsion velocity and acceleration. This behavior was observed at all three probe stations.

Fig. 12 presents a composite of the film thickness data collected at all three probe stations, for two expulsion cases. In this figure each curve represents the film thickness at a fixed distance (z) from the head of the bubble and moving with the bubble (Lagrangian system). These film thicknesses are plotted as a function of instantaneous

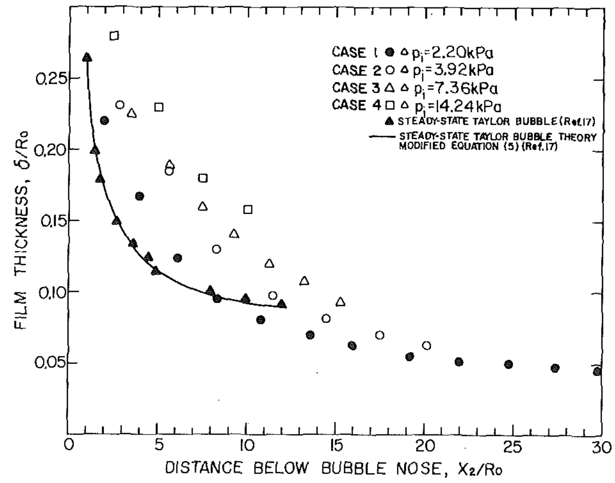

Fig. 10 Film thickness measured at station No. 2 versus distance X_2 below bubble nose

bubble velocity. Three points should be noted from these results. First, the film thickness at a given distance from the bubble nose increased with increasing bubble velocity. This behavior was found for all distances z, for both cases. Second, comparing the results of the two cases one finds differences in the thickness at the same distance z and the same instantaneous velocity. This indicates that local film thickness, at least in regions close to the head of the bubble, is dependent on the expulsion history and is not a function of velocity alone. Third, comparing film thicknesses at different z/R_0 for any given bubble velocity, a consistent trend is noted. In all cases film thickness δ/R_0 decreased with increasing z/R_0. This is consistent with the conclusions discussed for Figs. 9–11.

Fig. 13 also plots the film thicknesses observed in a Lagrangian system for the same two cases. Here the local film thicknesses are plotted as a function of instantaneous acceleration. Similar observations are made. For a given distance z, the film thickness increased with increasing acceleration for both cases. Again, the film thickness was evidently governed by expulsion history and was not dependent only on the instantaneous acceleration. Also, δ/R_0 decreased with increasing z/R_0 for any given acceleration.

The information in these two figures (12 and 13) are of the same nature as that presented by Kottowski in [15]. Similar effect of velocity on film thickness was reported. Kottowski, however, reported film thickness to decrease with increasing acceleration. This difference in behavior is undoubtedly caused by the interacting effects of velocity and acceleration. As noted previously, the film thickness is dependent on the expulsion history and is not a function of either instantaneous velocity or acceleration alone.

Fig. 14 presents the film thickness in an Eulerian frame of reference as observed at a fixed location on the channel (at the lowest probe station). This local film thickness is plotted as a function of time for the four different expulsion cases. Each curve represents one expulsion case and indicates that the thickness continuously decreased as time increased. These results strongly indicate that the neglect of drainage in the residual film could result in substantial error in film thickness estimates, until asymptotic film thickness is attained, as discussed subsequently. Comparing the results for the various cases it is seen that the local film thickness in this Eulerian frame of reference, at a given time t^*, decreased with increasing expulsion rate. While the differences are not overly large, there is certainly significant difference between the slowest and fastest voiding cases. Furthermore, the curves show a consistent trend with increasing voiding rate.

The results in Figs. 9–11 and 14 all indicate that δ/R_0 approaches an asymptotic value at large distances ($X/R_0 > 30.0$) below the head of the bubble. This asymptotic value of δ/R_0 appears to be 0.05, as measured at both stations 1 and 2. The data obtained at station 3 did

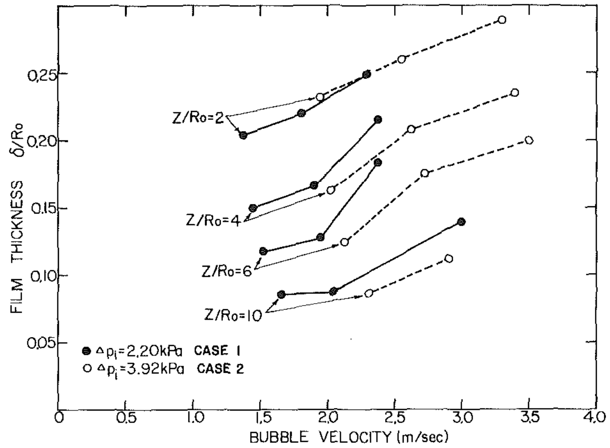

Fig. 12 Film thickness versus bubble velocity at fixed distances below bubble nose

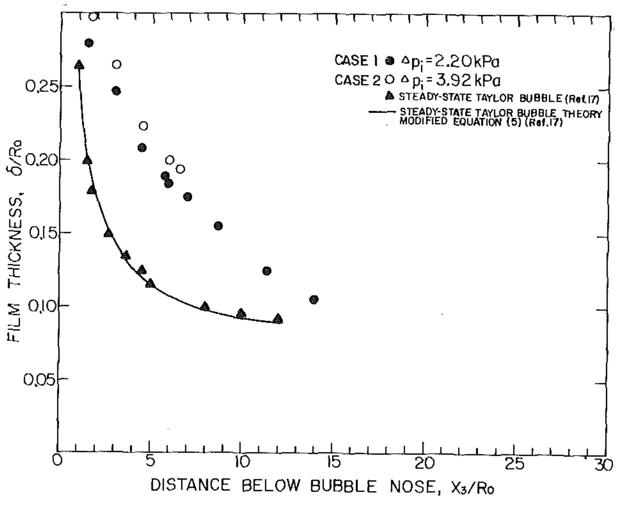

Fig. 11 Film thickness measured at station No. 3 versus distance X_3 below bubble nose

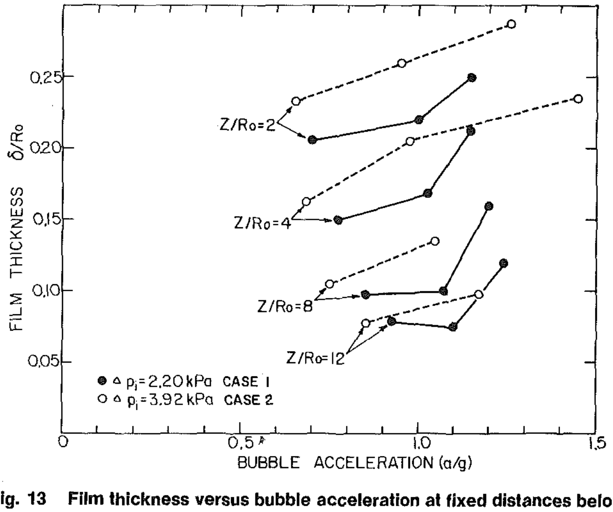

Fig. 13 Film thickness versus bubble acceleration at fixed distances below bubble nose

not extend to sufficiently large X_3/R_0 values to indicate this asymptotic film thickness. However, extrapolation of the data in Fig. 11 would seem to confirm this value. Thus, these results imply that transient single bubble expulsion results in an asymptotic void fraction of 0.90 for the expulsion rates encountered in this study. In the asymptotic region $X/R_0 > 30.0$, where film thickness remains constant with time, the assumption of zero net drainage in the film would be valid. For this region, the expression derived by Ford, et al. [12–14] for the film thickness should be valid:

$$\delta/R_0 = \frac{1}{2}[1 - V_L/V_B]$$

Fig. 15 shows the measured velocity ratio V_L/V_B as a function of time, for the four expulsion cases. These data indicate an asymptotic value of 0.905 for V_L/V_B in all expulsion cases. The resulting asymptotic film thickness (δ/R_0) obtained from the equation given then is 0.048. This is in good agreement with the value of 0.05 discussed previously from direct film thickness measurements. Thus, consistency between the independent measurements by photography and by capacitance gage is indicated. For comparison, the results of Ford, et al. [12–14] indicate a film thickness of $\delta/R_0 = 0.075$. No discrimination between asymptotic, local, or average thickness was made in [12–14].

Fig. 16 illustrates the variation of the average film thickness with time for the four expulsion cases. Through mass balance, average film thickness can be determined in terms of bubble and liquid displacements as

$$\delta_{avg}/R_0 = \frac{1}{2}\frac{X_B - X_w}{X_B}$$

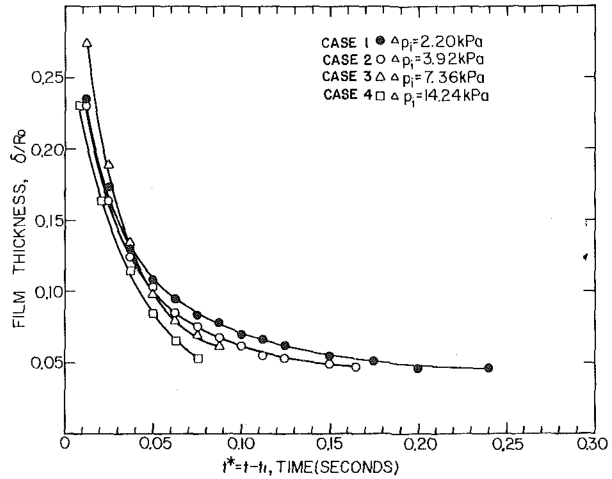

Fig. 14 Film thickness measured at station No. 1 versus time

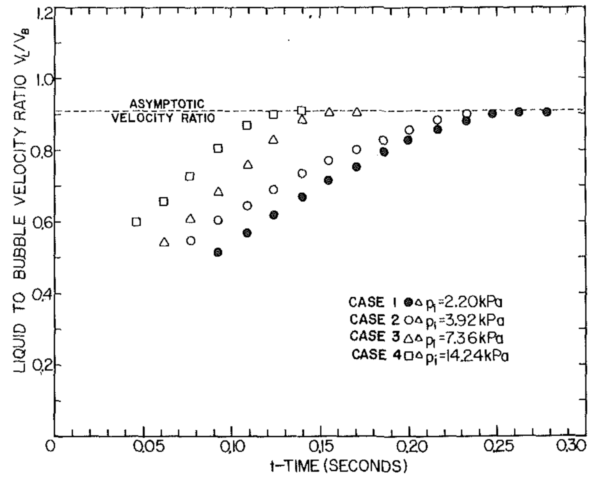

Fig. 15 Liquid to bubble velocity ratio versus time

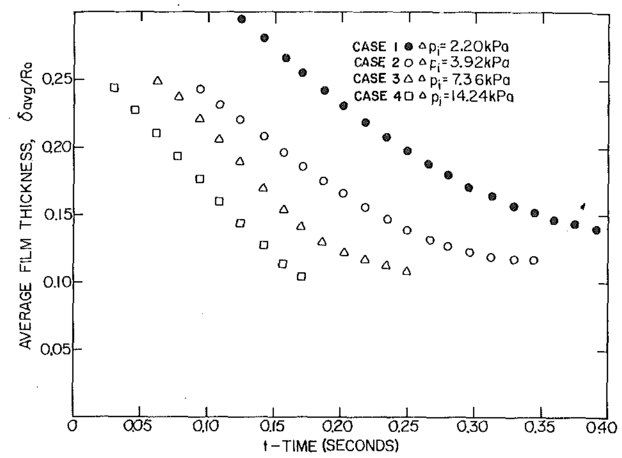

Fig. 16 Average film thickness over bubble length versus time

As is seen in the figure, in all four cases the average film thickness continuously decreased as expulsion progressed. Also, the rate of decrease of the average film thickness increased as the expulsion rate increased, i.e., as Δp_i increased. Similar behavior of average film thickness has been reported by Ford [12].

In attempting to relate these results to those reported by other investigators no comparable cases were found. Kottowski's [15] results were obtained in or close to the capillary flow regime, whereas in this study due to larger pipe diameter capillary effects were negligibly small. Maneri and Zuber [18] investigated the shape of bubbles rising in restricted media. Their experiments dealt with the steady-state rise of bubbles whose characteristic dimension was small compared with the duct. The present study dealt with accelerating rise of bubbles which occupied almost the entire duct cross section. Hence, the concept of film thickness is appropriate for this situation and meaningless for the problem considered by Maneri and Zuber.

Conclusions

The following conclusions can be drawn from this study, for transient voiding under the conditions tested.

A For nose and near regions ($X/R_0 \leq 30.0$):

1 For all expulsion cases, film thickness at fixed locations on the channel wall decreases as expulsion progresses. This implies that substantial flow occurs in the liquid film.

2 At equal distances below the bubble nose on the channel wall film thickness increases as the expulsion rate increases.

3 Film thickness at a fixed location on the channel wall decreases

Table 1 Experimental voiding cases

Case	Symbol	Plenum pressure^a	Δp_i^{b}	V_1^{c}	a_1/g^{d}
1	●	8.5 kPa	2.2 kPa	1.33 m/s	0.675
2	○	10.3 kPa	3.9 kPa	1.875 m/s	0.625
3	△	13.7 kPa	7.4 kPa	2.425 m/s	0.875
4	□	20.6 kPa	14.2 kPa	3.45 m/s	1.60

^{a}Plenum pressure above atmospheric
^{b}Δp_i = net driving head = (plenum pressure) − (initial liquid head)
^{c}Velocity of bubble nose when passing station No. 1
^{d}Acceleration of bubble nose when passing station No. 1

as time increases. The rate of change increases as the expulsion rate increases.

4 At fixed distances below the bubble nose and moving with the bubble (Lagrangian system) film thickness increases as the bubble velocity and acceleration increase.

5 Film thickness is dependent on expulsion history.

6 Average film thickness decreases as time progresses. The rate of change increases as expulsion rate increases.

B For asymptotic region ($X/R_0 > 30.0$):

1 Film thickness approaches a constant asymptotic value of $\delta/R_0 = 0.05$.

2 This asymptotic value is independent of voiding acceleration and velocity.

Acknowledgments

The authors wish to express their appreciation to Prof. Eppes, Dr. T. Özkaynak, and Mr. C. Dodge of Lehigh University for their assistance and recommendations during this study. Special thanks are extended to Messrs. J. Blackwood and D. Bright of Homer Research Labs for their help in data reduction.

References

1 LMFBR Program Plan,wash 1110, USAEC, Vol. 10—safety, 1968.

2 "Safety Problems of Liquid-Metal Cooled Fast Breeder Reactors," ANL 7657, 1970.

3 Peppler, W., et al., "Sodium Boiling and Fast Reactor Safety," Proceedings of the International Conference on the Safety of Fast Reactors, Aix-en-Provence, France, Sept. 19–22, 1968.

4 Spiller, K. H., Grass, G., and Perschke, D., "Superheating and Single Bubble Ejection in the Vaporization of Stagnating Liquid Metals," *Atomkernenergie*, Vol. 12, No. 3/4, 1967, pp. 111–114.

5 Dumitrescu, D. T., "Flow Past an Air Bubble in a Vertical Pipe," *Zeitschrift fuer Angewandte Mathematek und Mechanik*, Vol. 23, 1943, pp. 139–148.

6 Davies, R. M., and Taylor, G. I., "The Mechanics of Large Bubbles Rising Through Extended Liquids and Through Liquids in Tubes," *Proceedings of the Royal Society, London*, Vol. 200, Series A, 1950, pp. 375–390.

7 Griffith, P., and Wallis, G. B., "Two-Phase Slug Flow," JOURNAL OF HEAT TRANSFER, TRANS. ASME, Series C, Vol. 83, No. 3, Aug. 1961, pp. 307–320.

8 Moissis, R., and Griffith, P., "Entrance Effects in a Two-Phase Slug Flow," JOURNAL OF HEAT TRANSFER, TRANS. ASME, Series C, Vol. 84, No. 1, Feb. 1962, pp. 29–39.

9 Brown, R. A. S., "The Mechanics of Large Gas Bubbles in Tubes. I. Bubble Velocities in Stagnant Liquids," *Canadian Journal of Chemical Engineering*, Vol. 43, Oct. 1965, pp. 217–223.

10 Nicklin, D. J., Wilkes, J. O., and Davidson, J. F., "Two-Phase Flow in Vertical Tubes," *Transactions of the Institute of Chemical Engineers*, Vol. 40, 1962, pp. 61–68.

11 Kottowski, Von H., "Über die Ausbildung einer Restschicht beim Sieden von Alkalimetallen in Kanälen," *Atomkernenergie* (ATKE), Bd. 15, Lfg. 2, 1970, pp. 131–137.

12 Ford, W. D., "Bubble Growth and Collapse in Narrow Tubes With Nonuniform Initial Temperature Profiles," ANL-7746, 1970.

13 Fauske, H. K., Ford, W. D., and Grolmes, M. A., "Liquid Film Thickness for Slug Expulsion," *Trans. ANS*, Vol. 13, No. 1, 1970, p. 646.

14 Grolmes, M. A., Lambert, G. A., and Fauske, H. K., "Liquid Film Thickness for Single-Bubble Slug Ejection," *Trans. ANS*, Vol. 14, No. 1, 1971, pp. 242–243.

15 Kottowski, H. M., et al., "Measurement of the Liquid Metal Residual Film Left Behind Coolant Expulsion in Narrow Channels," *Proc. of Fast Reactor Safety Meeting*, Los Angeles, Conf-740401-P3, 1974, pp. 1173–1184.

16 Özgü, M. R., Chen, J. C., and Eberhardt, N., "A Capacitance Method for Measurement of Film Thickness in Two-Phase Flow," *Review of Scientific Instruments*, Vol. 44, No. 12, Dec. 1973, pp. 1714–1716.

17 Özgü, M. R., Chen, J. C., and Stenning, A. H., "Local Liquid Film Thickness Around Taylor Bubbles," JOURNAL OF HEAT TRANSFER, TRANS. ASME, Series C, Vol. 95, No. 3, Aug. 1973, pp. 425–427.

18 Maneri, C. C., and Zuber, N., "An Experimental Study of Plane Bubbles Rising at Inclination," *International Journal of Multiphase Flow*, Vol. 1, No. 5, Pergamon Press, 1974, pp. 623–645.

G. Hesse[1]
E. M. Sparrow
R. J. Goldstein

Department of Mechanical Engineering,
University of Minnesota,
Minneapolis, Minn.

Influence of Pressure on Film Boiling Heat Transfer

Experiments on film boiling of carbon dioxide were performed covering the range of pressures from the triple point to the critical point. Measurements were also made at supercritical pressures. Three different heating wire sizes were employed with diameters of 0.0508, 0.1, and 0.4 mm. The boiling curves, plotted in terms of heat flux and temperature difference, were found to be pressure dependent, with a more marked dependence for smaller diameter heating wires. The role of pressure level was exhibited in greater detail in a presentation in which the heat transfer coefficient is plotted against pressure at fixed values of heat flux. The most rapid variations of the heat transfer coefficient with pressure occur in the neighborhoods of the triple and critical points, with relatively gradual variations in evidence in the intermediate range of pressures. The curves of heat transfer coefficient versus pressure take on minimum values at the triple and critical points. Nusselt numbers evaluated from the experimental data agree satisfactorily with available predictive equations. Photographs of the vapor separation patterns revealed that with increasing pressure, the bubble columns which break away from the vapor film successively evolve into vapor columns and vapor sheets. As the critical pressure is approached, the height of the sheet diminishes.

Introduction

Although there is an extensive experimental literature dealing with film boiling, the influence of the pressure level on the heat transfer coefficient has not been established with certainty. The apparently conflicting trends that have sometimes been reported (for example, [1-3][2]) are due, at least in part, to differences in the range of pressures investigated, in the working fluid, and in the size of the heating wire. Another factor which contributes to the complexity of the pressure effect is that the fluid properties respond to pressure variation with different degrees of sensitivity depending on the pressure level.

The present experiments were undertaken to help clarify the effect of pressure level on film boiling heat transfer coefficients. The experiments were performed for saturation boiling on thin horizontal heated wires, with carbon dioxide as the working fluid. The pressure was varied over the entire range that is possible for a boiling liquid, that is, from the triple point to the critical point. Within the knowledge of the authors, these are the first experiments where the entire triple point—critical point range has been studied. Three heating wires were employed, with diameters of 0.4, 0.1, and 0.0508 mm. The heat flux was also varied as an independent parameter.

In the presentation of results, the influence of the pressure level on both the heat flux and the heat transfer coefficient are examined. In addition, photographs are presented to show how the pattern of vapor departure from the heated wire evolves as the pressure level is systematically varied. Nusselt numbers evaluated from the present measurements are compared with correlation equations from the literature in order to test the generality of the correlations.

Experimental Apparatus

The experiments were performed with an apparatus which was an adaptation of that employed in [4]. The description of the apparatus will, therefore, be limited to a broad overview, but with a more detailed discussion of those aspects which are specific to the present research.

A schematic diagram showing the main components of the test

---

[1] Present address: GEA Luftkühlergesellschaft, Bochum, Germany.

[2] Numbers in brackets designate References at end of paper.

Contributed by the Heat Transfer Division for publication in the JOURNAL OF HEAT TRANSFER. Manuscript received by the Heat Transfer Division October 6, 1975. Paper No. 76-HT-GG.

setup is presented in Fig. 1. The experiments were performed in a horizontal cylindrical pressure vessel, 165 mm in internal diameter and 110 mm long. Within the vessel, liquid carbon dioxide was boiled on a heated platinum wire mounted along the horizontal diameter midway between the end faces of the vessel. The pressure vessel itself was fully immersed in a circulating, thermostatically controlled bath which served to maintain constant temperature and, correspondingly, constant pressure during the measurement period. The circulating liquids were water and methanol, respectively, for the higher and lower temperature tests. Windows in the end faces of the pressure vessel enabled visual observations and photography of the vapor separation patterns.

Three different heating wire sizes were employed during the course of the experiments, with diameters of 0.4, 0.1, and 0.0508 mm, respectively. All wires were 110-mm long. The heating was accomplished by passing d-c current from a battery through the wire. To avoid end effects, two 0.0508-mm dia voltage taps were spot welded to the heating wire, 60 mm apart, thereby enabling measurement of the voltage drop in the central portion of the wire. The 60-mm long segment of wire served as the test section.

The temperature of the test section was determined by measuring its electrical resistance. The purity of the platinum was in the range required for precision platinum resistance thermometers. To insure the accuracy of the temperature measurement, the electrical resistance of the test section was carefully determined at 0°C with a Mueller bridge. The resistances of all the wires were measured before the data runs and, for verification, the resistance of one of the wires was remeasured after the runs, with no change being observed.

The 0°C resistances were employed in conjunction with the well-established relation for the relative change of resistance with temperature for pure platinum. Measurements of the test section voltage drop and of the current passing through the heating wire during a data run enabled the test section resistance to be evaluated, from which the temperature followed directly. The aforementioned voltage and current data, used in conjunction with the wire surface area, also gave the test section heat flux.

Other quantities measured during a data run included the pressure of the carbon dioxide vapor and the temperatures of the liquid and vapor carbon dioxide. For the latter, calibrated copper-constantan thermocouples were used. They were, respectively, positioned about 30 mm below the heating wire and 10 mm below the top of the pressure vessel. All electrical measurements were made with the aid of an electronic data acquisition system which required about 4 s to read the temperatures and voltage drops. Ten successive sets of such measurements, recorded over a total time span of about 50 s, were averaged to yield the final data.

Photographs were taken with a camera which viewed the test section through one of the windows while diffuse back lighting of controlled intensity was provided through the other window. A shutter speed of 1 ms was employed along with 35-mm black and white film (ASA 400).

Several additional precautions were taken to ensure the quality of the data. The carbon dioxide used during the experiments had a purity of 99.99 percent. Prior to assembly, all parts of the apparatus that would subsequently be contacted by the test fluid were thoroughly cleaned with acetone. In addition, prior to their calibration, each of the heating wires was annealed at a pressure of one Torr to relieve mechanical stresses and to clean the surface. The pressure vessel was purged two or three times with CO_2 gas before it was filled with the test fluid. The battery voltage was carefully monitored and, if necessary, regulated in order to maintain steady heating conditions for each set of operating parameters.

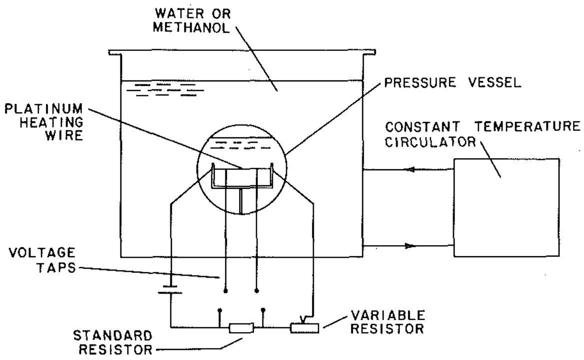

Fig. 1 Schematic diagram of the experimental apparatus

It is interesting to note that during the initial runs, an oil-like substance was observed to have been deposited on the heating wire. It is believed that this substance had dissolved from the neoprene seals (even though neoprene is recommended for CO_2 equipment). When the neoprene seals were replaced by Teflon seals, the oil-like substance no longer appeared.

Operational Observations and Experimental Procedure

Each data run, characterized by a saturation pressure p, was initiated by the establishment of nucleate boiling on the test section. Film boiling was then sought by increasing the heat flux. From preliminary experiments, it was found that the successful attainment of film boiling on the test section depended on the pressure level. The characteristic pressure levels varied slightly among the three heating wire diameters, so that nominal pressure values will be employed during the forthcoming discussion.

At pressure levels $p \geq 0.95p_c$, an increase in heat flux brought about film boiling along the entire length of the heating wire. On the other hand, for $p \leq 0.7p_c$, the initial manifestation of transition resulting from an increase in heat flux was the occurrence of film boiling on only part of the wire, while nucleate boiling continued on the remainder. The film boiling portion of the wire was observed to be glowing red. Further increases in heat flux led to burnout. In the intermediate regime, typified by observations at p

Nomenclature

B = Laplace parameter, $(\sigma/g(\rho_\ell - \rho_v))^{1/2}$
c_p = specific heat at constant pressure
D = diameter of heating wire
Gr = Grashof number, equation (5)
g = acceleration of gravity
h = heat transfer coefficient, $q/(T_w - T_{sat})$
i = enthalpy
i_{fg} = latent heat of vaporization
k = thermal conductivity
Nu = Nusselt number, hD/k_v
Pr = Prandtl number
Pr* = modified Prandtl number, equation (6)
Pr** = modified Prandtl number, equation (7)
p = pressure
p_c = critical pressure
q = heat transfer per unit time and area
Ra = Rayleigh number, GrPr_v
Ra* = modified Rayleigh number, equation (6)
T_w = temperature of heating wire
T_r = temperature ratio, T_{sat}/T_c
T_{sat} = saturation temperature
ΔT = temperature difference, $T_w - T_{sat}$
X,Y = correlation parameters, equation (12)
θ' = correlation parameter, equation (10)
μ = viscosity
ρ = density
σ = surface tension

Subscripts

ℓ = saturated liquid properties
v = vapor properties evaluated at $(T_w + T_{sat})/2$

$= 0.8p_c$, an initial increase in heat flux caused transition to film boiling on part of the wire, but a further increase brought about film boiling on the entire wire.

The foregoing behavior can be understood if account is taken of the character of the q versus ΔT boiling curve at various pressure levels. At pressures close to p_c, both q and ΔT at the point of departure from nucleate boiling (DNB) are relatively small. As the pressure decreases, the DNB values of q and ΔT increase.

With this as background, consider a situation where an initial nucleate boiling regime is brought to the point of DNB by an increase of heat flux and then, owing to a local random fluctuation, film boiling is established on part of the wire. Since electrical resistance increases with temperature, the presence of partial film boiling increases the overall resistance of the wire. If the applied voltage is constant, then the current decreases. Consequently, the heat flux at the nucleate boiling portion of the wire drops below the DNB value.

If the applied voltage is then increased to restore the heat flux in the nucleate boiling region, there will also be an increase of heat flux in the film boiling region. At pressure levels substantially below p_c, the DNB heat flux peak is so high that if the nucleate-boiling region of the wire is restored to the DNB level, the corresponding increase in the heat flux in the film boiling region of the wire causes burnout. On the other hand, at pressure levels near p_c, the relatively low DNB peak necessitates that the heat flux be increased only slightly to restore and to overpass DNB conditions, and thus to establish film boiling on the entire wire.

The findings of the preliminary experiments are, therefore, physically plausible. Their essential message is that at pressures substantially below p_c, pure film boiling cannot be attained by starting from established nucleate boiling and increasing the heat flux at constant pressure. This outcome motivated an exploration of experimental procedures which would enable film boiling data runs to be made in the lower range of pressures.

The procedure which proved to be most successful was as follows. First, film boiling was established on the wire at a pressure slightly below the critical, for instance, at $p = 0.9p_c$. Then, the pressure was decreased in small steps while the heat flux was maintained constant. At each step, sufficient time was allowed for equilibrium to be established before data were collected.

The success of this procedure, as measured by how low a pressure could be attained while maintaining film boiling on the test section, depended both on the wire diameter and on the heat flux level. In general, lower pressures could be reached for larger diameters and at higher heat fluxes. Thus, for example, for the 0.4-mm dia wire (the largest used during these experiments), it was possible to proceed all the way down to the triple-point pressure at both high and intermediate levels of heat flux.

At lower heat flux levels and/or for the smaller diameter wires, the procedure of step-by-step pressure reduction at a fixed heat flux ran into a natural limitation; namely, that for each pressure level and wire diameter, there is a minimum heat flux (Leidenfrost point) below which film boiling cannot exist. Nucleate boiling appeared near the ends of the wire and, with further reductions in pressure, it spread into the test section. As a consequence, the test section was no longer a region of pure film boiling. This behavior obviated further decreases in pressure at the fixed heat flux and, as a consequence, the triple point pressure was not reached at the low heat fluxes or for the smallest diameter heating wire. The pressure level at which step-by-step pressure reductions had to be terminated depended on the wire diameter; the smaller the diameter, the higher the pressure at termination.

When the nucleate boiling was observed to have moved into the test section, it was found that the spread could be arrested and film boiling re-established by increasing the heat flux to a higher level. This was possible because the temperature of the film boiling portion of the wire was well below the melting temperature (i.e., the wire was not glowing red). In this way, it was possible to continue the data collection but at a higher heat flux.

Other initiatives were made in an attempt to obtain data in the lower pressure range for low and intermediate heat fluxes. In one approach, from an established high heat flux—low pressure film boiling state reductions in heat flux are made at fixed pressure. This procedure met with a certain degree of success for the larger heating wires. However, for the smallest heat wire, it was not possible to obtain film boiling data below $p/p_c = 0.7$.

The ranges of pressure and heat flux where film boiling data collection was possible will be displayed later in one of the subsequent figures (i.e., Fig. 3).

Data Reduction

The quantities that are basic to all aspects of the presentation of the experimental results are the test section heat flux q and the temperature difference $(T_w - T_{\text{sat}})$ between the surface of the test section and the saturated liquid environment. The heat flux was evaluated from the product of the measured test section current and voltage drop, divided by the test section surface area. Three corrections for the heat flux were considered: (a) changes in test section dimensions owing to thermal expansion, (b) heat loss by conduction through the voltage taps, and (c) radiative heat transfer from the test section to the liquid environment. Calculations showed that dimension changes and voltage tap conduction (evaluated via one-dimensional fin theory) each affected the heat flux by 1 percent at the very most and, therefore, no corrections were made.

The net radiative flux q_r was found to be as large as 3 percent in some cases, and a subtractive radiation correction was applied to the input power in order to obtain the boiling heat flux. q_r was evaluated from

$$q_r = \epsilon\sigma(T_w{}^4 - T_{\text{sat}}{}^4) \qquad (1)$$

where ϵ is the hemispherical emittance of the platinum wire and σ is the Stefan-Boltzmann constant. Equation (1) is based on a model whereby the liquid environment behaves like a blackbody and the vapor film is radiatively nonparticipating owing to its small thickness. Values of ϵ were taken from [5] in the form of normal emittances and converted to hemispherical emittances. The emittance information was well represented by a straight line passing through the points $\epsilon = 0.071$, $T = 500$ K and $\epsilon = 0.156$, $T = 1000$ K.

The wire temperature was determined from the resistance-temperature relation for pure platinum, which is of the form [6]

$$R(T) = R_0(1 + C_1T + C_2T^2) \qquad (2)$$

where $C_1 = 3.90784 \times 10^{-3}$ and $C_2 = -0.578408 \times 10^{-6}$. The quantity R_0 is the resistance (in ohms) at 0°C, and T is in °C. As was noted earlier, R_0 was measured for all three heating wires. From equation (2), T can easily be expressed as an explicit function of R. With an input value of R deduced from the measured test section current and voltage drop, T is readily evaluated.

The temperature obtained in this way is the average for the cross section. The difference between the surface temperature and the average temperature was calculated via heat conduction theory and found to be negligible. Then, with the thus determined T_w and with the measured temperature T_{sat} of the saturated liquid environment, the difference $\Delta T = (T_w - T_{\text{sat}})$ was found.

The heat transfer coefficient was evaluated from its customary defintion

$$h = q/(T_w - T_{\text{sat}}) \qquad (3)$$

An error analysis for h gave an estimated error of 2–3 percent. For the evaluation of the Nusselt number (and for the Rayleigh number as well), various candidate characteristic lengths have been considered in the literature besides the heater wire diameter. These have included, for example, the Laplace parameter B (defined in the Nomenclature) and the critical wavelength $\lambda_c = 2\pi B$. The use of such characteristic lengths has not led to better data

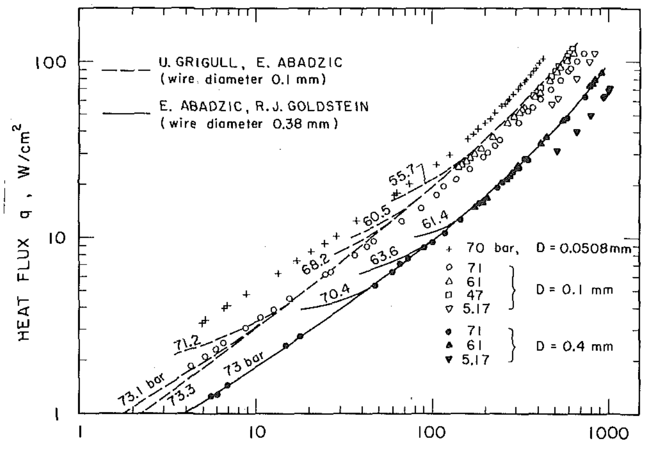

Fig. 2 Heat flux versus temperature film-boiling curve

correlation than is obtained with the heater wire diameter, so that the most recent correlations and syntheses have employed the latter. To facilitate comparison with the most recent literature, Nusselt numbers will be evaluated here via the definition

$$\mathrm{Nu} = hD/k_v \tag{4}$$

The vapor conductivity k_v and all other vapor properties (identified by subscript v) correspond to the film temperature $T_f = (T_w + T_{\mathrm{sat}})/2$.

All of the available correlations contain some sort of Grashof or Rayleigh number. In their basic form, these quantities are defined as

$$\mathrm{Gr} = \rho_v g(\rho_\ell - \rho_v)D^3/\mu_v{}^2, \qquad \mathrm{Ra} = \mathrm{GrPr}_v \tag{5}$$

in which the subscript ℓ refers to the properties of the saturated liquid. Modified Rayleigh numbers and Prandtl numbers have also been employed as correlating parameters. In the Pitschmann and Grigull correlation [1], which will be examined later, use is made of Ra*, where

$$\mathrm{Ra}^* = \mathrm{GrPr}^*, \qquad \mathrm{Pr}^* = ((i_v - i_\ell)/(T_w - T_{\mathrm{sat}}))\mu_v/k_v \tag{6}$$

where i denotes the enthalpy per unit mass. Nishikawa and coworkers [7] employ still another Prandtl number, Pr**, given by

$$\mathrm{Pr}^{**} = \mathrm{Pr}_v(1 + 3.33\, i_{fg}/c_{pv}(T_w - T_{\mathrm{sat}})) \tag{7}$$

Other special dimensionless groups that serve as correlation parameters will be defined later.

The thermophysical properties of carbon dioxide that were employed in the evaluation of the various dimensionless representations of the data were taken from [8].

Results and Discussion

Heat Transfer Results. The experimental results will first be presented in terms of the boiling curve variables, q and ΔT. These data are plotted in Fig. 2, where they group according to wire diameter and, for each wire, are parameterized by the pressure level (the critical pressure for carbon dioxide is 73.8 bar). Also shown for comparison are experimental results of Abadzic and co-workers [2, 4].

The results display an increase of q with ΔT, as is characteristic of the stable film boiling regime. A more major issue addressed in Fig. 2 is the effect of pressure level. The present data, which cover the entire pressure range from the triple point to the neighborhood of the critical point, indicate a 30–50 percent variation of q over this range, at a given ΔT. The data of [2, 4], which encompassed a smaller range of pressures (from 55.7 bar to near critical), could be represented by a single film boiling curve applicable to all pressures. Only near the respective minimum heat fluxes for each pressure do the results of [2, 4] display curve tails which separate from a common curve for each wire diameter. The present film boiling data, as well as those of Gorenflo[3] [9], do not display curve tails.

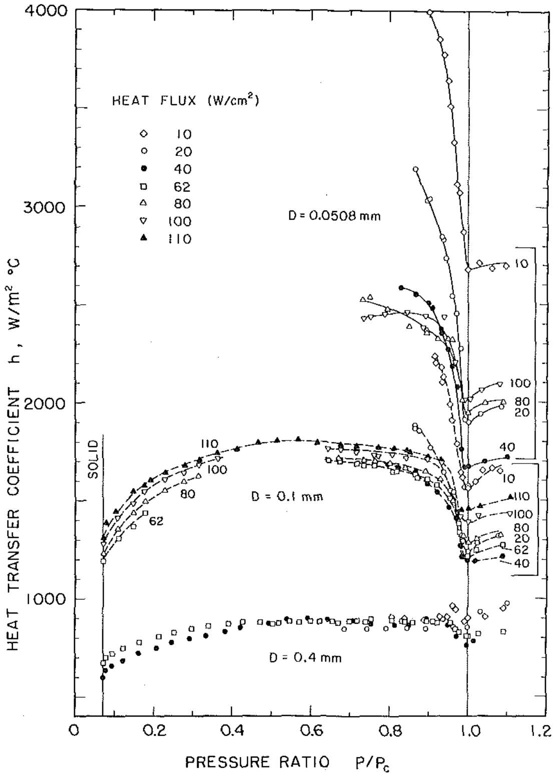

Fig. 3 Variation of the heat transfer coefficient with pressure

The aforementioned effect of pressure level can be attributed, at least in part, to changes in the thermophysical properties which occur as the pressure changes. Furthermore, it is not unreasonable to expect that these property changes will have a different impact on plane vapor films and on annular vapor films with appreciable curvature, owing to differences in the respective temperature profiles. The extent of the curvature can be keyed to the magnitude of the film thickness—radius ratio. A simple heat conduction model suggests that the vapor film surrounding the 0.1-mm dia wire possesses substantially greater curvature than that surrounding the 0.4-mm wire. The data of Fig. 2 show that the vapor film surrounding the smaller wire is more sensitive to pressure level than that surrounding the larger wire.

Heat transfer coefficients evaluated from the present measurements are plotted in Fig. 3 as a function of the pressure level expressed as the ratio p/p_c. The data cover the abscissa range from the triple point to supercritical conditions ($p/p_c > 1$). The heat flux q is used to parameterize the data.

The results for the three heating wire diameters separate from each other naturally. There is a marked increase in the magnitude of the transfer coefficients as the diameter decreases. This trend can be attributed, at least in part, to the increasing role of the curvature of the vapor film with decreasing wire diameter. It has been well established both in convective heat transfer problems (e.g., forced and natural convection flows about cylinders) and in heat conduction that surface curvature acts to augment the transfer coefficients.

---

[3] Gorenflo boiled four different liquids on an 8-mm dia tube.

The figure shows that the sensitivity of the transfer coefficients to pressure variations is markedly affected by the diameter of the heating wire. For the largest diameter of these experiments, 0.4 mm, the pressure effect is slight. With decreasing diameter, the influence of pressure becomes increasingly more important. The pressure insensitivity for large diameter heating surfaces has been noted earlier in [9, 10], whereas the increased pressure sensitivity for thin heating wires was identified in [3, 11].

It is particularly relevant to note that the pressure influence is greatest in the neighborhoods of the critical and triple points. This behavior is well illustrated by the results for the 0.1-mm wire, where h is seen to be relatively independent of pressure in the intermediate range of p/p_c and falls off rather sharply at both ends. Minimum values are attained at the triple and critical points. The results for the 0.0508-mm wire display a very high degree of sensitivity to pressure level.

Further inspection of the figure reveals that h is not independent of the magnitude of the heat flux. This dependence is believed due to the effect of variable fluid properties. The spread of the results with heat flux appears to increase as the diameter of the heating wire decreases. It appears that at pressures that are not too near the critical, higher heat transfer coefficients are associated with higher heat fluxes. The deviations from this trend that are in evidence at near critical pressures may be related to the various regimes of film boiling that can exist in that range. As will be noted later in connection with the discussion of the vapor separation patterns, the transitions between the regimes take place at different pressure levels, depending on the heat flux. Therefore, at a given pressure, the heat transfer coefficients at the various heat flux levels may correspond to different film boiling regimes.

In the supercritical region, the influence of pressure is relatively slight compared with that in the adjacent film boiling region. It is interesting to observe that the ordering of the curves in the supercritical region is the same for the 0.1 and 0.0508 mm wires, with those for 10 W/cm^2 and 40 W/cm^2, respectively, falling highest and lowest.

The interrupted curves indicate regions where pure film boiling could not be attained on the test section. As was noted earlier, these are regions where the applied heat flux is below the minimum value for film boiling.

It is relevant to employ the present data, which encompass a larger pressure range than that of previously available data, to examine the quality of several recent film boiling correlations.

Pitschmann and Grigull [1] deduced a relation between the Nusselt number and the modified Rayleigh number Ra*, respectively, defined by equations (4) and (6), by extending the classical Bromley model. When radiative transfer and thermal accommodation effects are neglected, the Pitschmann-Grigull equation takes the form

$$\mathrm{Nu} = 0.9\,(\mathrm{Ra}^*)^{0.08} + 0.8(\mathrm{Ra}^*)^{0.2} + 0.02(\mathrm{Ra}^*)^{0.4} \tag{8}$$

Equation (8) has been plotted in Fig. 4 along with the data of the present experiments. The data for the various heating wires are separately identified.

Overall, the agreement between the Pitschmann-Grigull prediction and the experimental data is seen to be very good, especially when note is taken of the large variations of h with heat flux, pressure, and wire diameter as evidenced by Fig. 3. There is, however, an interesting trend that is worthy of note. Namely, that for each heating wire, the data at the high end of the Ra* range tend to lie above the prediction curve. These high Ra* data correspond to operating conditions near the critical pressure and also at heat fluxes that were nearest to the minimum film boiling heat flux, and this suggests that the predictions may be less accurate in that region. A similar finding was reported in [4] on the basis of experiments involving a single heating wire.

Clements and Colver [12] carried out an extensive survey of the available predictions, empirical correlations, and experimental data for film boiling. Guided by the structure of the predictive equations and employing experimental data to fix a multiplicative constant, they proposed the following Nusselt number representation [13]

$$\mathrm{Nu} = 0.94(\mathrm{Ra}\theta' T_r{}^{-2})^{1/4} \tag{9}$$

where Nu and Ra are given by equations (4) and (5), and

$$\theta' = i_{fg}/c_{pv}(T_w - T_{\mathrm{sat}}) + 0.5 \tag{10}$$

$$T_r = T_{\mathrm{sat}}/T_c \tag{11}$$

The Clements-Colver correlation is compared with the present data in Fig. 5. It is seen from the figure that there is a systematic deviation between the correlation and the data that is ordered according to the diameter of the heating wire. The deviations of the data from the correlation that are in evidence in Fig. 5 are actually much smaller than those shown in the Clements-Colver paper [13].

Nishikawa and co-workers [7] employed a boundary layer integral-type analysis to deduce a Nusselt number prediction of the form

$$Y = 0.22 + 0.15X + 0.0058X^2 \tag{12}$$

where

$$Y = \log_{10}\mathrm{Nu}$$

$$X = \log_{10}(\mathrm{GrPr}^{**2}/(\mathrm{Pr}^{**} + 1.33))$$

in which Pr** is defined by equation (7). A comparison of the Nishikawa equation and the present data is made in Fig. 6. The overall agreement is generally satisfactory, but there appears to be a tendency for the correlation equation to fall above the data at higher values of the abscissa variable.

It appears that both the Pitschmann-Grigull and the Nishikawa equations provide satisfactory predictions of the present experimental data. The Clements-Colver equation is less satisfactory because its correlating parameters give rise to a systematic separation of the data according to heating wire diameter.

Boiling Phenomena. Photographic information showing patterns of vapor separation from thin wires during film boiling of carbon dioxide is available in [2, 4]. Photographic studies were also carried out as part of the present investigation in order to system-

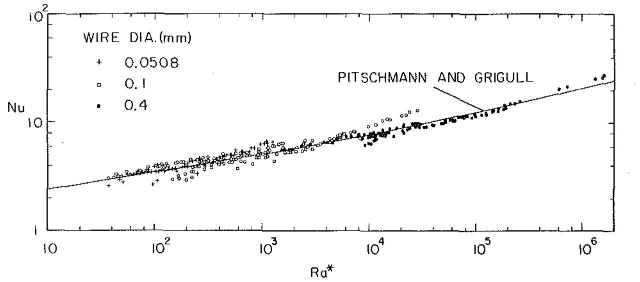

Fig. 4 Comparison of present Nusselt number results with the Pitschmann-Grigull equation

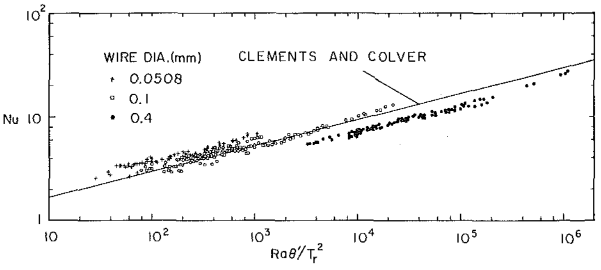

Fig. 5 Comparison of present Nusselt number results with the Clements-Colver equation

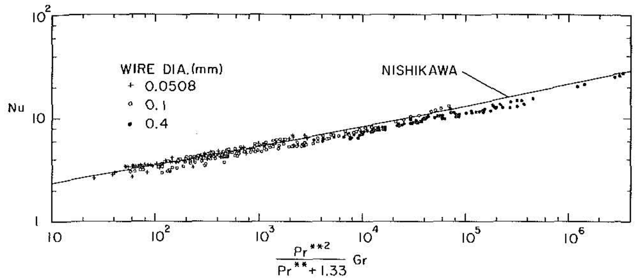

Fig. 6 Comparison of present Nusselt number results with the Nishikawa equation

atically examine the effect of pressure level on the vapor separation pattern. In addition, the effect of changes in heat flux at a fixed pressure level was also examined.

Each of Figs. 7 and 8 contains a succession of photographs in which the pressure is varied at a fixed heat flux, respectively for the 0.4- and 0.0508-mm heating wires. Among the photographs, Figs. 7(*a*) and 8(*a*) are special in that they portray the situation where steady-state film and nucleate boiling coexist side by side. This pattern of vapor separation was encountered when, starting with the operating conditions of Figs. 7(*b*) and 8(*b*), the pressure was reduced. Nucleate boiling, initiated at one or both ends of the wire, spread into part of the test section. Inasmuch as the electrical resistivities of the film and nucleat boiling portions of the wire are different (owing to differences in temperature), so also are the corresponding heat fluxes. In view of this, the fixed heat flux level specified for Figs. 7 and 8 does not apply to Figs. 7(*a*) and 8(*a*).

The vapor separation pattern portrayed in Figs. 7(*b*) and 8(*b*) is typical of that for all cases where film boiling exists in the range between the triple point and $p/p_c = 0.7 - 0.8$. Both the diameter of the bubbles which break away from the vapor film and the distance between bubble columns become larger with decreasing pressure and increasing wire diameter.

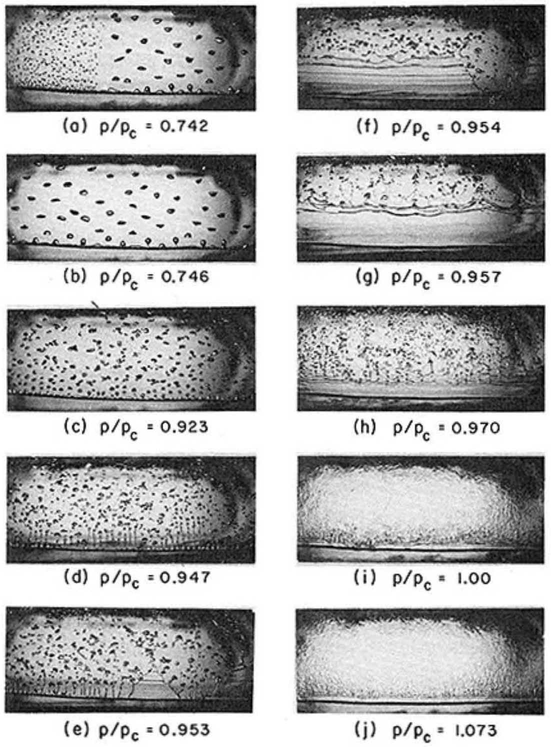

(a) $p/p_c = 0.742$
(b) $p/p_c = 0.746$
(c) $p/p_c = 0.923$
(d) $p/p_c = 0.947$
(e) $p/p_c = 0.953$
(f) $p/p_c = 0.954$
(g) $p/p_c = 0.957$
(h) $p/p_c = 0.970$
(i) $p/p_c = 1.00$
(j) $p/p_c = 1.073$

Fig. 7 Patterns of vapor separation as a function of pressure, 0.4-mm dia heating wire, q = 10 W/cm² (the viewing windows were approximately 25 by 75 mm)

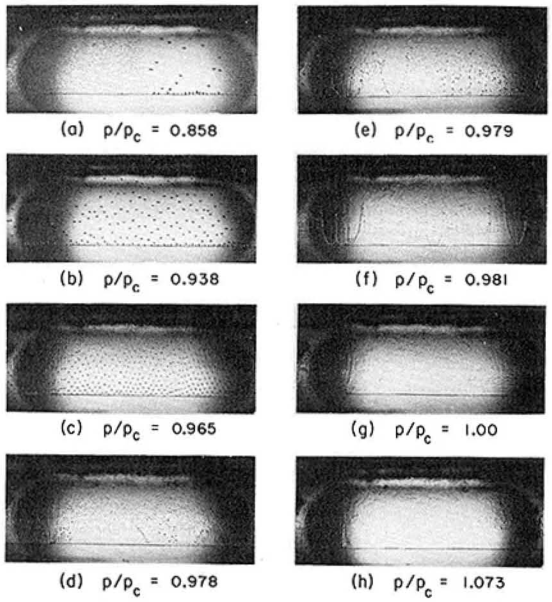

(a) $p/p_c = 0.858$
(b) $p/p_c = 0.938$
(c) $p/p_c = 0.965$
(d) $p/p_c = 0.978$
(e) $p/p_c = 0.979$
(f) $p/p_c = 0.981$
(g) $p/p_c = 1.00$
(h) $p/p_c = 1.073$

Fig. 8 Patterns of vapor separation as a function of pressure, 0.0508-mm dia heating wire, q = 10 W/cm²

Attention may now be focused on Fig. 7 in order to identify trends with increasing pressure level. Beginning with Fig. 7(*b*), it is seen that an increase in pressure causes the bubble columns to move closer together and to evolve into vapor columns. These columns successively develop into partial and complete vapor sheets[4] (Figs. 7(*e*), 7(*f*), and 7(*g*)). The sheets oscillate in the vertical direction. As the critical pressure is approached, the oscillations become less vigorous, and the vapor sheets diminish in height. The flow pattern at the critical point is not distinguishably different from that for supercritical natural convection.

The sequence of events portrayed in Fig. 8 for the thinner heating wire is similar to that just discussed for Fig. 7. The major difference is that the transitions in the vapor separation patterns occur at pressures nearer the critical.

From the study of photographs similar to those of Figs. 7 and 8, it was found that the transitions take place at lower pressures for higher heat flux levels.

Fig. 9 has been prepared to illustrate the effect of heat flux level, with pressure held fixed. From a careful examination of these photographs, the distance between bubble columns (often termed the wavelength λ) is seen to increase with increasing heat flux. For instance, for a 5-cm length of the test section, there are, on the average, 53 and 34 bubble columns, respectively, for heat fluxes of 10 and 100 W/m². The dependence of the wavelength on pressure and wire diameter has been discussed in [4].

Concluding Remarks

The present film boiling experiments appear to be the first where pressures covering the entire triple point—critical point range have been studied. The q, ΔT boiling curve is shown to be pressure dependent, with a more marked dependence for smaller diameter heating wires. The effects of pressure are more clearly portrayed when the heat transfer coefficient is plotted against pressure at fixed values of heat flux. The pressure influence is greatest in the neighborhoods of the triple and critical points, with

---

[4] A mechanism for the transition from column boiling to sheet boiling has recently been proposed by Berghmans [14].

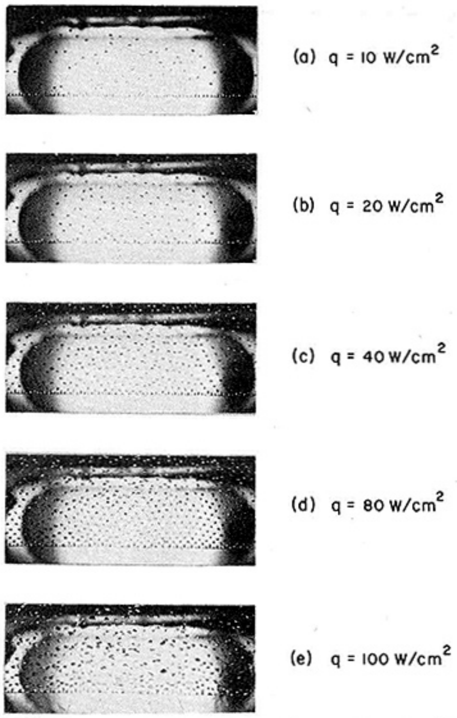

Fig. 9 Patterns of vapor separation as a function of heat flux, 0.0508-mm dia heating wire, $p/p_c = 0.891$

a lesser influence in the range of intermediate pressures. The sensitivity of the heat transfer coefficient to pressure level is markedly increased as the diameter of the heating wire decreases. The heat transfer coefficient is not independent of the heat flux level. For a given heat flux, minimum values of the transfer coefficient are attained at the triple and critical points.

Nusselt numbers evaluated from the experimental data were in satisfactory agreement with the prediction equations of Pitschmann and Grigull and of Nishikawa. Photographs revealed that with increasing pressure, the bubble columns which break away from the vapor film surrounding the wire successively evolve into vapor columns and vapor sheets. As the critical pressure is approached, the sheets diminish in height. The photographs also documented certain operating conditions where nucleate boiling encroached into an established film boiling regime subsequent to a decrease of pressure.

Acknowledgment

Post-doctoral scholarship support accorded to G. Hesse in 1972–1973 by the Deutsche Forschungsgemeinschaft, Bonn-Bad Godesberg, Germany, is gratefully acknowledged.

References

1 Pitschmann, P., and Grigull, U., "Film Boiling on Horizontal Cylinders," *Wärme- und Stoffübertragung*, Vol. 3, 1970, pp. 75–84.

2 Grigull, U., and Abadzic, E., "Heat Transfer From a Wire in the Critical Region, *Proc. Inst. Mech. Engrs.* (London), Vol. 182, Part 31, 1968, pp. 52–57.

3 Simoneau, R. J., and Baumeister, K. J., "Experimental Effects of Pressure, Subcooling, and Diameter on Thin-Wire Film Boiling of Liquid Nitrogen," *Adv. Cryo. Engng.*, Vol. 16, 1971, pp. 416–425.

4 Abadzic, E., and Goldstein, R. J., "Film Boiling and Free Convection Heat Transfer to Carbon Dioxide Near the Critical State," *International Journal of Heat and Mass Transfer*, Vol. 13, 1970, pp. 1163–1175.

5 Gubareff, G. G., Janssen, J. E., and Torborg, R. H., "Thermal Radiation Properties Survey," Honeywell, Inc., Minneapolis, Minn., 1960.

6 "Grundwerte der Messwiderstände für Widerstandsthermometer," Deutscher Normenausschuss, Berlin, DIN 43760, 1968.

7 Nishikawa, K., Ito, T., Kuroki, T., and Matsumoto, K., "Pool Film Boiling Heat Transfer From a Horizontal Cylinder to Saturated Liquids," *International Journal of Heat and Mass Transfer*, Vol. 15, 1972, pp. 853–862.

8 Vukalovich, M. P., and Altunin, V. V., *Thermophysical Properties of Carbon Dioxide*, Collet's Ltd., London and Wellingborough, 1968.

9 Gorenflo, D., Institut für Techn. Thermo., Universität Karlsruhe, personal communication.

10 Hesse, G., "Heat Transfer in Nucleate Boiling, Maximum Heat Flux, and Transition Boiling," *International Journal of Heat and Mass Transfer*, Vol. 16, 1973, pp 1611–1627.

11 Feurstein, G., and Hahne, E., "Heat Transfer in Pool Film Boiling of Carbon Dioxide," Int. Inst. of Refrigeration, Comm. B-1, B-2, and E-1, Freudenstadt 1972, Annex 1972–1, pp. 39–50.

12 Clements, L. D., and Colver, C. P., "Natural Convection Film Boiling Heat Transfer," *I and E Chem.*, Vol. 62, No. 9, 1970, pp. 26–46.

13 Clements, L. D., and Colver, C. P., "Generalized Correlation for Film Boiling," JOURNAL OF HEAT TRANSFER, Series C, Vol. 94, 1972, pp. 324–326.

14 Berghmans, J., "Film Boiling Near the Critical State," *International Journal of Heat and Mass Transfer*, Vol. 18, 1975, pp. 1127–1130.

L. C. Farrar
Aerojet Nuclear Co.,
Idaho Falls, Idaho

E. Marschall
Assoc. Professor,
Department of Mechanical and Environmental Engineering,
University of California,
Santa Barbara, Calif.

Film Boiling in a Scaling Liquid

Film boiling experiments were carried out in an aqueous-calcium sulfate solution. The experimental results indicate that scale formation on heating surfaces during evaporation of a calcium sulfate solution can be avoided under carefully controlled conditions. Experimental heat transfer results for both distilled water and aqueous calcium solutions compare very well with analytical predictions. In addition, for high heat fluxes, contact between liquid and heating surface was found to exist during stable film boiling in a quiescent, saturated or almost saturated liquid.

Introduction

Stable film boiling is commonly described as a mechanism in which the heating surface is completely separated from the boiling liquid by a continuous vapor film. Consequently, one should expect that the severe formation of scale on heating surfaces which is observed in nucleate boiling of aqueous salt solutions would not occur in film boiling, since there is no contact between the scaling liquid and the heating surface. Although numerous experimental and theoretical investigations of film boiling have been carried out, all those studies deal with pure, nonscaling liquids. No experiments or analyses are known which investigate film boiling in a scaling liquid. In the following, heat transfer and scale formation experiments are described, and experimental results are compared with a simplified theory on film boiling heat transfer. These experiments were carried out with distilled water and an aqueous-calcium sulfate solution as fluids. An almost completely submerged sphere was used as the heater element.

Heat Transfer Analysis

A quite successful analysis of film boiling from fully submerged spheres was carried out by Hendricks and Baumeister [1].[1] In a recent paper, Marschall and Farrar [2] adopted their approach to analyze film boiling from half-submerged spheres. Comparison with experimental data indicated that for the considered case the predicted Nusselt numbers were equal to or smaller than the experimentally obtained Nusselt numbers, thus the theory seemed to provide for conservative estimates of the heat transfer rates.

In the following study, an almost fully submerged sphere will be considered as indicated in Fig. 1. The employed model assumes that the sphere of radius R_0 is separated from the liquid by a vapor gap of constant thickness δ. The conservation equations for mass, momentum, and energy are formulated in terms of the coordinates r and θ. The position of the liquid level is measured by θ^*. To facilitate the analysis, it is assumed that the vapor flow in the gap between liquid and sphere is laminar and at steady state, and that inertia and body force terms can be neglected. The vapor participation in radiant energy exchange is assumed to be negligibly small. Thus, as shown in reference [1], the convective terms in the energy equation can be neglected if the latent heat of vaporization is replaced by an enthalpy difference which contains the latent heat. The solution of the conservation equations for the vapor flow in the gap with the aforementioned assumptions yields the following equation for the Nusselt number in the range $0 < \theta < \theta^*$, as demonstrated in references [2, 3]

$$\mathrm{Nu} = \frac{h}{k} R_0 = 1 + \frac{R_0}{\delta} + \frac{R_0}{k} \epsilon_w \sigma_r \frac{(T_w{}^4 - T_s{}^4)}{T_w - T_s} \tag{1}$$

The Nusselt number depends on the sphere radius R_0, emissivity ϵ_w of the heating surface, wall temperature T_w, saturation temperature T_s of the liquid, and the gap thickness δ. While for a given problem R_0, the temperatures T_w and T_s, and the emissivity ϵ_w are known, the gap thickness remains to be determined as a function of the boundary conditions.

The interface conditions at $r = R_0 + \delta$ are difficult to specify. It is obvious from visual observation that the liquid at the interface is not at rest. Thus, a complete solution of the problem requires additional consideration of the conservation equations in the liquid phase which would add drastically to the computational difficulty of the problem. Therefore, two limiting cases are being considered. In the first case, it is assumed that the vapor at the interface does not move in θ-direction. For this condition, in the following denot-

---

[1] Numbers in brackets designate References at end of paper.

Contributed by the Heat Transfer Division for publication in the JOURNAL OF HEAT TRANSFER. Manuscript received by the Heat Transfer Division October 10, 1975. Paper No. 76-HT-MM.

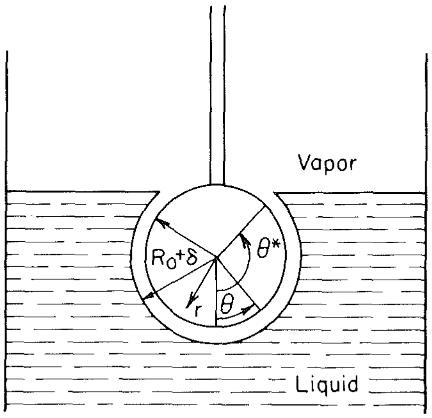

Fig. 1 Film boiling model

ed as nonslip condition, the gap thickness δ is found from

$$\left(\frac{\delta}{R_0}\right)^4 = -\left(\frac{2\epsilon_w\sigma_r(T_w{}^4 - T_s{}^4)}{\rho\mu^*\lambda_1{}^*c_4} + \frac{2k(T_w - T_s)}{R_0\rho\mu^*\lambda_1{}^*c_4}\right)\frac{\delta}{R_0} - \frac{2k(T_w - T_s)}{R_0\rho\mu^*\lambda_1{}^*c_4} \quad (2)$$

In the second case, it is assumed that the shear stress at the interface is zero. For this condition, in the following called slip conditions, the gap thickness δ can be calculated from

$$\left(\frac{\delta}{R_0}\right)^4 = \left[-\left(\frac{2\epsilon_w\sigma_r(T_w{}^4 - T_s{}^4)}{\rho\mu^*\lambda_1{}^*c_4} + \frac{2k(T_w - T_s)}{R_0\rho\mu^*\lambda_1{}^*c_4}\right)\frac{\delta}{R_0} - \frac{2k(T_w - T_s)}{R_0\rho\mu^*\lambda_1{}^*c_4}\right]\frac{1}{(1 + 3\phi)} \quad (3)$$

In equations (2) and (3) the following abbreviations have been used:

$$c_4 = \frac{\dfrac{1 - \cos\theta^*}{\rho\mu^{*2}}\left[\dfrac{1}{2}R_0\phi(\rho_\ell - \rho)g(1 - \cos\theta^*) + \dfrac{2\sigma}{R_0 + \delta}\right]}{12\left[\ell\mathrm{n}\cos^2\dfrac{\theta^*}{2} + \sin^2\dfrac{\theta^*}{2}\right]} \quad (4)$$

$$\lambda_1{}^* = [h_{fg} + c_{p\ell}(T_s - T_\ell) + \alpha c_p(T_w - T_s)] \quad (5)$$

$$\mu^* = \frac{\nu}{R_0} \quad (6)$$

$$\phi = \frac{R_0 + \delta}{R_0} \quad (7)$$

The term $\alpha c_p(T_w - T_s)$ in equation (5) accounts for vapor superheat and vapor inertia forces where α is a still undetermined coefficient of the order $0 < \alpha < 1$. All physical properties of the vapor are evaluated at the reference temperature $T_R = (T_s + T_w)/2$.

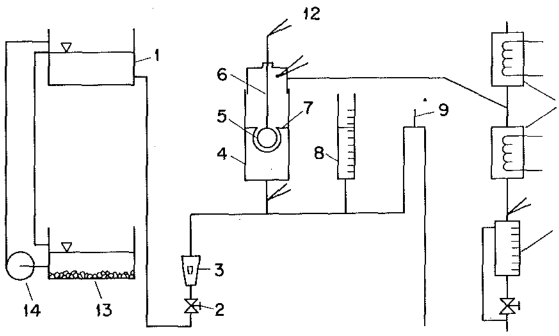

Fig. 2 Experimental apparatus

Data for the emissivity ϵ_w of inconel 600 were taken from reference [4] and fitted with an algebraic function of temperature. It should be noted that the heat transfer coefficient defined by equations (1) and (2)–(7) represents heat transferred by conduction, convection, and radiation.

Experimental Apparatus

A schematic of the film boiling apparatus is presented in Fig. 2. Distilled water or saturated calcium sulfate solution at a constant flowrate leaves the constant head tank (1), passes through a metering valve (2) and a flowmeter (3), and enters a glass pipe (4) of 4.5 cm ID. In the center of the glass pipe, a solid inconel sphere (5) of 1.905 cm dia is located which is supported by a thin-walled, stainless steel tube (6) of 0.318 cm OD. The inconel sphere serves as heating element; it is heated by a 2.5 kW induction heater operating at about 400 kHz. Inconel 600 was chosen because of its good corrosion resistance at high temperatures. The liquid level (7) in the glass pipe can be read from a graduated glass cylinder (8), and can be adjusted at any desired height with help of the overflow (9). The vapor produced in the glass pipe is completely condensed in the condensers (10); the condensate flow rate is determined with help of a graduated cylinder (11). The temperature of the inconel sphere is measured with a shielded thermocouple (12) which is inserted through the steel pipe, so that the thermocouple junction is positioned in the center of the sphere. Since only the surface of the sphere is heated by induction, the thermocouple measures the average surface temperature. Additional thermocouples are used to determine the vapor temperature, the temperature of the distilled water or the calcium sulfate solution entering the glass pipe, and the temperature of the condensate. The usual and well-publicized precautions are taken to ensure correct temperature measurements. A saturated solution of calcium sulfate is maintained by placing calcium sulfate particles into reservoir (13) with the distilled water, and continuously circulating the solution with the pump (14). The solution temperature can be controlled with the help of an immersion heater. Heat losses are prevented with a suf-

Nomenclature

A = surface area of submerged part of sphere
c_p = specific heat of vapor
$c_{p\ell}$ = specific heat of liquid
g = gravitational acceleration
h = heat transfer coefficient
h_{fg} = latent heat of vaporization
k = thermal conductivity
$\dot{m}$ = mass flow rate
Nu = Nusselt number
P = pressure
P_0 = pressure at liquid level

$\dot{Q}$ = heat flow
q_{rad} = radiant heat transfer
r = radial coordinate
R_0 = radius of sphere
T_ℓ = temperature of liquid
T_s = saturation temperature
T_v = vapor temperature
T_w = sphere temperature
μ^* = dimensionless velocity
v_r = radial velocity component
v_θ = theta velocity component

α = parameter defined by equation (15)
δ = gap thickness
ϵ_w = emissivity of sphere
θ = angular coordinate
$\lambda_1{}^*$ = modified latent heat (equation (5))
$\lambda_2{}^*$ = modified latent heat (equation (9))
ν = kinematic viscosity of vapor
ρ_ℓ = liquid density
σ = surface tension
σ_r = Stefan-Boltzmann constant

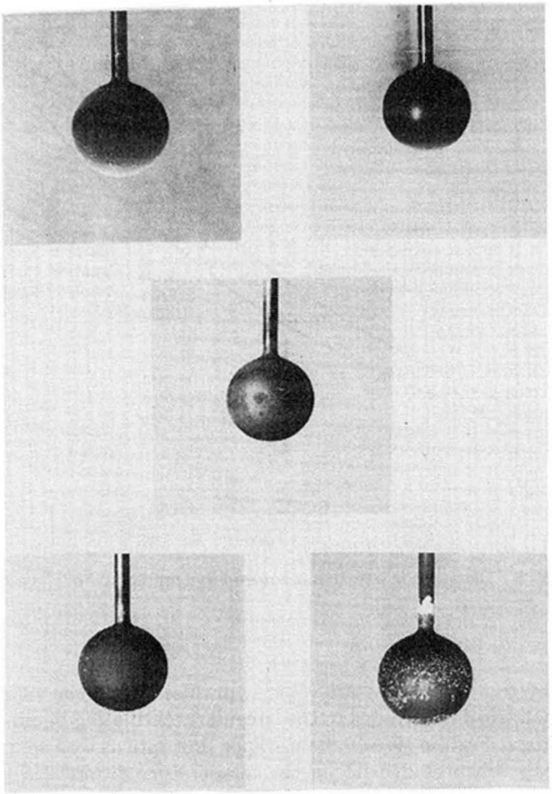

Fig. 3 Scale formation in film boiling

ficient thermal insulation.

Experimental Procedure and Data Evaluation

Data accumulation for the experiments was quite straightforward. The inconel sphere was heated by the induction heater until its surface temperature was sufficiently high to maintain stable film boiling. The liquid level was then adjusted to a height such that $\theta^* = 150$ deg. The value of $\theta^* = 150$ deg was chosen on the basis of preliminary experiments which revealed that for larger values of θ^* liquid would come into contact with the supporting, cooler steel tube and deposit large amounts of scale. Then, the power input to the sphere was chosen such that in steady-state conditions the difference between sphere temperature and saturation temperature $(T_w - T_s)$ would take on a value between 300 and 1000°C. Each experiment was carried out over a period of 24 hr. During the experiment, all temperatures and the condensate flow were constantly monitored. At steady-state conditions values of temperatures and condensate flow rate remained constant. Steady-state conditions were usually obtained after a period of 1–2 hr. Temperatures and condensate flow rate at the end of the 24-hr period which are identical with temperatures and condensate flowrate during the whole period of steady-state conditions provided the necessary information for the evaluation of the heat fluxes and Nusselt numbers.

The energy flow required to heat and vaporize the subcooled liquid and to produce the superheated vapor is given by

$$\dot{Q} = \dot{m}\lambda_2^* \tag{8}$$

where

$$\lambda_2^* = h_{fg} + c_{p\ell}(T_s - T_\ell) + c_p(T_v - T_s) \tag{9}$$

and $\dot{m}$ is the measured flow rate of the condensate.

The temperature T_ℓ of the subcooled liquid entering the glass pipe (4) was maintained at 46°C for all experiments. However, since the pool of liquid in the glass pipe is relatively small, the temperature of most of the liquid in the glass pipe is close to saturation temperature.

The heat flow from the sphere to the fluid can be written as

$$\dot{Q} = Ah(T_w - T_s) \tag{10}$$

where A is the area of the sphere submerged in the liquid, given by

$$A = 2\pi R_0^2(1 - \cos\theta^*) \tag{11}$$

The Nusselt number is defined as

$$\mathrm{Nu} = \frac{hR_0}{k} \tag{12}$$

Equations (8)–(12) can be combined in an expression that yields the Nusselt number in terms of known and measurable quantities:

$$\mathrm{Nu} = \frac{\lambda_2^*\dot{m}}{k2\pi R_0(1 - \cos\theta^*)(T_w - T_s)} \tag{13}$$

The Nusselt number as defined by equation (13) does not account for the following phenomena:

(*a*) Heat is conducted from the sphere into the supporting steel tube and transferred by conduction and convection to the vapor. Further, convective heat transfer occurs from the upper unsubmerged part of the sphere to the vapor.

(*b*) Vapor and liquid are in contact at the liquid level (7). Therefore, heat is transferred from the superheated vapor to the liquid by conduction and convection.

An estimation of both effects revealed that they are small as compared to the total heat transfer and of the same order of magnitude, thus, almost canceling each other out. Therefore, errors introduced by omitting these effects in the calculation of the Nusselt numbers are negligibly small.

The evaluation of the coefficient α in equation (9) is obtained by noting that

$$h_{fg} + c_{p\ell}(T_s - T_\ell) + \alpha c_p(T_w - T_s) = h_{fg} + c_{p\ell}(T_s - T_\ell) + c_p(T_v - T_s) \tag{14}$$

and, therefore,

$$\alpha = \frac{(T_v - T_s)}{(T_w - T_s)} \tag{15}$$

To evaluate the effectiveness of film boiling as a scale-free heating method for aqueous salt solutions, the spheres were removed after completion of each 24-hr test, and the surface conditions were noted and recorded by photographs.

Results

The photographs of Fig. 3 show the surface conditions of five spheres after 24-hr periods of film boiling in an aqueous-calcium sulfate solution. These results are representative of the effectiveness of the film boiling technique as a scale preventative measure over the complete range of temperature differences investigated.

After tests at temperature differences $(T_s - T_w)$ between 350 and 600°C, the submerged position of the sphere was always entirely covered with a very fine calcium sulfate powder (Fig. 3, upper left-hand corner). The amount of calcium sulfate deposited on the heating surfaces decreased with increasing temperature differences. As the temperature differences were raised to a range above 600°C but below 800°C, the calcium sulfate coating did not cover the entire submerged position of the sphere but was restricted to the lower pole area (Fig. 3, upper right-hand corner). At temperature differences between 800 and 850°C, sphere surfaces were found to be entirely scale free after the 24-hr test period (Fig. 3, middle). At temperature differences above this range, small distinct calcium sulfate spots began to appear on the sphere surfaces (Fig. 3, lower left-hand corner). With increasing temperature differences, the number of spots found after a test increased, too. While most spots were found at the lower pole and the equator of a sphere at temperature differences between 950 and 1000°C, calcium sulfate deposits could be found at almost any position (Fig. 3,

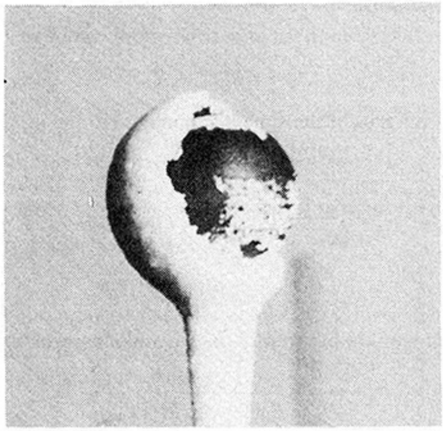

Fig. 4 Scale formation in nucleate boiling

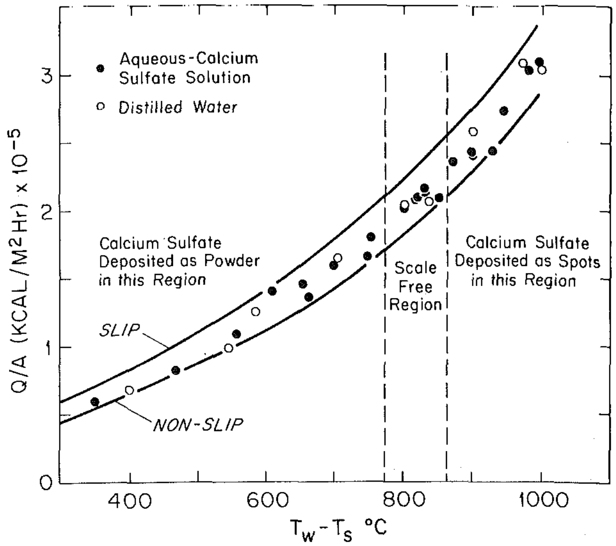

Fig. 5 Comparison between measured and predicted heat flow rates

lower right-hand corner).

It is proposed that at lower temperature differences small calcium sulfate particles form at or near the vapor-liquid interface, diffuse across the vapor film, and deposit on the heating surface. However, as the temperature differences are raised, heat fluxes increase and, therefore, more vapor is produced. The higher vapor flow prevents the small calcium sulfate particles from depositing on the heating surfaces. From visual observations and from photographic pictures taken, it is obvious that with increasing temperature differences the liquid-vapor interface takes on a more and more turbulent character. Not only do irregular waves appear on the interface, but droplets are carried with the vapor flow and ejected into the vapor space above the heating element. At temperature differences above 850°C, droplets apparently cross the vapor film, contact the sphere surface, and evaporate completely or partly, leaving a calcium sulfate deposit.

Although the film boiling experiments indicate that there exists only a small range of temperature differences, where scale formation can be prevented entirely, scale deposits, when they occur, are very light compared with scale formation experienced in nucleate boiling. Fig. 4 demonstrates the extent of scale accumulation during a 24-hr nucleate boiling test in an aqueous-calcium sulfate solution. The entire sphere was encased by scale deposits; however, some of the scale was removed for purposes of illustration.

Heat transfer results are represented in Fig. 5; for brevity, only heat fluxes are presented as function of temperature differences both for distilled water and aqueous-calcium sulfate solution, for spheres submerged to the $\theta^* = 150$ deg level. All data points are found to lie within the range which is bounded by the predicted heat fluxes for nonslip conditions (equations (1) and (2)) and slip conditions (equations (1) and (3)). The coefficient α in equation (5) was found by evaluating equation (15) for each experiment and fitting the result with help of a standard regression program yielding the following function

$$\alpha = 0.08677 + 0.00003(T_w - T_s) \tag{16}$$

Equation (16) specifies the dependence of α on temperature differences for the investigated range from $(T_w - T_s) = 350°C$ to $(T_w - T_s) = 1000°C$. Not only are the values of α according to equation (16) a function of the temperature differences $(T_w - T_s)$, but they are also substantially smaller than the constant value of $\alpha = 0.5$ suggested in reference [1] for laminar flow around a sphere.

The discrepancy between the theoretical value of $\alpha = 0.5$ and the values given by equation (16) is apprarently a consequence of the real character of vapor flow about the sphere. Due to the rapid, irregular movements of the liquid-vapor interface, the assumption of laminar vapor flow may be violated. The degree of possible turbulence in the vapor flow depends upon vapor flow rate as well as the disturbances at the vapor-liquid interface. Furthermore, the assumption of steady-state velocity profiles within the vapor gap cannot possibly hold due to the irregularly oscillating liquid-vapor interface. For the given system, vapor flow rate as well as interfacial disturbances depend on the temperature differences $(T_w - T_s)$. Consequently, equation (16) provides for more realistic values for α than the 0.5 predicted for laminar flow. It should be noted that the interfacial disturbances provide for increased contact area between liquid and vapor. This effect is also contained in the experimental value of α. The close agreement of theory and experiments demonstrated in Fig. 5 must be viewed with some caution, since experimental heat fluxes found for half-submerged spheres ($\theta^* = 90$ deg) are generally greater than those predicted for slip conditions in reference [2]. This statement also holds when the value of $\alpha = 0.5$ used in reference [2] is replaced by equation (16).

Conclusion

It has been demonstrated that film boiling provides for a possible method to maintain scale-free heating surfaces during the evaporation of salt solutions. However, for a scale-free evaporation temperature, differences $(T_w - T_s)$ have to be adjusted to a range in which the vapor velocities are large enough to prevent diffusion of salt particles from the liquid-vapor interface to the heating surface while the disturbances at the liquid-vapor interface are still not violent enough to cause liquid-solid contact.

A further result of this investigation is the clear indication of liquid-solid contact in the stable film boiling regime. It is generally accepted that when liquid droplets are placed in close proximity to very hot surfaces, a vapor film is generated between the liquid and heating surface preventing liquid-solid contact. This phenomenon is known as Leidenfrost boiling. A study conducted by Bradfield [5], however, revealed that when droplets of high velocity impinge upon a hot surface, liquid-solid contact can occur. The obvious extension of Bradfield's findings, and a result of this investigation, is that liquid-solid contact exists in regions of stable film boiling due to droplets which are ejected at the liquid-vapor interface with such force that they are able to cross the entire vapor gap and contact the heating surface.

Finally, the experimental data indicate that the theoretical equation (1) combined with the empirical equation (16) provides for reliable prediction of heat transfer for film boiling for more than half but not fully submerged spheres.

Acknowledgment

Support by the Academic Senate of the University of California-Santa Barbara in the form of computer funds is acknowledged.

References

1 Hendricks, R. C., and Baumeister, K. J., "Film Boiling From Submerged Spheres," NASA TN D-5124, 1969.

2 Marschall, E., and Farrar, L. C., "Film Boiling From a Partly Submerged Sphere," *International Journal of Heat and Mass Transfer*, Vol. 18, 1975, pp. 875–878.

3 Farrar, L. C., "Film Boiling From a Partially Submerged Sphere in Distilled Water and a Saturated Aqueous-Calcium Sulfate Solution," MS thesis, Department of Mechanical and Environmental Engineering, University of California, Santa Barbara, 1975.

4 Inconel Alloy 600, Huntington Alloy Products Division, The International Nickel Co.

5 Bradfield, W. S., "Liquid-Solid Contact in Stable Film Boiling," *I&EC Fundamentals*, Vol. 5, 1966, pp. 200–204.

G. Preiss[1]
P. C. Wayner, Jr.

Chemical and Environmental Engineering Department,
Rensselaer Polytechnic Institute,
Troy, N. Y.

Evaporation From a Capillary Tube

The heat transfer characteristics of an evaporating ethanol meniscus formed at the exit of a glass capillary tube were studied experimentally. The meniscus profile was photographed and was found to be a function of the evaporation rate and the initial hydrostatic head. The meniscus was found to be stable over a wide range of evaporation rates.

1 Introduction

The study of evaporation from a stable meniscus formed at the exit of a capillary tube is important to the understanding and design of change-of-phase heat transfer processes in porous media. Some initial studies of evaporation from a meniscus formed in a vertical groove have been made [1].[2] The closely related process of evaporation from a stable meniscus formed on a flat plate has also been experimentally studied [2, 3] and analyzed [4]. These experiments demonstrated that the evaporating meniscus was stable and that both the length and the average radius of curvature of the evaporating meniscus were smaller than those associated with the isothermal meniscus. A change in the contact angle was also possible. An analysis of the steady-state evaporating meniscus, which was based on the hypothesis that fluid flow in the meniscus resulted from a change in the meniscus profile, demonstrated that the available pressure gradient was sufficient to supply the necessary fluid flow [4]. Therefore, it appears that the removal of liquid by evaporation changes the meniscus profile which, in turn, changes the pressure distribution within the liquid. The fluid flow resulting from the pressure gradient gives a stable process. Power law solutions for evaporation from a finned surface in which fluid flow results from a curvature gradient have been presented [5]. The mechanics of flow in the evaporating meniscus are closely related to the isothermal rewetting problem [6, 7]. This paper concerns the design and use of experimental equipment to measure the heat transfer characteristics of a meniscus formed in a capillary. In particular, the profile of an evaporating meniscus formed at the exit of a capillary tube was photographed and was found to be a function of the evaporation rate and hydrostatic head. The results of the study support the hypothesis that fluid flow in and to an evaporating meniscus results from a curvature gradient [1–5].

2 Analysis

The following macroscopic analysis of evaporation from a stationary meniscus formed at the exit of a heated capillary tube will be used to analyze the experimental data. The heat flow rate required to evaporate the liquid flowing in a capillary tube is

$$Q_m = \bar{V} A \rho \lambda \tag{1}$$

The average velocity, $\bar{V}$, in a capillary tube of fixed length, L, can be determined by measuring the pressure drop across its length, ΔP.

$$\bar{V} = \frac{R^2}{8\mu L}(\Delta P) \tag{2}$$

The pressure difference across the liquid-vapor interface for a uniformly spherical meniscus is given by

$$(\Delta P)_{\ell v} = \frac{2\sigma \cos \theta}{R} \equiv \sigma K \tag{3}$$

Where K is defined as the total curvature of a spherical meniscus. Assuming that fluid flow in the capillary tube to the base of the meniscus with evaporation in the meniscus region results from a change in the meniscus curvature at the base of the meniscus from its nonevaporating value, the pressure drop for fluid flow is given by

$$\Delta P = (\sigma K)_E - (\sigma K)_{\mathrm{NE}} \tag{4}$$

A change in the meniscus profile can occur because the interline can move around the corner at the exit of the tube. The microscop-

---

[1] Present address: Naval Underwater Systems Center, New London, Conn.

[2] Numbers in brackets designate References at end of paper.

Contributed by the Heat Transfer Division for publication in the JOURNAL OF HEAT TRANSFER. Manuscript received by the Heat Transfer Division December 15, 1976. Paper No. 76-HT-NN.

ic processes in the liquid-solid vapor interline region that allow this to occur are not the subject of this macroscopic analysis that applies to the base of the meniscus. Combining equations (1), (2), and (4) gives

$$Q_M = \frac{\rho A \lambda R^2}{8 \mu L} [(\sigma K)_E - (\sigma K)_{\mathrm{NE}}] \tag{5}$$

Therefore, the heat flow rate for evaporation can be determined by measuring the change in the meniscus curvature at its base if it is assumed that all the fluid flowing in the tube is evaporated.

The average heat flow rate from the end of a vertical dry capillary tube which is heated is

$$Q_{\mathrm{NE}} = ha(\Delta T)_{\mathrm{NE}} \tag{6}$$

where ΔT is the average temperature difference between the tube and the surroundings. The average heat flow rate from the end of a heated capillary tube with an evaporating meniscus is

$$Q_E = Q_M + Q_T \tag{7}$$

where Q_M represents that portion due to the meniscus and Q_T represents that portion due to the tube itself. For the same experimental power input setting, $Q_{\mathrm{NE}} = Q_E$,

$$Q_M + Q_T = ha(\Delta T)_{\mathrm{NE}} \tag{8}$$

Assuming that the heat transfer process does not change for the solid tube portion, $Q_T = ha(\Delta T)_E$, gives

$$Q_M = Q_E \frac{[(\Delta T)_{\mathrm{NE}} - (\Delta T)_E]}{(\Delta T)_{\mathrm{NE}}} \tag{9}$$

Measuring the values of ΔT for the evaporating and nonevaporating cases at the same power input, equation (9) can be used to calculate Q_M. Equations (5) and (9) represent two independent methods of obtaining Q_M.

3 Experimental Equipment

Schematic diagrams of the test equipment are presented in Figs. 1 and 2. The meniscus was located at the exit of the vertical capillary tube which was enclosed in a glass test cell. The test cell was not airtight. An optical window in the test cell allowed undistorted viewing of the capillary tube. The capillary had an inside diameter of 5.85×10^{-4} m and an outside diameter of 5.55×10^{-3} m. A nickel resistive heater of approximately 6 ohms was vapor deposited on the flat surface of the capillary. Power connections were made to small tabs which were vapor deposited on opposite sides of the outside wall at the end of the capillary. The regulated d-c power input was measured using a precision registor and L & N K-4 potentiometer. Type K thermocouples were epoxied to various locations on and around the capillary tube to monitor the temperature distribution. The thermocouple output was measured with an accuracy of ±0.1 K. Only relative values of ΔT at the same location are needed in the macroscopic analysis of the data.

A 3 l liquid storage reservoir was connected to the subject capillary by a 0.44-m long constant diameter capillary (ID = 6.75×10^{-4} m) which was used as a flowmeter. The relative height of the liquid in the reservoir could be varied from run to run but remained constant during each run. The pressure drop across the flowmeter was measured with a manometer. A 10× microscope with a filar micrometer eyepiece was used to measure the liquid level change in the manometer. The difference in hydrostatic head between the liquid surface in the reservoir and the exit of the capillary tube was measured using a cathetometer and telescope arrangement having an accuracy of $\pm 5 \times 10^{-5}$ m.

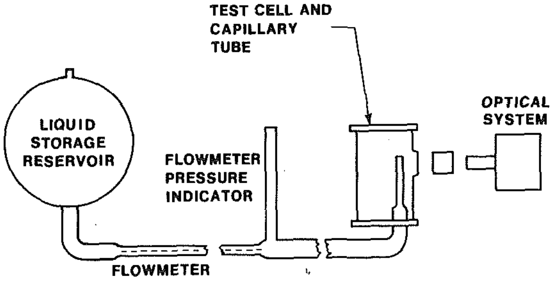

Fig. 1 Schematic diagram of experimental equipment (not to scale)

The optical setup used to photograph the meniscus profile is shown in Fig. 2. This particular system was picked because it highlighted the liquid-vapor interface and produced distinct pictures. A Graflex box camera with Polaroid black and white film was used to record the meniscus profile at a magnification of 60 times the actual size. A final magnification of 120 times the actual size was used to determine the curvature at the base of the meniscus. The curvature at the base was obtained by assuming a constant curvature profile between the base and the exit of the capillary tube. Although there is a curvature gradient between the base and the interline when there is evaporation, the macroscopic analysis only requires the curvature at the base.

The foregoing equipment was used with absolute-reagent quality ethyl alcohol as follows. The initial hydrostatic head was set by adjusting the level of the reservoir. The difference in the hydrostatic head between the reservoir and the capillary tube exit was measured for the isothermal case. A picture of the meniscus was taken after the system reached equilibrium. Then the power input was set at a given level. After equilibrium was reached, the power input, flow rate and temperature distribution were measured and a picture of the meniscus was taken. The previous readings were checked for stability. Data were taken at various increments of power input until the meniscus either became unstable by migrating down the tube or started to obviously sputter. In these tests, an attempt to measure the highest possible stable evaporation rate was not made. Tests were made for various hydrostatic heads, each time starting with an isothermal meniscus. For the purpose of calibration, the temperature and power input were also obtained for the dry tube.

4 Experimental Results

The measured hydrostatic head is plotted as a function of the

Nomenclature

A = flow area of capillary tube
a = external heat transfer area
h = heat transfer coefficient for solid part of capillary tube
K = curvature (see equation(3))
L = length
P = pressure
Q = heat flow rate

R = radius of capillary tube
T = temperature
$\bar{V}$ = average velocity
θ = apparent contact angle
λ = heat of vaporization
μ = viscosity
ρ = density

σ = surface tension

Subscripts

E = evaporating
lv = liquid-vapor interface
M = meniscus
NE = nonevaporating
T = capillary tube

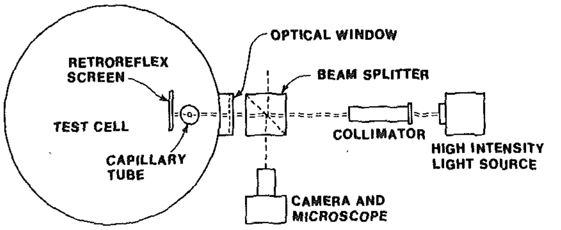

Fig. 2 Schematic diagram of optical arrangement (not to scale)

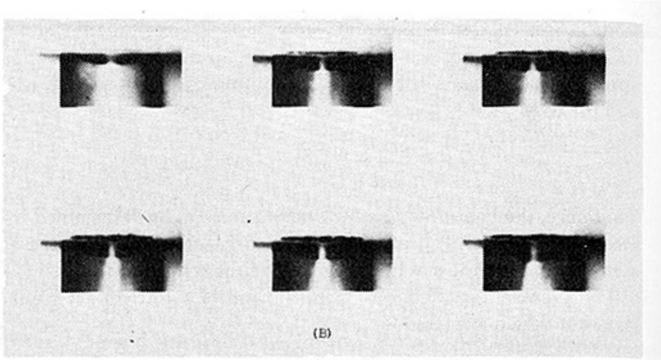

Fig. 4 Photographs of the evaporating meniscus profiles for various evaporation rates at a hydrostatic head of 10^{-2} m—from left to right the evaporation rates are 0, 0.019, 0.021, 0.049, 0.055, and 0.127 W

pressure drop across the meniscus based on the measured meniscus curvature for the isothermal case in Fig. 3. The dashed line represents the least square fit to the data. Deviations from the least square fit is a measure of the random errors present in the measurement of the curvature. The major error is believed due to a difficulty in locating exactly the top of the tube when measuring the curvature. Additional errors are associated with locating the vapor-liquid interface and the centerplane of the tube. The curvature measurements were adjusted for the effect of magnification due to the refraction of light rays at the air-glass and the ethanol-glass interfaces. The 45 deg line represents a literature surface tension value of 2.185×10^{-2} N/m at 25°C. Since our system was not completely closed, impurities could account for this difference. The least square curve based on the measured hydrostatic head was used in the nonisothermal results presented in the following.

A photograph of the meniscus profiles for various evaporation rates at a hydrostatic head of 1 cm are presented in Fig. 4. From left to right the evaporation rates are 0, 0.019, 0.021, 0.049, 0.055, and 0.127 W. These photographs clearly show the increase in meniscus curvature with an increase in evaporation rate.

In Fig. 5, the measured flow rate (evaporation rate) based on the flowmeter measurements is presented as a function of the measured meniscus suction potential based on the photographs for various hydrostatic heads.

Each run at a particular hydrostatic head is terminated close to the point where the meniscus was about to recede from the capillary exit or where sputtering or boiling was observed. The dashed line represents equation (5) which is the theoretical limit based on the assumption that all the suction potential is used to supply liquid directly to the base of a spherical evaporating meniscus. The surface tension was evaluated at room temperature for the nonevaporating case and at the atmospheric saturation temperature for the evaporating case. The scatter in the individual points results from taking the difference between relatively large numbers that are difficult to measure. The results clearly demonstrate that the evaporating meniscus is stable and that a change in its profile causes the flow of fluid to its base. An additional curvature gradient between the base of the meniscus and the liquid-solid-vapor interline, which was not measured in these experiments, results in fluid flow from the base to the point of evaporation. The deviation from the theoretical curve at the higher evaporation rates indicate that additional viscous losses were present. These could be due to recirculation resulting from a Maragoni effect. The highest heat flow rate of 0.160 W represents a heat flux of 5.97×10^5 W/m^2 based on the cross-sectional area of the pore.

In Fig. 6 the evaporation rate calculated using equation (5) is plotted versus the evaporation rate calculated using equation (9). These results demonstrate that a heat balance was obtained and also indicate that sputtering was minimal at these levels. Some preliminary, but incomplete, tests at higher evaporation rates demonstrated that a sputtering region is present before the meniscus becomes unstable.

In Fig. 7, the results for two runs at the same conditions are presented with the solid line showing the best fit to the data. These results indicate that a change in the process occurs at higher rates of evaporation. They also show the sensitivity of the evaporation rate to the power input at higher power inputs.

The above experimental design allows the heat sink capability of

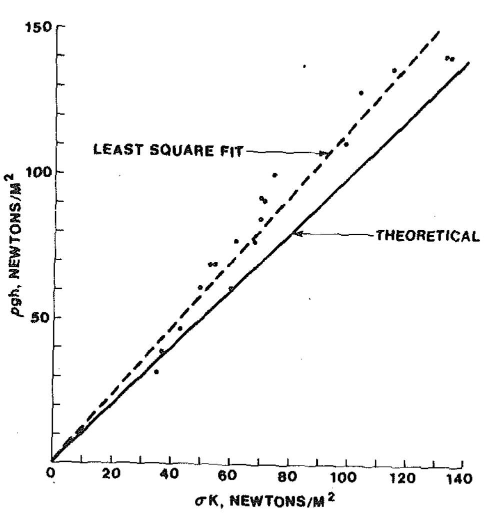

Fig. 3 Measured hydrostatic head versus measured curvature for the isothermal case

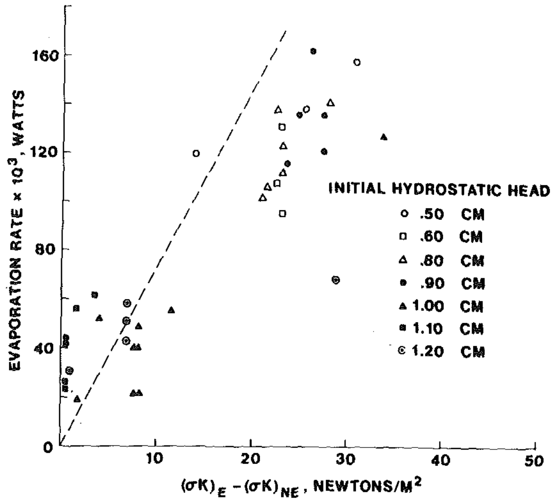

Fig. 5 Evaporation rate versus meniscus suction potential

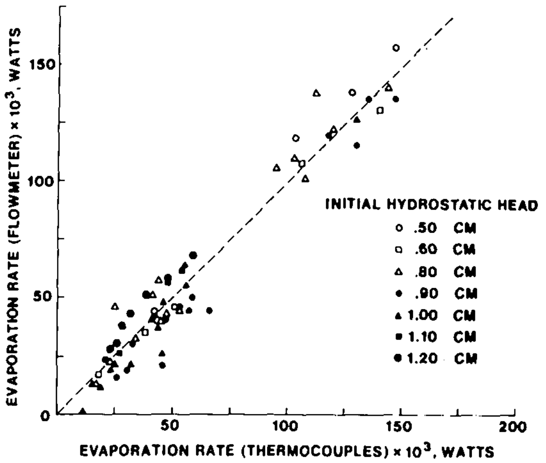

Fig. 6 Evaporation rate based on flowmeter versus evaporation rate based on temperature measurements

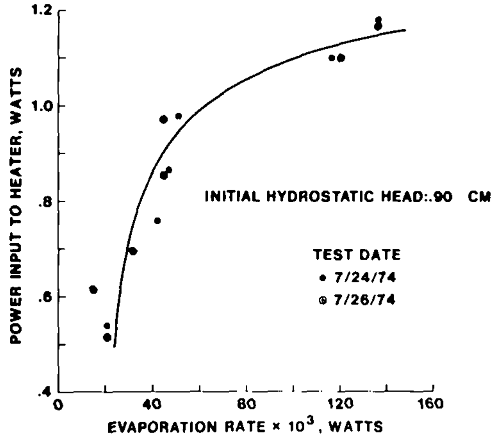

Fig. 7 Power input versus evaporation rate for an initial hydrostatic head of 0.9×10^{-2} m

a stable evaporating meniscus to be measured. It is anticipated that more extensive studies of this system will lead to greater use of the evaporating meniscus. Since the evaporating meniscus is stable for a range of evaporation rates, a porous media heat exchanger can be designed to advantageously use a fixed location for the surface of evaporation. In this way, the optimum paths for the flow of liquid and vapor can be selected.

5 Conclusions

1 An experimental technique to measure the suction potential and stability of an evaporating meniscus as a function of the evaporation rate and hydrostatic head was developed.

2 The evaporating meniscus at the exit of a capillary tube was found to be stable over a wide range of evaporation rates and hydrostatic heads.

3 Fluid flow to the base of a stable evaporating meniscus is caused by a change in its curvature.

6 Acknowledgment

The authors wish to acknowledge the support of the National Science Foundation (Grant No. GK 43116) and the Naval Underwater Systems Center, New London, Connecticut. This paper was presented at the 68th annual AIChE meeting, Los Angeles, Calif., Nov. 16–20, 1975.

References

1 Bressler, R. G., and Wyatt, P. W., "Surface Wetting Through Capillary Grooves," JOURNAL OF HEAT TRANSFER, TRANS. ASME, Series C, Vol. 92, 1970, pp. 126–132.

2 Wayner, P. C., Jr., and Coccio, C. L., "Heat and Mass Transfer in the Vicinity of the Interline Region of a Meniscus," *AIChE Journal*, Vol. 17, 1971, pp. 569–574.

3 Renk, F., and Wayner, P. C., Jr., "The Measurement of Fluid Flow and Heat Transfer in an Evaporating Meniscus," *Proceedings of the Fifth International Heat Transfer Conference*, Vol. 5, 1974, pp. 252–256.

4 Potash, M. L., Jr., and Wayner, P. C., Jr., "Evaporation From a Two Dimensional Extended Meniscus," *International Journal of Heat and Mass Transfer*, Vol. 15, 1972, pp. 1851–1863.

5 Edwards, D. K., Balakrishnan, A., and Catton, I., "Power Law Solutions for Evaporation From a Finned Surface," JOURNAL OF HEAT TRANSFER, TRANS. ASME, Series C, Vol. 96, 1974, pp. 423-425.

6 Ludviksson, V., and Lightfood, N., "Deformation of an Advancing Meniscus," *AIChE Journal*, Vol. 14, 1968, pp. 674-677.

7 Huh, C., and Scriven, L. E., "Hydrodynamic Model of Steady Motion of a Solid/Liquid/Fluid Contact Line," *Journal of Colloid and Interface Science*, Vol. 35, 1971, pp. 85–101.

H. Buchberg
I. Catton
D. K. Edwards

Energy and Kinetics Department,
School of Engineering,
University of California,
Los Angeles, Calif.

Natural Convection in Enclosed Spaces—A Review of Application to Solar Energy Collection

A useful solar-thermal converter requires effective control of heat losses from the hot absorber to the cooler surroundings. Based upon the theory and some experimental measurements it is shown that the spacing between the tilted hot solar absorber and successive glass covers should be in the range 4–8 cm to assure minimum gap conductance. Poor choice of spacing can significantly affect thermal conversion efficiency, particularly when the efficiency is low or when selective black absorbers are used. Recommended data for gap Nusselt number are presented as a function of the Rayleigh number for the high aspect ratios of interest in solar collector designs. It is also shown that a rectangular cell structure placed over a solar absorber is an effective device to suppress natural convection, if designed with the proper cell spacing d, height to spacing ratio L/d and width to spacing ratio W/d needed to give a cell Rayleigh number less than the critical value.

Introduction

A major concern of solar collector designers is the reduction of heat losses from the hot solar absorber to the cooler environment. Designers seek economic alternatives to minimize these losses, which result from conductive-convective and thermal radiative heat exchanges. In the case of fixed flat-plate collectors, which have the advantages of being able to operate during cloudy or hazy days with diffuse solar radiation and being capable of integration into a roof or wall structure, the designer may consider the employment of one or more transparent covers with or without a honeycomb core to limit convection and radiation heat losses. It is the purpose of this paper to summarize natural convection heat transfer developments applicable to the design of solar collectors and to illustrate their applicability.

Two geometries of widespread applicability are singled out in this paper: (1) the case of two parallel flat plates tilted and heated from below, and (2) the case of a honeycomb structure located between the two plates. In the first case it will be shown that conduction-convection heat losses decrease with an increase in plate spacing to reach an apparent minimum just as natural convection is initiated, then increase thereafter until a maximum is reached, and then fall gradually with further increase in plate spacing to reach values below the conduction minimum. The spacings at which the apparent minimum and maximum occur, change greatly with temperature difference and somewhat with temperature level. Solar heat collectors reported in the literature appear to be constructed in ignorance of this behavior, and even recommended design parameters seem erroneous in this respect. In the second case it will be shown that suppression of natural convection in honeycomb structures depends very critically upon the cell dimension as well as the cell dimension ratios. There have been reported in the literature failures of honeycomb to achieve desired results because of improper specification of the critical dimensional requirements. Also, the wall radiation effect upon initiation of natural convection appears to be neglected.

It will also be shown that a partial vacuum serves well to reduce convective heat losses.

Natural Convection Above Flat Plate Solar Absorbers

Use of Transparent Covers. Unless solar energy is collected at temperatures near ambient temperature, one or more transparent covers are used to reduce convective and thermal radiative heat losses. These losses are reduced when the temperature of the surface which finally interfaces with the surroundings is lowered. To maximize solar irradiance, flat plate collectors are tilted up from the horizontal plane and faced south in the northern hemisphere and north in the southern

---

Contributed by the Heat Transfer Division and presented at the Winter Annual Meeting, New York, N. Y. November , 1974, of THE AMERICAN SOCIETY OF MECHANICAL ENGINEERS. Revised manuscript received by the Heat Transfer Division December 29, 1975. Paper No. 74-WA/HT-12.

hemisphere. For year-round collection, the tilt angle τ, measured from the horizontal, is generally made equal to the latitude angle ϕ; but it may be as much as $\phi + 20$ deg or as little as $\phi - 20$ deg to favor winter or summer solar collection, respectively. Angles of tilt up to about 60 deg are of particular interest. Larger angles may be useful in the extreme northern and southern latitudes. The collector is generally several feet in extent, both up the slope (dimension d) and horizontally in the east-west direction (dimension W). Transparent covers are placed parallel to the absorber at a height L above it as shown in Fig. 1 to provide an insulating gap and protection from weathering. It has been customary to make the magnitude of L approximately 1 to 2.5 cm. Hottel [1][1] explained . . . "That experiment had shown that increasing the air space beyond ½ in. (1.27 cm) had little effect on reducing the conductance." Typically, a single glass cover is used with a nonselective black absorber for collection temperatures of approximately 25°C above ambient, or with a selective black absorber for collection temperatures of approximately 50°C above ambient. Additional transparent covers provide more thermal insulation for higher collection temperatures with either type of absorber, and are typically spaced 0.6–2.5 cm above the first one.

Natural convection over flat plate solar absorbers thus typically occurs in enclosed spaces of high aspect ratio (AR) d/L and high horizontal aspect ratio W/L with the $d \times W$ heated surface below and tilted up to as much as 60 deg from the horizontal. The cooled flat surface (cover glass) is above and parallel to the heated surface with temperature difference up to perhaps 80°C.

High Aspect Ratio (d/L) Spaces. In the vertical slot, there exists a base flow circulation up the heated surface and down the cooled one. The base flow becomes unstable as the Rayleigh number (Ra) increases with increasing space L or temperature difference. Ostrach [2] reviews this case in detail. A tilted air layer will exhibit such a base unicellular flow at any nonzero angle of inclination from the horizontal. For Ra > critical value, the results of Catton, et al. [3] can be used to determine the Nusselt number for the unicellular flow. They indicate that the contribution to heat transfer by the unicell will always be negligible for aspect ratios (20–200) of interest in solar collector design.

When the heated surface lies below the cooled one, as is the case in horizontal or tilted flat plate solar collectors, a (multi) cellular convection arises for high aspect ratio spaces when Ra exceeds $1708/\cos\tau$. It is this flow which significantly augments the heat loss from the hot surface.

Hart [4], in order to get a general idea of the motions possible in the tilted geometry, ran a series of flow visualization experiments in water.

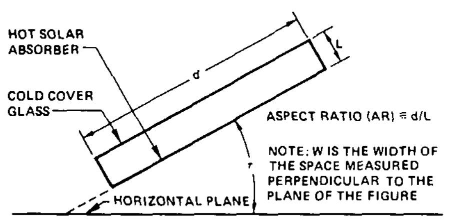

Fig. 1 Dimensions of a high aspect ratio enclosed space

For AR ≥ 25 and τ as high as 70 deg (20 deg from the vertical) and at Ra somewhat above critical, he observed longitudinal rolls with axes directed up slope, that is, a multicellular convection much like that for $\tau = 0$. As Ra was further increased, a "roll-dominated turbulence" was witnessed. At somewhat higher tilts, transverse travelling waves oriented across the slope are the first instabilities in the transverse unicellular convection. Hart presented theoretical results indicating that as Pr and/or AR are lowered, the tilt τ at which the longitudinal- or horizontal-like convection switches to transverse or vertical-like convection decreases. Arnold, et al. [5, 6] observed an apparent change in heat transfer mechanism at $\tau = 63$ deg for AR = 12 and $\tau = 58$ deg for AR = 6, both for relatively large Pr, since silicone oils were used. The apparent change manifests itself as a local minimum in Nu versus τ at constant Ra. Ozoe, et al. [7, 8, 9] indicate similar behavior for AR = 15.5 and 1, using air as well as higher Pr fluids.

Clever [10] showed that when the instability in an infinite Prandtl number fluid is in the form of longitudinal convection rolls in an inclined layer, it is theoretically correct to replace g in the critical Rayleigh number by $g \cos\tau$. He went on to show that the Nusselt number-Rayleigh number relationship for the horizontal layer would apply and did correlate data when Rayleigh number was modified by the replacement of g with $g \cos\tau$. Hollands, et al. [11] have recently shown that on theoretical grounds the infinite Prandtl number constraint may be relaxed, which confirms the experimental evidence. Thus, there exists a basis for scaling, by means of $g \cos\tau$ the extensive data for the horizontal layer, to the inclined layer case for large values of aspect ratio and values of τ to 60 deg.

New heat transfer data for inclined fluid layers, Ozoe, et al. [7], Hollands, et al. [11], and Arnold, et al. [6] have been obtained recently. It is of interest to examine a composite of these results and previous data. Fig. 2 presents a log-log plot of Nu versus Ra cos τ for $\tau = 0, 30, 45$, and 60 deg for natural convection across a confined fluid layer when the aspect ratio is large. In this paper the Nusselt number is defined as the ratio of the conductive-convective heat transferred to

---

[1] Numbers in brackets designate References at end of paper.

Nomenclature

a_e = equation (3)
b = equation (2)
C_L = convective gap conductance
d = spacing (up slope) or cell spacing
f = ratio of cell opening to solar absorber area
$F(a_e, b)$ = equation (5)
g = acceleration due to gravity
Gr = Grashof number
H_e = equation (4)
k = thermal conductivity
k_f = fluid thermal conductivity
k_w = wall thermal conductivity
L = height of enclosed space or gap
d/L = aspect ratio (AR)
Nu = Nusselt number
Pr = Prandtl number
G_s = solar irradiance
q_L = heat losses
q_u = solar power withdrawn or utilized
Ra = Rayleigh number $(g\beta\rho^2 c_p/k\mu)(\Delta T L^3)$
Ra_c = critical Rayleigh number
Ra_d = Rayleigh number based on cell spacing d, equation (7)
$S(a, b)$ = integration integral, equation (6)
t_w = wall half-thickness
$\bar{T}$ = mean absolute temperature in equation (4)
T_g = cover glass temperature
T_H = hot surface temperature
T_p = solar absorber plate temperature
ΔT = temperature difference between hot and cold surface
u_a = wind speed
W = width of space (E-W orientation)
W/d = horizontal aspect ratio
α_p = absorber solar absorptance
β = coefficient of thermal expansion
ϵ_p = absorber total hemispherical emittance
ϵ_w = wall total hemispherical emittance
η = solar collector efficiency
θ_s = incidence angle of the sun
ν = kinematic viscosity
τ = collector tilt angle (from the horizontal plane)
ϕ = latitude angle

the conductive heat transferred across a fluid layer of thickness L at an average temperature $(T_H - \Delta T/2)$. This ratio is equivalent to the ratio of an "effective " thermal conductivity to the thermal conductivity of the fluid layer at the average temperature.

Tabor [12] reviewed the literature on natural convection in enclosed fluid layers for the period up to 1955 and concluded that the U. S. National Bureau of Standards data [13] were the most reliable for solar collector design. The Tabor correlation of NBS air data for horizontal planes predicts values of Nu only slightly higher (3 percent or less) than the power law based on the Malkus-Catton-Edwards theory [14] and Silveston's [15] measurements including the Mull and Reiher air data. The correspondence of these three correlations is particularly good in the region $10^5 < \text{Ra} < 10^6$. It should be noted that the Hollands, et al., and O'Toole correlations predict lower values of Nu in this region. The O'Toole correlation was pulled down by low Pr Mercury data. The lower Goldstein and Chu [16] air data may be explained in large part by an aspect ratio effect. Arnold, et al. [6] indicate about a 6 percent increase in Nu when increasing from AR = 2 to 12 at Ra $\simeq 10^6$ for horizontal layers. In the region $1708 < \text{Ra} < 3000$ all investigators are in close agreement. In the region $3000 < \text{Ra} < 10^5$, the 70 data points of Edwards practically coincide with the O"Toole and Silveston [17], and Hollands, et al. [11] correlations. The Ozoe, et al., air data tend to fall above the correlations. Dropkin and Somerscales [18] have also presented data for natural convection in inclined liquid layers for Ra > 10^5.

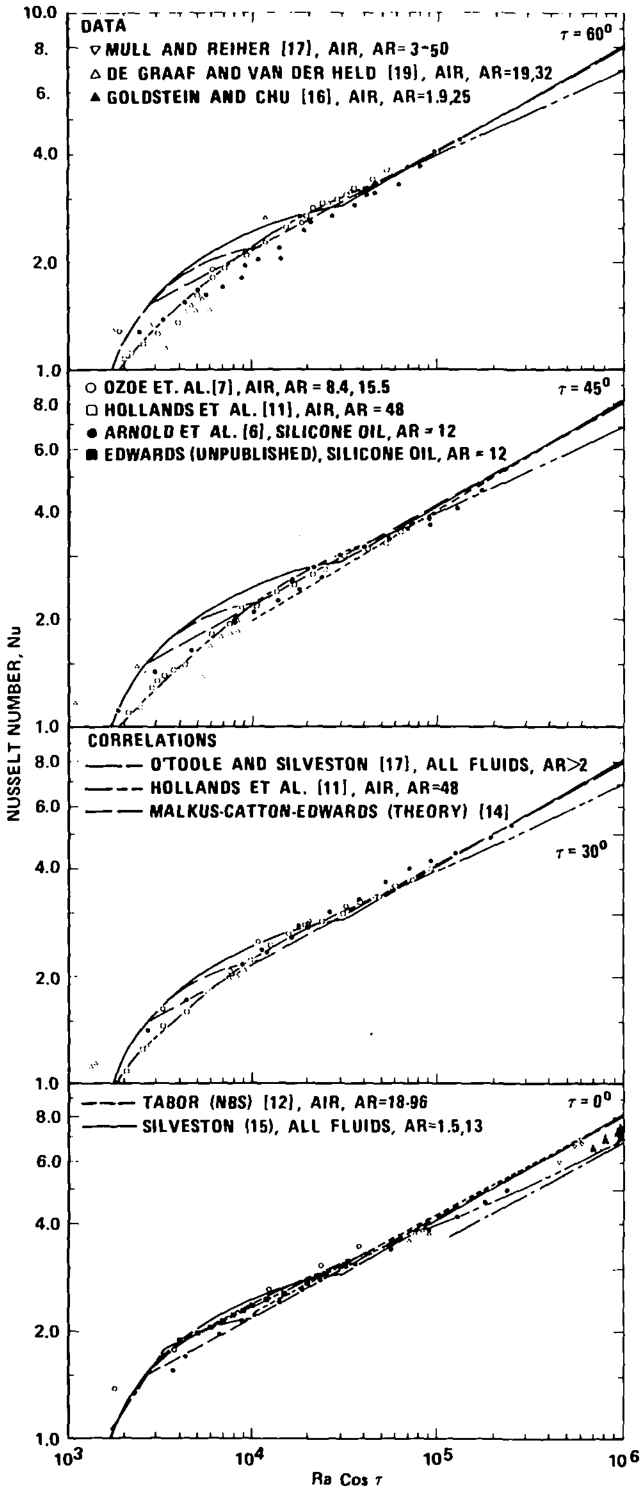

Fig. 2 Enclosed space heat transfer, higher aspect ratio (d/L), τ = 0, 30, 45, and 60 deg

Examination of data plotted as Nu versus Ra cos τ indicates that a three-region correlation based on the Mulkus-Catton-Edwards first mode, *the O"Toole and Silveston central region correlation and the* Catton power law fit to the theory would result in conservative design. In light of the recent inclined layer data, Hollands, et al. [11], Ozoe, et al. [7], and Arnold, et al. [6], a two-region correlation, by extending the high Ra power law fit to smaller Ra until it intersects the first-mode theoretical curve at Ra = 2500, appears to be useful. Fig. 2 indicates that as τ increases from 30 deg, the two region correlation becomes an upper bound on the new data. Another alternative is to use the Hollands, et al., correlation for all angles of inclination $\tau \leq 60$ deg. This correlation appears to fit well the data of Hollands, et al. [11] and de Graaf and van der Held [19]. The Tabor correlation of the $\tau = 45$ deg NBS data appears to be a reasonable fit of all of the data but on the lower bound through the central Ra region. In addition, this correlation has the weakness of being limited to $\tau = 45$ deg.

Recommended Gap Conductance (C_L) Calculation. The conductive-convective gap conductance (C_L) defined as (k/L) Nu depends on L, ΔT, and T_H. Three alternatives for calculating Nu were investigated.

1 three-region correlation

$$\text{Nu} = 1 + 1.446\left(1 - \frac{1708}{\text{Ra}\cos\tau}\right)^{\bullet} \quad \text{for } 1708 < \text{Ra}\cos\tau < 5900$$

$$\text{Nu} = 0.229\,(\text{Ra}\cos\tau)^{0.252} \quad \text{for } 5900 < \text{Ra}\cos\tau < 9.23 \times 10^4$$

$$\text{Nu} = 0.157\,(\text{Ra}\cos\tau)^{0.285} \quad \text{for } 9.23 \times 10^4 < \text{Ra}\cos\tau < 10^6$$

2 two-region correlation

$$\text{Nu} = 1 + 1.446\left(1 - \frac{1708}{\text{Ra}\cos\tau}\right)^{\bullet} \quad \text{for } 1708 < \text{Ra}\cos\tau < 2500$$

$$\text{Nu} = 0.157\,(\text{Ra}\cos\tau)^{0.285} \quad \text{for } 2500 < \text{Ra}\cos\tau < 10^6$$

3 Hollands, et al., correlation

$$\text{Nu} = 1 + 1.44\left[1 - \frac{1708}{\text{Ra}\cos\tau}\right]^{\bullet}\left(1 - \frac{(\sin 1.8\,\tau)^{1.6}\,1708}{\text{Ra}\cos\tau}\right) + \left[\left(\frac{\text{Ra}\cos\tau}{5830}\right)^{1/3} - 1\right]^{\bullet}$$

Note: dotted brackets go to zero when negative.

The thermal conductivity k is evaluated for an average gap temperature $(T_H - \Delta T/2)$.

Typical design curves for a tilted ($\tau = 40$ deg) collector are shown in Fig. 3 for each alternative calculational procedure. C_L is given as a function of L for values of ΔT between 5.56°C and 55.6°C when $T_H = 70$°C. The sharply decreasing curve on the left represents the conduction regime. When convection initiates for a particular ΔT, there is a sudden increase in C_L which reaches a peak value at some value of L. With further increase in L the gap conductance decreases and eventually drops below the previous minimum value. Because of space limitations, design curves are shown for only single values of T_H and τ. As T_H increases C_L peaks at increasing values of L, and

Table 1 Effect of spacing *L on collector performance*

Double Glazed Nonselective Absorber

$\alpha_p = 0.95$, $\epsilon_p = 0.95$

$\tau = 40^o$

L_2, cm	L_1, cm	Collector Efficiency, % *η_1	η_2	η_3
0.952	1.91	42.8	43.0	43.2
5.08	5.08	43.8	43.8	44.1
Area Reduction, %		2.3	1.9	2.1

$\tau = 0^o$

L_2, cm	L_1, cm	Collector Efficiency, % η_1	η_2	η_3
0.952	1.91	42.6	42.8	42.6
5.08	5.08	43.4	43.4	43.8
Area Reduction, %		1.9	1.4	2.8

Single Glazed Nonselective Absorber

$\alpha_p = 0.95$, $\epsilon_p = 0.95$

$\tau = 40^o$

L_1, cm	Collector Efficiency, % η_1	η_2	η_3
1.59	29.7	30.4	30.1
5.08	31.5	31.5	32.0
Area Reduction, %	6.1	3.6	6.7

$\tau = 0^o$

L_1, cm	Collector Efficiency, % η_1	η_2	η_3
1.59	29.1	29.8	29.2
5.08	31.0	31.0	31.6
Area Reduction, %	6.5	4.0	8.2

Single Glazed Selective Absorber

$\alpha_p = 0.91$, $\epsilon_p = 0.06$

$\tau = 40^o$

L_1, cm	Collector Efficiency, % η_1	η_2	η_3
1.59	49.1	50.5	50.8
5.08	53.2	53.2	54.6
Area Reduction, %	8.4	5.3	7.5

$\tau = 0^o$

L_1, cm	Collector Efficiency, % η_1	η_2	η_3
1.59	48.0	49.3	47.6
5.08	52.0	52.0	53.6
Area Reduction, %	8.3	5.5	12.6

*η_1 based on 3-region correlation

η_2 based on 2-region correlation

η_3 based on Hollands et al. correlation

the peak value drops slightly for a specified ΔT. Also as τ decreases toward zero tilt, for specified values of T_H and ΔT, the peak value of C_L increases and occurs at slightly lower values of L. To avoid peak values of gap conductance, the designer should use a value of L sufficiently beyond the occurrence of conductance peaks for the highest angle of tilt and for the highest absorber operating temperature.

It is interesting to note that the three-region correlation predicts the highest peak values of C_L and the Hollands, et al., correlation the lowest, but displaced to the right with a steeper drop in C_L beyond the peak. Because T_H and ΔT usually vary during solar collector operation, it appears that from a thermal performance standpoint, values of L in the range 4–8 cm are indicated, regardless of which correlation is used to calculate C_L. It is apparent, from the behavior illustrated in Fig. 3, how limited experimental results may lead to an erroneous conclusion regarding the best spacing L to minimize heat losses due to natural convection.

Effect of Spacing (*L*) on Collector Performance. To determine the effect of spacing L on solar collector performance, calculations were made for a single and double-glazed nonselective black and single-glazed selective black flat plate solar collector. The same operating conditions were imposed for each spacing; namely, inlet fluid temperature above ambient air = 63.9°C; solar irradiation = 789 W/m^2; water, mass flow rate = 227 kg/h.

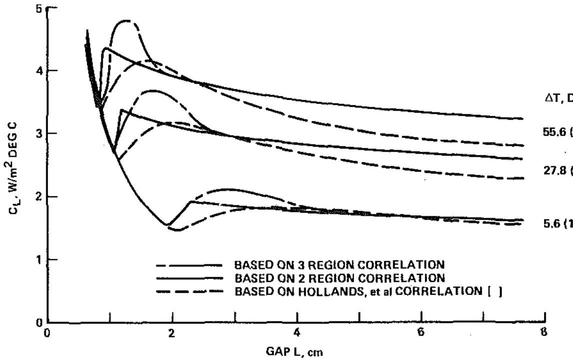

Fig. 3 Gap conductive-convective conductance C_L for T_H. = 70°C and τ = 40 deg

A reiterative steady-state analysis was employed to determine the glazing temperatures, absorber temperature, thermal power withdrawn and collector efficiency η. Each of the alternatives for C_L given in Fig. 3 were tested. The results given in Table 1 indicate that the dimension L is most important when a selective black absorber with low emittance is used. For the horizontal collector increasing L from 1.59 to 5.08 cm would reduce the collector area requirement from 5.5 to 12.6 percent, depending upon the correlation used. Tilting the collector 40 deg increases the efficiency slightly for the same solar irradiance. Increasing the gap dimensions for the single and double-glazed black collectors reduced the area requirements by 4–7 percent and about 2 percent, respectively.

If a solar collector was designed to operate at some value of τ and at fixed values of T_p and ΔT, one could specify dimension L corresponding to the "local" minimum C_L; however, collectors are usually designed to be operated at different locations under a variety of environmental conditions and for different service specifications. The angle of tilt, T_p and ΔT may vary widely. To predict the full impact of a particular value of L, one should sum the useful energy collected over an operating season. The best design approach, when it is cost effective, is to avoid the region of the "local" minimum and maximum values of C_L by using a sufficiently large value of L, say on the order of 4–8 cm.

Suppression of Convection by Cellular Structures

Use of Cellular Structures. Francia [20] recommended the use of honeycomb material over a solar absorber to reduce reradiation. He employed 15 mm dia glass tubes with an $L/d = 17$ in a tracking collector equipped with a six-to-one conical concentrator. Subsequent work was reported by Perrot, et al. [21], Hollands [22], and Charters [23]. Buchberg, et al. [24] indicated that a *rectangular* cellular structure with the long side of the rectangle running east-west was superior for fixed, flat-plate solar collectors because of higher solar transmittance to the absorber. Their cells were L high between the absorber surface and cover glass; W wide in the east-west direction, and d between the tilted side walls. Their first study indicated a broad optimum in cell configuration for L/d between 3–8 for a specified W/d of 3.4, and they recommended d = 0.53 cm for a 100°C collection temperature. They pointed out that, as an alternative to selectively transmitting glass, one could employ a selectively reflecting material such as an aluminized plastic-undercoated paper overcoated with solar-clear, infrared-opaque resin. Subsequently, they reported [25] actual performance data for such honeycomb $d = 0.53$ cm, $L/d = 7.11$, and $W/d = 3.4$ and two other cell configurations. Measurements showed heat losses q_L by both radiation and convection of 467 W/m^2 for an absorber temperature $T_p = 107°$C and cover glass temperature $T_g = 43°$C under solar irradiation $G_s = 962$ W/m^2 with the sun 11 deg off normal at noon and a wind speed $u_a = 4.7$ m/s; and $q_L = 391$ W/m^2 with $T_p = 72°$C, $T_g = 47°$C, and $G_s = 704$ W/m^2 with the $\theta_s = 46$ deg also at noon and $u_a = 2.3$ m/s.

Lalude and Buchberg [26] studied a transpired rectangular honeycomb system and recommended values of L/d between 4 and 5 for $T_p \leq 80°$C, $L/d = 6$–8 for $80°\text{C} \leq T_p \leq 95°$C, and $L/d \simeq 10$ for $T_p = 95°$C with $W/d = 6$.

The very rapid increase in Nu, once cellular convection (a roll in the $W \times L$ plane) initiates, dictates that such honeycomb solar collector covers be designed to suppress this mode of convection. The creeping convection, a roll in the $d \times L$ plane, has small effect for the small d/L aspect ratios employed.

Suppression of Cellular Convection. In the honeycomb solar collector with typical tilts of $\tau = 30$–40 deg, warm light air close to the absorber lies under cold heavy air close to the cover glass. There is thus a tendency for a perturbation to induce a warm upflow and a cold downflow. As mentioned previously for the case of a rectangle, the most damaging form of motion is a roll in the W-L plane. In the case of a circular or nearly circular cell cross section, the roll takes place around a diameter. Whether the three-dimensional disturbance grows into steady convection or is damped is governed by a Rayleigh number which is a ratio of the heat convection feeding the disturbance divided by the heat conduction damping the disturbance times the buoyant work liberated in the motion divided by the viscous work dissipated by it [27]. Both conduction within the walls and radiation from hot wall area to cold wall area (through transparent air) serve to modify the boundary conditions on the fluid so as to promote conduction in the fluid draining energy from the disturbance. If the critical Rayleigh number for a particular mode of cellular motion to be activated exceeds the actual Rayleigh number pertaining to the solar collector, that mode of cellular motion will be effectively suppressed.

The initiation of natural convection in enclosed spaces has been treated theoretically by Ostroumov [28] and Yih [29] for the infinitely tall circular cell and Ostrach and Pnueli [30] for arbitrary planform but perfectly conducting side walls. Catton and Edwards [31] reported measurements for side walls which approach being perfectly adiabatic or perfectly conducting. They subsequently developed an approximate theory for finite cylinders [32]. Wooding [33] treated the problem of initiation for the slot with adiabatic side walls.

The side walls used in solar collectors are neither perfectly insulating nor perfectly conducting. Ostroumov [28] gave the first treatment of arbitrarily conducting walls for an infinitely tall circular cylinder. Edwards [34] treated the slot planform for arbitrarily conducting side walls. Edwards and Sun [35] extended this treatment to the rectangular planform, deriving a simple, closed-form approximate solution, and presented experimental verification. Additional experimental verification was provided by Heitz and Westwater [36]. Sun and Edwards [37] also treated the circular cylinder of finite height with arbitrarily conducting side walls. Catton [38, 39] treated the rectangular enclosure more exactly. His comparison with their data was no better than that with the approximate relation. For this reason, and by virtue of its ease in use, the approximate relation of Edwards and Sun is recommended for design.

Edwards and Sun [40] predicted the effect of wall radiation mentioned in the foregoing and analyzed it for the circular cylinder. Its effect on initiation in the slot was also analyzed and experimentally verified [35]. The effect may, in theory, triple the initiation Rayleigh number in a circular cylinder, and it is larger for the slot. In practice, wall radiation increases the initiation Rayleigh number by a factor of two by tending to damp wall temperature perturbations just as wall conduction does. Hollands [41] reported that a thin-walled honeycomb gave experimental values of critical Rayleigh number intermediate to theoretical values for a perfectly conducting wall and an adiabatic wall, thus supporting the wall radiation effect, although the data were not compared with predictions of the magnitude.

The influence of tilt upon natural convection in honeycomb has received some attention. Sun [42] measured experimentally, using silicone oils, Nu versus Ra_L for four rectangular honeycombs, all with L approximately 18.8 mm and L/d approximately 4 but with W/d values of 2, 4, 8.6, and 15.2. Angles of tilt of 0, 15, 30, and 45 deg were investigated in the Nu range between 1 and 2. A value of critical Rayleigh number per se was not observed for the tilted cells, presumably because of the transverse natural circulation, a roll in the $d \times L$ plane. At a Rayleigh number equal to the experimentally observed critical value for the untilted cells, the Nusselt number for the $\tau = 45$ deg tilted cells was observed to be below 1.25. At higher values of Rayleigh number, the curves of Nu for the tilted cells merged with or crossed under those for the untilted cells. Additional data obtained by Arnold at tilts of 0, 15, 30, 60, and 90 deg suggest that Nu at a value of Ra equal to the critical value for $\tau = 0$ deg is 1.25 or less when $\tau \neq 0$ deg. The untilted cell Nu versus Ra curve lies approximately 10 percent above or below the tilted cell results in the vicinity of Nu = 2 for tilts up to 60 deg. At $\tau = 90$ deg the untilted honeycomb curve lies considerably above (about 40 percent at Nu = 2) that for the tilted honeycomb. Cane et al. [43] have presented air data for a 25.4 mm square honeycomb with $L/d = 3$ with tilts of 0, 30, and 60 deg. At an initiation Rayleigh number of approximately 1.2×10^5, Nu was approximately 1.25, and in the vicinity of Nu = 2 all three curves were within 10 percent of one another.

Recommended Design-Calculation Procedure. A design value of $\Delta T/L$ in the honeycomb cover material is found from the acceptable losses through the cover, accounting for both radiation and conduction. The radiation problem is described, for example, by Edwards and Tobin [44], Edwards and Bertak [45], and Amar and Edwards [46], as well as Buchberg, Lalude, and Edwards [25]. For design values of $\Delta T/L$ and L/d there is a maximum d which can be employed fixed in part by the relation

$$\text{Ra}_d = 12[1 + 2H_e](a_e{}^2 + b^2)^2/a_e{}^2 \tag{1}$$

where

$$b \doteq (\pi + 0.85)(d/L) \tag{2}$$

$$a_e{}^2 = b^2 + (\pi d/W)^2[1 + 1.260\,(d/W) + 2.132\,(d/W)^2 + \ldots] \tag{3}$$

$$H_e = (k_w t_w/k_f d) + (4\epsilon_w \sigma \bar{T}^3 d/k_f)F(a_e, b) \tag{4}$$

$$F(a_e, b) = \frac{1 - S(a_e, b)}{[1 - (1 - \epsilon_w)S(a_e, b)][a_e{}^2 + b^2]} \tag{5}$$

$$S(a_e, b) = \int_{-\infty}^{+\infty} \int_{-\infty}^{+\infty} \frac{\cos b\zeta \cos a\xi}{\pi[\zeta^2 + \xi^3 + 1]^2}\, d\xi d\zeta \tag{6}$$

The cell dimensions d, W, and L have been previously defined. The quantity k_w is wall conductivity, t_w is wall half-thickness, k_f is fluid conductivity, ϵ_w is wall emissivity, σ is the Stefan-Boltzmann constant in the radiation law, T is the mean absolute temperature, and $S(a_e, b)$ is the radiation integral tabulated in [35]. The remaining relation fixing d to $\Delta T/L$ is

$$\text{Ra}_d \equiv \frac{g\beta(\Delta T/L)d^4}{\nu^2}\,\text{Pr} \tag{7}$$

where β is the fluid expansion coefficient, the reciprocal of absolute temperature for an ideal gas, ν is kinematic viscosity of the fluid and Pr is Prandtl number.

To arrive at a working curve as is shown in Fig. 4, one proceeds backwards by choosing d, along with W/d, L/d, $\bar{T}$, ϵ_w, $k_w t_w$, and the properties $g\beta/\nu^2$, Pr, and k_f. Then one finds b, $a_e{}^2$, and $S(a_e, b)$ from equation (6), noting that $S(a, b) = S(b, a)$. Then there are found $F(a_e + b)$, H_e, and finally Ra_d. From the value of Ra_d and the chosen value of d together with the properties one finds $\Delta T/L$ as shown in Fig. 4. In this procedure the relatively minor influence of tilt for $\tau \leq 60$ deg is neglected. The value of d is thus that which gives Nu $\doteq$ 1 for the untilted collector and Nu $\leq$ 1.25 for the tilted one.

Note in the graph that rather small values of d are mandatory. This fact explains Charters' negative results [23] with $d = 1.0$ in. and

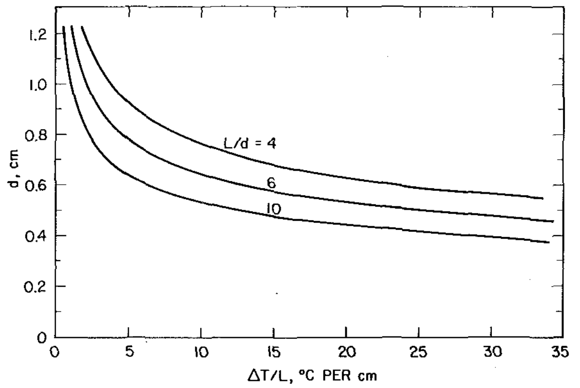

Fig. 4 Maximum cell spacing d to suppress convection as a Function of L/d and $\Delta T/L$ for a fixed $W/d = 6$

Buchberg, et al.'s positive experience [25] with $d = 0.21$ in. (and a smaller value of $W/d = 3.4$ than the value, $W/d = 6$, used for Fig. 4).

Design Recommendations

Designers of solar collectors have three main options for minimizing conduction-convection losses across enclosed spaces between a hot solar absorber and one or more cover glasses. One is to make the spacing large enough (4–8 cm) to reduce somewhat the convective gap conductance for the absorber temperatures and temperature differences encountered during collector operation. The increase in L from 1 cm to 4–8 cm requires additional housing material, which for larger area collectors would probably be an insignificant cost factor. Another problem to be considered is the increased edge shadow for large solar incidence angles. Again, this effect is generally insignificant in a large area system and can be offset by lining the vertical edge surface with a reflective foil.

The second option is to use a honeycomb structure of proper shape and dimensions in the space. While this step practically eliminates the effect of natural convection on the gap conductance, it, too, is not taken without some penalty. Aside from the additional cost, the honeycomb walls increase the effective thermal conductivity of the space so that it becomes important to use thin wall structures of low thermal conductivity. The area of honeycomb cell opening (for the recommended rectangular structures) per unit solar absorber area is given by

$$f = \left(\frac{1}{1 + 2t_w/d}\right)\left(\frac{1}{1 + 2t_w/W}\right)$$

It is recommended that for the values of d and W used, the wall thickness $2t_w$ be chosen to obtain a value of f not less than about 0.9. It should be pointed out that an important consideration in the choice of a rectangular cell shape is the need to maximize the solar transmittance of the honeycomb structure and to minimize its effective emittance of infrared radiation originating at the hot absorber plate.

As a third option, the designer may consider using vacuum to reduce convective heat transfer losses from solar collectors. The use of partial vacuum to prevent the initiation of natural convection in spaces between a hot absorber and cover glass is an interesting alternative in design, particularly for cylindrical absorbers and glazings which can most easily support the pressure difference and are perhaps easiest to seal. The concept usually employed, e.g., Speyer [47], is to use a sufficiently high vacuum that free molecule conduction is reached so that effective conductivity of the gas is greatly reduced. However, well before the free molecule conduction regime is reached, natural convection is virtually eliminated, as shown by Thompson and Sogin [48]. Since conduction in the gas, even at the ordinary atmospheric conductivity value, may be satisfactorily small, a partial vacuum may be used.

The effect of partial vacuum appears entirely through the density-squared term appearing in the numerator of the Rayleigh number. Recognizing that the density of an ideal gas varies linearly with pressure, the magnitude of ΔT which can be supported without convection rises with the inverse square of decreasing pressure for a given size L or d in the Rayleigh number and for a given critical value of Rayleigh number (for example, 1708). If 30°C is tolerable at 1 atm, 120°C is tolerable at ½ atm. (Of course, under these large ΔT conditions, the Boussinesq assumption that density difference is small compared to the density itself, must be viewed as only a crude approximation.)

Conclusions

1 The base or unicellular flow in high aspect ratio enclosed spaces above a hot solar absorber tilted up from the horizontal does not significantly affect heat transfer.

2 Any one of the three correlations examined for the determination of Nu for enclosed fluid layers is acceptable for solar collector design calculations.

3 To avoid having large free convection transfer in spaces above a hot solar absorber, the gap should be in the range of 4–8 cm. As suggested by Tabor [12], design tradeoffs including heat transfer across the space above the solar absorber, edge shading of the absorber, and cost ultimately determine the spacing to be selected.

4 The spacing of the cover glass above the solar absorber is particularly important when a selective black absorber with low emittance is used in a flat plate solar collector design.

5 A cellular structure placed over a solar absorber is an effective device to suppress natural convection, if designed with the proper L/d and W/d ratio and corresponding value of d calculated to give a cell Rayleigh number less than the critical value for $\tau = 0$ with account taken for conduction in the cell walls and radiation from hot to cold wall areas.

6 Natural convection above hot solar absorbers may be effectively suppressed with partial vacuum, the effect appearing entirely through the density-squared term in the Rayleigh number.

Recommendations For Research

Some uncertainty exists regarding the influence of the Prandtl number on heat transfer in enclosed fluid layers of large aspect ratio. Additional data for air in the range $1708 < \text{Ra} \cos \tau < 10^7$ would be useful for $0 < \tau < 90$. Data are particularly needed to assess the effect of leakage into and out of the enclosed space and the effect of nonisothermal surfaces. In the area of cellular apparatus, the wall-radiation-fluid-conduction effect needs further work. Equation (7) was evaluated for the infinite slot. End effects, in both the L and W directions, need to be elucidated and the effect of absorber plate emittance established. Work on the effects of intercell leakage through gaps between the honeycomb core and absorber and/or cover glass is underway at UCLA.

References

1 Hottel, Hoyt C., "Performance of Flat-Plate Solar Energy Collectors," *Space Heating With Solar Energy, Proceedings of a Course Symposium,* MIT Press, 1954, pp. 58–71.

2 Ostrach, S., "Natural Convection in Enclosures," *Adv. in Heat Transfer,* Vol. 8, 1972, pp. 161–227.

3 Catton, I., Ayyaswamy, P. S., and Clever, R. M., "Natural Convection Flow in a Finite, Rectangular Slot Arbitrarily Oriented With Respect to the Gravity Vector," *International Journal of Heat and Mass Transfer,* Vol. 17, 1974, pp. 173–184.

4 Hart, J. E., "Stability of the Flow in a Differentially Heated Inclined Box," *J. Fluid Mechanics,* Vol. 47, 1971, pp. 547–576.

5 Arnold, J. N., Bonaparte, P. N., Catton, I., and Edwards, D. K., "Experimental Investigation of Natural Convection in a Finite Rectangular Region Inclined at Various Angles from 0° to 180°, *Proceedings of the 1974 Heat Transfer and Fluid Mechanics Institute,* Stanford University Press, 1974, pp. 321–329.

6 Arnold, J. N., Catton, I., and Edwards, D. K., "Experimental Investigation of Natural Convection in Inclined Rectangular Regions of Differing Aspect Ratios," ASME Paper No. 75-HT-62, 1975.

7 Ozoe, H., Sayama, H., and Churchill, S. W., "Natural Convection in an Inclined Rectangular Channel at Various Aspect Ratios and Angles-Experimental Measurements," *International Journal of Heat and Mass Transfer,* in press.

8 Ozoe, H., Sayama, H., and Churchill, S. W., "Natural Convection in an Inclined Rectangular Channel Heated on One Side and Cooled on the Opposing Side," *International Journal of Heat and Mass Transfer*, Vol. 17, 1974, pp. 1209 1217.

9 Ozoe, H., Yamamoto, K., Sayama, H., and Churchill, S. W., "Natural Convection in an Inclined Square Channel," *International Journal of Heat and Mass Transfer*, Vol. 17, 1974, pp. 401–406.

10 Clever, R. M., "Finite Amplitude Longitudinal Convection Rolls in an Inclined Layer," JOURNAL OF HEAT TRANSFER, TRANS. ASME, Series C, Vol. 95, 1973, pp. 407–408.

11 Hollands, K. G. T., Unny, T. E., Raithby, G. D., and Konicek, L., "Free Convective Heat Transfer Across Inclined Air Layers," ASME Paper No. 75-HT-55, 1975.

12 Tabor, H., "Radiation, Convection, and Conduction Coefficients in Solar Collectors," *Bull. Res. Conc. of Israel*, Vol. 6C, 1958, pp. 155–176.

13 Housing Research Paper No. 32, "The Thermal Insulating Value of Airspaces," Housing and Home Finance Agency, U. S. Gov. Printing Office, Apr. 1954.

14 Catton, Ivan, "Natural Convection in Horizontal Layers," *The Physics of Fluids*, Vol. 9, No. 12, 1966, pp. 2521–2522.

15 Silveston, P. L., "Warmedurchgang in waagerechten Flussigkeitsschichten," *Forsch. Geg. Ing. Wes.*, Vol. 24, 1959, pp. 29–32, 56–69.

16 Goldstein, R. J., and Chu, T. Y., "Thermal Convection in a Horizontal Layer of Air," *Progress in Heat and Mass Transfer*, Vol. 2, 1969, pp. 55 75.

17 O'Toole, J. L., and Silveston, P. L., "Correlations of Convective Heat Transfer in Confined Horizontal Layers," Chemical Engineering Progress Symposium Series, V57, N32, 1961.

18 Dropkin, D., and Somerscales, E., "Heat Transfer by Natural Convection in Liquids Confined by Two Parallel Plates Which are Inclined at Various Angles With Respect to the Horizontal," JOURNAL OF HEAT TRANSFER, TRANS. ASME, Series C, Vol. 87, 1965, pp. 77–84.

19 de Graaf, J. G. A., and van der Held, E. F. M., "The Relation Between the Heat Transfer and the Convection Phenomena in Enclosed Plain Air Layers," *Appl. Sci. Res.*, Vol. 3, 1953, pp. 393–409.

20 Francia, G., "A New Collector of Solar Radiant Energy—Theory and Experimental Verification," United Nations Conference on New Sources of Energy, Rome, Italy, Paper F6, May 1961.

21 Perrot, M., et al., "Les Structures Cellulaires Antirayonnantes et Leurs Applications Industrielles," *Solar Energy*, Vol. 11, 1967, pp. 34–40.

22 Hollands, K. G. T., "Honeycomb Devices in Flat-Plate Solar Collectors," *Solar Energy*, Vol. 9, 1965, pp. 159 164.

23 Charters, W. W. S., and Peterson, L. F., "Free Convection Suppression Using Honeycomb Cellular Materials," *Solar Energy*, Vol. 13, 1972, pp. 353–361.

24 Buchberg, H., Edwards, D. K., and Lalude, O. A., "Design Considerations for Cellular Solar Collectors," ASME Paper No. 68-WA/SOL-3, 1968.

25 Buchberg, H., Lalude, O. A., and Edwards, D. K., "Performance Characteristics of Rectangular Honeycomb Solar-Thermal Converters," *Solar Energy*, Vol. 13, 1971, pp. 193-211.

26 Lalude, O. A., and Buchberg, H., "Design of Honeycomb Porous Bed Solar Air Heaters," *Solar Energy*, Vol. 13, 1971, pp. 223-242.

27 Edwards, D. K., Discussion of "Critical Rayleigh Numbers for Natural Convection of Water Confined in Square Cells With *L/D* from 0.5 to 8"," by Heitz, W. L., and Westwater, J. W., *Journal Heat Transfer*, TRANS. ASME, Series C, Vol. 93, 1971, pp. 195–196.

28 Ostroumov, G. A., "Free Convection Under Conditions of the Internal Problem," NACA TM 1407, 1958.

29 Yih, C. S., "Thermal Stability of Viscous Fluids," *Quarterly of Applied Mathematics*, Vol. 17, 1959, pp. 25–42.

30 Ostrach, S., and Pneuli, D., "The Thermal Stability of Completely Confined Fluids Inside Some Particular Configurations," JOURNAL OF HEAT TRANSFER, TRANS. ASME, Series C, Vol. 85, 1963, pp. 346-354.

31 Catton, I., and Edwards, D. K., "Effect of Side Walls on Natural Convection Between Horizontal Plates Heated From Below," JOURNAL OF HEAT TRANSFER, TRANS. ASME, Series C, Vol. 89, 1967, pp. 295-299.

32 Catton, I., and Edwards, D. K., "Initiation of Thermal Convection in Finite Right Circular Cylinders," *AIChE Journal*, Vol. 16, 1970, pp. 594–601.

33 Wooding, R. A., "Instability of a Viscous Liquid of Variable Density in a Vertical Hele-Shaw Cell," *J. Fluid Mechanics*, Vol. 7, 1960, pp. 501 515.

34 Edwards, D. K., "Suppression of Cellular Convection by Lateral Walls," JOURNAL OF HEAT TRANSFER, TRANS. ASME, Series C, Vol. 91, 1969, pp. 145 150; see also "Basic Heat Transfer Studies Related to the Use and Control of Solar Energy," UCLA Engineering Report 64 14, Mar. 1964.

35 Edwards, D. K., and Sun, W. M., "Prediction of the Onset of Natural convection in Rectangular Honeycomb Structures," Paper 7/62, 1970, International Solar Energy Society Conference, published by the Australian and New Zealand Section of the Society, 191 Royal Parade, Parkville, Victoria 3052.

36 Heitz, W. L., and Westwater, J. W., "Critical Rayleigh Numbers for Natural Convection of Water Confined in Square Cells with *L/D* from 0.5 to 8"," JOURNAL OF HEAT TRANSFER, TRANS. ASME, Series C, Vol. 93, 1971, pp. 188–195.

37 Sun, W. M., and Edwards, D. K., "Natural Convection in Cells With Finite Conducting Side Walls Heated From Below," Heat Transfer 1970, *Proceedings of the Fourth International Heat Transfer Conference*, Versailles, France, Paper NC 2.3, Elsevier Publishing Co., Amsterdam, Sept. 1970.

38 Catton, Ivan, "Effect of Wall Conduction on the Stability of a Fluid in a Rectangular Region Heated From Below," JOURNAL OF HEAT TRANSFER, TRANS. ASME, Series C, Vol. 94, 1972, pp. 446 452.

39 Catton, Ivan, "The Effect of Insulating Vertical Walls on the Onset of Motion in a Fluid Heated From Below," *International Journal of Heat and Mass Transfer*, Vol. 15, 1972, pp. 665–672.

40 Edwards, D. K., and Sun, W. M., "Effect of Wall Radiation on Thermal Instability in a Vertical Cylinder," *International Journal of Heat and Mass Transfer*, Vol. 14, 1971, pp. 15–18.

41 Hollands, K. G. T., "Natural Convection in Horizontal Thin-Walled Honeycomb Panels," JOURNAL OF HEAT TRANSFER, TRANS. ASME, Series C, Vol. 95, 1973, pp. 439-444.

42 Sun, W. M., "Effect of Arbitrary Wall Conduction and Radiation on Free Convection in a Cylinder," PhD dissertation, School of Engineering and Applied Science, University of California, Los Angeles, 1970.

43 Cane, R. L. D., Hollands, K. G. T., Raithby, G. D., and Unny, T. E., "Convection Suppression in Inclined Honeycombs," presented at the ISES 1975 Congress, UCLA, July 28–Aug. 1, 1975.

44 Edwards, D. K., and Tobin, R. D., "Effect of Polarization on Radiant Heat Transfer Through Long Passages," JOURNAL OF HEAT TRANSFER, TRANS. ASME, Series C, Vol. 89, 1967, pp. 132–138.

45 Edwards, D. K., and Bertak, I. V., "Imperfect Reflections in Thermal Radiation Transfer," *Progress in Astronautics and Aeronautics*, Vol. 24, 1971, pp. 143-165.

46 Amar, R. C., and Edwards, D. K., "Reflection and Transmission by Rough-Walled Passages," *Progress in Astronautics and Aeronautics*, Vol. 31, 1973, pp. 475–495.

47 Speyer, E., "Solar Energy Collection with Evacuated Tubes," ASME Paper No. 64-WA/SOL-2, 1964.

48 Thompson, H. A., and Sogin, H. H., "Experiments on the Onset of Thermal Convection in Horizontal Layers of Gases," *J. Fluid Mechanics*, Vol. 24, 1966, pp. 451 479.

K. G. T. Hollands
Assoc. Professor,
Thermal Engineering Group,
Department of Mechanical Engineering,
University of Waterloo,
Waterloo, Ontario, Canada

T. E. Unny
Professor,
Department of Civil Engineering,
University of Waterloo,
Waterloo, Ontario, Canada

G. D. Raithby
Assoc. Professor,
Thermal Engineering Group,
Department of Mechanical Engineering,
University of Waterloo,
Waterloo, Ontario, Canada

L. Konicek
CSICC Fellow,
Division of Building Research,
National Research Council,
Ottawa, Ontario, Canada

Free Convective Heat Transfer Across Inclined Air Layers

This paper presents new experimental measurements on free convective heat transfer rates through inclined air layers of high aspect ratio, heated from below. The Rayleigh number range covered is from subcritical to 10^5*; the range of the angle of inclination,* ϕ *measured from the horizontal is:* $0 < \phi < \sim 70$ *deg. Although it was anticipated that the results might be identical to the results for the horizontal layer if one replaced Ra by Ra cos* ϕ*, significant departures from this behavior were observed, particularly in the range* $1708 < Ra \cos \phi < 10^4$*,* $30 \text{ deg} \leq \phi < 60$ *deg. A recommended relationship giving the Nusselt number as a function of Ra cos* ϕ *and* ϕ *is reported. This relationship fits all data closely.*

Introduction

The free convective heat transfer across an inclined air layer of large aspect ratio and heated from below is of importance in a number of engineering situations. It is of particular importance in solar energy flat-plate collectors where it can constitute the main mode of heat loss. However, except for the limiting cases of vertical and horizontal layers, which have been studied extensively, the inclined layer has been the subject of very few experimental investigations.

The principle investigation was carried out by De Graaf and Van der Held in 1952 [1, 2].[1] These authors performed measurements of the heat transport at settings for the angle ϕ (Fig. 1) ranging from 0 to 90 deg in 10-deg steps, covered a Rayleigh number range of approximately 10^3–10^5. They also observed the flow pattern of the air under varying conditions. Other measurements have been reported only sporadically: thus, a U. S. Government Housing Research Paper [3] reports extensive measurements but all at $\phi = 45$ deg; Hollands and Konicek [4] reported measurements at 15 deg intervals in ϕ, but only near the critical Rayleigh number. Extensive experiments involving liquids were reported by Dropkin and Somerscales [5]; however, their Rayleigh number range (10^5–10^9) was above that of interest for solar collectors (approximately from 10^3 to 10^5) moreover the significant Prandtl number effect on the heat transport argues against the use of their results for predicting heat transport across gas layers.

Since the De Graaf-Van der Held study, considerable progress has been made in the theory of natural convection in fluid layers. As a consequence and because of the importance of the problem it was decided to undertake a new set of measurements, using recent theory to assist in interpreting results and obtaining the correlation equations. These measurements, a new theoretical result, and the resultant correlation equations are described in this paper. This study is restricted to a range for the angle ϕ from 0 to ~70 deg. It covers values of Ra ranging from subcritical (Ra < 1708/cos ϕ) to 10^5, although there is reason to expect that the correlation equation will be valid for higher Rayleigh numbers.

Basic Theory

Conductive Regime. Provided the Rayleigh number is sufficiently small, the fluid motion consists of one large cell (called the base flow), with the fluid rising near the hot surface, falling near the cold surface, but with the streamlines parallel to the bounding surfaces everywhere except at the extreme ends of the slot where the fluid

---

[1] Numbers in brackets designate References at end of paper.

Contributed by the Heat Transfer Division of THE AMERICAN SOCIETY OF MECHANICAL ENGINEERS and presented at the AIChE-ASME National Heat Transfer Conference, San Francisco, Calif., August 10–13, 1975. Revised manuscript received by the Heat Transfer Division December 29, 1975. Paper No. 75-HT-55.

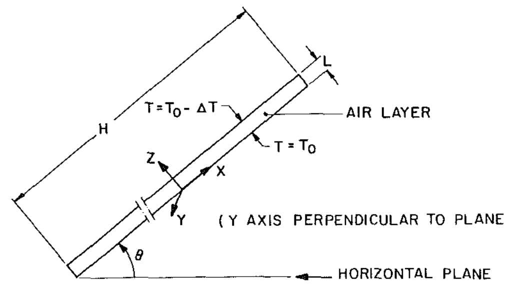

Fig. 1 **Sketch of air layer showing important dimensional quantities**

turns. The heat transfer in this flow regime is consequently purely conductive (i.e., Nu = 1) except at the extreme ends where there is some convective heat transport associated with the fluid turning; however, as the aspect ratio (= H/L, Fig. 1) of the slot becomes increasingly large, the contribution of this convective heat transfer to the average Nusselt number for the slot becomes vanishingly small, so that the average Nusselt number approaches unity. This conductive regime exists for air provided the Rayleigh number is less than a critical value, Ra_c given by $\mathrm{Ra}_c = 1708/\cos\phi$ [6–9, 4]. Consequently we have:

$$\mathrm{Nu} = 1 \qquad \mathrm{Ra} < 1708/\cos\phi,\ \phi < \sim 70 \text{ deg} \tag{1}$$

Immediate—Postconductive Regime. For $\mathrm{Ra} = \mathrm{Ra}_c$ the base flow is marginally unstable, the incipient flow theoretically consisting of steady longitudinal rolls (i.e., rolls with their axis along the upslope), provided $\phi < \sim 70$ deg. De Graaf and Van der Held [1, 2] have observed these rolls for $\phi < 20$ deg and found that they persist up to Rayleigh numbers of about 30,000. For $\phi \geq 30$ deg they did not observe the rolls but rather report a direct transition to "turbulence" from the base flow. Using water, Hart [8] observed the rolls up to $\mathrm{Ra} \simeq 5000$ for all $\phi < 70$ deg.

Recently, Clever [10] demonstrated analytically that, provided two conditions are satisfied, the Nusselt number is a function of Ra cos ϕ only (rather than Ra and ϕ separately). The first condition is that the Prandtl number be infinite; the second is that the fluid flow and temperature fields be X-independent, where X is measured in the longitudinal direction (Fig. 1). A flow pattern consisting of longitudinal rolls satisfies the second condition. It follows from this result that

$$\mathrm{Nu} = \mathrm{Nu}_H(\mathrm{Ra}\cos\phi)$$

where $\mathrm{Nu}_H(\mathrm{Ra})$ denotes the Nusselt number dependence on the Rayleigh number applying to the horizontal layer. This is a useful result since the horizontal layer has been studied extensively. For Rayleigh numbers up to about 8000, Nu_H is known to be expressible by [11]:

$$\mathrm{Nu}_H = 1.44\,(1 - 1708/\mathrm{Ra})$$

independent of the Prandtl number. Combining equations (2) and (3) it follows that provided both of Clever's conditions are met, we expect:

$$\mathrm{Nu} = 1.44\,(1 - 1708/\mathrm{Ra}\cos\phi) \tag{4}$$

in the immediate postconductive regime.

Of course the first condition ($\mathrm{Pr} = \infty$) on Clever's result limits its utility considerably. We have re-examined Clever's analysis and found that in fact this condition can be relaxed. The proof of this new result is given in the Appendix to this paper. Consequently, equation (4) should be valid provided only that the flow consists of longitudinal rolls (or is X-independent).

Clever [10] presented some experimental evidence that his result is valid for air, using the data of [2]. However, since his plot shows only two data points in the range $1708 < \mathrm{Ra}\cos\phi < 10^4$, there is insufficient evidence to conclude its validity in this range.

High Rayleigh Number Regime. At very high Rayleigh numbers it is expected that the flow should take up a boundary layer structure, the resistance to heat transfer lying exclusively in two boundary layers, one on each of the bounding surfaces. The thermal resistance of each boundary layer is expected to be the same as that on a single heated, facing up, inclined plate in an infinite environment. In [12, 13], arguments are presented for taking the "conduction thickness," Δ_t, (defined as that thickness of stagnant fluid offering the same resistance to heat transfer as the actual boundary layer), the following expression:

$$\Delta_t = \frac{1}{C_t}\left\{\frac{\nu\alpha}{g\beta\Delta T_{BL}\cos\phi}\right\}^{1/3}$$

for $\phi < \sim 70$ deg where ΔT_{BL} is the temperature difference across the boundary layer. The value of C_t depends only on the Prandtl number. Based on measurements on single horizontal plates, its value for air is 0.14 [14]. The overall conductance, h, of two such boundary layers with overall temperature difference $\Delta T = 2\Delta T_{BL}$ is:

$$h = \frac{k}{2\Delta_t} = \frac{C_t}{2^{4/3}}\,k\left\{\frac{g\beta\Delta T\cos\phi}{\nu\alpha}\right\}^{1/3}$$

giving a Nusselt number of:

$$\mathrm{Nu} = \frac{C_t}{2^{4/3}}(\mathrm{Ra}\cos\phi)^{1/3} = \left(\frac{\mathrm{Ra}\cos\phi}{5830}\right)^{1/3} \tag{5}$$

Expected Correlation. Again the Nusselt number for the inclined layer is obtained from the Nu-Ra relation applying to the horizontal layer, but using Ra cos ϕ for Ra. Since such a procedure is found to be applicable to all three regimes discussed previously, it might therefore be anticipated to apply over the full Rayleigh number range,

Nomenclature

g = acceleration of gravity [m/s^2]
H = length of air layer (see Fig. 1) [m]
k = thermal conditivity of air [W/m K]
L = width of air layer (see Fig. 1) [m]
Nu = Nusselt number for natural convective heat transfer across the air layer = $qL/k\Delta T$
Nu_2 = quantity defined by equation (9)
Pr = Prandtl number = ν/α
p = pressure [N/m^2]
q = heat flux across air layer [W/m^2]
Ra = Rayleigh number = $\dfrac{g\beta\Delta TL^3}{\nu\alpha}$
Ra_c = critical Rayleigh number for stability of base flow
T = temperature of air, [K]
ΔT = temperature difference across air layer, [K]
t = time [s]
u, v, w = fluid velocities in x-, y-, z-directions, respectively [m/s]
X, Y, Z = spatial coordinates of any point in the fluid layer, (see Fig. 1), [m]
$x, y, z = x = X/L;\ y = Y/L;\ Z = z/L$
α = thermal diffusivity of air, [m^2/s]
β = coefficient of thermal expansion of air, [K^{-1}]
θ = dimensionless temperature
μ = fluid viscosity [kg/ms]
ν = kinematic viscosity of air, [m^2/s]
ρ = density of air, [kg/m^3]
ϕ = angle of air layer from horizontal, (see Fig. 1)

Subscripts

0 = at $z = 0$
H = horizontal position

as has recently been suggested by Buchburg, et al. [15]. Recently an empirical Nu-Ra relationship for the horizontal air layer, which has equations (1), (3), and (5) with $\phi = 0$ as special cases, was arrived at by three of the authors [14]. The expression is:

$$\mathrm{Nu}_H = 1 + 1.44\left[1 - \frac{1708}{\mathrm{Ra}}\right]^{\bullet} + \left[\left(\frac{\mathrm{Ra}}{5830}\right)^{1/3} - 1\right]^{\bullet} \tag{6}$$

where $[\ ]^{\bullet}$ is defined by:

$$[X]^{\bullet} = (|X| + X)/2 \tag{7}$$

where X is any quantity. Equation (6) has been found to fit very closely all available horizontal data for air for Rayleigh numbers up to 10^8 and is expected to be valid in the limit $\mathrm{Ra} \rightarrow \infty$. Replacing Ra by Ra cos ϕ in equation (6) as suggested in the foregoing gives:

$$\mathrm{Nu} = 1 + 1.44\left[1 - \frac{1708}{\mathrm{Ra}\cos\phi}\right]^{\bullet} + \left[\left(\frac{\mathrm{Ra}\cos\phi}{5830}\right)^{1/3} - 1\right]^{\bullet} \tag{8}$$

and this equation will be used for comparison with experimental results. The support for this equation is weakest in the immediate postconductive regime ($1708 < \mathrm{Ra}\cos\phi < \sim 10^4$) for 30 deg $< \phi <$ 60 deg since longitudinal rolls have not been observed in this regime for air.

Experiment

Apparatus. The apparatus used in the experiment is essentially the same as that used previously to measure critical Rayleigh numbers for inclined air layers [4, 18] and for horizontal air layers constrained by a honeycomb [16] and, hence, has been fully described elsewhere. Sketched in Fig. 2, it contains the air layer between two parallel isothermal copper plates, each 56 × 61 × 1 cm. The upper plate is cooled and the lower heated, by two thermostatically controlled water streams which pass through tubes soldered to the rear side of each plate, thereby maintaining a uniform temperature difference (of the order of 10 K and measured by four copper-constantan thermocouples) across the air layer. The heat flux is measured at the lower plate and only in the central 13 × 13 cm area of that plate. The air layer is bounded at the periphery of the plates by means of aluminum foil stretched from one plate to the other and firmly attached to each plate. This foil maintains a linear temperature rise from the cold to the hot plate, thereby assuring no net loss of heat from the air layer at the periphery. The plates are inserted into a vacuum (or pressure) vessel in which the air pressure can be varied from 10 Pa to 700*k* Pa. This provision for varying the pressure permits varying the Rayleigh number over a wide range without altering the plate spacing (or layer width, L) or the temperature difference. The whole system, including the vacuum vessel can be rotated about a horizontal axis so as to provide any value of ϕ desired.

The apparatus has been checked for dynamic similarity in the horizontal case [14] by making sets of measurements with different plate spacings and/or different temperature differences, with the result that, when nondimensionalized, the data lie closely together. Such a check for the inclined layer, with $\phi = 15$ deg, is shown in Fig. 3 where dimensionless results for two different temperature differences are plotted on the same graph. The data are seen to lie closely together. The slight disagreement around Ra = 17,000 is thought to be associated with the hysteresis effect noted by Krishnamurti [17] around this Rayleigh number.

Procedure. Runs were taken with settings for ϕ of 15, 30, 45, 60, and 75 deg. In all runs the plate spacing (or layer width, L) was 1.27 cm (0.50 in.). The temperature difference, ΔT, was nominally between 12 and 15 K for all runs except at $\phi = 15$ deg where runs were made at two different temperature difference settings, as discussed in the foregoing. In each run, the air pressure was increased in approximately 5 percent steps from slightly subcritical up to 700*k* Pa (100 psia), the maximum pressure permissible for the vessel, giving roughly 10 percent steps in the Rayleigh number, up to a maximum Ra of about 10^5. Readings of heat flux, temperature difference and pressure were taken at each step in pressure.

The setting for the layer width, L of 1.27 cm (0.5 in.) was chosen as a compromise: too low a value limits the maximum Rayleigh number attainable; too high a value gives too low a value for the aspect ratio of the slot (H/L), and does not permit a proper sampling of the rolls or cells for the heat flux measurement. The actual aspect ratio was $H/L = 48$. Since the heat transfer was measured only at the central fifth of the length of the slot it is considered that the "turn-around" region of the base flow was not included in the heat flux measurement. Consequently, the measured results should correspond essentially to an infinite aspect ratio slot.

Results

The experimental results for ϕ = 15, 30, 45, and 60 deg are plotted in Fig. 4 in the form of Nu versus Ra cos ϕ. Those data points, indicated as being from the present study, but having Nu < 1.4, are in fact taken from [4]. (This latter article was concerned with transition, rather than heat transfer.) Also shown, for comparison, are the data of De Graaf and Van der Held [1, 2]. (In the cases of $\phi = 15$ deg and $\phi = 45$ deg, the Nusselt numbers shown for these workers are actually arithmetic means of their measurements for ϕ= 10 deg and 20 deg, and for $\phi = 40$ deg and 50 deg, respectively. This procedure was necessary since their step size in ϕ was 10 deg rather than 15 deg.) Although possessing greater scatter and a less uniform coverage of the Rayleigh number range, their data are in good agreement with the present data. This is of particular interest since these workers measured the heat transfer over the total area of the slot rather than just over the central region as was done in the present study. The close agreement between the two sets of data substantiates that the convective heat transfer associated with the turn-around region of the base flow (including its counterpart at supercritical Rayleigh numbers) does not contribute significantly to the overall heat transfer across the layer. Also shown in Fig. 4 is the recommended correlation of the Housing Report [3] as reported by Tabor [19], for $\phi = 45$ deg, which agrees quite well with the present data although lying slightly below it.

Comparison With Expected Correlation Equation

Equation (8) is plotted in Fig. 4 to permit the comparison suggested earlier. For $\phi = 15$ deg the data are seen to agree well with this equation. Since longitudinal rolls are observed at this angle for Ra up to 30,000 [2, 3], the agreement up to this Rayleigh number represents experimental verification of Clever's result and of its extension given in the Appendix. It is also noted that for high Rayleigh numbers the data are asymptotic to equation (5), thereby giving some experimental validation for this equation.

For ϕ = 30, 45, and 60 deg significant departures from equation (8) are observed, particularly in the immediate postconductive regime. The significance of these departures is a matter for further investigation both experimentally and theoretically. There has not been any published reports so far indicating experimental verification of the existence of longitudinal rolls (x-independent flows) at these angles of inclination for air. Hence, these departures need not necessarily represent any disagreement with the theory presented herein. The fact that Hart [8] observed longitudinal rolls in water for Ra up to 5000 and greater also has no necessary relevance to the present results, because the stability phenomena in inclined layers are strongly Prandtl number dependent [9].

It is to be noted here that the theoretical finding of x-independent flows in the postinstability regime is based on linear stability analysis which assume both the Boussinesq approximation and the validity of Squires theorem, and hence assume the existence of only two-dimensional disturbances [6–9]. Departures from these assumptions may lead to three-dimensional flows in the postinstability regime. Perhaps these are the flows that are observed as "turbulence" by De Graaf and Van der Held. Clearly further theoretical analysis as well as flow visualization studies and heat transfer measurements for air layers at these angles of inclination are warranted.

Revised Correlation Equation

Since equation (8) does not fit the data well, a modified form, which does, was sought. In Fig. 5, the data for $\phi = 30$ deg are plotted in the

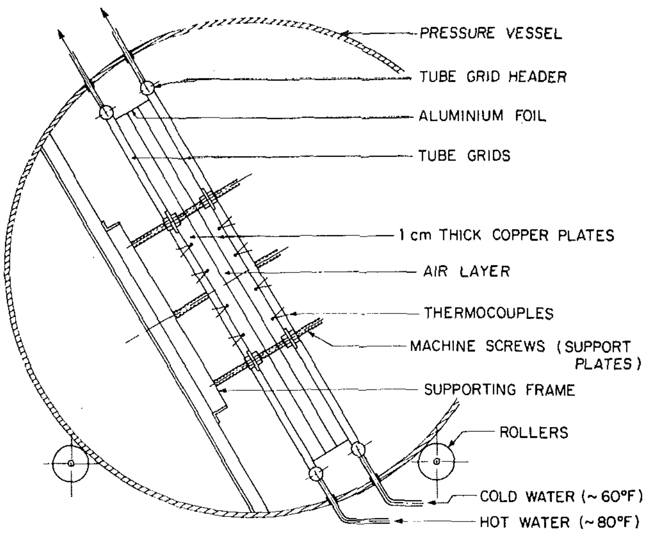

Fig. 2 Sketch of experimental apparatus

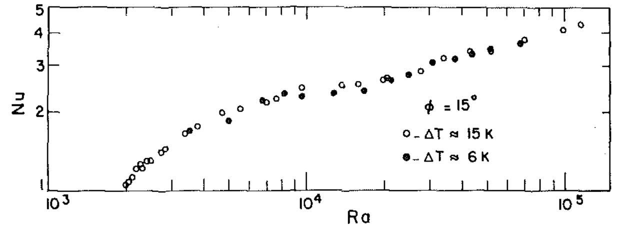

Fig. 3 Plot of experimental data at ϕ = 15 deg showing runs at two different temperatures differences

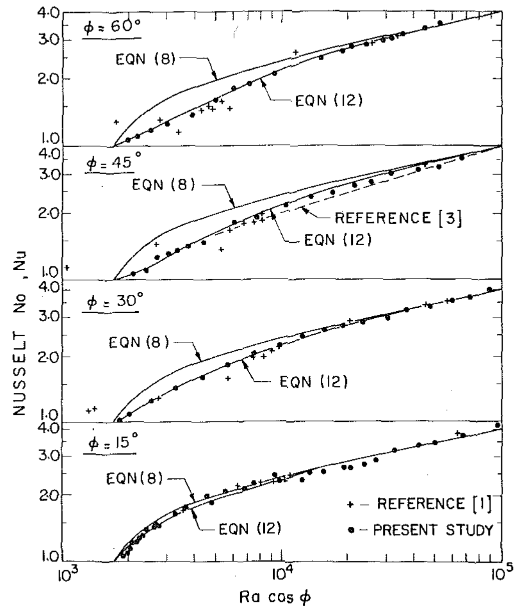

Fig. 4 Plot of experimental results for values for ϕ of 15, 30, 45, and 60 deg

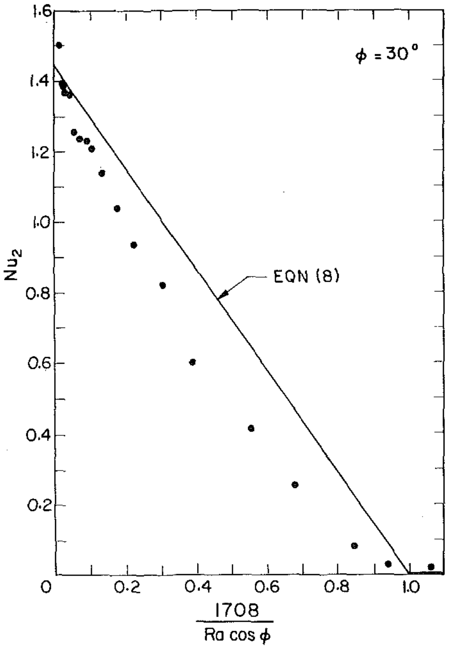

Fig. 5 Plot of measured Nu_2 for ϕ = 30 deg

Table 1 Fitted values of $f(\phi)$ (rounded)

ϕ	15 deg	30 deg	45 deg	60 deg	0 deg
$f(\phi)$	0.25	0.75	1.00	0.95	0.0
$(\sin 1.8\phi)^{1.6}$	0.283	0.712	0.980	0.923	0.0

form Nu_2 versus $1708/(Ra \cos \phi)$, where Nu_2 is defined by:

$$\mathrm{Nu}_2 = \mathrm{Nu} - 1 - \left[\left(\frac{\mathrm{Ra}\cos\phi}{5830}\right)^{1/3} - 1\right]^{\bullet} \tag{9}$$

If equation (8) were valid, the data would fall on the straight line shown, (as is in fact observed when $\phi = 0$). However, although the intercepts are correct, the data appear to give a parabolic rather than linear fit. Plots for ϕ = 45 deg and 60 deg show similar behavior. The following parabolic equation for Nu_2 was found to fit the data:

$$\mathrm{Nu}_2 = 1.44\left[1 - \frac{1708}{\mathrm{Ra}\cos\phi}\right]^{\bullet}\left(1 - f(\phi)\frac{1708}{\mathrm{Ra}\cos\phi}\right) \tag{10}$$

provided the function $f(\phi)$ was properly chosen. Values of $f(\phi)$ obtained by fitting equation (10) to the data are given in Table 1. The function:

$$f(\phi) \approx (\sin 1.8\phi)^{1.6} \tag{11}$$

was found to be reasonable fit to $f(\phi)$, as indicated in Table 1. Combining equations (9), (10) and (11), there results:

$$\mathrm{Nu} = 1 + 1.44\left[1 - \frac{1708}{\mathrm{Ra}\cos\phi}\right]^{\bullet}\left(1 - \frac{(\sin 1.8\phi)^{1.6}\,1708}{\mathrm{Ra}\cos\phi}\right) + \left[\left(\frac{\mathrm{Ra}\cos\phi}{5830}\right)^{1/3} - 1\right]^{\bullet} \quad \phi \le 60 \text{ deg} \tag{12}$$

This equation is plotted in Fig. 4 and is seen to fit the data closely. The maximum deviation of the data from equation (12) is about 5 percent,

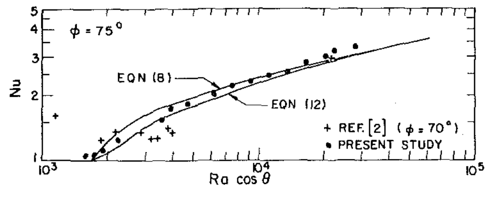

Fig. 6 Plot of experimental results for ϕ = 75 deg

the average deviation is less than 2 percent. Equation (12) is, therefore, the recommended correlation equation.

The question arises: to what upper limit on ϕ is equation (12) valid? Fig. 6 shows the comparison between equation (12) and the next angle for which we have data, namely $\phi = 75$ deg. Clearly, equation (12) is not as accurate for ϕ this large. It is known that at this angle, the first instability of the conductive state is a shear flow instability rather than a buoyant instability, and for this reason we have not used the data at this angle in fitting $f(\phi)$, choosing rather to treat it as part of a separate study. However, equation (12) can be used for ϕ up to 75 deg if errors of up to 10 percent in Nu are acceptable.

Conclusions

1 Based on the results of measurements reported in this paper, equation (12) is recommended for calculating Nusselt numbers for free convective heat exchange through tilted air layers of high aspect ratio, having $0 \leq \phi \leq 60$ deg and $0 < \mathrm{Ra} \leq 10^5$. This equation can be expected to give values for Nu with a maximum error about 5 percent. Equation (12) may also be used for ϕ up to 75 percent but errors of up to 10 percent may be expected. From analogy with the horizontal layer, equation (12) is expected to be valid for $\mathrm{Ra} > 10^5$, but except at $\phi = 0$, experimental confirmation is lacking.

2 Provided only that the fluid flow is X-independent, the Nusselt number is a function of Ra cos ϕ only, regardless of the Prandtl number. This result has been demonstrated analytically for all ϕ, and verified experimentally for air at $\phi = 15$ deg.

3 For 30 deg $\leq \phi \leq$ 60 deg, the Nusselt number is not a function of Ra cos ϕ only. Further research is necessary to clarify this interesting result.

Acknowledgments

This work was supported in part by a grant from the National Research Council of Canada. The authors also wish to acknowledge support received from the National Science Foundation of the United States under Grant No. AER-74-09110 of their program AER-T/RANN/SOLAR ENERGY. Thanks is expressed to Professor P. L. Silveston for calling the De Graaf thesis [1] to our attention, and to Mr. Doug Cane and Mr. S. Rajaram for assistance in correlating the data.

References

1 De Graaf, J. G. A., "Het Verband Tussen de Warmte-overgang en de Stromingsverschijnselen in Gesloten Spouwen," PhD thesis, University of Utrecht, published by Drukkerij Fa. Schotanus & Jens, Utrecht, 1952.

2 De Graff, J. G. A., and Van der Held, E. F. M., "The Relation Between the Heat Transfer and Convection Phenomena in Enclosed Plane Air Layers," *Appl. Sci. Res.*, Vol. 3, 1953, pp. 393–409.

3 Housing Research Paper No. 32, Housing and Home Finance Agency, U. S. Government Printing Office, Apr. 1954.

4 Hollands, K. G. T., and Konicek, L., "Experimental Study of the Stability of Differentially Heated Inclined Air Layers," *International Journal of Heat and Mass Transfer*, Vol. 16, 1973, pp. 1467–1476.

5 Dropkin, D., and Somerscales, E., "Heat Transfer by Natural Convection in Liquids Confined by Two Parallel Plates Which are Inclined at Various Angles With Respect to Horizontal," JOURNAL OF HEAT TRANSFER TRAN. ASME, Series C., Vol. 87, 1965, pp. 77–84.

6 Birikh, R. V., Gershuni, G. Z., Zhukhovuskii, E. M., and Rudokov, R. N., "Hydrodynamic and Thermal Instability of Steady Convective Flow," *PMM*, Vol. 32, No. 2, 1968, pp. 256–263.

7 Gershuni, G. Z., and Zhukhovitskii, E. M., "Stability of Plane-Parallel Convective Motion With Respect to Spatial Perturbations," *PMM*, Vol. 33, 1969, p. 830.

8 Hart, J., "Stability of the Flow in a Differentially Heated Inclined Box," *Journal of Fluid Mechanics*, Vol. 47, 1971, p. 547.

9 Unny, T. E., "Thermal Instability in Differentially Heated Inclined Fluid Layers," *Applied Mechanics*, Vol. 39, No. 1, 1972, pp. 41–46.

10 Clever, R. M., "Finite Amplitude Longitudinal Convection Rolls in an Inclined Layer," JOURNAL OF HEAT TRANSFER, TRANS. ASME, Series C., Vol. 95, No. 3, 1973, pp. 407–408.

11 Hollands, K. G. T., "Convectional Heat Transport Between Rigid Horizontal Boundaries after Instability," *Physics Fluids*, Vol. 8, 1965, pp. 389–390.

12 Raithby, G. D., and Hollands, K. G. T., "A General Method of Obtaining Approximate Solutions to Laminar and Turbulent Free Convection Problems," *Advances in Heat Transfer*, Vol. 12, Academic Press, 1974.

13 Raithby, G. D., and Hollands, K. G. T., "Laminar and Turbulent Heat Transfer by Natural Convection," *International Journal of Heat and Mass Transfer*, Vol. 17, 1974, pp. 1620–1622.

14 Hollands, K. G. T., Raithby, G. D., and Konicek, L., "Correlation Equations for Free Convection Heat Transfer in Horizontal Layers of Air and Water," *International Journal of Heat and Mass Transfer*, Vol. 18, 1975, pp. 879–884.

15 Buchberg, H., Catton, Ivan, and Edwards, D. K., "Natural Convection in Enclosed Spaces: A Review of Application to Solar Energy Collection," ASME Paper No. 74-WA/HT-12, Nov. 1974.

16 Hollands, K. G. T., "Natural Convections in Horizontal Thin-Walled Honeycomb Panels," JOURNAL OF HEAT TRANSFER, TRANS. ASME, Series C, Vol. 95, 1973, pp. 439–444.

17 Krishnamurti, R., "On the Transition of Turbulent Convection, Part 1, The Transition From Two- to Three-Dimensional Flow," *Journal of Fluid Mechanics*, Vol. 42, Part 2, 1970, pp. 295–307.

18 Konicek, L., "Experimental Determination of Critical Rayleigh Numbers and Heat Transfer Through Horizontal and Inclined Air Layers," MASc thesis, University of Waterloo, Waterloo, Canada, 1971.

19 Tabor, H., "Radiation, Convection and Conduction Coefficients in Solar Collectors," *Bull Res. Counc. of Israel*, Vol. 6C, 1958, pp. 155–176.

APPENDIX

Referring to Fig. 1, the following governing equations are readily derived from the fundamental conservation equations, assuming the Boussinesq approximation:

$$\frac{\partial u}{\partial x} + \frac{\partial v}{\partial y} + \frac{\partial w}{\partial z} = 0$$

$$\frac{1}{\mathrm{Pr}}\frac{Du}{Dt} + \frac{\mathrm{Ra}}{\mathrm{Pr}}\sin\phi\left\{F(z)\frac{\partial u}{\partial x} + F'(z)w\right\} - \sin\phi\,\theta + \frac{\partial \mathrm{p}}{\partial \mathrm{x}} = \nabla^2 \mathrm{u}$$

$$\frac{1}{\mathrm{Pr}}\frac{Dv}{Dt} + \frac{\mathrm{Ra}}{\mathrm{Pr}}\sin\phi\,F(z)\frac{\partial v}{\partial x} + \frac{\partial p}{\partial y} = \nabla^2 v$$

$$\frac{1}{\mathrm{Pr}}\frac{Dw}{Dt} + \frac{\mathrm{Ra}}{\mathrm{Pr}}\sin\phi\,F(z)\frac{\partial w}{\partial x} - \cos\phi\theta + \frac{\partial p}{\partial z} = \nabla^2 w$$

$$\frac{D\theta}{Dt} + \mathrm{Ra}\sin\phi\,F(z)\frac{\partial \theta}{\partial x} - \mathrm{Ra}w = \nabla^2\theta$$

where $F(z) = (4z^3 - 6z^2 + 2z)/24$. In these equations, u, v, w, θ, and p represent the *departure* of the x, y, and z velocity components, temperature and pressure, respectively, from their corresponding values in the conduction regime. (The conduction regime is characterized by $u = v = 0$ and $\partial w/\partial x = 0$; solutions for this regime are given for example, in [9].) All quantities have been dedimensionalized, using the scale α/L for velocity, $\rho\alpha^2/L^2$ for pressure, $\nu\alpha/g\beta L^3$ for temperature; L^2/α for time; and L for length. The boundary conditions are: $u = v = w = \theta = 0$ at $z = 0, 1$. The Nusselt number is given by:

$$\mathrm{Nu} = 1 + \frac{1}{\mathrm{Ra}}\left(\frac{\partial\theta}{\partial z}\right)_{z=0}$$

If now, the velocity and temperature fields are assumed to be x-independent, all terms in $\partial/\partial x$ vanish. In the resulting equations, if Ra, θ and u are scaled according to: $\tilde{\theta} = \theta\cos\phi$; $\widetilde{\mathrm{Ra}} = \mathrm{Ra}\cos\phi$; and $\tilde{u} = u/\tan\phi$, there results:

$$\frac{\partial v}{\partial y} + \frac{\partial w}{\partial z} = 0$$

$$\frac{1}{\mathrm{Pr}}\left(\frac{\partial\tilde{u}}{\partial\tau} + v\frac{\partial\tilde{u}}{\partial y} + w\frac{\partial\tilde{u}}{\partial z}\right) + \frac{\mathrm{R\tilde{a}}}{\mathrm{Pr}}F'(z)w - \tilde{\theta} = \nabla^2\tilde{u}$$

$$\frac{1}{\mathrm{Pr}}\left(\frac{\partial v}{\partial\tau} + v\frac{\partial v}{\partial y} + w\frac{\partial v}{\partial z}\right) + \frac{\partial p}{\partial y} = \nabla^2 v$$

$$\frac{1}{\mathrm{Pr}}\left(\frac{\partial w}{\partial\tau} + v\frac{\partial w}{\partial y} + w\frac{\partial w}{\partial z}\right) + \frac{\partial p}{\partial z} - \tilde{\theta} = \nabla^2 w$$

$$\frac{\partial\tilde{\theta}}{\partial\tau} + v\frac{\partial\tilde{\theta}}{\partial y} + w\frac{\partial\tilde{\theta}}{\partial z} - \widetilde{\mathrm{Ra}}w = \nabla^2\tilde{\theta}$$

with $\tilde{u} = v = w = \tilde{\theta} = 0$ at $z = 0, 1$; and the Nusselt number is

$$\mathrm{Nu} = 1 + \frac{1}{\widetilde{\mathrm{Ra}}}\left(\frac{\partial\tilde{\theta}}{\partial z}\right)_{z=0}$$

Since these equations and boundary conditions are all independent of ϕ it follows that $\tilde{\theta}$ and Nu are dependent only upon $\widetilde{\mathrm{Ra}}$ and Pr, as required.

H. H.-S. Chu[1]
Graduate Student.

S. W. Churchill
Professor.

C. V. S. Patterson
Professor.

Department of Chemical and Biochemical Engineering,
University of Pennsylvania,
Philadelphia, Pa.

The Effect of Heater Size, Location, Aspect Ratio, and Boundary Conditions on Two-Dimensional, Laminar, Natural Convection in Rectangular Channels

The effect of localized heating in rectangular channels was studied by solving the partial differential equations for the conservation of mass, momentum, and energy numerically using an unsteady state formulation and the alternating-direction-implicit method. The heating element was a long, horizontal, isothermal strip located in one, otherwise-insulated vertical wall. The opposing wall was maintained at a lower uniform temperature and the upper and lower surfaces were insulated or maintained at the lower temperature. Computations were carried out for $Pr = 0.7$, $0 \leq Ra \leq 10^5$, a complete range of heater widths and locations and a wide range of aspect ratios. Flow visualization studies and comparison with prior computed results for a limiting case confirm the validity of the computed values. The computed rates of heat transfer and circulation provide guidance for locating heaters or coolers.

Introduction

Natural convection in enclosures has received increasing attention in recent years. This attention is due in part to recognition of the importance of this process in many diverse applications such as home heating, solar collectors, cryogenic storage, thermal insulation, crystal growth, nuclear reactor design, and furnace design. Interest has also been generated by improved facility in the solution of the partial differential equations describing the process. These solutions have generally been limited to two-dimensional, laminar motion in enclosures in which the bounding walls were taken to be isothermal, uniformly heated, and perfectly insulated.

In many applications heating takes place over a narrow segment of one of the vertical walls. The objective of this investigation has been to determine the influence of the size and location of the heating element on the flow field and on the rate of heat transfer in such a situation. Most practical applications involve turbulent three-dimensional motion. However, such behavior is beyond present theoretical capabilities. Hence it was decided to confine the investigation to conditions such that the motion is laminar and essentially two-dimensional. This problem is of some practical importance as well as being a stepping stone to the more general one. Even with the foregoing restrictions the possible boundary conditions are almost unlimited. The following conditions were, therefore, selected merely as illustrative. The enclosure is a long horizontal channel with a rectangular cross section. The heating element is a long, horizontal, isothermal strip in an otherwise-insulated, vertical wall. The width and location of the heating element are considered variables. The opposing vertical wall is maintained at a uniform lower temperature. The upper and lower surfaces are insulated or maintained at the lower temperature. The coordinate system and thermal boundary conditions for this problem are shown in Fig. 1. The calculations and experiments were carried out for aspect ratios (h/w) from 0.4 to 5, a range of Rayleigh numbers from 0 to 10^5 and for $Pr = 0.7$.

Theoretical solutions were sought by solving numerically the

---

[1] Currently with Exxon Production Research Co., Houston, Texas.

Contributed by the Heat Transfer Division for publication in the JOURNAL OF HEAT TRANSFER. Manuscript received by the Heat Transfer Division June 2, 1975. Paper No. 76-HT-W.

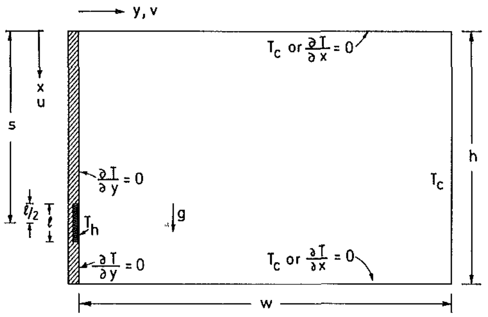

Fig. 1 Coordinate system and thermal boundary conditions

partial differential equations governing the conservation of mass, momentum, and energy. These computations were checked against prior solutions for limiting cases. Experiments were carried out to provide a check on the applicability of the mathematical model for the chosen conditions.

Further details concerning all aspects of this work are given by Chu [1].[2]

Prior Work

Natural convection in a square, horizontal channel with the vertical walls at uniform temperature has received detailed attention. This work has recently been reviewed by Probert, et al. [2] and will be referred to only in comparison with the results of this investigation. Torrance and Rockett [3] studied natural convection induced by a small, circular disk at uniform temperature in the floor of circular and rectangular enclosures by solving simplified, two-dimensional partial differential equations numerically for Pr = 0.7 and 4 $\times 10^4 < \mathrm{Gr} < 4 \times 10^{10}$. They found that the flow patterns were not affected significantly by heater location except when the disk was located within a few diameters of the vertical walls. Torrance, et al. [4] photographed the flow patterns for these conditions and found excellent agreement with the theoretical predictions. Erb [5] has carried out similar studies in a horizontal cylinder.

Mathematical Model

To represent the problem described in the Introduction the general equations of motion were simplified by adopting the well-known Boussinesq approximation for the gravitational term, assuming physical properties otherwise constant and neglecting dissipation. Nondimensionalizing the simplified equations, eliminating the pressure between the two momentum equations and introducing a dimensionless stream function and vorticity then result in

$$\frac{\partial \zeta}{\partial \tau} + \mathrm{U}\frac{\partial \zeta}{\partial X} + V\frac{\partial \zeta}{\partial Y} + \mathrm{Gr}\frac{\partial \Phi}{\partial Y} + \frac{\partial^2 \zeta}{\partial X^2} + \frac{\partial^2 \zeta}{\partial Y^2} \tag{1}$$

$$\frac{\partial \Phi}{\partial \tau} + U\frac{\partial \Phi}{\partial X} + V\frac{\partial \Phi}{\partial Y} = \frac{1}{\mathrm{Pr}}\left(\frac{\partial^2 \Phi}{\partial X^2} + \frac{\partial^2 \Phi}{\partial Y^2}\right) \tag{2}$$

where

$$-\zeta = \frac{\partial^2 \psi}{\partial X^2} + \frac{\partial^2 \psi}{\partial Y^2} \tag{3}$$

and

$$U = \frac{\partial \psi}{\partial Y} \text{ and } V = -\frac{\partial \psi}{\partial X} \tag{4}$$

The initial and boundary conditions are

at $\tau = 0, 0 \le X \le 1, 0 \le Y \le w/h$

$$\Phi = \Phi_0(X, Y) \text{ and } \zeta = \zeta_0(X, Y) \tag{5}$$

at $S - \frac{L}{2} \le X \le S + \frac{L}{2}, Y = 0, \tau > 0$

$$\Phi = 1, \psi = 0, \text{ and } \frac{\partial \psi}{\partial Y} = 0 \tag{6}$$

at $0 \le X < S - \frac{L}{2}, Y = 0, \tau > 0; S + \frac{L}{2} < X \le 1, Y = 0, \tau > 0$

$$\frac{\partial \Phi}{\partial Y} = 0, \psi = 0, \text{ and } \frac{\partial \psi}{\partial Y} = 0 \tag{7}$$

at $Y = w/h, 0 \le X \le 1, \tau > 0$

$$\Phi = 0, \psi = 0, \frac{\partial \psi}{\partial Y} = 0 \tag{8}$$

at $X = 0, 1, 0 \le Y \le w/h, \tau > 0$

"Isothermal" Case

$$\Phi = 0, \psi = 0, \frac{\partial \psi}{\partial X} = 0 \tag{9}$$

"Adiabatic" Case

$$\frac{\partial \Phi}{\partial Y} = 0, \psi = 0, \frac{\partial \psi}{\partial X} = 0 \tag{10}$$

The dimensionless symbols are all defined in the Nomenclature.

---

[2] Numbers in brackets designate References at end of paper.

Nomenclature

g = gravitational acceleration
$\mathrm{Gr} = g\beta\,(T_h - T_c c)h^3/\nu^2$ = Grashof number
h = height of enclosure
k = thermal conductivity of fluid
$L = \ell/h$ = dimensionless width of heating element
ℓ = width of heating element
$\mathrm{Nu} = q\ell/k(T_h - T_c)$ = mean Nusselt number
$\mathrm{Pr} = \nu/\alpha$ = Prandtl number
q = mean heat flux density through heated strip
$\mathrm{Ra} = g\beta(T_h - T_c)h^3/\nu\alpha$ = Rayleigh number based on height of channel
$\mathrm{Ra}' = g\beta(T_h - T_c)w^3/\nu\alpha$ = alternative Rayleigh number based on width of channel
s = distance of center of heating element from top of enclosure
$S = s/h$ = dimensionless location of heating element
t = time
T = temperature
u = velocity component in x-direction
$U = uh/\nu$ = dimensionless velocity component in X-direction
v = velocity component in y-direction
$V = vh/\nu$ = dimensionless velocity component in Y-direction
w = width and height of enclosure
x = distance from top of enclosure
$X = x/h$ = dimensionless distance from top of enclosure
y = distance from wall containing heating element
$Y = y/h$ = dimensionless distance from wall containing heating element
α = thermal diffusivity
β = volumetric coefficient of expansion with temperature
$\zeta = \partial V/\partial X - \partial U/\partial Y$ = dimensionless vorticity
ν = kinematic viscosity
$\tau = t\nu/h^2$ = dimensionless time
$\Phi = (T - T_c)/(T_h - T_c)$ = dimensionless temperature
ψ = dimensionless stream function (see equation (4))

Subscripts

c = cold surfaces
h = hot surface
max = maximum

Numerical Procedure

A detailed discussion of the problems of convergence and stability connected with the numerical solution of this problem is beyond the scope of this paper and has been presented elsewhere [6]. The procedures and relevant conclusions in this regard are, however, summarized in the following paragraphs.

The derivatives in the mathematical model (equations (1)–(10)) were first approximated by finite differences at a series of grid points. The resulting set of algebraic equations was then solved with the assistance of a digital computer. The spatial derivatives of temperature, vorticity, and stream function were approximated by second-order central differences. First-order differences were used for the time derivatives. The finite-difference equations were formulated and solved using the ADI (alternating-direction-implicit) method developed by Douglas and Peaceman [7] for conduction and adapted by Wilkes and Churchill [8], Samuels and Churchill [9], Ozoe and Churchill [10], and others for natural convection in enclosures. The temperature field at $\tau + \Delta\tau$ was obtained by solving in tri-diagonal form the finite-difference approximations of equation (2) for the two half-time steps. The vorticity field was computed similarly using the advanced temperatures but leaving the vorticities of the boundaries at their prior value. The stream function field was calculated from the advanced vorticity using a fictitious unsteady-state term and hence the ADI method, as proposed by Samuels [11]. The velocity components were computed from the stream function using fourth-order differences for greater accuracy, as proposed by Wilkes [12]. The temperature gradient was calculated at both the hot strip and the cold wall using first-, second-, and third-order differences. The mean heat flux was then obtained by integration using Simpson's rule. The trapezoidal rule was used for the end point whenever an even number of grid points was encountered. The mean heat flux was also calculated at each vertical cross section using a second-order central difference for the conductive term and the central value for the convective term, and integrating as before.

Since only the steady-state behavior was sought, the choice of initial conditions was arbitrary. Some calculations were started from uniform temperature and no motion. However, less computing time was required if the steady-state solution for one situation (Gr, S, and L) was used as the starting condition for another situation.

The finite difference representation was nonconservative. This proved to have an unexpected advantage for the steady-state results. When a coarse grid-size was used the mean heat flux calculated at the cold surface fell above and at the hot surface fell below the true value. As the grid size was decreased these fluxes converged to the same value, providing a useful measure of the rate of convergence. The error for a given grid-size increased with the Grashof number. For the hot surface the third-order approximation for the temperature gradient was found to converge most rapidly but for the cold surface the first-order approximation was best. The heat flux calculated at the central plane was more accurate than at the surfaces. (Here accuracy is defined as agreement with the value obtained by extrapolation of the results for several grid-sizes to zero grid-size, as illustrated in references [1, 6].)

Calculations with the ADI method are unconditionally stable for any $\Delta\tau$ for linear problems. However, for coupled, nonlinear problems an optimum $\Delta\tau$ generally exists and must be found by trial and error. For pure conduction $\Delta\tau = 0.01$ was found to be satisfactory. As Ra increased it was found desirable to decrease $\Delta\tau$ to avoid oscillations and a value of $\Delta\tau = 0.0005$ was used at $\mathrm{Ra} = 10^5$. A satisfactory approximation for the steady state was generally attained before τ reached 1.0.

The corresponding CPU-time on the University of Pennsylvania IBM-370/65 computer was 10–15 s for a square channel with the isothermal boundary condition and a 10 × 10 grid. A 20 × 20 grid required three times as long. The adiabatic boundary condition required a 50–100 percent increase in computing time. For aspect ratios other than 1.0 the computing time was roughly proportional to the number of grid points.

The calculations were effectively limited to $\mathrm{Ra} \leq 10^5$ by numerical instability associated with the boundary condition for vorticity. Iteration for these values would probably have extended the range of Ra but would have required excessive computer time.

Experimental Work

A 25.4 × 25.4 × 152.4-mm cavity was formed by a 5.08-mm thick copper block and a 31.75-mm thick Plexiglas block. A 5.08-mm strip of Nichrome resistance ribbon was used as the heater. A second copper block and heater were installed on the other side of the Plexiglas block to minimize heat losses. The copper blocks were clamped to the Plexiglas block and could be adjusted up and down to vary the location of the heating strip within the cavity. Clear Plexiglas plugs were mounted on the ends of the cavity to permit viewing. Thermocouples were mounted at various locations on the heater strips, on the copper block, and in the Plexiglas block. The entire apparatus was immersed in a water bath maintained at uniform temperature.

Cigarette smoke was used to visualize the flow pattern. Illumination was provided through a vertical slit in the copper block. Photographs were taken with a Nikon F 35 mm camera and Kodak Tri-X film. The lamp was turned on only when taking pictures.

Test of Results

The experimental streamlines in Fig. 2 for a square isothermal channel, with $\mathrm{Ra} = 100{,}000$, $\ell/h = 0.2$ and $s/h = 0.8$ can be compared with the computed stream function in the right lower quadrant of Fig. 4. The agreement is excellent in all respects even though the walls of the cell were not exactly isothermal and adiabatic in the experiments. Similar agreement was observed for all experimental conditions, assuring that the correct mode of circulation was computed.

The heat transfer rates computed for the limiting case of a completely heated wall ($\ell/h = 1.0$) in a square channel with insulated top and bottom surfaces are in excellent agreement with the computed results of previous investigators, including Wilkes and Churchill [8], de Vahl Davis [13], Elder [14], MacGregor and Emery [15], and Boyack and Kearney [16].

These comparisons together with the tests for convergence, stability, independence from the initial condition, and independence from the size of the time step, suggest that the numerical results are a valid solution of the mathematical model.

Temperature and Stream Function Fields

The computed stream functions and isotherms for a 20 × 20 grid in a square isothermal channel with $\mathrm{Ra} = 100{,}000$ and $\ell/h = 0.2$ are plotted as bands in Figs. 3 and 4 for several heater locations. The isothermal bands, each representing 10 percent of the overall temperature difference, are quite distorted and the outward ones have a stomach-like shape. The greater displacement of the bands from the heater indicates that the rate of heat transfer increases as the heater is lowered. Fig. 4 suggests that this increase in heat transfer is associated with lessened drag across the top wall, and

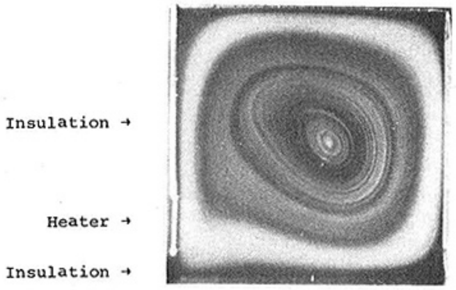

Fig. 2 **Experimental streamlines for strong convection in a square channel cooled on three sides—Ra = 100,000, $s/h = 0.8$, $\ell/h = 0.2$**

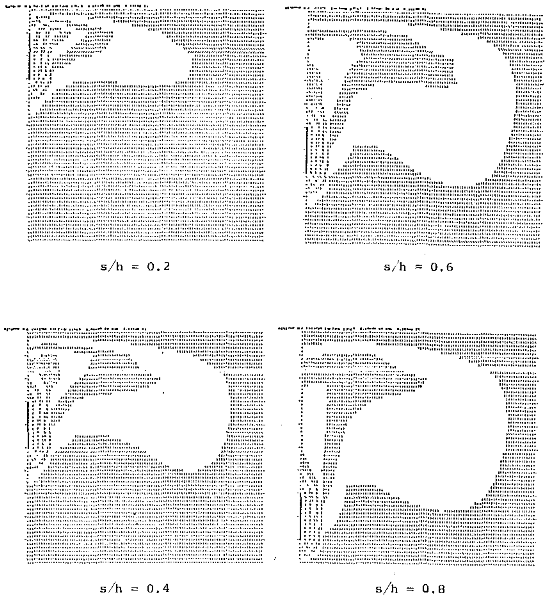

s/h = 0.2 s/h = 0.6

s/h = 0.4 s/h = 0.8

Fig. 3 Computed isotherms for strong convection in a square channel cooled on three sides with various heater locations—Ra = 100,000, ℓ/h = 0.2 ($\Delta X = \Delta Y = 0.05$)

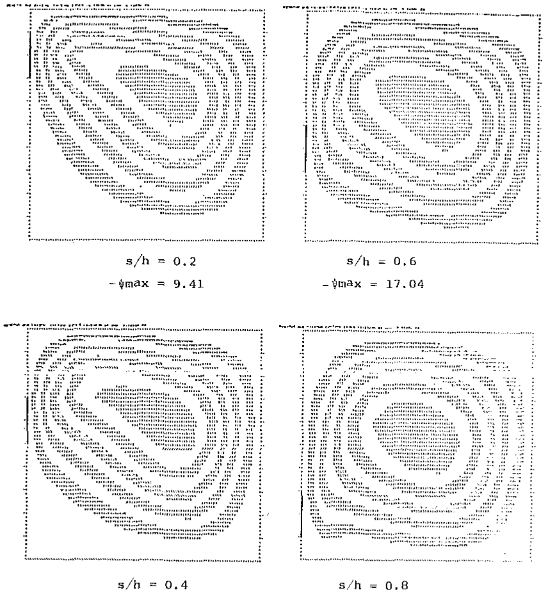

s/h = 0.2, $-\psi_{max}$ = 9.41 s/h = 0.6, $-\psi_{max}$ = 17.04

s/h = 0.4, $-\psi_{max}$ = 13.27 s/h = 0.8, $-\psi_{max}$ = 19.46

Fig. 4 Computed streamlines for strong convection in a square channel cooled on three sides with various heater locations—Ra = 100,000, ℓ/h = 0.2 ($\Delta X = \Delta Y = 0.05$)

with more symmetrical and stronger circulation. The stream function bands represent 10 percent of the range from 0 at the wall to the indicated maximum value at the center of circulation. These values differ somewhat from those in subsequent plots owing to the difference in grid size. The waviness in the outer stream function along the bottom for s/h = 0.8 actually developed into a secondary circulation as Ra was increased still further.

Effect of Heater Location

Figs. 5, 6, and 7 illustrate the dependence of ψ_{max} and Nu on heater location for ℓ/h = 0.2 in a square channel with Ra as a parameter. These values were computed for a 10 × 10 grid but the trends do not differ significantly from those obtained by extrapolation of values for ΔX = 0.2, 0.1, and 0.05 to zero grid-size. The values of ψ_{max} do not differ greatly for the two boundary conditions and are plotted together. The rates of heat transfer are much higher for the isothermal condition and are plotted separately to avoid confusion. As the Rayleigh number increases the heater location for maximum circulation shifts downward (s/h increases). The increased space available for development of the flow after heating is presumably responsible for this behavior. As Ra is increased the heater location for maximum heat transfer shifts from the top to the bottom of the cavity because of the increase in circulation noted in the foregoing. For the isothermal boundary condition Nu must approach infinity when the heater reaches the top and bottom ($s/h \rightarrow$ 0.1 and 0.9 for ℓ/h = 0.2) for all Ra. These singularities do not exist for the adiabatic case. Figs. 6 and 7 also demonstrate that conduction is the predominant mechanism for heat transfer up to Ra = 1000 even though some circulation occurs for all Ra > 0.

These same values of Nu and ψ_{max} are plotted versus each other in Figs. 8 and 9, revealing a surprisingly complex relationship between the rate of heat transfer and the rate of circulation. For the adiabatic case in Fig. 8 either a high or low rate of circulation can be attained for the same rate of heat transfer by the choice of heater location. Conversely, the same rate of circulation (as measured by ψ_{max}) can be attained for two different rates of heat transfer. This multiplicity also occurs for the isothermal case but the range is more restricted as indicated in Fig. 9.

Effect of Heater Size

Figs. 10 and 11 illustrate the dependence on heater size in a square channel with a centrally located heater (s/h = 0.5). These calculated values are also for a 10 × 10 grid. As the heater size is increased above 20 percent of the wall height the circulation is seen to increase only slightly. The rate of heat transfer behaves similarly for the adiabatic case but approaches infinity.

It should be noted that the mean Nusselt number for the cooled surface with the entire cooled perimeter as the characteristic

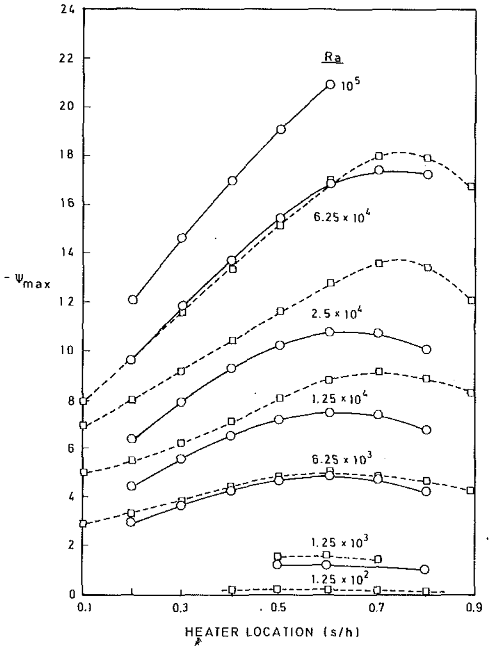

Fig. 5 Effect of heater location and Rayleigh number on rate of circulation in a square channel—ℓ/h = 0.2 ($\Delta X = \Delta Y = 0.1$)
—O— isothermal horizontal walls
- - - □ - - - *adiabatic horizontal walls*

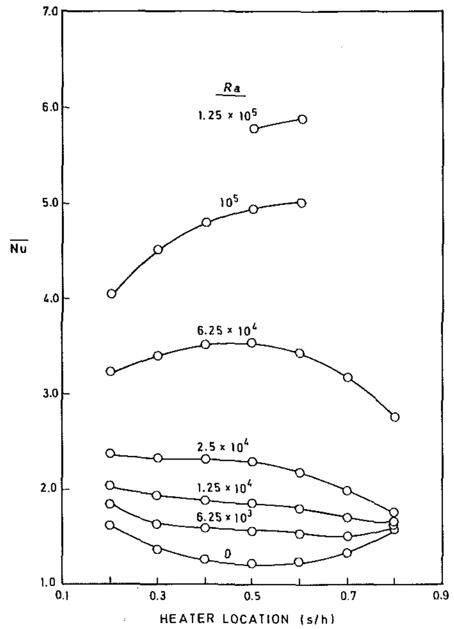

Fig. 6 Effect of heater location and Rayleigh number on rate of heat transfer in a square channel with cooled horizontal walls—$\ell/h = 0.2$ ($\Delta X = \Delta Y = 0.1$)

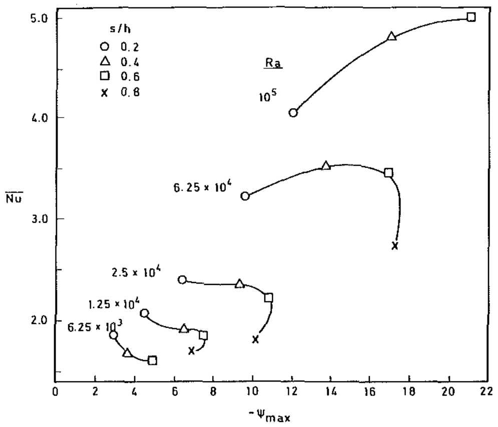

Fig. 9 Relationship between rates of heat transfer and circulation in a square channel with cooled horizontal walls—$\ell/h = 0.2$ ($\Delta X = \Delta Y = 0.1$)

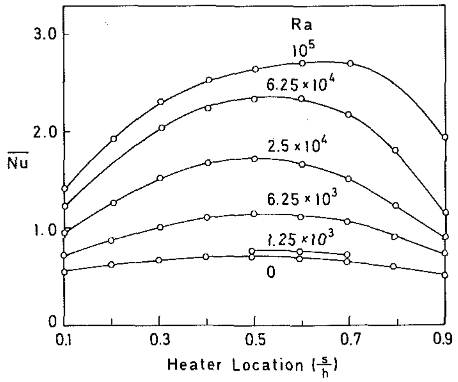

Fig. 7 Effect of heater location and Rayleigh number on rate of heat transfer in a square channel with insulated horizontal walls—$\ell/h = 0.2$ ($\Delta X = \Delta Y = 0.1$)

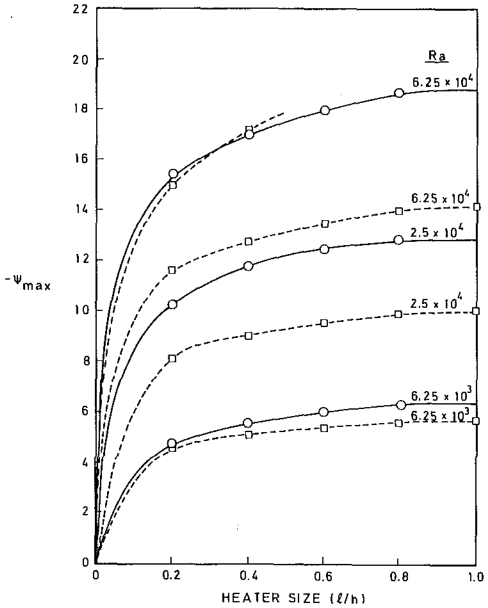

Fig. 10 Effect of heater size and Rayleigh number on rate of circulation in a square channel—$s/h = 0.5$ ($\Delta X = \Delta Y = 0.1$)

—○— isothermal horizontal walls

- - - □ - - - *adiabatic horizontal walls*

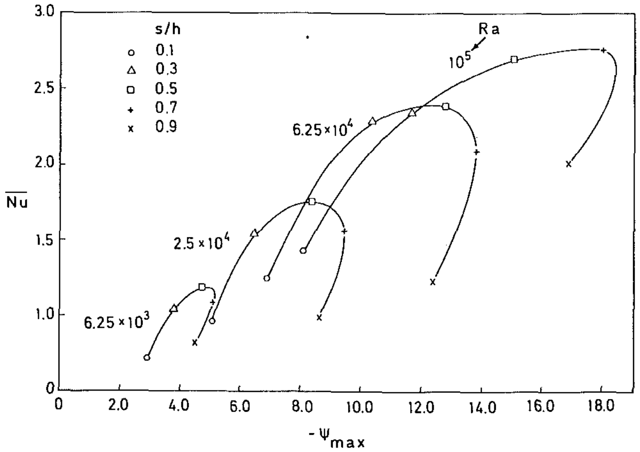

***Fig. 8* Relationship between rates of heat transfer and circulation in a square channel with insulated horizontal walls—$\ell/h = 0.2$ ($\Delta X = \Delta Y = 0.1$)**

length is numerically equal to the mean Nusselt number for the heating element with ℓ as the characteristic length.

The variation of $\overline{Nu}$ with ℓ/h predicted by boundary layer theory (using half the temperature difference in Ra, and ℓ as the characteristic length) is included in Fig. 11 for Ra = 62,500. The computed rate for the enclosure with cooled top and bottom surfaces is significantly greater than this prediction indicating that the increased cooling predominates over the increased drag. The opposite discrepancy is obtained for insulated top and bottom walls.

Effect of Aspect Ratio

For a given heater size and location the effect of aspect ratio (h/w) can be investigated by varying either the height or the width of the channel while keeping the same heater width and location. The former condition will be considered first with the invariant width of the cavity used as the characteristic length in the alternative Rayleigh number, Ra′. The stream functions and isotherms in the upper square section of channels with aspect ratios of 2.0, 3.0, 3.4, and 5 are shown in Fig. 12 for the isothermal case and the indi-

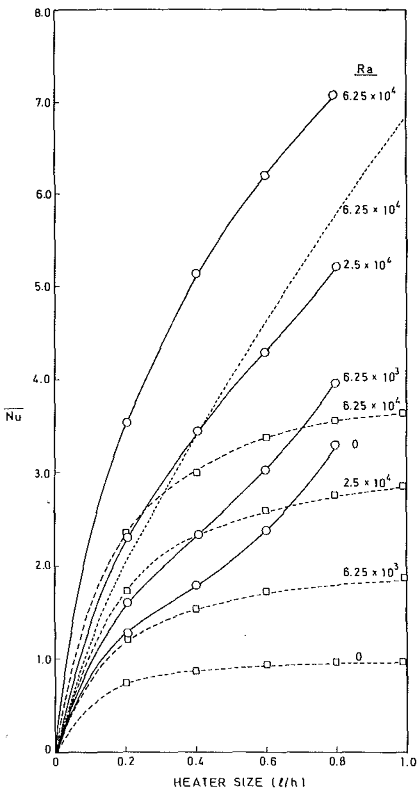

Fig. 11 Effect of heater size and Rayleigh number on rate of heat transfer in a square channel—$s/h = 0.5$ ($\Delta X = \Delta Y = 0.1$)
—O— isothermal horizontal walls
- - - □ - - - adiabatic horizontal walls
. . . . boundary layer theory

cated illustrative conditions. It can be seen that a secondary flow with circulation in the opposite direction develops at the upper surface as the height increases. Somewhat similar behavior was attained as Ra′ was increased form 6250 to 25,000 for a fixed aspect ratio of 4.0. The secondary cell eventually weakens the primary circulation as indicated in Fig. 13 for the isothermal case. For pure conduction the rate of heat transfer decreases as the aspect ratio increases as indicated in Fig. 4. For large Ra′ the rate of heat transfer decreases, the increase being due to greater circulation and the decrease due to the greater distance to the cold horizontal wall. Intermediate behavior is observed for intermediate values of Ra′.

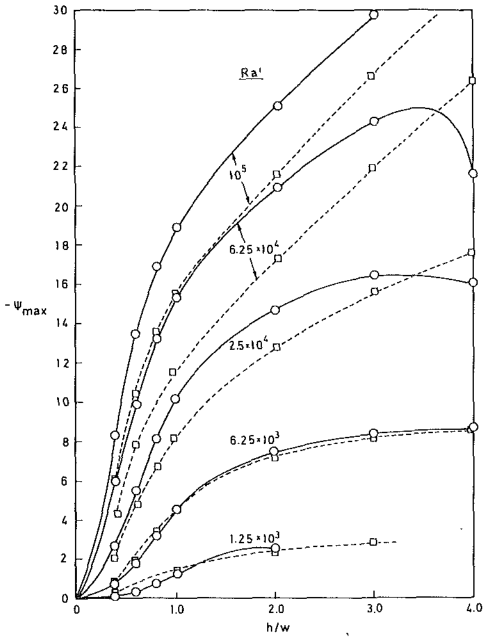

Fig. 13 Effect of cavity height and Rayleigh number on rate of circulation—$\ell/w = 0.2$, $s/h = 0.5$ ($\Delta X = \Delta Y = 0.1$)

Secondary motion does not occur for the adiabatic boundary condition. Hence the dependence of $\psi_{\max}$ and $\overline{\mathrm{Nu}}$ on h/w is quite different. However, the rate of heat transfer for the two boundary conditions is seen to approach the same value as the aspect ratio increases.

The effect of varying the width of the cavity while keeping the width and location of the heating element constant is finally considered with the characteristic length in the Rayleigh number, Ra, now chosen to be the fixed height of the cavity. The variation of

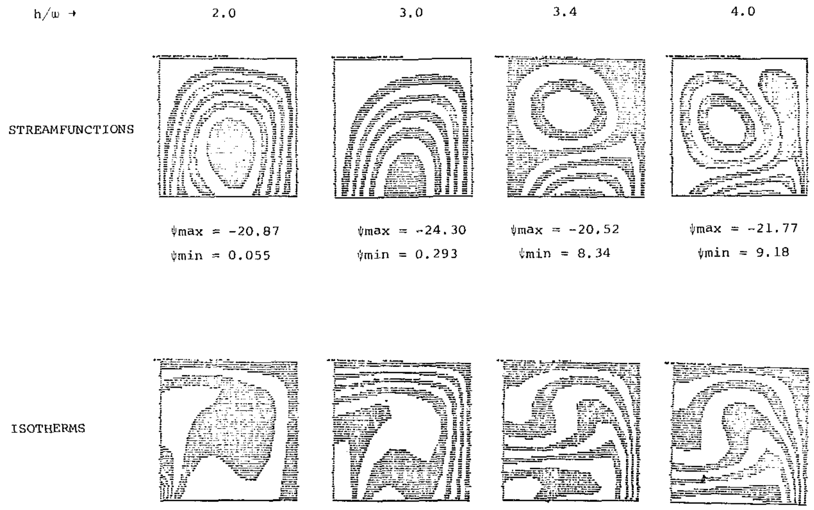

Fig. 12 Effect of cavity height on stream functions and isotherms in the upper square section of channels with cooled horizontal walls—$Ra' = 62{,}500$, $\ell/w = 0.2$, $s/h = 0.5$, ($\Delta X = \Delta Y = 0.1$)

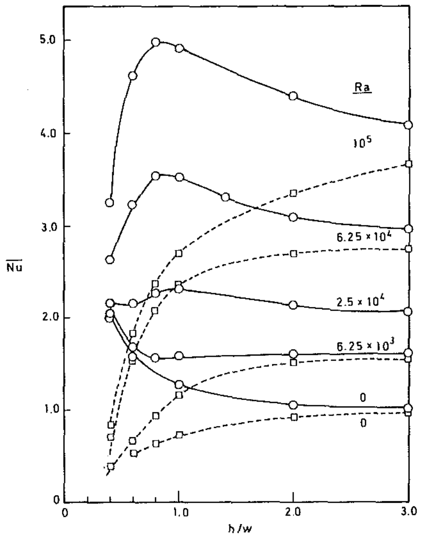

Fig. 14 Effect of cavity height and Rayleigh number on rate of heat transfer—$\ell/w = 0.2$, $s/h = 0.5$ ($\Delta X = \Delta Y = 0.1$)

$\psi_{\max}$ and Nu is shown in Figs. 5 and 6. For the isothermal case $\psi_{\max}$ increases for all Ra as the width is increased. Nu also increases, except for pure conduction (Ra → 0). The behavior for insulated horizontal surfaces is more complicated. At high Ra a maximum and then a minimum in the rate of circulation is observed as the width is increased owing to the competitive effects of decreased drag and decreased heat transfer. The minimum disappears as Ra decreases. As the width decreases, the rate of circulation necessarily becomes the same as for isothermal horizontal surfaces. The rate of heat transfer generally decreases as the width increases. The rates of heat transfer for the two boundary conditions again approach one another as the width is decreased.

Discussion

A computer program has been developed for the computation of the temperature and velocity field in two-dimensional laminar natural convection with a heater in the form of a long, horizontal, isothermal strip of arbitrary width and location on an otherwise-insulated, vertical wall of a rectangular channel. The computed flow patterns were found to be in agreement with experimental results, and the computed heat transfer rates for limiting conditions with prior computations. Illustrative numerical results have been presented herein for $\mathrm{Pr} = 0.7$. Numerical values are presented only for finite grid-size but the values obtained from the computer can readily be extrapolated to zero grid-size if desired.

The relationship between the circulation pattern and the rate of heat transfer has been found to be quite complex, and indicates the possibility of maximizing or minimizing the rate of circulation for a given rate of heat transfer or vice versa. Conduction was observed to be the predominant mechanism for heat transfer for $\mathrm{Ra} < 1000$ even though some circulation occurs for all $\mathrm{Ra} > 0$. The results herein, when expressed in terms of Ra, S, and L, would be expected to be approximately valid for any Newtonian fluid with $\mathrm{Pr} > 0.7$ [10].

Boundary layer theory for a vertical heated plate does not appear to be useful for prediction or correlation of the computed values.

The choice of the characteristic dimension in the Rayleigh number is arbitrary but affects the magnitude significantly. For example the use of the width of the heating element instead of the height of the enclosure would decrease the indicated magnitudes of Ra by a factor of $(\ell/h)^3 = 8 \times 10^{-3}$ for $\ell/h = 0.2$.

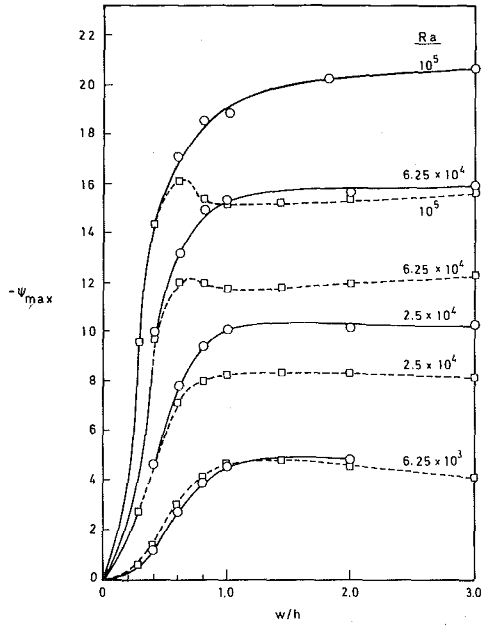

Fig. 15 Effect of cavity width and Rayleigh number on rate of circulation—$\ell/h = 0.2$, $s/h = 0.5$ ($\Delta X = \Delta Y = 0.1$)

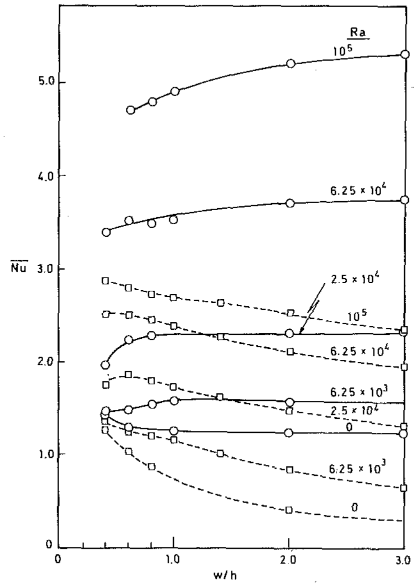

Fig. 16 Effect of cavity width and Rayleigh number on rate of heat transfer—$\ell/h = 0.2$, $s/h = 0.5$, ($\Delta X = \Delta Y = 0.1$)

References

1 Chu, H. H.-S., "Natural Convection in a Closed Cavity With Localized Heating on One Vertical Wall," PhD thesis, University of Pennsylvania, Philadelphia, 1974.

2 Probert, D., Brooks, R. G., and Dixon, M., "Heat Transfer Across Rectangular Cavities," *Chemical Process Engineering,* Heat Transfer Survey, Vol. 42, 1970, pp. 35–40.

3 Torrance, K. E., and Rockett, J. A., "Numerical Study of Natural Convection in an Enclosure With Localized Heating From Below-Creeping Flow to the Onset of Laminar Instability," *J. Fluid Mech.,* Vol. 36, 1969, pp. 33–54.

4 Torrance, K. E., Orloff, L., and Rockett, J. A., "Experiments on Natural Convection in Enclosures With Localized Heating From Below," *J. Fluid Mech.,* Vol. 36, 1969, pp. 21–31.

5 Erb, R. I., "Interferometric Study of Natural Convection Inside a Horizontal Cylindrical Cavity," MS thesis, Air Force Institute of Technology, Mar. 1965.

6 Chu, H. H.-S., and Churchill, S. W., "The Development and Testing of a Numerical Solution for Laminar Natural Convection in Enclosures," Preprint No. 57c, 80th National Meeting, AIChE, Boston, Sept. 1975.

7 Douglas, J., Jr., and Peaceman, D. W., "Numerical Solution of Two-Dimensional Heat Flow Problems," *AIChE Journal*, Vol. 1, 1955, pp. 502–512.

8 Wilkes, J. O., and Churchill, S. W., "The Finite-Difference Computation of Natural Convection in a Rectangular Enclosure," *AIChE Journal*, Vol. 12, 1966, pp. 161–166.

9 Samuels, M. R., and Churchill, S. W., "Stability of a Fluid in a Rectangular Region Heated From Below," *AIChE Journal*, Vol. 13, 1967, pp. 77–85.

10 Ozoe, H., and Churchill, S. W., "Hydrodynamic Stability and Natural Convection in Ostwald-deWaele and Ellis Fluids: The Development of a Numerical Solution," *AIChE Journal*, Vol. 18, pp. 1196–1207.

11 Samuels, M. R., "Stability of a Fluid in a Long Horizontal Rectangular Cylinder Heated From Below," PhD thesis, University of Michigan, Ann Arbor, 1966.

12 Wilkes, J. O., "The Finite Difference Computation of Natural Convection in an Enclosed Rectangle," PhD thesis, University of Michigan, Ann Arbor, 1963.

13 deVahl Davis, G., "Laminar Natural Convection in an Enclosed Rectangular Cavity," *International Journal of Heat and Mass Transfer*, Vol. 11, 1968, pp. 1675–1692.

14 Elder, J. W., "Numerical Experiments With Free Convection in a Vertical Slot," *Journal of Fluid Mechanics*, Vol. 24, 1966, pp. 823–843.

15 MacGregor, R. K., and Emery, H. A., "Free Convection Through Vertical Plane Layers—Moderate and High Prandtl Number Fluids," JOURNAL OF HEAT TRANSFER, TRANS. ASME, Series C, Vol. 91, 1969, pp. 391–403.

16 Boyack, B. E., and Kearney, D. W., "Heat Transfer by Laminar Natural Convection for Low Aspect Ratio Cavities," ASME Paper No. 72-HT-52.

H. Ozoe
Department of Industrial and Mechanical
Engineering, School of Engineering,
Okayama University,
Okayama, Japan

K. Yamamoto
Kobe Steel, Ltd.,
Kobe, Japan

S. W. Churchill
Department of Chemical and Biochemical
Engineering, University of Pennsylvania,
Philadelphia, Pa.

H. Sayama
Department of Industrial and
Mechanical Engineering,
School of Engineering,
Okayama University,
Okayama, Japan

Three-Dimensional, Numerical Analysis of Laminar Natural Convection in a Confined Fluid Heated From Below

An improved model and algorithm were developed for the numerical solution of three-dimensional, laminar natural convection in enclosures. Illustrative calculations were carried out for heating from below in a cubical box, a long channel with a square cross section and in the region between infinite, horizontal plates. The results are in good agreement with prior experimental and theoretical results. For the infinite flat plates the three-dimensional model correctly produces a two-dimensional solution. For the cube the solution produces different stable solutions depending on the initial conditions. A fluid-particle path is shown to be a good method of illustrating the three-dimensional motion. In the cube and in each cubical cell in the channel this streak-line was found to consist of a pair of double helices.

Introduction

Three-dimensional analysis is difficult because three nonlinear momentum equations must be solved in addition to the mass and work by Aziz and Hellums [1][1] who computed the fluid motion and temperature field in a cube heated from below. Except for limiting cases, natural convection in a confined fluid is necessarily three-dimensional and the proliferation of two-dimensional, numerical solutions in the literature is based on mathematical convenience and perhaps reasonable approximation rather than on exact correspondence to the physical world.

Three-dimensional analysis is difficult because three nonlinear momentum equations must be solved in addition to the mass and energy equations. The boundary conditions are also much more complicated than for two-dimensional convection. Detail and error in the numerical integration increase by perhaps an order of magnitude over two-dimensional calculations. Numerical instability is also more of a problem. As a consequence the requirements of time and memory are severe even by the standard of modern computers.

Aziz and Hellums carried out numerical integrations for a horizontal, diagonal roll-cell in a cube heated from below and obtained Nu = 1.65 for Pr = 1.0 and Ra = 3500. However Catton [2] obtained 3446 for the critical Rayleigh number (Nu → 1.0) by perturbation methods and Heitz and Westwater [3] obtained nearly the same value experimentally. This discrepancy is discussed in connection with the numerical results obtained herein.

The objective of this paper is to develop a more general, efficient and accurate computational scheme for three-dimensional natural convection. Three geometrical configurations with heating from below were chosen for test calculations: the region between infinite, horizontal plates; a cubical enclosure; and a long channel with a square cross section. The vertical sides of the cube and channel are assumed to be perfect insulators.

Mathematical Model

Three-dimensional, laminar, natural convection in a fluid with constant physical properties, other than the density in the buoyancy term, and with negligible viscous dissipation can be represented by the following equations for the conservation of mass, energy, and momentum:

$$\nabla \cdot \vec{v} = 0 \qquad (1)$$

---

[1] Numbers in brackets designate References at end of paper.

Contributed by the Heat Transfer Division for publication in the JOURNAL OF HEAT TRANSFER. Manuscript received by the Heat Transfer Division November 13, 1975. Paper No. 76-HT-RR.

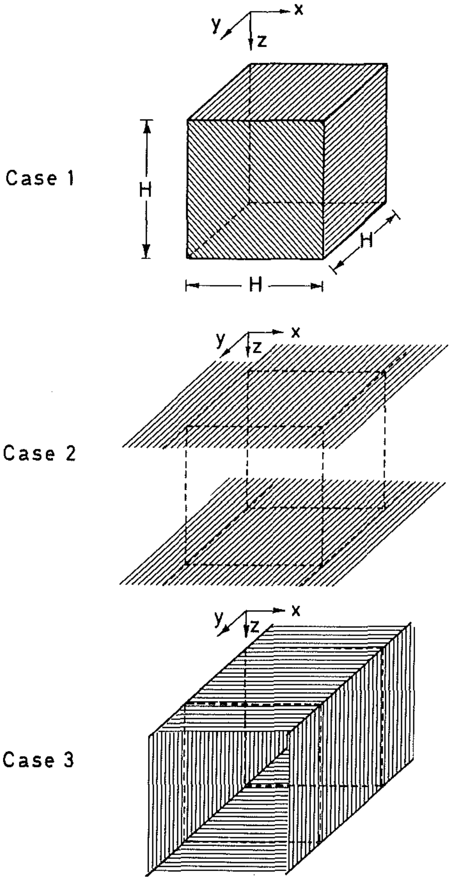

Fig. 1 Geometrical configurations
Case 1—cubical enclosure
Case 2—infinite horizontal plates
Case 3—channel with a square cross-section

and

$$\frac{DT}{Dt} = \alpha\nabla^2 T \tag{2}$$

$$\frac{D\vec{v}}{Dt} = -\frac{\nabla P'}{\rho_0} + \nu\nabla^2\vec{v} + \begin{pmatrix} 0 \\ 0 \\ -g\beta(T - T_0) \end{pmatrix} \tag{3}$$

In equation (3), the gravity vector has been taken to be in the z-direction as indicated in Fig. 1. The equation of state for the fluid was assumed to be

$$\rho = \rho_0/[1 + \beta(T - T_0)] \tag{4}$$

and the pressure to be represented by a dynamic plus a static term, such that

$$\nabla P \equiv \nabla P' + \vec{g}\rho_0 \tag{5}$$

Following Aziz and Hellums [1], a three-dimensional vorticity and vector potential were introduced to expedite the numerical solution of the model. Assuming $\rho = \rho_0$ in the dynamic pressure term, taking cross-derivatives of the three components of equation (3) with x, y, and z and subtracting to eliminate the dynamic pressure terms, then introducing the vorticity for the derivatives of the velocity components and finally dedimensionalizing gives

$$\frac{1}{\mathrm{Pr}}\left(\frac{D\vec{\Omega}}{D\tau} - (\vec{\Omega}\cdot\bar{\nabla})\vec{V}\right) = \begin{pmatrix} -\mathrm{Ra}\dfrac{\partial\phi}{\partial Y} \\ +\mathrm{Ra}\dfrac{\partial\phi}{\partial X} \\ 0 \end{pmatrix} + \bar{\nabla}^2\vec{\Omega} \tag{6}$$

The dimensionless vorticity is here defined as the curl of the dimensionless velocity in terms of the dimensionless coordinates:

$$\vec{\Omega} \equiv \bar{\nabla} X \vec{V} \tag{7}$$

A dimensionless vector potential is then defined such that its curl equals the dimensionless velocity vector:

$$\vec{V} \equiv \bar{\nabla} X \vec{\psi} \tag{8}$$

This vector potential satisfied equation (1), i.e.,

$$\bar{\nabla}\cdot\vec{V} = \bar{\nabla}\cdot(\bar{\nabla} X \vec{\psi}) = 0 \tag{9}$$

and can be required to be solenoidal, i.e.,

Nomenclature

$\vec{g}$ = gravitational vector
g = acceleration due to gravity in z-direction
H = distance between plates, height of channel and sides of cube
k = thermal conductivity
Nu = mean Nusselt number = $qH/k(T_h - T_c)$
P = pressure
P' = dynamic pressure (see equation (5))
Pr = Prandtl number = ν/α
q = mean heat flux density over surface
Ra = Rayleigh number = $g\beta(T_h - T_c)H^3/\alpha\nu$
T = temperature
T_c = temperature of cold plate
T_h = temperature of hot plate
T_0 = initial temperature = $(T_h + T_c)/2$
t = time
u = velocity component in x-direction
U = dimensionless velocity component in X-direction = uH/α
$\vec{v}$ = vector velocity
$\vec{V}$ = dimensionless vector velocity = $\vec{v}H/\alpha$
v = velocity component in y-direction
V = dimensionless velocity component in Y-direction = vH/α
w = velocity component in z-direction (downward)
W = dimensionless velocity component in Z-direction (downward), wH/α
x = horizontal coordinate (across channel)
X = dimensionless horizontal coordinate (across channel) = x/H
y = horizontal coordinate (down channel)
Y = dimensionless horizontal coordinate (down channel) = y/H
z = vertical (downward) coordinate
Z = dimensionless vertical (downward) coordinate = z/H
α = thermal diffusivity
β = volumetric coefficient of expansion with temperature
θ = fictitious dimensionless time in equation (15)
ν = kinematic viscosity
ρ = density
ρ_0 = density at T_0
τ = dimensionless time = $t\alpha/H^2$
ϕ = dimensionless temperature = $(T - T_0)/(T_h - T_c)$
$\vec{\psi}$ = vector potential (see equation (8))
ψ_i = i-component of vector potential
$\vec{\Omega}$ = vorticity vector (see equation (7))
Ω_i = i-component of vorticity vector

Operators

$\nabla = i(\partial/\partial x) + j(\partial/\partial y) + k(\partial/\partial z)$
$\bar{\nabla} = i(\partial/\partial X) + j(\partial/\partial Y) + k(\partial/\partial Z)$
$D/Dt = (\partial/\partial t) + u(\partial/\partial x) + v(\partial/\partial y) + w(\partial/\partial z)$
$D/D\tau = (\partial/\partial\tau) + U(\partial/\partial X) + V(\partial/\partial Y) + W(\partial/\partial Z)$
σ = of the order of

$$\bar{\nabla}\cdot\vec{\psi} = 0 \tag{10}$$

The vorticity is then related to the vector potential as follows:

$$\vec{\Omega} = \bar{\nabla}X\vec{V} = \bar{\nabla}X(\bar{\nabla}X\vec{\psi}) = \bar{\nabla}(\bar{\nabla}\cdot\vec{\psi}) - \bar{\nabla}^2\vec{\psi} = -\bar{\nabla}^2\vec{\psi} \tag{11}$$

The vorticity and temperature fields are obtained by solving equation (6) simultaneously with the energy equation in nondimensional form:

$$\frac{D\phi}{D\tau} = \bar{\nabla}^2\phi \tag{12}$$

For the solenoidal case the vector potential can then be obtained by solving equation (11). The velocity is finally obtained from the vector potential through equation (8).

Boundary Conditions

The conditions on velocity and temperature follow from physical intuition. At $Z = 0$ and 1, the dimensionless temperatures are $-\frac{1}{2}$ and $\frac{1}{2}$, respectively, and on all vertical walls the derivative of temperature normal to the wall is zero. On all rigid walls the three components of the velocity are zero. The boundary conditions on the vector potential are not so obvious. Since the principal difficulty in developing a solution arose from their specification some discussion of this problem seems appropriate. The conditions for the cubical enclosure will be discussed here and then the modifications for the other geometries later.

Aziz and Hellums [1] used the following conditions for the vector potential on the rigid walls at $X = 0$ and 1 as proposed by Hirasaki and Hellums [4]

$$\partial\psi_x/\partial X = \psi_y = \psi_z = 0 \tag{13}$$

Similar conditions follow for the $Y = 0$ and 1 and $Z = 0$ and 1 walls. The boundary conditions on the vorticity follow from those on the velocity under the presumption that the tangential derivatives of the velocity components are zero at the wall, but not necessarily the normal derivatives. For example for the walls at $X = 0$ and 1

$$\Omega_x = 0,\ \Omega_y = -\frac{\partial W}{\partial X},\quad \Omega_z = \frac{\partial V}{\partial X} \tag{14}$$

The vorticity at the wall can be computed in two ways: (1) directly from the velocity gradient as in equation (14); or (2) from the vector potential. Initially, this second method was tried. However the resulting velocity components did not extrapolate smoothly to zero at the boundaries. This suggests that the computed vector potential in the fluid does not couple strongly with the primitive condition that the velocity components be zero on the walls.

The boundary conditions used by Aziz and Hellums for the vector potential can also be applied directly. These conditions require only that the normal component of the velocity be zero at the walls. For example to satisfy $V = W = 0$ at the $X = 0$ and 1 walls it is necessary that $\partial\psi_x/\partial Z = \partial\psi_z/\partial X$ and $\partial\psi_y/\partial X = \partial\psi_x/\partial Y$. This requires the simultaneous calculation of ψ_x, ψ_y and ψ_z because of the coupled conditions on the walls. This process is both awkward and time consuming and was, therefore, not tried.

As a fourth method all three components of the vector potential and two of the normal derivatives were equated to zero on each wall. The vorticity was computed from equation (11) but at different grid points than the vector potential, thus avoiding over-specification of the vorticity at the walls. This combination of boundary conditions was found to be satisfactory for all three geometrical configurations considered herein. However when subsequently tried for an inclined square channel it failed to yield the oblique roll-cell which has been observed experimentally. Hence, it cannot be relied on to produce the correct mode of circulation.

Computation of the vorticity at the wall directly from the velocity gradient through equation (14) thus proved to be more successful than any of the other three methods and was finally used to obtain the results reported herein. The velocity components computed in this way extrapolate smoothly to the wall. When the vorticity on the wall is calculated from the velocity gradients it is corrected strongly from step to step. This procedure also resulted in better satisfaction of the solenoidal condition on the vector potential. The boundary conditions on the vector potential provided by equation (13) do not assure that the tangential velocity components are zero on the walls but that condition is satisfied implicitly through computation of the vorticity at the wall from the velocity.

Numerical Method

Equations (6) and (12) were solved by finite difference methods using the general three-dimensional ADI (alternating direction-implicit) method developed by Brian [5]. This computational procedure differs slightly from that used by Aziz and Hellums [1].

The first and second derivatives were approximated by central differences and the time derivatives by a first-order forward difference. Applying the ADI method to equations (6) and (12) produces first-order algebraic equations with a coefficient matrix of three diagonal components. The unknowns are solved line by line in the X-, Y-, and Z-directions. This numerical procedure is a simple extension of that for two dimensions. Because of the limited memory of the available computer the sides of the cube were divided into only eight segments, yielding $9^3 = 729$ grid points. The steady-state solution was obtained as the limit of transient calculations using a dimensionless time step of 0.001. For each time step 9 × 9 or 7 × 7 matrices were solved about one thousand times by the Thomas method [6] to obtain the temperature and the three components of the vorticity. The three components of the vector potential were then obtained from the vorticity using equation (11) with an added, fictitious, unsteady term as proposed by Samuels and Churchill [7]:

$$\frac{\partial\vec{\Psi}}{\partial\theta} = \vec{\Omega} + \frac{\partial^2\vec{\Psi}}{\partial X^2} + \frac{\partial^2\vec{\Psi}}{\partial Y^2} + \frac{\partial^2\vec{\Psi}}{\partial Z^2} \tag{15}$$

20 s were required to advance one time step on the NEAC TYPE 2200/500 computer at the Okayama University Computing Center. This computer is about 1/10th as fast as an IBM 360/75. From 200 to 500 time-steps were required to approach the steady-state closely enough. The computations were limited to $\Pr = 10$ but the results would be expected to provide a good approximation for all $\Pr \geq 1$, just as they are known to for two-dimensional calculations [7].

Numerical Results

Case I—Cubical Enclosure Heated From Below. Aziz and Hellums [1] computed a roll-cell with a horizontal and diagonal axis. In order to obtain this same mode of circulation the numerical calculations herein were started from $\phi = 0$ with two hot and two cold finite-difference elements located in the $Z = 0.5$ plane as shown in Fig. 2(*a*). Calculations were also started from $\phi = 0$ with the series of hot and cold finite-difference elements located in the $Z = 0.5$ plane as shown in Fig. 2(*b*). The resulting roll-cell had an axis horizontal and parallel to the $Y = 0$ and 1 walls as indicated. Both of these modes of circulation were stable according to the numerical analysis. Other stable modes might also be computed with different initial conditions. The computations for the second (nondiagonal) mode were carried out for Ra = 4000, 6000, and 8000. The mean Nusselt numbers computed at the $Z = 0.5$ plane are listed in Table 1. The critical Rayleigh

Table 1 Computed values of Nu at $Z = 0.5$ for $\Delta X = \Delta Y = \Delta Z = 0.125$

Ra	Cubical box	Infinite horizontal plates	Long channel with square cross section
2000	—	1.451	—
2600	—	—	1.258
3000	—	—	1.455
4000	1.165	1.966	1.801
6000	1.535	—	2.213
8000	1.746	2.617	2.482

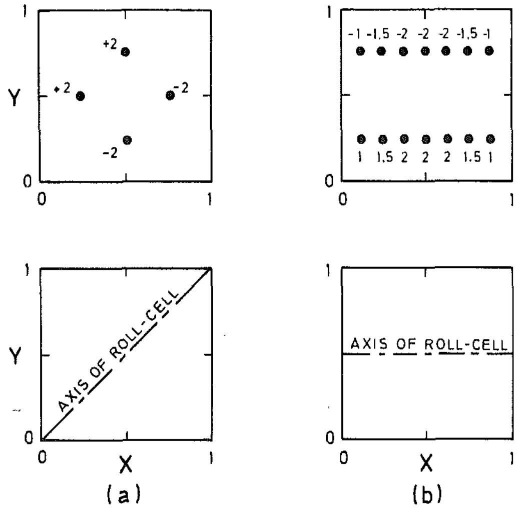

Fig. 2 Dependence of mode of circulation in a cubical enclosure on location of initial hot and cold finite-difference elements centered in the $Z = 0.5$ plane (numbers are initial values of ϕ): (*a*) for diagonal roll cell; (*b*) for parallel roll cell

number obtained by extrapolation to Nu = 1 is approximately 3500 which agrees closely with the previously mentioned computed and experimental values of Catton [2] and of Heitz and Westwater [3].

Computed values of Nu for the diagonal mode were in reasonable agreement with those of Aziz and Hellums and, hence, significantly in excess of the above-mentioned experimental results. Therefore, it is tentatively concluded that the nondiagonal mode is the physically preferred one. The stability of various modes of circulation and the preferred mode can however be determined only by experimental observations of the circulation pattern and this objective will be pursued in a continuation of this work.

Illustrative values of the dimensionless components of the velocity are plotted in Fig. 3. The several lines for each plot and the finite values for the U-component itself indicate three-dimensional effects, i.e., the effect of the drag of the walls at the ends of the roll-cell (X = 0 and 1).

The flow characteristics can be visualized somewhat better by a streak-line, i.e., the path traced by a particle of the fluid. Such a line was computed by starting at a point in the fluid and calculating the subsequent location after a small time increment using a Runge-Kutta technique. The velocity components were known only at the grid points, hence a second-order interpolating equation was used to compute the values at intermediate locations. A satisfactory eventual return to the initial point indicated that the numerical error in this calculation was not serious.

A partial trajectory of a particle starting from $X = 0.375$, $Y = 0.1875$, $Z = 0.1875$ is shown in Fig. 4. The particle circulates helically toward the $X = 0$ plane with a radius of gyration of about 0.45. The radius of gyration begins to decrease as the axial velocity decreases to zero and continues to decrease as the axial velocity reverses sign at about $X = 0.1$. If the streak line were continued, the radius of gyration would begin to increase again at about $X = 0.3$ and, after another reversal in the sign of the axial velocity at about $X = 0.4$ the streak line would return to the starting point. This same pattern occurs for the other half of the roll-cell between $X = 0.5$ and 1.0. Thus the circulation consists of a pair of double (concentric) helices (or spirals). This type of pattern has probably been observed experimentally but apparently has not been described quantitatively before.

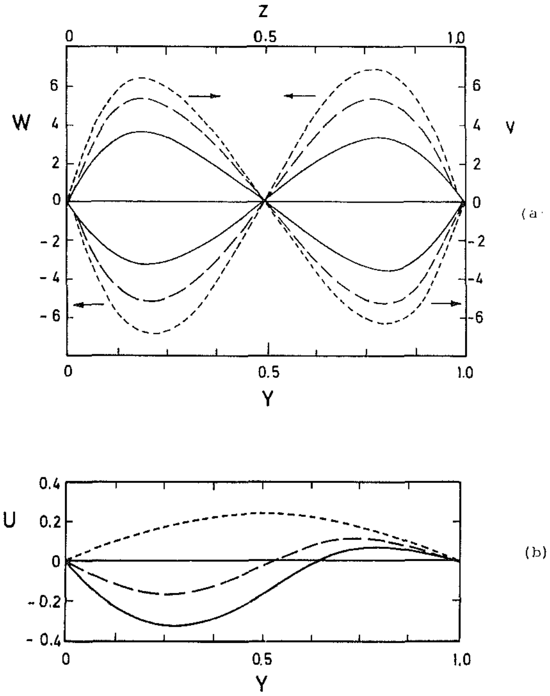

Fig. 3 Illustrative traces of the velocity components for a parallel roll cell in a cubical enclosure with Ra = 4000 and Pr = 10:

(*a*) W at $Z = 0.5$ —— $X = 0.125$; ----- $X = 0.250$; ----- $X = 0.500$

V at $Y = 0.5$

(*b*) U at $X = 0.375$ —— $Z = 0.125$; ----- $Z = 0.250$; ----- $Z = 0.500$

Case 2—Region Between Infinite Horizontal Plates Heated From Below. To simulate natural convection between infinite horizontal plates, a cubical cell was postulated whose four vertical faces are fluid interfaces and whose horizontal faces are rigid walls.

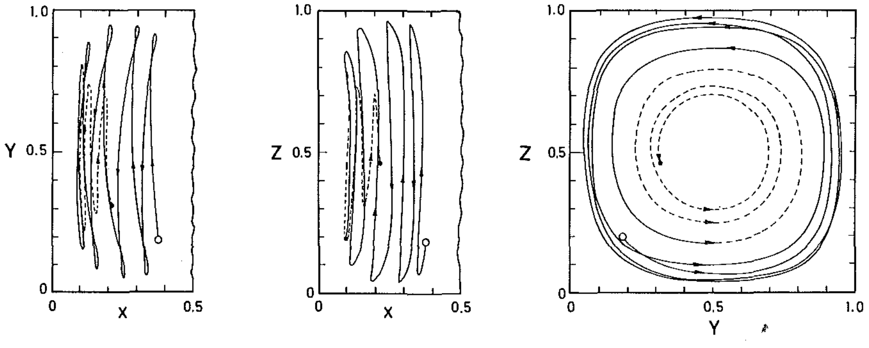

Fig. 4 Traces of fluid particle path in a cubical enclosure with Ra = 4000 and Pr = 10: ○ starting point at $X = 0.375$, $Y = Z = 0.1875$; ● end point at $\tau = 50$

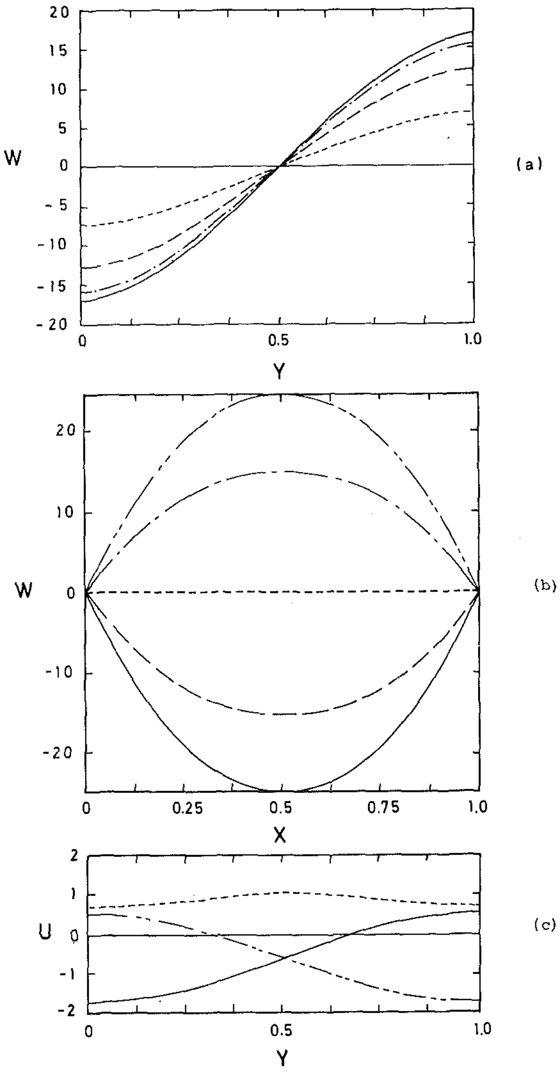

Fig. 5 Illustrative traces of the velocity components for a long channel with square cross-section at Pr = 10:
(*a*) Downward velocity component *W* at *Z* = 0.5, Ra = 4000
- - - - -*X* = 0.125 and 0.875
— — —*X* = 0.250 and 0.750
—•—•—*X* = 0.375 and 0.625
———*X* = 0.500
(*b*) Downward velocity component *W* at *Z* = 0.5, Ra = 6000
———*Y* = 0.00
— — —*Y* = 0.25
- - - - - - - *Y* = 0.50
— - — -*Y* = 0.75
— - - —*Y* = 1.00
(*c*) Axial velocity component *U* at *X* = 0.25, Ra = 4000
———*Z* = 0.125
- - - - - - - *Z* = 0.500
— - - - *Z* = 0.875

A boundary condition for the fluid interfaces does not appear to have been formulated before for the three-dimensional numerical calculations. At the $Y = 0$ and 1 planes $\psi_x = \partial\psi_y/\partial Y = \psi_z = 0$ should hold since the normal velocity component on this interface is zero just as for a rigid wall. The additional condition is that the normal derivatives of the components of the tangential velocity be zero. Thus, at the $Y = 0$ and 1 planes $\partial U/\partial Y = \partial W/\partial Y = \partial V/\partial X = \partial V/\partial Z = 0$. For the vector potential the following conditions were then derived for the $Y = 0$ and 1 planes:

$$\left.\begin{aligned}\frac{\partial U}{\partial Y}=\frac{\partial}{\partial Y}\left(\frac{\partial\psi_z}{\partial Y}-\frac{\partial\psi_y}{\partial Z}\right)=\frac{\partial^2\psi_z}{\partial Y^2}-\frac{\partial}{\partial Z}\left(\frac{\partial\psi_y}{\partial Y}\right)=\frac{\partial^2\psi_z}{\partial Y^2}=0\\ V=\frac{\partial\psi_x}{\partial Z}-\frac{\partial\psi_z}{\partial X}=0\\ \frac{\partial W}{\partial Y}=\frac{\partial}{\partial Y}\left(\frac{\partial\psi_y}{\partial X}-\frac{\partial\psi_x}{\partial Y}\right)=-\frac{\partial^2\psi_x}{\partial Y^2}+\frac{\partial}{\partial X}\left(\frac{\partial\psi_y}{\partial Y}\right)=-\frac{\partial^2\psi_x}{\partial Y^2}=0\end{aligned}\right\}\quad(16)$$

Thus the second derivatives of ψ_x and ψ_z should vanish. These conditions were used to obtain the tangential velocity components at the fluid interface. The conditions for the vorticity follow directly. The boundary conditions may then be illustrated for $X = 0$ and 1 as follows:

$$\frac{\partial\psi_x}{\partial X}=\psi_y=\psi_x=\frac{\partial^2\psi_y}{\partial X^2}=\frac{\partial^2\psi_z}{\partial X^2}=\Omega_y=\Omega_z=0 \qquad (17)$$

Computations were carried out for Pr = 10 and Ra = 2000, 3000, and 6000. The results for Nu are included in Table 1. For Ra = 6000, the magnitude of the Y and Z components of the vector potential, ψ_y and ψ_z, was found to be O (10^{-6}) or less whereas ψ_x was O (1). The magnitude of the axial velocity component U was O (10^{-5}), whereas V and W were equal on all X-planes and exceeded 20 in magnitude. These results indicate that the steady convective mode is two-dimensional in agreement with the results of Lipps and Sommerville [8] who found with incomplete calculations that the transient behavior was three-dimensional but the steady behavior two-dimensional.

An earlier, two-dimensional computer program with the vorticity at the walls computed from the vector potential rather than from the velocity [9, 10] was employed for the same grid-size, Ra and Pr. For Ra = 3000, Nu = 1.931 was obtained as compared to the value of 1.966 in Table 1. The small difference is presumably due to the different method of computing the vorticity at the wall. The velocity and temperature fields showed similar agreement. Lipps and Sommerville concluded that the width of the two-dimensional cell was not exactly equal to the height, as assumed here. This choice may introduce some small error into the computed results.

The fact that an essentially two-dimensional flow field in accordance with prior experimental observations and computed results was obtained from the three-dimensional formulation seems to assure that the extension of the boundary conditions and numerical scheme herein to three dimensions is sound.

Case 3—A Long Square Channel Heated From Below. A series of roll-cells with axes horizontal and perpendicular to the long dimension of the channel and with width almost equal to height is known to be the stable mode of circulation for this configuration. As an approximate, three-dimensional model for this flow a cube was selected with one opposing pair of rigid vertical walls and another opposing pair of frictionless fluid interfaces. The boundary conditions for this situation follow from the arguments for the prior two cases and are illustrated for $X = 0$ and 1 as follows:

$$\frac{\partial\psi_x}{\partial X}=\psi_y=\psi_z=\Omega_x=0,\quad \Omega_y=-\frac{\partial W}{\partial X},\quad \Omega_z=\frac{\partial V}{\partial X} \qquad (18)$$

The computed conditions and results are included in Table 1. The critical Rayleigh number obtained from extrapolation to Nu = 1 was 2300 which agrees reasonably well with the prediction of 2453 by Catton for a channel length-to-width-ratio of 10. Illustrative plots of the velocity components are shown in Fig. 5. The several curves in each plot and the finite values of U again indicate that the motion is three-dimensional. A fluid particle-path obtained by the same procedure as described for Case 1 is shown in Fig. 6. A pair of double helices occurs for this geometry as well as for Case 1 although the details are different.

Comparison of Nu for Cases 1, 2, and 3 and Prior Studies. The computed values of Nu are plotted versus Ra in Fig. 7. The prior results for infinite, horizontal plates obtained from two-dimensional calculations by Ozoe and Churchill [11] and experimentally by Silveston [12] are included; also the experimental results of Ozoe, et al. [9] for a long channel with a square cross section. The theoretical critical Rayleigh numbers obtained by Catton [2] for a cube and a channel with a square cross section and by Pellow and Southwell [13]

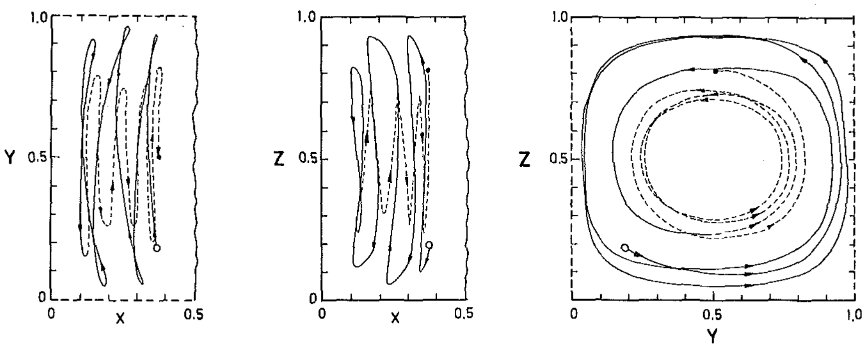

Fig. 6 Traces of fluid particle path in a long channel with a square cross-section with Ra = 4000 and Pr = 10: ○ starting point at $X = 0.375$, $Y = Z = 0.1875$; ● end point at $\tau = 15.4$

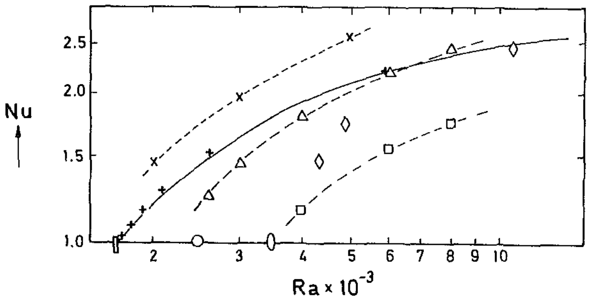

Fig. 7 Mean Nusselt number for three geometrical cases:

- - X - - infinite horizontal plates } This work
- - Δ - - square channel } $\Delta X = \Delta Y = \Delta Z = 0.125$
- - □ - - cubical box }
+ infinite horizontal plates—Ozoe and Churchill [11], $\Delta X = \Delta Y = \Delta Z \rightarrow 0$
——— infinite horizontal plates—Silveston [12], experimental
◊ *square channel—Ozoe, et al.,* [9], *experimental*
▯ infinite horizontal plates—Pellow and Southwell [13], theoretical
○ square channel—Catton [2], theoretical
0 cubical box—Catton [2], theoretical

for infinite horizontal plates are plotted as well.

Conclusions

The mathematical formulation and the computer algorithm developed in this investigation appear to be suitable for the computation of natural convection in enclosures. For infinite horizontal plates heated from below the calculations produced a two-dimensional motion in agreement with prior theoretical and experimental results. For a cubical enclosure, two stable, three-dimensional circulations were computed. The computed mode of circulation depends on the initial conditions. Experiments are therefore needed to determine the physically stable mode or modes. The results for a diagonal roll-cell are in reasonable agreement with the prior results of Aziz and Hellums [1] for that mode. Despite the large finite grid-size the results for a roll-cell with its axis parallel to a pair of the side walls are in good agreement with the prior theoretical results of Catton [2] and the experimental results of Heitz and Westwater [3].

The results for a channel with square cross-section are in fair agreement with the theoretical results of Catton [2] and the experimental results of Ozoe, et al. [9]. The numerical discrepancies are presumably due to the use of a finite grid-size for the calculations.

A plot of the computed path of a fluid particle appears to be useful for illustrating the complex, three-dimensional fluid motion. Such plots reveal that the motion both in the cube and in the individual cells of the square channel consists of a symmetrical pair of double helices.

References

1 Aziz, K., and Hellums, J. D., "Numerical Solution of the Three-Dimensional Equations of Motion for Laminar Convection," *Physics of Fluids*, Vol. 10, 1967, pp. 314–324.

2 Catton, I., "The Effect of Insulating Vertical Walls on the Onset of Motion in a Fluid Heated From Below," *International Journal of Heat and Mass Transfer*, Vol. 15, 1972, pp. 665–672.

3 Heitz, W. L., and Westwater, J. W., "Critical Rayleigh Numbers for Natural Convection of Water Confined in Square Cells With L/D from 0.5 to 8," JOURNAL OF HEAT TRANSFER, TRANS. ASME, Series C, Vol. 93, 1971, pp. 188–196.

4 Hirasaki, G. J., and Hellums, J. D., "A General Formulation of the Boundary Conditions on the Vector Potential in Three-Dimensional Hydrodynamics," *Quarterly of Applied Mathematics*, Vol. 26, 1968, pp. 331–342.

5 Brian, P. L. T., "A Finite Difference Method of High-Order Accuracy for the Solution of Three-Dimensional Transient Heat Conduction," *AIChE Journal*, Vol. 7, 1961, pp. 367–370.

6 Ames, W. F., *Nonlinear Partial Differential Equations in Engineering*, Academic Press, N.Y., 1965, p. 341.

7 Samuels, M. R., and Churchill, S. W., "Stability of a Fluid in a Rectangular Region Heated From Below," *AIChE Journal*, Vol. 13, 1967, pp. 77–85.

8 Lipps, F. P., and Sommerville, R. C. J., "Dynamics of Variable Wavelength in Finite Amplitude Benard Convection," *Physics of Fluids*, Vol. 14, 1965, pp. 759–765.

9 Ozoe, H., Sayama, H., and Churchill, S. W., "Natural Convection in an Inclined Square Channel," *International Journal of Heat and Mass Transfer*, Vol. 17, 1974, pp. 401–406.

10 Ozoe, H., Yamamoto, K., Sayama, H., and Churchill, S. W., "Natural Circulation in an Inclined Rectangular Channel Heated on One Side and Cooled on the Opposing Side," *International Journal of Heat and Mass Transfer*, Vol. 17, 1974, pp. 1209–1217.

11 Ozoe, H., and Churchill, S. W., "Hydrodynamic Stability and Natural Convection in Ostwald-de Waele and Ellis Fluids; the Development of a Numerical Solution," *AIChE Journal*, Vol. 18, 1972, pp. 1196–1207.

12 Chandrasekhar, S., *Hydrodynamic and Hydromagnetic Stability*, Oxford University Press, 1961, p. 68.

13 Pellow, A., and Southwell, R. V., "On Maintained Convective Motion in a Fluid Heated From Below," *Proceedings of the Royal Society* (London), Series A, Vol. 176, 1940, pp. 312–343.

G. M. Harpole
I. Catton

Department of Energy and Kinetics,
University of California,
Los Angeles, Calif.

Laminar Natural Convection About Downward Facing Heated Blunt Bodies to Liquid Metals

The laminar boundary layer equations for free convection over bodies of arbitrary shape (i.e., a three-term series expansion) and with arbitrary surface heat flux or surface temperature are solved in local Cartesian coordinates. Both two-dimensional bodies (e.g., horizontal cylinders) and axisymmetric bodies (e.g., spheres) with finite radii of curvature at their stagnation points are considered. A Blasius series expansion is applied to convert from partial to ordinary differential equations. An additional transformation removes the surface shape dependence and the surface heat flux or surface temperature dependence of the equations. A second-order-correct, finite-difference method is used to solve the resulting equations. Tables of results for low Prandtl numbers are presented, from which local Nusselt numbers can be computed.

Introduction

Some proposed designs for liquid-metal fast breeder reactors include a core catcher as part of the post-accident heat removal and containment system. One proposed core catcher design consists of a hemispherical dome of stainless steel. This dome would be situated below the reactor vessel, where it would catch falling debris and molten fuel should a melt-down accident occur. A pool of liquid metal below the dome would remove heat by natural convection. One part of what is needed to compute the dome thickness and temperature distribution is the solution to low Prandtl number natural convection about downward facing surfaces with nonuniform surface heat fluxes.

Free convection from various downward facing bodies has been studied previously, but little of it at low Prandtl numbers, and none of it general enough for application to core catchers. Laminar free convection from the very restricted class of two-dimensional and axisymmetric bodies which admit similarity solutions was solved by Braun, Ostrach, and Heighway [1].[1] They considered variable surface temperature. Cygan and Richardson [2] used an integral method with transcendental functions for temperature and velocity profiles to solve free convection from isothermal horizontal cylinders to low Prandtl number fluids. Chiang and Kaye [3] used a Blasius series expansion to find local Nusselt numbers for laminar free convection from a horizontal cylinder with a prescribed surface heat flux or surface temperature. Richardson and Gogus [4] solved the first term of Chiang and Kaye's expansion for low Prandtl number free convection from an isothermal cylinder. Chiang, Ossin, and Tien [5] applied the same Blasius series method to spheres with a prescribed surface heat flux or surface temperature. Koh and Price [6, 7, 8] transformed Chiang and Kaye's cylinder equations further, to make them independent of the arbitrary surface heat flux or temperature. Fox [9] proposed treating arbitrary surface shapes as in Schlichting [10] for forced convection. Saville and Churchill [11] presented a Görtler-type series expansion for free convection from a horizontal cylinder and used it for a low Prandtl number solution to the isothermal horizontal cylinder [12]. Wilks [13] extended the Saville-Churchill analysis to two-dimensional bodies of constant heat flux. Lin and Chao [14] presented series solutions of the form first proposed by Merk to free convection from isothermal surfaces of arbitrary shape. Peterka and Richardson [15] solved second-order boundary layer equations for an isothermal horizontal cylinder.

No work has been found which considers natural convection from nonisothermal surfaces of arbitrary shape. Until now, the only low-Prandtl-number solution to natural convection from a two-dimensional body has been for an isothermal cylinder [4, 12]

---

[1] Numbers in brackets designate References at end of paper.

Contributed by the Heat Transfer Division for publication in the JOURNAL OF HEAT TRANSFER. Manuscript received by the Heat Transfer Division August 13, 1975. Paper No. 76-HT-HH.

and there was no low-Prandtl-number solution to natural convection from any axisymmetric bodies. The present work solves the laminar natural convection heat transfer problem, from any arbitrary blunt nosed two-dimensional or axisymmetric body, with either an arbitrary surface heat flux or an arbitrary surface temperature, for low Prandtl numbers.

Analysis

The well known laminar boundary layer equations for steady-state free convection in local Cartesian coordinates (see Fig. 1) are

$$(ur^{*n})_{x^*} + (vr^{*n})_{y^*} = 0$$

$$uu_{x^*} + vu_{y^*} = \nu u_{y^*y^*} + g\beta\theta \sin\gamma$$

$$u\theta_{x^*} + v\theta_{y^*} = \alpha\theta_{y^*y^*} \tag{1}$$

where

$$n = 0 \text{ for two-dimensional bodies}$$

$$= 1 \text{ for axisymmetric bodies}$$

If a stream function ψ is defined such that

$$u = \psi_{y^*}, \quad v = -\left(\psi_{x^*} + n\psi \frac{r^*_{x^*}}{r^*}\right) \tag{2}$$

then equations (1) become

$$M_yM_{xy} - M_{yy}\left\{M_x + nM\frac{\cos\gamma}{r}\right\} = \Pr M_{yyy} + \phi \sin\gamma$$

$$M_y\phi_x - \phi_y\left\{M_x + nM\frac{\cos\gamma}{r}\right\} = \phi_{yy} \tag{3}$$

when the equations are made dimensionless with

$$x = \frac{x^*}{R}, r = \frac{r^*}{R}$$

$$y = (\mathrm{GrPr}^2)^{1/4}y^*/R, \quad M = (\mathrm{GrPr}^2)^{-1/4}\psi/\alpha, \quad \phi = \theta/\theta_{w0} \tag{4}$$

for specified surface temperature, and

$$y = (\overline{\mathrm{Gr}}\mathrm{Pr}^2)^{1/5}y^*/R, \quad M = (\overline{\mathrm{Gr}}\mathrm{Pr}^2)^{-1/5}\psi/\alpha,$$

$$\phi = \theta(\overline{\mathrm{Gr}}\mathrm{Pr}^2)^{1/5}k/q_0R \tag{5}$$

for the specified surface heat flux case.

Choosing the specified surface heat flux or temperature to be of the form

$$q = q_0(1 + a_1x^2 + a_2x^4) \text{ or } \theta_w = \theta_{w0}(1 + a_1x^2 + a_2x^4) \tag{6}$$

the dimensionless boundary conditions become

$$y = 0: \quad M = M_x = M_y = 0$$

$$-\phi_y = 1 + a_1x^2 + a_2x^4 \text{ or } \phi = 1 + a_1x^2 + a_2x^4 \tag{7}$$

$$y \to \infty: \quad M_y \to 0, \phi \to 0$$

If the surface shape is described by, see Appendix,

$$\sin\gamma = x + s_1x^3 + s_2x^5 + \ldots, \text{ and thus}$$

$$\frac{\cos\gamma}{r} = \frac{1}{x} - \frac{1}{3}x - \left(\frac{4}{5}s_1 + \frac{7}{45}\right)x^3 - \ldots \tag{8}$$

then the following Blasius series expansions can be used to convert equations (3) to ordinary differential equations:

$$M(x, y) = xf_0(y) + x^3f_1(y) + x^5f_2(y) + \ldots$$

$$\phi(x, y) = g_0(y) + x^2g_1(y) + x^4g_2(y) + \ldots \tag{9}$$

Substitution of the Blasius series expansion into equations (3) and grouping like powers of x results in pairs of equations of the form

$$\Pr f_j''' + \alpha_1f_j'' + \alpha_2f_j' + \alpha_3f_j + \alpha_4g_j + \alpha_5 = 0$$

$$g_j'' + \alpha_1g_j' + \alpha_6g_j + \alpha_7f_j + \alpha_8 = 0 \tag{10}$$

The first pair of equations are nonlinear and succeeding pairs are linear. In this work the series given by equations (9) are truncated to three terms.

The surface shape dependence can be removed from equations (10) and the surface heat flux or temperature dependence can be removed from the boundary conditions with the following transformations

$$f_0 = F_1 \qquad g_0 = G_1$$

$$f_1 = a_1F_2 + s_1F_3 \qquad g_1 = a_1G_2 + s_1G_3$$

$$f_2 = a_2F_4 + a_1^2F_5 + s_1a_1F_6 + s_1^2F_7 + s_2F_8$$

$$g_2 = a_2G_4 + a_1^2G_5 + s_1a_1G_6 + s_1^2G_7 + s_2G_8 \tag{11}$$

for two-dimensional bodies, and

$$f_0 = F_1 \qquad g_0 = G_1$$

$$f_1 = a_1F_2 + s_1F_3 + F_4 \qquad g_1 = a_1G_2 + s_1G_3 + G_4$$

$$f_2 = a_2F_5 + a_1^2F_6 + s_1a_1F_7 + s_1^2F_8 + s_2F_9 + s_1F_{10} + a_1F_{11} + F_{12}$$

$$g_2 = a_2G_5 + a_1^2G_6 + s_1a_1G_7 + s_1^2G_8 + s_2G_9 + s_1G_{10} + a_1G_{11} + G_{12} \tag{12}$$

for axisymmetric bodies. When equations (10) are transformed by equations (11) or (12), and when terms containing a_1, s_1, s_1a_1, etc., are grouped as the like powers of x were, these groups become pairs of equations of the form

Nomenclature

a_1, a_2 = surface heat flux or temperature parameters
f, g = functions defined by equation (9)
F, G = functions defined by equations (11) or (12)
g = gravitational acceleration
Gr = Grashof number, $g\beta\theta_{w0}R^2/\nu^2$
$\overline{\mathrm{Gr}}$ = modified Grashof number, $g\beta q_0R^4/k\nu^2$
k = thermal conductivity
M = dimensionless stream function
$\overline{\mathrm{Nu}}$ = average Nusselt number, $\bar{q}R/k\bar{\theta}$
Pr = Prandtl number, ν/α
q = surface heat flux, $-(k\partial\theta/\partial y^*)_w$
r = dimensionless distance from the symmetric axis
R = radius of curvature at the stagnation point
s_1, s_2 = surface shape parameters
T = temperature
u = x-direction velocity component
v = y-direction velocity component
x = dimensionless coordinate along the surface, see Fig. 1
y = dimensionless coordinate normal to the surface
α = thermal diffusivity
β = thermal expansion coefficient
γ = angle between the surface normal and the vertical, see Fig. 1
$\theta = T - T_\infty$
ν = kinematic viscosity
ϕ = dimensionless temperature
ψ = stream function

Subscripts

j = for the jth equation
w = at the surface
0, $w0$ = at the stagnation point
∞ = ambient

Superscripts

$*$ = a dimensional quantity
$'$ = derivative with respect to y

Table 1 Coefficients for equations (13) when bodies are two-dimensional

j	α_2	α_3	α_5	α_6	α_7	α_8
1	$-F_1'$	0	0	0	0	0
2	$-4F_1'$	$3F_1''$	0	$-2F_1'$	$3G_1'$	0
3	$-4F_1'$	$3F_1''$	G_1	$-2F_1'$	$3G_1'$	0
4	$-6F_1'$	$5F_1''$	0	$-4F_1'$	$5G_1'$	0
5	$-6F_1'$	$5F_1''$	$3(G_2G_2''-G_2'^2)$	$-4F_1'$	$5G_1'$	$3F_2'G_2'-2F_2G_2$
6	$-6F_1'$	$5F_1''$	$3(F_2''F_3+F_3''F_2)-6F_2'F_3'+G_2$	$-4F_1'$	$5G_1'$	$3(F_2G_3'+F_3G_2')-2(F_2'G_3+F_3'G_2)$
7	$-6F_1'$	$5F_1''$	$3(F_3''F_3-F_3'^2)+G_3$	$-4F_1'$	$5G_1'$	$3F_3G_3'-2F_3'G_3$
8	$-6F_1'$	$5F_1''$	G_1	$-4F_1'$	$5G_1'$	0

$\alpha_1 = F_1$, $\alpha_4 = 1$ all j

$$\Pr F_j''' + \alpha_1 F_j'' + \alpha_2 F_j' + \alpha_3 F_j + \alpha_4 G_j + \alpha_5 = 0$$

$$G_j'' + \alpha_1 G_j' + \alpha_6 G_j + \alpha_7 F_j + \alpha_8 = 0 \qquad (13)$$

with the α's being given in Tables 1 and 2. There are eight pairs of equations for two-dimensional bodies and twelve pairs for axisymmetric bodies. The boundary conditions which are needed for equations (13) are

$$F_j(0) = F_j'(0) = F_j'(\infty) = G_j(\infty) = 0 \quad \text{for all } j$$

$$G_j'(0) = -1 \text{ or } G_j(0) = 1 \quad \text{for } n = 0 \text{ and } j = 1, 2, \text{ and } 4$$

$$\text{for } n = 1 \text{ and } j = 1, 2, \text{ and } 5$$

$$G_j'(0) = 0 \text{ or } G_j(0) = 0 \quad \text{for other } j \qquad (14)$$

The first pair of equations (13) are nonlinear (e.g., $\alpha_1 = 2F_1$, $\alpha_2 = -F_1'$), and succeeding pairs are all linear, in that the α's come from solutions to preceding pairs of equations.

Equations (13) were solved using a finite difference method which utilized three-point central differencing. In solving the nonlinear equations (the first pair of equations (13)) an iteration procedure was used which linearized the equations to be solved at each iterate. The linearization was accomplished by letting $F_1{}^i = F_1{}^{i-1} + (F_1{}^i - F_1{}^{i-1})$ and $G_1{}^i = G_1{}^{i-1} + (G_1{}^i - G_1{}^{i-1})$ and dropping second order terms (e.g., $(F_1{}^i - F_1{}^{i-1})(G_1{}^i - G_1{}^{i-1})$). This is essentially Newton's method applied at each node point of the difference equations. Convergence was obtained with three iterations using

$$G_1{}^0 = \exp\{-y\}, \quad F_1{}^{0\prime} = \exp\{-y\} - \exp\{-y/\sqrt{\Pr}\} \qquad (15)$$

as initial guesses. A node point spacing of 0.0125 and a maximum y of 12.5 were used. A detailed description of this method can be found in reference [16].

Results

Two-dimensional and axisymmetric local Cartesian coordinate equations were solved for both the arbitrary surface heat flux case and the arbitrary surface temperature case for Prandtl numbers 0.0, 0.004, 0.006, 0.008, and 0.010, and the results (surface temperature or heat flux) are tabulated in Tables 3 and 4. For zero Prandtl number, the equations were solved by a singular perturbation technique, dropping the no slip boundary condition.

The local temperature for the specified heat flux case or the local heat flux for the specified temperature case can be found from Tables 3 and 4 in the following way. Use the values given in the tables in equations (11) or (12) to obtain values of terms in the Blasius expansion which include variable wall heat flux or temperature and shape. The local temperature for the arbitrary surface heat flux is then given by

Table 2 Coefficients for equations (13) when bodies are axisymmetric

j	α_2	α_3	α_5	α_6	α_7	α_8
1	$-F_1'$	0	0	0	0	0
2	$-4F_1'$	$4F_1''$	0	$-2F_1'$	$4G_1'$	0
3	$-4F_1'$	$4F_1''$	G_1	$-2F_1'$	$4G_1'$	0
4	$-4F_1'$	$4F_1''$	$-F_1F_1''/3$	$-2F_1'$	$4G_1'$	$-F_1G_1'/3$
5	$-6F_1'$	$6F_1''$	0	$-4F_1'$	$6G_1'$	0
6	$-6F_1'$	$6F_1''$	$4F_2F_2''-3F_2'^2$	$-4F_1'$	$6G_1'$	$4F_2G_2'-2F_2'G_2$
7	$-6F_1'$	$6F_1''$	$4(F_2''F_3+F_3''F_2)-6F_2F_3$	$-4F_1'$	$6G_1'$	$4(F_2G_3'+F_3G_2')-2(G_2F_3'+G_3F_2')$
8	$-6F_1'$	$6F_1''$	$G_3-3F_3'^2+4F_3F_3''$	$-4F_1'$	$6G_1'$	$4F_3G_3'-2G_3F_3'$
9	$-6F_1'$	$6F_1''$	G_1	$-4F_1'$	$6G_1'$	0
10	$-6F_1'$	$6F_1''$	$4(F_3''F_4+F_4''F_3)-6F_3'F_4'+G_4$ $- 4F_1F_1''/5-(F_1''F_3+F_1F_3'')/3$	$-4F_1'$	$6G_1'$	$4(F_3G_4'+F_4G_3')-4F_1G_1/5$ $-(G_1'F_3+G_3'F_1)/3-2(G_3F_4'+G_4F_3')$
11	$-6F_1'$	$6F_1''$	$4(F_2''F_4+F_4''F_2)-6F_2'F_4'$ $-(F_1''F_2+F_2''F_1)/3$	$-4F_1'$	$6G_1'$	$4(F_2G_4'+F_4G_2')-(G_1F_2+G_2F_1)/3$ $-2(G_2G_4'+G_4F_2')$
12	$-6F_1'$	$6F_1''$	$4F_4''F_4-3F_4'^2-7F_1''F_1/45$ $-(F_1''F_4+F_1F_4'')/3$	$-4F_1'$	$6G_1'$	$4F_4G_4'-7F_1G_1'/45-2G_4F_4'$ $-(G_1'F_4-F_1G_4')/3$

$\alpha_1 = 2F_1$, $\alpha_4 = 1$ all j

Table 3 Results for two-dimensional bodies

j	Arbitrary Surface Heat Flux					Arbitrary Surface Temperature				
	$G_j(0)$					$G_j'(0)$				
	Pr=0.0	.004	.006	.008	.010	Pr=0.0	.004	.006	.008	.010
1	1.476	1.512	1.520	1.527	1.533	-0.616	-0.596	-0.592	-0.589	-0.586
2	0.640	0.643	0.650	0.656	0.661	-1.480	-1.404	-1.387	-1.373	-1.361
3	-0.142	-0.146	-0.148	-0.150	-0.151	-0.137	-0.135	-0.135	-0.134	-0.134
4	0.488	0.489	0.496	0.502	0.506	-1.978	-1.850	-1.820	-1.797	-1.777
5	-0.0206	-0.0229	-0.0235	-0.0240	-0.0245	-0.153	-0.155	-0.155	-0.154	-0.153
6	-0.0717	-0.0775	-0.0793	-0.0808	-0.0821	-0.251	-0.253	-0.252	-0.252	-0.251
7	0.0415	0.0450	0.0463	0.0473	0.0482	0.0310	0.0321	0.0323	0.0324	0.0326
8	-0.0853	-0.0898	-0.0918	-0.0935	-0.0950	-0.108	-0.109	-0.110	-0.110	-0.110

$$T_w - T_\infty = (g_0(0) + g_1(0)x^2 + g_2(0)x^4)(q_0R/k)(\overline{\mathrm{Gr}}\mathrm{Pr}^2)^{-1/5} \quad (16)$$

The local heat flux for the arbitrary surface temperature case is given by

$$q = -(g_0'(0) + g_1'(0)x^2 + g_2'(0)x^4)(k(T_{w0} - T_\infty)/R)(\mathrm{GrPr}^2)^{1/4} \quad (17)$$

Average Nusselt numbers can be obtained by integrating equations (6) and (16) or (17) from zero to a maximum x value x_m. For a given heat flux

$$\overline{\mathrm{Nu}} = \frac{(1 + a_1x_m{}^2/3 + a_2x_m{}^4/5)}{(g_0(0) + g_1(0)x_m{}^2/3 + g_2(0)x_m{}^4/5)}(\overline{\mathrm{Gr}}\mathrm{Pr}^2)^{1/5} \quad (18)$$

For a given temperature

$$\overline{\mathrm{Nu}} = \frac{-(g_0'(0) + g_1'(0)x_m{}^2/3 + g_2'(0)x_m{}^4/5)}{(1 + a_1x_m{}^2/3 + a_2x_m{}^4/5)}(\mathrm{GrPr}^2)^{1/4} \quad (19)$$

Most previous work was for Prandtl numbers of 0.7 or 0.72. Results were obtained for many of the cases reported in previous works [3–8, 14, 15]. There was agreement to four significant figures in nearly every case and three significant figures in all cases.

It was shown by Harpole [16] that local Cartesian boundary layer equations will break down when $(\mathrm{GrPr}^2)^{1/4} < 20$. This was done by a second-order correct boundary layer analysis which is not reported here. Even the second-order boundary layer analysis is invalid when $(\mathrm{GrPr}^2)^{1/4} < 3$. Hence, low Gr, low Pr regimes require further attention and the present work is only valid for high Gr, low Pr regimes.

At high Gr, one usually anticipates transition to turbulence. In the present work, the stabilizing effect of a downward facing heated surface is believed to delay transition to extremely high Gr. No work was found which addressed the transition question for downward facing heated surfaces when the Pr was low.

The series expansions which represent wall temperature or heat flux, equations (16) or (17), were found to be highly convergent for uniform heat flux or temperature and divergent only with drastic nonuniformities in surface heat flux or temperature.

The solutions are general. They apply to any arbitrary blunt nosed two-dimensional or axisymmetric surface with any arbitrary surface heat flux or temperature.

References

1 Braun, W. H., Ostrach, S., and Heighway, J. E., "Free-Convection Similarity Flows About Two-Dimensional and Axisymmetric Bodies With Closed Lower Ends," *International Journal of Heat and Mass Transfer*, Vol. 2, 1961, pp. 121–135.

2 Cygan, D. A., and Richardson, P. D., "A Transcendental Approximation for Natural Convection at Small Prandtl Numbers," *Can. J. Chem. Engr.*, Vol. 46, 1968, pp. 321–324.

3 Chiang, T., and Kaye, J., "On Laminar Free Convection From a Horizontal Cylinder," *Proceedings 4th U.S. Nat. Cong. Applied Mech.*, Berkeley, Calif., 1962.

4 Richardson, P. D., and Gogus, Y., "Natural Convection From a Hori-

Table 4 Results for axisymmetric bodies

j	Arbitrary Surface Heat Flux					Arbitrary Surface Temperature				
	$G_j(0)$					$G_j'(0)$				
	Pr=0.0	.004	.006	.008	.010	Pr=0.0	.004	.006	.008	.010
1	1.211	1.243	1.251	1.257	1.263	-0.790	-0.762	-0.756	-0.751	-0.747
2	0.660	0.662	0.669	0.674	0.679	-1.501	-1.432	-1.416	-1.402	-1.391
3	-0.150	-0.153	-0.155	-0.156	-0.158	-0.181	-0.176	-0.175	-0.174	-0.173
4	0.0257	0.0256	0.0258	0.0259	0.0260	0.0310	0.0295	0.0291	0.0288	0.0286
5	0.528	0.525	0.532	0.537	0.542	-1.913	-1.809	-1.783	-1.762	-1.744
6	-0.0317	-0.0333	-0.0340	-0.0345	-0.0350	-0.173	-0.171	-0.170	-0.169	-0.168
7	-0.0866	-0.0900	-0.0916	-0.0929	-0.0941	-0.292	-0.288	-0.287	-0.285	-0.284
8	0.0560	0.0578	0.0588	0.0598	0.0606	0.0517	0.0511	0.0509	0.0509	0.0508
9	-0.104	-0.106	-0.108	-0.109	-0.111	-0.156	-0.154	-0.153	-0.153	-0.153
10	0.0395	0.0388	0.0390	0.0392	0.0393	0.0671	0.0634	0.0625	0.0618	0.0612
11	0.0035	0.0036	0.0037	0.0038	0.0039	0.0164	0.0169	0.0169	0.0169	0.0169
12	0.0074	0.0073	0.0074	0.0074	0.0075	0.0127	0.0119	0.0117	0.0116	0.0114

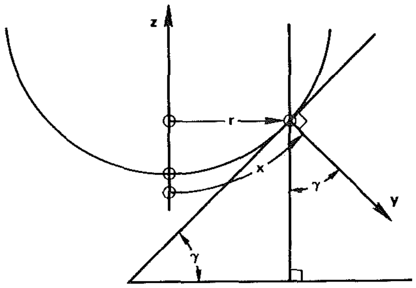

Fig. 1 Cartesian and local Cartesian coordinates

zontal Cylinder: An Examination of Profiles," *Can. J. Chem. Engr.*, Vol. 51, 1973, pp. 507–510.

5 Chiang, T., Ossin, A., and Tien, C. L., "Laminar Free Convection From a Sphere," JOURNAL OF HEAT TRANSFER, TRANS. ASME, Series C, Vol. 86, 1964, pp. 537–542.

6 Koh, J. C. Y., and Price, J. F., "Laminar Free Convection From a Nonisothermal Cylinder," JOURNAL OF HEAT TRANSFER, TRANS. ASME, Series C, Vol. 87, 1965, pp. 237–242.

7 Koh, J. C. Y., "Laminar Free Convection From a Horizontal Cylinder With Prescribed Surface Heat Flux," *International Journal of Heat and Mass Transfer*, Vol. 7, 1964, pp. 811–823.

8 Koh, J. C. Y., and Price, J. F., "Laminar Free Convection From a Horizontal Cylinder With Prescribed Surface Heat Flux," Boeing Science Research Laboratory, Seattle, Wash., Math. Note D1-82-0282, 1962.

9 Fox, J., Discussion of "Laminar Free Convection From a Sphere," JOURNAL OF HEAT TRANSFER, TRANS. ASME, Series C, Vol. 86, 1964, p. 543.

10 Schlichting, H., *Boundary-Layer Theory*, Sixth ed., McGraw-Hill, New York, 1968, p. 224.

11 Saville, D. A., and Churchill, S. W., "Laminar Free Convection in Boundary Layers Near Horizontal Cylinders and Vertical Axisymmetric Bodies," *J. Fluid Mech.*, Vol. 29, 1967, pp. 391–399.

12 Saville, D. A., and Churchill, S. W., "Free Convection at Low Prandtl Numbers in Laminar Boundary Layers," *Indust. Eng. Chem. Fund.*, Vol. 8, 1969, pp. 329–332.

13 Wilks, G., "External Natural Convection About Two-Dimensional Bodies With Constant Heat Flux," *International Journal of Heat and Mass Transfer*, Vol. 15, 1972, pp. 351–354.

14 Lin, F. N., and Chao, B. T., "Laminar Free Convection Over Two-Dimensional and Axisymmetric Bodies of Arbitrary Contour," JOURNAL OF HEAT TRANSFER, TRANS. ASME, Series C, Vol. 96, 1974, pp. 435–442.

15 Peterka, J. A., and Richardson, P. D., "Natural Convection From a Horizontal Cylinder at Moderate Grashof Numbers," *International Journal of Heat and Mass Transfer*, Vol. 12, 1969, pp. 749–752.

16 Harpole, G. M., "Laminar Natural Convection From Blunt Bodies With Arbitrary Surface Heat Flux or Surface Temperatures," MS Thesis, School of Engineering and Applied Science, University of California, Los Angeles, 1975.

APPENDIX

Computing Surface Shape Parameters

Given an arbitrary blunt surface $z(r)$ in Cartesian coordinates, it is desirable to obtain s_1 and s_2 for the expansion given by equation (8). As can be seen from Fig. 1,

$$\frac{dz}{dr} = \tan\gamma \tag{20}$$

And from a trigonometric identity

$$\sin\gamma = \frac{\tan\gamma}{(1+\tan^2\gamma)^{1/2}} = \frac{(dz/dr)}{(1+(dz/dr)^2)^{1/2}} = (1 + (dz/dr)^{-2})^{-1/2} \tag{21}$$

Taking third and fifth derivatives of the expansion given by equation (8) there results

$$\left.\frac{d^3(\sin\gamma)}{dx^3}\right|_{x=0} = 6s_1, \quad \left.\frac{d^5(\sin\gamma)}{dx^5}\right|_{x=0} = 120s_2 \tag{22}$$

Taking the third and fifth derivatives with respect to x of equation (21), using the chain rule with

$$\frac{dr}{dx} = (1 + (dz/dr)^2)^{-1/2} \tag{23}$$

equations (22) give s_1 and s_2.

$$s_1 = \frac{1}{6}\left(\left.\frac{d^4z}{dr^4}\right|_{r=0} - 4\right)$$
$$s_2 = \frac{1}{120}\left(\left.\frac{d^6z}{dr^6}\right|_{r=0} - 44\left.\frac{d^4z}{dr^4}\right|_{r=0} + 88\right) \tag{24}$$

Note that because x is scaled with R, the radius of curvature at the stagnation point, z and r must also be scaled with R, thus $z(r)$ has a unit radius of curvature at $r = 0$. Therefore, a Taylor expansion of z will have the form

$$z(r) = \frac{1}{2}r^2 + ar^4 + br^6 + \ldots \tag{25}$$

which yields

$$s_1 = 4a - \frac{2}{3}$$
$$s_2 = 6b - \frac{44a}{5} + \frac{11}{15} \tag{26}$$

For a parabola, $a = b = 0$. For a circle ($z = 1 - (1 - r^2)^{1/2}$), $a = 1/8$ and $b = 1/16$. For $z = \cosh(r) - 1$, $a = 1/24$ and $b = 1/720$.

V. E. Schrock
Professor.
Mem. ASME

A. D. K. Laird
Professor.
Mem. ASME

Lawrence Berkeley Laboratory,
University of California, Berkeley, Calif.

Physical Modeling of Combined Forced and Natural Convection in Wet Geothermal Formations

Wet geothermal formations or reservoirs are of great current interest as a new energy source. Such formations have the potential for large quantities of energy at temperatures of interest for power production and other uses. In these reservoirs the ground water usually contains dissolved solids in such high concentration as to pose a serious disposal problem. For this reason and also to maintain the water table, in most cases, the water will be reinjected into the reservoir after the useful energy has been extracted. Efficient utilization of the potential of a given reservoir requires optimum location of costly producing and reinjection wells. Selection of well location must be based upon an understanding of the heat and mass flows within the reservoir. In this paper, we present some general considerations for physical modeling as well as the results obtained from a laboratory model having two wells to simulate a geothermal energy extraction loop.

Introduction

The potential for utilizing geothermal energy has been described extensively in several references, for example, Kruger and Otte [1].[1] Geothermal energy, resulting from radioactive decay within the earth, flows to the surface by conduction and convection at an average heat flux that is about four orders of magnitude lower than the average radiant flux from the sun. It is, however, about the same order of magnitude as the current total worldwide utilization rate of energy for all purposes and from all sources. This is an immense energy rate which would be useless to us if we had to deal only with the average flux at the surface temperature. Fortunately, local fluxes vary by large factors from the average and relatively large regions have already been identified [2] in which the geothermal temperatures and stimulated (in a few cases natural) energy fluxes are in the range of interest for power production.

The cream of geothermal energy appears in volcanically active regions where the molten core approaches the earth's surface through fissures in solid rock and occasionally vents. Additionally, convection of ground water is often a powerful mechanism for energy transport and is responsible for the natural geysers. Geysers are usually associated with "steam-dominated" geothermal reservoirs. The major use of geothermal energy up till now has been power produced from steam-dominated reservoirs, notably in Italy and California, which together generate about 1000 MW of electricity. These high-quality sites are rare, however, and the great potential for geothermal energy is probably to be found in the much more extensive liquid-dominated reservoirs of the type already utilized for space heating and power production in Iceland and New Zealand. In addition, large quantities of energy are available from the stored energy in hot dry rock which can, in principle, be harvested by reaching below the thermal resistance of a few thousand meters of earth, even in locations of normal geothermal gradient [3].

The natural convection in wet geothermal reservoirs is of prime importance in the transport of energy. Understanding this process is essential to the interpretation of the natural geological formation and is also necessary in predicting the effect on the natural system of the extraction of energy. Calculations are made difficult by the complexities of geometry, spatial variations and anisotropic character of physical properties, nonuniform boundary conditions, etc. However, natural convection in liquid-saturated porous media with isotropic properties has been studied extensively for simple geometries using numerical mathematical methods [4–11]. Experiments on these problems have been scarce by comparison and it is only recently that they have been motivated by the geothermal application. Schrock, et al. [12] made experimental measurements of natural convection

---

[1] Numbers in brackets designate References at end of paper.

Contributed by the Heat Transfer Division and presented at the Winter Annual Meeting, Houston, Texas, November 30–December 5, 1975 of THE AMERICAN SOCIETY OF MECHANICAL ENGINEERS. Revised manuscript received by the Heat Transfer Division March 10, 1976. Paper No. 75-WA/HT-70.

from heated cylinders buried in a liquid-saturated porous medium. Their studies were conducted in the context of radioisotope fuel capsule safety but are related to the problem of the natural energy flow in geothermal reservoirs. The data agreed well with theoretical predictions [10] and permitted extension of the empirical correlation, by numerical computations, into the higher range of Rayleigh numbers that could not be reached experimentally without pressurizing the equipment to suppress boiling. The case of boiling may also be of interest in the geothermal application and was studied experimentally.

Recently new physical modeling experiments have been started at Stanford University to study flashing blowdown of hot water in crushed rock [13] and phase change in low permeability porous media [14]. At the University of Hawaii, Cheng and Takahaski [15] are building a model in which they will attempt to model the Hawaiian geothermal system. The types of geothermal systems to be encountered are even more diverse than this brief introduction would suggest. Thus, physical modeling in the geothermal field is in its infancy and some of the early attempts will bear little similarity to one another. Experiments underway at Berkeley, and described in this paper, are aimed at understanding the changes that will take place in a wet geothermal reservoir as energy is extracted using producing and reinjection wells. With sufficient knowledge of the combined forced and natural convection, it should be possible to optimize the number and location of wells for the most effective withdrawal of energy.

As a starting point, we selected a very simple case of a homogeneous system, initially at isothermal conditions and with one source and one sink. Because numerical computation methods were being developed in parallel, we chose for simplicity to make a two-dimensional model. More realistic three-dimensional models will be built later. The model used much of the same equipment as employed in the buried cylinder studies [12]. These experiments provide essential data for testing numerical computation methods.

Modeling

The governing dimensionless parameters may be deduced from the "macroscopic" partial differential equations expressing conservation of mass, momentum, and energy [10]. The following assumptions are made:

1 The porous medium is fixed, homogeneous, and isotropic for both mass and energy transport.

2 The properties of the solid-fluid combination are independent of temperature except for the fluid density which depends linearly upon temperature.

3 The fluid flow resistance is governed by Darcy's law (Re based on d_p is less than unity).

These assumptions together with order of magnitude arguments applied to the full set of equations give a simplified dimensionless set as follows:

Continuity

$$(\vec{\nabla} \cdot \vec{V})^* = 0 \tag{1}$$

Momentum

$$(\vec{V})^* = -(\nabla p + T\vec{g})^* \tag{2}$$

Energy

$$(\rho C_p)_m{}^* \left(\frac{\partial T}{\partial t}\right)^* + \mathrm{Ra}[\vec{\nabla} \cdot (\vec{V}T)]^* - (\nabla^2 T)^* = 0 \tag{3}$$

where the asterisk denotes dimensionless quantities. The nondimensionalization is discussed in the appendix.

If these equations are applied to the two-dimensional system shown in Fig. 1, we have the following additional equations.

Initially the system is assumed to be isothermal with no fluid motion.

Thus

$$T^* \cdot (w, y, o) = 0 \tag{4}$$

$$(\vec{V})^*(x, y, o) = 0 \tag{5}$$

$$p^*(x, y, o) = 0 \tag{6}$$

The boundaries of the region are impermeable and adiabatic, so

$$\left(\frac{\partial T}{\partial n}\right)^* = 0 \tag{7}$$

$$(V_n)^* = 0 \tag{8}$$

The fluid source (injection) has the same flow strength as the sink (producing well). The source is taken to be of constant strength and the injected fluid is at a constant temperature; therefore, the source (finite cylinder of radius R) and sink may be expressed as

$$|(\vec{V})^*|_s = \frac{\Phi}{V_c} \frac{\dot{Q}}{2\pi R} \tag{9}$$

From these equations, we conclude that the system variables $(\vec{V})^*$, T^*, p^* are functions of time t^* in a generalized sense for specific values of the parameters Ra, $(\rho C_p)_m{}^*$ and $|(\vec{V})^*|_s$ and similar geometry, i.e., h/w, a/h, b/h all fixed.

Therefore, the physical model must have, in addition to similar geometry, the same parameters as the geothermal reservoir, i.e., Ra, $(\rho C_p)_m{}^*$, $|(\vec{V})^*|_s$, and the initial conditions and the boundary conditions must be similar.

Nomenclature

a = characteristic length, equation (A-2)
b = depth to source and sink below sand surface
C_p = specific heat at constant pressure
d = half distance between the centers of the cylinders
d_p = diameter of typical particle in porous media
g = gravitational acceleration
h = height of sand bed
k = thermal conductivity
K = permeability of isotropic porous medium, length squared units
L = characteristic length, equation (A-2)
Pr = Prandtl number
$\dot{Q}$ = volumetric flow rate per unit length
R = radius of the cylinder
Ra = Rayleigh number
Re = Reynolds number
t = time
T = temperature
$\vec{v}$ = local velocity
v_s = radial velocity at the surface of the source
$V = \Phi v$ = superficial velocity
w = width of sand bed
α = thermal diffusivity
β = volume expansivity
μ = dynamic viscosity coefficient
ν = kinematic viscosity coefficient
ρ = density
Φ = porosity

Subscripts

c = characteristic quantity
f = property of fluid component
m = property of saturated porous medium
o = initial isothermal state
s = property of solid component or value at surface of the source

Superscripts

$\hat{}$ = unit vector
$*$ = dimensionless quantity
$\rightarrow$ = vector

Other Notations

$\langle\ \rangle$ = volume average

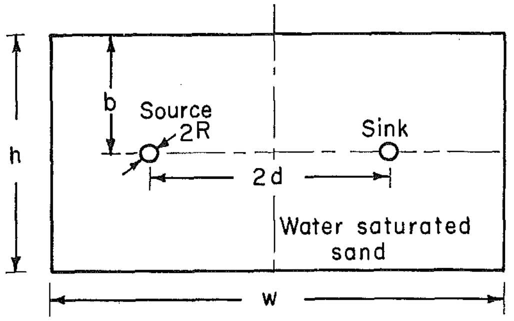

Fig. 1 Idealized geothermal reservoir with simple extraction and injection (elevation view)

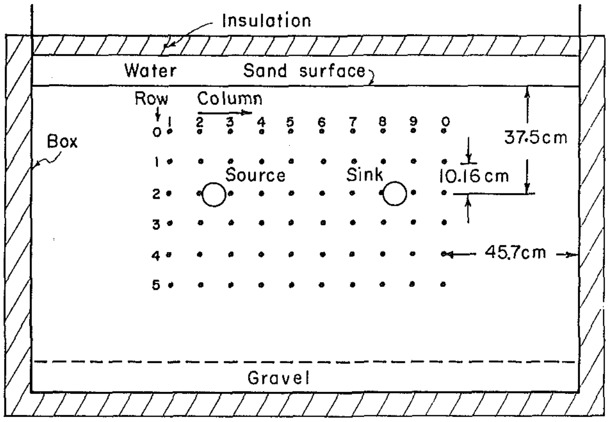

Fig. 3 Thermocouple grid—thermocouples numbered by row and column (elevation view)

It is interesting to note that the characterization of the relative roles of natural and forced convection by the ratio Gr/Re^2 as for a pure liquid system [17] does not appear in the present problem. This is because the Reynolds number based upon pore size is small ($Re < 1$). The use of the Darcy law is permitted and in this case liquid inertia plays no role. However, this is not to say that there is not a forced convection influence. Rather the source (and sink) boundary conditions provide information needed for the forced convective motion. When no temperature differences exist the flow is essentially a potential flow whose dimensionless distribution is fixed by the geometry and whose magnitude is proportional to the source-sink strength. The characteristic velocity (equation (A-7)) is based upon the buoyant force, hence the dimensionless source-sink condition expressed by equation (9) represents, qualitatively, a relationship between the forced and natural convection effects in the present problem.

The equipment and experimental conditions were chosen more for convenience and availability of equipment than as an attempt to model a specific geothermal reservoir. There has, therefore, been no attempt to interpret the results in terms of prototype behavior through the foregoing analysis. The prototype is very probably three-dimensional in character whereas we have attempted to produce two-dimensional fields in our experiment. However, the experimental data are in the Darcy regime and can, therefore, be used for comparison with two-dimensional computer models based upon the foregoing equations. Also, this analysis may be employed to relate the results of future larger models to the results of the present experiments in order to help establish scaling laws. It is worth noting that the experimental value of $|(\vec{V})^*|_s$ was on the order 10^{-2}–10^{-1}, indicating that significant natural convection should occur and its existence is inferred by the measured transient temperature fields.

Experimental Equipment and Procedure

The experiments were carried out in a rectangular box 1.1 m wide, 1.85 m long, and 1.2 m deep. The box was insulated on its sides, top, and bottom and filled with Monterey Crystal Amber sand (12 mesh) for which previous measurements of permeability, porosity, and effective thermal conductivity had been made [16]. A summary of the sand properties is given in Table 1. In order to facilitate establishing the desired initial condition, a layer of gravel was spread across the bottom of the tank and piping provided to introduce heated water at the bottom and remove it from a thin layer of water on top of the sand bed. The gravel served the purpose of spreading the flow uniformly so the sand bed could be uniformly heated in a minimum period of time. The gravel depth totaled approximately 15 cm and was applied in three layers of decreasing coarseness ranging from 2.5 to 0.5 cm. A stainless steel screen was applied between layers to keep the sand from mixing with the gravel. The heating loop consisted of a centrifugal pump with maximum flow rate of 2.5×10^{-3} m^3/s (40 gpm) and a steam heated shell and tube heat exchanger. A temperature controller was used to maintain a constant temperature of the water entering the tank during warm-up. A schematic of this system is shown in Fig. 2.

Simulation of producing and reinjection wells was accomplished by the use of sintered ceramic tubes 6 cm in diameter and 74 cm long having a pore size of approximately 10 μm. The tubes were placed horizontally in the sand bed, as shown in Fig. 2. One end of each tube was closed and the other ends were connected to piping of the energy extraction loop. The energy extraction loop consisted of a pump, flowmeter, heat exchanger, and several thermocouples to measure the loop temperatures, particularly the water entering and leaving the sand bed.

To permit observation of the spatial temperature distribution during transient cool down of the sand bed, a grid of 60 thermocouples

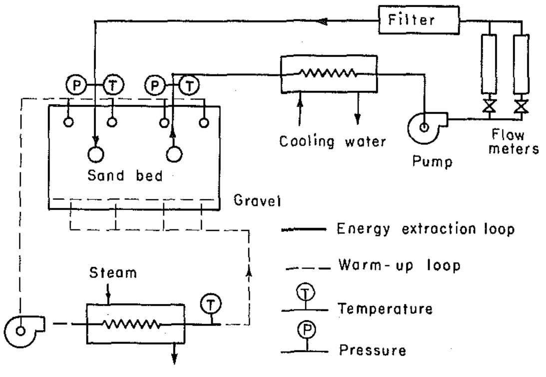

Fig. 2 Schematic of experimental system

Table 1 Properties of Monterey Crystal Amber Sand (12 Mesh)*

Mean grain size, m (ft)	10^{-3}	(0.33×10^{-2})
Bulk density, kg/m^3 (lb/ft^3)	1.986×10^{3}	(124.5)
Porosity, dimensionless	0.386	
Permeability, m^2 (darcies)	3.68×10^{-11}	(373)
Bulk thermal conductivity W/m °C $\left(\frac{\text{Btu}}{\text{hr ft °F}}\right)$	2.59	(1.50)
Bulk thermal diffusity $\frac{\text{m}^2}{\text{sec}}\left(\frac{\text{ft}^2}{\text{hr}}\right)$	9.05×10^{-7}	(0.035)
Bulk specific heat kJ/kg °C (Btu/lb °F)	1.45	(0.347)

*Water saturated at 37 °C

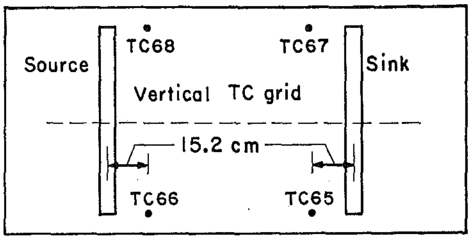

Fig. 4 Plan view—thermocouple location

Table 2 Test Conditions

Test number	T_i,C	T_S,C	Flow rate $m^3/s \times 10^5$
5a	72.5	28.8	3.15
5b	72.5	28.4	3.15
6	72.5	30.0	6.31
7	48.8	27.2	3.15
8	49.3	26.8	6.31
9a	73.2	27.9	6.31
9b	72.5	27.8	6.31
9c	72.6	27.5	6.31
10	39.4	24.8	6.30
11	37.9	25.6	3.15

was mounted in the longest vertical midplane. The positions of thermocouples in the grid are shown in Fig. 3. The geometry chosen was intended to produce a two-dimensional field. To observe possible three-dimensional effects, four fixed thermocouples were mounted in the horizontal plane at the level of the source and sink at lateral positions near the tank walls, as shown in Fig. 4. In addition, a stainless-steel sheathed thermocouple could be used as a probe to observe the temperature at any location.

A Hewlett-Packard model 20100 data logger was employed to record the outputs of the thermocouples. The system used crossbar scanning and printed digital output on tape at frequent intervals.

The experimental procedure was to establish the sand bed at an initial isothermal condition by operating the warm-up loop with the extraction loop turned off. During warm-up the water temperature entering the sand bed was held constant. When the sand bed reached an isothermal condition, the warm-up loop was turned off and the energy extraction loop actuated.

Tests have been conducted for three nominal values of initial temperature, 72.5, 49, and 38°C, a nominal source temperature of 26°C, and two flow rates in the extraction loop 6.31×10^{-5} m^3/s (1 gpm) and 3.15×10^{-5} m^3/s (0.5 gpm). The actual test conditions are listed in Table 2. Some of the tests were repeated because of difficulties that arose such as malfunctioning of several thermocouples or departure from the desired test conditions and also to determine the reproducibility of the results.

Results and Discussion

The experimental results are principally the temperature histories at the fixed positions in the thermocouple grid and of the water extracted from the sand bed and the water reinjected into the bed. Because of the large number of thermocouples, it is not practical to present all these temporal histories here. By interpolating between grid temperatures at selected times, it was possible to present an overall view of the development of isotherms in the sand bed.

For test number 5b, Fig. 5 shows the temperatures at the outlet and inlet (sink and source) and the temperature of the cooling water. Except for a slight transient caused by change in cooling water temperature during the first 5 min of the test, the injected water remained quite constant in time. Fig. 6 shows the lateral differences in temperature history which indicate that the plane of the thermocouple grid was cooled more rapidly than the region near the box walls. This is because the source and sink tubes did not extend the full width of the box. Convective motion has a small component up the side walls of the tank and down the center of the box but the main convective motion is probably parallel to the plane of the thermocouple grid.

Figs. 7 and 8 show the histories at some selected locations, also for test number 5b. Fig. 8 shows a curious effect consisting of a non-monatonic trend at certain locations. A tentative explanation for this behavior, which was also observed in other runs, is that we did not succeed in creating a truly two-dimensional system. The porous tubes simulating the wells did not extend the full width of the tank (see Fig. 4). Thus, the regions along the sides of the tank receive less cold water and it is likely that thermal convection cells are established in transverse vertical planes. It is possible that interaction of these cells with the main thermal convection in the longitudinal vertical plane causes the effect observed in Fig. 8. Fig. 9 shows the isotherms in the plane of the thermocouple grid for times of 1.5, 3.0, 5.0, and 7.0 hr, respectively, for run 5b. These figures suggest that a very pronounced natural convective flow is superimposed on the pump-driven flow. If pump-driven flow dominates, we would expect symmetry in the isotherms about the line passing through the source and sink.

Similar evolutions of temperature fields are shown in Fig. 10 for test number 6, Fig. 11 for test number 11, and Fig. 12 for test number 10. Test number 6 has the same initial temperature as number 5b but twice the source flow. The higher source flow clearly diminishes the effect of natural convection but it remains a significant factor in determining the positions of isotherms.

Reducing the initial temperature (lower Ra) has a pronounced in-

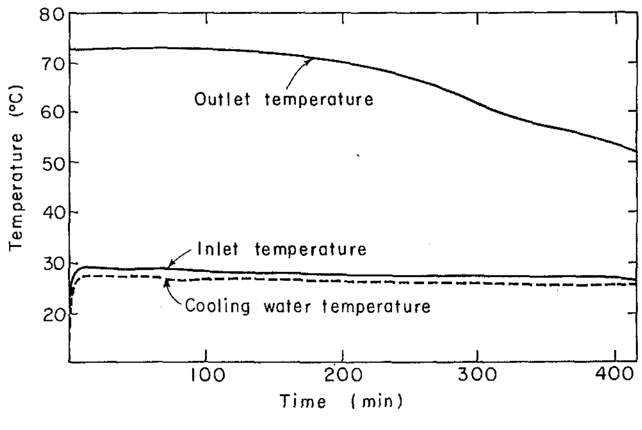

Fig. 5 Inlet and outlet temperatures, run 5b

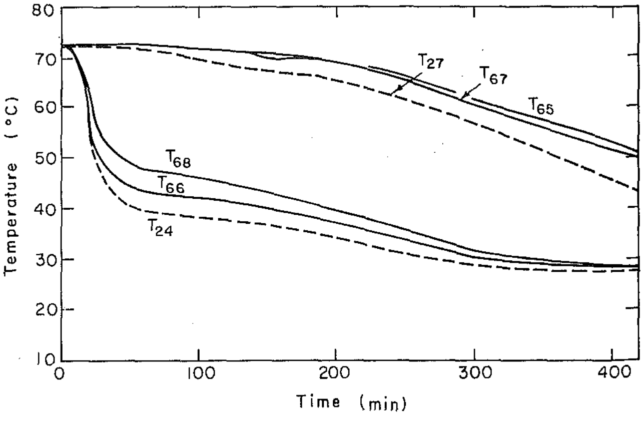

Fig. 6 Grid point temperatures, run 5b, at locations shown in Figs. 3 and 4

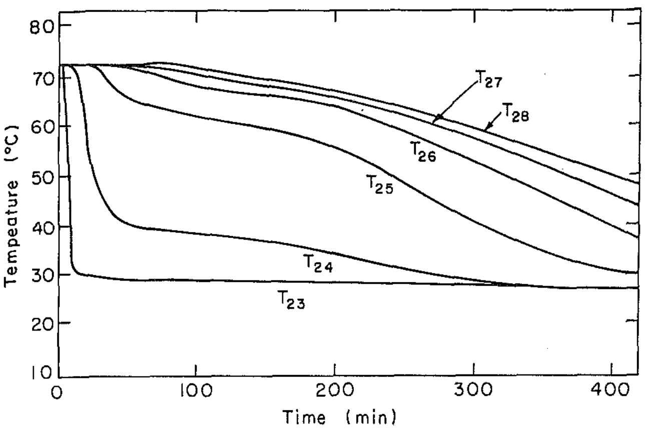

Fig. 7 Grid point temperatures, run 5b, at locations shown in Fig. 3

fluence upon the role of natural convection, as seen for tests 10 and 11, for which the nominal initial temperature was only 80°C, i.e., ΔT of 13°C compared with 43°C in tests 5b and 6. In both tests 10 and 11 the small amount of natural convection develops very slowly. The higher source flow of test 10 still has a noticeable influence in reducing natural convection compared to test 11.

Unfortunately, at this time there is no suitable experimental technique for measuring the velocity field and it can only be inferred by the temperature field. In the absence of thermal convection, the two-dimensional flow field can be described as a potential flow. If it is further assumed that there is no heat diffusion and that the thermal capacity in the sand is negligible, the temperature field would consist of two regions, one at the original temperature and one at the temperature of the water pumped into the bed. The position of the front at any time can be determined from the potential flow solution. Calculations of this type were made that predicted front shapes similar to the isotherms measured in tests 10 and 11. However, the spreading of isotherms shows the influence of heat diffusion and local energy exchange between the liquid and solid. Departure from symmetry shows the influence of thermal convection.

The data reported here reveal significant three-dimensional effects. In order to simplify comparisons with numerical computations, several modifications in the experimental equipment were made for future tests to obtain a closer approach to a two-dimensional system. The real geothermal system is certainly three-dimensional and future models will have to take this into consideration, as will numerical computations. Our first attempt to use physical modeling for the geothermal problem indicates that the concept is promising. However, the experiments are cumbersome to set up and require extensive in situ instrumentation and will therefore be time consuming and expensive. There is a need to develop new instrumentation for flow and pressure measurements and to develop model laws for cases where

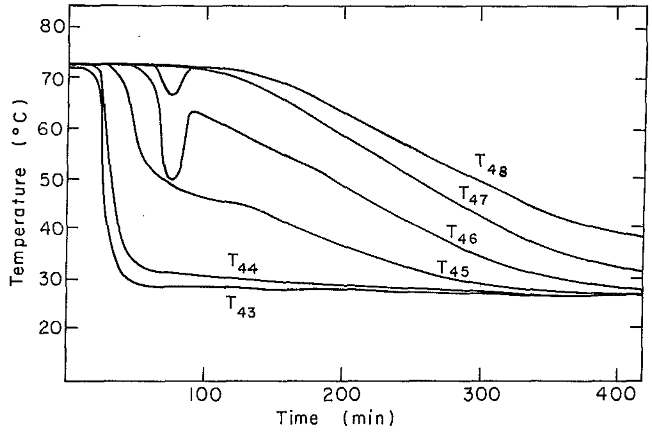

Fig. 8 Grid point temperatures, run 5b, at locations shown in Fig. 3

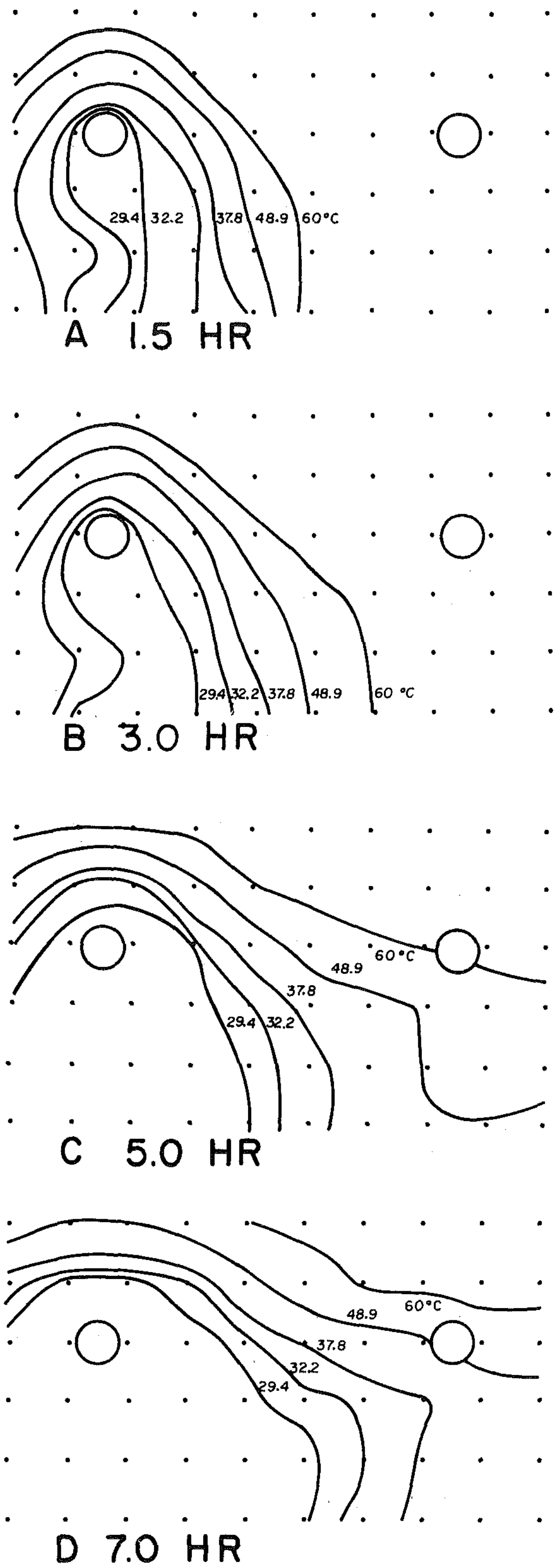

Fig. 9 Positions of isotherms as a function of elapsed time from start of injection, test 5b: initial temperature, 72.5 C; injection temperature, 28.4 C; flow rate, 31.5 × 10^{-5} m^3/s. Grid points, source, and sink are as shown in Fig. 3.

inhomogeneities and turbulence exists.

Conclusions

Experiments have been performed on the combined effects of forced and natural convection in a liquid-saturated porous medium in a system intended to simulate a wet geothermal system. Within the range of parameters explored, the flow patterns inferred by temperature field measurements reveal a natural convection effect that develops slowly and is most pronounced when the source flow is low and

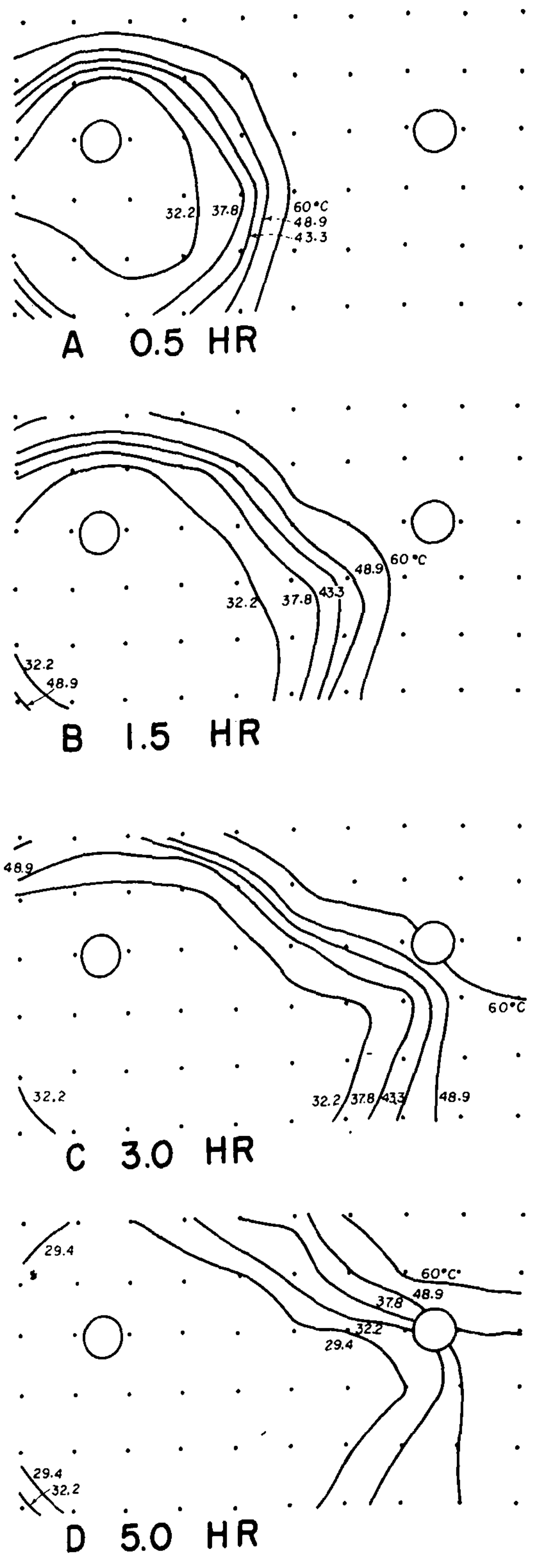

Fig. 10 Positions of isotherms as a function of elapsed time from start of injection, test 6: initial temperature, 72.5 C; injection temperature, 30.0 C; flow rate, 6.31 × 10^{-5} m^3/s

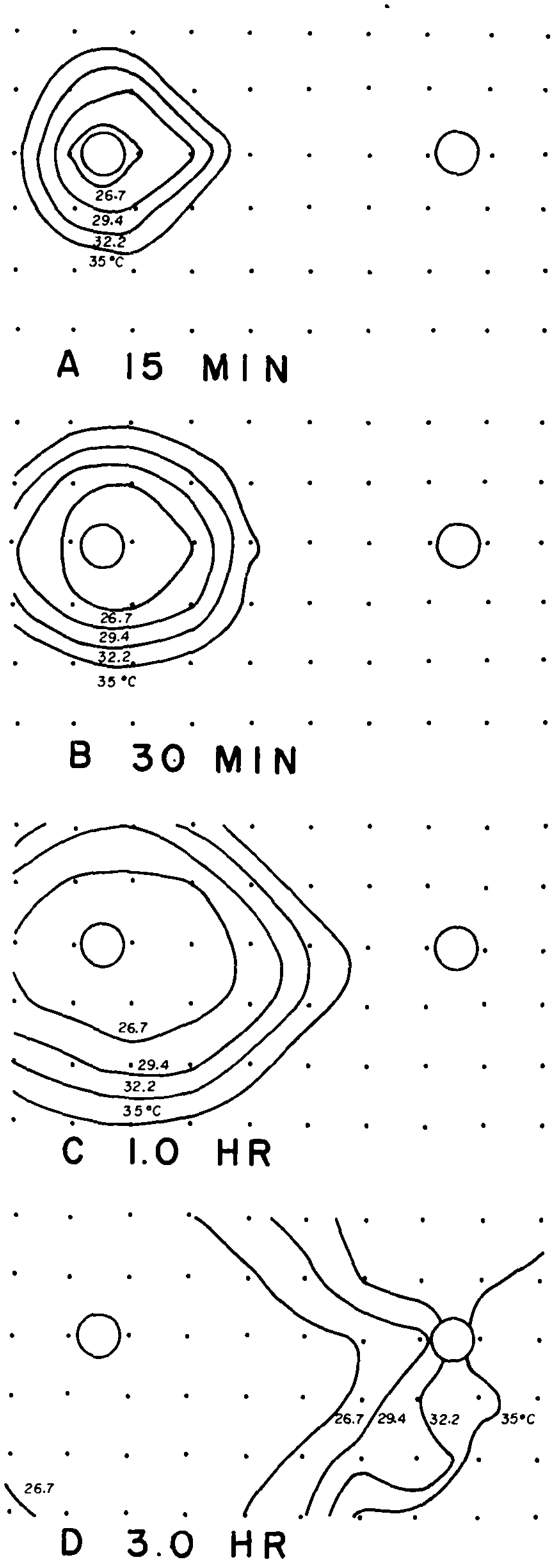

Fig. 11 Positions of isotherms as a function of elapsed time from start of injection, test 11: initial temperature, 37.9 C; injection temperature, 25.6 C; flow rate, 3.15 × 10^{-5} m^3/s

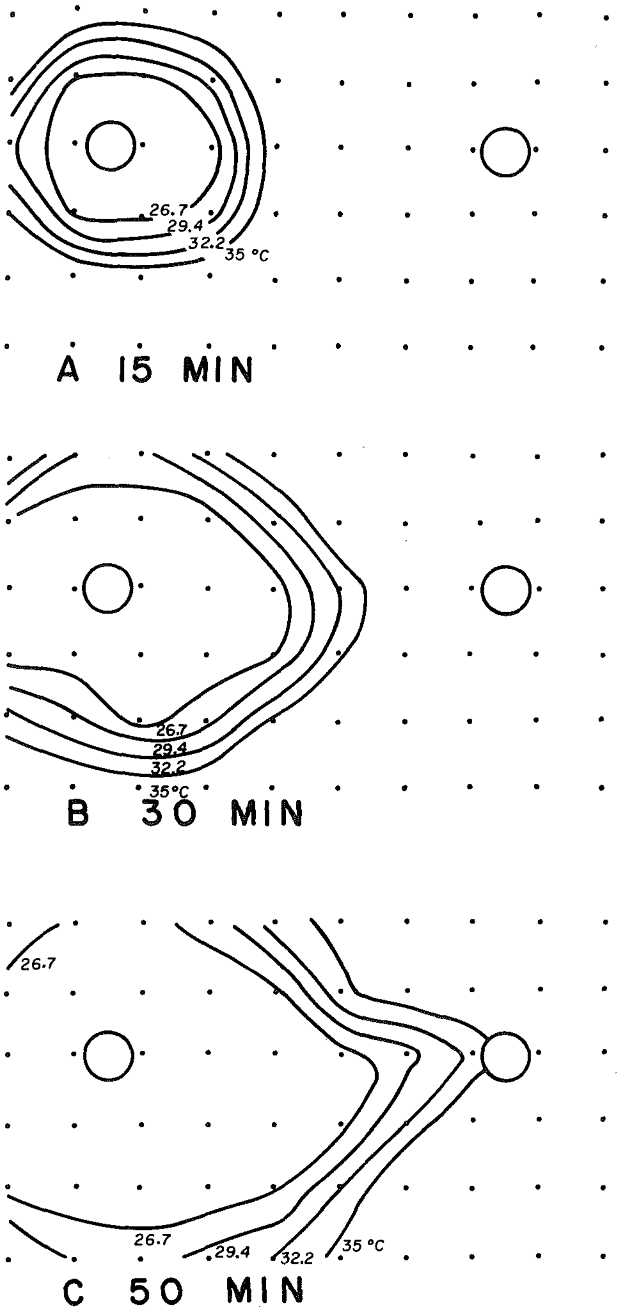

Fig. 12 Positions of isotherms as a function of elapsed time from start of injection, test 10: initial temperature, 39.4 C; injection temperature, 24.8 C; flow rate, 6.30 × 10^{-5} m^3/s

the temperature difference is large. The results will be useful for checking numerical computations and were intended as a first step toward developing the capability to physically model geothermal reservoirs. When more extensive data of this type are available covering a range of sizes and geometries, it will be possible to verify the scaling requirements for model experiments. It may also be possible to use such model experiments to determine optimum spacing between production and injection wells.

The experiments are cumbersome to set up and new experimental techniques would greatly aid in the development of this method.

Acknowledgments

This work was supported by the U. S. Energy Research and Development Administration-Lawrence Berkeley Laboratory Geothermal Project and the Sea Water Conversion Laboratory, University of California, Berkeley. We are indebted to Mr. David Theroux and Mr. T.-M. Shih who assisted with the experimental program and the staff of the Sea Water Conversion Laboratory, particularly Mr. Robert Buckland, who supervised the experimental setup.

References

1 Kruger, P., and Otte, C., ed., *Geothermal Energy,* Stanford University Press, Stanford, Calif., 1973.

2 Koenig, J. B., "Worldwide Status of Geothermal Resources Development," *Geothermal Energy,* Chapter 2, 1973, pp. 15–58.

3 Smith, M., Potter, R., Brown, D., and Aamodot, R. L., "Induction and Growth of Fractures in Hot Rock," *Geothermal Energy,* Chapter 4, 1973, pp. 251–268.

4 Wooding, R. A., "Steady State Free Thermal Convection of Liquid in a Saturated Permeable Medium," *Journal of Fluid Mechanics,* Vol. 2, 1957, pp. 273–285.

5 Donaldson, I. G., "The Simulation of Geothermal Systems with a Simple Convection Model," *Geothermics,* Vol. 2, 1970, pp. 649-–654.

6 Holst, P. H., and Aziz, K., "A Theoretical and Experimental Study of Chemical Engineers, Vol. 50, 1972, pp. 232–241.

7 Elder, J. W., "Steady Free Convection in a Porous Medium Heated From Below," *Journal of Fluid Mechanics,* Vol. 27, 1967, pp. 29–48.

8 Combarnous, M. A., and Bia, P., "Combined Free and Forced Convection in Porous Media," *Society of Petroleum Engineers Journal,* 1971, pp. 399–405.

9 Combarnous, M. A., and Bories, S. A., "Thermal Convection in Saturated Porous Media," Report G. E. 11, Institut Français de Petrole et Institute de Mecanique des Fluides de Toulouse, France, 1973.

10 Fernandez, R. T., "Natural Convection from Cylinders Buried in Porous Media," PhD thesis, University of California, Berkeley, 1972.

11 Lasseter, T. J., "Underground Storage of Liquified Natural Gas in Cavities Created by Nuclear Explosives," Pd thesis, University of California, Berkeley, June 1974.

12 Schrock, V. E., Fernandez, R. T., and Kesavan, K., "Heat Transfer from Cylinders Embedded in a Liquid Filled Porous Medium," *Proceedings of the 4th International Heat Transfer Conference,* Vol. VII, Paper CT 3.6, Paris/Versailles, Sept. 1970.

13 Kruger, P., Stanford University, private communication, 1974.

14 Ramey, F., Stanford University, private communication, 1974.

15 Cheng, P., and Takahashi, P., "Modeling of Hawaiian Geothermal Resources," University of Hawaii—NSF Geothermal Project, Technical Report No. 1, Nov. 1973.

16 Schrock. V. E., and Kesavan, K., "Heat Transfer from Radioisotopic Heat Sources Buried in the Ocean Floor," U. S. NRD-TRC-86.

17 Gebhart, B., *Heat Transfer,* McGraw-Hill, New York, 1961, pp. 273–274.

Appendix

In the nondimensionalization of the governing equations, some choices must be made of characteristic quantities. The quantities chosen are identified as follows:

$$T_c = T_o - T_s \quad \text{characteristic temperature} \tag{A-1}$$

$$L_c = 2(d^2 - R^2)^{1/2} = a \quad \text{characteristic length} \tag{A-2}$$

$$\rho_c = \rho_o \quad \text{characteristic density} \tag{A-3}$$

$$\Delta\rho_c = \rho_o \beta_f T_c \quad \text{characteristic density difference} \tag{A-4}$$

$$t_c = L_c{}^2/\alpha_{mf} \quad \text{characteristic time} \tag{A-5}$$

060

$$P_c = L_c \rho_o g \beta_f T_c \quad \text{characteristic pressure} \tag{A-6}$$

$$V_c = K g \beta_f T_c/\nu_f \quad \text{characteristic velocity} \tag{A-7}$$

Using these quantities the dimensionless dependent variables are:

$$(\vec{V})^* \equiv \frac{\vec{V}}{V_c} \tag{A-8}$$

$$T^* \equiv \frac{(T_o - \langle T \rangle)}{T_c} \tag{A-9}$$

$$p^* \equiv \frac{(\langle p \rangle - p_o)}{p_c} \tag{A-10}$$

$$\rho_f^* \equiv \langle \rho_f \rangle / \rho_c \tag{A-11}$$

and the dimensionless independent variables are

$$\mathrm{Ra} = \mathrm{PrGr} \quad \text{Rayleigh number} \tag{A-12}$$

where

$$\mathrm{Gr} \equiv aKg\beta_f T_c/\nu_f^2 \quad \text{Grashof number} \tag{A-12a}$$

$$\mathrm{Pr} \equiv \nu_f/\alpha_{mf} \quad \text{Prandtl number} \tag{A-12b}$$

$$N_{\Delta\rho} \equiv \beta_f T_c \quad \text{dimensionless density difference parameter} \tag{A-13}$$

$$(\rho C_p)_m{}^* \equiv (\rho C_p)_m/\rho_c C_{pf} \quad \text{dimensionless heat capacity parameter} \tag{A-14}$$

$$t^* \equiv t/t_c = \frac{t\alpha_{mf}}{L_c{}^2} \quad \text{dimensionless time} \tag{A-16}$$

$$\nabla^* \equiv L_c\nabla \quad \text{dimensionless del operator} \tag{A-17}$$

D. M. Burch
R. W. Allen
B. A. Peavy

Department of Mechanical Engineering,
University of Maryland,
College Park, Md.

Transient Temperature Distributions Within Porous Slabs Subjected to Sudden Transpiration Heating

This paper investigates the transient temperature distribution within packed beds after being subjected to single blow heating. Numerical solutions are derived for the fluid and solid temperatures that include the effect of forced convection heat transfer at the fluid-exit surface. An inlet-face heat transfer coefficient is specified that includes both the effect of small scale inlet-face convective heat transfer and heat conduction in the oncoming transpirant. The boundary conditions do not require fluid or solid temperatures to be specified at the bounding surfaces. Charts are presented for predicting the response times for packed bed heat exchangers and chemical reactors covering a wide range of parameters.

1 Introduction

Transient temperature distributions develop in the hot startup of packed bed heat exchangers and chemical reactors. In the single blow heating of a packed bed heat exchanger, an initially isothermal packed bed is suddenly exposed to a flow of high temperature transpiring fluid (usually a gas) for the purposes of storing thermal energy. In chemical reactor applications, a high-temperature catalyst gas is suddenly forced to pass through an initially isothermal porous slab and into a reaction zone, in order to increase the rate of chemical reaction taking place between the species of a fluid mixture flowing in the reaction zone.

Previous solutions [1–3][1] in the literature for the single blow heating of packed beds took the fluid temperature at the fluid-entry surface to be initially elevated and held at a constant value throughout the transient adjustment. In the related transpiration heat transfer problems in which the forcing function is a step increase in the rate of internal heat generation [4] or a step increase in the rate of convective heating at the fluid-exit surface [5], the assumption that the fluid-entry temperature is identically equal to the temperature of the oncoming fluid is usually not seriously violated. However, for packed beds subjected to single blow heating, the fluid-entry temperature will change throughout the transient adjustment. Upon approaching within several pore diameters of the fluid-entry surface, the fluid will accelerate toward its first pore or fluid-entry point. The accelerated lateral fluid motion in the vicinity of the stagnation point for each solid particle at the bounding surface will give rise to small-scale convective heat transfer between the bulk of the approaching fluid and the solid material at the bounding surface. This small-scale convective heat transfer and the heat conduction in the oncoming fluid will cause the fluid-entry temperature to change through out the transient adjustment in response to physical processes taking place.

The present paper presents numerical solutions for predicting solid and fluid temperatures within packed bed heat exchangers and chemical reactors after being subjected to single blow heating. An inlet-face heat transfer coefficient is specified that includes the effect of both small-scale convective heat transfer and heat conduction in the oncoming transpirant, permitting the fluid-entry temperature to change through out the transient adjustment in response to physical processes. Furthermore, these solutions include the effect of forced convection heat transfer at the fluid-exit surface (the case of the chemical reactor). An exact analytic solution for the limiting case of

---

[1] Numbers in brackets designate References at end of paper.

Contributed by the Heat Transfer Division for publication in the JOURNAL OF HEAT TRANSFER. Manuscript received by the Heat Transfer Division September 2, 1975. Paper No. 76-HT-LL.

equal gas and matrix temperature is also derived. This solution is used to develop charts for predicting the response times for packed bed heat exchangers and chemical reactors covering a wide range of parameters. Analytic solutions for predicting the steady-state fluid and matrix temperatures that occur within packed beds are also presented. Koh [6] developed a similar analytical solution that required solid temperatures to be specified at the bounding surfaces. The authors of the present paper feel that such a formulation has the disadvantage that an experiment must be first performed to measure bounding surface temperatures before steady-state profiles can be predicted.

2 Analysis

Assumptions made in the analysis are outlined in the following:

1 Thermal, physical, and transport properties are constant.

2 Heat conduction in the solid material and fluid flow through the interstices are one-dimensional in a direction normal to the bounding surfaces.

3 Thermal storage within the fluid is neglected.

4 Heat conduction within the fluid is neglected.

From the foregoing assumptions, it is seen that heat conduction in the solid material and in a direction transverse to the fluid flow is neglected. This condition occurs when the transverse thermal resistance of the solid matrix particles is small in comparison to the thermal resistance of the interstitial convective film between gas and matrix; that is, the separate solid particles within the matrix are at very nearly uniform temperature in a plane parallel to the faces. In terms of a Biot number, h_sR/K_m, based on a mean particle radius, R, the foregoing condition is met when this Biot number is less than 0.1.

With the foregoing assumptions, a heat balance may be performed on the solid material of an elemental slice of the packed bed system of Fig. 1. The sum of the heat transferred by internal convection between the fluid and the matrix and the net heat conducted into the solid material must equal to the energy stored in the solid material, giving the partial differential equation:

$$\frac{\partial^2 T_m}{\partial x^2} + \frac{h_v}{K_m}(T_g - T_m) = \frac{1}{\alpha_m}\frac{\partial T_m}{\partial t}$$

$$\text{or } \frac{\partial^2 \theta}{\partial \xi^2} + \mathrm{Bi}_m(\nu - \theta) = \frac{\partial \theta}{\partial F_0} \qquad (1)$$

Correlations for predicting the volumetric heat transfer coefficient, h_v, may be found in references [7–8]. Performing a similar heat balance on the fluid contained in an elemental slice, the decrease in fluid enthalpy must be equal to the interstitial heat transfer between the fluid and matrix, giving the partial differential equation:

$$-GC_g\frac{\partial T_g}{\partial x} = h_v(T_g - T_m)$$

$$\text{or } -g\frac{\partial \nu}{\partial \xi} = \mathrm{Bi}_m(\nu - \theta) \qquad (2)$$

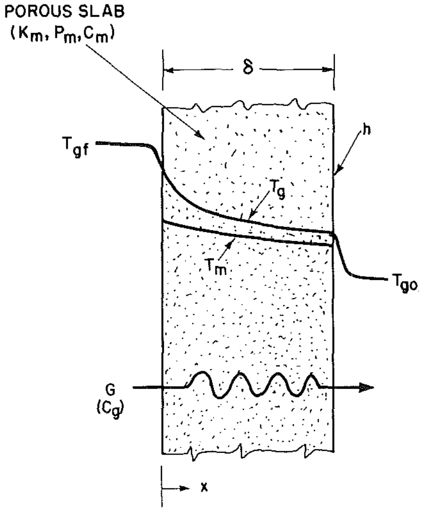

Fig. 1 Packed bed system

For a plane at the fluid-entry face, the net heat transferred to the matrix from the oncoming fluid must equal to the loss in fluid enthalpy, or

$$GC_g(T_{gf} - T_g) = h_f(T_{gf} - T_m) \quad \text{at } x = 0$$

$$\text{or } (1 - \nu) = \mathrm{St}(1 - \theta) \quad \text{at } \xi = 0 \qquad (3)$$

Here h_f is the inlet-face heat-transfer coefficient and includes the effect of both small-scale inlet-face convective heat transfer and heat conduction in the oncoming fluid, and St, the inlet-face Stanton number is based on h_f. The specification of an inlet-face heat transfer coefficient is a more general formulation than the fluid conduction condition used by Bernicker [16]. The energy transferred from the oncoming fluid must also be equal to the heat conducted into the matrix, hence

$$h_f(T_{gf} - T_m) = -K_m\frac{\partial T_m}{\partial x} \quad \text{at } x = 0$$

$$\text{or } g\,\mathrm{St}(\theta - 1) = \frac{\partial \theta}{\partial \xi} \quad \text{at } \xi = 0 \qquad (4)$$

The inlet-face heat transfer coefficient may be estimated from correlations for predicting the heat transfer coefficient in the vicinity of a stagnation point of blunt-nosed two-dimensional or axisymmetric

Nomenclature

Bi_m = interstitial heat transfer number, $\mathrm{Bi}_m = h_v\delta^2/K_m$
C = specific heat
Fo = dimensionless time (Fourier modulus), Fo = $\alpha t/\delta^2$
g = dimensionless mass flow rate of transpirant, $g = GC\delta/K_m$
G = superficial mass flux of transpirant approaching fluid-entry surface
h = forced convection heat-transfer coefficient at fluid-exit surface
h_f = inlet-face heat-transfer coefficient
h_s = internal heat-transfer coefficient per unit surface area
h_v = internal heat-transfer coefficient per unit bed volume
H = Biot number at fluid-exit surface, $H = h\delta/K_m$
K = thermal conductivity
M_1, M_2 = roots of characteristic equation
R = particle radius
St = inlet-face Stanton number, St = h_f/GC_g
t = time
T = temperature
x = distance from fluid-entry surface
α = thermal diffusivity, $\alpha = K/\rho c$
β_n = roots of characteristic equation
δ = slab thickness
θ = dimensionless (solid) matrix temperature, $\theta = (T_m - T_{g0})/(T_{gf} - T_{g0})$
$\lambda = \Delta\mathrm{Fo}/(\Delta\xi)^2$
ξ = dimensionless distance from fluid-entry surface, $\xi = x/\delta$
ρ = density
ν = dimensionless fluid temperature, $\nu = (T_g - T_{g0})/(T_{gf} - T_{g0})$
ϕ = time-dependent portion of solution
ψ = steady-state portion of solution or empirical coefficient that depends on particle shape

Subscripts

f = bulk fluid stream approaching fluid-entry surface
g = transpirant
m = (solid) matrix
n = the nth node or nth term
0 = initial reference temperature
R = mean particle radius

bodies [9]. At the fluid-exit surface, the heat lost by forced convection heat-transfer must equal to the energy conducted from the solid matrix material:

$$-K_m \frac{\partial T_m}{\partial x} = h(T_m - T_{g0}) \quad \text{at } x = \delta$$

$$-\frac{\partial \theta}{\partial \xi} = H\theta \text{ at } \xi = 1 \tag{5}$$

Correlations for predicting the fluid-exit heat transfer coefficient, h, with boundary layer suction and blowing may be found in references [10–14]. The solid and fluid are initially at the reference temperature T_{g0}, or

$$\theta = \nu = 0 \quad \text{for Fo} \leq 0 \quad 0 \leq \xi \leq 1 \tag{6}$$

Setting the right side of equation (1) equal to zero, the steady-state solution to the foregoing system of equations is found to be:

$$\theta - 1 = \frac{H\left(\frac{M_2}{g} - \text{St}\right)e^{M_1\xi} - H\left(\frac{M_1}{g} - \text{St}\right)e^{M_2\xi}}{e^{M_2}(H + M_2)\left(\frac{M_1}{g} - \text{St}\right) - e^{M_1}(H + M_1)\left(\frac{M_2}{g} - \text{St}\right)} \tag{7}$$

$$\nu - 1 = \frac{H\left(\frac{M_2}{g} - \text{St}\right)\frac{M_1}{g}e^{M_1\xi} - \text{H}\left(\frac{M_1}{g} - \text{St}\right)\frac{M_2}{g}e^{M_2\xi}}{e^{M_2}(H + M_2)\left(\frac{M_1}{g} - \text{St}\right) - e^{M_1}(H + M_1)\left(\frac{M_2}{g} - \text{St}\right)} \tag{8}$$

$$M_{1,2} = -\frac{\text{Bi}_m}{2g} \pm \sqrt{\left(\frac{\text{Bi}_m}{2g}\right)^2 + \text{Bi}_m}$$

Koh [6] presented a similar steady-state solution, but his selection of boundary conditions required the matrix temperatures at the bounding surfaces be specified. The foregoing steady-state solution eliminates this requirement.

A time-dependent solution to the foregoing system of equations was obtained using a finite difference technique. The position of nodes within the packed bed are shown in Fig. 2. Note that there are n nodes and n-2 subdivisions for the packed bed. This nodal arrangement has the advantage that it permits boundary conditions to be converted directly into finite difference equations. Making use of finite difference formulas [15] for first and second derivatives, differential equations (1) and (2) and the boundary conditions (3)–(5) may be readily converted into implicit form difference equations. In summary, the equations for the solid temperatures at the n nodes are:

$$\begin{gathered}
\theta_1\left(1 + \frac{g\text{St}\Delta\xi}{2}\right) - \theta_2 = \frac{g\text{St}\Delta\xi}{2} \\
-2\lambda\theta_1 + (3\lambda + \text{Bi}_m\,\Delta\text{Fo} + 1)\theta_2 - \lambda\theta_3 = \theta_2{}' + \text{Bi}_m\Delta\text{Fo}\nu_2 \\
+ \\
\cdot \\
\cdot \\
\cdot \\
-\lambda\theta_{i-1} + (2\lambda + \text{Bi}_m\Delta\text{Fo} + 1)\theta_i - \lambda\theta_{i+1} = \theta_i{}' + \text{Bi}_m\Delta\text{Fo}\nu_i \qquad (9) \\
+ \\
\cdot \\
\cdot \\
\cdot \\
-\lambda\theta_{n-2} + (3\lambda + \text{Bi}_m\Delta\text{Fo} + 1)\,\theta_{n-1} - 2\lambda\theta_n = \theta'_{n-1} + \text{Bi}_m\Delta\text{Fo}\nu_{n-1} \\
\theta_n\left(1 + \frac{\Delta\xi}{2}H\right) - \theta_{n-1} = 0
\end{gathered}$$

and the equations for the fluid temperature at the n nodes

$$\begin{gathered}
\nu_1 = (1 - \text{St}) + \text{St}\theta_1 \\
-g\nu_1 + \left(\frac{g}{2} + \text{Bi}_m\Delta\xi\right)\nu_2 + \frac{g}{2}\nu_3 = \text{Bi}_m\Delta\xi\theta_2 \\
+ \\
\cdot \\
\cdot \\
\cdot \\
\nu_{i+1} + \frac{2\text{Bi}_m\Delta\xi}{g}\nu_i - \nu_{i-1} = \frac{2\text{Bi}_m\Delta\xi}{g}\theta_i \qquad (10) \\
+ \\
\cdot \\
\cdot \\
\cdot \\
-\frac{g}{2}\nu_{n-2} + \left(\text{Bi}_m\Delta\xi - \frac{g}{2}\right)\nu_{n-1} + g\nu_n = \text{Bi}_m\Delta\xi\theta_{n-1} \\
\left(1 + \frac{4g}{\text{Bi}_m\Delta\xi}\right)\nu_n + \left(1 - \frac{4g}{\text{Bi}_m\Delta\xi}\right)\nu_{n-1} = \theta_{n-1} + \theta_n
\end{gathered}$$

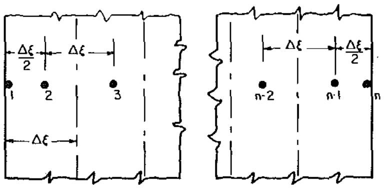

Fig. 2 Location of nodes for the finite difference analysis

The two foregoing sets of equations are linear algebraic systems of equations of the form $Ay = B$. As in the case of the differential equations (1) and (2), the two matrix systems of equations are also coupled. Note, also, that the coefficient matrix for both systems is tridiagonal. To obtain a time-dependent solution, it is necessary to solve iteratively the two foregoing coupled systems for consecutive time steps.

To provide a check on the convergence of the finite difference equations, the limiting case of infinite interstitial heat transfer between the fluid and matrix for which the fluid and matrix temperature become equal is derived in the following. The condition of equal gas and matrix temperature is approached in an actual packed bed in which the interstitial heat-transfer number, Bi_m, becomes large. The foregoing system of equations reduces to:

$$\frac{\partial^2\theta}{\partial\xi^2} - g\frac{\partial\theta}{\partial\xi} = \frac{\partial\theta}{\partial\text{Fo}} \tag{11}$$

$$-\frac{\partial\theta}{\partial\xi} = H\theta \quad \text{at } \xi = 1 \tag{12}$$

$$g(\theta - 1) = \frac{\partial\theta}{\partial\xi} \quad \text{at } \xi = 0 \tag{13}$$

$$\theta = 0 \quad \text{for Fo} \leq 0 \quad 0 \leq \xi \leq 1 \tag{14}$$

Assuming a solution of the form

$$\theta(\xi,\text{Fo}) = \psi(\xi) + \phi(\xi,\text{Fo})$$

the general solution to (11) becomes

$$\theta = A_0 + B_0 e^{g\xi} + \sum_{n=1}^{\infty} \exp\left[\frac{g}{2}\xi - \left(\beta_n{}^2 + \frac{g^2}{4}\right)\text{Fo}\right] \times [A_n \cos(\beta_n\xi) + B_n \sin(\beta_n\xi)] \tag{15}$$

Application of boundary condition (13) leads to:

$$A_0 = 1 \tag{16}$$

$$A_n = B_n\left(\frac{2\beta_n}{g}\right) \tag{17}$$

Boundary condition (12) gives

$$B_0 = -A_0 e^{-g}\frac{H}{H + g} \tag{18}$$

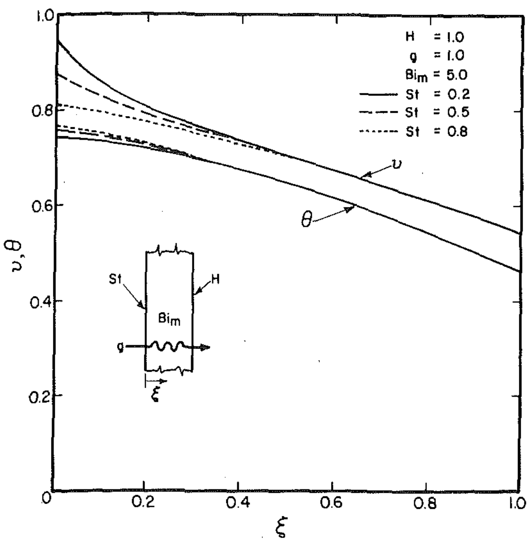

Fig. 3 The effect of the inlet-face Stanton number on the steady-state temperature distribution within a regenerator

and leads to the characteristic equation:

$$\tan(\beta_n) = \frac{\beta_n(H+g)}{\beta_n{}^2 - \frac{g}{2}\left(H + \frac{g}{2}\right)} \tag{19}$$

The eigen values β_n are the roots of the foregoing transcendental equation. Introducing (16), (17), and (18) into (15) gives

$$\theta = 1 - \frac{H}{H+g} e^{g(\xi-1)} + \sum_{n=1}^{\infty} A_n \exp\left[\frac{g}{2}\xi - \left(\beta_n{}^2 + \frac{g^2}{4}\right)\mathrm{Fo}\right] \times \left[\cos(\beta_n\xi) + \left(\frac{g}{2\beta_n}\right)\sin(\beta_n\xi)\right] \tag{20}$$

Applying the initial condition (14) leads to the following relation:

$$-e^{-g/2\xi} + \frac{H}{H+g} e^{g(\xi/2-1)} = \sum_{n=1}^{\infty} A_n \left[\cos(\beta_n\xi) + \left(\frac{g}{2\beta_n}\right)\sin(\beta_n\xi)\right] \tag{21}$$

The Sturm-Liouville theorem may be used to obtain the orthogonality property:

$$\int_0^1 \left[\cos(\beta_n\xi) + \left(\frac{g}{2\beta_n}\right)\sin(\beta_n\xi)\right]\left[\cos(\beta_m\xi) + \left(\frac{g}{2\beta_m}\right)\sin(\beta_m\xi)\right] d\xi = 0 \quad \text{for } n \neq m \tag{22}$$

Multiplying equation (21) by the factor $[\cos(\beta_m\xi) + (g/2\beta_m)\sin(\beta_m\xi)]$, applying the orthogonal relation (22), evaluating the integrals, and making use of (19) gives the series coefficient:

$$A_n = \frac{-2\beta_n{}^2 g}{\left(\beta_n{}^2 + \frac{g^2}{4}\right)^2 \left[1 + \frac{\beta_n{}^2 + g/2(H+g/2)}{\beta_n{}^2(H+g)}\sin^2(\beta_n)\right]} \tag{23}$$

The final time-dependent solution is given by equation (20). The finite difference solution was checked against the solution of equation (20). It was found that for 10 subdivisions of the matrix (n = 12), the finite difference solution converged to the solution of equation (20) as the interstitical Biot number, Bi$_m$, was made large.

3 Discussion of Results

The effect of inlet-face heat transfer on the steady-state temperature distribution within a packed bed subjected to single blow heating is shown in Fig. 3. For this analysis a Biot number $H = 1$, a transpirant flow rate $g = 1$, and an interstitial heat transfer number Bi$_m$ = 5 were selected. Separate steady-state fluid and matrix temperature distributions were obtained using equations (7) and (8) for inlet-face Stanton numbers equal to 0.2, 0.5, and 0.8 and are plotted in Fig. 3. Notice that the effect of the inlet-face Stanton number is confined to an entrance region. For this particular example, the *inlet-face Stanton number has no effect on the steady-state temperature* distribution for the right half of the packed bed. Also, note that for high inlet-face Stanton numbers (such as St = 0.8), most of the change in fluid temperature takes place in the fluid region in front of the packed bed, rather than inside the matrix. Another important observation is that the fluid-entry temperature at $\xi = 0$ differs significantly from the upstream supply condition ($\nu = 1$). Thus, the assumption that the fluid-entry temperature is equal to the upstream supply condition may not be a good one for packed beds subjected to single blow heating.

The system of finite difference equations (9) and (10) were solved numerically for the fluid and matrix temperature. For the analysis, an interstitial heat transfer number Bi$_m$ = 5, a Biot number at the fluid-exit surface $H = 1$, a transpirant flow rate $g = 1$, and an inlet-face Stanton number *St = 0.4 were used. Matrix and fluid temperature* distributions within a packed bed for various elapsed times (Fourier numbers) after the start of single blow heating are shown with solid *lines in Fig. 4. The limiting case of infinite interstitial heat transfer* between the fluid and matrix for which the matrix and fluid temperature become equal are shown with broken lines in the plots of Fig. 4. Initially (Fo = 0) the matrix and the fluid are at the reference state, T_0, or $\theta = \nu = 0$. A short time after the start of single blow heating (Fo = 0.02), the transpiring fluid temperature has risen significantly over the left half of the packed bed. The heat capacity of the solid matrix causes its temperature to be elevated only in a narrow entrance region. As time progresses, heat is progressively transferred by internal convection to the solid matrix, and its temperature gradually rises, until a steady-state condition (Fo = ∞) is reached. Note that, when forced convection heat transfer is present at the fluid-exit surface (H

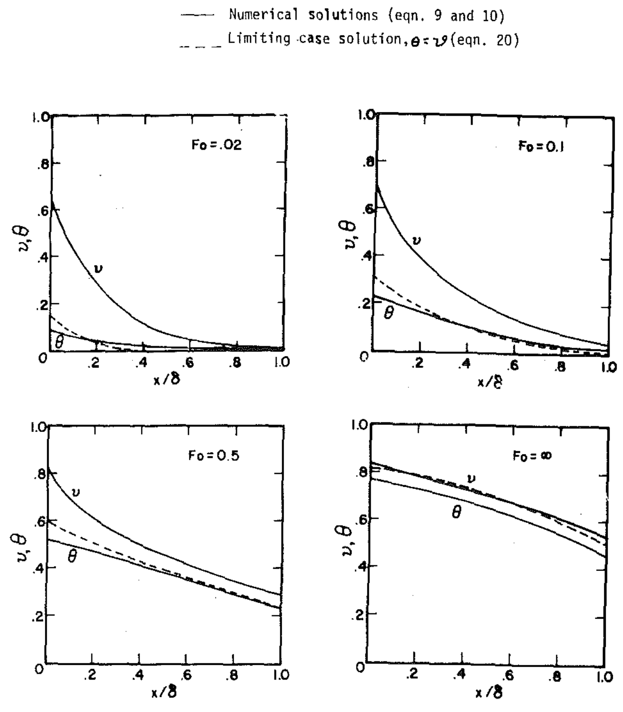

Fig. 4 Transient temperature distribution within a packed bed subjected to single blow heating (St = 0.4, g = 1, H = 1, and Bi$_m$ = 5)

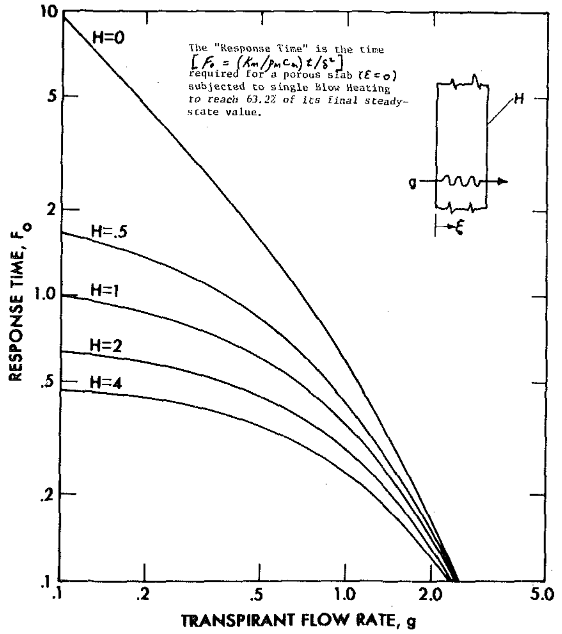

Fig. 5(*a*) Response times for fluid-entry surface

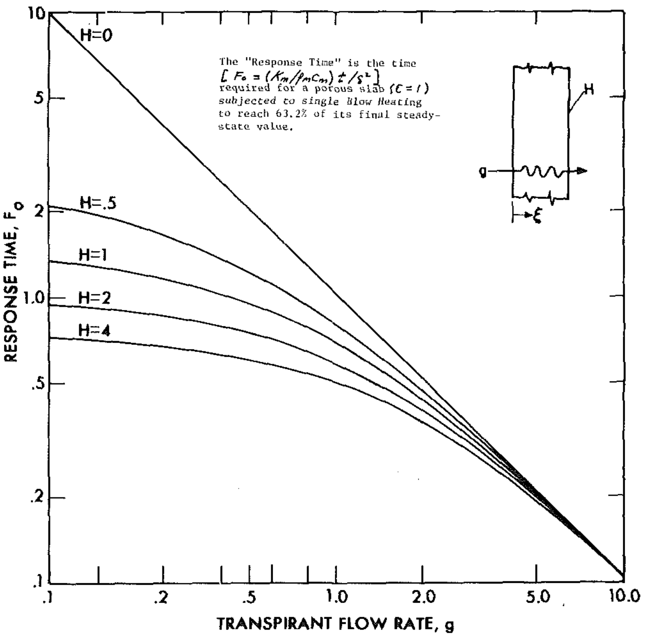

Fig. 5(*b*) Response times for fluid-exit surface

> 0), the matrix-to-gas temperature difference is initially large at the beginning of the transient adjustment and decreases to minimum in the steady-state.

It is interesting to note that in the foregoing plots of Fig. 4, that during the early stage of the transient development that the exact solution for the limiting case $\theta = \nu$ tends to follow the matrix temperature. During the latter stage of the transient temperature development, it lies between the matrix and gas temperature distributions, whereas in the steady state it tends to be closer to the fluid temperature distribution than the matrix temperature distribution. Another very interesting feature of the transient development profiles of Fig. 4 is that the fluid-entry temperature varies significantly during the transient adjustment. Thus the assumption that the fluid-entry temperature is suddenly elevated and held at a constant value through out the transient adjustment is seen to be inconsistent with actual matrix behavior for the packed bed subjected to single blow heating.

Of particular interest is the time required for a packed bed subjected to single blow heating to reach a new steady-state condition. A characterizing parameter for this matrix property is the "response time" which is defined as the time (Fourier number) required for the solid temperature at some point in the packed bed to reach 63.2 percent of it final steady-state value. The limiting case solution $\theta = \nu$ (equation (20)) was used to generate response times for a wide range of transpirant flow rates, g, and forced convection heat transfer rates, H, at the fluid-exit surface. A Biot number $H = 0$ applies to the case of a packed bed heat exchanger, whereas a Biot number $H > 0$ applies to the case of a chemical reactor.

Response times are plotted for a wide range of parameters for the fluid-entry surface (Fig. 5(*a*)) and the fluid-exit surface (Fig. 5(*b*)). Note that for any particular condition that more time is required for the fluid-exit surface to reach a steady-state condition than the fluid-entry surface. Note, that as both the transpirant flow rate, g, and the rate of forced convection heat transfer, H, are made to increase, the difference between the response times at the separate surfaces also becomes greater. Also, note that the effect of increasing g and H is to decrease the response time at both surfaces of the matrix. And finally, as g becomes large, the effect of H vanishes.

The foregoing response time charts are in a strict sense applicable only to the limiting case of infinite interstitial heat transfer between fluid and matrix. However, these charts predicted approximate response times for packed beds having finite interstitial heat transfer. For example, for $\mathrm{Bi}_m = 20$, the percent error was 4 percent at the fluid-exit surface and 5 percent at the fluid-entry surface. For $\mathrm{Bi}_m = 5$, the error was 6 percent at the fluid-exit surface and 20 percent at the fluid-entry surface. Thus, the foregoing charts may be used to give approximate values for response times for actual packed beds.

References

1 Schumann, T. E. W., "Heat Transfer: A Liquid Flowing Through a Porous Prism," *Journal of Franklin Institute,* Vol. 208, 1929, pp. 405–416.

2 Creswick, F. A., "A Digital Computer Solution of the Equations for Transient Heating of Porous Solid Including the Effects of Longitudinal Conduction," *Industrial Mathematics,* 1957, pp. 61–69.

3 Moreland, F. E., "Solution of the Single Blow Problem With Longitudinal Conduction by Numerical Inversion of Laplace Transforms," MS thesis, United States Naval Post Graduate School, Monterey, Calif., 1964.

4 Choudhurry, W. U., El-Wakil, M. M., "Heat Transfer and Flow Characteristics in a Conductive Porous Media With Energy Generation," *Proceedings of Fourth International Heat Transfer Conference,* Versailles, France, Aug., 1970.

5 Curry, D. M., and Cox, J. E., "The Effect of Porous Material Characteristics on the Internal Heat and Mass Transfer," ASME Paper No. 73-HT-49, 1973.

6 Koh, J. C. Y., del Casal, E. P., Evans, R. W., and Deriugin, V., "Fluid Flow and Heat Transfer in High-Temperature Porous Matrices for Transpiration Cooling," AFFDL-TR-66–70, May, 1966.

7 Bird, R. B., Steward, W. C., and Lightfoot, E. N., *Transport Phenomena, Wiley,* New York, 1960.

8 Kays, W. M., and London, A. L., *Compact Heat Exchangers,* The National Press, Palo Alto, Calif., 1955.

9 Kays, W. M. Convective Heat and Mass Transfer, McGraw Hill, New York, 1966.

10 Mickley, H. A., Ross, R. C. Squyers, A. L., and Stewart, A. L., "Heat and Momentum Transfer for Flow Over a Flat Plate With Blowing or Suction," NASA TN 3208, 1954.

11 Hartnett, J. P., and Eckert, E. R. G., "Mass Transfer Cooling in a Liminar Boundary Layer With Constant Fluid Properties," TRANS. ASME, Vol. 79, 1957, pp. 247.

12 Moffat, R. J., and Kays, W. M., "The Turbulent Boundary Layer on a Porous Plate: Experimental Heat Transfer With Uniform Blowing and Suction," *International Journal of Heat and Mass Transfer,* Vol. 11, 1968, pp. 1547.

13 Whitten, D. G., "The Turbulent Boundary Layer on a Porous Plate: Experimental Heat Transfer With Variable Suction, Blowing and Surface Temperature," PhD dissertation, Stanford University, 1967.

14 Tori, K., Nishewaki, N., and Hirata, M., "Heat Transfer and Skin Friction in Turbulent Boundary Layer With Mass Injection," *Proceedings 3d International Heat Transfer Conference,* AIChE and ASME, 1966.

15 Carnaham, B., Luther, H. A., Wilkes, J. O., *Applied Numerical Methods,* Wiley, New York, 1969.

16. Bernicker, R. P., "An Investigation of Porous Wall Cooling," ASME Paper No. 60-WA-233, Aug., 1960.

R. W. Johnson
Research Engineer
Whirlpool Corp.,
Benton Harboer, Mich.

A. M. Dhanak
Professor of Mechanical Engineering,
Michigan State University,
East Lansing, Mich.

Heat Transfer in Laminar Flow Past a Rectangular Cavity With Fluid Injection

The paper describes an analytical and experimental study of the effects of fluid injection on heat transfer in laminar air flow over a long square cavity. The Reynolds number (based on cavity width) ranged in value from 10 to 1000. The injection (of air) at the cavity wall was varied in velocity from 0 to 5 percent of the main stream. The results indicate the greatest reduction in heat transfer to be occurring at the reattachment point. An expression is suggested for predicting the approximate reduction in heat-transfer rate from the entire cavity surface.

Introduction

Heat transfer in cavity flows of either laminar or turbulent character has been a subject of a number of publications in recent times [1–10].[1] A review on this subject can be found in reference [11]. Some of the studies, especially those dealing with laminar flow, have been made possible largely by the development of better low-velocity measurement techniques and by the availability of high-speed computers for the analytical calculations of the complex temperature and flow fields in the cavity.

Motivation for study of cavity flow comes from a desire to better describe the flow and heat transfer in the vicinity of various irregularities which may be present on a surface, either by design or otherwise. The flow field in question will be laminar in nature under conditions of very low velocities or small cavities as, for example, in the case of flow over certain types of surface roughness, fabrication seams, or cavities on an ablating surface. Injection may be present in slots on certain types of aerodynamic surfaces and in some lubrication problems. This study deals with such laminar flow situations.

"The present study [12] consists of two parts, one analytical and the other experimental in character. The analytical portion is a numerical study which differs from previous numerical investigations in that the two-dimensional Navier-Stokes and energy equations are solved fully for the region above the cavity as well as within it. In addition, the region near the reattachment corner is solved in detail and injection of fluid through the cavity bottom is considered. In studying the entire field with a numerical technique, no attempt is made to delineate and analyze in detail any individual region such as a shear layer, wake, or reattachment zone. Instead, the capabilities of the numerical method to accommodate a variety of boundary conditions and complex geometries are used to advantage in studying both overall and local heat transfer phenomena. While solutions for high Reynolds number flow are difficult using numerical techniques such as the method employed in this study, this is not considered a major disadvantage since, for such flows, the assumption of laminar flow also breaks down."

Analytical Study

The specific flow geometry to be considered is a square cavity with sides of length B located in one of two parallel plates spaced a distance B apart (Fig. 1). The plates and cavity walls are considered to be at a uniform temperature, T_w. Fully developed Poiseuille flow is assumed to exist upstream of the cavity. The temperature field is also considered fully developed. Uniform injection of fluid at a temperature T_w is assumed to take place through the bottom wall of the cavity. The flow inside and over the cavity is assumed to be steady, laminar, Newtonian, and incompressible with constant properties. Effects of viscous dissipation are considered to be negligible.

The velocity and temperature fields are described by the usual Navier-Stokes and energy equations, written nondimensionally in terms of stream function and vorticity as follows:

$$\frac{\partial^2 \psi}{\partial \bar{x}^2} + \frac{\partial^2 \psi}{\partial \bar{y}^2} = -\omega \qquad (1)$$

$$\frac{\partial^2 \omega}{\partial \bar{x}^2} + \frac{\partial^2 \omega}{\partial \bar{y}^2} = \mathrm{Re}\left[\frac{\partial \psi}{\partial \bar{y}}\frac{\partial \omega}{\partial \bar{x}} - \frac{\partial \psi}{\partial \bar{x}}\frac{\partial \omega}{\partial \bar{y}}\right] \qquad (2)$$

and

---

[1] Numbers in brackets designate References at end of paper.

Contributed by the Heat Transfer Division of THE AMERICAN SOCIETY OF MECHANICAL ENGINEERS and presented at the AIChE-ASME National Heat Transfer Conference, San Francisco, Calif., August 10–13, 1975. Revised manuscript received by the Heat Transfer Division December 12, 1975. Paper No. 75-HT-58.

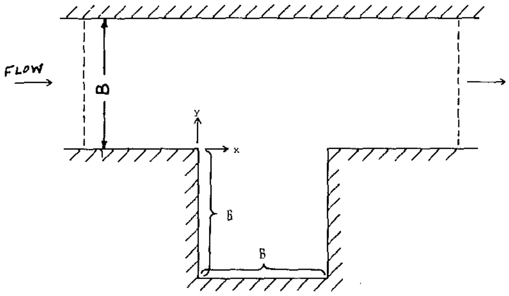

Fig. 1 Flow geometry for analytical study

$$\frac{\partial^2\theta}{\partial\bar{x}^2} + \frac{\partial^2\theta}{\partial\bar{y}^2} = \mathrm{PrRe}\left[\frac{\partial\psi}{\partial\bar{y}}\frac{\partial\theta}{\partial\bar{x}} - \frac{\partial\psi}{\partial\bar{x}}\frac{\partial\theta}{\partial\bar{y}}\right] \qquad (3)$$

which is similar in form to equation (2).

Equations (1), (2), and (4) are put into finite difference form with the use of the relations

$$\begin{aligned}\frac{\partial P}{\partial\bar{x}} &= \frac{P_{i+1,j} - P_{i-1,j}}{2b}\\ \frac{\partial P}{\partial\bar{y}} &= \frac{P_{i,j+1} - P_{i,j-1}}{2\beta b}\\ \frac{\partial^2 P}{\partial\bar{x}^2} &= \frac{P_{i+1,j} - 2P_{i,j} + P_{i-1,j}}{b^2}\\ \frac{\partial^2 P}{\partial\bar{y}^2} &= \frac{P_{i,j+1} - 2P_{i,j} + P_{i,j-1}}{\beta^2 b^2}\end{aligned} \qquad (4)$$

where $P_{i,j}$ represents the value of any property, P, at the i,jth location of a mesh system with points spaced as shown in the following:

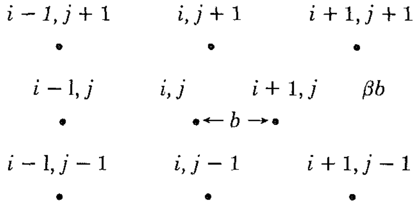

After introducing equation (4), along with relaxation parameters, α_1, α_2, and α_3, the governing equations are put into the form

$$\psi_{i,j}{}^n = (1-\alpha_1)\psi_{i,j}{}^{n-1} + \frac{\alpha_1}{2(1+\beta^2)}\left[\beta^2(\psi_{i+1,j}{}^{n-1} + \psi_{i-1,j}{}^n + b^2\omega_{i,j}) + \psi_{i,j+1}{}^{n-1} + \psi_{i,j-1}{}^n\right] \qquad (5)$$

$$\omega_{i,j}{}^n = (1-\alpha_2)\omega_{i,j}{}^{n-1} + \frac{\alpha_2}{2(1+\beta^2)}\left[(\beta^2 + C)\omega_{i-1,j}{}^n + (\beta^2 - C)\omega_{i+1,j}{}^{n-1} + (1-D)\omega_{i,j-1}{}^n + (1+D)\omega_{i,j+1}{}^{n-1}\right] \qquad (6)$$

$$\theta_{i,j}{}^n = (1-\alpha_3)\theta_{i,j}{}^{n-1} + \frac{\alpha_3}{2(1+\beta^2)}\left[(\beta^2 + C')\theta_{i-1,j}{}^n + (\beta^2 - C')\theta_{i+1,j}{}^{n-1} + (1-D')\theta_{i,j-1}{}^n + (1+D')\theta_{i,j+1}{}^{n-1}\right] \qquad (7)$$

where C, D, C', D' are as given below.[2]

These relations apply at all points except, of course, on the boundaries. The boundary points require special attention and will be discussed later.

The method used for the solution of these equations, the so-called "over-relaxation" method, is somewhat similar to that used by Mills [13], Burggraf [2], and others with the exception that the relaxation factors here have been taken as functions of local velocity in order to obtain rapid convergence over a wide range of Reynolds numbers.

The proper choice of values of α_1, α_2, and α_3 is essential to a stable and rapid convergence of the iterative procedure. Stability of the solutions was particularly sensitive to the choice of values of α_2 and α_3. When a single value was assigned to either of these and used for all points in the field for all iterations, the procedure was either unstable or convergence was deemed excessively slow. However, it was found that by choosing these parameters as functions of local velocity at each step it was possible to achieve convergence of the iterative process in reasonable times for all values of Reynolds numbers included in this study.

An analysis similar to Russell's [14] for the case with a rectangular mesh system resulted in expressions of the same general form for α_i [12]. However, since the square-root function encountered

---

[2] $$C = \frac{\mathrm{Re}\beta}{4}(\psi_{i,j+1} - \psi_{i,j-1});\ C' = \mathrm{Pr}C$$
$$D = \frac{\mathrm{Re}\beta}{4}(\psi_{i+1,j} - \psi_{i-1,j});\ D' = \mathrm{Pr}D \qquad (7a)$$

Nomenclature

b = mesh size in x-direction
B = cavity width
C, D, C', D' = parameters defined in text
h = convection coefficient = $(q_w/A)/(T_w - T_c)$
k = thermal conductivity of fluid
Nu = cavity Nusselt number = hB/k
P = any one of the dependent variables: ψ, ω, or θ
Pr = Prandtl number
q = heat-transfer rate from cavity *with* fluid injection
q_0 = heat-transfer rate from cavity *without* fluid injection
Re = cavity Reynolds number = UB/ν
T = local temperature
u = local x-component of velocity (Note: $\bar{u} = u/U$)
U = average flow velocity in channel
v = local y-component of velocity (Note: $\bar{v} = v/U$)
v_i = ratio of injection velocity at cavity to the average mainstream velocity
x = horizontal coordinate, Fig. 1
$\bar{x} = x/B$
y = vertical coordinate, Fig. 1
$\bar{y} = y/B$
α_1 = relaxation factor for ψ difference equation
α_2 = relaxation factor for ω difference equation
α_3 = relaxation factor for θ difference equation
β = ratio of mesh size in y-direction to that in x-direction
ν = kinematic viscosity of fluid
ψ = *dimensionless* stream function = (stream function)/(UB)
ω = *dimensionless* vorticity = (vorticity)/(U/B)
θ = *dimensionless* temperature = $(T - T_w)/(T_c - T_w)$

Subscripts

c = condition at channel center, upstream from cavity
i = denotes position in x-direction (except in v_i)
j = denotes position in y-direction
w = condition at wall
0 = boundary point
l = neighboring point
n = denotes direction normal to boundary

Superscript

n = iteration index

took a relatively large amount of computer time, it was found more expedient to use the following simplified relations:

$$\alpha_1 = 1.2 \tag{8}$$

$$\alpha_2 = \frac{K_1}{K_2 + C + D} \tag{9}$$

$$\alpha_3 = \frac{K_1}{K_2 + C' + D'} \tag{10}$$

where K_1 and K_2 were constants which were varied systematically in a trial and error fashion to determine the best values for rapid and stable convergence. Values used ranged between 1 and 4.

These expressions are somewhat more conservative than the derived optimum expressions [12]. Hence, they will usually result in more iterations being required before convergence. However, because of stability criteria, an underestimation of α_i is much less serious than is an overestimation of α_i.

The choice of values for b and β, which determine the mesh size, is also a compromise. A fine mesh is desirable for stability and accuracy of the solution, while a coarse mesh is desired to limit computer time. After some experimentation, a value of $0.04B$ was chosen for b and a value of 0.5 was chosen for β. These were used for all regions except near the reattachment corner where a reduced mesh size was required because of the large velocity and temperature gradients in that region [12].

A more complete discussion concerning the choice of relaxation factors and mesh size may be found in reference [12] along with listings of the computer programs used in the study.

In the solution of the equations, calculations were continued until the residual, R, was less than 10^{-5} for all points within the flow field. Here R was taken as the change in value for the properties, ψ and θ, between two successive iterations. Using this convergence criteria and with judicious initial guesses of ψ, ω, and θ (taken from results of solutions for lower Reynolds numbers) typical solution times required were 5–10 min on the CDC 6500.

Boundary Conditions

One boundary condition for the Navier-Stokes equations at each of the solid walls can be immediately written as

$$\frac{\partial \psi}{\partial t} = \text{a constant}$$

along each wall, where t is the coordinate parallel to the wall. (The constant is zero when there is no injection of fluid through the wall and $-\bar{v}_i$ when the relative injection velocity at the wall is $\bar{v}_i$.) The other condition required at these walls can be derived from the condition that there is no slip at the wall, i.e., $(\partial\psi/\partial n)_w = 0$, and the resulting relation is written as

$$\omega_0 = \frac{2}{b^2}(\psi_0 - \psi_1)$$

At the upstream and downstream boundaries of the field in the channel, however, the boundary conditions are not quite so explicit. The effects of the cavity on the external flow may be felt for an indefinite distance—both upstream and downstream. However, to obtain a manageable field size it is necessary to impose some conditions which may be only an approximation to physical reality by taking "boundaries" at a relatively short distance upstream and downstream of the cavity. The upstream boundary was chosen at a distance, $0.8B$, upstream of the cavity with the downstream boundary at a distance, B, downstream of the cavity. After trying various conditions at these boundaries, it was found that best results were achieved by using the relations

$$\frac{\partial \psi}{\partial \bar{x}} = 0, \qquad \frac{\partial \omega}{\partial \bar{x}} = 0, \qquad \frac{\partial \theta}{\partial \bar{x}} = -\frac{\theta\,\mathrm{Nu}}{\mathrm{Pr}\,\mathrm{Re}}$$

which physically correspond to fully developed flow and temperature fields. In difference form these were expressed as

$$\psi_0 = \psi_1, \qquad \omega_0 = \omega_1$$

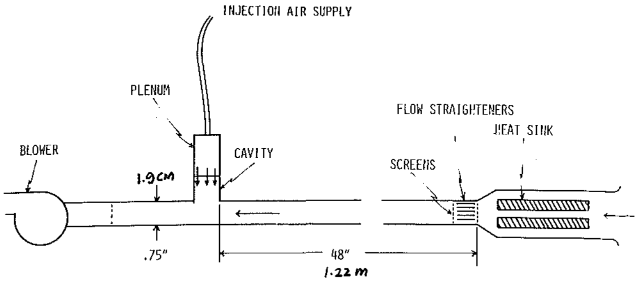

Fig. 2 Schematic of experimental flow system

$$\theta_0 = \theta_1/(1 + b\,\mathrm{Nu}/\mathrm{Pr}\,\mathrm{Re}) \text{ upstream}$$

$$\theta_0 = \theta_1/(1 - b\,\mathrm{Nu}/\mathrm{Pr}\,\mathrm{Re}) \text{ downstream}$$

where the subscript 0 refers to the boundary point, and the subscript 1 refers to the adjacent point in each case. Preliminary solutions were computed with ψ and ω actually specified to impose fully developed flow between parallel plates at these boundaries. However, at the higher Reynolds numbers, slight irregularities (which physically would correspond to very small oscillations in the flow) were present in the ψ field near these boundaries. Specifying the derivative boundary conditions eliminated these irregularities while still allowing satisfactory convergence rates when using a good initial guess of the solution.

Experimental Study

A supporting experimental study of the flow patterns, velocities, and temperature distributions within and above the cavity was conducted using the system depicted in Fig. 2. Air was drawn through a flow channel of rectangular cross section with a square cavity in one of the walls. With an aspect ratio of 26.7 for the channel and a developing flow section 64 times the plate spacing in length, flow in the system was essentially two-dimensional and fully developed. The velocity profile was experimentally verified to be parabolic upstream of the cavity. The channel walls were constructed of aluminum plates which were held at the desired temperature by means of electrical heating wires (Fig. 3). Uniformity of temperature was obtained by variations in the wire spacings and by individual control of the seven separate heating circuits. To allow uniform injection of air through the bottom wall of the cavity it was constructed of a ¼-in. thick plate of graphite with an overall porosity of 20 percent. Filtered air from a high-pressure air supply was used to pressurize a plenum constructed over the cavity bottom (Fig. 3). The flow rate of this injected air was controlled by means of a pressure-regulating valve and measured with a laminar-flow element. Its temperature was adjusted to equal the cavity wall temperature prior to its delivery to the plenum.

Velocities at points within and above the cavity were measured using a hot-wire anemometer which was modified to improve its sensitivity to the small velocities [12]. Calibration of the wires used was accomplished by centering the probe in a separate tube, 1.510 in. in diameter, in which a fully developed laminar flow had been established. Flow rates in the tube were measured by means of a laminar-flow element [15] for part of the range of interest and by means of a thin-plate orifice section for the remainder of the range. Agreement between the two measuring devices was excellent over the range where *both* were judged to be accurate.

Temperature measurements were made with 30-gauge copper-constantan thermocouples and a K3 potentiometer. Wall temperatures were measured with thermocouples attached to the wall at 13 selected locations. Traverses were made with a probe which was positioned by means of a traversing mechanism which was also used for positioning the hot-wire anemometer probe [12]. The thermocouple probe was constructed with the 30-gauge wires ex-

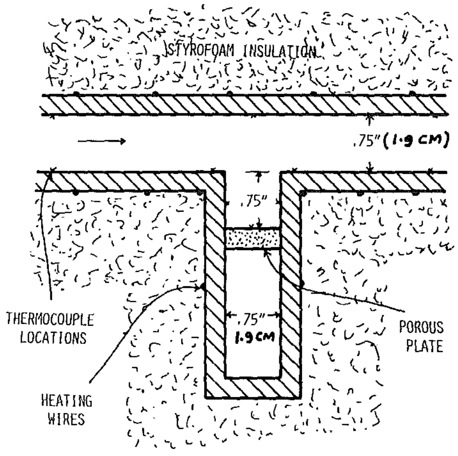

Fig. 3 Cross section of cavity

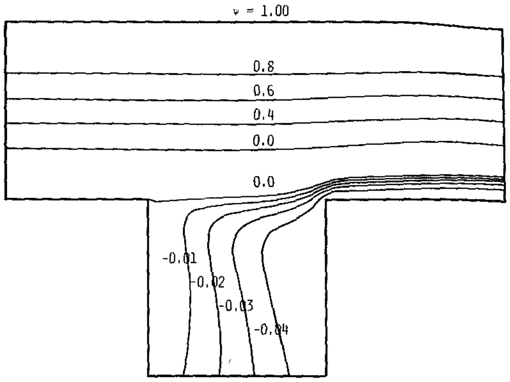

Fig. 5 Analytical streamline patterns, Re = 100, 5 percent injection

tending 3.2 cm to the junction from a small diameter steel tube inserted through the back wall of the cavity and bent at a 90 deg angle in the direction of the measuring point. Prior to their installation, all thermocouples were calibrated.

Discussion of Results

Streamline patterns within and above the cavity were drawn from the calculated stream function values and by interpolating between points when necessary. A representative streamline plot is shown in Fig. 4. The large central vortex appearing in this figure is similar to that observed by previous authors when considering flow in a "closed" cavity. It persisted in the cavity even at the rates of injection of 1 and 2 percent through the cavity bottom. However, when a 5 percent injection rate was used, the vortex was no longer present and the flow pattern appeared as in Fig. 5. (Note that the streamline spacing as drawn in these figures is not indicative of local velocity since the differences in stream function magnitude is not the same between all adjacent lines.) Small secondary vortices appeared in the lower corners of the cavity for flow without injection at Reynolds numbers of 500 and 1000. At lower flow rates or when fluid injection was added, these vortices were not evident, however. Photographs of flow visualization obtained by introducing smoke into the channel upstream of the cavity confirmed these results.

Velocity profiles were obtained from the calculated stream function data as well as from the experimental measurements and are shown in Fig. 6 for comparison purposes. In all cases it is seen that the magnitude of the velocity at points within the cavity is quite small when compared to the free-stream value. At the cavity closure $(y = 0)$, the velocity varied from 16 percent of the free stream velocity for the case with a Reynolds number of 1000 to nearly 35 percent of average free-stream velocity for the case with a Reynolds number of 100.

Isotherms, also obtained by linearly interpolating between points on the temperature map as given by the numerical results, are shown in Figs. 7 and 8 for cases with a Reynolds number of 100 and injection rates of 0 and 5 percent, respectively. The addition of injection greatly suppresses heat transfer to the lower parts of the cavity and further creates a large region of essentially uniform temperature in the bottom half of the cavity. This effect can also be seen from Fig. 9 where temperature profiles are plotted at the position $x/B = 0.5$ for flow with a Reynolds number of 500 and a variety of injection rates. Thermocouple data from the experimental studies showed generally good agreement with the numerical predictions.

The Nusselt number along the walls of the cavity was calculated from the temperature gradient, $(\partial\theta/\partial n)_{\mathrm{wall}}$, as obtained from the numerical solutions. The distribution is shown in Fig. 10 for various injection rates. (To interpret the figure it may be helpful to

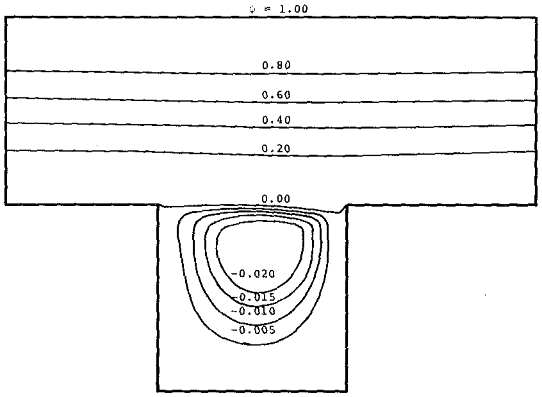

Fig. 4 Analytical streamline patterns, Re = 100, no injection

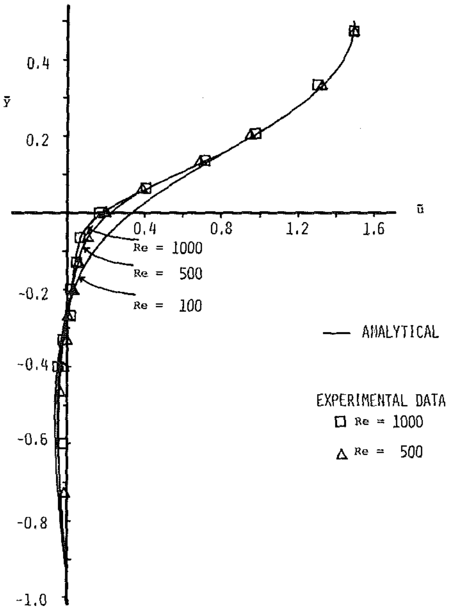

Fig. 6 Analytical and experimental velocity profiles showing Reynolds number effect, $\bar{x} = 0.5$, no injection

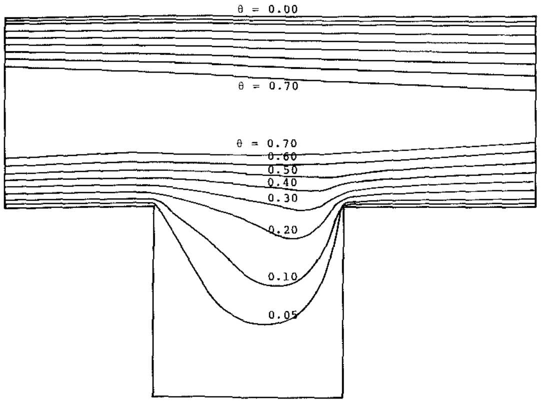

Fig. 7 Analytical isotherm patterns, Re = 100, no injection

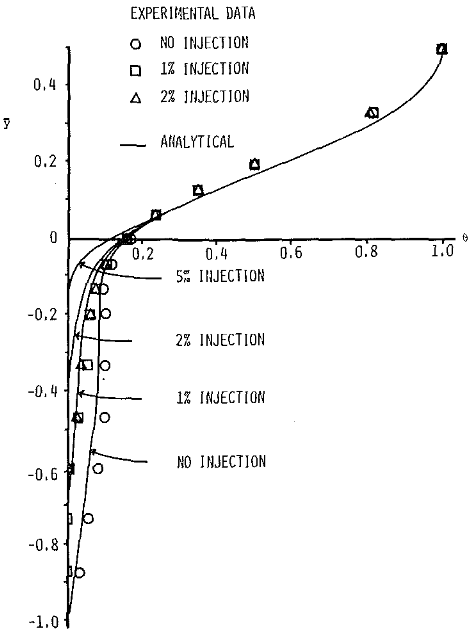

Fig. 9 Analytical and experimental temperature profiles showing effect of injection, $\bar{x}$ = 0.5, Re = 500

consider the sides of the cavity folded out to lie in the plane of the cavity bottom.)

It is evident that the heat-transfer rate at the bottom wall is very low in all cases—nearly zero for the cases with injection. In the case with no injection the Nusselt number at the downstream wall near the reattachment corner becomes very high. However, it is in this region that the greatest reduction of heat transfer occurs when fluid is injected into the cavity. This trend is in general agreement with the predictions of Bales and Korst [1].

Of particular interest is the effect of fluid injection on the overall heat-transfer rate from the cavity. Chapman [10] analytically predicted a reduction of the heat-transfer rate which could be expressed in terms of q/q_0 as a function of $\bar{v}_i$ Re$^{0.5}$. Fig. 11 shows a comparison between Chapman's prediction and the present results. His analysis was done for the temperature boundary conditions which were applied at $y = -\infty$ and considered only the jet-mixing region as the determining factor in overall heat transfer. The results of the present study indicate that for the geometry considered, a somewhat different Reynolds number dependency exists. The results are well correlated when q/q_0 is plotted as a function of $\bar{v}_i$ Re$^{0.77}$, as shown in Fig. 12. An empirical expression which approximates the curve representing the calculated results is given as

$$\frac{q}{q_0} \simeq \exp\,(-0.43\,\bar{v}_i\,\mathrm{Re}^{0.77}) \tag{11}$$

It is of interest to note that Chapman's analysis predicted a reduction of the heat-transfer rate to zero when $\bar{v}_i$ Re$^{0.5}$ reached 1.2 while the present results indicate that the heat-transfer rate approaches zero only for very large values of $\bar{v}_i$ Re$^{0.77}$. This difference is not surprising in view of the fact that Chapman's study dealt with a single component, i.e., the mixing region, whereas the present study was also concerned with phenomena taking place within the cavity and near the important recompression region.

In conclusion, it was found that the numerical techniques employed in the study were well suited for the detailed investigation of laminar flow and heat transfer in the vicinity of a wall cavity. Of particular value is the ability to consider the temperature and flow fields both above and within the cavity and to study the important region near the reattachment corner in considerable detail with a view toward determining overall heat transfer rates. The results indicate that fluid injection through the cavity has significant effects on the flow patterns and the heat-transfer rates. The greatest reduction in heat transfer is evidenced especially at the reattachment point on the downstream cavity wall. The magnitude of the overall reduction of heat transfer with injection was found to be of the same order of magnitude as reported by previous investigators. However, a somewhat different dependency on Reynolds number and injection rate was observed.

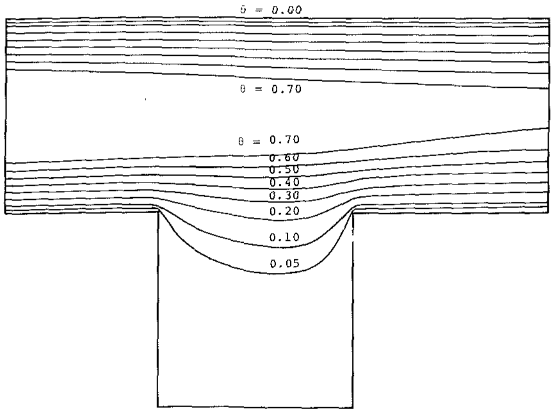

Fig. 8 Analytical isotherm patterns, Re = 100, 5 percent injection

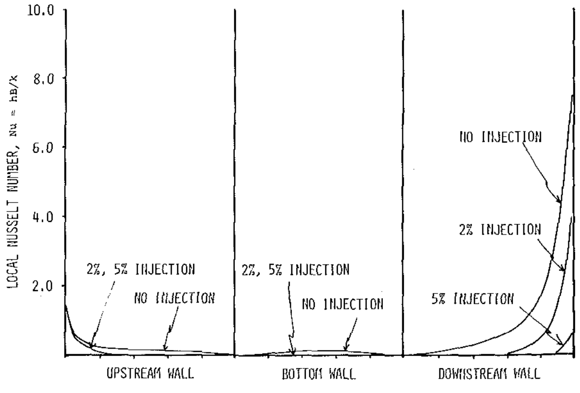

Fig. 10 Analytical local Nusselt number along cavity walls, showing effect of injection, Re = 500

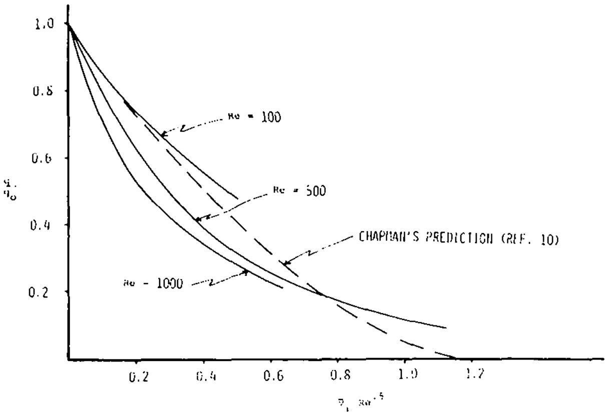

Fig. 11 Effect of injection on heat transfer—comparison with Chapman's results

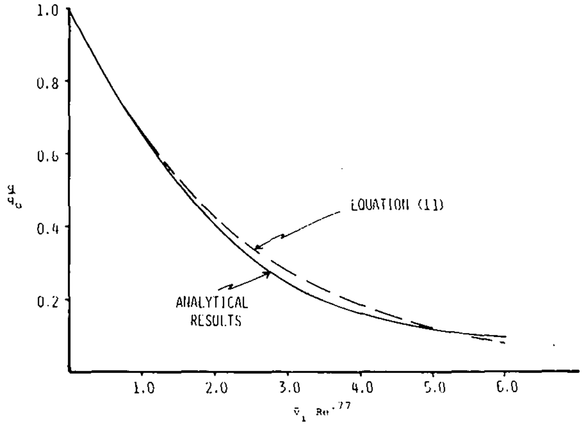

Fig. 12 Effect of injection on heat transfer

References

1 Bales, E. L., and Korst, H. H., "Heat Transfer Within and Across Nearly Circular Cavities," ASME Paper No. 74-WA/HT-62, 1974.

2 Burggraf, O. R., "A Model of Separated Flow in Rectangular Cavities at High Reynolds Number," *Proceedings of the 1965 Heat Transfer and Fluid Mechanics Institute*, Stanford University Press, Stanford, Calif., 1965, pp. 190–231.

3 Haugen, R. L., and Dhanak, A. M., "Heat Transfer in Turbulent Boundary Layer Separation Over a Surface Cavity," JOURNAL OF HEAT TRANSFER, TRANS. ASME, Series C, Vol. 89, No. 4, Nov. 1967, pp. 335-341.

4 White, R. A., "Some Results on the Heat Transfer Within Resonating Cavities at Subsonic and Supersonic Mach Numbers," *Journal of Basic Engineering*, TRANS. ASME, Series D., Vol. 93, No. 4, Dec. 1971, pp. 537–542.

5 Reihman, R. C., and Sabersky, R. H., "Laminar Flow Over Rectangular Cavities," *International Journal of Heat and Mass Transfer*, Vol. 11, 1968, pp. 1083-1085.

6 Nicoll, K. M., "A Study of Laminar Hypersonic Cavity Flows," *AIAA Journal*, Vol. 2, 1964, p. 1535.

7 Presser, K. H., "Empirische Gleichungen Zur Berechnung der Stoff- Und Wärmeübertragung für den Spezialfall der Abgerissenen Strömung," *International Journal of Heat and Mass Transfer*, Vol. 15, 1972, pp. 2447–2471.

8 Fox, J., "Heat Transfer and Air Flow in a Transverse Rectangular Notch," *International Journal of Heat and Mass Transfer*, Vol. 8, 1965, pp. 269–279.

9 Charwat, A. F., Dewey, C. F., Roose, J. N., and Hitz, J. A., "An Investigation of Separated Flows –Part II; Flow in the Cavity and Heat Transfer," *Journal of the Aero-Space Sciences*, Vol. 28, 1961, pp. 513-527.

10 Chapman, D. R., "A Theoretical Analysis of Heat Transfer in Regions of Separated Flow," NACA TN 3792, 1956.

11 Chilcott, R. E., "A Review of Separated and Reattaching Flows With Heat Transfer," *International Journal of Heat and Mass Transfer*, Vol. 10, 1967, pp. 783-797.

12 Johnson, R. W., "Heat and Momentum Transfer in Laminar Flow Past a Rectangular Cavity with Fluid Injection," PhD thesis, Michigan State University, 1970.

13 Mills, R. D., "Numerical Solutions of the Viscous Flow Equations for a Class of Closed Flows," *Journal of the Royal Aeronautical Society*, Vol. 69, Oct. 1965, pp. 714-718.

14 Russel, D. B., "On Obtaining Solutions to the Navier-Stokes Equations With Automatic Digital Computers," A.R.C.R. & M. 3331, May 1962.

15 Johnson, R. W., and Dhanak, A. M., "Calibration of Constant-Temperature Hot-Wire Anemometers for Low-Velocity Air Flow Measurements," *Proceedings of DISA Conference on Fluid Dynamic Measurements in the Industrial and Medical Environments*, University of Leicester, U.K., Apr. 1972.

E. M. Sparrow
N. Cur

Department of Mechanical Engineering,
University of Minnesota,
Minneapolis, Minn.

Characteristics of Hollow Glass Microspheres as an Insulating Material and an Opacifier

Thermal conductivity measurements were performed to determine the characteristics of hollow glass microspheres as an insulating material and as an opacifying agent for other insulations. The experiments were carried out with a radial flow heat transfer apparatus especially designed to suppress extraneous heat transfers, both internal and external to the heated section, and to provide uniform temperatures on the bounding surfaces. Three types of microsphere insulations were investigated, differing in bulk density and in the presence or absence of an aluminizing coating. The thermal conductivity of the microsphere insulations was found to be about one and a half times that of stagnant air over a wide temperature range. Additional experiments, involving the use of an opacifier (powdered silicon), demonstrated that radiative transfer has a minor effect on the thermal conductivity of microsphere insulations. This finding was corroborated by the fact that the high-temperature conductivity of the aluminized microspheres was not appreciably different from that of the uncoated microspheres. Another set of experiments was performed in which microsphere insulation was added to opacify silica aerogel, a fine powder insulation that is markedly affected by radiative transfer. The presence of the microspheres brought about reductions in conductivity of almost a factor of two at an optimum mixture ratio of the constituents. Furthermore, it was found that the conductivity of such a mixture was lower than that of either constituent, thereby illustrating their synergistic interaction.

Introduction

Insulating materials possessing an interesting variety of thermal, structural, durability, and installation characteristics have been produced by innovative contemporary technology. An example of such insulating materials is hollow glass microspheres, a granular-type insulation for which the production techniques have only recently been perfected. The thermal conductivity characteristics of the hollow microsphere insulation have been investigated in [1][1] for the range of temperatures relevant to cryogenics and under vacuum conditions ($<10^{-6}$ Torr). The present study was undertaken to investigate the characteristics of the microsphere insulation at higher temperatures (mean insulation temperatures up to 250°C (500°F)) and at atmospheric pressure.

The experiments to be described here encompass three research objectives: the effect of (*a*) bulk density; (*b*) addition of an opacifier on the thermal conductivity of the microsphere insulation; (*c*) the effectiveness of the hollow microspheres as an opacifier when mixed with other granular insulations. The first two of these objectives were part of the original research plan. The third was undertaken when it was found that the conductivity of the microsphere insulation is essentially unaffected by the addition of an opacifying material, thereby suggesting that the blockage of radiation by the microspheres is comparable to that by the opacifier.

Hollow microsphere insulations possess a number of attractive attributes. As will be demonstrated later, they have low thermal conductivity (about 1½ times the conductivity of stagnant air) at atmosphere pressure and do not require opacification at higher temperatures. They are light in weight, but possess sufficient mechanical strength so as not to settle or compact in the presence of

---

[1] Numbers in brackets designate References at end of paper.

Contributed by the Heat Transfer Division for publication in the JOURNAL OF HEAT TRANSFER. Manuscript received by the Heat Transfer Division October 15, 1975. Paper No. 76-HT-OO.

vibration or moderate compressive load. When poured, they flow like a fluid and are, therefore, able to fully fill the space to be insulated, yet they exhibit a lesser tendency to be airborne than do fine powder insulations. Finally, hollow microsphere insulations are moderate in cost (on the order of one-fourth the cost of silica aerogel).

The conductivity measurements were performed with the aid of a specially designed radial heat flow apparatus. In addition to guard heating at both ends of the annular test section, low conductivity insulations were installed both internal and external to the heated section in order to further suppress extraneous heat losses. As a result of these measures, a high degree of temperature uniformity was achieved at the bounding surfaces of the annulus at all operating conditions of the experiments.

Three types of hollow microsphere insulations were employed in the experiments.[2] The first two types, designated, respectively, as B25B and B15B (manufacturer's designations), were characterized by bulk densities of 0.127 and 0.087 g/cm^3. These materials enabled an assessment of the effect of bulk density. The third type, which consisted of half-aluminized hollow microspheres, was studied in connection with the possible influence of radiative transfer at higher temperature levels. All of the investigated insulations encompassed a range of microsphere diameters, as will be indicated later. The mean microsphere diameter was on the order of 100 μm (0.004 in.), with a wall thickness of approximately 1 μm (0.00004 in.). The individual microspheres are filled with a gas mixture of SO_2 and O_2 at a total pressure of about $\frac{1}{3}$ atm, the component gases being present in a ratio of roughly 2:1.

For the experiments on the role of opacifying materials, finely powdered silicon was employed as an opacifier for the microsphere insulation. In subsequent experiments, the microspheres were used as an opacifying material for silica aerogel insulation. To provide comparisons with the results of the latter experiments, conductivity measurements were also made for silica aerogel insulation, both unopacified and opacified with powdered silicon.

Within the knowledge of the authors, the only prior experiments concerned with the characteristics of hollow microsphere insulations are those of [1], mentioned previously. A detailed analysis of the heat conduction process in the walls of a hollow microsphere and in the region of contact of adjacent microspheres was performed in [2], without consideration of radiation and conduction in the spaces interior to and between the microspheres. The radiation transfer was analyzed in [3] but, as yet, the complexity of the problem has precluded a predictive theory including all relevant transport mechanisms. A number of analytical models have been proposed for predicting the thermal conductivities of granular insulating materials, and these are well summarized in [4]. Owing to the fact that the microsphere insulation consists of a three-component mixture (spherical glass shell, interior $SO_2 - O_2$ mixture, air in pore spaces), with a range of particle diameters, the existing models do not appear to be applicable. For example, the microsphere insulation does not fall within any of the seven categories of three-component mixtures considered in [5]. As a consequence, it does not appear that predictions are presently available against which to compare the results to be reported here.

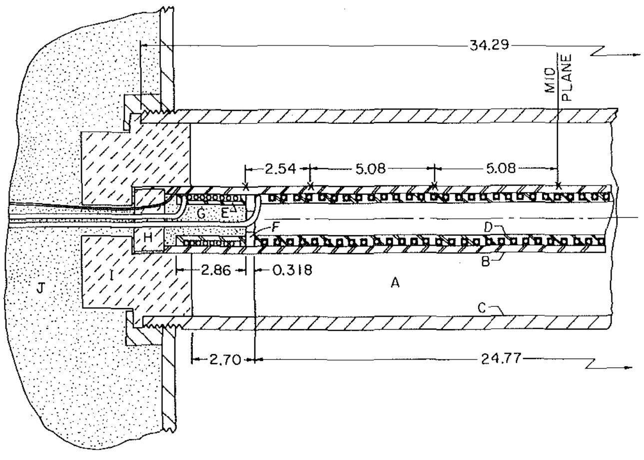

Fig. 1 Schematic diagram of the thermal conductivity apparatus

Experimental Apparatus and Procedure

The apparatus that was employed for the thermal conductivity measurements is shown in cross sectional view in Fig. 1. The design was aimed at minimizing extraneous heat transfers both internal and external to the apparatus. The insulation material to be investigated is contained in the annular space A bounded by the concentric cylinders B and C. The inner bounding cylinder is made of copper, with an outside diameter of 2.67 cm (1.05 in.) and a wall thickness of 0.290 cm (0.114 in.). The outer bounding cylinder is of brass and has an inside diameter of 7.77 cm (3.06 in.) and a 0.559 cm (0.22 in.) wall. The length dimensions (in centimeters) of these and other components are indicated in the figure.

The main heater D, fabricated by winding sheathed double-conductor resistance wire onto a helically grooved copper core, was tightly press fitted into cylinder B. Flanking each end of the main heater is a guard heater E, made up of a copper spool wound with the sheathed resistance wire. To minimize extraneous heat transfer between the main heater and the respective guard heaters, a disk F of Min-K insulation was employed as a separator. Min-K was selected for this function because it is a rigid material capable of accommodating high temperatures and yet has a thermal conductivity substantially less than that of air (e.g., almost 30 percent less at a temperature of 300°C). The Min-K disk shown in the figure has an aperture to permit the passage of the main heater power leads. Once the leads were installed, this aperture was closed with high temperature fibrous insulation. The Min-K disk at the other end of the main heater is solid.

A number of features were incorporated into the apparatus to suppress end losses. The hollow bore G of the guard heater was filled with microsphere insulation. Min-K disks H were employed to close the ends of the inner cylinder B, and cylindrical blocks I of Min-K served to seal the ends of the annular space A. To further diminish end losses, each end cap was interfaced with a large bed J of silica aerogel insulation, whose thermal conductivity at moderate temperatures is less than that of air.

Surface temperatures on the inner bounding cylinder of the annulus were measured with the aid of ten 30-gage iron-constantan

---

[2] All manufactured by 3M Company, St. Paul, Minn.

Nomenclature

k = thermal conductivity

k_m = mean thermal conductivity, equations (2) and (3)

L = length of main heater

Q = power input to main heater

r_i = inner radius of insulation annulus

r_0 = outer radius of insulation annulus

T = temperature

T_{av} = average temperature of insulation, $\frac{1}{2}(T_i + T_0)$

T_i = temperature at r_i

T_0 = temperature at r_0

T^* = temperature corresponding to k_m

ρ_b = bulk density of insulation sample

ρ_t = true density of solids

thermocouples which had been calibrated prior to their installation. The axial positions of the thermocouple junctions are identified in Fig. 1 by the x-symbols. At the midplane, there are four thermocouples deployed at 90 deg intervals around the circumference, whereas single thermocouples are situated at each of the other axial stations. The thermocouple leads were placed in shallow axial grooves that had been machined into the surface of the cylinder. The dimensions of the grooves were chosen to be the minimum that could accommodate the wires. Good contact between the junctions and the cylinder was assured by the use of copper oxide cement. The edges of the grooves were peened against the junctions and the lead wires to ensure positive positioning. As indicated in Fig. 1, the lead wires were brought out from the ends of the apparatus.

Owing to the guard heating and the other measures aimed at suppressing extraneous heat losses, a high degree of uniformity was attained among the thermocouple readings. For example, at the lowest temperature level of the experiments (inner-cylinder temperature of about 130°C (265°F)), temperature uniformity among the thermocouples was within 0.02°C. At the highest temperature level, at which the inner-cylinder temperature was about 420°C (790°F), uniformity was within 0.15°C. The axial heat transfer induced in the wall of the inner cylinder by these temperature variations was estimated, at maximum, to be about two percent of the power input to the main heater.

Temperature measurements on the outer bounding cylinder were made at three axial stations by means of 12 thermocouples. At each station, four thermocouples were circumferentially distributed at 90 deg intervals. As a matter of convenience, the thermocouples were installed on the outer surface of the cylinder rather than on the inner surface. Calculations indicated that at the highest heat flux of the experiments, the temperature drop across the cylinder wall is only about 0.02°C (~0.04°F). Therefore, the placement of the thermocouples on the outside surface is not a source of error. The temperature uniformity among these thermocouples was even better than the aforementioned uniformity for the inner-cylinder thermocouples. The thermocouple wires were laid in axial grooves similar to those on the inner cylinder.

The thermocouple outputs were read with a digital voltmeter to within one microvolt. The main heater and the two guard heaters were each energized by a separate d-c power supply. Heater power inputs were determined either by a laboratory-grade (¼ percent) wattmeter or by voltage and shunt current measurements, depending on the power level.

The inner bounding surface (i.e., the heating surface) of the insulation annulus was coated with a continuous black oxide film, whereas the outer bounding surface was lightly oxidized. According to [10], the radiation properties of the bounding surfaces are of no particular relevance for optically thick insulation systems. As will be seen later, the insulation system investigated in the present experiments is optically thick.

For the determination of the bulk density of the various insulation samples, measurements of mass were made with a precision balance accurate to within 0.1 mg. The mass of a typical sample was on the order of 200 g. The same balance was employed to weigh the components of the insulation mixtures that were used in the opacification studies.

Particular care was exercised in inserting the insulation materials into the test section, both with a view to maintaining concentric positioning of the bounding cylinders and to avoiding nonuniform packing and voids. The filling operation was performed with the axis of the apparatus vertical and with the lower end of the annulus sealed. The insulation sample was introduced in discrete stages through the upper end of the annulus, which was open for this purpose. Each stage was marked by shaking, tapping, and compacting with a wire loop in order to achieve a solid packing. Once the annulus had been filled, the upper end was sealed, and the apparatus positioned with its axis horizontal in readiness for the experiments.

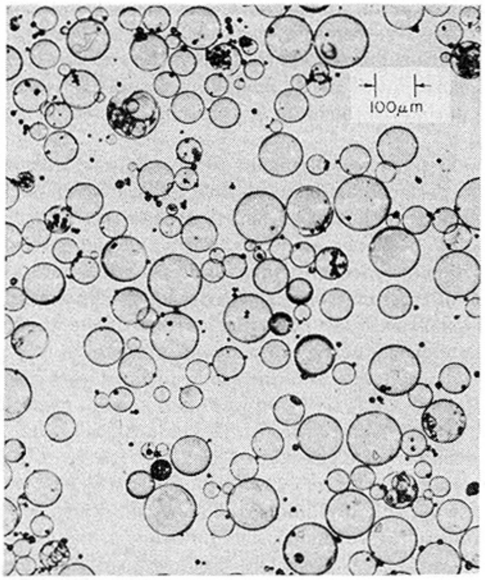

Fig. 2 Photomicrograph of typical constituents of type B25B insulation

One indication of the uniformity attained by the aforementioned packing procedure was the total absence of systematic circumferential temperature variations. Furthermore, verification experiments, based on independent packings of insulation samples, yielded highly consistent results.

Care was also taken in the mixing of components to obtain the insulation samples for the investigation of opacifying materials. To facilitate the attainment of uniformity, samples several times larger than needed to fill the test section were prepared.

In the conduct of the experiments, it was found that 15–20 hr had to be allowed to attain steady state after a major change in input power level. Subsequent to the attainment of an initial steady state, a succession of small adjustments of the guard heaters was made in order to achieve the desired uniformity of the temperature of the inner cylinder. Owing to the time lapse needed to attain steady state after each such adjustment, between two and three days were required for each data point.

Description of the Investigated Insulations

The hollow glass microsphere insulations have already been described in general terms in the Introduction, and further details will be given here. A photomicrograph of the typical constituents of type B25B microsphere insulation is presented in Fig. 2. The photograph shows size distribution and composition, but does not display the true packing arrangement encountered in a bed of insulation. This is because the deployment of a thin layer of microspheres on a microscope slide is necessarily different from that in a packed bed.

In the photograph, the bubble-like spherical objects are the hollow microspheres. The smaller, darker objects are bits of solid glass (the so-called beads). By making use of the scale indicated in the figure, it is seen that the diameters of the hollow microspheres range in size from 140 to 20 μm (0.0055–0.0008 in.). The beads are generally of smaller diameter, typically about 10 μm (0.0004 in.).

Quantitative information about the densities and size distributions of the microsphere insulations is given in Table 1. The table lists the three types of microsphere insulations that were mentioned in the Introduction. The ρ_b column gives the bulk densities (in g/cm^3) of the respective insulations as they were packed in the thermal conductivity apparatus. The next column of the table indicates the true density ρ_t of the solids, that is, the mass of the solids (hollow microspheres plus beads) divided by the volume occupied by these solids (including the volume of the hollow bore of the microspheres). The true density was measured by an air pycnometer [6].

The lower values of ρ_b and ρ_t for the B15B insulation, relative to those for the B25B insulation, are due primarily to a diminished number of beads and also to relatively thinner walls for the hollow microspheres. The still lower densities for the half aluminized microsphere insulation is the result of further elimination of beads.

The void fraction (or porosity) ϵ, which is the ratio of the volume of the pore spaces between the solids to the total volume occupied by the insulation, can be evaluated as $1 - (\rho_b/\rho_t)$. It is interesting to note that the void fractions of the B25B and B15B insulations differ only slightly, which suggests that the gaseous conduction in the pore spaces should not be very different in the two cases. Furthermore, for the microsphere insulations, the pore space conduction should not be affected by mean free path effects, whose influence is related to the ratio of the mean free path to a characteristic dimension of the pores. According to [10], such a characteristic dimension may be estimated from the relation $0.67D/(1 - \epsilon)$, where D is the diameter of a typical microsphere ($\sim$100 μm). When this estimate is used along with the mean free path for air at atmosphere pressure, the aforementioned ratio is on the order of 10^{-3}, which indicates that the pore space heat conduction follows the conventional laws for continua.

Information about the distribution of particle sizes in the microsphere insulations is provided by the last three columns of the table. The numbers 95, 50, and 5, which head the respective columns, represent volume percentages. The entries in the table are best explained by an illustration. For example, the number 144 (which appears directly under the 95 percent heading) indicates that for the B25B insulation, 95 percent of the volume of the solids is made up of particles whose diameters are smaller than (or equal to) 144 μm. The other entries have a corresponding meaning. The tabulated results indicate that the particles constituting the B15B insulation are, on the average, somewhat smaller than those of the other insulations and also that there are relatively few very small particles in the half-aluminized insulation. The size distributions listed in Table 1 were obtained by means of a Coulter counter [6].

For the opacification studies, two other materials were employed in addition to those of Table 1. One is powdered silicon, which is a commonly used opacifier. The powdered silicon used in the present experiments was described by the manufacturer[3] as containing one percent iron and consisting of particles which pass through a 100 mesh screen (149 μm openings). Microscopic examination of the powdered silicon revealed the presence of 15–100 μm chunks and a 1–2 μm dust.

The other material is silica aerogel (Santocel A, Monsanto), a well known powder insulation. The thermal conductivity of silica aerogel is markedly affected by radiative transfer at higher temperatures and, for this reason, it was selected for opacification studies in which the hollow microspheres are employed as an opacifying agent. The bulk density of a sample of the silica aerogel insulation, as packed in the thermal conductivity apparatus, was 0.088 g/cm^3.

Data Reduction

Thermal conductivity values were evaluated from the measured temperatures and power inputs by employing the governing equation for steady radial heat flow between concentric cylinders. When the thermal conductivity is a function of temperature, this equation takes the form

$$Q = \frac{2\pi L(T_i - T_0)}{\ln (r_0/r_i)} \left[\frac{1}{(T_i - T_0)} \int_{T_0}^{T_i} k dT \right] \tag{1}$$

where T_i and T_0 are the temperatures at the inner and outer bounding surfaces of the annulus and Q is the rate of heat transfer corresponding to the axial length L. It is natural to define a mean thermal conductivity k_m as

Table 1 Characteristics of microsphere insulations

Type	ρ_b	ρ_t	Size distribution 95	50	5
B25B	0.127	0.241	144	102	36
B15B	0.087	0.160	129	88	26
Half Al.	0.071	0.117	145	97	63

$$k_m = \frac{1}{(T_i - T_0)} \int_{T_0}^{T_i} k dT \tag{2}$$

so that, from equation (1),

$$k_m = \frac{Q \ln (r_0/r_i)}{2\pi L(T_i - T_0)} \tag{3}$$

Equation (3) was employed to evaluate the thermal conductivity. For Q, the power input to the main heater was used, recognizing the possibility of an uncertainty of up to two percent owing to axial conduction in the inner cylinder as discussed earlier. L is the length of the main heater, and T_i and T_0 are the measured inner and outer surface temperatures, respectively at radii r_i and r_0.

Next, it is relevant to consider the temperature which is to be associated with a thermal conductivity value deduced from equation (3). In the literature which deals with insulating materials, it is usual to employ the average of the inner and outer surface temperatures, that is

$$T_{\text{av}} = \tfrac{1}{2}(T_i + T_0) \tag{4}$$

Alternatively, the numerical value of k_m may be introduced into the relation $k = k(T)$, and the temperature T^* corresponding to this k_m value can be solved for. If the $k(T)$ relation is linear, then $T_{\text{av}} = T^*$. Otherwise, there are deviations between T_{av} and T^*, the extent of which depends on the degree of nonlinearity of the $k(T)$ relation.

As will be demonstrated shortly, the $k(T)$ relation for each of the hollow microsphere insulations is very nearly linear, so that $T_{\text{av}} \approx T^*$. On the other hand, the silica aerogel insulation employed in the opacification studies has a moderately nonlinear $k(T)$, both without and with an opacifying agent. The extent of the deviations between T_{av} and T^* for the aerogel will be discussed later, in conjunction with the presentation of results.

For all cases, the measured thermal conductivities will be plotted as a function of T_{av} in order to have the presentation of results be consistent with the currently standard procedure.

Thermal Conductivity of Microsphere Insulations

The measured thermal conductivities of the hollow microsphere insulations are plotted as a function of temperature in Fig. 3. Two ordinate scales are used for the thermal conductivity, one for SI units (right-hand ordinate) and the other for English engineering units (left-hand ordinate). Correspondingly, separate abscissa scales in °C and °F are employed for the temperature. On account of the moderate variations of the thermal conductivity in the temperature range investigated, an expanded ordinate scale has been adopted (note the indicated vertical height corresponding to a two percent change in conductivity). The results for the three types of microsphere insulations are identified by different data symbols, and faired curves have been passed through the data points to provide continuity.

Also shown in the figure for reference purposes is a dashed line which represents the intrinsic thermal conductivity of air. With regard to the transfer of heat across an actual air layer, the purely conductive transport may be augmented by natural convection and by radiation, so that the effective thermal conductivity may be very much larger than the intrinsic conductivity. Therefore, although the intrinsic thermal conductivity of air is a convenient ref-

---

[3] Union Carbide Metals Division.

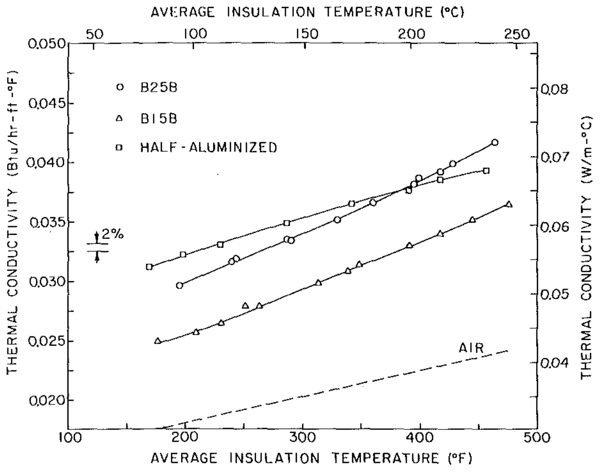

Fig. 3 Thermal conductivity of hollow microsphere insulations

erence quantity, it should not be regarded as an absolute standard for judging the quality of an insulating material. In particular, even if the conductivity of an insulating material exceeds the intrinsic conductivity of air, it still may be a more effective barrier to heat transfer than an air layer.

The conductivity values shown in Fig. 3 are more than fifty times larger than those reported in [1] for hollow microsphere insulations under high vacuum ($<10^{-6}$ Torr) and at cryogenic temperatures. A part of the increase can be attributed to temperature-related increases in the thermal conductivities of the glass walls of the microspheres and of the gases contained within the microspheres. In addition, radiative transfer is increased as the temperature level is raised. A further major factor in accounting for the larger conductivity values encountered in the present investigation is gaseous conduction in the pore spaces.

Attention will now be turned to the uncoated microspheres, i.e., types B25B and B15B. From the figure, it is seen that the thermal conductivities of the B25B and B15B insulations are, respectively, about 1.67 and 1.45 times that of air. Therefore, the insulating quality of the microspheres is comparable to that of fine powder insulations and superior to that of most fibrous insulations. Furthermore, the microsphere insulations do not exhibit rapid increases in thermal conductivity at higher temperatures, as occurs for a number of granular and powder insulations owing to the effect of radiative transfer.

The conductivity of the B15B insulation is about 15 percent lower than that of B25B insulation. This ordering is consistent with the fact that the bulk density of the former is lower (by about 30 percent) than that of the latter. The percentage difference in the thermal conductivities of the two insulations is about half the percentage difference in the corresponding bulk densities. In assessing this outcome, it should be noted that whereas a reduction in bulk density has a direct effect on the conduction paths through the solids, other heat flow paths may be affected to a lesser extent. For instance, as discussed in connection with Table 1, the pore space volumes for the B25B and B15B insulations are approximately the same, suggesting comparable contributions of pore-space gaseous conduction. Another factor which may influence the nonproportionate response of the conductivity to the bulk density is the difference in the size distributions of the two insulations as evidenced by Table 1.

The variation of the conductivity with temperature is seen to be nearly linear. For the B25B and B15B insulations, the following linear $k(T)$ relations represent the data to well within one percent.

$$k = 0.02081 + 0.0000444T, \quad \text{B25B} \tag{5}$$

$$k = 0.01742 + 0.0000396T, \quad \text{B15B} \tag{6}$$

where k is in Btu/hr-ft-°F, and T is in °F. The possible causes of the conductivity increase with temperature are of two types: (*a*) increases in the conductivities of the constituent materials, (*b*) activation of additional transfer mechanisms. It can be verified [7, 8] that the thermal conductivities of all the constituents of the B25B and B15B insulations (borosilicate glass, air, SO_2 and O_2) do increase with temperature. Radiative transfer may be activated at higher temperatures, and this possibility will be examined shortly. Natural convection is negligible at all the temperature levels of the experiments, as will be documented later.

The results for the half aluminized microsphere insulation will now be considered. Although this insulation has the lowest bulk density among those investigated (Table 1), its conductivity is higher than the others for temperatures in the lower and middle part of the abscissa range of Fig. 3. The reason for this outcome is that the aluminum coating on the microspheres provides an augmented conduction path, thereby diminishing the thermal resistance. The thermal conductivity of the aluminum is about two orders of magnitude greater than that of borosilicate glass [7, 9, 10]. The thickness of the aluminum film has been estimated to be in the range of 0.03–0.1 μm, although the process by which it is applied does not permit an accurate film thickness assessment. As noted earlier, the wall thickness of the microspheres is on the order of 1 μm. The increase of the conductivity with temperature is more gradual for the half aluminized microsphere insulation than for the other insulations, so that the curves cross at higher temperatures. This more gradual slope might, at first thought, be believed due, at least in part, to the effectiveness of the coating in blocking thermal radiation. However, the results that will be presented shortly indicate that radiation is not a major factor in microsphere insulations. Of seemingly greater relevance with respect to the aforementioned gradual slope is the fact that the thermal conductivity of pure aluminum decreases with increasing temperature in the range of the present experiments [9, p. 9]. This is in contrast to the conductivities of the constituents of the B25B and B15B insulations which, as has been already noted, increase with temperature.

The conductivity data for the half aluminized microsphere insulation can be represented to well within one percent by the linear relation

$$k = 0.02655 + 0.0000285T \tag{7}$$

where the units are the same as those of equations (5) and (6). The results of Fig. 3 indicate that coating the microspheres does not lead to improved insulating qualities in the temperature range investigated here.

To explore the possible influence of radiative transfer on the measured thermal conductivities of the uncoated microsphere insulations, experiments were performed in which an opacifying material, powdered silicon, was employed. The amounts of powdered silicon added to the microsphere insulation were characterized by the ratio

$$\text{mass ratio} = \frac{\text{mass of powdered silicon}}{\text{mass of unopacified microsphere insulation}} \tag{8}$$

The results of these experiments are presented in Fig. 4. The ordinate of the figure is the ratio of the conductivity in the presence of the opacifier to that in the absence of the opacifier. The average temperature of the insulation is plotted on the abscissa, with separate scales for SI and for English units. The various mass ratios are depicted by the symbols identified in the legend. The open and closed symbols are for the B25B and B15B insulations, respectively.

In appraising Fig. 4, cognizance has to be taken of the highly expanded ordinate scale. It is then seen that for the most part, there is a difference of only a few percent between the conductivities with and without the opacifier. Even for the extreme case of a 95 percent mass ratio, the change in conductivity was only 11–14 percent—an increase.

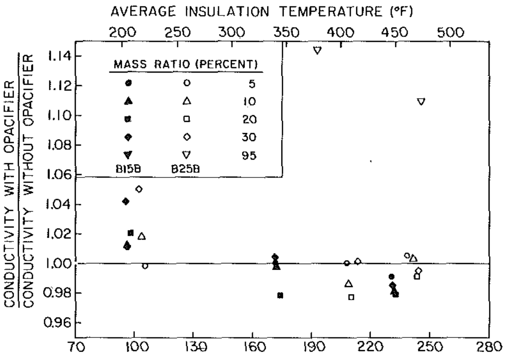

Fig. 4 Effect of an additive opacifying agent (powdered silicon) on the thermal conductivity of microsphere insulations—the mass ratio is defined in equation (8)

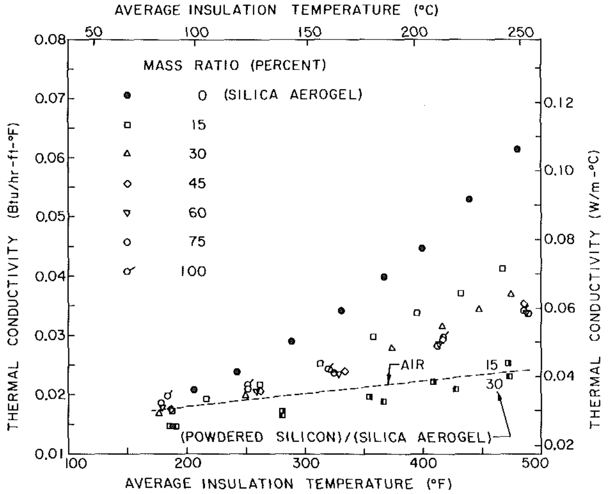

Fig. 5 Effect of B25B microsphere insulation as an opacifying agent on the thermal conductivity of silica aerogel insulation—the mass ratio is defined in equation (9)

It might appear from the results of Fig. 4 that the powdered silicon was not performing its function as an opacifier. Yet, as will be demonstrated shortly, powdered silicon is a highly effective opacifying agent. It may, therefore, be concluded that radiation is so effectively blocked by the microspheres themselves that there is very little radiation that remains to be blocked by the powdered silicon.

The aforementioned results clearly establish that hollow microsphere insulations can be employed over a wide range of temperatures without requiring additive opacifying agents. This is a distinct advantage compared with many granular and powder insulations, which require additives to opacify radiative transfer at higher temperatures.

The disposition of the data points in Fig. 4, although suggestive of scatter, is actually indicative of an orderly pattern. The addition of the powdered silicon not only blocks radiative transfer (albeit to a very small extent), but also provides alternative conduction paths. This is why an increase in thermal conductivity is in evidence at the higher mass ratios.

Before leaving this section, the role of natural convection will be discussed. It will first be demonstrated that the heat transfer through the air in the pore spaces is by conduction and not by natural convection. For this purpose, a pore space Rayleigh number may be evaluated. If the diameter D of a typical microsphere ($\sim$100 μm) is used as the characteristic dimension, then the Rayleigh number is found to be about 10^{-5}. As an alternative, the pore space Rayleigh number may be defined with the square root of the permeability as the characteristic dimension. From the Carmen-Kozeny relationship [11], the permeability of a bed of spheres is given by $\kappa = \epsilon^3 D^2/180(1-\epsilon)^2$, where ϵ is the void fraction. The pore Rayleigh number based on $\kappa^{1/2}$ is about 2×10^{-9}. Either of these Rayleigh numbers is smaller by many orders of magnitude than that at which the influence of natural convection is first manifested in enclosed spaces [12].

It is also of interest to consider the possible existence of larger scale natural convection currents circulating through the insulation bed as a whole. From the analysis of simpler porous media systems (e.g., [13]), the onset of convection is found to depend on a Rayleigh number based on the product of the permeability and a typical dimension of the porous bed as well as on a weighted solid-fluid thermal conductivity. The evaluation of such a Rayleigh number for the present case yields a value of about 0.002, which is appreciably smaller than the value $4\pi^2$ ($\sim$40) given by linear stability theory as the threshold for the initiation of convective motions.

Application of Microspheres as an Opacifier

The results presented in the foregoing section suggest that hollow glass microspheres might serve as a highly effective opacifier when mixed with other granular or powder insulations. To investigate this, experiments were performed in which type B25B microsphere insulation was added to silica aerogel (Santocel A, Monsanto), a fine powder insulation which is markedly affected by radiative transfer at higher temperatures. To characterize the microsphere-aerogel mixtures, the following ratio was employed

$$\text{mass ratio} = \frac{\text{mass of B25B insulation}}{\text{mass of unopacified silica aerogel}} \tag{9}$$

The results of these opacification experiments are presented in Fig. 5, where the thermal conductivity is plotted as a function of temperature. As before, dual scales are employed for SI and English units. The experiments were performed for mass ratios from 0 to 100 percent, which covers the range from unopacified silica aerogel to equal masses of microspheres and aerogel. Curves have not been faired through the data because they would be confusingly overlapped for the intermediate and high mass ratios.

The data for the unopacified silica aerogel (black circles) represent the baseline against which the other data are to be compared. The large increase in the thermal conductivity of the aerogel with temperature (a factor of three over the investigated temperature range) confirms the significant influence of radiative transfer.

As witnessed by the reductions in thermal conductivity at higher temperatures, the addition of microsphere insulation is a highly effective means of diminishing radiative transfer in the silica aerogel. The reduction in conductivity is relatively sharp when small amounts of microsphere insulation are added. Further, but increasingly gradual, reductions can be achieved when more microspheres are added. Finally, a point is reached where further additions of microsphere insulation cause the conductivity to increase.

These trends are clearly illustrated in Fig. 6, which is a cross plot of the data of Fig. 5. In Fig. 6, the thermal conductivity at each of several fixed temperatures is plotted as a function of the mass ratio defined by equation (9). The figure shows that the use of an opacified mixture characterized by a 60 percent mass ratio leads to a minimum thermal conductivity at all temperatures except for the lowest (where radiative effects are small and an opacifier would not normally be used). At the highest average insulation temperature of these experiments ($\sim$475°F), the thermal conductivity of the optimally opacified aerogel is about half of that for the unopacified aerogel.

The increase in thermal conductivity in evidence in Fig. 6 at the higher mass ratios is an indication that the heat conduction in the microspheres, which is intrinsically greater than that in the aerogel, is beginning to assert itself.

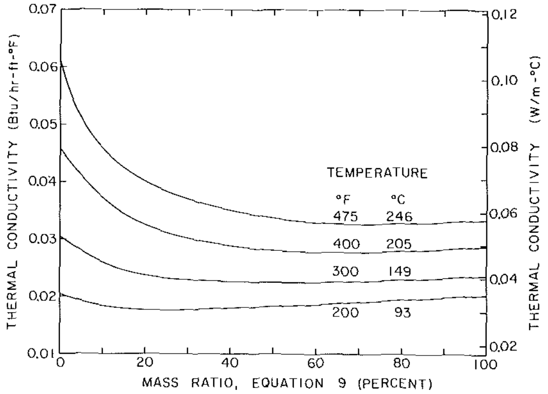

Fig. 6 Variation of the thermal conductivity of microsphere/aerogel mixtures as a function of the mass ratio of the constituents

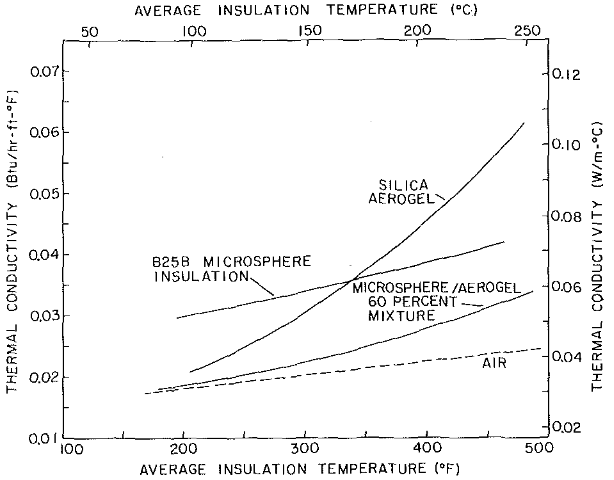

Fig. 7 Comparison of the thermal conductivities of microsphere insulation, silica aerogel insulation, and a mixture of the two

The results of Figs. 3, 5, and 6 enable the quantitative display of a behavior which, although known, is not well documented in the literature. The behavior to be displayed is the synergistic interaction of two insulating materials such that the thermal conductivity of the mixture is less than that of the components. For this purpose, Fig. 7 brings together the thermal conductivity-temperature characteristics for silica aerogel insulation, B25B microsphere insulation, and a mixture of the two having a 60 percent mass ratio (equation (9)). It is evident from the figure that in the temperature range considered, the mixture is superior to either component in insulation quality.

Before concluding, two additional matters will be discussed. The first has to do with the nonlinearity of the $k(T)$ relation for silica aerogel and its opacified mixtures (Fig. 5). As noted in the Data Reduction section following equation (4), the temperatures T_{av} and T^* may be different when $k(T)$ is nonlinear. To examine the extent of the deviation between T_{av} and T^*, calculations were performed for silica aerogel, whose $k(T)$ relation is more nonlinear than that of the other cases. By numerically integrating the $k(T)$ distribution over the entire available temperature range, a mean conductivity k_m was evaluated in accordance with equation (2) and, with this, a T^* value was deduced. It was found that T^* is about 5°C (9°F) larger than T_{av}. This is a minor deviation, so that if the results had been plotted as a function of T^*, they would not differ significantly from those plotted as a function of T_{av}.

Finally, mention will be made of the data shown at the bottom of Fig. 5. These data were obtained from experiments in which silica aerogel was opacified with powdered silicon. Mass ratios (powdered silicon ÷ silica aerogel) of 15 and 30 percent were employed. The reduction in conductivity brought about by the addition of the powdered silicon is seen to be truly remarkable. Indeed, for the 30 percent mass ratio, the conductivity of the mixture is below that of air over the entire temperature range investigated.

The data of Fig. 5 for the 15 percent powdered silicon-silica aerogel mixture represent the only results of the present investigation which overlap with the published literature [14]. In the range of overlap, 200–300°F, the agreement between the two sets of results is excellent, thereby lending support to the effectiveness of the present experimental apparatus.

Concluding Remarks

Carefully executed experiments have been performed to investigate the characteristics of hollow glass microspheres as an insulating material and as an opacifying agent for other insulations. The thermal conductivity of the microsphere insulation was found to be about one and a half times that of stagnant air in the investigated temperature range (average insulation temperatures ranging from 75 to 250°C (170–480°F). Therefore, the insulating quality of the microspheres is comparable to that of fine powder insulations and superior to that of most fibrous insulations. It was also established that radiative transfer has a minor effect on the thermal conductivity of the microsphere insulations, so that additive opacifiers need not be employed. These characteristics, taken together with light weight, mechanical strength, fluidity, minimal airborne dispersion, high temperature capability, and moderate cost, cause microsphere insulations to be highly attractive for practical application.

The thermal conductivities of the microsphere insulations were found to increase nearly linearly with temperature. Equations (5), (6), and (7) represent the data to well within one percent.

For the uncoated microspheres, the conductivity of type B15B was about 15 percent lower than that of type B25B, owing to its lower bulk density. On the other hand, the former is more costly than the latter. Owing to the fact that radiative transfer is not an important factor, coating the microspheres with a thin aluminum film does not lead to improved insulating qualities.

Experiments were performed in which type B25B microsphere insulation was added to opacify silica aerogel, a fine powder insulation that is strongly affected by radiative transfer. The microspheres were found to be a highly effective opacifier, reducing the conductivity of the unopacified aerogel by nearly a factor of two at the highest average insulation temperature of the experiments (~475°F). A mixture in which the mass of the microspheres is about 60 percent of the mass of the unopacified aerogel yielded the greatest reduction. The thermal conductivity of such a mixture was lower than that of either constituent, thereby illustrating their synergistic interaction.

Supplemental experiments showed that powdered silicon is an even more effective opacifying agent than the microspheres.

Acknowledgment

This research was supported by Grant GI-34871, initially funded by NSF/RANN and subsequently by ERDA. The contributions of Mr. F. W. Larsen to the initial design of the experimental apparatus are gratefully acknowledged.

References

1 Cunnington, G. R., and Tien, C. L., "Heat Transfer in Microsphere Cryogenic Insulation," *Advances in Cryogenic Engineering*, Vol. 18, 1973, pp. 103–117.

2 Chan, C. K., and Tien, C. L., "Conductance of Packed Spheres in Vacuum," JOURNAL OF HEAT TRANSFER, TRANS. ASME, Series C, Vol. 95, 1973, pp. 302–308.

3 Chan, C. K., and Tien, C. L., "Radiative Transfer in Packed Spheres," JOURNAL OF HEAT TRANSFER, TRANS. ASME, Series C, Vol. 96, 1974, pp. 52–58.

4 Vachon, R. I., Prakouras, A. G., Crane, R., and Khader, M. S., "Thermal Conductivity of Heterogeneous Mixtures and Lunar Soils," Department of Mechanical Engineering, Auburn University, Auburn, Alabama, Oct. 1973.

5 Cheng, S. C., and Vachon, R. I., "The Prediction of the Thermal Conductivity of Two and Three Phase Solid Heterogeneous Mixtures," *International Journal of Heat and Mass Transfer*, Vol. 12, 1969, pp. 249–264.

6 Howell, Peter A., 3M Company, St. Paul, Minn., personal communications.

7 Touloukian, Y. S., Powell, R. W., Ho, C. Y., and Klemens, P. G., *Thermal Conductivity, Nonmetallic Solids*, IFI/Plenum, New York, 1970.

8 Touloukian, Y. S., Liley, P. E., and Saxena, S. C., *Thermal Conductivity, Nonmetallic Liquids and Gases*, IFI/Plenum, New York, 1970.

9 Touloukian, Y. S., Powell, R. W., Ho, C. Y., and Klemens, P. G., *Thermal Conductivity, Metallic Elements and Alloys*, IFI/Plenum, New York, 1970.

10 Tien, C. L., and Cunnington, G. R., "Cryogenic Insulation Heat Transfer," *Advances in Heat Transfer*, Vol. 9, 1973, pp. 349–417.

11 Carmen, P. C., "Fluid Flow Through Granular Beds," *Transactions of the Institution of Chemical Engineers*, Vol. 15, 1937, pp. 150–166.

12 Ostrach, S., "Natural Convection in Enclosures," *Advances in Heat Transfer*, Vol. 8, 1972, pp. 161–227.

13 Elder, J. W., "Steady Free Convection in a Porous Medium Heated From Below," *Journal of Fluid Mechanics*, Vol. 27, 1967, pp. 29–48.

14 Santocel, A Silica Aerogel, Technical Bulletin I-180, Monsanto, St. Louis, Mo.

R. E. Mayle
F. C. Kopper
Mem. ASME

Pratt and Whitney Aircraft,
East Hartford, Conn.

Adiabatic Wall Effectiveness of a Turbulent Boundary Layer With Slot Injection

An analysis is presented which extends the theoretical work of Weighardt and determines the adiabatic wall effectiveness of a turbulent boundary layer in a constant free-stream velocity flow heated or cooled by the discharge of a secondary fluid through a slot. A comparison of the analysis with the experimental results of Wieghardt is made and it is found that the streamwise decay in adiabatic wall effectiveness, except in the immediate region of the slot, may be explained by considering the thermal boundary layer growth within the hydrodynamic boundary layer.

Introduction

Since 1943, when Wieghardt reported his work on "Hot-Air Discharge For De-Icing" [1],[1] many analyses have been performed to determine the adiabatic wall temperature of a turbulent boundary layer heated (or cooled) by an injection of secondary fluid through a slot. Most of the work involves combining the energy integral equation with assumptions and/or empirical information concerning the effects of injection on the turbulent boundary layer near the slot and entrainment downstream of the slot [2, 3]. In general, all of these analyses provide an analytic expression for the adiabatic wall effectiveness (a dimensionless adiabatic wall temperature) and describe the qualitative behavior exhibited experimentally far downstream of the slot, while only a few agree reasonably well with the data for a variety of situations. The important point to be made here is that each analysis implicitly assumes the thermal boundary layer thickness is either equal or proportional to the velocity boundary layer thickness, an assumption which is only appropriate a large number of boundary layer thicknesses downstream of the slot. The numerical solution techniques which have been presented more recently [4] inherently allow for not only an independent growth of the thermal boundary layer within the velocity boundary layer but also a diffusion of the shear layer that initially exists between the injected and free-stream fluid. As a result, they have the ability to determine the adiabatic wall effectiveness closer to the slot than could be previously accomplished, and in general, do well downstream. A detailed discussion of most theoretical work and comparison with experiments may be found in the comprehensive article by Goldstein [5].

The analysis performed in this study provides an approximate solution to the energy differential equation for the turbulent boundary layer downstream of the slot. This approach was taken by Wieghardt in his original paper, but only carried through to the point where he determined the functional form for the temperature profile. Upon investigating the related problem of an infinite line source of heat in a turbulent boundary layer, Frost [6], who was mainly concerned with thermal and mass diffusion in the lower atmosphere, found a solution for the temperature and mass concentration distributions where the shear layer thickness remained constant. Tribus and Klein [7], using an integration kernel developed from a solution for the problem of heat transfer with a step change in wall temperature, presented a result which included the effects of vertical heat and mass advection. However, the latter analysis implicitly assumes an initial $1/7$-power-law temperature profile and, although generally not mentioned, is quite dependent on the kernel used. More recently, Haji-Sheikh [8] presented an integral boundary layer analysis using the assumption that the thermal boundary layer grows as if the wall temperature after the slot is maintained constant. In the following analysis, the temperature profile shape and thermal boundary layer development is not assumed and the advection of fluid in the direction normal to the wall is considered. The analysis, however, is confined to the case of a low-speed, zero-pressure-gradient turbulent boundary layer where the physical properties of the slot and free-stream fluids are considered both identical and constant.

---

[1] Numbers in brackets designate References at end of paper.

Contributed by the Heat Transfer Division for publication in the JOURNAL OF HEAT TRANSFER. Manuscript received by the Heat Transfer Division October 20, 1975. Paper No. 76-HT-JJ.

Analysis

A turbulent boundary layer on an adiabatic wall and heated or cooled by the discharge of a secondary fluid through a slot in the wall at right angles to the flow is examined. The increase in shear layer thickness and the formation of a thermal boundary layer, which occur in the immediate vicinity of the slot as a result of the injection process, are presumed to occur at the slot. From this point onward, the shear layer is considered to develop as an undisturbed turbulent boundary layer on a flat plate, but with a different effective origin to account for the thickening, and possibly a different velocity profile shape than that without injection. Accordingly, as shown in Fig. 1, the origin of the coordinate system for the analysis is positioned a distance x_0 upstream of the slot, where x_0 is the length required for a zero pressure-gradient turbulent boundary layer to grow to the same thickness, δ_0, as the shear layer which exists immediately downstream of the slot with injection. Consequently, the origin of the coordinate system is a function of all the factors which determine δ_0, such as the upstream boundary layer, slot geometry and mass flow, etc. Similarly, the thermal boundary layer thickness at $x = x_0$, i.e., δ_{t0}, is also dependent on the same factors and must be determined from either a suitable analysis of the slot vicinity or an experimental correlation.

The equations of continuity, momentum, and energy for a turbulent boundary layer with zero-pressure gradient may be expressed as

$$\frac{\partial(\rho u)}{\partial x} + \frac{\partial(\rho v)}{\partial y} = 0$$

$$\rho u \frac{\partial u}{\partial x} + \rho v \frac{\partial u}{\partial y} = \frac{\partial}{\partial y}\left[\rho(\nu + \epsilon_M)\frac{\partial u}{\partial y}\right]$$

$$\rho c_p u \frac{\partial \theta}{\partial x} + \rho c_p v \frac{\partial \theta}{\partial y} = \frac{\partial}{\partial y}\left[\rho c_p(\alpha + \epsilon_H)\frac{\partial \theta}{\partial y}\right]$$

where $\theta = T - T_\infty$ is the temperature difference referenced to the free-stream temperature, T_∞.

The boundary conditions are for $y = 0$: $u = v = 0$, $(\partial\theta/\partial y) = 0$ (adiabatic wall) and for $y = \infty$: $u = u_\infty$, $\theta = 0$.

If the mass-averaged, slot air temperature difference, $\theta_s = T_s - T_\infty$, is small compared to the free-stream temperature, the physical properties of the slot and free-stream air may be treated as identical and constant and the integrated energy equation for the boundary layer downstream of the slot becomes

$$\int_0^\infty \rho u \theta dy = (\rho u)_s \theta_s s, \; x \geq x_0 \tag{1}$$

where $(\rho u)_s$ is the average slot mass flux and s the slot width.

As first shown by Weighardt and subsequently by many other investigators, the temperature profiles are affinitive downstream of injection. Thus, $\theta = \theta_w(x) G[y/\delta_t]$ where θ_w is the adiabatic wall temperature and δ_t a thermal boundary layer thickness defined by

$$\delta_t(x) = \int_0^\infty \frac{\theta}{\theta_w} dy \tag{2}$$

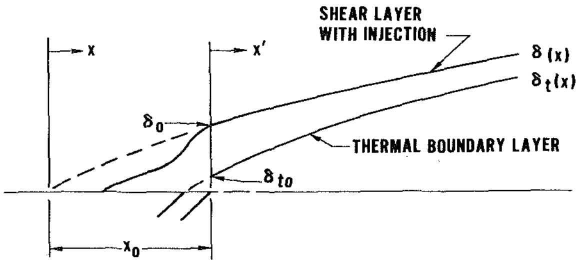

Fig. 1 Streamwise coordinate system

The mass-velocity profiles are assumed to have a simple power-law form, i.e., $\rho u = (\rho u)_\infty [y/\delta(x)]^n$ where n varies slightly with the momentum thickness Reynolds number and is about 1/7 for moderate Reynolds numbers. Then from the continuity equation with $(\rho u)_\infty$constant,

$$\rho v = \frac{n}{1+n}(\rho u)_\infty \left(\frac{y}{\delta}\right)^{1+n} \delta'$$

where a prime denotes differentiation with respect to the argument. Substituting the given expressions for θ, ρu, and ρv into the energy equation,

$$(\rho u)_\infty \delta_t \left(\frac{y}{\delta}\right)^n G \left\{\frac{\theta_w'}{\theta_w} + \left(\frac{y}{\delta_t}\right)\frac{G'}{G}\left[\frac{n}{1+n}\frac{\delta'}{\delta} - \frac{\delta_t'}{\delta_t}\right]\right\} = \frac{d}{dy}[\rho(\alpha + \epsilon_H)G']$$

Differentiating equation (1) with respect to x,

$$\frac{d}{dx}\int_0^\infty \rho u \theta dy = 0$$

which upon substituting for ρu and θ becomes

$$\frac{n}{1+n}\frac{\delta'}{\delta} - \frac{\delta_t'}{\delta_t} - \frac{1}{1+n}\frac{\theta_w'}{\theta_w} = 0 \tag{3}$$

Here, a small error was introduced by evaluating the integral using $\rho u = (\rho u)_\infty (y/\delta)^n$, $0 \leq y \leq \infty$ rather than $\rho u = (\rho u)_\infty (y/\delta)^n$, $0 \leq y \leq \delta$ and $\rho u = (\rho u)_\infty$, $y \geq \delta$. However, an evaluation of this error after determining the function $G[y/\delta_t]$ (see the following) showed it to be less than one percent for δ/δ_t's greater than one.

Nomenclature

c_p = specific heat at constant pressure
M = injection-to-free-stream mass flux ratio
n = exponent in velocity profile power-law
Pr = molecular Prandtl number
Pr_T = average turbulent Prandtl number
s = slot width normal to the slot mass flow direction
T = absolute temperature
u, v = velocity components in x- and y-direction, respectively
x, y = spatial coordinates parallel and normal to the wall, respectively
x' = spatial coordinate measured from slot
α = thermal diffusivity
Δ = ratio of velocity-to-thermal boundary layer thickness
δ = velocity boundary layer thickness
δ_t = thermal boundary layer thickness, see equation (2)
ϵ_H = thermal eddy diffusivity
ϵ_M = momentum eddy diffusivity
η = adiabatic wall effectiveness
θ = temperature referenced to free-stream temperature
μ = absolute viscosity
ν = kinematic viscosity
ρ = density

Subscripts

0 = evaluated at slot location
∞ = free-stream state
s = slot state
w = evaluated at wall

Substituting equation (3) into the energy equation,

$$\frac{1}{1+n}(\rho u)_\infty \delta_t \left(\frac{\delta_t}{\delta}\right)^n \frac{\theta_w'}{\theta_w}\left[\left(\frac{y}{\delta_t}\right)^{1+n} G\right]' = \frac{d}{dy}\left[\rho(\alpha + \epsilon_H)G'\right]$$

At this point Wieghardt assumed $\epsilon_H \gg \alpha$ and $\epsilon_H = \epsilon_H(x)$. Interestingly, *the latter is not such a bad assumption since near the wall* and at the edge of a boundary layer where ϵ_H typically changes most rapidly, *the derivative of the temperature in the y-direction*, i.e., G', is nearly zero by virtue of the adiabatic wall and constant free-stream temperature boundary conditions. This situation, providing the thermal layer is not imbedded too deeply within the boundary layer, is quite different from that for flow over a heated wall where the turbulent transport of heat by the flow near the wall, i.e., within the sublayer, is crucial. Using $\epsilon_H \gg \alpha$ and $\rho\epsilon_H = \rho_\infty\bar{\epsilon}_H(x)$,

$$\frac{G''}{[(y/\delta_t)^{1+n}G]'} = -K_1 = \frac{1}{1+n}\frac{u_\infty \delta_t^2}{\bar{\epsilon}_H}\left(\frac{\delta_t}{\delta}\right)^n \frac{\theta_w'}{\theta_w} \qquad (4)$$

where K_1 is a constant to be determined.

The first equality in (4) is an ordinary differential equation for $G[y/\delta_t]$, *the solution of which, with the appropriate boundary conditions*, was presented by Wieghardt, viz.,

$$G\left[\frac{y}{\delta_t}\right] = \frac{\theta}{\theta_w} = \exp\left\{-\left[\Gamma\left(\frac{3+n}{2+n}\right)\left(\frac{y}{\delta_t}\right)\right]^{2+n}\right\} \qquad (5)$$

where $\Gamma(z)$ denotes the Gamma function. Here, equation (2) was used to determine $K_1(n) = (2+n)[\Gamma((3+n)/(2+n))]^{2+n}$. Values of K_1 and $K_1/(2+n)$ are given in Table 1. Equation (5), generally with $n = 1/6$, has been compared to measured temperature distributions at various distances from the slot by numerous investigators with good results. Wieghardt's original comparisons are shown in Fig. 2.

The second equality in equation (4) is an equation relating $\theta_w(x)$ and $\delta_t(x)$ providing $\delta(x)$ and $\bar{\epsilon}_H(x)$ are known. Although Wieghardt recognized this, it was here that he returned to the energy balance, equation (1), and deduced $\theta_w \propto \delta^{-1}$ far downstream of the slot. However, since equation (3) is another independent equation relating θ_w and δ_t, two ordinary differential equations for these quantities can be formed and their solutions sought. Normally this would be approached with some hesitancy because of the assumptions already made, but after the success Reynolds [9] had in solving the more difficult problem of heat transfer to a turbulent boundary layer with a step change in wall temperature by an approximate method, where somewhat questionable assumptions were made regarding ϵ_H at the wall, it becomes interesting to pursue.

In order to appreciate the thermal boundary layer development within the shear layer and its role in determining the adiabatic wall effectiveness, it is best to proceed by deriving an expression for the ratio of these thicknesses, $\Delta = \delta/\delta_t$. Hence, by eliminating θ_w between equations (3) and (4) and using the definition for Δ,

$$\frac{\Delta'}{\Delta} - \frac{1}{1+n}\frac{\delta'}{\delta} + K_1\frac{\bar{\epsilon}_H}{u_\infty \delta^2}\Delta^{2+n} = 0 \qquad (6)$$

The thermal eddy diffusivity $\bar{\epsilon}_H$ may be evaluated by introducing a turbulent Prandtl number, Pr_T, such that $\bar{\epsilon}_H(x) = \bar{\epsilon}_M(x)/\mathrm{Pr}_T$, where Pr_T is assumed constant and $\bar{\epsilon}_M$ is the average eddy diffusivity through the boundary layer, i.e., $\bar{\epsilon}_M = 1/\delta \int_0^\delta \epsilon_M(x, y)dy$. The eddy diffusivity, $\epsilon_M(x, y)$, can be determined by integrating the momentum equation with respect to y from $y = 0$ to y after assuming $\epsilon_M \gg \nu$ and using the power-law form for the velocity profiles, and then combining this result with that found by continuing the integration to $y = \delta$ in order to eliminate the wall shear stress. The result of this series of calculations is

$$\bar{\epsilon}_H = \frac{1}{\mathrm{Pr}_T}\frac{1}{(1+n)}\frac{1}{(2-n)(3+n)}u_\infty \delta\delta'$$

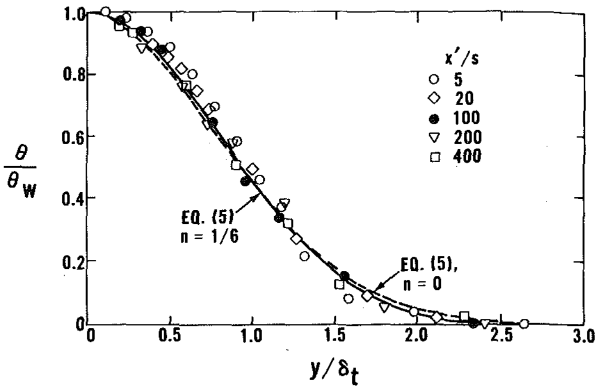

Fig. 2 Wieghardt's dimensionless temperature profiles for M = 0.74 and s = 10 mm

Substituting this expression into equation (6) and assuming the *shear layer downstream of the slot develops as an ordinary turbulent boundary layer on a flat plate*, $\delta \propto x^{4/5}$, an ordinary differen*tial equation for* $\Delta(x)$ *is found*, viz.,

$$\frac{\Delta'}{\Delta} + \frac{1}{1+n}\left[\frac{1}{\mathrm{Pr}_T}\frac{1}{K_2}\Delta^{2+n} - 1\right]\frac{4}{5}\frac{1}{x} = 0$$

where values of $K_2 = (2-n)(3+n)/K_1$ are given in Table 1. The solution to this differential equation with $\Delta = \delta_0/\delta_{t_0} \equiv \Delta_0$, at $x = x_0$ is

$$\Delta = \left\{\frac{\mathrm{Pr}_T K_2}{1 - [1 - \mathrm{Pr}_T K_2 \Delta_0^{-(2+n)}](x_0/x)^{4(2+n)/5(1+n)}}\right\}^{1/(2+n)}$$

And as might be expected intuitively, Δ approaches a constant, viz., $(\mathrm{Pr}_T K_2)^{1/(2+n)}$ for large values of x/x_0. Equating this expression to experimental data (see Fig. 3 and the following discussion) at large streamwise distances gives $\mathrm{Pr}_T = 0.65$ (for $n = 1/7$) which, *although somewhat lower than the generally accepted value of 0.8*, really implies the proportionality constant in $\bar{\epsilon}_H \propto u_\infty \delta\delta'$ should be about 0.23 rather than 0.187 if $\mathrm{Pr}_T = 0.8$. For $n = 1/7$ and $\mathrm{Pr}_T = 0.65$,

$$\Delta = \frac{1.475}{[1 - (1 - 2.3\Delta_0^{-15/7})(x_0/x)^{3/2}]^{7/15}} \qquad (7)$$

The adiabatic effectiveness is defined as $\eta = \theta_w/\theta_s$ and may be *found from equation (1) to be given by*

$$\eta = \frac{1}{K_3}Ms\frac{\delta^n}{\delta_t^{1+n}} = \frac{1}{K_3}\frac{\Delta^{1+n}}{(\delta/Ms)}$$

where M is the mass flux ratio $(\rho u)_s/(\rho u)_\infty$ and

$$K_3(n) = \int_0^\infty z^n \exp\left(-\frac{K_1}{(2+n)}z^{2+n}\right)dz$$

$$= \frac{1}{1+n}\Gamma\left(\frac{3+2n}{2+n}\right)\Big/\left[\Gamma\left(\frac{3+n}{2+n}\right)\right]^{(1+n)}$$

The values of $K_3(n)$, all nearly unity, are given in Table 1. Far downstream of the slot, Δ is constant and $\eta \propto \delta^{-1}$, as inferred by Wieghardt. The adiabatic effectiveness at intermediate distances may be found by substituting $\Delta(x)$ in the given equation and as-

Table 1

n	1/4	1/5	1/6	1/7	1/8	0
K_1	1.71	1.68	1.67	1.65	1.64	1.57
K_2	3.32	3.42	3.48	3.54	3.57	3.82
K_3	0.828	0.857	0.877	0.892	0.906	1.00
$K_1/(2+n)$	0.760	0.765	0.768	0.771	0.772	0.785

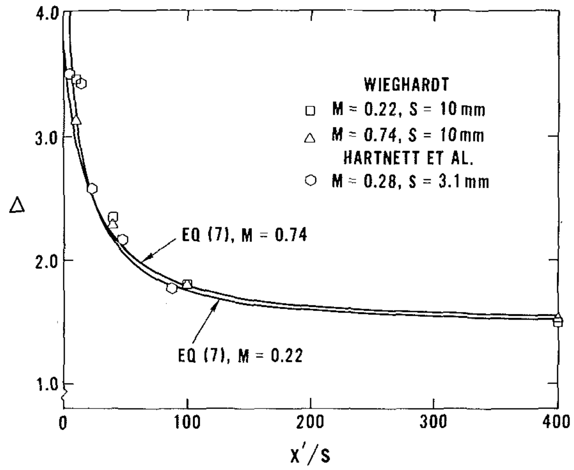

Fig. 3 Streamwise variation of velocity-to-thermal boundary layer thickness ratio

suming the turbulent boundary layer downstream of the slot grows according to

$$\delta = 0.058 \left[\frac{(1+n)(1+2n)}{n}\right]^{4/5} \left[\frac{(\rho u)_\infty x}{\mu}\right]^{-1/5} x$$

which is the solution to the momentum equation where the shear stress is given by the Blasius resistance formula (see [9]). Accordingly,

$$\eta = \frac{17.25}{K_3} \left[\frac{n}{(1+n)(1+2n)}\right]^{4/5} \left[\frac{(\rho u)_s s}{\mu}\right]^{1/5} \left(\frac{x}{Ms}\right)^{-4/5}$$
$$\times \left\{\frac{\mathrm{Pr}_T K_2}{1 - [1 - \mathrm{Pr}_T K_2 \Delta_0{}^{-(2+n)}](x_0/x)^{4(2+n)/5(1+n)}}\right\}^{(1+n)/(2+n)}$$

where the initial conditions, Δ_0 and x_0 must be provided by either an analysis for the flow in the slot vicinity or experiment. For $n = 1/7$ and $\mathrm{Pr}_T = 0.65$ this becomes

$$\eta = 4.67 \left[\frac{(\rho u)_s s}{\mu}\right]^{1/5} \left(\frac{x}{Ms}\right)^{-4/5}$$
$$\times [1 - (1 - 2.3\Delta_0{}^{-15/7})(x_0/x)^{3/2}]^{-8/15} \quad (8)$$

Near the slot, the adiabatic effectiveness is approximately given by

$$\eta \doteq \frac{17.25}{K_3} \left[\frac{n}{(1+n)(1+2n)}\right]^{4/5} \Delta_0{}^{(1+n)}$$
$$\times \left[\frac{(\rho u)_s s}{\mu}\right]^{1/5} \left(\frac{x_0}{Ms}\right)^{-4/5} \left[1 - \frac{4}{5} \frac{\Delta_0{}^{(2+n)}}{\mathrm{Pr}_T K_2} \frac{x'}{x_0}\right]$$

If for the moment $x' = 0$ is considered to be the last position where $\eta = 1$, then after some manipulation find $\delta_{t_0} \approx 1.4\, Ms$ which is only slightly larger than the effective displacement thickness of the injected air.

Far downstream, i.e., $x/x_0 \gg 1$, the adiabatic effectiveness is given by

$$\eta \doteq \frac{17.25}{K_3} \left[\frac{n}{(1+n)(1+2n)}\right]^{4/5} (\mathrm{Pr}_T K_2)^{(1+n)/(2+n)}$$
$$\times \left[\frac{(\rho u)_s s}{\mu}\right]^{1/5} \left(\frac{x'}{Ms}\right)^{-4/5}$$

which for $n = 1/7$ and $\mathrm{Pr}_T = 0.65$, interestingly, is virtually identical to the result found by Tribus and Klein [7] using Rubesin's integration kernel and $\mathrm{Pr} = 0.72$, viz.,

$$\eta = 4.62 \left[\frac{(\rho u)_s s}{\mu}\right]^{1/5} \left(\frac{x'}{Ms}\right)^{-4/5}$$

(note that the coefficient is close to that in equation (8)). But the streamwise decay of η, had they included an initial length, x_0, in their analysis, would have been much less than that described by equation (8).

Comparison of Analysis With Experiments

Most experimental work to date has been concerned with adiabatic (or impervious) wall effectiveness measurements for a variety of slot configurations, whereas only a few have included detailed temperature or species and velocity measurements both near and downstream of the slot. One of these experimental studies is, notably, that of Wieghardt. His work included, for a number of mass flux ratios, sufficient temperature and velocity profile information from which initial thermal velocity boundary layer thicknesses may be determined. Consequently, Wieghardt's results will be used for most of the comparisons to follow.

Wieghardt's adiabatic wall effectiveness results can be found in [1] plotted as η versus x', η versus x'/s, and η versus x'/Ms in Figs. 7, 8, and 10, respectively. The data points used in the following comparison for each mass flux ratio were extracted and replotted from these figures, leaving out any indistinguishable point. Here, it should be noted that there is a discrepancy in Wieghardt's presentation of his $M = 0.22$ and 0.36 data. Specifically, although Wieghardt's Figs. 8 and 10 *are consistent with each other, they are not* in agreement with his Fig. 7 (the data as reported in the latter figure being considerably lower). However, since a heat balance can be made for the $M = 0.22$ test case using the results as Weighardt presented them in Figs. 8 and 10, the results as reported in these figures are considered correct and used here for the comparisons, while those in Fig. 7 are disregarded. Incidently, Wieghardt's conclusions are also based on Figs. 8 and 10.

Velocity and temperature profile measurements for $M = 0.22$, 0.74, and 1.01 test conditions with $s = 10$ mm are also available in [1]. Therefore, the initial values of Δ_0 and x_0 could be determined reasonably well for these mass flux ratios as follows:

1 The velocity boundary layer thickness was found by plotting $\rho u/(\rho u)_\infty$ *profiles for a given mass flux ratio, M, on log-log paper,* fitting a straight line to the data in the wake region and taking the y-value at $\rho u/(\rho u)_\infty = 1$ as δ.

2 The values of δ_0 and x_0 were determined by plotting $\delta^{5/4}$ against the distance from the slot, $x' = x - x_0$, fitting the line $\delta^{5/4} = (0.376)^{5/4} [(\nu/u_\infty)^{1/4} x]$ to the data and extrapolating back to the $x' = 0$ and $\delta = 0$ intercepts, respectively (Wieghardt's boundary layer development downstream of the slot agreed reasonably well with that determined for a 1/7-profile, hence $n = 1/7$ is used for all of the calculations).

3 Values of δ_{t0} were found by extrapolating a curve passing through $\delta_t(x')$ data points to the slot location.

In order to compare the analysis with adiabatic effectiveness measurements reported by Wieghardt for his other mass flux ratios, the initial values had to be determined through interpolation. Here, values of δ_0 and δ_{t0} for the $M = 0.22$ and 0.74 test conditions were plotted against Ms and those for other mass flux ratios found by linear interpolation. Results from this series of calculations and the corresponding values of Δ_0 and x_0 are presented in Table 2 where the values obtained by interpolation are marked.

In Fig. 3, the streamwise variation in Δ as calculated from equation (7) is compared to experimental results. The results of Hartnett, et al. [10] are also included since the slot geometry, mass flux ratio and initial conditions are similar to Wieghardt's (see Table 2). The curves, however, were calculated specifically for Wieghardt's $M = 0.22$ and 0.74 test conditions. Accordingly, the agreement is quite good.

From Fig. 3 it is apparent that there are at least two distinct regions of thermal boundary layer growth. One, which starts near the slot and extends to $x'/s \approx 100$, is distinguished by a rather rapid increase in the thermal layer thickness within the velocity boundary layer, while the other, $x'/s > 100$, is characterized by a growth nearly proportional to that of the velocity boundary layer. The latter corresponds to the generally accepted "far downstream" region. Eckert and Birkebak [11] noted three distinct regions "in which

Table 2

M	0.22	0.28	0.36	0.45	0.74	1.01	0.28[b]
s (mm)	10	10.7	10(10.7?)	10.7	10	10	3.1
u_∞ (m/s)	32	33	31.5	33	16.2	16.2	50
$\frac{\rho_s u_s s}{\mu}$	4700	6600	7700	10600	7900	10800	2880
δ_0/s	1.9	1.9*[a]	2.1*	2.2*	2.7	2.7	2.2
δ_{t0}/s	0.30	0.33*	0.40*	0.46*	0.7	0.75	0.49
Δ_0	6.3	5.8*	5.3*	4.7*	3.9	3.6	4.5
x_0/s	90	92*	97*	100*	120	120	93

[a] Values obtained by interpolation (see text).
[b] Results from Hartnett, et al. [10].

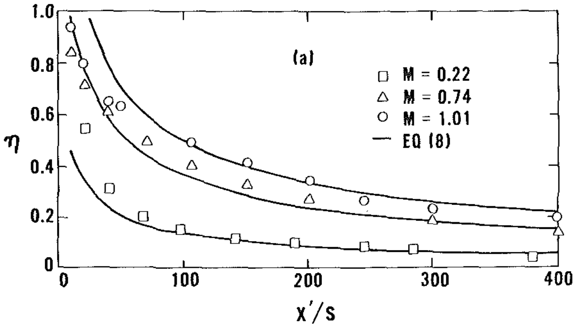

Fig. 4(a)

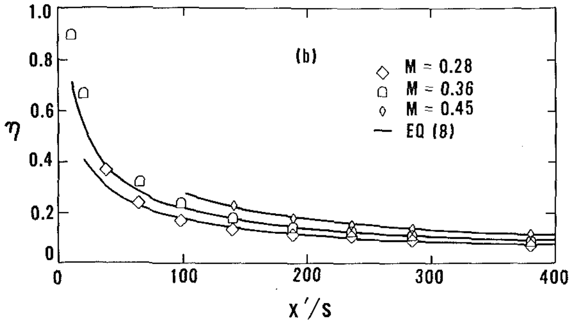

Fig. 4(b)

Fig. 4 Comparison of analysis with Wieghardt's adiabatic wall effectiveness results

the effectiveness . . . follows different laws," viz., $x'/s < 6$, $6 < x'/s < 60$ and $x'/s > 60$. It is noteworthy that the last two correspond more or less with the regions mentioned in the foregoing. However, while the suggestion was made that the different behavior results from adjustments in the velocity profile, it appears that, at least in the region around $x'/s = 60$, the thermal boundary layer growth within the shear layer is more important.

Wieghardt's adiabatic wall effectiveness results for six mass flux ratios and the corresponding curves calculated from equation (8) of the analysis are shown in Figs. 4(*a*) and 4(*b*). The agreement is seen to be quite good away from the slot, as should be expected, and reasonable near the slot. The discrepancies near the slot, as mentioned before, may be attributed to the fact that, in general, the actual velocity profiles are not similar until between 10 and 40 slot widths (see [1]) downstream of the slot. In particular, the $1/7$ profile used in the present calculations is fuller than the actual velocity profiles for the low mass flux ratios and less full for the higher mass flux ratios. As a consequence, the energy within the boundary layer for the appropriate slot excess energy is initially overestimated for the low and underestimated for the high mass flux ratios. Evidence of the latter may be seen in Fig. 4(*a*) where the calculated adiabatic wall effectivenesses for $M = 0.74$ and 1.01 become greater than one at the slot.

Conclusions

The adiabatic wall effectiveness of a turbulent boundary layer heated or cooled by a secondary fluid discharged through a slot depends to a large extent on the subsequent growth of the thermal boundary layer within the shear layer, and contrary to the situation of heat transfer to a turbulent boundary layer from a wall, it appears that its growth may be determined quite accurately by assuming the thermal eddy diffusivity is a function of the streamwise distance alone. Near the slot, however, where the velocity profiles are most distorted as a result of the injection process, a variation in the shape of the profiles must be considered in order to properly account for the distribution in streamwise flux of thermal energy.

Finally, it should be mentioned that the main problem in determining the adiabatic wall effectiveness lies in evaluating the effect of injection on the flow in the immediate vicinity of the slot. Of all the works in the field, only a few address the problem and even then, not in sufficient detail. As a result, the shear layer thickness, thermal boundary layer thickness, and profile shapes immediately downstream of injection cannot as yet be satisfactorily related to the slot geometry, free stream-to-slot mass and momentum flux ratio, and shear layer thickness before the slot.

References

1 Wieghardt, K., "Hot-Air Discharge for De-Icing," AAF Translation No. F-TS919-RE, Air Material Command, Aug. 1946.

2 Kutateladze, S. S. and Leont'ev, A. I., "Film Cooling with Turbulent Gaseous Boundary Layer," *Thermal Physics High Temperature*, Vol. 1, 1963, pp. 281–290.

3 Goldstein, R. J., and Haji-Sheikh, A., "Prediction of Film Cooling Effectiveness," *Japan Soc. Mech. Engr. 1967 Semi-Intern. Symp.*, 1967, pp. 213–218.

4 Kacker, S. C., Pai, B. R., and Whitelaw, J. H., "The Prediction of Wall Jet Flows With Particular Reference to Film Cooling," *Progress in Heat and Mass Transfer*, Vol. 2, Macmillan (Pergamon), New York, 1969, pp. 163–186.

5 Goldstein, R. J., "Film Cooling," *Adv. Heat Transfer*, Vol. 7, Academic Press, New York, 1971, pp. 321–379.

6 Frost, R., "Turbulence and Diffusion in the Lower Atmosphere," *Proceedings of the Royal Society*, London, Series A, Vol. 186, 1946, p. 20.

7 Tribus, M., and Klein, J., "Force Convection From Nonisothermal Surfaces," *Heat Transfer Symposium, University of Michigan, 1952*, 1953, pp. 211–235.

8 Haji-Skeikh, A., "Flow Parameters on a Film-Cooled Surface," *Heat Transfer 1970*, Elsevier Vol. 2, 1970.

9 Reynolds, W. C., "Heat Transfer in the Turbulent Incompressible Boundary Layer With Constant and Variable Wall Temperature," PhD thesis, Stanford University, 1957 (also Reynolds, W. C., Kays, W. M., and Kline, S. J., NASA memo 12-2-58W, 1958).

10 Hartnett, J. P., Birkebak, R. C., and Eckert, E. R. G., "Velocity Distributions, Temperature Distributions, Effectiveness and Heat Transfer for Air Injected Through a Tangential Slot Into a Turbulent Boundary Layer," JOURNAL OF HEAT TRANSFER, TRANS. ASME, Series C, Vol. 83, 1961, pp. 293–306.

11 Eckert, E. R. G., and Birkebak, R. C., "Effects of Slot Geometry on Film Cooling," in *Heat Transfer Thermodynamics and Education, Boelter Anniversary Volume*, H. A. Johnson, ed., McGraw-Hill, New York, 1964.

R. S. Colladay
Head, Turbomachinery Fundamentals Section,
NASA-Lewis Research Center,
Cleveland, Ohio. Mem., ASME

L. M. Russell
Aerospace Engineer,
NASA-Lewis Research Center,
Cleveland, Ohio

Streakline Flow Visualization of Discrete Hole Film Cooling for Gas Turbine Applications

Film injection from discrete holes in a three row staggered array with 5-dia spacing was studied for three hole angles: (1) normal, (2) slanted 30 deg to the surface in the direction of the mainstream, and (3) slanted 30 deg to the surface and 45 deg laterally to the mainstream. The ratio of the boundary layer thickness-to-hole diameter and the Reynolds number were typical of gas turbine film cooling applications. Results from two different injection locations are presented to show the effect of boundary layer thickness on film penetration and mixing. Detailed streaklines showing the turbulent motion of the injected air were obtained by photographing very small neutrally-buoyant helium filled "soap" bubbles which follow the flow field. Unlike smoke, which diffuses rapidly in the high turbulent mixing region associated with discrete hole blowing, the bubble streaklines passing downstream injection locations are clearly identifiable and can be traced back to their point of ejection.

Introduction

Increases in turbine inlet temperature and pressure have reached the point where heat flux levels are too high to adequately cool hot section gas turbine components by convection alone. Some film cooling is generally required to protect the metal parts from the hot gas stream. The most practical method currently used for film cooling aircraft turbines is to inject the cooling air from discrete holes in the surface of the blades. It is important that the film be injected in the most efficient manner possible in order to provide the desired heat transfer protection with a minimum disruption of the mainstream. Poorly designed film injection schemes can lead to mainstream momentum losses which severely reduce turbine aerodynamic efficiency and, in some instances, even increase heat transfer to the surface.

There has been considerable emphasis recently in experimental heat transfer studies related to discrete hole film cooling. Erikson [1][1] and his predecessors at the University of Minnesota investigated adiabatic wall film effectiveness and augmented heat transfer coefficients due to blowing for one hole and a single row of holes at various injection angles and center-to-center spacings. Reference [1], the last in a series of reports on this study, includes a complete bibliography of earlier reports in the series. Liess [2] has made a similar study for a single row of injection holes with a freestream static pressure distribution typical of turbine blade applications. Crawford, Choe, Kays, and Moffat, at Stanford University, have investigated the heat transfer characteristics of full coverage film cooling from multiple rows of discrete holes arranged in a staggered array. Hole spacings of 5 and 10 dia were studied. Normal injection results from this study are presented in references [3, 4] and reference [5] is a summary data report containing all of the test results for both normal and 30 deg injection. Metzger, Takeuchi, and Kuenstler [6] examined surface averaged heat transfer rates associated with a full coverage pattern of discrete holes oriented normal to the surface. Mayle and Camarata [7] investigated the adiabatic wall film effectiveness associated with full coverage film cooling from compound angle injection at various hole spacings. Analytical and experimental work in this same area has been the subject of several reports from Imperial College, [8, 9].

While all of these investigations have contributed to the quantitative data needed to develop reliable analytical models of film cooling, they have also suggested the need for a better understanding of the fluid dynamics encountered when film air is injected through

---

[1] Numbers in brackets designate References at end of paper.

Contributed by the Heat Transfer Division and presented at the Winter Annual Meeting, Houston, Texas, November, 1975, of THE AMERICAN SOCIETY OF MECHANICAL ENGINEERS. Revised manuscript received by the Heat Transfer Division March 3, 1976. Paper No. 75-WA/HT-12.

discrete holes into a turbulent boundary layer. One particularly effective method of acquiring this understanding is through the use of flow visualization studies. Such studies are helpful in gaining an insight into the complex interaction of the injected film and the mainstream. Erikson [1] used CO_2 fog to visualize the flow field surrounding a single injection hole. However, the fog diffused so rapidly due to the high turbulent mixing in the injection region that only the large scale turbulent motion near the hole was visible.

In the present study, air seeded with small neutrally buoyant helium-filled bubbles, was injected into a turbulent boundary layer through discrete holes in the test surface of an ambient air-wind tunnel. The paths traced by the bubbles map streakline patterns of the injected film air mixing with the mainstream. Unlike fog or smoke which diffuses rapidly, the bubble streaklines are clearly identifiable as continuous thread-like streaks which can be traced through the film injection region.

Streakline patterns of the flow field associated with film injection from discrete holes in a three row staggered array with 5-dia spacing are presented for three hole angles typically encountered in turbine cooling applications. The holes were angled (1) normal to the surface, (2) slanted 30 deg to the surface in the direction of the mainstream, and (3) slanted 30 deg to the surface and 45 deg laterally to the mainstream. The momentum thickness Reynolds number just upstream of the injection holes was 2165 and the ratio of the boundary layer thickness-to-hole diameter was 1.75. A boundary layer thickness-to-hole diameter ratio of 2.4 at the same Reynolds number was also run by moving the injection location further downstream from the inlet nozzle.

Experimental Apparatus and Procedure

Bubble Generator. The system for generating neutrally-buoyant bubbles, described in detail in the manufacturer's report [10], consists of a head which is the device that actually forms the bubbles and a console containing micrometering valves which control the flow of helium, bubble solution, and air to the head. A drawing illustrating the basic features of the head is shown in Fig. 1. Neutrally buoyant helium-filled bubbles about 1 mm in diameter, form on the tip of the concentric tubes and are blown off the tip by a continuous blast of air flowing through the shroud passage. The bubble solution flows through the annular passage and is formed into a bubble inflated with the helium passing through the inner concentric tube. The desired bubble size and neutral buoyancy are achieved by proper adjustment of the air, the bubble solution, and the helium flow rates. As many as 300 bubbles per s can be formed in this device.

Rig. The flow visualization test rig, shown in schematic form in Fig. 2, consists of a transparent plastic tunnel through which ambient room air is drawn into a vacuum exhaust line. Its construction provides flexibility for testing a large number of film injection hole geometries and boundary layer configurations appropriate to turbine and combustor cooling applications. The test configuration for this study consisted of a zero pressure gradient mainstream flow over a flat surface containing discrete film injection holes. At the point of injection, the mainstream boundary layer was fully turbulent. A further description of the details of the rig is given in reference [11]. There are three separate air flow sources: (1) the primary mainstream air; (2) the bubble generator air; and (3) the secondary film injection air.

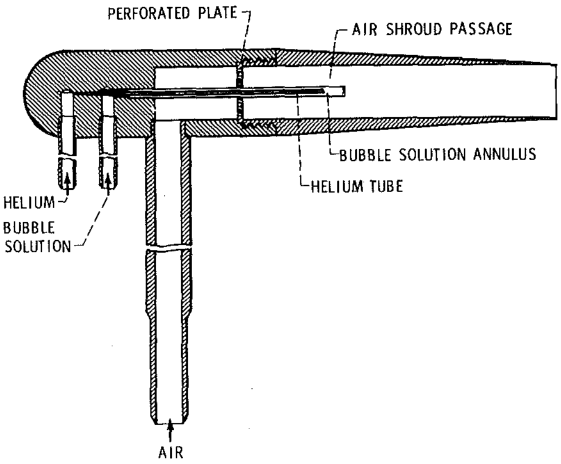

Fig. 1 Bubble generator head

The tunnel, 0.381 by 0.152 m in cross section, is sectioned into four parts: a test section 0.61-m long and three spacing sections each 0.91-m long. The sections can be put in any order to allow for a boundary layer development length upstream of the first film injection location anywhere from several centimeters to over 2.7 m. Having the option of injecting the film air at different axial locations downstream of the inlet provides flexibility in adjusting the boundary layer thickness-to-hole diameter δ/D, and the momentum thickness Reynolds number Re_θ at the point of injection when the hole diameter can not be changed significantly. The minimum hole diameter is limited to about 1.3 cms to avoid excessive bubble breakage in the holes.

The helium filled bubbles are injected into a plenum which serves as a collection chamber for the bubbles and the film air. The air, seeded with the bubbles, then passes through the film injection holes in the floor of the test section. The small quantity of air used by the bubble generator to blow the bubbles off the tip of the annulus as they form, ends up as part of the film air in the plenum. However, this bubble air flow cannot be varied since it is adjusted and then fixed to give optimum bubble formation. Consequently, to provide variable film injection air flow rates, additional secondary air is also supplied to the plenum. The plenum box is clamped onto the bottom of the test section for easy removal when another test plate with a different hole configuration is to be tested. Rotameters were used to measure the helium and bubble generator air flow rates and a hot wire flow meter was used in the secondary air leg for accurate measurement over a wide range of film air flow rates.

When the bubbles pass through the film injection holes, they are illuminated by a high intensity quartz arc lamp. The resulting reflection off the bubble surface appears as a streak across the photographic film if the exposure is relatively long. The light beam was directed axially down the tunnel as shown in the sketch in Fig. 2. With a well-focused and collimated light beam, the bubbles are illuminated as soon as they leave the holes without the beam striking any of the tunnel surfaces. This insures good contrast with a bright bubble streak against a black background.

Test Section. The 0.38 by 0.61-m floor of the test section which contains the film injection holes is easily removed to allow bottom plates with different hole configurations to be installed without affecting the rest of the test section or the plenum chamber. The floor and back side of the test section are made of wood and finished glossy

Nomenclature

d = film injection hole diameter
m = film-to-mainstream velocity ratio or blowing rate (u_f/u_∞ for constant density)
Re_θ = momentum thickness Reynolds number

u_f = film injection velocity
u_∞ = freestream velocity
u^+ = dimensionless velocity, $u/\sqrt{\tau_w/\rho}$
y = coordinate normal to the surface
y^+ = dimensionless distance, $y\sqrt{\tau_w/\rho}/\nu$

δ = boundary layer thickness
θ = boundary layer momentum thickness
ν = kinematic viscosity
ρ = density
τ_w = shear stress at the wall

black to give maximum contrast with the bubble streaklines. The top and front face are clear plastic.

Three different film injection arrays were studied. Sketches of the three configurations are given in Fig. 3. They are: (1) normal injection with the holes oriented 90 deg to the surface, (2) slanted in-line injection with the holes angled 30 deg to the surface and in-line with the mainstream, and (3) compound angle injection with the holes again 30 deg to the surface, but rotated 45 deg laterally to the mainstream. In all three cases, the holes were spaced 5 dia apart as measured from the hole center line. The holes formed a staggered array representing the center portion of three rows of holes. In Fig. 3(*b*) and 3(*c*), the hole axes for both the in-line and compound angle holes make an angle of 30 deg with the plane of the paper. Tubes which extend into the plenum were inserted into the holes in the plate and finished off flush with the test surface to provide a hole length-to-diameter ratio typical of aircraft turbine applications. The delivery tubes for this study had a 1.27-cm ID and were 6.35-cm long.

Results and Discussion

A fully turbulent boundary layer existed in the region of the film injection holes and the freestream turbulence intensity, measured by a hot wire probe, was 2 percent. The film-to-mainstream velocity ratio was varied by changing the mass flow rate of the secondary or film air while keeping the mainstream velocity constant at 15.5 m/s. The velocity profile through the boundary layer was surveyed with a total pressure probe just upstream of the injection holes. The dimensionless profile at the duct center line in Fig. 4 shows the typical logarithmic distribution in the wall region, characteristic of a turbulent boundary layer on a smooth wall. Surveys off the center line showed less than a 1 percent spanwise variation in the profile within the injection region. The boundary layer thickness defined by the 99 percent value of the freestream velocity, was 2.22 cms. The boundary layer thickness-to-injection hole diameter ratio was then 1.75 at the upstream injection location. The boundary layer momentum thickness θ and shape factor were 0.215 and 1.31 cm, respectively, so the momentum thickness Reynolds number was 2165 at the upstream hole location.

Photographs of the film streaklines were taken both from the top looking down on the test surface and from the side. The two viewing angles are illustrated in Fig. 5 which shows the test section with two cameras mounted in the positions used when taking photographs. The top view photographs show the spreading characteristics of the film as it leaves the holes and the side view photographs show the degree of penetration of the film into the mainstream relative to the boundary layer thickness and the surface. All of the side view photographs were taken with the two outer holes in the four hole array plugged to give a plane view of the two center holes. The film from the upstream hole passes directly over the downstream hole.

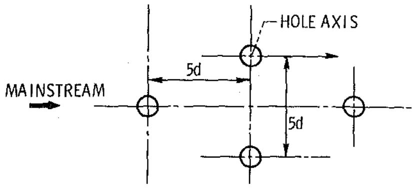

(a) NORMAL.

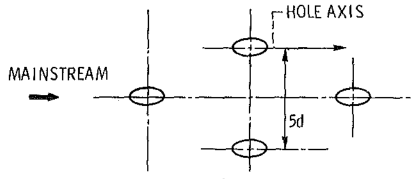

(b) SLANTED 30° IN-LINE.

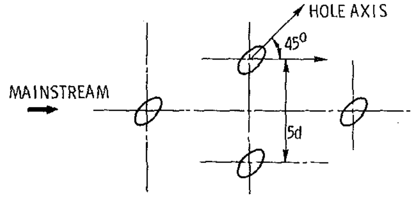

(c) COMPOUND ANGLE 30° BY 45°.

Fig. 3 Top view of the three injection arrays

Normal Injection. Streaklines traced by a film injected into a turbulent boundary layer from holes oriented normal to the surface are shown in Fig. 6. The streaklines in the figures are black on a white background because the photographs are negative images printed from color transparencies. Top and side view photographs are included for a low ($m = 0.3$) and a high ($m = 0.8$) blowing rate. Also included is a close-up view of the region surrounding the upstream hole. The top view clearly illustrates the counter-rotating vortices extending downstream of each injection hole. This vortex pattern has been well documented in earlier studies. The top view also shows that the film spreads about one-and-a-half hole diameters for a blowing rate of 0.3 and slightly more for the higher blowing rate.

From the side view, note that the film separates from the surface even at a low blowing rate of 0.3. The boundary layer thickness δ just upstream of the first injection hole is indicated on the side view photograph. At the high blowing rate, most of the film mixes with the freestream rather than providing a protective film adjacent to the surface.

Notice the sharp "kinks" in the streaklines in the close-up views, particularly at the highest blowing rate. The tortuous path traced by a bubble indicates a very high intensity, small scale turbulence

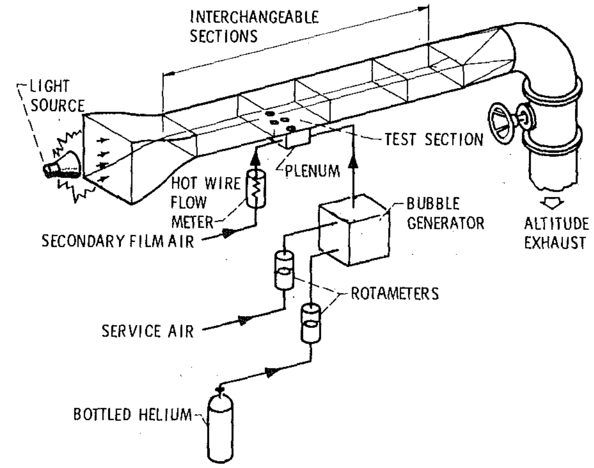

Fig. 2 Film cooling flow visualization rig

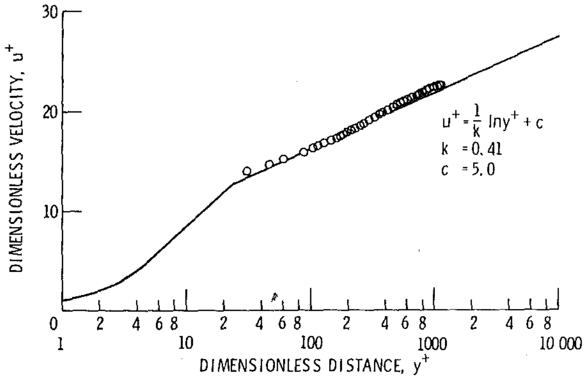

Fig. 4 Boundary layer profile at the upstream injection location

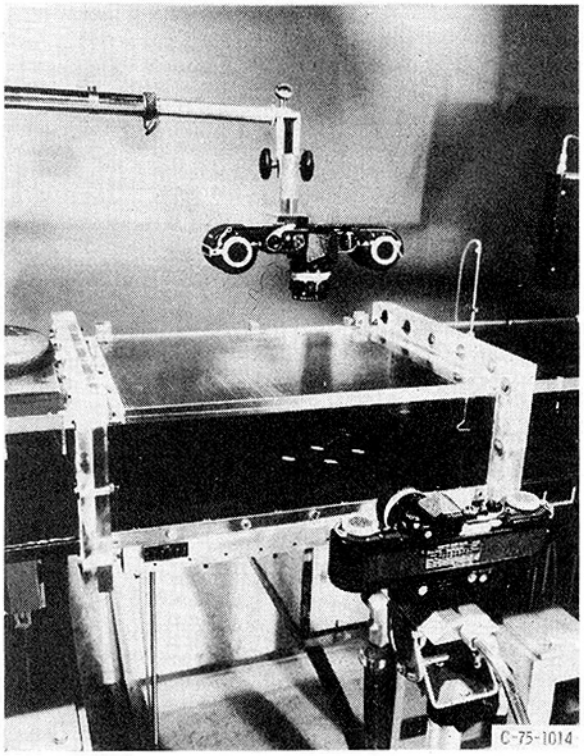

Fig. 5 Test section with top and side view camera positions

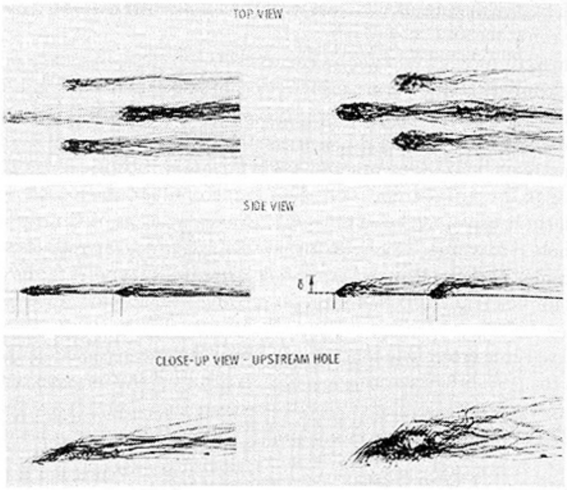

Fig. 6 Streakline pattern for film injection from holes normal to the surface

structure in the vortex region just downstream of an injection hole. This high turbulence is detrimental because it increases the heat transfer coefficient [4] and causes extensive mixing of the film air with the mainstream. Also, when normal injection is used for film cooling turbine blades, substantial aerodynamic losses in the mainstream occur [12], resulting in a decrease in turbine efficiency.

Note that as the bubbles get caught up in one of the vortices, their trajectory is in a direction nearly normal to the surface, suggesting a very high velocity transfer of mass between the wall region and the outer boundary layer. There is also evidence of recirculating flow since some of the streaklines slope back upstream.

One should be careful not to interpret the streakline coverage of the surface far downstream of the holes as representing effective film coverage. The streaks do not depict the diffusion that normally takes place when the cooler film air is injected into the mainstream. While the streaklines still look bright at the far downstream edge of the photographs, data for normal injection [1, 4] indicate that through turbulent mixing and diffusion, the film quickly loses much of its effectiveness.

Slanted In-Line Injection. The streakline pattern associated with film injection from holes angled 30 deg to the surface, in-line with the mainstream is given in Fig. 7. For this geometry, blowing rates have nominal values of 0.3, 0.8, and 1.4 were photographed. A top and side full field view, and a close-up side view of the region surrounding the downstream hole are included.

Notice that in general, the streaklines are much smoother than with normal injection, indicating a much larger scale and lower intensity turbulence for 30 deg injection. Only at the highest blowing rate do the streaklines exhibit the character indicative of high intensity, small scale turbulence. The counter-rotating vortex pattern is not nearly as evident as it was for the normal injection case. Evidence of entrainment of the freestream fluid down to the wall can be seen, however, as the streaklines coming from the center of the hole wrap around the outside and then under the jet. The pattern is more subtle than with normal holes because the scale at which the streaklines interwind is much larger—on the order of the hole diameter. The top view shows almost no spreading of the film as it extends downstream until it encounters another injection hole. Then, most of the upstream film tends to split to either side of the downstream jet.

At a blowing rate of 0.3 notice from the full field side view that the film remains very near the surface. The thickness of the film layer is much less than the thickness of the boundary layer entering the injection region. It has been observed in these and other tests [1, 5] that at a blowing rate of about 0.5 the film jet begins to separate from the surface allowing the mainstream air to wrap around beneath the jets. At a blowing rate of 0.8, the full field, side view photograph clearly shows that the film has separated from the surface. At the high blowing rate (m = 1.4), the film penetrates into the freestream and offers little protection to the surface. Also, as one would expect, the downstream film has a steeper trajectory across the boundary layer because of the momentum deficit in the incident boundary layer near the wall created by the upstream injection.

The close-up view shows the downstream jet passing right through the film from the upstream hole. Note also the high turbulence generated for the case of m = 1.4 compared to the lower blowing rates. It has been observed that when the velocity of the jet exceeds that of the mainstream, there is a change in the character of the turbulence near the injection holes. When $m < 1$, the streaks are smooth and gently undulating. When $m > 1$, very jagged streaks appear.

Compound Angle Injection. The distinctive features of the streakline pattern associated with film injection at a compound angle 30 deg to the surface and 45 deg lateral to the mainstream are illustrated in Figs. 8 and 9. For this injection configuration, the oblique angle that the film makes with the mainstream generates a single vortex filament downstream of each hole. This vortex motion begins forming at blowing rates of about 0.3 (Fig. 8(a)) and becomes most pronounced at blowing rates between 0.7 and 0.9. Notice the very tight "winding" of the streaklines in Fig. 8(b) for a blowing rate of 0.75. A close-up top view of the region surrounding the upstream injection location for this blowing rate is shown in Fig. 8(c). The most important feature of compound angle injection is that this strong vortex motion keeps the film attached to the surface even at the high blowing rates. This can be seen from Fig. 9 which compares the compound angle injection at a low and a high blowing rate. Notice that there is very little difference in the penetration distance between a blowing rate of 0.3 and 0.9. Even at a velocity ratio of 0.9, the film remains close to the surface. Note particularly how the downstream film lies underneath the film from the upstream hole. Recall, in Fig. 7(b), that for the in-line injection, most of the film separated from the surface at a blowing rate of 0.8.

With compound angle injection, the mainstream flow must turn the film jets, so there is a slight aerodynamic penalty in turbine effi-

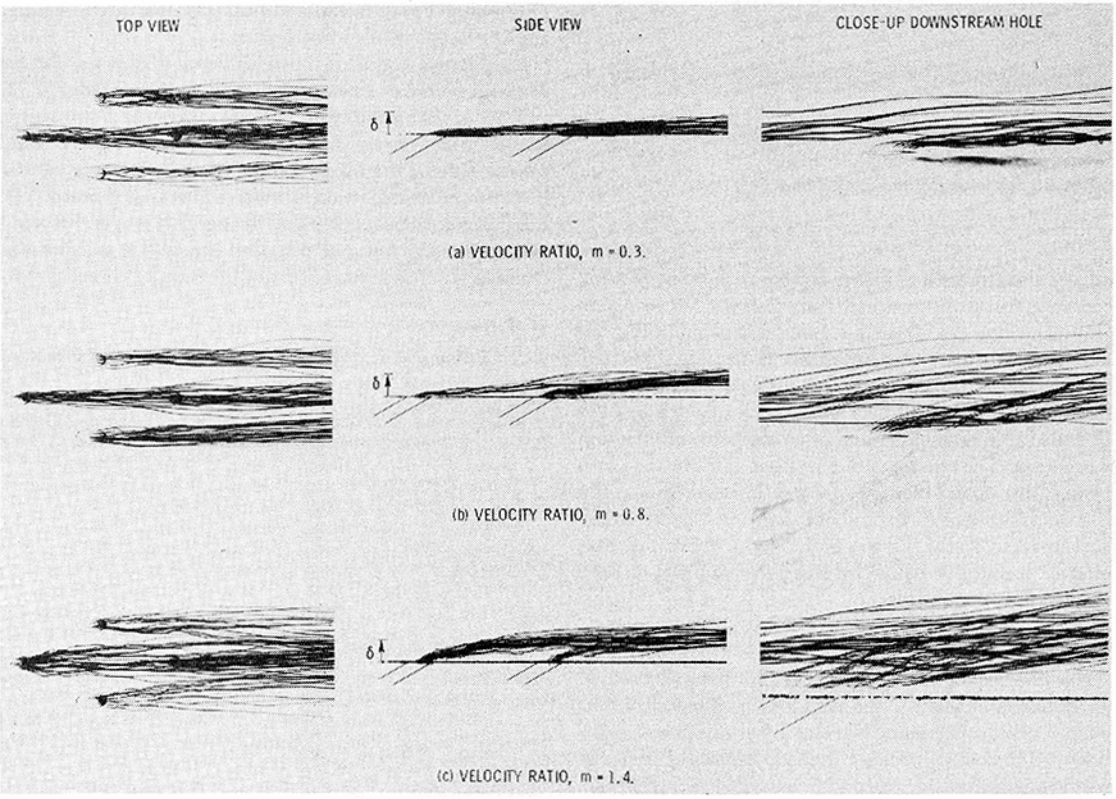

(a) VELOCITY RATIO, m = 0.3.

(b) VELOCITY RATIO, m = 0.8.

(c) VELOCITY RATIO, m = 1.4.

Fig. 7 Streaklines for film injection from holes angled 30 deg to the surface in-line with the mainstream

ciency associated with this type of film cooling [13] compared to the in-line case providing the blowing rate is low enough that separation is not a problem.

Effect of Boundary Layer Thickness. To determine the effect that the initial boundary layer thickness has on the distance that the film jet penetrates into the mainstream, the 30 deg in-line injection

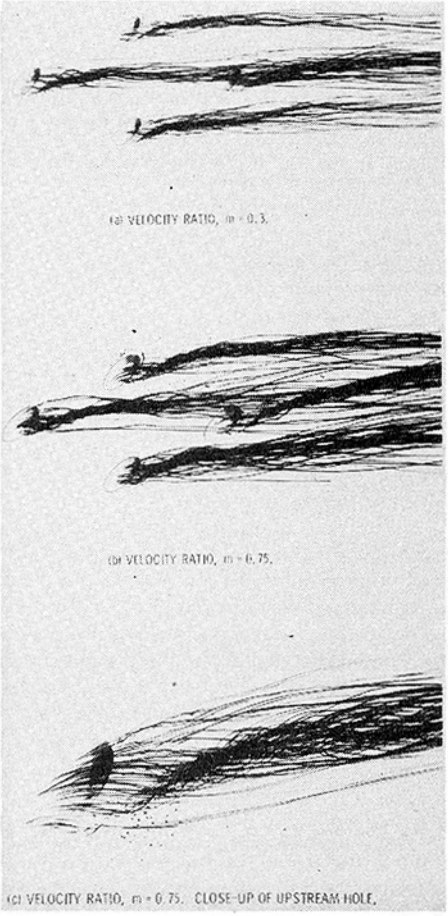

(a) VELOCITY RATIO, m = 0.3.

(b) VELOCITY RATIO, m = 0.75.

(c) VELOCITY RATIO, m = 0.75. CLOSE-UP OF UPSTREAM HOLE.

Fig. 8 Compound angle film injection—top view

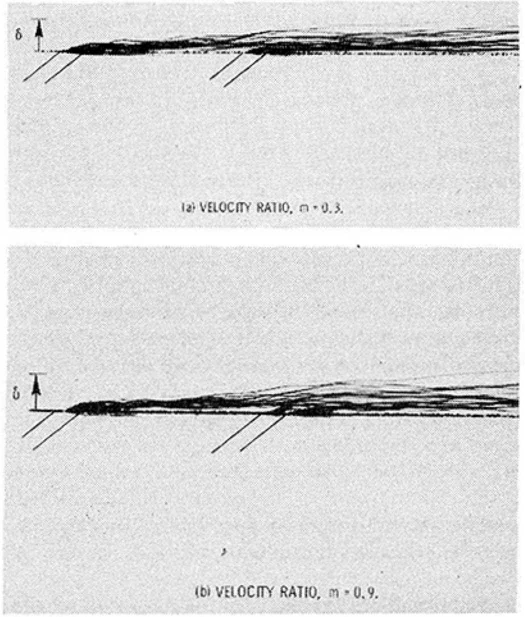

(a) VELOCITY RATIO, m = 0.3.

(b) VELOCITY RATIO, m = 0.9.

Fig. 9 Compound angle injection—side view

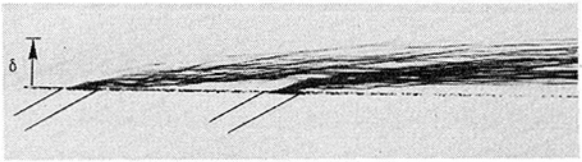

Fig. 10 In-line, 30 deg injection into a thick boundary layer, $m = 0.8$

configuration was also run with a thicker boundary layer by moving the injection location further downstream from the inlet nozzle. A side view photograph showing the streakline pattern is given in Fig. 10. The boundary layer thickness was increased 37 percent over that which existed for the results discussed previously. The blowing rate was 0.8, the same as in Fig. 7(*b*). The freestream velocity was decreased to give the same Reynolds number at the point of injection as in the earlier results. The upstream film jet penetrates further with the thicker boundary layer, but the penetration relative to the boundary layer thickness appears to be about the same. The trajectory of the downstream jet looks the same in both figures which indicates that its penetration is controlled more by the upstream injection than the initial boundary layer thickness.

Concluding Remarks

In discrete hole film cooling for turbine applications, the film should be injected at as shallow an angle to the surface as possible within the limits set by fabrication constraints. Normal injection is a very inefficient method of film cooling because the film separates from the surface even at low blowing rates. A counter-rotating vortex motion downstream of the injection hole generates excessive turbulent mixing which dissipates the film, increases the heat transfer coefficient, and increases aerodynamic losses in the turbine.

For injection holes angled 30 deg to the surface in-line with the mainstream, the film layer remains attached to the surface as long as the blowing rate does not exceed about 0.5. At higher blowing rates, the mainstream will wrap around and underneath the separated film jet, reducing its effectiveness. But high film injection velocities cannot always be avoided in turbine cooling applications because of the pressure drop needed across the outer shell of the airfoil to insure that a positive flow direction is always maintained. High blowing rates are a particular problem with multiple rows of film cooling holes fed from a common supply plenum and discharging into a region of rapidly varying freestream static pressure.

To delay separation to much higher blowing rates, film cooling holes can be oriented at a compound angle to the surface and mainstream in local areas on the turbine blade where the boundary layer has a tendency to separate such as in the diffusion region on the suction or convex side of the blade. Where the blowing rate can be kept low however, in-line injection is preferred because it causes less turbulent mixing and consequently the film persists longer. Also, in-line injection results in a lower aerodynamic penalty in turbine efficiency because most of the momentum of the film jet is recovered.

References

1 Erikson, V. L., "Film Cooling Effectiveness and Heat Transfer With Injection Through Holes," Report HTL-TR-102 (NASA CR-72991), University of Minnesota, 1971.

2 Liess, C., "Film Cooling With Ejection From a Row of Inclined Circular Holes—An Experimental Study for the Application to Gas Turbine Blades," Technical Note 97, von Karman Institute for Fluid Mechanics, 1973.

3 Choe, H., Kays, W. M., and Moffat, R. J., "The Superposition Approach to Film Cooling," ASME Paper No. 74-WA/HT-27, 1974.

4 Choe, H., Kays, W. M., and Moffat, R. J., "The Turbulent Boundary Layer On A Full-Coverage Film-Cooled Surface: An Experimental Heat Transfer Study With Normal Injection," NASA CR-2642, 1976.

5 Crawford, M. E., Choe, H., Kays, W. M., and Moffat, R. J., "Full-Coverage Film Cooling Heat Transfer Studies—A Summary of the Data for Normal-Hole Injection and 30° Slant-Hole Injection," NASA CR-2648, 1976.

6 Metzger, D. E., Takeuchi, D. I., and Kuenstler, P. A., "Effectiveness and Heat Transfer With Full-Coverage Film Cooling," *Journal of Engineering for Power*, TRANS. ASME, Series A, Vol. 95, 1973.

7 Mayle, R. E., and Camarata, F. J., "Multihole Cooling Film Effectiveness and Heat Transfer," TRANS. ASME, Series C, JHT, Vol. 97, 1975, pp. 534–538.

8 LeBrocq, P. V., Launder, B. E., and Priddin, C. H., "Discrete Hole Injection as a Means of Transpiration Cooling—An Experimental Study," Imperial College of Science and Technology, Report HTS/71/37, 1971.

9 Launder, B. E., and York, J., "Discrete Hole Cooling in the Presence of Freestream Turbulence and a Strong Favorable Pressure Gradient," Imperial College of Science and Technology, Report HTS/73/9, 1973.

10 Hale, R. W., Tan, P., Stowell, R. C., and Ordway, D. E., "Development of an Integrated System for Flow Visualization in Air Using Neutrally-Buoyant Bubbles," Sage Action Inc. Report 7107, 1971.

11 Colladay, R. S., Russell, L. M., and Lane, J. M., "Streakline Flow Visualization of Discrete Hole Film Cooling With Holes Inclined 30° to the Surface," NASA TN D-8175, 1976.

12 Prust, H. W., Jr., Schum, H. J., and Szanca, E. M., "Cold-Air Investigation of a Turbine With Transpiration-Cooled Stator Blades—I. Performance of a Stator With Discrete Hole Blading," NASA TM X-2094, 1970.

13 "Aeronautical Propulsion," NASA-Lewis Research Center Conference, May, 1975, NASA SP-381, pp. 229–288.

S. W. Hong[1]
Research Assistant.
Assoc. Mem. ASME

A. E. Bergles
Professor and Chairman.
Mem. ASME

Department of Mechanical Engineering
and Engineering Research Institute,
Iowa State University,
Ames, Iowa

Augmentation of Laminar Flow Heat Transfer in Tubes by Means of Twisted-Tape Inserts

Heat transfer coefficients for laminar flow of water and ethylene glycol in an electrically heated metal tube with two twisted-tape inserts were determined experimentally. The Nusselt number for fully developed flow was found to be a function of tape twist ratio, Reynolds number, and Prandtl number. These Nusselt numbers were as much as nine times the empty tube constant property values. The correlation of these data is in fair agreement with the only available analytical predictions. The friction factor is affected by tape twist only at high Reynolds numbers, in accordance with analytical predictions. The performance of these augmented tubes is compared with that of empty tubes under similar heating conditions.

Introduction

Laminar flow heat transfer in tubes occurs in a wide variety of engineering applications. The following examples can be cited: heating or cooling of viscous liquids in the chemical and food industries, heating or cooling of oils, cooling of space suits, heating of the circulating fluid in solar collectors, heat transfer in compact heat exchangers, and cooling or warming of blood during surgical operations. In addition, in cases where normal heat exchanger operation is in turbulent flow, off-design operation and operation during start-up or shut-down periods may result in laminar flow conditions. When laminar flow heat transfer occurs, it usually represents the dominant thermal resistance in a heat exchanger.

Even with the substantial natural enhancement of superimposed free convection, heat transfer coefficients are generally low for laminar flow in ordinary tubes [1].[2] In recent years, the requirement for more efficient heat transfer systems has stimulated interest in augmentative heat transfer methods. Use of artificially roughened surfaces, use of extended surfaces, use of inlet vortex generators, vibration of the surface or fluid, application of electrostatic fields, and the insertion in tubes of objects such as twisted tapes, coiled wires, or spinners are a few examples of such augmentative techniques. Existing systems can often be improved by using an augmentative method, while in other applications, such as the design of heat exchangers for use in space vehicles, an augmentative scheme may be mandatory in order for the system to function properly and meet the size limitations imposed. Detailed surveys of the many augmentative methods presently employed are given in references [2, 3]. A recent survey focused on laminar flow heat transfer augmentation in tubes is given in reference [4].

Devices which establish a swirl in the fluid are particularly attractive augmentative schemes for forced convection systems. Full-length, twisted-tape inserts have been found to improve heat transfer by up to 100 percent for turbulent flow of water [2].

Tape inserts are inexpensive and they can be easily employed to improve the performance of existing systems. Date and Singham [5] and Date [6] have reported analytical results that suggest that swirl flow improves heat transfer to viscous liquids by as much as a factor of nearly 70. However, there appear to be no published experimental data to confirm the large predicted effects of swirl flow. Twisted tapes, of course, involve increased pressure drop and, thus, pumping power. The benefits of twisted-tape inserts must be viewed in terms of the constraints of the particular application: fixed flow rate, fixed pressure drop, fixed pumping power, etc.

The present study of twisted-tape inserts had two primary goals: (1) obtain laminar flow data under carefully controlled conditions, and from these data develop the first experimentally based correlation for predicting the associated heat transfer coefficients, (2) compare the heat transfer performance of tubes having tape-generated swirl

---

[1] Present address: M/C 195, General Electric Co., San Jose, Calif.

[2] Numbers in brackets designate References at end of paper.

Contributed by the Heat Transfer Division for publication in the JOURNAL OF HEAT TRANSFER. Manuscript received by the Heat Transfer Division November 13, 1975. Paper No. 76-HT-QQ.

flow with the performance of empty tubes under similar heating conditions.

Experimental Apparatus

The test facility utilized in this investigation was constructed in the ISU Heat Transfer Laboratory. A schematic layout of the test loop is shown in Fig. 1. It is a closed loop, low pressure system with all piping made of copper tube and brass fittings. The working fluid was circulated with a small centrifugal pump. An accumulator was used to insure a stable flow. Two flowmeters were installed in parallel to measure a wide range of flow rates.

The test section was a 304 stainless steel tube with a twisted tape installed in the 1.22-m heated length. The inside tube diameter and wall thickness were 10.2 and 0.51 mm, respectively. The tube was heated by a d-c current passed directly through the tube wall.

The tapes used for this investigation were made of a strip of 302 stainless steel, 0.46-mm thick and 9.7-mm wide. The strips were covered at both edges by 2.5-mm wide strips of black No. 33 Scotch electrical tape. To assure good electric insulation, the tape assemblies were baked in a furnace at 260°C for about one minute to set the adhesive. The tapes were twisted by clamping each tape to the ceiling, attaching weights to one end, and then twisting to the desired specifications. The tapes were lubricated with a soap solution and pulled into the tube. After tape installation, the average total clearance between the tube wall and the tape was approximately 0.2 mm. The electrical resistance between the twisted tape and the test tube was measured to be 5–10 KΩ before and after testing. With this electrical resistance, it was reasonable to assume that there was no heat generated in the tape. This situation closely approximates real applications where removable tapes are inserted in existing heat exchanger tubes.

Fluid temperature measurements were made at the inlet and exit of the test section. The outside wall temperature was measured at two axial locations, 0.48 and 1.12 m from the onset of heating. Eight thermocouples were placed 45 deg apart, circumferentially, insulated from the tube with thin strips of insulating paper. The tube was then heavily insulated with glass fiber insulation to minimize heat loss.

The pressure drop was measured with a longer test section (3.2 m) having a $y = 3.125$ tape insert. A U-tube manometer was formed by attaching standpipes to pressure taps at either end of the test section.

Experimental Procedure and Data Reduction

Distilled water and ethylene glycol were chosen as working fluids, since they provide a substantial variation in Prandtl number and a wide range of laminar Reynolds numbers.

At the beginning of a series of tests, the loop was filled with the liquid from the top of the supply/degassing tank, and air was bled from all high points of the system. Liquid was then circulated through the heated tank to reduce the gas content. The gas content (measured by an Aire-Ometer) was below 10 cc/l for water and less than 6 cc/l for ethylene glycol.

The experiments generally proceeded by increasing power to the heated section (flow rate and inlet temperature remaining constant). At each power setting, data were recorded concerning the test-section flow rate, inlet and exit fluid temperatures, current, voltage drop, outer tube wall temperatures, and pressure drop. The present system variables for water and ethylene glycol were as follows:

Twist ratio (tube diameters per 180-deg rotation of the tape): $y = 2.45, 5.08$

Water:	Flow rate: 20–34 kg/hr Heat flux: 500–38,500 W/m^2 (Prandtl number: 3–7) (Reynolds number: 83–2460)
Ethylene Glycol:	Flow rate: 6.5–136 kg/hr Heat flux: 5200–27,600 W/m^2 (Prandtl number: 84–192) (Reynolds number: 13–390)

Heat input was determined from the measured electrical power input as corrected for heat loss through the outer wall (estimated to be 1.5 percent [1]). This value generally agreed with the value determined from the enthalpy rise of the fluid; however, the latter method was not reliable due to lack of a motorized mixing chamber at the tube outlet.

The local bulk temperature at the measuring section was computed from the inlet temperature, flow rate, and actual power input. A linear variation in bulk temperature from the inlet to the exit of the heated length was assumed. The tube wall temperature drop was calculated by considering the steady-state, one-dimensional heat conduction equation with uniform heat generation inside the cylindrical tubes. This correction, less than 0.5 K, was applied uniformly around the circumference of the metal tube. The circumferential average wall temperature was computed from the eight inner wall temperature readings by Simpson's rule of numerical integration. The wall temperature and bulk temperature were combined with the heat flux to give the heat transfer coefficient and the Nusselt number.

Pressure drop data were obtained for water and ethylene glycol

Nomenclature

a = tube radius
A = cross-sectional flow area
A_s = cross-sectional flow area with twisted tape, $A - \delta D$
Be = viscosity parameters, $(-1/\mu)(d\mu/dT)\Delta T$
C_p = constant pressure specific heat
D = inside tube diameter
f = Fanning friction factor, $2g_c D\Delta p/(L\rho\bar{w}^2)$
g = gravitational acceleration
G = mass flux, $\dot{m}/A_s$
Gr_f = Grashof number based on radius and film temperature, $g\beta\rho^2a^3\Delta T/\mu^2$
$\mathrm{Gr}_f{}^*$ = modified Grashof number based on radius and film temperature, $g\beta\rho^2a^3\Delta T^*/\mu^2$
$\bar{h}$ = circumferential average heat transfer coefficients, $q''/(\bar{T}_w - T_b)$
H = pitch for 180-deg rotation of tape
k = fluid thermal conductivity
k_f = tape thermal conductivity
k_w = tube wall thermal conductivity
L = length between two pressure taps
$\dot{m}$ = mass flow rate
Nu_s = Nusselt number for swirl flow, $\bar{h}D/k$
N = number of tubes in a tube bundle
Nu_f = Nusselt number for empty tube based on film temperature, $\bar{h}(2a)/k$
Pr = Prandtl number, $\mu C_p/k$
Pw^* = tube wall parameter, $kD/k(k_wt)$
Δp = pressure drop
q'' = rate of heat transfer per unit area
Re_s = Reynolds number for swirl flow, GD/μ
T_b = bulk fluid temperature
T_w = temperature at wall
t = tube wall thickness
ΔT = temperature difference, $\bar{T}_w - T_b$
ΔT^* = modified temperature difference, $q''a/k$
$\bar{w}$ = bulk average velocity in axial direction
y = twist ratio, H/D
Z = distance along heated section
α = thermal diffusivity, $k/\rho C_p$
β = coefficient of thermal expansion, $(-1/\rho)(\partial/\partial T)_p$
δ = thickness of tape
μ = viscosity
ρ = density

Subscripts

b = evaluated at bulk liquid temperature
f = evaluated at liquid film temperature, $(\bar{T}_w - T_b)/2$
s = swirl flow
w = evaluated at tube wall temperature

Liquid properties are evaluated at the bulk temperature unless otherwise specified.

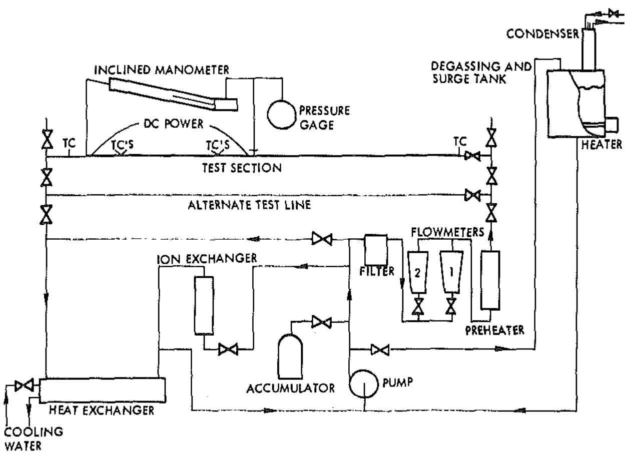

Fig. 1 Schematic layout of test loop

under isothermal conditions. The pressure gradient was presumed uniform and characteristic of fully developed swirl flow.

Further details of the apparatus, procedure, and data reduction are given in reference [4].

Heat Transfer and Pressure Drop Results

Wall Temperature Variation. Typical temperature variations around the tube wall for various flows and heat fluxes for water are shown in Fig. 2. The local tape locations are 90 and 120 deg for twist ratios y = 5.08 and 2.45, respectively. The location of maxima and minima for the two tape twists (upper two sets of curves) are different in such a way as to suggest that the temperature profiles are related to tape orientation rather than tube orientation. This is as expected since the secondary flow generated by the tapes should be much stornger than any buoyancy-induced secondary flow.

The circumferential variation of tube wall temperature is small, with the maximum and minimum temperatures generally differing by less than 6 K. A rather uniform wall temperature is reasonable due to the flow mixing and the high conductance of the tube wall.

Heat Transfer Results. The experimental laminar swirl flow heat transfer results are presented in Fig. 3 in terms of the twist ratio, y, and the traditional dimensionless groups: Nu, Pr, Re_s, Z/DRe_sPr. The inside tube diameter rather than the hydraulic diameter was used in these parameters in order to best show the improvement obtainable with swirl flow over a comparable empty tube flow. Since the tape inhibits free convection, the Grashof number or Rayleigh number, important parameters in empty tube laminar flow, are unimportant in swirl flow. The fin parameter suggested in reference [6] and the tube wall parameter developed in reference [8] were also ignored.

The variation of the Nusselt number as a function of reduced length for various Re_s and y is shown in Fig. 3 for water and ethylene glycol. The baseline shown in Fig. 3 represents the limiting analytical solution for $y \to \infty$, as presented in reference [4] for pure forced convection in a semicircular tube with the flat side insulated. It should be noted that the actual limiting curve will be somewhat higher since the tube and tape define a circular sector which is smaller than a semicircle. No analytical solution for a circular sector is available; however, the correction for the present case is estimated from [9] to be less than 6 percent.

It is evident from Fig. 3 that for constant y, and with essentially constant Prandtl and Reynolds numbers, Nusselt number is not significantly dependent on Z/D. This corresponds to the classical interpretation of the fully developed condition; hence, it is concluded that fully developed conditions were obtained prior to the first measuring section. Assuming that Nusselt number is independent of axial length for fixed Re_s, Pr, and y, a correlation of the following form was sought:

$$\text{Nu} = f(\text{Re}_s, \text{Pr}, y) \quad (1)$$

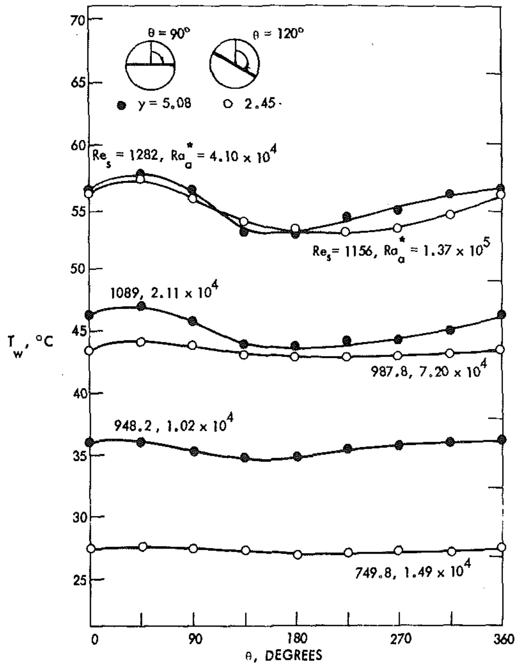

Fig. 2 Circumferential wall temperature variaton with various Re_s, Ra_a^*, and y for water

Plots with this interpretation of all the data are shown in Figs. 4 and 5 for y = 5.08 and 2.45, respectively. It is apparent that the tighter tape twist (lower y value) produces an increase in heat transfer coefficients. It may also be observed that Nu varies essentially as Re_s^m for high Reynolds number flow. This would suggest a linearized correlation for the high Reynolds number region, similar to the usual correlation for turbulent flow in empty tubes. Estimated straight-line representations of the four sets of data are indicated in Fig. 6; the maximum deviation of the data from each line is 20 percent. The heat transfer coefficient clearly increases with increasing Reynolds and Prandtl numbers and decreasing twist ratio. It should be noted that the present data do not exhibit any inflections which might denote a transition to turbulent flow.

Correlation of Data. As shown in Fig. 6, the ethylene glycol data for both twist ratios are well above the water data at constant Reynolds number. Following the suggestion from Date and Singham [5],

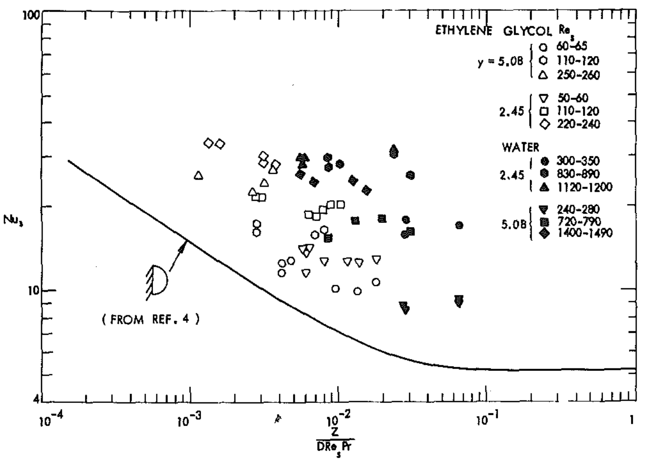

Fig. 3 Nusselt number as a function of reduced axial length for water and ethylene glycol

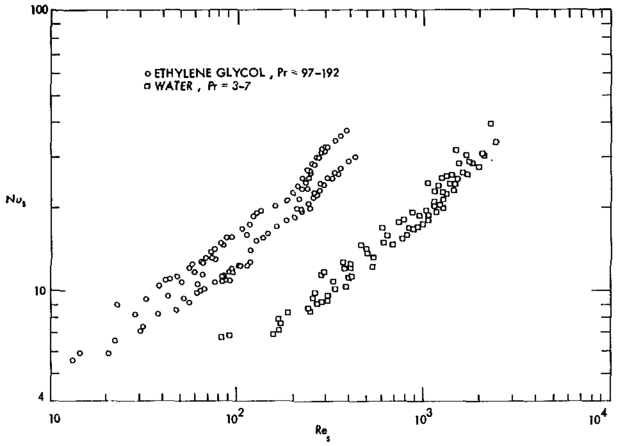

Fig. 4 Fully developed heat transfer results for water and ethylene glycol with $y = 5.08$

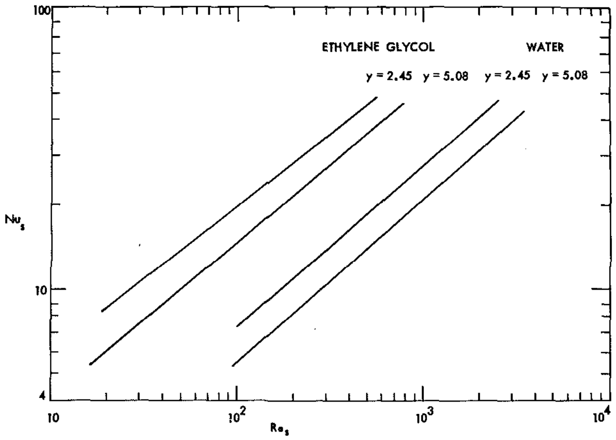

Fig. 6 Linearized representation of data for water and ethylene glycol

the parameters Re_s and y were combined as one single parameter Re_s/y. This parameter is similar to the Dean number in curved pipe flow, which accounts for the centrifugal force effect. The final straight-line correlation given in Fig. 7 for all data with $\mathrm{Re}_s/y > 10$ is

$$\mathrm{Nu}_s = 0.383\,\mathrm{Pr}^{0.35}(\mathrm{Re}_s/y)^{0.622} \qquad (2)$$

In order to reduce the scatter of experimental data, different procedures were tried for reducing the four sets of heat transfer data. No significant improvement in the correlation was obtained by using the film temperature or other technique to account for radial variations in fluid properties.

It was, therefore, decided to simply use bulk temperature for evaluation of all fluid properties.

It is evident that equation (2) is not suitable for correlation of low Re_s/y values. As Re_s/y decreases, the Nusselt number should approach the asymptotic value for a tube with a straight tape. Following the procedure suggested by Churchill and Usagi [7], the following alternate correlation was obtained:

$$\mathrm{Nu}_s = 5.172\{1 + 5.484 \times 10^{-3}\mathrm{Pr}^{0.7}(\mathrm{Re}_s/y)^{1.25}\}^{0.5} \qquad (3)$$

In the interest of generality the coefficient has been kept as the semicircular tube value of 5.172 rather than incorporating the small adjustment noted above. The recommended correlation is compared with the data in Fig. 8. It is seen that equation (3) shows reasonable correlation for all values of Re_s/y. The standard deviation of the data from the correlation is 16.4 percent.

Comparison With Analytical Prediction. The only analytical prediction of laminar swirl flow generated by twisted-tape inserts is given by Date and Singham [5] and Date [6]. One important parameter used in their analysis is the fin parameter, representing the fin effect of the twisted tape, which is defined as

$$C_{\mathrm{fin}} = \frac{k_w \delta}{kD} \qquad (4)$$

In the present investigation, the twisted tape was covered by electrical insulation tape to prevent electric contact beteeen the tape and the tube wall. C_{fin} in this study, therefore, approaches zero (approximately 0.124 for ethylene glycol). A low value of C_{fin} is also expected to be the case in many practical applications since loose-fitting tapes are desirable from the standpoint of insertion and removal for tube cleaning.

A comparison of the present heat transfer correlation with the limited analytical results for $C_{\mathrm{fin}} = 0$ is presented in Fig. 9. In addition to the computed results given in references [5, 6] unpublished data are included [8].[3] The agreement is only fair, particularly with regard to the effect of Prandtl number. Additional analytical predictions for $C_{\mathrm{fin}} = 1.85$ and ∞ and Pr up to 500 suggest a very strong influence of

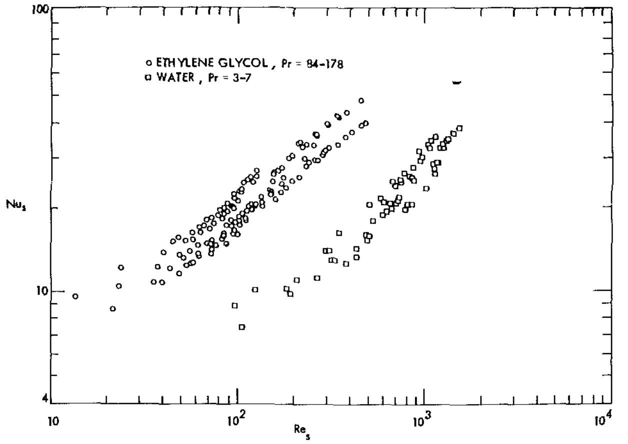

Fig. 5 Fully developed heat transfer results for water and ethylene glycol with $y = 2.45$

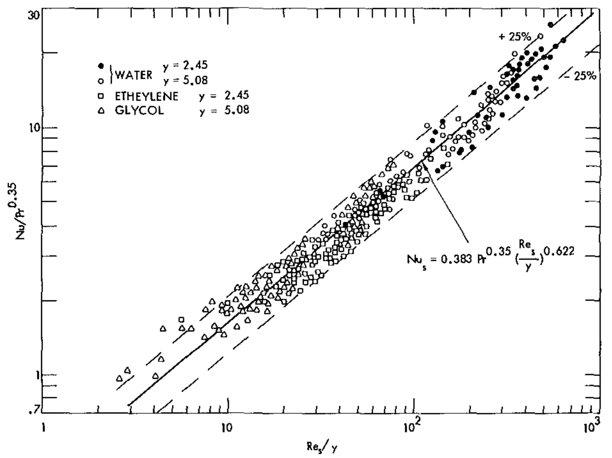

Fig. 7 Correlation of heat transfer results for laminar swirl flow

---

[3] The results given in references [6, 7] should be increased by a factor of 2.0 to account for a computation error [8].

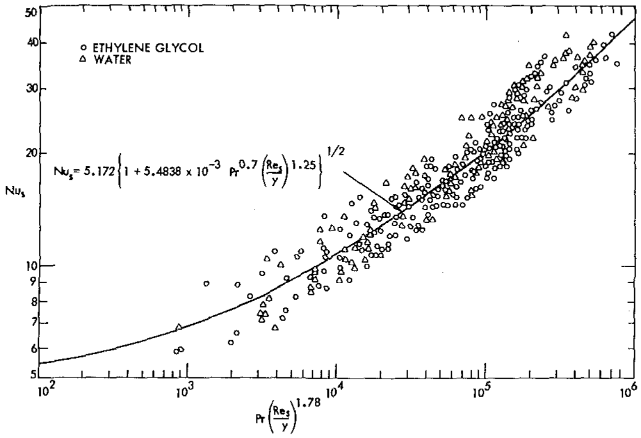

Fig. 8 **Final correlation of heat transfer results**

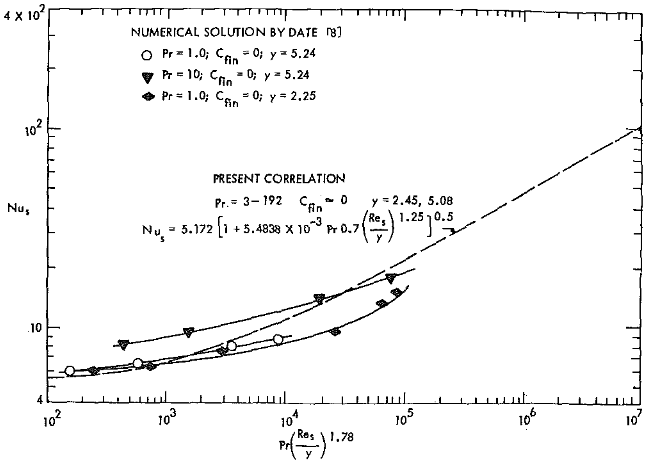

Fig. 9 **Comparison of present heat transfer correlation with previous analytical predictions**

Prandtl number on the Nusselt number. Although a direct comparison is not possible, the present results do not appear to confirm this analytical trend.

Pressure Drop

Friction factor data for both water and ethylene glycol under isothermal conditions are presented in Fig. 10. The reference curve, $f = 183.6/\mathrm{Re}_s$ was obtained from the analytical results of Sparrow and Hiji-Sheikh [9] for the circular sector corresponding to the present tube-tape assembly. The effect of tape twist is evident only at large Reynolds numbers, where the data tend to rise above the reference curve. The present data are in quantitative agreement with the analytical results of Date and Singham [5] and Date [6] for a semicircular tube. The resolution of the instrumentation was not adequate to accurately assess the small reductions in pressure drop with heating.

It is important to note that the increase in pressure drop with tape-generated swirl flow is less than the increase in heat transfer coefficient (at constant Reynolds number). The maximum increase in heat transfer coefficient is ten times the empty tube constant property value, while the corresponding pressure drop is less than four times the empty tube pressure drop. This is in contrast to turbulent flow, where comparable increases in heat transfer coefficient are accompanied by pressure drops which are several orders of magnitude greater than the empty tube values [10].

Applications

The final objective of this study is to compare the swirl flow results with the heat transfer performance of ordinary tubes. The heat transfer results for an empty horizontal metal tube presented by Morcos and Bergles [1] were correlated as follows:

$$\mathrm{Nu}_f = 0.377\,\mathrm{Gr}_f^{0.256}\mathrm{Pr}_f^{0.31}/Pw_f^{*0.09} \qquad (5)$$

where $Pw^* = (k/k_w)\,(D/t)$ and the subscript f indicates that all physical properties are evaluated at the film temperature. By introducing $\Delta T^* = q''a/k$ into the Grashof number, equation (5) can be rewritten as follows:

$$\mathrm{Nu}_f = 0.45\,\mathrm{Gr}_f^{*0.204}\mathrm{Pr}_f^{0.256}/Pw_f^{*0.072} \qquad (6)$$

It is seen that the Nusselt number for an ordinary tube depends on the Grashof number, the Prandtl number, and the tube wall parameter. However, in the laminar swirl tube flow Nusselt number is a function only of Pr and Re_s/y as indicated by equation (2) or equation (3).

Consider as a first goal increasing heat transfer for fixed geometry. The heat duty ratio of tubes with a twisted tape and without a twisted tape is obtained from equations (2) and (5) as follows:

$$\frac{q_s}{q_o} = \left\{\frac{\mathrm{Nu}_s}{\mathrm{Nu}_f}\right\}_{\Delta T,N,D,L} = \frac{1.015\,\mathrm{Pr}^{0.35}(\mathrm{Re}_s/y)^{0.622}Pw_f^{*0.09}}{\mathrm{Gr}_f^{0.256}\mathrm{Pr}_f^{0.31}} \qquad (7)$$

Equation (8) reveals that the Nusselt number ratio depends rather strongly on Re_s/y and Gr_f and weakly on Pw^* and Pr for the same working fluid. For high flow rates and low heat fluxes, a large improvement in heat transfer coefficient is obtained. Since the Nusselt number for the empty tube flow is independent of Reynolds number, the usual coupling of augmented and empty tubes is not present. Hence, equation (7) is valid for a constraint of fixed flow rate, pressure drop, or pumping power. A Nusselt number ratio of 1.9 is achieved for ethylene glycol with $\mathrm{Re}_s = 216.5$, $\mathrm{Gr}_f = 2.708 \times 10^3$, $y = 5.08$, $\mathrm{Pr} = 159$, and $Pw_f^* = 0.167$.

A second objective frequently encountered in equipment design is to reduce exchanger size. This goal is usually associated with a fixed heat duty. With this objective and any of the hydraulic constraints, the Nusselt number ratio is obtained as follows:

$$\frac{A_0}{A_s} = \frac{N_0L_0}{N_sL_s} = \left\{\frac{\mathrm{Nu}_s}{\mathrm{Nu}_f}\right\}_{\Delta T,q} = \frac{0.851\,\mathrm{Pr}^{0.35}(\mathrm{Re}_s/y)^{0.622}Pw_f^{*0.072}}{\mathrm{Gr}_f^{*0.204}\mathrm{Pr}_f^{0.246}} \qquad (8)$$

where N_0 and N_s are number of exchanger tubes without twisted tape inserts and with twisted tapes, respectively. A length ratio, L_s/L_0 of 0.37 is obtained for water with $\mathrm{Pr} = 6.85$, $\mathrm{Re}_s = 805.3$, $\mathrm{Gr}_f^* = 1.69 \times$

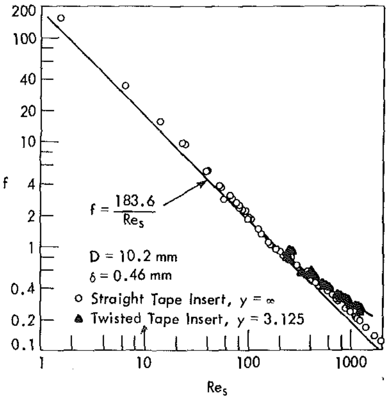

Fig. 10 **Friction factor data for various tape inserts**

10^4, $y = 2.45$, and $Pw_f{}^* = 0.386$.

It is emphasized that these improvements are evaluated relative to "free-convection-augmented" heat transfer in normal tubes. The augmentation with swirl flow may be more or less dependent on the conditions of the reference exchanger.

Concluding Remarks

An experimental study has been conducted to investigate heat transfer augmentation by means of twisted-tape inserts in laminar flow. The investigation focused on fully-developed laminar flow heat transfer and pressure drop in horizontal tubes with uniform axial heat flux. The heat transfer results indicate that the Nusselt number is a function of tape twist ratio, Reynolds number, and Prandtl number. Nusselt numbers greater than 40 were obtained. The recommended heat transfer correlation is given in equation (3).

This correlation is in fair agreement with the analytical prediction given in references [6, 7]. The analytical results are limited, however, and it appears that the effect of certain variables, Prandtl number in particular, is not predicted well by the analysis.

The pressure drop data indicate that the friction factor depends primarily on Reynolds number. Swirl flow increases the friction factor somewhat at higher Reynolds number.

The constant-condition comparisons of Nusselt number for tubes with twisted-tape inserts and without tapes are given by equations (7) and (8). The reference data include the significant effects of free convection. If the objective is to increase heat transfer at constant geometry, equation (7) indicates that the heat transfer can be improved by a factor of two or three. With fixed heat duty, the exchanger can be reduced in size by inserting twisted tapes according to the ratio given in equation (9). The performance ratios are valid regardless of the hydraulic constraint (constant flow rate, constant pumping power, constant pressure drop).

Further tests should be run to confirm the correlation over a wider range of conditions. Tests in the transitional Reynolds number range would provide the basis for development of a composite correlation for laminar and turbulent flow. Visual studies would help clarify the mechanism of augmentation in laminar flow.

Acknowledgments

This study was supported by the National Science Foundation through Grant GK-36851 and by the Engineering Research Institute, Iowa State University. Mr. S. D. Joshi provided the pressure drop data presented in this paper.

References

1 Morcos, S. M., and Bergles, A. E., "Experimental Investigation of Combined Forced and Free Laminar Convection in Horizontal Tubes," JOURNAL OF HEAT TRANSFER,TRANS. ASME, Series C, Vol. 97, 1975, pp. 212–219.

2 Bergles, A. E., "Survey and Evaluation of Techniques to Augment Convective Heat Transfer," *Progress in Heat and Mass Transfer*, Vol. 1, Pergamon Press, New York, 1969, pp. 331–334.

3 Bergles, A. E., "Recent Developments in Convective Heat Transfer Augmentation," *Applied Mechanics Reviews*, Vol. 26, 1973, pp. 675–682.

4 Hong, S. W., and Bergles, A. E., "Augmentation of Laminar Flow Heat Transfer in Tubes by Means of Twisted-Tape Inserts," ISU Heat Transfer Laboratory Report HTL-5, Engineering Research Institute ISU-ERI-23-Ames-75011, Dec. 1974.

5 Date, A. W., and Singham, J. R., "Numerical Prediction of Friction and Heat Transfer Characteristics of Fully-Developed Laminar Flow in Tubes Containing Twisted Tapes," ASME Paper No. 72-HT-17, 1972.

6 Date, A. W., "Prediction of Fully-Developed Flow in a Tube Containing a Twisted-Tape," *International Journal of Heat and Mass Transfer*, Vol. 17, 1974, pp. 845–859.

7 Churchill, S. W., and Usagi, R., "A General Expression for the Correlation of Rates of Transfer and Other Phenomena," *AIChE Journal*, Vol. 18, 1972, pp. 1121–1128.

8 Date, A. W., Personal communication, July 23, 1975.

9 Sparrow, E. M., and Sheikh, A., "Flow and Heat Transfer in Ducts of Arbitrary Shape with Arbitrary Thermal Boundary Conditions," JOURNAL OF HEAT TRANSFER, TRANS. ASME, Series C, Vol. 88, 1966, pp. 351–358.

10 Megerlin, F. E., Murphy, R. W., and Bergles, A. E., "Augmentation of Heat Transfer in Tubes by Use of Mesh and Brush Inserts," JOURNAL OF HEAT TRANSFER, TRANS. ASME, Series C, Vol. 96, 1974, pp. 145–151.

J. H. Masliyah
K. Nandakumar[1]

**Department of Chemistry and Chemical Engineering,
University of Saskatchewan,
SASKATOON, Sask. Canada**

Heat Transfer in Internally Finned Tubes

Heat transfer characteristics for a laminar forced convection fully developed flow in an internally finned circular tube with axially uniform heat flux with peripherally uniform temperature are obtained using a finite element method. For a given fin geometry, the Nusselt number based on inside tube diameter was higher than that for a smooth tube. Also, it was found that for maximum heat transfer there exists an optimum fin number for a given fin configuration. The internal fins are of triangular shape.

Introduction

The need for high performance thermal systems has stimulated research interest in methods to augment or intensify heat transfer. As excellent review of many enhancement techniques is presented by Bergles [1].[2] Use of forged internal fins in tubes is one such method which is finding increasing use in recent years. Such fins could be either straight or helical in geometry. Some experimental findings on pressure drop and heat transfer characteristics in both laminar and turbulent flow are given by Watkinson, et al. [2, 3].

A theoretical investigation of fully developed laminar forced convective heat transfer in internally finned tubes with zero fin thickness, has been conducted by Hu and Chang [4]. In their work they considered fully developed velocity and temperature profiles together with a uniform heat flux around the walls of each cross section as well as uniform heat input per unit length in the axial direction.

In the present work, fins of triangular shape (finite thickness) as shown in Fig. 1 will be considered. The energy equation will be solved subject to the boundary condition of axially uniform heat flux (i.e., constant heat input per unit length) with peripherally uniform temperature. The temperature along the fin is assumed to be equal to the wall temperature which will be closely realized only for metals of high thermal conductivity.

Mathematical Formulation

The energy equation, neglecting axial conduction and heat generation due to viscous dissipation, is given by

$$\frac{k}{\rho C_p}\left[\frac{\partial^2 T}{\partial x'^2}+\frac{\partial^2 T}{\partial y'^2}\right]=w'\frac{\partial T}{\partial z'} \qquad (1)$$

where T and w' are the local fluid temperature and velocity, respectively. Heat balance over a unit length gives

$$\frac{\partial T}{\partial z'}=\frac{Q}{\rho A'\bar{w}'C_p} \qquad (2)$$

where Q is the heat transfer rate per unit length of the tube and A' is the flow cross-sectional area. Combining equations (1) and (2) yields

$$\left[\frac{\partial^2 T}{\partial x'^2}+\frac{\partial^2 T}{\partial y'^2}\right]k=\frac{w'}{\bar{w}'}\frac{Q}{A'} \qquad (3)$$

Introducing the dimensionless quantities

$$\phi=\frac{T-Tw}{Q/k},\ x'/R=x,\ y'/R=y,\ A'/R^2=A$$

$$w=\frac{-w'}{\left(\frac{g_c}{\mu}\frac{dP'}{dz'}R^2\right)} \quad \text{and} \quad \bar{w}=\frac{-\bar{w}'}{\left(\frac{g_c}{\mu}\frac{dP'}{dz'}R^2\right)} \qquad (4)$$

equation (3) becomes

$$\frac{\partial^2\phi}{\partial x^2}+\frac{\partial^2\phi}{\partial y^2}=\frac{w}{A\bar{w}} \qquad (5)$$

Equation (5) defines the temperature field subject to appropriate boundary conditions. The local velocity w and the average velocity $\bar{w}$ are provided by the solution of the momentum equation [5].

A variational integral for the energy equation (5) is given by

$$I(\phi)=\int\int_A\left[\left(\frac{\partial\phi}{\partial x}\right)^2+\left(\frac{\partial\phi}{\partial y}\right)^2+\frac{2w}{A\bar{w}}\phi\right]dxdy \qquad (6)$$

The boundary conditions are

(i) $\phi=0$ on the pipe and fin walls

(ii) $\partial\phi/\partial n=0$ along lines of symmetry ($\theta=0$ and $\theta=\alpha$)

The finite element method was used in minimizing equation (6)

---

[1] Present address: Chemical Engineering Department, Princeton University, Princeton, N.J.

[2] Numbers in brackets designate References at end of paper

Contributed by the Heat Transfer Division for publication in the JOURNAL OF HEAT TRANSFER. Manuscript received by the Heat Transfer Division August 29, 1975. Paper No. 76-HT-SS.

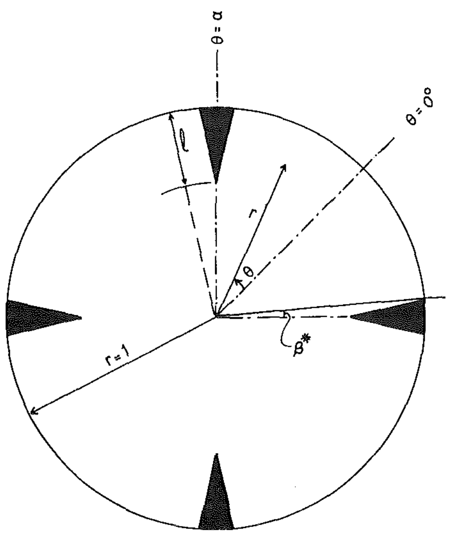

Fig. 1 Finned tube geometry

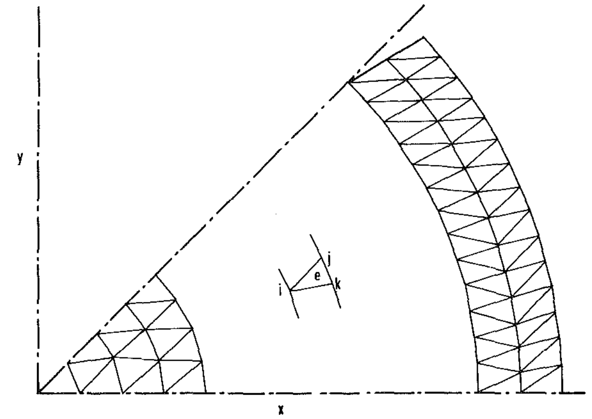

Fig. 2 Finite elements grid

where such a minimization is equivalent to a direct solution of equation (5). The entire flow regime was divided into E triangular elements as shown in Fig. 2. A first degree polynomial was used to describe the temperature within a triangular element. The boundary conditions were introduced into the resulting system of linear equations in the manner suggested by [6] and they were solved by Gaussian elimination method in double precision. The solution provides the dimensionless fluid temperature, ϕ, as a function of position.

The heat transfer coefficient, h_i, based on the inside tube diameter, is defined as

$$Q\Delta z' = h_i(T_w - T_b)\Delta z' = 2\pi R$$

leading to

$$h_i = \frac{Q}{2\pi R(T_w - T_b)} \tag{7}$$

The Nusselt number based on inside tube diameter is then given by

$$\mathrm{Nu}_i = 2h_iR/k = -1/(\pi\phi_b) \tag{8}$$

where

$$\phi_b = \frac{(T_b - T_w)}{Q/k} \quad \text{and } T_b = \frac{\int\int_A wTdA}{\bar{w}A}$$

Another form of heat transfer coefficient, h_e, based on the equivalent tube diameter is defined as

$$\Delta z'Q = h_e(T_w - T_b)C'\Delta z'$$

leading to

$$\mathrm{Nu}_e = h_eDe'/k = -De/(C\phi_b) \tag{9}$$

where Nu_e is the Nusselt number based on the equivalent diameter. The Nusselt number, Nu_i, is a more useful quantity defining the effectiveness of a finned tube to a designer.

The friction coefficient, f, is given by

$$f = \frac{2A'g_c}{C'\rho\bar{w}'^2}\frac{dP}{dz'} \tag{10}$$

Nomenclature

A = dimensionless cross-sectional flow area $(= A'/R^2)$
C = dimensionless wetted perimeter $(= C'/R)$
C_p = specific heat, J/kg°C
De = dimensionless equivalent diameter $(= De'/R = 4A/C)$
D_0 = dimensionless tube diameter $(= D_0/R = 2)$
E = total number of finite elements
f = Fanning friction factor
$(f\mathrm{Re})_d$ = design fRe, defined by equation (13)
g_c = proportionality constant in Newton's second law of motion, (kg/kgf)(m/s^2)
ℓ = dimensionless fin length $(= \ell'/R)$
$\dot{m}$ = mass flow rate, kg/s
n = normal vector
N = number of fins
Nu_i = Nusselt number based on inside diameter
Nu_e = Nusselt number based on equivalent diameter
P' = dimensional pressure, kgf/m^2
Q = heat transfer rate per unit tube length, J/(ms)
R = tube radius, m
Re = Reynolds number $(= \bar{w}'\rho De'/\mu)$
T = temperature, °C
w = dimensionless local velocity

$$\left(= \frac{-w'}{\frac{g_c}{\mu}\frac{dP'}{dz'}R^2}\right)$$

$\bar{w}$ = dimensionless average velocity

$$\left(= \frac{-\bar{w}'}{\frac{g_c}{\mu}\frac{dP'}{dz'}R^2}\right)$$

x = x-coordinate, dimensionless $(= x'/R)$
y = y-coordinate, dimensionless $(= y'/R)$
z' = axial coordinate, m
α = semiangle of fin separation
β^* = half fin angle, degrees
β^+ = half fin angle, radians
γ = circular sector opening angle
θ = angular coordinate
μ = fluid, viscosity, kg/ms
ρ = fluid density, kg/m^3
ϕ = dimensionless temperature, $(= (T - T_w)/(Q/k))$

Superscripts

— = average value
′ = dimensional quantity
(e) = element e

Subscripts

b = bulk value
e = based on equivalent diameter
i = based on inside diameter
o = based on inside diameter
i, j, k = indices of triangular element (e)
w = wall value

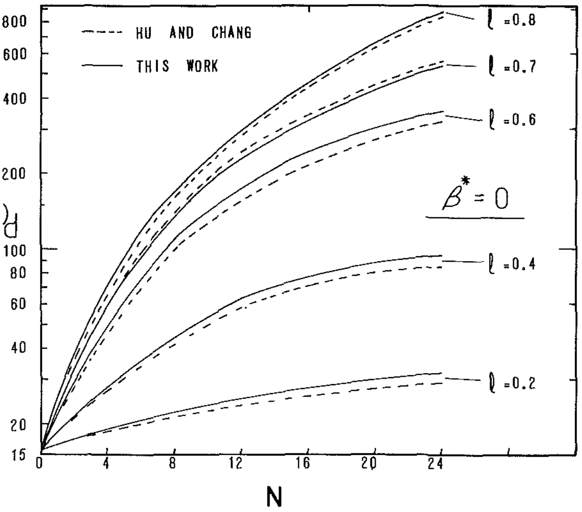

Fig. 3 Variation of $(f\text{Re})_d$ with fin number for $\beta^* = 0$ deg

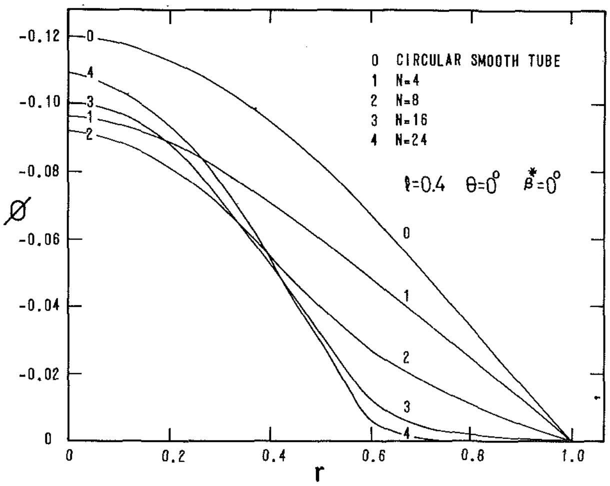

Fig. 4 Dimensionless temperature variation in radial direction for $\ell = 0.4$ and $\beta^* = 0$ deg along $\theta = 0$ deg

Defining $\text{Re} = \rho De\bar{w}'/\mu$ and introducing the dimensionless quantities, equation (10) yields

$$f\text{Re} = 8A^2/C^2\bar{w} \qquad (11)$$

The wetted perimeter, C', and the flow area, A' are given by:

$$C' = 2\pi R + 2N[(R - \ell')^2 + R^2 - 2R(R - \ell') \cos \beta^+]^{1/2} - 2N\beta^+ R$$

and

$$A' = \pi R^2 - N\beta^+ R^2 + NR(R - \ell') \sin \beta^+$$

A more useful correlation for fRe from a design point of view can be given by[3]

$$(f\text{Re})_d = f\text{Re} \cdot (A'^3/C'^2)_{\text{finless}}/(A'^3/C'^2)_{\text{finned}} \qquad (12)$$

where

$$(f\text{Re})_d = \frac{g_c\rho}{2\mu\,\dot{m}}\frac{\Delta P}{dz'}(D_e'^2A')_{\text{finless}} \qquad (13)$$

and $\dot{m}$ is the mass flow rate.

Discussion of Results

When the fin thickness is zero, equation (12) reduces to $(f\text{Re})_d = (f\text{Re})(2R/De')^2$. Using the notation of Hu and Chang, $(f\text{Re})_d$, is the quantity $[f\text{Re}_0(D_0/De)]$ which is used in their work and which gave a better correlation for the friction factor. Consequently, the results of this study are to be compared with their work using $(f\text{Re})_d$ for the case of $\beta^* = 0$ deg. Fig. 3 shows the variation of $(f\text{Re})_d$ with the fin number for a zero fin thickness. The results of Hu and Chang are included for comparison. Hu and Chang used a semianalytical approach to obtain $(f\text{Re})_d$ values. In general, the agreement is fairly good especially for $\ell \geq 0.7$. It should be pointed out that in the present analysis, the temperature variation within an element was assumed to be linear and consequently an inherent approximation to the general solution exists. No special numerical consideration was found to be necessary at the fin tip. As the flow is rectilinear, the only flow boundary condition is that of no-slip. The typical singularity of the vorticity and consequently that of shear stress does not appear in the solution. To avoid any numerical instability, fRe and Nu_i were evaluated using the bulk velocity and the bulk temperature, respectively, rather than from velocity and temperature gradients at the solid surface.

The variation of the dimensionless temperature, ϕ, with radial position along $\theta = 0$ deg, for various number of fins, is shown in Figs. 4 and 5 for $\ell = 0.4$ and 0.8, respectively. Because of the manner by which the temperature was dimensionalized, a large negative value of ϕ indicates a low value of T. The maximum value of ϕ is zero and it is equivalent to having the temperature, T, equal to the wall temperature, T_w. Figs. 4 and 5 show that the dimensionless fluid temperature near the tube wall, within the fin region, increases with the increase of the number of fins. However, the fluid temperature near the tube centre away from the fins first increases with an increase in N but decreases with further increase in the number of fins. For both $\ell = 0.4$ and 0.8 such a reversal occurred between $N = 8$ and $N = 16$. For $\ell = 0.4$, the general shape of the temperature distribution is not very much different from that of a smooth tube especially for low values of N.

When the fin number is large, $N \geq 16$ and $\ell > 0.7$, the fin tips are close to each other and they act as an artificial envelope where the fluid velocity approaches zero and the dimensionless temperature, ϕ, becomes nearly zero. This situation leads to the formation of two regions; a fin region which extends from the tube wall to the fin tips and a core region extending from the fin tips to the tube center. The

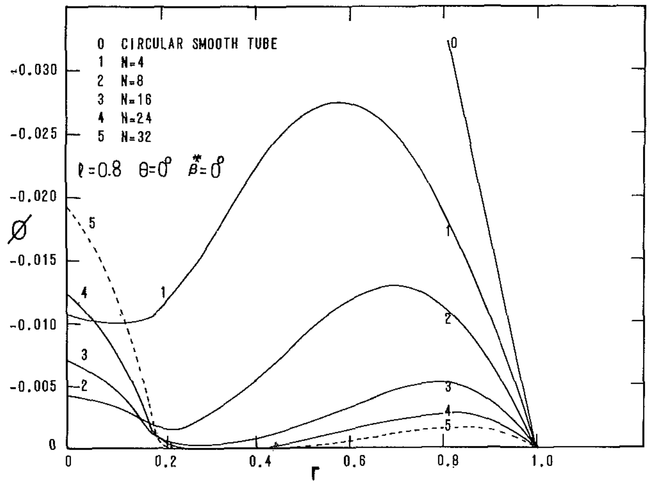

Fig. 5 Dimensionless temperature variation in radial direction for $\ell = 0.8$ and $\beta^* = 0$ deg along $\theta = 0$ deg

---

[3] Equations (12) and (13) were suggested by Dr. R. H. Shah, of Harrison Radiators.

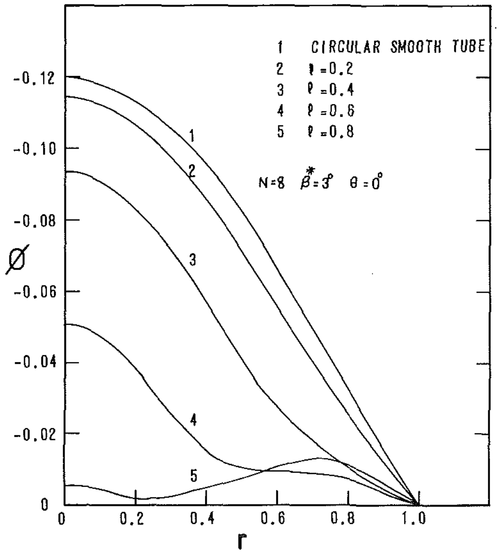

Fig. 6 Dimensionless temperature variation in radial direction along $\theta = 0$ deg for $N = 8$ and $\beta^* = 3$ deg

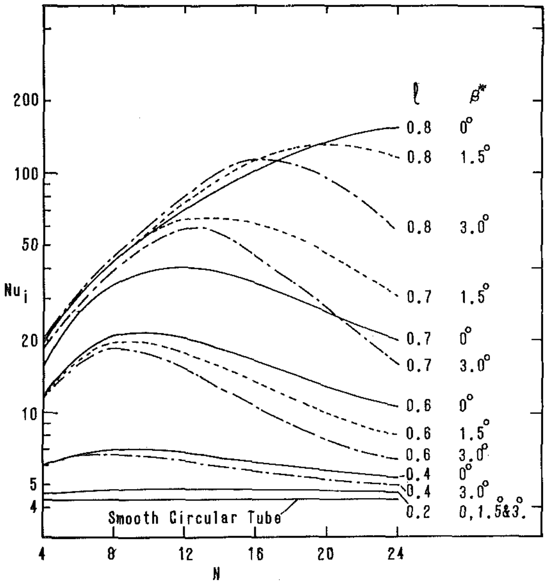

Fig. 8 Nusselt number variation with fin number

fin region is very much the same as for the flow in a circular sector and the core region approaches that for a finless circular tube. Such two regimes are evident from Fig. 5.

The effect of the fin length on the temperature distribution along $\theta = 0$ deg for $\beta^* = 3$ and $N = 8$ is shown in Fig. 6. For $\ell = 0.2$, the temperature variation is similar to that of a smooth tube indicating that short fins do not alter to a great extent the temperature profile. As ℓ is increased, the influence of the fin length becomes much more pronounced. For $\ell = 0.8$, the minimum fluid temperature no longer occurs at the tube center but shifts towards the fin region. The dimensionless temperature distribution along $\theta \approx \alpha$ with $\ell = 0.8$ is given in Fig. 7 for $\beta^* = 0$ and 3 deg. The influence of the fin thickness on the temperature variation near the tube center is more pronounced when N is large.

The variation of the limiting Nusselt number Nu$_i$, based on the inside diameter, with the number of fins N is shown in Fig. 8 for $\beta^* = 0$, 1.5, and 3 deg. In the range studied, it is shown that for a given fin length, the Nusselt number which is a measure of the heat transfer coefficient does not necessarily increase with an increase in the number of fins. Nu$_i$ exhibits a maximum for a given ℓ and such a maximum value occurs at $8 < N < 14$ for $0.2 \leq \ell \leq 0.7$ for all values of β^*. The existence of such a maximum can be explained in that by increasing the number of fins for a given ℓ, the fluid velocity either near the fins tips (for $\ell \geq 0.7$) or in the fin tube region (for $\ell \leq 0.7$) becomes low. In these regions, the temperature gradients are small, as shown in Fig. 4 and 5, and consequently the fluid acts as an insulator between the inner fluid core and the wall. For low values of N, the increase in the surface area due to the presence of the fins over rides the "fluid insulating effect," and Nu$_i$ increases with N. However, as N is further increased the effect of the fluid insulation dominates and Nu$_i$ decreases with an increase in N.

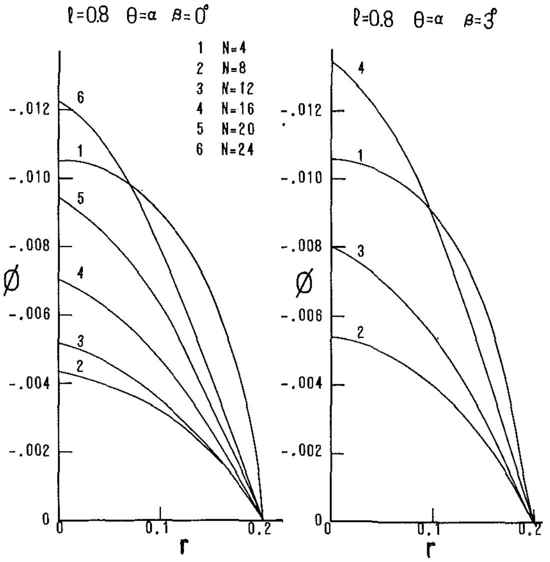

Fig. 7 Dimensionless temperature variation in radial direction along $\theta = \alpha$ with $\ell = 0.8$ for $\beta^* = 0$ and 3 deg

For $\ell = 0.8$ and $\beta^* = 0$ deg a maximum also occurs as it was found that at $N = 60$, Nu$_i$ = 34 which is lower than that given at $N = 24$, as shown in Fig. 8. The effect of β^* on Nu$_i$ for a given ℓ is dependent on the value of ℓ itself. For $\ell \leq 0.2$, Nu$_i$ is a very weak function of β^* and for $0.2 \leq \ell \leq 0.7$ and a given N, Nu$_i$ increases with decrease in β^*. However, for $\ell > 0.7$, the effect of β^* on Nu$_i$ becomes more complicated as is shown in Fig. 8.

In all the cases considered, the Nusselt number for the finned tubes was found to be higher than that for a smooth tube. In certain cases, the improvement in heat transfer was as high as 20 fold. As only the limiting flow case of fully developed velocity and temperature profiles was considered, the Nusselt number thus evaluated is independent of the Reynolds number and consequently the usual engineering comparison of "constant power" cannot be made [2, 3].

Tabulated values for the Nusselt number and fRe for the various fin geometry are given in Table 1.

Limiting Cases

In order to gain confidence in any numerical procedure it is desirable to consider limiting cases especially when the answer for such cases is already known with some certainty.

For the case of an internally finned tube, when the fin length is zero, one obtains a smooth finless tube. Here the finite element method gave fRe = 16.06 and Nu$_i$ = 4.34 compared with the exact values of 16 and 4.3636, respectively, leading to a maximum error of less than 0.6 percent.

Another limiting case considered is that for $\ell = 1$ and $\beta^* = 0$ deg, here one obtains a circular sector. The problem of fluid flow and heat

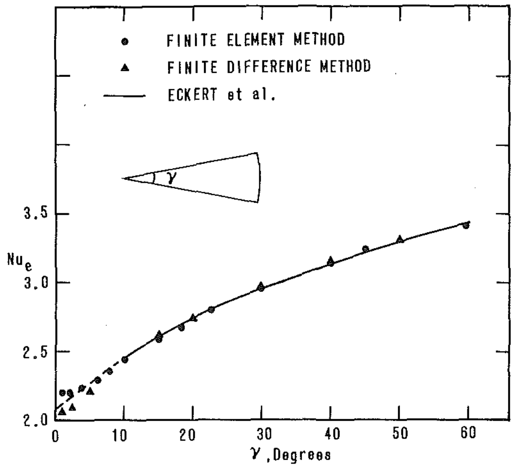

Fig. 9 Nusselt number variation with circular sector opening angle

Table 1 Values of fRe and Nu_i for finned tubes

$\beta^* = 0^0$

	ℓ=0.2		ℓ=0.4		ℓ=0.6		ℓ=0.7		ℓ=0.8	
N	fRe	Nu_i	fRe	Nu_i	fRe	Nu_i	fRe	Nu_i	fRe	Nu_i
4	12.15	4.58	12.75	6.05	16.17	11.82	16.58	15.34	18.02	19.30
8	9.83	4.74	11.54	6.98	17.34	21.10	17.74	34.27	18.48	42.58
12	8.21	4.77	10.05	6.65	16.59	20.52	17.27	40.92	18.43	72.27
16	6.92	4.74	8.44	6.09	14.96	16.22	16.13	34.45	18.25	106.5
20	5.87	4.68	7.00	5.64	13.15	12.73	14.75	26.07	18.00	138.3
24	5.01	4.62	5.81	5.32	11.42	10.41	13.33	19.83	17.68	156.9

$\beta^* = 1.5^0$

	ℓ=0.2		ℓ=0.4		ℓ=0.6		ℓ=0.7		ℓ=0.8	
N	fRe	Nu_i	fRe	Nu_i	fRe	Nu_i	fRe	Nu_i	fRe	Nu_i
4	12.58	4.58	12.93	6.03	16.25	11.72	18.77	18.02	18.07	19.29
8	10.36	4.73	11.64	6.85	17.29	20.01	20.46	43.26	18.67	43.60
12	8.71	4.75	9.91	6.42	16.16	12.82	20.54	64.58	18.74	76.17
16	7.34	4.71	8.07	5.82	14.03	13.15	19.86	63.21	18.63	112.1
20	6.18	4.64	6.44	5.37	11.71	9.95	18.70	46.17	18.35	131.9
24	5.22	4.58	5.13	5.07	9.57	8.02	17.19	30.86	17.87	117.5

$\beta^* = 3^0$

	ℓ=0.2		ℓ=0.4		ℓ=0.6		ℓ=0.7		ℓ=0.8	
N	fRe	Nu_i	fRe	Nu_i	fRe	Nu_i	fRe	Nu_i	fRe	Nu_i
4	12.98	4.58	13.13	6.00	16.33	11.63	18.70	17.82	18.12	19.29
8	10.87	4.71	11.72	6.71	17.20	18.87	20.47	43.31	18.88	44.88
12	9.19	4.73	9.74	6.19	15.59	15.30	20.45	58.88	19.10	80.81
16	7.73	4.67	7.63	5.57	12.84	10.64	19.35	45.28	19.02	112.4
20	6.47	4.60	5.83	5.14	9.96	7.91	17.37	26.75	18.54	98.2
24	5.40	4.54	4.42	4.87	7.44	6.42	14.77	16.01	17.45	56.04

transfer in circular sectors had been solved numerically by Eckert, et al. [7], where they used a collocation method for solution. It was felt desirable to resolve the circular sector case with finite difference method where second order central difference formulae are used to represent the derivatives of both the momentum and the energy equations. The results given by the finite difference method could be considered as the "true solution" to the problem. A 21 × 21 grid was used and it was found that the results from a 15 × 15 grid agreed within 0.5–1 percent with the smaller grid. A comparison between the finite element, the finite difference and the collocation methods is shown in Fig. 9. The agreement between the three techniques as given by the value of Nu_e is good and for $\gamma > 5$ deg, the finite element technique is in excellent agreement with that of the finite difference method. This is a further proof of the validity of the results presented in this work.

It is of interest to note that even though the equivalent diameter of a circular sector as $\gamma \rightarrow 0$ approaches that of infinite parallel plates or that of a rectangular channel with an aspect ratio of infinity, the Nusselt number as given for the circular sector is about one quarter smaller than that of parallel plates or that of a rectangular channel with an aspect ratio of infinity [8].

Conclusion

The analysis of fully developed laminar flow in internally finned tubes indicates that the Nusselt number, based on the tube diameter, is a strong function of the fin length and fin thickness. Also there exists an optimum fin number for a given fin configuration. A similar conclusion was also reached by Hu and Chang for the analysis of fully developed laminar flow where a constant and uniform heat flux is assumed to apply over the tube and fin surfaces.

In all cases considered, the Nusselt number was higher than that for a finless tube. As in fully developed velocity and temperature fields of a laminar flow, the Nusselt number becomes independent of Reynolds number, the constant power criterion to compare finned and finless tubes cannot be utilized. Here, for a given mass flow rate, the larger the number of fins and their length, the higher is the tube wall stress.

It should be pointed out that the optimum number of fins as found in the present analysis was obtained in a rather idealized situation, namely: 100 percent fin efficiency, fully developed fluid and temperature fields and constant fluid properties. However, such an analysis is the first step that should be taken before the more realistic situation is considered. Moreover, in certain circumstances such an idealization is quite applicable and the present findings of improved heat transfer coefficients are useful in the design of compact heat exchangers.

Acknowledgment

The authors wish to thank the University of Saskatchewan for financial aid and Prof. Paul Watkinson for his encouragement to initiate this research project.

References

1 Bergles, A. E., "Survey and Evaluation of Techniques to Augment Convective Heat and Mass Transfer," *Progress in Heat and Mass Transfer*, Vol. 1, Pergamon Press, Elmsford, N. Y., 1969, pp. 331–424.

2 Watkinson, A. P., Miletti, D. L., and Tarassoff, P., "Turbulent Heat Transfer and Pressure Drop in Internally Finned Tubes," AIChE *Symposium Series*, Vol. 69, No. 131, 1973, pp. 94–103.

3 Watkinson, A. P., Miletti, D. L., and Kubanek, G. R., "Heat Transfer and Pressure Drop of Internally Finned Tubes in Laminar Oil Flow," ASME Paper No. 75-HT-41, presented at the AIChE-ASME Heat Transfer Conference, San Francisco, Cal., Aug. 1975.

4 Hu, M. H., and Chang, Y. P., "Optimization of Finned Tubes for Heat Transfer in Laminar Flow," JOURNAL OF HEAT TRANSFER, TRANS. ASME, Series C, Vol. 95, 1973, pp. 332–338.

5 Nandakumar, K., and Masliyah, J. H., "Fully Developed Viscous Flow in Internally Finned Tubes," The *Chem. Eng. Journal*, Vol. 10, 1975, pp. 113–120.

6 Myers, G. E., *Analytical Methods in Conduction Heat Transfer*, McGraw-Hill, New York, 1971.

7 Eckert, E. R. G., Irvine, T. F., Jr., and Yen, J. T., "Local Laminar Heat Transfer in Wedge-Shaped Passages," TRANS. ASME, Vol. 81, 1959, pp. 1433–1438.

8 Sparrow, E. M., and Siegel, R., "A Variational Method for Fully Developed Laminar Heat Transfer in Ducts," TRANS. ASME, Vol. 81, 1959 pp. 157–167.

P. Carajilescov
Instituto Tecnológico de Aeronáutica,
São Jose dos Campos, Brazil

N. E. Todreas
Massachusetts Institute of Technology,
Cambridge, Mass.

Experimental and Analytical Study of Axial Turbulent Flows in an Interior Subchannel of a Bare Rod Bundle

Reactor fuel elements generally consist of rod bundles with the coolant flowing axially through the bundles in the space between the rods. Heat transfer calculations form an important part in the design of such elements, which can only be carried out if information of the velocity field is available. A one-equation statistical model of turbulence is applied to compute the detailed description of velocity field (axial and secondary flows) and the wall shear stress distribution of steady, fully developed turbulent flows with incompressible, temperature-independent fluid, flowing through triangular arrays of rods with different aspect ratios (P/D). Also experimental measurements of the distributions of the axial velocity, turbulence kinetic energy, and Reynolds stresses were performed using a laser Doppler anemometer (LDA), operating in a "fringe" mode with forward scattering, in a simulated interior subchannel of a triangular rod array with P/D = 1.123 and $L/D_H = 77$. From the experimental results, a new mixing length distribution is proposed. Comparisons between the analytical results and the results of this experiment as well as other experimental data available in the literature are presented. The results are in good agreement.

1 Introduction

Nuclear reactor fuel elements generally consist of rod bundles in which each rod is composed of fissile material cladded by a suitable canning. In the space between the rods, the coolant flows axially through the bundle.

The present trend of reactor thermo-hydraulics analysis is the use of combined approaches of lumped and distributed parameter methods. The lumped parameter approach would yield the average temperature of the flow in the subchannel and the application of the distributed parameter method would then provide the fuel element surface temperature distribution through a multiregion thermal analysis, since, in many cases, the surface temperature of the fuel rods limits the thermal power that can be generated by the reactor.

In the present study, a one-equation statistical model of turbulence is applied to an interior subchannel of a bare rod bundle with smooth rods (see Fig. 1). Some of the constants involved in the analytical model were deduced from the experimental data obtained with a laser Doppler anemometer (LDA) within a test section with cross section simulating an interior subchannel of a bare rod bundle with triangular array with $P/D = 1.123$ and $L/D_H = 77$.

2 Theoretical Background Information

For a steady, fully developed turbulent flow with incompressible, temperature-independent property fluid and neglecting body forces, the Navier-Stokes and continuity equations are reduced to the axial momentum, vorticity, and stream function equations.

These equations can be written in the general form:

$$a_\phi \left[\frac{1}{r}\frac{\partial}{\partial r}\Phi\frac{\partial\psi}{\partial\theta} - \frac{\partial}{r\partial\theta}\Phi\frac{\partial\psi}{\partial r} \right] - \left[\frac{1}{r}\frac{\partial}{\partial r} r\left(b_\phi\frac{\partial\Phi}{\partial r}\right) + \frac{\partial}{r\partial\theta}\left(b_\phi\frac{\partial\Phi}{r\partial\theta}\right) \right] = S_\phi \quad (1)$$

Contributed by the Heat Transfer Division and presented at the Winter Annual Meeting, Houston, Texas, November 30–December 5, 1975, of THE AMERICAN SOCIETY OF MECHANICAL ENGINEERS. Revised Manuscript received by the Heat Transfer Division January 22, 1976. Paper No. 75-WA/HT-51.

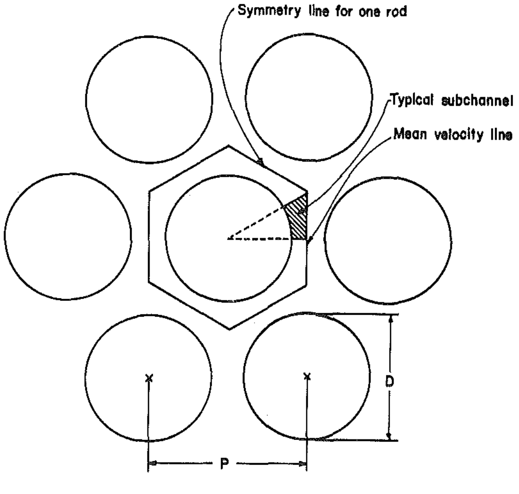

Fig. 1 Fuel bundle geometry with triangular array of rods

Table 1 Differential equations and boundary conditions

PARAMETERS OF DIFFERENTIAL EQUATIONS

Φ	a_ϕ	b_ϕ	s_ϕ
v_z	1	$1+\frac{\nu_T}{\nu}$	$-\frac{1}{\rho\nu}\frac{\partial p}{\partial z}$
ω	1	1	$-\frac{1}{\nu}\frac{\partial}{r\partial\theta}\left[\frac{1}{r}\frac{\partial}{\partial r}r\,(\overline{v_\theta'^2}-\overline{v_r'^2})\right]$ $-\frac{1}{\nu r}(\overline{rv_r'v_\theta'})\left[\frac{\partial}{\partial r}\frac{1}{r}\frac{\partial}{\partial r}r-\frac{\partial^2}{r^2\partial\theta^2}\right]$
ψ	0	1	$\frac{\omega}{\nu}$
K	1	$1+\frac{\nu_T}{\nu\sigma_k}$	$\frac{\nu_T}{\nu}\left[(\frac{\partial v_z}{\partial r})^2+(\frac{\partial v_z}{r\partial\theta})^2\right]-\frac{c_D K^{3/2}}{\ell}$

BOUNDARY CONDITIONS

Wall	Mean Velocity Line	$\theta = 0°$ and $\theta = \theta_{max}$
$v_z = \frac{v_\tau}{\kappa}\log\frac{Ev_\tau y}{\nu}$	$\frac{\partial v_z}{\partial r} = \frac{\partial v_z}{r\partial\theta}\tan\theta$	$\frac{\partial v_z}{\partial\theta} = 0$
$\omega_o = -\frac{\omega_1}{2} - \frac{3\nu}{(r_1-R)^2}$ (*)	$\omega = 0$	$\omega = 0$
$\psi_o = 0$	$\psi = 0$	$\psi = 0$
$K = \frac{c_\nu}{c_D\kappa^2}v_\tau^2$	$\frac{\partial K}{\partial r} = \frac{\partial K}{r\partial\theta}\tan\theta$	$\frac{\partial K}{\partial\theta} = 0$

* See Reference 16

where the parameters are given in Table 1. Reference [1][1] provides full details of the derivation of these equations.

3 Review of the Literature

The methods designed to provide the Reynolds stresses can be generally classified into three categories: (*a*) The phenomenological turbulence models, where an attempt is made to explain the behavior of turbulent eddies and how the turbulent shear stresses are created. Prandtl's mixing length theory and Buleev's model [2] are in this group. These two approaches have been applied to rod bundles [3, 4]. (*b*) The eddy diffusivity methods, where the turbulent shear stresses are related to axial velocity gradients by an exchange or eddy diffusivity coefficient, obtained experimentally or deduced on theoretical grounds. Nijsing [5] has applied this approach to rod bundles. (*c*) Higher-order closure models. This group of models assumes that the fluctuations are random in nature and that a few of the statistical properties of turbulence are supposed to obey laws of generation, dissipation, and transport.

The one- and two-equation models relate the Reynolds stresses to axial velocity gradients with the exchange coefficient or turbulent viscosity, ν_T, given by

$$\nu_T = c_\nu K^{1/2}\ell \qquad (2)$$

where K is the turbulence kinetic energy, ℓ is a mixing length, and c_ν is a constant. K is calculated by a transport equation. ℓ can be given either by an algebraic expression [6] (one-equation model) or a transport equation of a related property (two-equation model). As far as the authors know, none of these models have been applied to rod bundles.

Regarding methods applied to rod bundles, it is worth also mentioning the method developed by Ibragimov and coworkers [8] and used by Bender and Magee [9]. Here a wall shear stress distribution is given by a semiempirical formula and universal velocity distributions are taken along radial lines.

Rod bundle experimental data, using a Pitot tube, for the axial velocity distribution, have been reported by Eifler and Nijsing [10] and Subbotin [11]. Kjellström [12] and Trupp and Azad [13] used hot wire anemometers to measure velocity, turbulent intensities, and cross correlations, for different Re but at $P/D \geq 1.20$. Hall and

---

[1] Numbers in brackets designate References at end of paper.

Nomenclature

c_1 = constant in pressure-velocity gradient correlation
c_2 = constant in main rate of strain-turbulence correlation
c_D = constant in the dissipation rate of TKE
c_ν = constant in turbulent viscosity
d_f = distance between two consecutive fringes in probe volume
D = rod diameter
D_H = hydraulic diameter of subchannel
E = constant in "law of the wall"
K = turbulence kinetic energy
ℓ = mixing length
L = length of test section from inlet to measuring station
P = pitch of rod array
p = time-averaged pressure
r = radial coordinate
Re = Reynolds number
v_b = bulk velocity
v_i = time-averaged velocity component in the direction i
v_i' = fluctuating component of velocity in the direction i
v_τ = local friction velocity $[\equiv (\tau_w/\rho)^{1/2}]$
y = distance from rod to point of interest in the radial direction
$\hat{y}$ = distance from rod wall to maximum velocity line
z = axial direction of flow
ϵ = dissipation rate of turbulence kinetic energy
ψ = stream function defined by $\bar{v}_\theta \equiv -\nu(\partial\psi/\partial r)$; $\bar{v}_r \equiv \nu(\partial\psi/r\partial\theta)$
κ = constant in "law of the wall"
ν = kinematic viscosity
ν_T = turbulent viscosity
ρ = fluid density
θ = angular coordinate
τ_w = wall shear stress
ω = vorticity

Svenningsson [20] also attempted measurements of secondary flow in similar geometries. Rowe and coworkers [14] used a laser Doppler anemometer in the study of the turbulent crossflow mixing processes in different rod bundle subchannels.

4 Analytical Method

In this work, a one-equation statistical turbulence model is adopted. The transport equation for the turbulence kinetic energy, K, is

$$\frac{1}{r}\frac{\partial}{\partial r}rK\left(\frac{\partial\psi}{r\partial\theta}\right)-\frac{\partial}{r\partial\theta}K\left(\frac{\partial\psi}{\partial r}\right)-\frac{1}{r}\frac{\partial}{\partial r}r\left[\frac{\partial K}{\partial r}-\frac{\overline{v_r'K'}}{\nu}\right]$$
$$-\frac{\partial}{r\partial\theta}\left[\frac{\partial K}{r\partial\theta}-\frac{\overline{v_\theta'K'}}{\nu}\right]=-\frac{c_DK^{3/2}}{\nu\ell}$$
$$-\frac{1}{\nu}\left[\overline{v_r'v_z'}\left(\frac{\partial v_z}{\partial r}\right)+\overline{v_\theta'v_z'}\left(\frac{\partial v_z}{r\partial\theta}\right)\right] \quad (3)$$

where c_D is a constant, and, as an approximation, $\overline{v_i'K'}$ is evaluated as

$$\overline{v_i'K'}\simeq-\frac{\nu_T}{\sigma_k}\left(\frac{\partial K}{\partial\xi_i}\right) \quad (4)$$

where σ_k can be understood as an effective Prandtl number.

The mixing length distribution adopted is

$$\frac{\ell}{\hat{y}}=\frac{y}{\hat{y}} \quad \text{for } 0\le\frac{y}{\hat{y}}\le 0.44,$$
$$\frac{\ell}{\hat{y}}=0.44+0.66\sin\left[\frac{\pi}{0.38}\left(\frac{y}{\hat{y}}-0.44\right)\right], \quad \text{for } 0.44\le\frac{y}{\hat{y}}\le 1.0 \quad (5)$$

where $\hat{y}$ is the radial distance from the rod wall to the maximum velocity line. This distribution was obtained experimentally in this investigation, as will be discussed later.

Regarding the vorticity source term, Brundrett and Baines [15] observed that, for square ducts,

$$I_\omega\simeq-\frac{1}{\nu r}\frac{\partial}{\partial\theta}\frac{1}{r}\frac{\partial}{\partial r}r(\overline{v_\theta'^2}-\overline{v_r'^2}) \quad (6)$$

This is assumed here to be true also for rod bundles.

Following Launder and Ying's [6] approach that assumes for the transport equations for the normal Reynolds stresses in the tangential and radial directions:

(*a*) convection and diffusion are negligible near the solid wall;

(*b*) all turbulent intensity is produced in the axial direction and part of it is redistributed into the tangential and radial direction by pressure fluctuations;

(*c*) dissipation is assumed isotropic in the vorticity generating region (regions near solid walls).

The pressure redistributions of $\overline{v_\theta'^2}$ and $\overline{v_r'^2}$ are made equal to their dissipations, that is,

$$\overline{\frac{p'}{\rho}\frac{\partial v_\theta'}{r\partial\theta}}\simeq\frac{\epsilon}{3} \quad (7)$$

$$\overline{\frac{p'}{\rho}\frac{\partial v_r'}{\partial r}}\simeq\frac{\epsilon}{3} \quad (8)$$

where ϵ is the dissipation rate of turbulence kinetic energy. So, an approximate equation for $(\overline{v_\theta'^2}-\overline{v_r'^2})$ *is written as*

$$\overline{\frac{p'}{\rho}\left(\frac{\partial v_\theta'}{r\partial\theta}\frac{\partial v_r'}{\partial r}\right)}\simeq 0 \quad (9)$$

Hanjalić and Launder [7] showed that the correlation between pressure and velocity-gradient fluctuations arises mainly from two kinds of physical interactions. The first has its origin in the interaction between the main rate of strain and turbulence and the second from mutual interaction between turbulence components. Hence

$$\overline{\frac{p'}{\rho}\frac{\partial v_\ell'}{\partial\xi_m}}=\Phi_{\ell m,1}+\Phi_{\ell m,2} \quad (10)$$

where $\Phi_{\ell m,1}$ and $\Phi_{\ell m,2}$ represent the two interaction processes as discussed.

Following the procedure described in reference [7], which, for simplicity, will be omitted, equation (9) is finally reduced to

$$(\overline{v_\theta'^2}-\overline{v_r'^2})\simeq-c\ell^2\left[\left(\frac{\partial v_z}{r\partial\theta}\right)^2-\left(\frac{\partial v_z}{\partial r}\right)^2\right] \quad (11)$$

with

$$c=\frac{c_\nu}{c_D}\frac{2(6c_2-2)}{11(c_1-2c_2)} \quad (12)$$

where c_1 and c_2 are constants. This is the approach adopted in the present calculation.

Due to steep gradients of the velocity and turbulence kinetic energy distribution near the solid wall that would require very fine mesh space in the numerical procedure, the velocity over that region is assumed to be described by the universal velocity profile

$$v_z=\frac{v_\tau}{\kappa}\log\frac{Ev_\tau y}{\nu} \quad (13)$$

and the turbulence kinetic energy, neglecting diffusion and convection, is given by

$$K=\frac{c_\nu}{c_D\kappa^2}v_\tau^2 \quad (14)$$

The system of differential equations of Table 1 with the approximations of equations (6), (11), (13), and (14) were converted to finite difference form and solved by the method of successive displacements subject to the boundary conditions listed in Table 1. The constants of the model are given in Table 2. The convergence criteria used was that recommended by Gosman, et al. [16] which is based on the rate of the change of a variable to the maximum previous value in the field, $\phi_{\text{MAX}}^{(n-1)}$, i.e.,

$$\left|\frac{\phi_{i,j}^{(n)}-\phi_{i,j}^{(n-1)}}{\phi_{\text{MAX}}^{(n-1)}}\right|_{\text{MAX}}\le\lambda$$

where n denotes the nth iteration. λ here was taken equal to 0.0001. Complete details of the numerical procedure and the calculational grid utilized can be found in reference [1].

5 Experimental Apparatus

Measurements of the mean axial velocity, turbulent intensities, and pressure drop were performed in water flowing within a test section with a cross section shown in Fig. 2, using a laser Doppler anemometer (LDA). The symmetry of the assembled test section and the adequacy of the entrance configuration were checked by extensive measurements confirming the symmetry of the mean axial velocity at the measuring station. At this measuring station, windows were provided (as shown, also, in Fig. 2) on the four sides of the test section. To reduce refraction of the beams on curved

Table 2 Parameters of the model

Parameter	Value	Basis	Reference
c_ν	0.180	Mixing Length-distance from wall, for points near wall	this work
c_D	0.38	From measurements of K and v_τ	this work
κ	0.4186	Correlation of experimental data	Patel [17]
E	9.8	Correlation of experimental data	Patel [17]
σ_k	1.3	Arbitrarily taken. Results insensible to small variations	this work
c_1	3.0	Decay of non-isotropic turbulent flow in absence of velocity gradients	Rotta [18]
c_2	0.37	Nearly isotropic turbulent shear flow	Champagne et al [19]
ℓ	eq.(5)	From measurements	this work

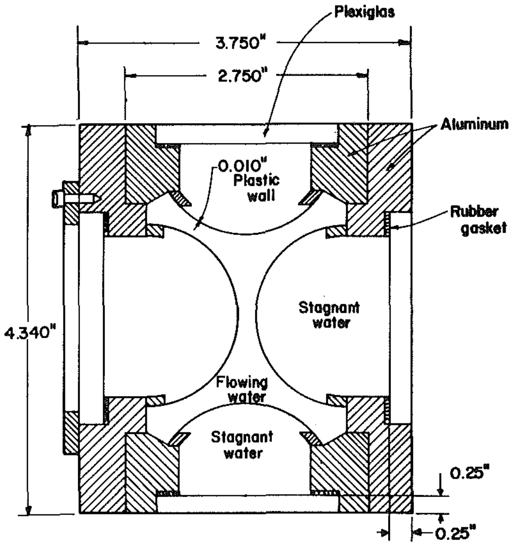

Fig. 2 Cross-sectional view of test section

surfaces of materials with different refractive indices to admissible levels, hollow rods were used at the measuring station, with apertures ½ in. wide. The hollow rods were covered by a thin plastic film, 0.010 in. thick, with water present on both sides of the film. A closed loop was used to circulate the water.

A schematic layout of the LDA is shown in Fig. 3. The LDA was operated in the "dual scattered beam mode" or "fringe mode."

All measurements were made in cartesian coordinates on individual velocity components along either axes x, y, and z or coordinates 1, 2, 3, and 4 at 45 deg to the axes x, z and y, z, respectively. The turbulence kinetic energy was obtained from the measured turbulent intensities by:

$$K = \frac{1}{2}(\overline{v_x'^2} + \overline{v_y'^2} + \overline{v_z'^2}) \tag{15}$$

and the cross correlations were also obtained from individual velocity component measurements by:

$$\begin{aligned}\overline{v_r'v_z'} &= \overline{v_x'v_z'}\cos\theta + \overline{v_y'v_z'}\sin\theta \\ &= \frac{1}{2}(\overline{v_1'^2} - \overline{v_2'^2})\cos\theta + \frac{1}{2}(\overline{v_3'^2} - \overline{v_4'^2})\sin\theta \qquad (16)\\ \overline{v_\theta'v_z'} &= \overline{v_y'v_z'}\cos\theta - \overline{v_x'v_z'}\sin\theta \\ &= \frac{1}{2}(\overline{v_3'^2} - \overline{v_4'^2})\cos\theta - \frac{1}{2}(\overline{v_1'^2} - \overline{v_2'^2})\sin\theta \qquad (17)\end{aligned}$$

Because the region separating the rods was so small, slight deviations in the measuring position would introduce large errors in the results from equations (15)–(17). Such deviations would occur if the measurements were attempted by trying to repeatedly bring a set of crossed beams to a measuring position. Consequently we defined each measuring position by focusing two sets of crossed beams and then performed the individual velocity component measurements sequentially. Simultaneous two component measurements which would have led to even smaller errors were not taken due to lack of a second tracker unit.

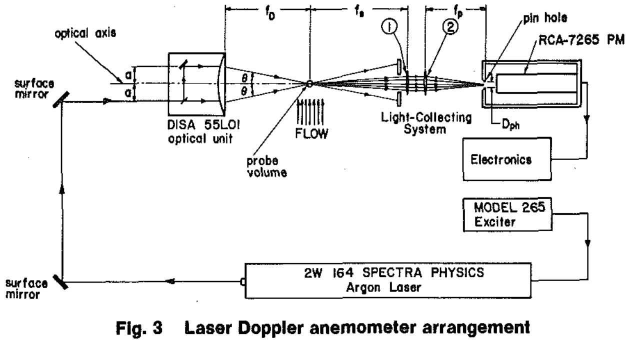

Fig. 3 Laser Doppler anemometer arrangement

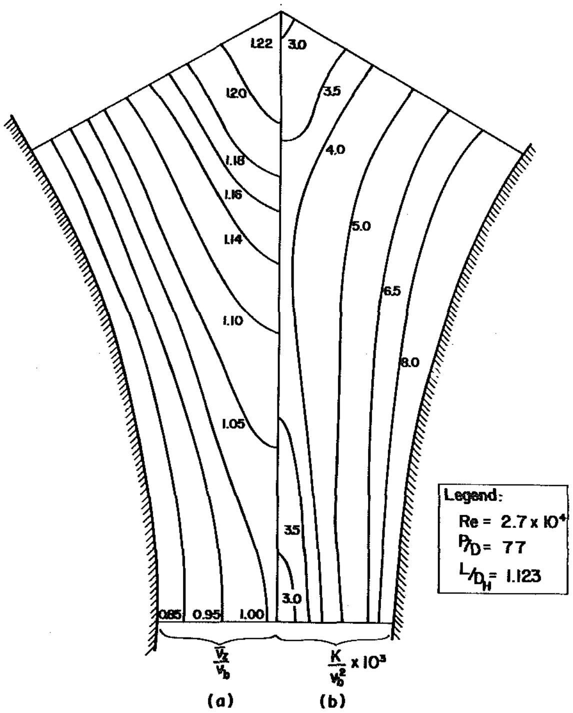

Fig. 4 Measured contour plots for normalized axial velocity and turbulent kinetic energy

An inclined manometer was used to measure the axial pressure drop between two tap holes drilled symmetrically with respect to the windows.

More details of this experiment design are provided by Carajilescov [1].

6 Results

The experimental measurements were performed along 11 radial lines, 3 deg apart, for Re = 2.7 × 10^4. Figs. 4(a), 4(b), and 5 show the distributions of v_z, K, and $\overline{v_r'v_z'}$. The values of $\overline{v_\theta'v_z'}$ obtained were very scattered due to their expected small values and the large experimental errors involved since the cross correlation was not directly measured. From these experimental data, the mixing length distribution was calculated by

$$c_\nu \ell = -\frac{\overline{v_r'v_z'}}{K^{1/2}\dfrac{\partial v_z}{\partial r}} \tag{18}$$

Its distribution is shown in Fig. 6 compared to the expression suggested by Buleev [2] which has been widely adopted. The average overall angular position was correlated in the form of equation (5), taking $\ell = y$ for points near wall. Based on this approach, c_ν was determined to be equal to 0.180.

From measurements of the pressure drop, the turbulent velocity, v_τ, was determined to be 7.4 × 10^{-2} m/s. With this value and the turbulence kinetic energy distribution, using equation (14), it was found that c_D equaled 0.30. However, better analytical results

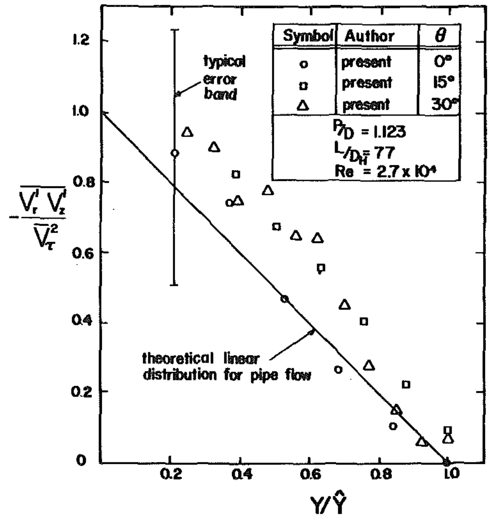

Fig. 5 Normalized Reynolds stress

were obtained with $c_D = 0.38$, which is the value adopted here. All computations were tried, then, with the constants shown in Table 2. However, since $c_\nu = 0.22$ and $c_D = 0.41$ are the most common values found in the literature, computations with those values are used for comparison. Ibragimov's method [8], used in the VELVET II code, was used also to obtain axial velocity and wall shear stress distributions for comparisons with the predictions of the method developed here.

Fig. 7 shows a comparison of the axial velocity distribution between the experimental results and the analytical models, for several angular positions. The error bands represent uncertainties in measurements associated with the electronics used in the experiment. Measurements performed at different times for same operating conditions showed that the error associated with the reproducibility of the data was very small compared to the electronics error. The present results are in close agreement with the experimental data. Predictions of wall shear stress distributions are shown in Figs. 8 and 9. The departure of the wall shear stress distribution from the simpler one predicted by the Ibragimov method can be explained by observing the shape of secondary flow streamlines, Figs. 10(*a*) and 10(*b*), predicted by the present method. Of the two swirls of secondary flows predicted, the closest to the gap is very weak compared to the other centered around $\theta \simeq$ (20–24) deg which practically affects only regions where θ is larger than about 12 deg. So, this strongest loop tends to homogenize only the wall shear stress distribution for large values of θ, while the region near the gap is not sensibly affected by secondary flows.

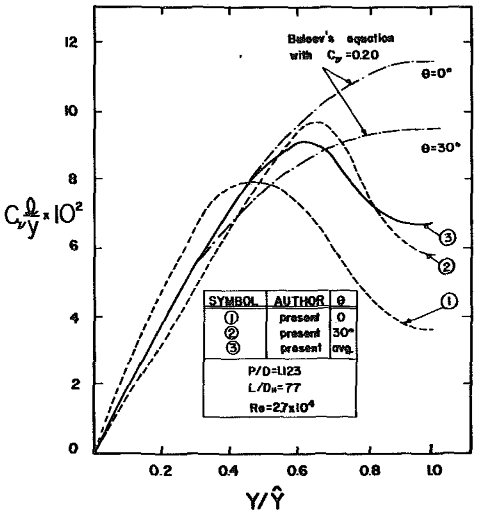

Fig. 6 Mixing length distribution

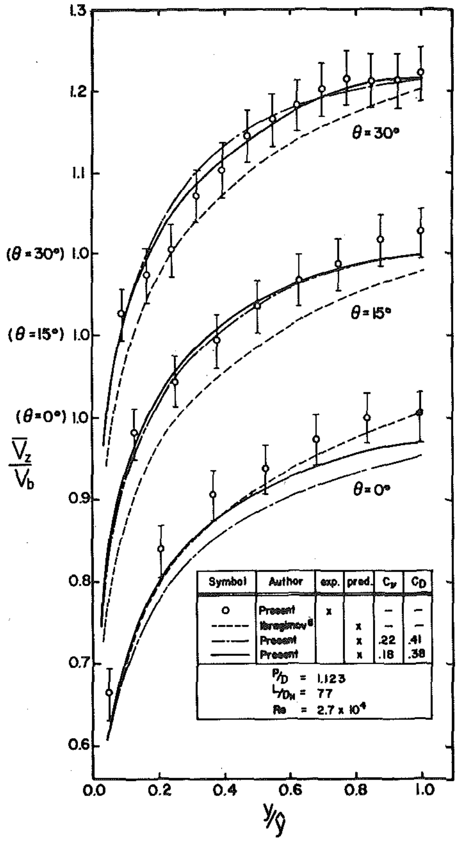

Fig. 7 Comparison between experimental and analytical axial velocity distributions

The effect of the Reynolds number, Re, on axial and secondary flow distributions was also studied. It was observed that the wall shear stress distribution becomes more uniform as Re increases. This is in contrast to the prediction of wall shear stress distribution using Ibragimov's method which is not affected by Re, since it is based only on geometric considerations. The secondary flows were found to increase with Re, (Fig. 11), although significant changes were not observed in the location of the secondary flow

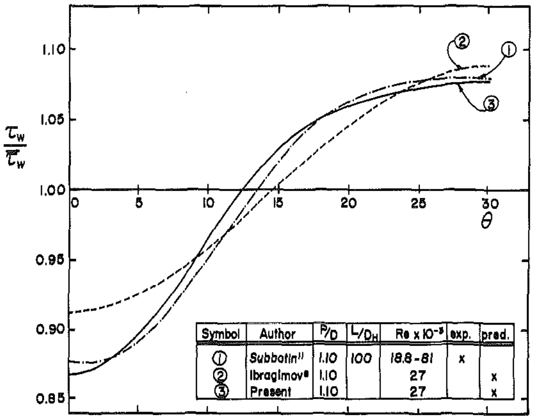

Fig. 8 Wall shear stress distribution for $P/D = 1.10$

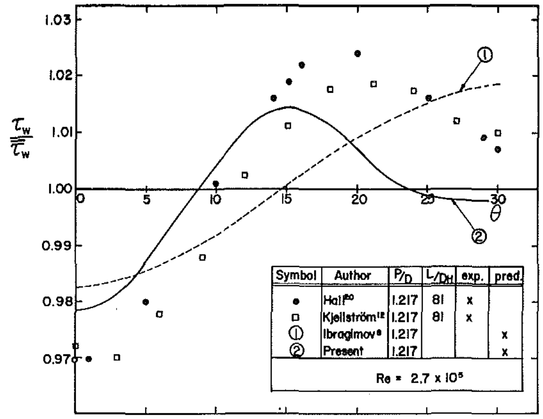

Fig. 9 Wall shear stress distribution for $P/D = 1.217$

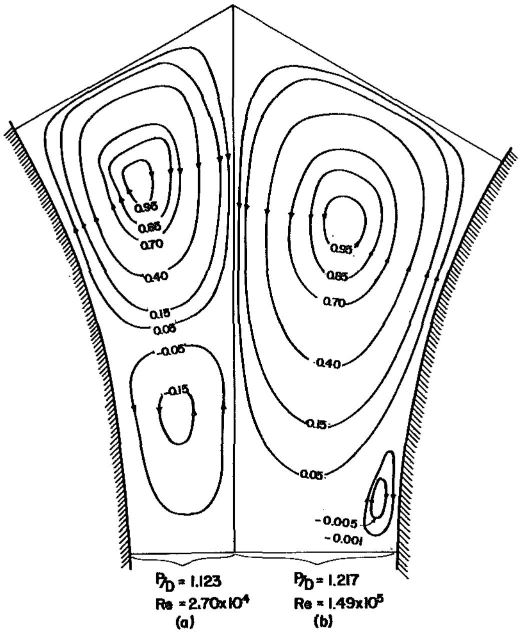

Fig. 10 Predicted normalized streamlines

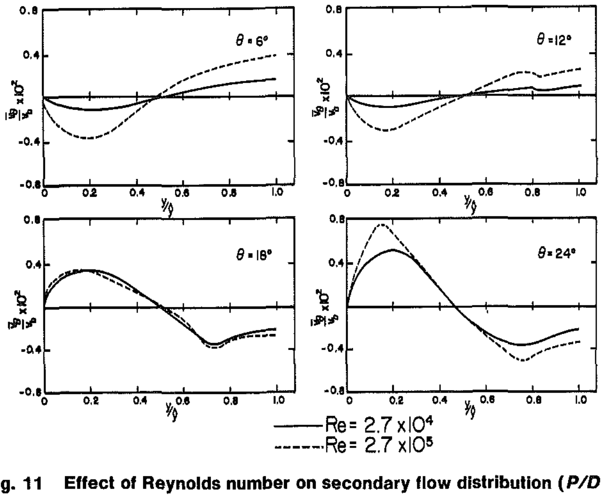

Fig. 11 Effect of Reynolds number on secondary flow distribution ($P/D = 1.123$)

swirls. Experimentally, a search conducted for secondary flows was inconclusive. However, the experimental error involved precluded identification of secondary flows having magnitude less than 0.67 percent of the bulk axial velocity. It was, therefore, concluded that the secondary flows within the test region (P/D = 1.123) at Reynolds number of 2.7×10^4 were less than 0.67 percent of the bulk axial velocity. The predictions are in agreement with this limitation.

7 Conclusions

Simple statistical models of turbulence, such as the one presented here, adopting the algebraic stress model expressed by equation (11) proposed by Launder and Ying [6], can provide reasonable predictions of axial velocity, wall shear stress, eddy diffusivity distribution, and friction factor for rod bundle subchannels. Also this model compared to previous approaches can take into account secondary flow effects without substantial increase in complexity. The predicted pattern of two swirls of secondary flows seems consistent with the good predictions of the wall shear stress distribution. This overall calculational model can provide the necessary hydrodynamic information to perform calculations of the temperature fields in coolant regions of rod bundles. However, it is anticipated that increased ease in numerical calculations can be achieved by treating the governing equations in terms of the variables of pressure and velocity rather than those employed here of vorticity and stream function.

Regarding the experimental aspects of this work, attention should be directed to our utilization of LDA in a geometry necessitating curved surfaces. Refraction problems certainly represent one of the major limitations of LDA in such geometries. The technique introduced here of designing to use thin transparent films can overcome this difficulty in many situations. Additionally the experimental search for secondary flows concluded that $\bar{v}_s/\bar{v}_b$ was equal to or less than 0.67 percent, a result in agreement with the analytic predictions for the test geometry at the Reynolds number of 2.7×10^4 investigated.

8 Acknowledgments

This research was conducted as part of the "Coolant Mixing in LMFBR Rod Bundles," contract AT(11-1)-224 sponsored by the USAEC at MIT. The authors gratefully acknowledge this support.

Pedro Carajilescov wants to thank the FAPESP—Fundação de Amparo a Pesquisa do Estado de São Paulo—Brazil, for granting him a fellowship during the preparation of this work.

The authors are grateful to David Gwinn, Francis L. Woodworth, and Albert T. Supple, Jr., members of the MIT Reactor staff, for the useful discussions during the design of the test section.

References

1 Carajilescov, P., "Experimental and Analytical Study of Axial Turbulent Flows in an Interior Subchannel of a Bare Rod Bundle," PhD thesis, Nuclear Engineering Department, MIT, Mar. 1975.

2 Buleev, N. I., "Theoretical Model of the Mechanism of Turbulent Exchange in Fluid Flow," AERE Translation 957, 1963.

3 Bender, D. J., and Switick, D. M., "Turbulent Velocity Distribution in a Rod Bundle," ASME Paper No. 68-WA/HT-36, 1969.

4 Ramm, H., and Johannsen, K., "Hydrodynamics and Heat Transfer in Regular Arrays of Circular Tubes," 1972 International Seminar on Recent Developments in Heat Exchangers, International Centre for Heat and Mass Transfer, Trogir, Yugoslavia, 1972.

5 Nijsing, R., "Heat Exchange and Heat Exchanger With Liquid Metals," AGARD-LS-57-72, 1972.

6 Launder, B. E., and Ying, W. M., "Prediction of Flow and Heat Transfer in Ducts of Square Cross-Section," *The Institution of Mechanical Engineering, Proceedings,* Vol. 187, 1973, 37/73, pp. 455–461.

7 Hanjalić, K., and Launder, B. E., "A Reynolds Stress Model of Turbulence and Its Application to Thin Shear Flows," *Journal of Fluid Mechanics,* Vol. 52, Part 4, 1972, pp. 609–638.

8 Ibragimov, M. Kh., et al., "Calculation of the Tangential Stresses at the Wall of a Channel and the Velocity Distribution in a Turbulent Flow of Liquid," *Soviet Atomic Energy,* Vol. 21, No. 2, 1966, pp. 731–739.

9 Bender, D. J., and Magee, P. M., "Turbulent Heat Transfer in a Rod Bundle With Liquid Metal Coolant," GEAP-10052, 1969.

10 Eifler, W., and Nijsing, R., "Experimental Investigation of Velocity Distribution and Flow Resistance in a Triangular Array of Parallel Rods," *Nucl. Eng. Des.*, Vol. 5, 1967, pp. 22–42.

11 Subbotin, V. I., et al., "Velocity Field of Turbulent Fluid Flow in a Longitudinal Streamline of Clusters of Rods," AEC-tr-7189, 1971.

12 Kjellström, B., "Studies of Turbulent Flow Parallel to a Rod Bundle of Triangular Array," Report AE-RV-196, AB Atomenergi, Sweden, 1971.

13 Trupp, A. C., and Azad, R. S., "The Structure of Turbulent Flow in Triangular Array Rod Bundles," Department of Mechanical Engineering, University of Manitoba, Winnipeg, Canada, 1973.

14 Rowe, D. S., et al., "Implications Concerning Rod Bundle Crossflow Mixing Based on Measurements of Turbulent Flow Structure," *International Journal of Heat and Mass Transfer*, Vol. 17, 1974, pp. 407–419.

15 Brundrett, E., and Baines, W. D., "The Production and Diffusion of Vorticity in Duct Flow," *Journal of Fluid Mechanics*, Vol. 19, 1964, pp. 375–394.

16 Gosman, A. D., et al., *Heat and Mass Transfer in Recirculating Flows*, Academic Press, London, 1969.

17 Patel, V. C., "Calibration of the Preston Tube and Limitations on Its Use in Pressure Gradients," *Journal of Fluid Mechanics*, Vol. 23, Part 1, 1965, pp. 185–208.

18 Rotta, J., "Turbulent Boundary Layers in Incompressible Flow," in *Progress in Aeronautical Sciences*, Vol. 2, A. Ferri, et al., ed., Macmillan, 1962.

19 Champagne, F. H., et al., "Experiments on Nearly Homogeneous Shear Flow," *Journal of Fluid Mechanics*, Vol. 41, Part 1, 1970, pp. 81–139.

20 Hall, Ch., and Svenningsson, P. J., "Secondary Flow Velocities in a Rod Bundle of Triangular Array," Report AE-RL-1326, AB Atomenergi, Sweden, 1971.

Choong Se Kim

Chemical Engineering Division,
Argonne National Laboratory,
Argonne, Ill.

Paul M. Chung

Department of Energy Engineering,
University of Illinois at Chicago Circle,
Chicago, Ill.

An Asymptotic, Thermo-Diffusive Ignition Theory of Porous Solid Fuels

The governing equations of thermal ignition are analyzed for porous solid fuel, such as coal, of various two-dimensional and axisymmetric geometries by the Laplace asymptotic method. Mass diffusion of the gaseous oxidant through the porous fuel is included. The nonlinear partial differential equations of energy and mass balances in time-space coordinates containing the Arrhenius volumic chemical reaction terms are analyzed. By employing the Laplace asymptotic technique and by invoking a certain limit theorem, the governing equations are reduced to a first order ordinary differential equation governing the fuel surface temperature, which is readily solved numerically. Detailed discussion of the effects of the various governing parameters on ignition is presented. Because of the basically closed-form nature of the solutions obtained, many general and fundamental aspects of the ignition criteria hitherto unknown are found.

Ignition of Solid Fuels

Conditions leading to the state of self-sustaining combustion when a solid fuel is exposed to a gaseous oxidant have been of great interest in many industrial applications. Because of the complexity of the coupled effects of heat and mass transfer involved, the details of the transient ignition processes of solid fuels have not been completely elucidated.

Ignition is preceded by a thermal induction period during which the surface layer of the fuel is heated to a temperature at which exothermic chemical reaction can commence at a substantial rate. This is followed by a period in which the run-away exothermic reaction becomes the dominant heat source which leads to ignition. The surface temperature history is initially indistinguishable from that of an inert solid. After the chemical heating rate becomes comparable to the external heating rate, the rate of surface temperature rise rapidly increases and attains the characteristics of a thermal shock as soon as the surface temperature reaches a certain value commonly called the "ignition temperature." We define "ignition delay time" as the amount of the heating time required for establishment of the precipitous increase of surface temperature associated with the thermal shock.

When the solid fuel is impervious to gaseous diffusion, the heterogeneous reaction and ignition are limited to the fuel surface. This problem was analyzed in references [1-3].[1]

When the fuel contains solid oxidizer, the exothermic chemical reaction will occur homogeneously in the condensed phase of the fuel. Existing solutions of the solid fuel ignition according to this theory have been obtained by integrating the governing equations numerically [4, 5] or by a certain asymptotic technique [6].

On the other hand, when the fuel is porous such that the diffusivity of the oxidizing gas through the porous solid fuel is substantial, it is known that gas-solid heterogeneous reaction takes place volumically throughout the porous fuel phase. The gas-solid reactions taking place in zones of substantial width in porous solids have been investigated by many engineers (see, for instance, references [7, 8]). However, either a steady-state or an isothermal assumption had to be made in order to solve the partial differential equations governing the mass and energy balances because of the mathematical difficulties. Usually, the ignition is strongly dependent upon the temperature as well as upon the reactant concentrations. Furthermore, ignition, by nature, is a rapid transient process from one state of no reaction to another

---

Contributed by the Heat Transfer Division of THE AMERICAN SOCIETY OF MECHANICAL ENGINEERS and presented at the AIChE-ASME National Heat Transfer Conference, August 10-13, 1975. Revised manuscript received by the Heat Transfer Division March 8, 1976. Paper No. 75-HT-20.

[1] Numbers in brackets designate References at end of paper.

state of self-sustaining combustion. Therefore, the isothermal assumption or the quasi-steady-state assumption is unrealistic and often leads to erroneous results. Hence, there exists a rather immediate need for a study of the ignition criteria of porous solid fuels in which diffusional effects, thermal effects, and transient behavior are all included.

In the present study, a "thermo-diffusive theory" is proposed for porous fuel ignition. This model is distinguished from other existing ones by the mass diffusion of gaseous oxidant through the porous solid fuel phase. Consequently, solid-gas reactions are considered to occur volumically throughout the porous fuel.

The activation energies of most fuels of engineering interest are very large. The large activation energy which engenders the thermal shock inherently has been the basic cause of the mathematical difficulties in the analyses of most ignition problems. Such difficulty manifests itself most critically in the direct numerical integrations [4, 5] of the governing equations. The asymptotic method to be employed in this paper is particularly well suited for analysis of the large activation-energy fuels.

A Semi-Infinite Slab With Constant Energy and Gaseous Oxidant Fluxes at the Fuel Surface

Description of the Problem. The model being considered herein is a one-dimensional, time-dependent system as illustrated in Fig. 1, with the porous fuel in $x \geq 0$. Commencing at $t = 0$, energy is supplied at a constant rate, $\dot{q}$, at the surface of the fuel. The gaseous oxidant is supplied at a constant rate, $\dot{m}$, at the fuel surface as well for $t \geq 0$. A single step exothermic reaction of Arrhenius type is assumed to take place throughout the porous fuel volumically. For mathematical convenience, all physical properties of the system are considered constant.[2] It is further assumed that the phase changes, such as formation of ash layer or devolatilization of the solid fuel, do not occur during the ignition since the time period involved for the ignition is very short.

The starting point of the analysis is the governing equations of the gaseous oxidant and the temperature of the fuel, written as,

$$\frac{\partial C_A}{\partial t} = D_{eA}\frac{\partial^2 C_A}{\partial x^2} - k_0 C_A{}^n \exp(-E/\mathcal{R}T) \tag{1}$$

$$\rho c_p \frac{\partial T}{\partial t} = \lambda \frac{\partial^2 T}{\partial x^2} + Q k_0 C_A{}^n \exp(-E/\mathcal{R}T) \tag{2}$$

The boundary conditions at the fuel surface are given as

$$-\lambda\frac{\partial T}{\partial x} = \dot{q}, \quad -D_{eA}\frac{\partial C_A}{\partial x} = \dot{m}, \quad \text{at } x = 0 \tag{3}$$

On physical ground, the other set of boundary conditions is given as

$$\frac{\partial T}{\partial x} = 0, \quad \frac{\partial C_A}{\partial x} = 0 \quad \text{at } x = \infty \tag{4}$$

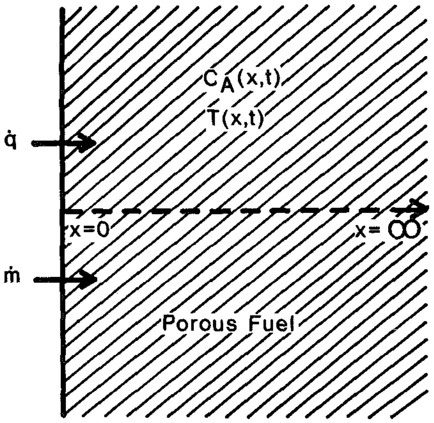

Fig. 1 A semi-infinite slab with constant heat and gaseous oxidant fluxes at the fuel surface

The initial conditions are

$$T = T_0, \quad C_A = C_{A0}, \quad \text{for } t = 0 \tag{5}$$

Analysis. We define the following nondimensionalized variables.

$$\theta = (T - T_0)/T_0, \quad Y = (C_A - C_{A0})/C_{A0}$$

$$\tau = \dot{q}^2 t/(\rho c_p \lambda T_0{}^2), \quad \xi = \dot{q}x/\lambda T_0 \tag{6}$$

In the previous equations, θ, Y, τ, and ξ denote, respectively, nondimensionalized temperature, gaseous oxidant concentration, time, and distance from the fuel surface. Symbols not defined in the text are defined in the Nomenclature. We also define the following nondimensionalized parameters.

$$\beta = E/\mathcal{R}T_0, \quad A = Qk_0\lambda T_0 C_{A0}{}^n/\dot{q}^2, \quad B = QC_{A0}/(\rho c_p T_0) \tag{7}$$

Note that the parameter A signifies the relative importance of the chemical and external heating rates, and the parameter B is the ratio of the chemical energy available in the exothermic reaction to the initial sensible energy. The nondimensional activation energy, β, controls to a large degree the characteristics of the ignition curve. The larger the β, it is expected that the ignition will take place more precipitously. As it was mentioned earlier, the asymptotic method to be employed is best suited for the large values of β which represents most ignition problems of engineering interest. It is considered in the following that $\beta \gg 1$.

Equations (1)–(5) can be written in terms of the nondimensionalized variables and parameters as

$$\frac{\partial Y}{\partial \tau} = \text{Le}\frac{\partial^2 Y}{\partial \xi^2} - (A/B)(1 + Y)^n \exp[-\beta/(1 + \theta)] \tag{8}$$

$$\frac{\partial \theta}{\partial \tau} = \frac{\partial^2 \theta}{\partial \xi^2} + A(1 + Y)^n \exp[-\beta/(1 + \theta)] \tag{9}$$

Nomenclature

C_A = concentration of gaseous oxidant
C_{A0} = initial concentration of gaseous oxidant in the porous fuel
c_p = specific heat of porous fuel
D_{eA} = effective mass diffusivity of oxidizing gas in the porous fuel
E = activation energy of fuel combustion
k_0 = pre-exponential factor of reaction rate constant
$\dot{m}$ = constant rate of gaseous oxidant flux at the fuel surface
n = order of reaction based on the gaseous oxidant concentration
Q = heat of reaction per mole of oxidizing gas
$\dot{q}$ = constant rate of heat flux at the fuel surface
$\mathcal{R}$ = gas constant
T = temperature
T_0 = initial temperature of porous fuel
t = time
x = distance from the fuel surface
λ = thermal conductivity of fuel
ρ = density of fuel
τ_c = nondimensional ignition delay time

---

[2] The constant property restrictions can be readily relaxed by appropriate transformations (see reference [1]) resulting in the same mathematical form of the governing equations as the one analyzed herein.

$$\frac{\partial\theta}{\partial\xi}(0,\tau) = -1, \quad \frac{\partial Y}{\partial\xi}(0,\tau) = -\lambda T_0\dot{m}/D_{eA}\dot{q}C_{A0} \tag{10}$$

$$\frac{\partial\theta}{\partial\xi}(\infty,\tau) = \frac{\partial Y}{\partial\xi}(\infty,\tau) = 0, \quad \theta(\xi,0) = Y(\xi,0) = 0 \tag{11}$$

where Le is a Lewis number defined as

$$\mathrm{Le} = D_{eA}\rho c_p/\lambda \tag{12}$$

The Lewis number is the ratio of effective mass diffusivity to thermal diffusivity. Note that the present model becomes identical to condensed phase thermal theory (see references [4–6]) in the limit of zero Lewis numbers. In the condensed phase theory, the nonporous solid fuel is considered to consist of a mixture of the fuel and oxidant. Throughout the present analysis, Lewis number is considered as unity for the porous fuel since the unity Lewis number assumption alleviates mathematical difficulties without the loss of important features of the problem.

We define a combined variable $H(\xi,\tau)$ as

$$H(\xi,\tau) = \theta(\xi,\tau) + BY(\xi,\tau) \tag{13}$$

Then, equations (8) and (9) are first combined to give

$$\frac{\partial H}{\partial\tau} = \frac{\partial^2 H}{\partial\xi^2} \tag{14}$$

The boundary conditions and initial conditions to be satisfied by the foregoing equation are written, from equations (10) and (11), as

$$\frac{\partial H}{\partial\xi}(0,\tau) = -\dot{h}, \quad \frac{\partial H}{\partial\xi}(\infty,\tau) = H(\xi,0) = 0 \tag{15}$$

where $\dot{h}$ represents the combined rate of heat and mass fluxes defined as

$$\dot{h} = 1 + QC_{A0}\dot{m}/\dot{q} \tag{16}$$

Solution of the foregoing partial differential equation is available elsewhere (see reference [9], for instance). It is

$$H(\xi,\tau) = 2\dot{h}[(\tau/\pi)^{1/2}\exp(-\xi^2/4\tau) - (\xi/2)\,\mathrm{erfc}\,(\xi/2\sqrt{\tau})] \tag{17}$$

Equation (9) is then written, with the use of equations (13) and (17), as

$$\frac{\partial\theta}{\partial\tau} = \frac{\partial^2\theta}{\partial\xi^2} + A\{1 + (2\dot{h}/B)[(\tau/\pi)^{1/2}\exp(-\xi^2/4\tau) - (\xi/2)\,\mathrm{erfc}\,(\xi/2\sqrt{\tau})] - \theta/B\}^n \exp[-\beta/(1+\theta)] \tag{18}$$

Now the problem at hand is to solve the foregoing highly nonlinear partial differential equation satisfying equations (10) and (11).

We first carry out a Laplace transformation of equation (18) with respect to the space variable as

$$\bar{\theta}(s,\tau) = \int_0^\infty \exp(-s\xi)\theta(\xi,\tau)d\xi \tag{19}$$

where $\bar{\theta}$ and s are, respectively, the temperature and space variable on a transformation plane. Then, we obtain

$$\frac{d\bar{\theta}}{d\tau} - s^2\bar{\theta} = 1 - s\theta(0,\tau) + AI_1 \tag{20}$$

where

$$I_1 = \int_0^\infty d\xi\exp(-s\xi)\{1 + (2\dot{h}/B)[(\tau/\pi)^{1/2}\exp(-\xi^2/4\tau) - (\xi/2)\,\mathrm{erfc}\,(\xi/2\sqrt{\tau})] - \theta(\xi,\tau)/B\}^n \exp\{-\beta/[1+\theta(\xi,\tau)]\} \tag{21}$$

Now let us consider the integral I_1 whose integrand is highly nonlinear. On physical grounds, we know that the temperature will have a maximum value at the fuel surface where heat is supplied at a constant rate. We also see that the function

$$\{1 + (2\dot{h}/B)[(\tau/\pi)^{1/2}\exp(-\xi^2/4\tau) - (\xi/2)\,\mathrm{erfc}\,(\xi/2\sqrt{\tau})] - \theta/B\}^n$$

is slowly varying in ξ as compared to the exponential function, $\exp\{-\beta/[1+\theta(\xi,\tau)]\}$, of I_1 where β is large. Therefore, the integral I_1 can be approximated by the Laplace asymptotic method (see reference [10]) for large β's as follows. (The readers are referred to reference [11] for the detailed derivations.)

$$I_1 \simeq [1 + (2\dot{h}/B)(\tau/\pi)^{1/2} - \theta(0,\tau)/B]^n \exp\{-\beta/[1+\theta(0,\tau)]\} \cdot \{s + \beta/[1+\theta(0,\tau)]^2\}^{-1} \tag{22}$$

Now, solving equation (20) for $\bar{\theta}(s,\tau)$, we obtain

$$\bar{\theta}(s,\tau) = \exp(s^2\tau)\int_0^\tau \mathrm{d}\eta\exp(-s^2\eta)[1 - s\theta(0,\eta)] + A\exp(s^2\tau)\int_0^\tau d\eta\exp(-s^2\eta)I_1(\eta) \tag{23}$$

where η is a dummy variable.

Let us now consider the integral I_2 which is defined as

$$I_2 = \int_0^\tau d\eta\exp(-s^2\eta)I_1(\eta) \tag{24}$$

We know on physical ground that the surface temperature is a monotonically increasing function of time. We also see in the integrand that the function

$$\exp(-s^2\eta)[1 + (2\dot{h}/B)(\eta/\pi)^{1/2} - \theta(0,\eta)/B]^n\{s + \beta/[1+\theta(0,\eta)]^2\}^{-1}$$

is slowly varying in η as compared to the function, $\exp\{-\beta/[1+\theta(0,\eta)]\}$. Thus, the integral I_2 is approximated for large β's, by the Laplace method (see reference [11] for details) as

$$I_2 \simeq \exp(-s^2\tau)[1 + (2\dot{h}/B)(\tau/\pi)^{1/2} - \theta(0,\tau)/B]^n \cdot \{s + \beta/[1+\theta(0,\tau)]^2\}^{-1}\exp\{-\beta/[1+\theta(0,\tau)]\} \cdot \left\{\beta\frac{d\theta}{d\tau}(0,\tau)/[1+\theta(0,\tau)]^2\right\}^{-1} \tag{25}$$

We substitute the above equation into equation (23) and obtain

$$\bar{\theta}(s,\tau) = \exp(s^2\tau)\int_0^\tau d\eta\exp(-s^2\eta)[1 - s\theta(0,\eta)] + A[1 + (2\dot{h}/B)(\tau/\pi)^{1/2} - \theta(0,\eta)/B]^n\{s + \beta/[1+\theta(0,\tau)]^2\}^{-1} \left\{[1+\theta(0,\tau)]^2/\beta\frac{d\theta}{d\tau}(0,\tau)\right\}\exp\{-\beta/[1+\theta(0,\tau)]\} \tag{26}$$

Inverse Laplace transformation of the foregoing equation which is obtainable only numerically will give the complete solution for the temperature as a function of time and space. However, if the inverse transformation were to be obtained numerically, the numerical computational work involved would be such that there is no real advantage of solving the problem by the present method as compared to numerically integrating the partial differential equation, equation (18), directly. However, an examination of the physical problem shows that the ignition will take place in the surface layer of the fuel. On this physical ground, the ignition criteria of porous fuel can be obtained by studying the fuel temperature histories near the surface. Therefore, we seek an asymptotic solution which is valid in the neighborhood of the fuel surface.

Applying a limit theorem given in [12]

$$\lim_{\xi\to0}\theta(\xi,\tau) = \lim_{s\to\infty}s\bar{\theta}(\mathrm{s},\tau) \tag{27}$$

to equation (26), we obtain

$$\theta(0,\tau) = \lim_{s\to\infty}s\exp(s^2\tau)\int_0^\tau d\eta\exp(-s^2\eta)[1 - s\theta(0,\eta)] + A[1 + (2\dot{h}/B)(\tau/\pi)^{1/2} - \theta(0,\tau)/B]^n\left\{[1+\theta(0,\tau)]^2/\beta\frac{d\theta}{d\tau}(0,\tau)\right\} \cdot \exp\{-\beta/[1+\theta(0,\tau)]\} \tag{28}$$

Note that the second term on the right-hand side of equation (28) represents the contribution of the exothermic chemical reaction to

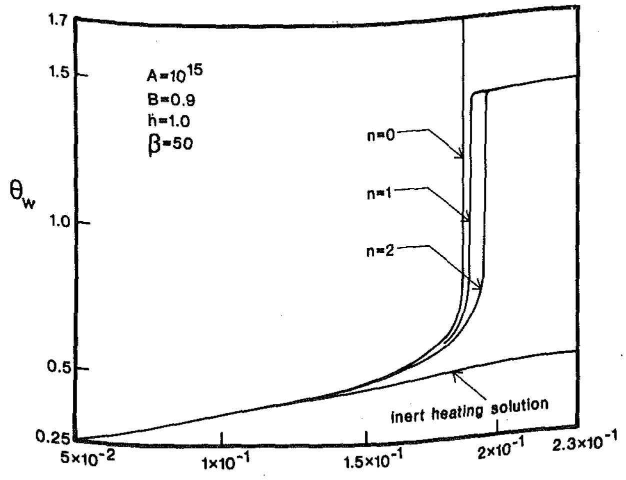

Fig. 2 Surface temperature-time histories for various order reactions based on gaseous oxidant concentrations

the surface temperature rise. On the other hand, the first term on the right-hand side of equation (28) represents the contribution of external heating to the surface temperature increase. We know that this term is equivalent to the solution of the corresponding chemically inert heating problem. This solution at the fuel surface will replace the first term on the right-hand side of equation (28).

The governing equation of this heating problem of an inert solid is obtained simply by setting $A = 0$ to equation (9) as

$$\frac{\partial \theta_I}{\partial \tau} = \frac{\partial^2 \theta_I}{\partial \xi^2} \tag{29}$$

where the subscript I denotes the inert heating problem. The boundary conditions and initial condition to be satisfied by the above equation are given by equations (10) and (11).

The solution of the foregoing boundary value problem is available elsewhere, and it is

$$\theta_I(\xi, \tau) = 2[(\tau/\pi)^{1/2} \exp(-\xi^2/4\tau) - (\xi/2) \operatorname{erfc}(\xi/2\sqrt{\tau})] \tag{30}$$

And in the neighborhood of fuel surface, we have

$$\lim_{\xi \to 0} \theta_I(\xi, \tau) = 2(\tau/\pi)^{1/2} \tag{31}$$

Replacing the first term on the right-hand side of equation (28) by the foregoing expression, we finally obtain the expression for the fuel surface temperature as

$$\theta(0, \tau) = 2(\tau/\pi)^{1/2} + A[1 + (2\dot{h}/B)(\tau/\pi)^{1/2} - \theta(0, \tau)/B]^n \cdot \left\{[1 + \theta(0, \tau)]^2/\beta \frac{d\theta}{d\tau}(0, \tau)\right\} \exp\{-\beta/[1 + \theta(0, \tau)]\} \tag{32}$$

Rewriting with θ_w denoting the surface temperature,

$$\frac{d\theta_w}{d\tau} = [A \exp(-\beta)/\beta][1 + (2\dot{h}/B)(\tau/\pi)^{1/2} - \theta_w/B]^n (1 + \theta_w)^2 \cdot [\theta_w - 2(\tau/\pi)^{1/2}]^{-1} \exp[\beta\theta_w/(1 + \theta_w)] \tag{33}$$

The foregoing equation is integrated numerically for θ_w.

Results and Discussion. Numerical computation of equation (33) was carried out for the following ranges of parameters.

$$\beta = 30\text{–}80 \quad A = 10^9\text{–}10^{27} \quad B = 0.9 \quad \dot{h} = 1.0\text{–}3.0 \quad n = 0, 1, 2 \tag{34}$$

Typical surface temperature histories are shown in Fig. 2 for the zeroth, first, and the second order reactions based on the gaseous oxidant concentration. The solution for the inert heating problem is also shown for a reference. As it is seen from the solution, the full temperature-time histories at the fuel surface leading to a self-sustained combustion can be obtained by the present method.

When the reaction order based on the gaseous oxidant concentration is zero, the present "thermo-diffusive theory" for a porous solid fuel becomes identical to the "thermal theory" (see references [4–6]) in which the diffusional effect of oxidizing gas is neglected. Bradley's exact numerical solution [5] for a semi-infinite fuel geometry is the only existing solution that can judge the accuracy of the present asymptotic method applied for $n = 0$. Fig. 3 compares the present solution of the ignition delay time with Bradley's numerical results for $n = 0$. The solid lines describe the present solution whereas the circles show Bradley's exact numerical results. This comparison shows that the ignition delay time predicted by the present method is sufficiently accurate for β's down to 30. In fact, it was found that a sufficient accuracy is attained down to β of 10. Furthermore, Bradley's numerical method faces rather severe difficulties, and its accuracy wanes as β increases. On the other hand, the accuracy of the present asymptotic method increases as β is increased. This is because the Laplace method used herein becomes asymptotically exact as $\beta \to \infty$. Therefore, the present results might even be more reliable than those obtained by a purely numerical method for large β's representing many practical ignition problems.

It was also found, from the present solutions, that the ignition delay time varied by no more than 10 percent as the reaction order varied from 0 to 2.

Fig. 4 shows the surface temperature-time histories for several β's. As β decreases, that is, as either the activation energy decreases or the initial temperature of the fuel slab increases, the ignition occurs faster.

Effect of the rate of mass transfer of oxidizing gas at the fuel surface on the ignition delay time is shown in Fig. 5 for $\beta = 40 \sim 80$ and for $n = 2$. From the definition of $\dot{h}$ given by equation (16), we have

$$\dot{m} = \dot{q}(\dot{h} - 1)/(QC_{A0}) \tag{35}$$

Therefore, $\dot{h} = 1$ represents the condition of no oxidizing gas supply at the fuel surface. Also, $\dot{h} = 2$ and $\dot{h} = 3$, respectively, correspond to $\dot{m} = \dot{q}/(QC_{A0})$ and $2\dot{q}/(QC_{A0})$. We can see that ignition occurs earlier as we increase the supply of the gaseous oxidant to the fuel surface. Note that ignition will still take place for $\dot{m} = 0$ since certain amount of gaseous oxidant is initially available within the porous solid fuel.

Finite Fuel Geometries

The present asymptotic method is now applied to the ignition problems of porous solid fuels of finite geometries. A slab of finite thickness, an infinitely long circular cylinder, and a sphere will be

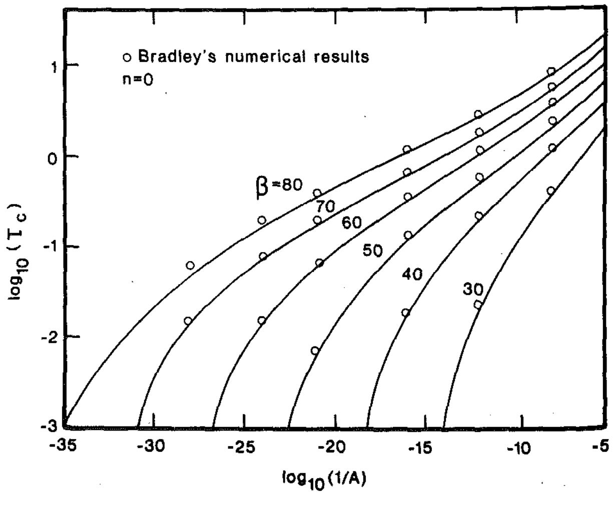

Fig. 3 Comparison with exact numerical solution where B = 0.9 and $\dot{h}$ = 1.0

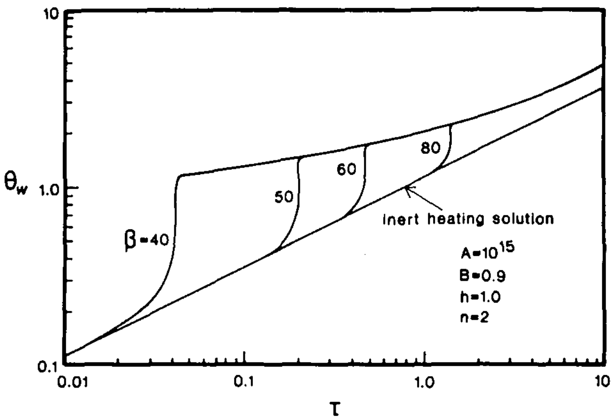

Fig. 4 Surface temperature histories for various β's ($n = 2$)

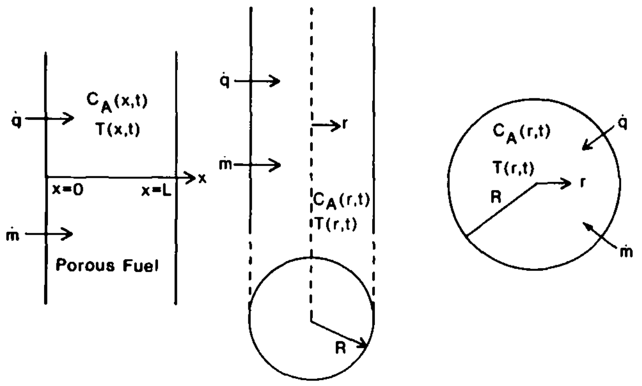

Fig. 6 Finite fuel geometries

considered.

Description of the Problem. We consider one-dimensional, time-dependent systems as illustrated in Fig. 6. Heat and gaseous oxidant are supplied at constant rates to the fuel at $x = 0$ for a slab, and at $r = R$ for a cylinder and a sphere. The other fuel surface of the slab at $x = L$ is assumed to be impervious to heat and mass. Symmetry condition was considered to be the other set of boundary conditions for the cylinder and the sphere.

Analysis. Governing equations for mass and energy balances can be written as

$$\frac{\partial C_A}{\partial t} = D_{eA}\nabla^2 C_A - k_0 C_A{}^n \exp\left(-E/\mathcal{R}T\right) \tag{36}$$

$$\rho c_p \frac{\partial T}{\partial t} = \lambda\nabla^2 T + Qk_0 C_A{}^n \exp\left(-E/\mathcal{R}T\right) \tag{37}$$

The boundary conditions are

$$\mp \lambda\nabla T = \dot{q} \quad \text{at } x = 0, r = R \tag{38}$$

$$\mp D_{eA}\nabla C_A = \dot{m} \quad \text{at } x = 0, r = R \tag{39}$$

$$\nabla T = \nabla C_A = 0 \quad \text{at } x = L, r = 0 \tag{40}$$

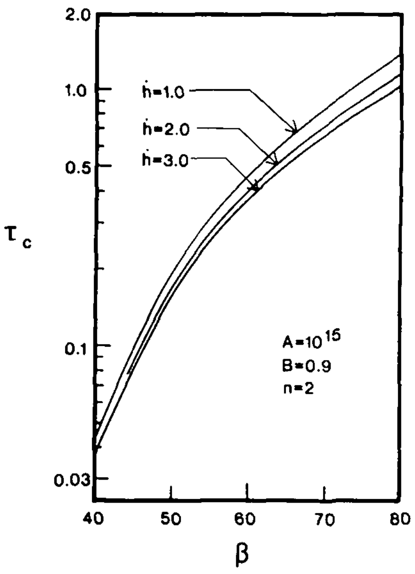

Fig. 5 Effect of gaseous oxidant flux at the fuel surface on ignition delay time

The initial conditions are written, for completeness, as

$$T = T_0, \quad \text{at } t = 0 \qquad C_A = C_{A0}, \quad \text{at } t = 0 \tag{41}$$

The governing equations are manipulated and combined to a single nonlinear partial differential equation by considering the effective Lewis number to be one.

$$\frac{\partial\theta}{\partial\tau} = \nabla^2\theta + A[1 + (1/B)(H - \theta)]^n \exp\left[-\beta/(1 + \theta)\right] \tag{42}$$

The procedure of deriving the above equation is essentially the same as that for the semi-infinite slab. Hence, the details are not repeated herein. In the previous equation, all the nondimensionalized variables and parameters are defined in the same way as for the semi-infinite slab. H represents the solution of the combined equations. They are

for a finite slab:

$$H(\xi, \tau) = \dot{h}\tau/\bar{L} + \dot{h}\bar{L}\{[3(\bar{L} - \xi)^2 - \bar{L}^2]/6\bar{L}^2 - (2/\pi^2)\sum_{n=1}^{\infty}\frac{(-1)^n}{n^2}\exp\left(-n^2\pi^2\tau/\bar{L}^2\right)\cos\left[n\pi(\bar{L} - \xi)/\bar{L}\right]\} \tag{43}$$

where

$$\bar{L} = \dot{q}L/\lambda T_0 \tag{44}$$

for a cylinder:

$$H(\bar{r}, \tau) = 2\dot{h}\tau/\bar{R} + \dot{h}\bar{R}[\bar{r}^2/2\bar{R}^2 - (1/4) - 2\sum_{n=1}^{\infty}\exp\left(-\alpha_n{}^2\tau/\bar{R}^2\right)J_0(\bar{r}\alpha_n/\bar{R})/\alpha_n{}^2 J_0(\alpha_n)] \tag{45}$$

where

$$\bar{r} = \dot{q}r/\lambda T_0, \quad \bar{R} = \dot{q}R/\lambda T_0, \tag{46}$$

and α_n, $n = 1, 2 \ldots$, are the roots of the equation,

$$J_1(\alpha) = 0 \tag{47}$$

In the previous equations J_0 and J_1 denote, respectively, the Bessel function of order zero and that of order one. Continuing, we have,

for a sphere:

$$H(\bar{r}, \tau) = 3\dot{h}\tau/\bar{R} + \dot{h}(5\bar{r}^2 - 3\bar{R}^2)/10\bar{R} - (2\dot{h}\bar{R}^2/\bar{r})\sum_{n=1}^{\infty}\frac{\sin(\bar{r}\gamma_n/\bar{R})}{\gamma_n{}^2\sin\gamma_n}\exp\left(-\gamma_n{}^2\tau/\bar{R}^2\right) \tag{48}$$

where γ_n, $n = 1, 2 \ldots$, are the roots of the equation,

$$\tan\gamma = \gamma \tag{49}$$

We define new space variables ϕ and ψ such that the present igni-

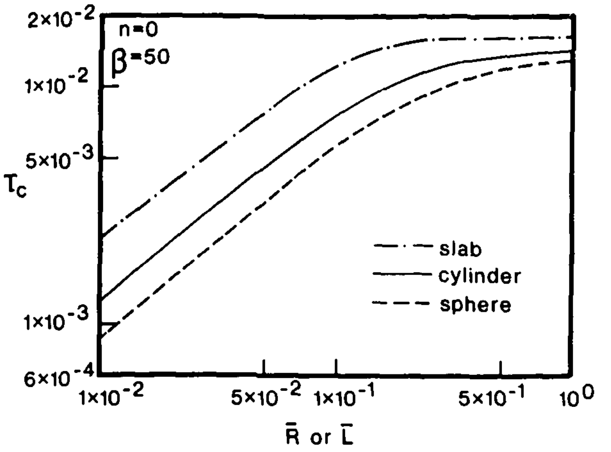

Fig. 7 Surface temperature histories for finite fuel geometries for $A = 10^{20}$, $B = 0.9$ and $\hat{h} = 1.0$

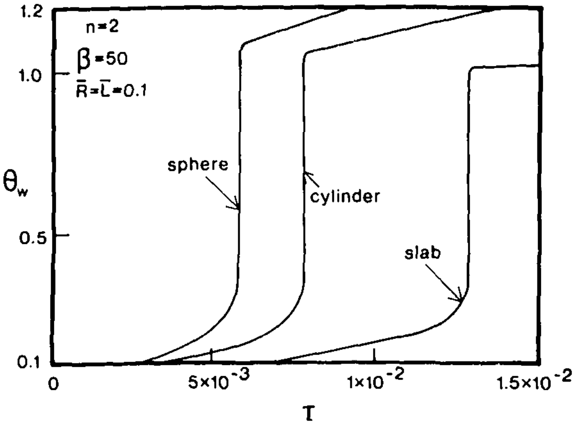

Fig. 8 Effect of fuel body size on ignition delay time for $A = 10^{20}$, $B = 0.9$ and $\hat{h} = 1.0$

tion problems of finite fuel geometries can be reduced to forms which are amenable to analyses by the Laplace method as

$$\phi = 1/(\bar{L} - \xi) - 1/\bar{L} \quad \text{for a slab} \tag{50}$$

$$\psi = 1/\bar{r} - 1/\bar{R} \quad \text{for a cylinder and a sphere} \tag{51}$$

By using the foregoing variables, we transform the finite fuel geometries into the semi-infinite slabs in (ϕ, τ) and (ψ, τ) planes.

Laplace transformation of the governing equations in new coordinates is first carried out with respect to the space variables. Then the Laplace method is applied twice to evaluate asymptotically but in closed forms the nonlinear integrals resulting from the exothermic chemical reaction terms. By invoking a limit theorem given by equation (27), we finally obtain ordinary differential equations governing the fuel surface temperatures. The procedures are not repeated herein since they are quite similar to those carried out for the semi-infinite slab. (The readers are referred to reference [11] for the detailed derivations.) The equations can be written, with θ_w denoting the surface temperatures, as

$$\frac{d\theta_w}{d\tau} = [A \exp(-\beta)/\beta][1 + (H_w/B) - (\theta_w/B)]^n (1 + \theta_w)^2 \cdot \exp[\beta\theta_w/(1 + \theta_w)](\theta_w - \theta_{Iw})^{-1} \tag{52}$$

In the previous equation, θ_{Iw} and H_w denote, respectively, the solutions of the corresponding inert heating problems and the solutions of the combined equations which are valid at the fuel surfaces. H_w is related with θ_{Iw}, for all the fuel geometries being considered, simply by the equation,

$$H_w = \hat{h}\theta_{Iw} \tag{53}$$

The corresponding inert heating solutions are

for a finite slab:

$$\theta_{Iw} = (\tau/\bar{L}) + \bar{L}[(1/3) - (2/\pi^2) \sum_{n=1}^{\infty} (1/n^2) \exp(-n^2\pi^2\tau/\bar{L}^2)] \tag{54}$$

for a cylinder:

$$\theta_{Iw} = (2\tau/\bar{R}) + \bar{R}[(1/4) - 2 \sum_{n=1}^{\infty} (1/\alpha_n^2) \exp(-\alpha_n^2\tau/\bar{R}^2)] \tag{55}$$

for a sphere:

$$\theta_{Iw} = (3\tau/\bar{R}) + \bar{R}[(1/5) - 2 \sum_{n=1}^{\infty} (1/\gamma_n^2) \exp(-\gamma_n^2\tau/\bar{R}^2)] \tag{56}$$

Equation (52) is integrated numerically for θ_w with the use of equations (53)–(56).

Results and Discussion. The effects of the body size and geometrical shapes of porous solid fuels on the ignition characteristics are presented in Figs. 7 and 8. Other features of ignition problems are not repeated here, since they are fundamentally the same as those discussed earlier for the semi-infinite slab.

It is seen in both figures that the ignition delay time is the shortest for the sphere and the longest for the slab when all other factors are equal. Note that $\bar{R}$ and $\bar{L}$, respectively, denote the normalized radius and thickness as defined by equations (46) and (44). Fig. 8 shows the effects of body size and geometry of porous fuels on the ignition delay times. It shows that the ignition delay times become longer as the fuel sizes increase and approach the value for the semi-infinite slab asymptotically. It also specifies certain ranges in which the body size and geometrical shape of the porous fuel have significant effects on ignition delay times.

Few experimental results have been reported on the ignition of solid fuels of finite body size. Thomas [13] investigated the effect of particle size on ignition when coal particles are subjected to hot air at constant temperature. He found that the smaller the particle the faster the ignition occurs. Tien and Turkdogan [14] showed that the oxidation rates are greater for smaller particles of electrode graphite in various conditions. They also reported that the oxidation rate was fastest for the spherical particles and slowest for the slabs. These results are for the steady-state combustion processes, not for ignition. However, since we know that faster oxidation rate will result in faster ignition, their experimental results are congruent with the present solutions.

It is the best knowledge of the present authors that there have not been any theoretical studies on the solid fuel ignition of finite bodies which are comparable with the present analysis. It is hoped that there will be exact numerical solutions which can judge the accuracy of the present asymptotic solution by the Laplace method.

Concluding Remarks

In the present study, a "thermo-diffusive theory" has been proposed for the porous solid fuels. Governing equations of mass and energy have been analyzed for the porous fuel of various two-dimensional, axisymmetric geometries by using the Laplace asymptotic method first employed in the surface ignition problems by Yung and Chung [1].

Governing equations have been manipulated and combined to a single highly nonlinear partial differential equation by considering the effective Lewis number to be one. The Lewis number could be considerably different from one, depending on the porosity and the conductivity of the solid fuel. However, the present analysis is intended to demonstrate the asymptotic tool with which the ignition of the high-activation energy fuel can be analyzed without incurring undo algebraic complexities. Furthermore, the present method can be readily applied to the cases of Lewis numbers different from one, and such analysis has been carried out by Ahluwalia [15]. This work includes the discussion of the significance of oxidant diffusion in the ignition processes and comparison with the condensed phase ignition.

Complete solutions for the fuel surface temperature leading to combustion have been obtained for the zeroth, first and second order reactions based on the gaseous oxidant concentration. The effects of the various governing parameters, such as the activation energy, the ratio of chemical heating to external heating, the rate of oxidizing gas supply at the fuel surface, etc., on ignition have been discussed. Also, the effects of the body size and geometrical shape of porous fuel on the ignition criteria have been discussed. It is seen that the accuracy of the present method increases for large β's of practical interest.

Because of the basically closed-form nature of the solutions obtained, many general and fundamental aspects of the ignition criteria hitherto unknown have been found.

References

1 Yung, S. C., and Chung, P. M., "Asymptotic and Numerical Solutions of Certain Heterogeneous Ignition Problems," *Proceedings of 1974 Heat Transfer & Fluid Mechanics Institute*, Stanford University Press, 1974.

2 Bradley, H. H., Jr., and Williams, F. A., "Theory of Radiant and Hypergolic Ignition of Solid Propellants," *Comb. Sci. & Tech.*, Vol. 2, 1970, pp. 41–52.

3 Linan, A., and Crespo, A., "An Asymptotic Analysis of Radiant and Hypergolic Heterogeneous Ignition of Solid Propellants," *Comb. Sci. & Tech.*, Vol. 6, 1972, pp. 223–232.

4 Hicks, B. L., "Theory of Ignition Considered as a Thermal Reaction," *J. of Chem. Phys.*, Vol. 22, No. 3, 1954.

5 Bradley, H. H., Jr., "Theory of Ignition of a Reactive Solid by Constant Energy Flux," *Comb. Sci. & Tech.*, Vol. 2, 1970, pp. 11–20.

6 Linan, A., and Williams, F. A., "Theory of Ignition of a Reactive Solid by Constant Energy Flux," *Comb. Sci. & Tech.*, Vol. 3, 1971, pp. 91–98.

7 Wen, C. Y., "Noncatalytic Heterogeneous Solid-Fluid Reaction Models," *I & EC*, Vol. 60, No. 9, 1968.

8 Wen, C. Y., and Wang, S. C., "Thermal and Diffusional Effects of Noncatalytic Solid-Gas Reactions," *I & EC*, Vol. 62, No. 8, 1970.

9 Carslaw, H. S., and Jaeger, J. C., *Conduction of Heat in Solid*, London, Oxford University Press, Second ed., 1959.

10 De Bruijn, N. G., *Asymptotic Methods in Analysis*, Intersciences Publishers, Inc., 1958.

11 Kim, C., "An Asymptotic Ignition of Porous Solid Fuels," PhD thesis, University of Illinois at Chicago Circle, 1974.

12 Widder, D. V., *The Laplace Transform*, Princeton University Press, Princeton, 1941.

13 Thomas, G. R., Stevenson, A. J., and Evans, D. J., "Ignition of Coal Particles Without Temperature Jump," *Comb. & Flame*, Vol. 21, 1973, pp. 133–136.

14 Tien, R. H., and Turkdogan, E. T., "Mathematical Analysis of Nonisothermal Mass Transfer Process—Application to Oxidation of Carbon with CO_2-CO Mixtures," *Carbon*, Vol. 10, 1972, pp. 35–49.

15 Ahluwalia, R., and Chung, P. M., to be published.

P. Hutchinson
Theoretical Physics Division,
A. E. R. E. Harwell,
Oxfordshire, England.

E. E. Khalil
J. H. Whitelaw
G. Wigley

Department of Mechanical Engineering,
Imperial College,
London, England

The Calculation of Furnace-Flow Properties and Their Experimental Verification

Measurements of mean axial velocity, and the corresponding normal stress are reported for the isothermal flow of air and for a combusting mixture of natural gas in an axisymmetric furnace enclosure with a coaxial burner. Temperature and wall heat flux measurements were also obtained for the combusting flow. The swirl number of the flow was 0.5. The measurements are compared with the results of a calculation procedure incorporating a two equation turbulence model and a one step reaction model. The combustion model allowed fuel and oxygen to coexist at the same place but not at the same time. The comparison indicates that the calculation procedure qualitatively represents the measurements but that quantitative differences exist. The argument is sufficiently close, however, to justify the use of the method for some design purposes.

Introduction

In an earlier paper, reference [1],[1] the authors reported measurements of velocity components and the corresponding normal stresses obtained in a model furnace by laser-Doppler anemometry. This paper reports new measurements obtained in the same furnace at a higher flow rate and, in addition, compares them with values obtained with a numerical design method. The measurements have been extended to include values of mean temperature and wall-heat flux. The inlet, swirl numbers of the flow were zero and approximately 0.52 for the isothermal air flow and, for reasons of flame stability, the zero swirl flow was not measured for the combusting mixture of natural gas and air. The calculations were obtained with the aid of a computer program originated by Gosman and Pun [2] and developed by Khalil and Whitelaw [3] for furnace configurations. The program solves, in finite-difference form, the two-dimensional elliptic forms of appropriate conservation equations.

The purpose of the research program, of which the present work forms a part, is to develop a design procedure for cylindrical furnaces. Since the conservation equations embodied in this procedure have been time averaged, the equations are not exact and include assumptions which may be classified as belonging to the turbulence or combustion models. It is, therefore, necessary to quantitatively assess the reliability of the procedure by comparison with experiments and the present experimental program is designed to meet this need. In contrast to previous experimental investigations, for example references [4–6], the present use of laser-Doppler anemometry allows the determination of Reynolds stresses and these provide a more sensitive test of the turbulence model than does the mean velocity. The previous computational investigations of Khalil and Whitelaw [3, 7] demonstrated, by comparison with the experiments of references [1, 4–6], that a two equation turbulence model allowed reasonable prediction of velocity and normal stresses and that a one step representation of the chemical reaction was also satisfactory. The comparisons of references [3, 7] were deficient in that only the data of reference [1] provided measured initial conditions but they did not include temperature or heat flux information. The measurements described here include initial conditions and provide velocity, temperature and heat-flux information obtained in the same flow configuration.

The following sections of the paper consider, in turn, the computational method and its physical assumptions; the flow configuration, associated instrumentation and procedures; and the results of computational and experimental investigations. The implications

---

[1] Numbers in brackets designate References at end of paper.

Contributed by the Heat Transfer Division of THE AMERICAN SOCIETY OF MECANICAL ENGINEERS and presented at the AIChE-ASME National Heat Transfer Conference, San Francisco, Calif., August 10–13, 1975. Revised manuscript received by the Heat Transfer Division November 12, 1975. Paper No. 75-HT-8.

Table 1

Variable ϕ	a_1	b_1	b_2	S_ϕ
U	1	μ_{eff}	μ_{eff}	$\frac{\partial}{\partial x}(\mu_{\text{eff}}\frac{\partial U}{\partial x}) + \frac{1}{r}\frac{\partial}{\partial r}(\mu_{\text{eff}} r\frac{\partial V}{\partial x}) - \frac{\partial P}{\partial x}$
V	1	μ_{eff}	μ_{eff}	$\frac{\partial}{\partial x}(\mu_{\text{eff}}\frac{\partial U}{\partial r}) + \frac{1}{r}\frac{\partial}{\partial r}(\mu_{\text{eff}} r\frac{\partial V}{\partial r}) - \frac{2\mu_{\text{eff}} V}{r^2} + \frac{\rho W^2}{r} -$
W	1	μ_{eff}	μ_{eff}	$-(\frac{\mu_{\text{eff}}}{r^2} + \frac{\rho V}{r} + \frac{1}{r}\frac{\partial \mu_{\text{eff}}}{\partial r})W$
k	1	$\frac{\mu_{\text{eff}}}{\sigma_k}$	$\frac{\mu_{\text{eff}}}{\sigma_k}$	$G_{k_1} - \rho\epsilon$
ϵ	1	$\frac{\mu_{\text{eff}}}{\sigma_\epsilon}$	$\frac{\mu_{\text{eff}}}{\sigma_\epsilon}$	$\frac{\epsilon}{k}(C_1 G_{k_1} - C_2\rho\epsilon)$
f	1	$\frac{\mu_{\text{eff}}}{\sigma_f}$	$\frac{\mu_{\text{eff}}}{\sigma_f}$	0
h	1	$\frac{\mu_{\text{eff}}}{\sigma_h}$	$\frac{\mu_{\text{eff}}}{\sigma_h}$	0
g	1	$\frac{\mu_{\text{eff}}}{\sigma_g}$	$\frac{\mu_{\text{eff}}}{\sigma_g}$	$C_{g_1} G_{g_1} - C_{g_2}\rho\frac{\epsilon}{k}g$
m_{fu}	1	$\frac{\mu_{\text{eff}}\mu}{\sigma_{\text{fu}}}$	$\frac{\mu_{\text{eff}}}{\sigma_{\text{fu}}}$	R_{fu}

$$G_{k1} = \mu_{\text{eff}}\left[2\left(\left(\frac{\partial U}{\partial x}\right)^2 + \left(\frac{\partial V}{\partial r}\right)^2 + \left(\frac{V}{r}\right)^2\right) + \left(\frac{\partial W}{\partial x}\right)^2 + \left(r\frac{\partial}{\partial r}\left(\frac{W}{r}\right)\right)^2 + \left(\frac{\partial U}{\partial r} + \frac{\partial V}{\partial x}\right)^2\right]$$

$$G_{g1} = \mu_{\text{eff}}\left[\left(\frac{\partial m_{\text{fu}}}{\partial x}\right)^2 + \left(\frac{\partial m_{\text{fu}}}{\text{d}r}\right)^2\right]$$

of the comparisons are discussed and specific conclusions stated in the closing sections.

Calculation Procedure

The present section presents the conservation equations and corresponding boundary conditions and comments briefly on the thermodynamic properties, the turbulence model, the combustion models, and the solution procedure. Further details of the solution procedure may be found in references [2, 3]. The equations and physical assumptions are given in detail in references [3, 7].

Equations and Boundary Conditions. The conservation equations, apart from mass continuity, had the common form:

$$a_1\left[\frac{\partial}{\partial x}(\rho U\phi) + \frac{1}{r}\frac{\partial}{\partial r}r(\rho V\phi)\right] = \frac{\partial}{\partial x}\left(b_1\frac{\partial\phi}{\partial x}\right) + \frac{1}{r}\frac{\partial}{\partial r}\left(rb_2\frac{\partial\phi}{\partial r}\right) + S_\phi \quad (1)$$

where the corresponding values of a_1, b_1, b_2 and S_ϕ are given in Table 1. The dependent variables include three components of the time-averaged velocity, total enthalpy and species properties and are to be calculated at values of the independent variables x and r. The use of time-average equations and the effective viscosity hy-

Nomenclature

a_0, b_0, c_0, d_0 = constants in specific heat equation
b_1, b_2 = constants
C_p = specific heat at constant pressure
C_1, C_2 = constants in turbulence model
C_{g1}, C_{g2} = constants in combustion model
C_D = constant
C_R = eddy-break-up constant
D = diameter
E = constant of law of wall
f = mixture fraction = $(\varphi - \varphi_A)/(\varphi_F - \varphi_A)$
g = square of the fluctuation of concentration
h = stagnation enthalpy
H_{fu} = heat of reaction of fuel
i = stoichiometric mass of oxygen per unit mass of fuel
k = kinetic energy of turbulence = $\frac{1}{2}(u^2 + v^2 + \bar{w}^2)$
K = constant in log law
M = molecular weight
m = mass fraction
P = pressure
Q = heat flux
R = universal gas constant
r = radial distance from axis of symmetry
R_0 = burner outer radius
Re = Reynolds number
R_ϕ = residual value
S = swirl number defined as; $\int WU\rho r^2 dr / (\int \rho U^2 r dr) R_0$
s_ϕ = source or sink term of any variable
T = absolute temperature
U = fluid mean velocity in the axial direction
u = fluctuation component of axial velocity
V = radial mean velocity
v = fluctuation component of radial velocity
W = mean tangential velocity
w = fluctuation component of tangential velocity
x = axial distance from burner exit
y = radial distance from burner centre line
y_a = width of burner annulus
μ = viscosity
ρ = density
σ_ϕ = Schmidt and Prandtl numbers for any variable ϕ
ϵ = dissipation of energy
$\varphi = (m_{fu} - m_{ox}/i)$
ϕ = general dependent variable
eff = effective (including the effects of turbulence)
fu = fuel
i = species
ox = oxidant
f = furnace
A = air stream
F = fuel stream
w = wall

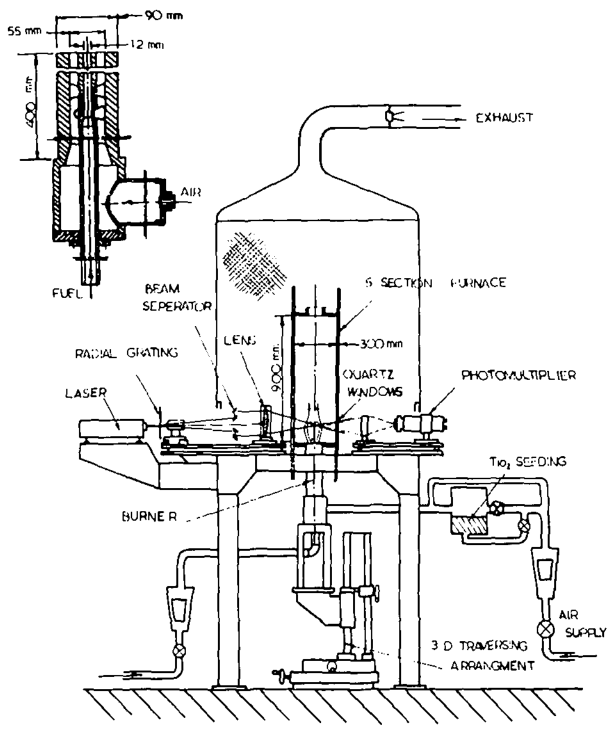

Fig. 1 Arrangement of furnace, burner and laser—Doppler anemometer

pothesis implied by Table 1 requires equations for turbulent kinetic energy and dissipation rate and constitute a model of turbulence. The equations for species concentration and species concentration fluctuations represent the combustion processes and will be referred to as the combustion model.

Boundary conditions are required for each of the equations of Table 1 and, wherever possible, these were obtained by measurement. Fig. 1 shows the geometry of the present furnace and shows a symmetry axis; this provides a boundary condition of the form $\partial\phi/\partial r = 0$ for one boundary of the solution domain. The velocities were assumed zero at all walls and the measurements provided the corresponding wall temperature conditions. The gradients of m_i, f, and g were assumed zero at all walls. At the inlet, the dissipation rate was determined from the equation

$$\epsilon = C_D \frac{k^{3/2}}{0.03y_a} \qquad (2)$$

which stems from a mixing length assumption: all other properties were taken from measurements. At the exit, all gradients were assumed to be zero; as was shown in references [3, 7], this assumption has a negligible influence on the upstream flow.

Thermodynamic Properties. The local density of the gaseous mixtures was obtained from the perfect gas law and Dalton's law of partial pressures. Values of specific heat were obtained from equations of the form:

$$\bar{C}_{p_i} = a_{0_i} + b_{0_i}T + c_{0_i}T^2 + d_{0_i}T^3 \qquad (3)$$

$$\bar{C}_{p_{\text{mix}}} = \sum_i m_i \bar{C}_{p_i} \qquad (4)$$

with the constants suggested in reference [8]. The total enthalpy of the mixture was defined as

$$h = m_{\text{fu}}H_{\text{fu}} + m_i\bar{C}_{p_i}T + (U^2 + V^2 + W^2)/2 \qquad (5)$$

with the heat of reaction, H_{fu}, taken as 4.97×10^4 kJ/kg.

Turbulence Model. The turbulence model involves the solution of the equations for k and ϵ together with the equations

$$-\overline{\rho uv} = C_D\rho\frac{k^2}{\epsilon}\left(\frac{\partial U}{\partial y} + \frac{\partial V}{\partial x}\right), \; -\overline{\rho uw} = C_D\rho\frac{k^2}{\epsilon}\left(\frac{\partial W}{\partial x}\right) \qquad (6)$$

The diffusion and dissipation terms in the k and ϵ equations are simplified representations of the exact terms and, although based on reasonable assumptions, have not been tested directly. The validity of this two-equation turbulence model has been tested by comparing calculations, obtained from the solution of boundary-layer equations including appropriate forms of the k and ϵ equations, with measurements also obtained in boundary-layer type flows. It has not been extensively tested in elliptic flows and the comparison of Section 4 help to meet this need.

Combustion Models. A one step, finite reaction rate model has been assumed for all calculations of section 4. It requires the solution of equations for f, g, and m_{fu} and represents the source term in the fuel equation by

$$R_{\text{fu}} = m_{\text{fu}}\,\rho^2\, m_{\text{Ox}} 10^{10} \exp(-1.84 \times 10^4/T) \qquad (7)$$

$$\text{or } R_{\text{fu}} = C_R g^{1/2}(\rho\epsilon/k) \qquad (8)$$

whichever is the smaller.

The time variation of f was assumed to have a square wave form, corresponding to a double delta function probability distribution, i.e.

$$f_+ = f + g^{1/2}, f_- = f - g^{1/2} \qquad (9)$$

except where the value of f_+ would exceed unity or f_- fall below zero. In these regions, the factor α defined by

$$f = \alpha f_+ + (1 - \alpha)f_- \qquad (10)$$

was adjusted to insure that f_+ was unity or f_- zero. This procedure allowed fuel and oxygen to exist at the same place but at different times. The local temperature of the mixture was determined from the enthalpy obtained from the simultaneous solution of the h–equation. From the definition of h given in equation 5, T_+ and T_- are calculated corresponding to values of $m_{\text{fu}+}$ and $m_{\text{fu}-}$. Values of mean temperature were then obtained from an equation similar to equation (10).

The values of constants in the turbulence and combustion models are listed in Table 2 and are consistent with those proposed in reference [9]: they have not been modified for the present calculations.

Solution Procedure. The differential equations represented by equation (1) and Table 1 were expressed in the finite-difference form of reference [2] and solved by the algorithm of that paper. The present calculations were performed with a grid composed of 20 × 20 nodes and allowed the solution of the 10 equations in approximately 8 min of CDC 6600 cp time; in the absence of swirl, this time reduced to 6 min and in the absence of swirl and combustion to 4 min. These times were achieved with the help of wall functions which linked the wall value to first grid nodes located in the logarithmic region of the boundary layer [9].

The distribution and number of grid nodes was investigated in reference [3] and the present arrangement was based on that experience. Convergence was assumed when the maximum residual, i.e.

$$[\text{convection} + \text{diffusion} + \text{source}]_{j+1}/\phi_j$$

was less than 10^{-4} at any grid node. After 30 iterations, all calculations were observed to converge monotonically. Approximately 250 iterations were required to satisfy the above convergence criterion.

Table 2 Turbulence and combustion model constants

Constant	Value
C_1	1.44
C_2	1.92
C_D	0.09
K	0.42
E	8.8
C_{g_1}	2.8
C_{g_2}	2.0
C_R	1.0

$\sigma_\epsilon = 1.22; \sigma_k = \sigma_h = \sigma_{fu} = \sigma_g = \sigma_f = .9$

Experimental Procedure

The model furnace and burner arrangements, the instrumentation and the experimental procedures are described briefly and separately in the following paragraphs. With the exception of temperature and heat-flux measurements, the instrumentation is similar to that described in reference [1]; the furnace and burner are also similar but were operated at higher flow rates and, as a consequence, the furnace cooling water was directed to a heat exchanger.

Furnace and Burner Arrangements. Fig. 1 shows, in line-diagram form, the outline and dimensions of the furnace enclosure and the layout of the laser-Doppler anemometer. For the isothermal measurements, a plexiglass enclosure was used and allowed measurements of the three orthogonal velocity components at all locations in the enclosure except in the vicinity of the wall. For the combusting measurements, a double-skinned steel enclosure of the same internal dimensions was used; it was water cooled in five separate axial sections and one section was fitted with windows to allow the transmission of light beams. The bottom plate of the furnace was also water cooled. The finite dimensions of the windows limited the range of locations at which the radial velocity component could be measured.

The burner arrangement is also shown on Fig. 1. For the isothermal measurements, the Reynolds number of the flow in the annulus was 4.7×10^4, corresponding to a mean axial velocity of 12.85 m/s, and that of the central jet flow 0.55×10^4; vane swirlers were added to produce a swirling annulus flow with a swirl number of 0.52. For the combusting measurement, natural gas (CH_4—94.4 percent, N_2—1.40 percent C_2H_6—3.1 percent); was supplied through the central jet to provide an initial mixture fraction corresponding to stoichiometric combustion.

The furnace and burner arrangement was traversed with respect to the laser-Doppler anemometer. The precision of translation in the horizontal plane was of the order of 1.0 mm and, in the vertical plane 2 mm. In this vertical plane, the burner top and bottom plates were moved vertically within the fixed steel enclosure.

The measurements were obtained without seeding the flow although residual titarium dioxide particles in the pipework did contribute to the particulate content of the flow.

Instrumentation. Velocity measurements were obtained with a laser-Doppler anemometer comprising an argon ion laser, a bleached radial diffraction grating and a focussing lens, a light collection arrangement, a photomultiplier and a bank of filters whose output was read automatically and transferred to paper tape. The laser was operated at 488 nm with a power output of approximately 130 MW. The radial grating had a total of 18,000 lines, equispaced in angle. on a radius of 130 mm and was rotated at velocities up to 5000 rpm. The bleaching process allowed 55 percent of the incident light energy to be concentrated into the two first order beams; further details of the performance characteristics of bleached gratings have been provided by Wigley [10]. Measurements were made with frequency shifts from −3.01 MHz to 3.01 MHz. The focussing lens had a focal distance of 400 mm and the forward-scattered light was collected by a lens of diameter 25 mm and focal length 200 mm: it was passed through a 0.75 mm pinhole to the photomultiplier (EMI 9635QB) cathode. The resulting control volume dimensions corresponded to a length of 2.4 mm and a diameter of 0.21 mm. The signal from the photomultiplier was high pass filtered at 600 kHz, amplified, low pass filtered at 10 MHz; limited to 100 mV and supplied to the filter bank described in detail by Baker [11]. In the filter bank the input signal was presented to 60 parallel filters with centre frequencies ranging from 0.631 MHz to 9.55 MHz in a logarithmic progression. After a threshold level had been set to reduce system noise, the filter bank logic established the most resonant of the filters and provided a voltage proportional to this frequency. The voltage analogue signal was supplied to a time analyser which time averaged the signal, and its square, to give values of the mean and rms velocities. The voltage analogue was further used to trigger a constant current which charged a capacitor, associated with a resonant filter, for the length of time of the Doppler burst. By scanning and logging the accumulated charges in the sixty individual capacitor stores, a histogram display was produced and is related to the probability distribution of Doppler frequencies. Statistical analysis of the histogram yielded the mean and rms velocities and higher moments.

The local temperature of the combusting gas was measured with a miniature suction pyrometer. The gas was sucked isokinetically into the probe and over a platinum–platinum 13 percent rhodium thermocouple calibrated between 1100 and 1800 K with a precision of ±20 K: at temperatures below 1100 K, the instrument was at least as precise on this calibration. The temperature of the furnace wall was obtained from chromel alumel thermocouples welded to the surface. The flow rates of water to each of the five sections of the enclosure were measured by rotameter and, together with the temperature of the water at inlet and outlet, allowed the calculation of the wall heat flux.

Results

The measurements presented in this section relate to a swirl number of 0.5 and to isothermal and combusting flow. Preliminary measurements with a swirl number of zero indicated that the flame was not stabilised on the burner and, since this was physically undesirable and could not be satisfactorily represented by the calculation method, they were not persued. The swirl number was determined by assuming profiles of nondimensional velocity and normal stresses, similar to those of reference [1] and calculating the profiles of velocity and normal stresses at downstream locations: the profiles at 0.1 D_f and 0.166 D_f, shown on the following figures were in closest agreement with a swirl number of 0.5 for both isothermal and combusting flow and confirm the measurement of reference [1].

Figs. 2 and 3 present measured profiles of the axial mean velocity and the corresponding normal stress at locations downstream of the burner with isothermal air flow. The calculated profiles are also shown and the general agreement supports the view that the calculation method is satisfactory for isothermal flows and may be applied to combusting flows with the knowledge that the turbulence model is likely to be adequate. As can be seen, the distribution of mean axial velocity is complex with a substantial region of recirculation which begins at the burner exit and extends, away from the centre line, to one furnace diameter downstream. The corresponding fluctuation velocity is comparatively large close to the burner and tends to a uniform and lower value at downstream locations. The calculated normal stress is, of course, based on the solution of an equation for turbulence kinetic energy and assumes that $\overline{u^2} = \frac{2}{3}k$.

Figs. 4 and 5 present measurements corresponding to those of Figs. 2 and 3 but relate to the combusting flow. The axial velocity and corresponding normal stress are larger in the combusting case, particularly in the region of the reaction zone. Indeed the region of the reaction zone can readily be recognized from the measurements. Once again, the calculated profiles are in general agreement with the measurements although quantitative differences, particularly in the reaction zone, are present. Mean and rms tangential velocity profiles are presented in Fig. 6 at two axial locations close to the burner exit for the burning case; they show that the larger tangential velocities are only slightly smaller than the corresponding axial velocities and that the normal stresses have a similar relationship.

The center-line velocity distributions for the isothermal and combusting flows are shown on Fig. 7. Only two measurements were obtained for the isothermal flow due to the very low particle concentration in this region. Comparison of the measured and calculated distributions indicates general agreement although the measured wake development is faster than that calculated. The region of center-line recirculation is substantial for the combusting flow and the comparison of the two distributions is similar to those reported in reference [1]. The figure also presents calculated distributions of axial velocity for a range of swirl numbers and shows

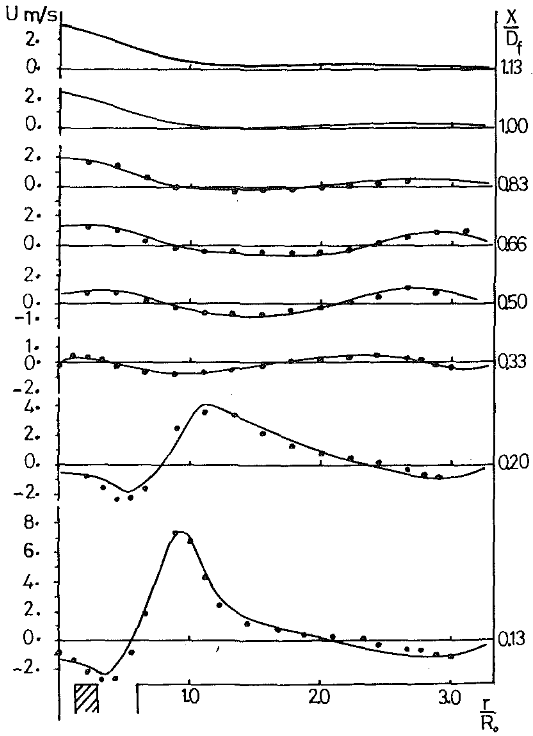

Fig. 2 Measured and calculated profiles of mean axial velocity: isothermal flow . . . measured values, —calculated values

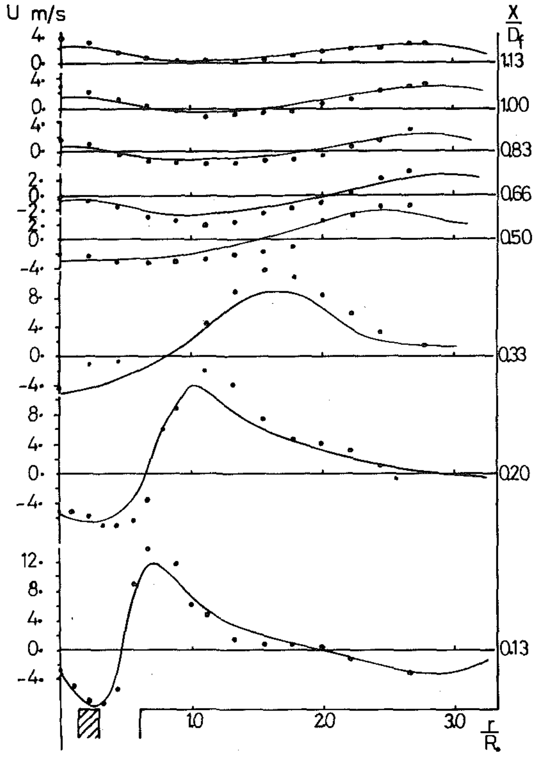

Fig. 4 Measured and calculated profiles of mean axial velocity: combusting flow . . . measured values, —calculated values

that the location and magnitude of the recirculation region are very dependent on the swirl number.

Measured and calculated temperature profiles are presented in Fig. 8 and can be related to the recirculation regions indicated by Fig. 4. They reveal temperature minima, close to the water-cooled base plate and in the region of forward velocity. The two temperature maxima, on either side of the minimum values, represent the edges of the reaction zone.

Figs. 9 and 10 present center-line distributions of mean temper-

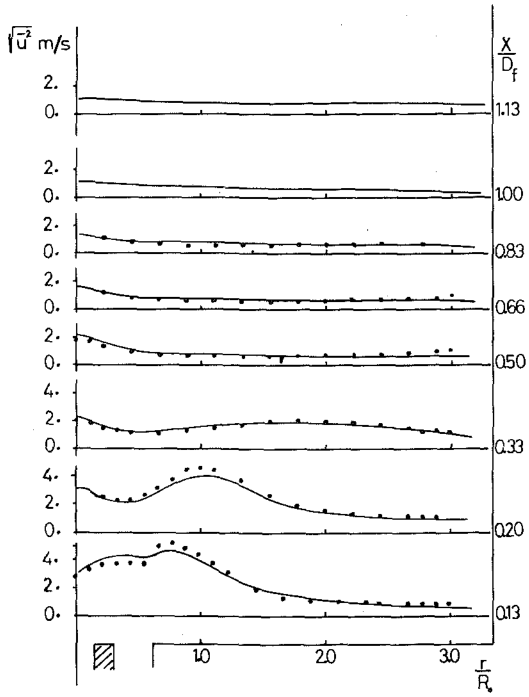

Fig. 3 Measured and calculated profiles of axial normal stress: isothermal flow . . . measured values, —calculated values

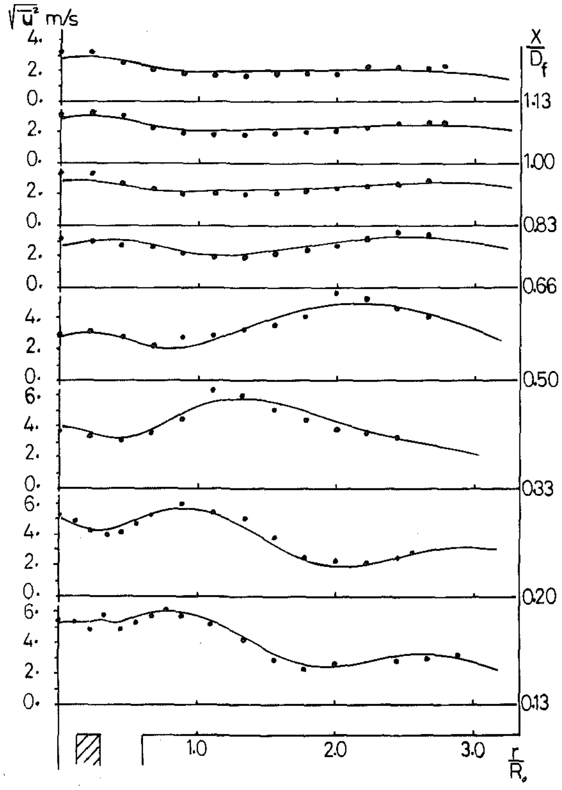

Fig. 5 Measured and calculated profiles of axial normal stress: combusting flow . . . measured values, —calculated values

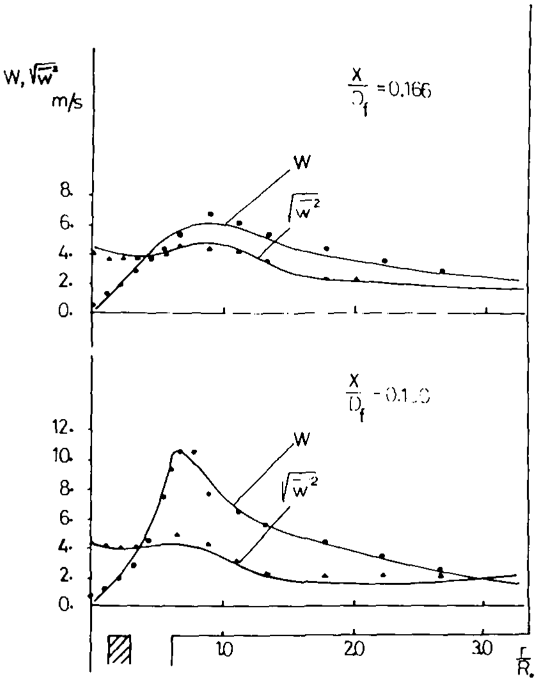

Fig. 6 Measured and calculated profiles of mean tangential velocity and the corresponding normal stress: combusting flow . . . measured values, —calculated values

ature and wall-heat flux respectively. Measured and calculated values may be compared for the case of a swirl number of 0.5 and the influence of swirl deduced from the calculations. The temperature results indicate that, as far as the center line is concerned the highest swirl number leads to the most rapid rise in temperature. The heat-flux results confirm this and suggest that the present furnace would be operated more effectively with higher flow rates of air and fuel.

Discussion and Conclusions

The comparisons of the previous section show that the calculated results are in general agreement with the measurements but that quantitative differences remain to be explained. Similar calculations, performed with the same physical information but with a different numerical scheme [7] show that differences of up to 15 percent can be introduced by the numerical arrangement although the rms difference was less than 5 percent. It must be presumed, therefore, that a substantial part of the differences indicated on the previous figures must be attributed to the physical content of the calculation method or to errors of measurement, with the former as the main source.

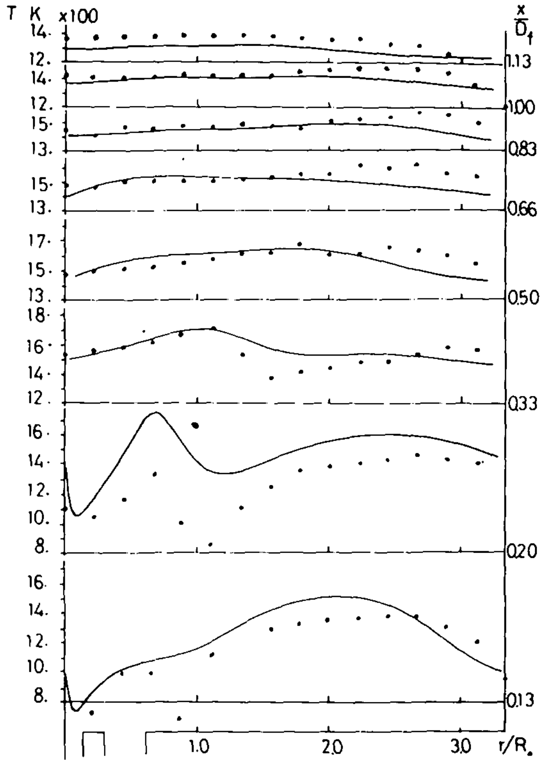

Fig. 8 Measured and calculated profiles of mean temperature . . . measured values, —calculated values

The turbulence model may be assessed from the results of Figs. 2 and 3 and appears to result in differences from the measurements which exceed the experimental scatter and which amount to up to 40 percent of the maximum velocity in the appropriate axial plane. The largest disagreements are in the wake and suggest that the two-equation turbulence model is inadequate in such regions. This conclusion is substantiated by the calculations of Pope and Whitelaw [12] for separated—wake flows. It is noteworthy that the two equation model also assumes isotropy of the normal stresses which is undoubtedly incorrect.

The major source of imprecision for the furnace calculations is the combustion model. The present calculations were repeated

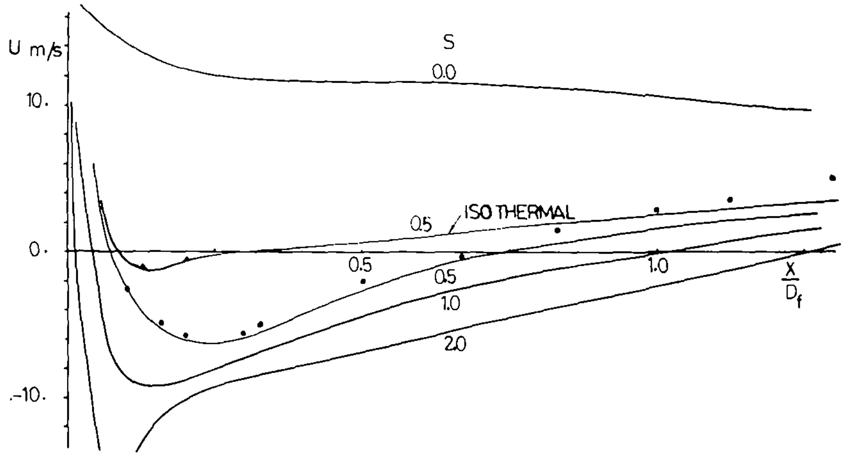

Fig. 7 Measured and calculated center-line distributions of axial mean velocity . . . measured values, —calculated values

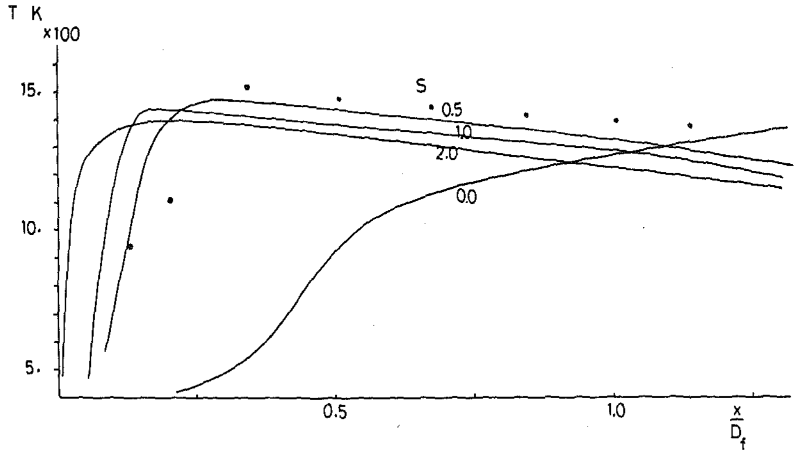

Fig. 9 Measured and calculated center-line distributions of mean temperature . . . measured values, —calculated values

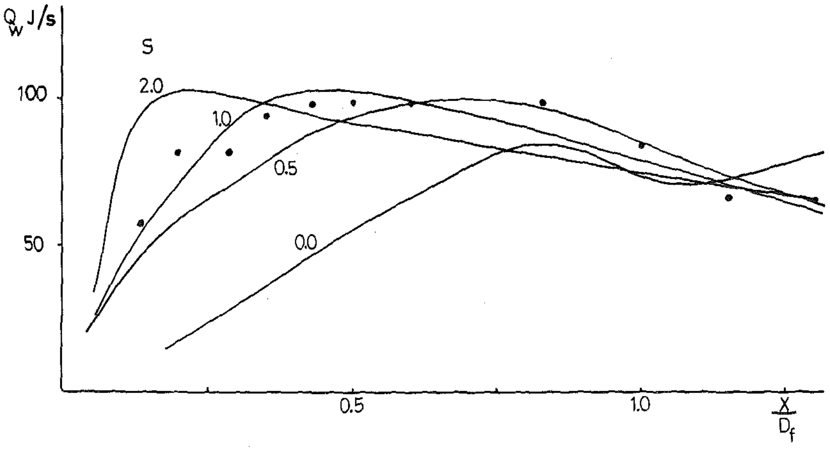

Fig. 10 Measured and calculated distributions of wall-heat flux . . . measured values, —calculated values

with the alternative assumption of infinite-reaction rate and the results were different from those presented here; the differences were not, however, significant when compared with the differences from the experimental data. Instant reaction is undoubtedly an over simplification and the faults in the present model must be traced and corrected. Since the eddy-break up equation controls the reaction for most of the solution domain it may be concluded that it is in need of improvement. Also, the square-wave variation of the mixture fraction with time is a simplification which has not been directly tested for flows of this type. These two assumptions are the most likely reasons for the discrepancies of, for example, Fig. 8 and work is presently in hand to improve them.

In spite of the emphasis of the previous paragraphs on the need to improve the calculation procedure, the results show that trends have been predicted correctly with the present assumptions and consequently the calculation procedure contribute to design in its present form. This is the major conclusion of the present investigation.

Acknowledgments

The present work was carried out with the financial assistance of the AERE, Harwell. Grateful thanks are due to Dr. J. Rhines of British Gas Corp., Solihull for assistance and advice on suction pyrometer measurements.

References

1 Baker, R. J., Hutchinson, P., Khalil, E. E., and Whitelaw, J. H., "Measurements of Three Orthogonal Velocity Components in Confined Coaxial Jet Flows With and Without Swirl and Combustion," *Proceedings 15th Symposium on Combustion*, 1974, p. 533.

2 Gosman, A. D., and Pun, W. M., Lecture notes for course entitled "Calculation of Recirculating Flows," Imperial College, Mechanical Engineering Department, 1973.

3 Hutchinson, P., Khail, E. E., and Whitelaw, J. H., "The Calculation of Wall Heat-Transfer Rate and Pollution Formation in Axi-Symmetric Furnaces," Fourth Members Conference of the IFRF, 1976.

4 Fricker, N., van Heyden, L., and Michelfelder, S., "Investigations Into the Combustion of Natural Gas in Multiple Burner Systems," International Flame Research Foundation document F35/a/5, 1971.

5 Fricker, N., and Wu, H. L., "An Investigation of the Behaviour of swirling Jet Flames in a Narrow Cylindrical Furnace," International Flame Research Foundation, 2nd Members Conference, 1971.

6 Gunther, R., and Lenze, B., "Exchange Coefficients and Mathematical Models of Jet Diffusion Flames," *Proceedings 14th Symposium on Combustion*, 1972, p. 675.

7 Khalil, E. E., and Whitelaw, J. H., "The Calculation of Local-Flow Properties in Two-Dimensional Furnaces," Imperial College, Mechanical Engineering Department Report HTS/74/38, see also I.J.H.M.T. Vol. 18, 1975, p. 775.

8 JANAF thermochemical tables, National Bureau of Standards, USA: NSRDS NBS 37, COM-71-50363, 1971.

9 Launder, B. E. and Spalding, D. B. *Mathematical Models of Turbulence*. Academic, 1972.

10 Wigley, G., "The Application of Radial Diffraction Gratings to Laser

Anemometry," AERE Report 7886, 1974.

11 Baker, R. J., "The Application of a Filter Bank to Measurements of Turbulence in a Fully Developed Jet Flow, *Proceedings of 2nd International Workshop on Laser Velocimetry,* Purdue University, 1974.

12 Pope, S. B., and Whitelaw, J. M., "The Calculation of Near-Wake Flaws," *Journal of Fluid Mechanics*, Vol. 73, 1976, p. 9.

A. F. Emery
R. E. Short
A. W. Guy
K. K. Kraning

University of Washington,
Seattle, Wash.

J. C. Lin

Wayne State University,
Detroit, Mich.

The Numerical Thermal Simulation of the Human Body When Undergoing Exercise or Nonionizing Electromagnetic Irradiation

The human body was modeled by a finite difference numerical procedure to determine the effect of simulating the sweating rate by different analytical models. Six different models were used in which the hypothalamus, muscle, average skin, and local skin temperatures were used as the controlling parameters for the rate of local sweating. These different models were tested by comparing their predictions of local temperatures for an exercising man with measured values. The computer program was then used to compute the thermal response of a man subjected to microwave irradiation of the entire body and the head only. Transient head and body temperatures and sweating rates were computed and compared with the temperature changes due to an equivalent exercise level. Significant differences in the results found by using the different sweat models point out the need for further work in determining accurate analytical descriptions of this major mode of body heat loss.

1 Introduction

In man, as in all homeotherms, the precise regulation of the internal body temperature is necessary for life. If the central body temperature falls much below 34°C, the temperature regulation is impaired, while if it rises much above 41°C, the central nervous system deteriorates and severe convulsions occur. The determination of the body temperatures under changing ambient conditions, variation of metabolic heat, and the absorption of nonionizing radiation requires a detailed study of the modes by which heat is transferred within the body to the skin and from the body surface to the ambient atmosphere. The transfer to the skin surface occurs by conduction through bones, tissue, fat, and skin and by convection accompanying the circulation of blood. Heat transfer also occurs between large arteries, large veins, and tissues due to temperature differences. The convective mode is of greatest importance to the body's thermal well-being because of its effectiveness in minimizing the temperature differences within the body. Furthermore, the variation of convection by the constriction or dilation of the cutaneous capillaries controls the internal heat distribution by reapportionment of the blood flow and the effective body insulation by increasing or decreasing the distance that the heat must flow through from the superficial layer to the superficial epidermis. This vasomotor state of the peripheral vessels is subject to thermoregulatory action and will be discussed in more detail in Section 2.

Once the heat has reached the body surface, it is then lost to the environment by the usual modes of conduction, convection, radiation, passive diffusion of water vapor through the skin, and by res-

---

Contributed by the Heat Transfer Division for publication in the JOURNAL OF HEAT TRANSFER. Manuscript received by the Heat Transfer Division June 5, 1975. Paper No. 76-HT-KK.

piration losses, none of which mechanisms are subject to thermoregulation. Sweating, the evaporation of fluid secreted from specialized glands within the skin, is subject to thermoregulation, with the secretion being in proportion to the stimulus. The quantity of heat lost by sweating is dependent upon the amount of sweat secreted and upon the portion which can evaporate. Under normal conditions, convection accounts for 40 percent of the total heat loss, radiation for 45 percent, conduction for 7 percent, respiration for 8 percent, passive diffusion for 7 percent, and sweating for 0 percent. However, under some conditions, sweating becomes the dominant heat loss mechanism.

One of the major concerns of this study was to determine the adequacy of the many different sweat models available in computing the changing body temperatures for the markedly different thermal loading caused by changes in ambient conditions, exercise, and electromagnetic deposition. Once sweating is initiated, the skin temperature often drops significantly, but nonuniformly, thus changing the conduction and convection patterns in the body and thereby reacting with the distribution of sweating.

2 The Thermal Model

The thermal models of man are usually based upon a division of the body into smaller anatomical structures with each treated by the usual conservation of energy equations,

$$\rho c \frac{\partial T}{\partial t} = \nabla(k\nabla T) + C + D + M + R + S + H \qquad (1)$$

where C is the heat *convected* by the blood; D, the passive *diffusion* of water vapor through the skin; M, the *metabolic* heat generation; R, the *respiratory* heat loss; S, the heat lost due to *sweating;* and H, the convective and radiative loss from the skin. Different models have been developed for the subdivision according to the purpose of the study. A survey of some of the different numerical and mathematical models of the human body is given by Fan [17].[1]

The model used herein, illustrated in Fig. 1, is assumed to be divided into 10 segments, representing the head, trunk, arms, hands, and legs following the work of Stolwijk [47], and Stolwijk and Hardy [48]. Each segment is further divided into a core region, muscle layer, fat layer, and skin. A common blood supply links the segments.

The conduction term, the convection term C, and the metabolic heat M are applicable to all of the segments. Thermal conductivity values were taken from references [11–14, 46–48, 51, 52, 54]. The convection term was expressed in the form,

$$C = \dot{m}_{b\ell} c_{b\ell} (T_{b\ell} - T) \qquad (2)$$

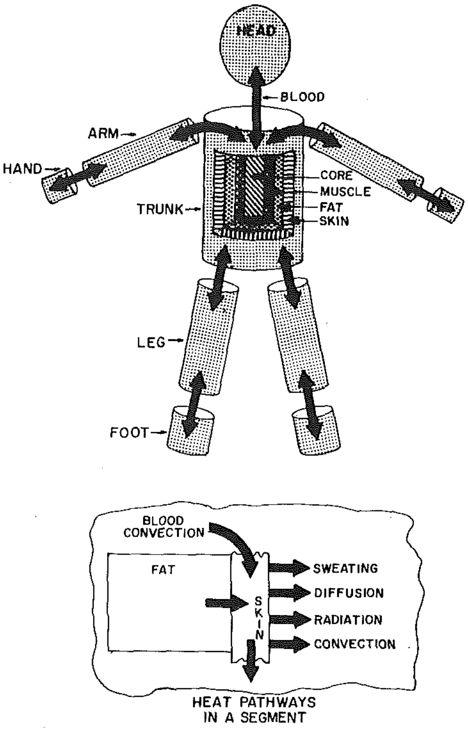

Fig. 1 Thermal schematic of the human body

which is based upon the assumptions that: (*a*) the blood enters the tissue volume at the common arterial temperature $T_{b\ell}$ (e.g., there is no heat exchanged with the blood while it is en route to the vascular bed); (*b*) after perfusing the tissue the blood exits at the local tissue temperature T. This last assumption, described by Pennes [35] and Perl [36], is based upon the micron distances in the capillaries and the small blood flows involved, and although it is commonly used in biological heat transfer simulation, it has never been completely experimentally verified.[2] Emery [16] has successfully utilized this assumption in modeling the temperatures in the rabbit eyes. The influences varying the blood flow rates caused by thermoregulation are most strongly felt in evaluating the heat exchange to the skin. Unfortunately, the skin blood flow regulation has not been well quantified. Benzinger [4], Stolwijk [47], Wissler [54], Brenglemann [7], Wyss [56], and Johnson [25] discuss the thermoregulation of the skin blood flow in detail. We chose to use

---

[1] Numbers in brackets designate References at end of paper.

[2] See reference [55] for a criticism of equation (2).

Nomenclature

A_{Du} = Dubois body area
B = the product, $\dot{m}c$
c = specific heat
C = heat convected by the blood
D = passive diffusion heat flux
E = electric field
h = surface heat transfer coefficient
H = convective and radiative heat flux
k = thermal conductivity, wave propagation constant
K = conductance
$\dot{m}$ = flow rate
M = metabolic heat generation
$N = \mathrm{N}^2 = \epsilon_1 + i\epsilon_2$, relative complex dielectric constant
P = pressure
Q = heat flux
R = respiratory heat flux, radius
S = sweating heat flux
t = time
T = temperature
$\hat{x}, \hat{y}, \hat{z}$ = rectangular Cartesian coordinates
ϵ_1, ϵ_2 = relative dielectric constants
$\hat{\theta}, \hat{\phi}$ = spherical coordinates
ρ = density
ω = frequency
σ = electrical conductivity

Subscripts

a = ambient
$b\ell$ = blood
ex = expired air
h = hypothalamic
m = muscle
r = rectal
res = respiratory
s = skin
sw = sweat

Wyss' formulation:

$$\dot{m}_{b\ell} = \alpha(T_{ra} - T_{ra0}) + \beta(T_s - 33.0) - \delta(-\dot{T}_s) + \gamma \qquad (3)$$

where T_{ra} is the right arterial temperature, T_{ra0} is the reference value of T_{ra}, T_s and $\dot{T}_s$ are the skin temperature and time rate of change and γ is the basal blood flow.

As the metabolic rate in active muscle increases, so too must the blood flow rate in order to replenish the muscle with oxygen and to carry away the excessive metabolic heat. Stolwijk [47] considered the muscle blood flow to consist of the basal flow plus 1 l/hr per kcal/hr of heat production. Pirnay [37] suggests a value of 0.82 as determined for the total metabolic increase. The blood flow through the areas of the body excluding the muscle and skin areas is assumed to remain at a constant basal level. This is not entirely accurate in many circumstances, but there is not sufficient information to quantify the changes. For example, during strenuous exercise the blood flow to the gut decreases and hepatic temperatures in excess of 41°C have been measured due to the decreased liver flow [40].

The respiratory loss, R, is estimated, by assuming that the expired air has come to thermal equilibrium with the core temperature of the trunk and is saturated [28] and using Fanger's [18] estimate of the ventilation rate, to be,

$$Q_{\text{res}} = M\{0.0023(44 - P_a) + 0.0014(T_{\text{ex}} - T_a)\} \qquad (4)$$

Mitchell, Nadel, and Stolwijk [30] have verified this expression by measuring the rate of respiratory water loss during different levels of bicycle exercise over a range of environmental conditions.

The radiative and convective heat losses from the skin are treated in the standard engineering manner assuming that the skin is a black body and the area is a fraction of the duBois area [15]. The convective coefficients were taken from the manikin studies of Nielsen and Pedersen [34] and Winslow [53]. The remaining term in equation (1) is the heat loss from the skin by sweating. This loss is a function of surface area, the ambient humidity, and the nature of the thermosensitive sites within the body from which originate the different signals which control sweating. The location of and precise nature of the thermoreceptors which produce the signals is still open to question, since many of the experimental observations were based upon animals other than man and it cannot be conclusively stated that the same sites and characteristics exist in man also. In general, the importance of an internal or core temperature is accepted, although it is not yet well defined as a function of the different specific core regions. Furthermore, there is considerable question about the influence of the local skin temperature and whether the sweating response is an additive function of the several impulses or a multiplicative function. A good background description of the sweating mechanism and the associated experiments can be found in reference [22]. Typical of the two types of response are Benzinger's additive equation [5],

$$\frac{Q_{sw}}{A_{\text{Du}}} = 15.7(T_h - T_{h0}) + \beta(\bar{T}_s - \bar{T}_{s0}) \text{ W/m}^2 \qquad (5)$$

(where T_{h0} and T_{s0} are the datum values for the hypothalamic and mean skin temperatures). These datum values (frequently termed set points) are the temperatures which the thermoregulatory mechanism attempts to maintain and it is not uncommon for investigators to assume that the set point is a variable temperature which depends on a number of physiological conditions. Benzinger, through tests on several subjects, suggested that $\beta = 1.6$ kcal/kg-hr-°C for $T_s < 33°\text{C}$ and $= 0$ for $T_s > 33°\text{C}$. According to this, the mean skin temperature is a slight inhibiting effect for $T < 33°\text{C}$ and ineffective for $T > 33°\text{C}$, thus the sweat drive is almost entirely a function of central body temperature. Because of this, many workers have questioned his results. Stolwijk and Hardy [21, 49] tested subjects for thermal transients and recommended,

$$\frac{Q_{sw}}{A_{\text{Du}}} = 5.8 + 93(T_e - 37.18) + 20.9(\bar{T}_s - 33.0) \text{ W/m}^2 \qquad (6)$$

where T_e is the tympanic temperature. This additive relationship could not fit all of the data, and experiments which incorporated exposures to a wider range of environmental conditions led to the multiplicative relationship.

$$\frac{Q_{sw}}{A_{\text{Du}}} = 11.6 + 81.4(T_e - 36.6)(\bar{T}_s - 33.5) \text{ W/m}^2 \qquad (7)$$

This expression is adequate for a sedentary subject, but does not adequately account for exercise and other physiological changes, although it allows for a substantial mean skin effect.

Stolwijk and Hardy and Stolwijk and Gagge [45, 50] have evaluated different sweating models to determine their accuracy in determining the effects of various levels of exercise and the transient effects. Some of these findings differed with those of Beaumont and Bullard [2], although the conditions were not quite the same. At any rate, no linear combination of temperatures could be found to characterize sweating both during or after exercise. They proposed either,

$$\frac{Q_{sw}}{A_{\text{Du}}} = 79(T_h - 36.6)(\bar{T}_s - 34.1) + 233(\bar{T}_m - 35.88) \times (T_h - 36.6) \text{ W/m}^2 \qquad (8a)$$

or

$$\frac{Q_{sw}}{A_{\text{Du}}} = 132.6(T_h - 36.6) + 19.8(\bar{T}_s - 33.3) \text{ W/m}^2 \qquad (8b)$$

Probably the most detailed work is that of Nadel, Bullard, and Stolwijk [31], who considered the effects of local and time derivative effects, skin wettedness, and degree of acclimation to exercise, and proposed,

$$\begin{array}{l}\text{Local}\\ \text{Sweat} = \{\alpha(T_{es} - T_{es0}) + \beta(\bar{T}_s - \bar{T}_{s0})\}e^{(T_s - T_{s0})/\delta}\\ \text{Rate}\end{array} \qquad (9)$$

Further studies indicated the effects of the time rate of change of the skin temperature, local variations in sweating, reabsorption of the sweat, and the subject's acclimation to exercise. However, at this time only the chest [32] and arm [23] local sweat rates have been quantified.

Nadel, et al. [33] also presented two simplified expressions which could be used in describing whole body evaporation, for thermal equilibrium,

$$\frac{Q_{sw}}{A_{\text{Du}}} = \{229(T_{es} - 36.7) + 26.7(\bar{T}_s - 34)\}e^{(\Sigma T_s - 34)/10} \text{ W/m}^2 \qquad (10)$$

and for exercise:

$$\frac{Q_{sw}}{A_{\text{Du}}} = \{128.1(T_{es} - 36.4) + 8.0\,(\bar{T}_s - 34)\}e^{(\Sigma T_s - 34)/10} \text{ W/m}^2 \qquad (11)$$

All of the previous sweat expressions predict the rate of evaporation heat loss assuming that all of the sweat secreted will evaporate. Using Fick's law and the heat transfer-mass diffusion analogy leads to a maximum evaporative heat loss of [6, 10, 42],

$$Q_{\max} = 2.14 h_c A_s (P_s - P_a) \qquad (12)$$

Sweating in excess of this amount is evidenced as liquid secretion and has no influence on the thermal state of the person.

3 Numerical Algorithim

The numerical algorithim predicts the temperatures of different areas of the body in response to specific stimuli in the form of surface or volume irradiation, ambient temperature, air speed variation, metabolic rates, or any combination thereof. The model does not include shivering so that the air temperature must be in excess of 28°C for a nude subject in still air, although lower temperatures are permissible if the metabolic rate is higher. The energy equation (1) is represented in a finite difference form as,

Table 1 Resting man in an environment of 28°C, 50 percent r.h.

	Core	Muscle	Fat	Skin
Head	36.76°C	35.82	35.27	34.93
Normal Hypothalamic	36.7			
Trunk	36.85	37.12	34.58	33.25
Normal Rectal	37.0			
Arms	35.92	35.52	34.31	34.07
Hands	34.33	34.25	34.18	34.07
Legs	36.67	36.25	34.57,	34.05
Feet	34.26	34.17	34.12	34.04
Blood	36.67		Mean Skin	33.80
			Normal Skin	33-34

$$(\rho c)\frac{T_i^{n+1} - T_i^n}{\Delta t} = K_{i,i-1}(\tilde{T}_{i-1} - \tilde{T}_i) + K_{i,i+1}(\tilde{T}_{i+1} - \tilde{T}_i) + \tilde{B}_i(T_{b\ell} - \tilde{T}_i) + \tilde{M}_i + \tilde{R}_i + \tilde{S}_i \quad (13)$$

where the terms denoted by tildes represent time averages according to

$$\tilde{B}_i = \alpha b_i^n + (1 - \alpha)B_i^{n+1} \quad 0 \leq \alpha \leq 1 \quad (14).$$

Letting $\alpha = 1$ gives an explicit algorithim which is subject to time step limitations, while values of $\alpha \leq 0.5$ yield an implicit scheme with no stability restrictions. The blood flow and sweating terms, which are functions of temperature, were expressed in a Taylor series as,

$$S_i(T) = \alpha S_i|_{T0}(T^n - T_0) + (1 - \alpha)S_i|_{T0}(T^{n+1} - T_0) \quad (15)$$

to permit a more accurate evaluation of the temperatures and where T represents the different temperatures in the sweating equation. The resulting simultaneous equations were solved by a standard banded matrix inversion routine modified to consider global variables.

4 Changes in Ambient Temperature

The set of equations (13) were first solved under the assumptions of the blood flow rate being basal, and no sweating. The environmental conditions were consistent with Fanger's [18] thermal comfort conditions for a nude sedentary individual. Table 1 lists the computed temperatures and some typical measured values. When comparing the values, certain points must be kept in mind. Actual body temperatures corresponding to the computed values are impossible to measure in-vivo and skin temperatures are easily measured but are the most variable and least important in their influence on the health and well-being of the individual. The normal oral temperature of a resting person is commonly taken as 36.7°—a value often chosen as the hypothalamic set point. This compares well with the computed head core temperature of 36.8°C. Rectal temperature under the same conditions is 37.0°C while the computed value is 36.9°C. The slight depression is due to our consideration of the trunk as one mass and since the upper trunk is largely lung tissue and subject to a greater heat loss than the lower trunk, the average can be expected to be lower than that of the lower trunk. The mean skin temperature was computed to be 33.8°C which is in the range of 33.0–34.0°C generally accepted as the mean skin set point.

Fig. 2 and Table 2 display the results obtained for a step change in ambient temperature using the sweat equation (10). Whereas the skin temperature decreases during exercise because the rise in core temperatures intensifies the sweating, the skin temperatures rise due to external heating. Shortly after the initial rise, sweating begins and the skin temperatures fall. Only in the 37°C case is thermal equilibrium achieved after 90 min.

Houdas [23] conducted a study of resting subjects exposed to changes in ambient temperature and his results are compared to the computed values in Table 2.

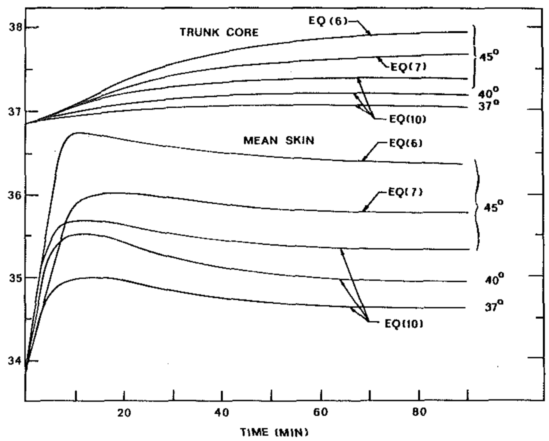

Fig. 2 Effect of changes in ambient temperature on tissue temperature (initial ambient temperature of 28°C)

The computed core temperatures are in good agreement but the skin temperatures are significantly lower. This latter comparison is less important, since it is the internal temperature which determines the thermal well-being of the person. Roemer and Horvath [44] used experimental data of skin blood flow, metabolism, and arterial blood flow in conjunction with a closed form solution to estimate the importance of the skin and rectal temperatures in establishing an effective body temperature. Because the experiment only considered a reduction in ambient temperature, it is not clear that their calculated proportions would be valid for increased ambient temperatures or energy deposition.

The most important conclusion to be drawn from these calculations for heating due to changes in ambient temperature is that there is no significant difference between the additive, multiplicative, or exponential sweat rate equations for external heating of the body, although each equation is sensitive to the coefficients used (e.g., equations (5) and (6)).

5 Effects of Exercise

Using the temperatures of Table 1 as the set point values, a series of numerical tests were made for different levels of metabolism, using several sweat rate equations. Both transient and steady state temperatures were obtained. Table 3 lists some temperatures for the four sweat equations used.

Figs. 3 and 4 illustrate the variation of temperature and total heat loss during exercise. As would be expected, the core temperatures increase with time and metabolic activity. Except for the highest metabolic rate, the skin temperature experiences a progressive decrease with increasing activity. At 506 W/m^2, the mean skin temperature exhibits only a slight decrease and this begins to increase after 25 min. At this level of activity, most of the skin surface is sweating at the maximum allowable level which is insufficient to adequately cool the body. The dashed lines in Fig. 4 indicate the condition of thermal equilibrium and at 90 min the transient heat loss is within 4 percent of the steady-state values. This is consistent with most researchers' feeling that approximately 90

Table 2 Measured [23] and computed temperatures 90 min after a step change in ambient temperature from an initial value of 28°C

Ambient Temperature	T_r	T_s	T_r	T_s	T_r	T_s	T_r	T_s
	Houdas [23]		Eq. 10		Eq. 6		Eq. 7	
37°C	37.05	36.3	37.10	34.62	37.37	35.22	37.21	34.81
40°C	37.20	36.4	37.23	34.95	37.62	35.67	37.38	35.09
45°C	37.45	36.7	37.45	35.34	37.95	36.36	37.68	35.77

Table 3 Metabolic level of 350 kcal/m^2-hr (407 W/m^2)

Sweat Equation	Type	Q_{sw} Watts	Head Core	Leg Muscle	Leg Fat	Mean Skin
Eq. 5	Additive	434	38.08°C	38.54	30.04	28.45
6	Additive	547	40.81°C	41.63	34.46	32.29
8b	Additive	544	41.89°C	42.78	36.52	34.11
7	Additive	493	39.15°C	39.75	32.76	30.65
11	Exponential	467	39.59°C	40.24	33.84	31.71
8a	Multiplicative	475	38.63°C	39.19	33.83	31.66

min is necessary for thermal equilibrium after a step change in activity or environmental conditions. The head core temperatures shown in Fig. 3 indicate that a level of 407 W/m^2 is the maximum steady output realizable in man. At this level the equilibrium temperature of 39.5°C is almost equal to that at which hyperthermia and a deterioration of central nervous system begins. According to Brown [9], a level of 407 W/m^2 is the maximum for a person in good physical condition. At a metabolic state of 506 W/m^2 dangerously high head core temperatures result after 30 min. Saltin [46] observed peak muscle temperatures of 40°C at exhaustion, which according to Fig. 3 would occur near 20 min at 506 W/m^2 but not until 60 min at 407 W/m^2.

6 Nonionizing Microwave Absorption in the Body

The basic microwave problem was taken to be the absorption of a plane nonionizing electromagnetic wave which deposited either 10 W in the head or 100 W in the body. This corresponds to R. F. power density levels of 120 MW/cm^2 at 100 MHz or 590 MW/cm^2 at 20 MHz as shown by the electromagnetic solution [20] for the body, or 1000 MW/cm^2 at 100 MHz for the head. Johnson and Guy [24] give an excellent review of the basic electromagnetic wave effects in biological materials and Barrett and Myers [3] present an inversion of the deposition problem in which electromagnetic emission is used to measure tissue temperatures.[3] It is possible that their method might be used in conjunction with the deposition experiments to validate the use of numerical predictive methods. Fig. 5 shows the results using the additive sweat equation when the power is deposited entirely in one type of tissue. The simulation permitted increased blood flow to the skin because of skin temperature changes, but the blood flow to the other tissues, the metabolism, and the respiration were fixed at the basal values.

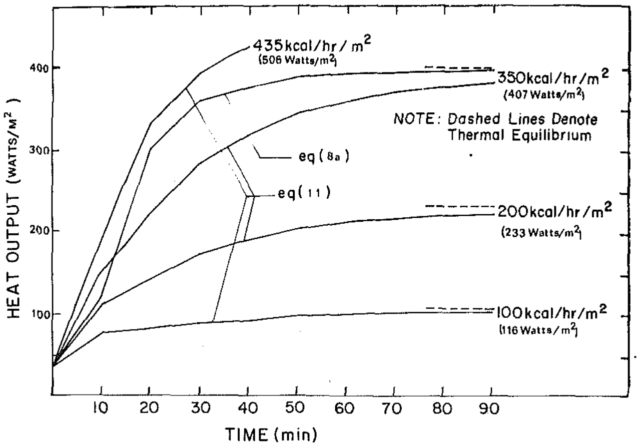

Fig. 4 Effect of exercise on net heat loss from the body

When the power is deposited into the brain (the head core tissue), there is a small rise in core temperature since it is well protected by the perfusing blood, but a significant fall in the surrounding tissue temperatures because of the sweating caused by the hypothalamic temperature rise. When the energy is deposited in the other tissues, the lack of a rise in the hypothalamic temperatures, again caused by the high rate of perfusing blood, inhibits sweating, with the result that the other tissue temperatures must rise considerably to transfer the heat.

After obtaining a basic feeling for the effects of energy deposited selectively within the body, it is necessary to estimate the precise nature of the electromagnetic deposition.

In order to quantify the power deposition from an electromagnetic field and the internal distribution as a function of frequency and tissue layers, and in the absence of a solution applicable to the human shape, two spherical models were chosen to model man: a homogeneous mass of muscle tissue, multilayered sphere whose core of muscle tissue is surrounded by two concentric layers of fat (or low loss dielectric), and skin.

For a plane wave linearly polarized in the x-direction and propagating along the positive z-direction, the exact Mie formulation adapted for the multilayered situation was used for calculating the absorbed power densities and their spatial distributions. The complex dielectric constants $\epsilon = \epsilon_1 + i\epsilon_2$ appropriate for biologic

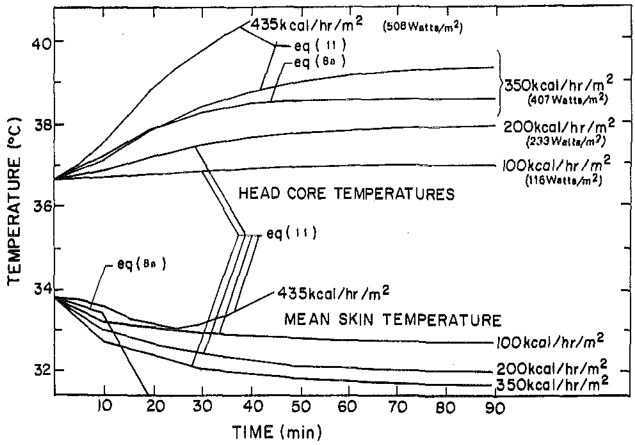

Fig. 3 Effect of exercise on tissue temperatures

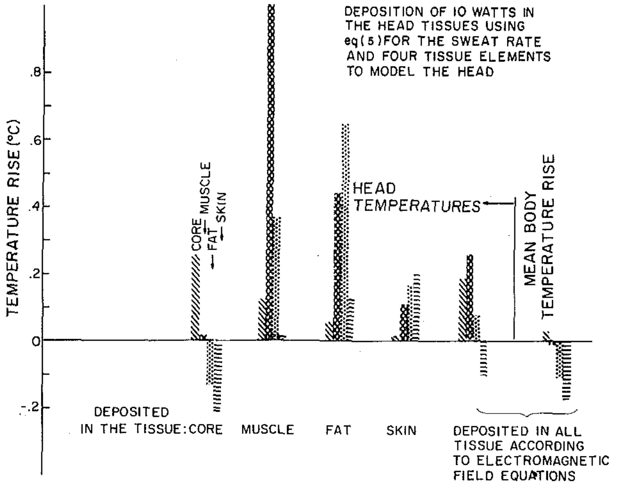

Fig. 5 Effect of the deposition of 10 W in the head tissues

---

[3] Reference [1] presents a current review of the different safety standards associated with nonionizing microwave radiation.

tissues are given in reference [24] for the frequencies considered.

For spherical 70 kg man, the sphere radius of the body is approximately 0.25 m and of the brain is 0.07 m and in the range of frequencies considered the Bessel series solution can be simplified to,

$$E = E_0 e^{-i\omega t}\left[\frac{3}{N^2}\hat{x} + i\,\frac{kR}{2}\left(\cos\phi\hat{\theta} - \cos\theta\sin\phi\hat{\phi}\right)\right] \tag{16}$$

Quasi-static Electric Term   Quasi-static Magnetic Term

This simplified solution is within 10 percent of the exact solution for frequencies less than 20 MHz for the body and 100 MHz for the head.

The time average power density inside a homogeneous sphere due to this electric field can be expressed as,

$$W_L = \frac{1}{2}\sigma E_0{}^2\left[\frac{9}{\epsilon_1{}^2 + \epsilon_2{}^2} - \frac{3\epsilon_2 kR\cos\theta}{\epsilon_1{}^2 + \epsilon_1{}^2} + \left(\frac{kR}{2}\right)^2\left(\cos^2\phi + \cos^2\theta\sin^2\phi\right)\right] \tag{17}$$

which indicates that the power absorption will be greatest at the leading edge of the sphere, and along the x and z axis, the absorbed power is proportional to x^2 and z^2 since for the body $kz/2$, $kx/2 \gg 3/|N^2|$. Numerical computations indicate that skin and fat have very little effect on the absorption pattern in the muscle.

The effect of tissue membranes has been investigated by placing a thin shell (10^{-6} m thick) of low dielectric and loss tangent material at various positions inside the sphere. Aside from the local absorption minima, the dielectric produces no change in the maximum absorbed power, average absorbed power, nor in the spatial distribution of absorbed power. This is not surprising, since the electromagnetic field in the spherical model of man is predominantly circular and does not cut across the dielectric membrane in this model.

For frequencies below 100 MHz and 20 MHz the absorption in the head and body, respectively, behave as the square of the frequency, and in general the head absorption is an order of magnitude smaller than the corresponding absorption for the whole body model. The distributions of the absorbed power density inside the brain is similar to that of the whole body. The only difference is that in this case the ratio of the absorption by the leading surface is much higher than that at the trailing surface. This results from the change in relative magnitude and phase between the electric fields induced in the sphere by the incident electric and magnetic fields.

Based on these observations, it is safe to assume that the maximum human exposure to E.M. field can be estimated from the whole body model and there is no selective absorption by the head itself. When the total energy deposited in the head is distributed according to the electromagnetic field equation (17), the resulting temperatures are closer to the case of brain (core) deposition, than to any of the other cases or to any weighted mean temperature of the four individual cases. This points out the need for treating each deposition problem individually. The high hypothalamic temperatures associated with either the core or the distributed depositions result in considerable sweating and a depression of all but the core body temperatures as indicated in Fig. 5. The 10 W input to the head, about 2 W/kg, corresponds to 133 W deposition to the rest of the body. However, an input of only 100 W to the body core or muscle creates a very elevated brain temperature rise, far in excess of that caused by the 10 W to the head. Furthermore, different from the head core deposition, it was found that deposition in the body core causes almost equal temperature rises in both the body and the head core. No electromagnetic field solutions are available for deposition in the head-body configuration, but since the deposition distribution in the head, according to the electromagnetic field equations, was not significantly different from a distribution according to the tissue mass, the case of 100 W deposited in the body was examined using the tissue mass distribution. Fig. 6 illustrates the mean head and body temperature rises. Although the deposition per tissue mass is approximately the same for head or body deposition, the results are significantly different because the head deposition is mitigated by the cooling of perfusing blood in the body with its large sweating surface while the body deposition has only the small unheated head surface for cooling. Both of these effects are associated with the nonlinear sweat interaction with various body temperatures.

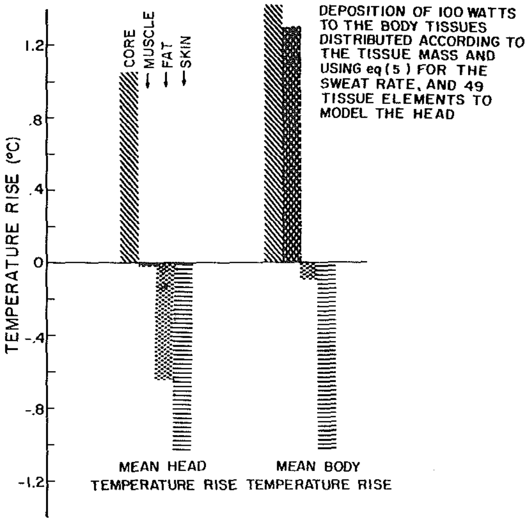

Fig. 6 Effect of the deposition of 100 W in the body tissues

For an incident plane wave, propagating in the z-direction with an electric field polarized in the x-direction, the electromagnetic field equations (17) show a strong spatial variation with a majority of the deposition occurring in the muscle. To account for this strong spatial variation (maximum/average deposition = 3) the head was modeled by 49 tissue elements rather than the 4 previously used and the resulting temperatures were weighted to give the mean tissue values. From Fig. 5, the simple 4 element model is seen to compare very well with 49 element head, suggesting that the effect of the high blood perfusion rate in the head ameliorates the strong variation of energy deposition.

It was previously noted that the body thermal responses to exercise and to a change in ambient temperature were slightly influenced by the form of the sweat equation used (see Fig. 3 and Table 3) but there was no overriding preference for any special sweat model. Fig. 7 illustrates the effect of using Nadel's sweat model (equation (10)) for electromagnetic deposition in the head and it is readily apparent that the use of the two sweat models is not at all comparable and the difference points up the need for more exactly defined sweat models.

The deposition of 100 W to the body is approximately equivalent to extra energy of exercise associated with the total metabolic rate of 116 W/m^2, although in the latter case the additional heat is almost totally confined to the muscle; the temperatures listed in Table 4 were found.

Although there are some differences, the general agreement is good. The basic difference between the two calculations is that in exercise the total blood flow increases in proportion to the rate of exercise and thus the hypothalamus is aware of the increased muscle temperature and initiates sweating whereas the blood flow during deposition is assumed to vary only in the skin tissue.

It is speculated that for long time irradiation, the effect of the elevated tissue temperature on the blood flow is comparable to that produced by increased metabolic rates. Using this assump-

Table 4

	100 Watts	Exercise
Head Core	ΔT=.15°C	.36
Skin	-.1	-1.1
Body Muscle	1.5	.85
Skin	∿0	-.39

tion, it would be possible to estimate a revised blood flow distribution in the muscle, but because of the lack of a tissue temperature-perfusion relationship for the other tissues, a complete redistribution is not possible. Consequently, all irradiation calculations were done using the basal perfusion since it is likely that this will yield a safe estimate of the effect of irradiation.

Koroxandis, et al. [26] indirectly heated the body core by immersing the feet and legs in hot water. They found a 2.5–12 fold increase in skin blood flow, a 60 percent increase in cardiac output accompanied by a 70 percent increase in heart rate and a 2°C increase in core temperature.

Grollman [19] found a 58 percent increase in cardiac output associated with a pyrogen induced fever. Since fever is an upward resetting of the set point temperatures, an increase in heat storage occurs in all the tissues [8]. This is not unlike the E.M. deposition, but again it is not completely analogous because of the different set points of the thermoregulatory system in the two cases and because of the differing cardiac distribution.

The temperature rises associated with these different E.M. depositions may be termed "physiologic" in that temperature regulation in a normal subject would remain efficient and stable [29] but this stability would undoubtedly result in some physiological stress. The greatest burden would be on the circulation by increasing the skin blood flow. This increase will be accompanied by increased heart rate, cardiac output, and diversion of the blood from the splanchnic areas, [19, 26, 27, 39, 40, 41, 43]. Unfortunately, there are no experimental data on circulatory changes in man undergoing body heating from internal sources to substantiate these predictions.

Conclusions

The numerical simulation of the human body to thermal response to exercise or to changes in ambient conditions was computed using different sweat rate models and all were found to be satisfactory. However, when these different models were applied to the case of deposited electromagnetic energy, very different thermal results were obtained. These disparate results emphasize the need for more accurate sweat rate models if numerical simulations of humans are to be made.

Acknowledgment

This work was partially supported by the United States Air Force Contract F41609-73-C-0002 and Social and Rehabilitation Services Contract 16-P-56818/0-13 and the authors wish to thank Dr. J. W. Frazer for his advice and encouragement.

References

1 Anon, "IMPI Policy Statement, Safety From Microwave Hazards in Using Microwave Power Equipment," *Journal of Microwave Power,* Vol. 10, 1975, pp. 333–341.

2 van Beaumont, W., and Bullard, R. W., "Sweating: Its Rapid Response to Muscular Work," *Science,* Vol. 141, 1963, pp. 643–646.

3 Barrett, A. H., and Myers, P. C., "Subcutaneous Temperatures: A Method of Noninvasive Sensing," *Science,* Vol. 190, 1975, pp. 669–671.

4 Benzinger, T. H., "Heat Regulation: Homeostasis of Central Temperature in Man," *Physiol. Rev.,* Vol. 49, 1969, pp. 671–759.

5 Benzinger, T. H., Kitzinger, C., and Pratt, A. W., "The Human Thermostat," *Temperature—Its Measurement and Control in Science and Industry,* Vol. 3, Part 3, J. D. Hardy, ed., Reinhold, New York, 1965.

6 Brebner, D. F., Kerslake, D. M., and Waddel, J. L., "The Relationship Between the Coefficients for Heat Exchange by Convection and by Evaporation in Man," *J. Physiol.,* Vol. 141, 1958, pp. 164–168.

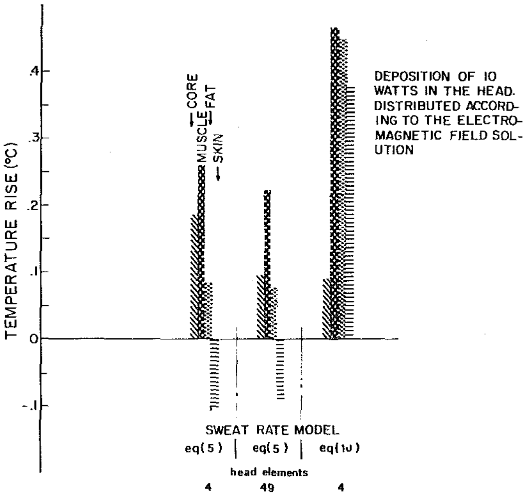

Fig. 7 Effect of the deposition of 10 W in the head tissues distributed according to the electromagnetic field solution

7 Brengelmann, G. L., Wyss, C., and Powell, L. B., "Control of Forearm Skin Blood Flow During Periods of Steadily Increasing Skin Temperature," *J. Appl. Physiol.,* Vol. 35, 1973, pp. 77–84.

8 Brengelmann, G., and Brown, A. C., "Temperature Regulation," T. C. Ruch, and H. T. Patton, eds., *Physiol. and Biophys.,* 19th ed., Philadelphia, Saunders, 1965.

9 Brown, A. C., and Brengelmann, G. L., "Energy Metabolism," *Physiology and Biophysics,* T. C. Ruch and H. D. Patton, eds., Philadelphia, Pa., W. B. Saunders, 1960.

10 Buettner, K. J. K., "Veroff," *Preuss Met. Inst.,* 1963.

11 Chato, J. C., "Heat Transfer in Bioengineering," *Lectures on Advanced Heat Transfer,* B. T. Chao, ed., University of Illinois, 1969.

12 Chato, J. C., "A Method for the Measurement of Thermal Properties of Biological Materials," *Thermal Problems in Biotechnology,* ASME, 1968, pp. 16–25.

13 Cooper, T. E., *Bio-Heat Transfer Studies,* PhD dissertation, University of California, Berkeley, 1970.

14 Crosbie, R. J., Hardy, J. D., and Fessenden, E., "Electrical Annals of Simulation of Temperature Regulation in Man," *Temperature—Its Measurement and Control in Science and Industry,* Vol. 3, Part 3, J. D. Hardy, ed., Reinhold, New York, 1965.

15 Dubois, D., and Dubois, E. F., "Clinical Calorimetry: Tenth Paper, A Formula to Estimate the Approximate Surface Area if Height and Weight are Known," *Arch. Int. Med.,* Vol. 17, 1915, pp. 863–871.

16 Emery, A. F., et al., "Microwave Induced Temperature Rises in Rabbit Eyes in Cataract Research," JOURNAL OF HEAT TRANSFER, TRANS. ASME, Series C, Vol. 97, 1975, pp. 123–128.

17 Fan, L. T., Hsu, F. T., and Huang, C. L., "A Review on Mathematical Models of the Human Thermal System," *Transactions IEEE,* Vol. BME-18, 1971, pp. 218–234.

18 Fanger, P. O., *Thermal Comfort: An Analysis and Applications in Environmental Engineering,* McGraw-Hill, New York, 1972.

19 Grollman, A., "Variations in Cardiac Output in Man: The Cardiac Output of Man During the Malaise and Pyrexia Following Injection of Typhoid Vaccine," *J. Clin. Invest.* Vol. 8, 1929, p. 25.

20 Guy, A. W., Johnson, C. C., Lin, J. C., Emery, A. F., and Kraning, Kenneth K., "Electromagnetic Power Deposition in Man Exposed to High-Frequency Fields and the Associated Thermal and Physiologic Consequences," *USAF Interim Report, SAM-TR-73-13,* Dec. 1973, pp. 67.

21 Hardy, J. D., and Stolwijk, J. A. J., "Partitional Calorimetric Studies of Man During Exposures to Thermal Transients," *J. Appl. Physiol.,* Vol. 21, 1966, pp. 1799–1806.

22 *Physiological and Behaviorial Temperature Regulation,* Hardy, J. D., Gagge, A. P., and Stolwijk, J. A. J., eds., Charles C Thomas, Springfield, Ill., 1970.

23 Houdas, Y., Colin, J., Timbal, J., Boutelier, C., and Guieu, J. D., "Skin Temperatures in Warm Environments and the Control of Sweat Evaporation," *J. Appl. Physiol.,* Vol. 33, 1972, pp. 99–104.

24 Johnson, C. C., and Guy, A. W., "Non-Ionizing Electromagnetic Wave Effects in Biological Materials and Systems," *Proceedings IEEE,* Vol. 60, 1972, pp. 692–718.

25 Johnson, J. M., Rowell, L. B., and Brengelmann, G. L., "Modification of the Skin Blood Flow—Body Temperature Relationship by Upright Exercise," Submitted to *J. Appl. Physiol.,* 1974.

26 Koroxenidis, G. T., Shepherd, J. T., and Marshall, R. J., "Cardiovascular Response to Acute Heat Stress," *J. Appl. Physiol.,* Vol. 16, 1961, p. 869.

27 Kraning, K. K., Belding, H. S., and Hertig, B. A., "Use of Sweating

Rate to Predict Other Physiological Responses to Heat," *J. Appl. Physiol.*, Vol. 21, 1966, p. 111.

28 McCutchan, J. W., and Taylor, C. L., "Respiratory Heat Exchange With Varying Temperatures and Humidity of Inspired Air," *J. Appl. Physiol.*, Vol. 4, 1951, pp. 121–135.

29 Minard, D., and Copman, L., "Elevation of Body Temperature in Disease," J. D. Hardy, ed., *Temperature: Its Measurement and Control in Science and Industry*, Vol. 3, Part 3, New York, Reinhold, 1963.

30 Mitchell, J. W., Nadel, E. R., and Stolwijk, J. A. J., "Respiratory Weight Losses During Exercise," *J. Appl. Physiol.*, Vol. 32, 1972, pp. 474–476.

31 Nadel, E. R., Bullard, R. W., and Stolwijk, J. A. J., "Importance of Skin Temperature in the Regulation of Sweating," *J. Appl. Physiol.*, Vol. 31, 1971, pp. 80–87.

32 Nadel, E. R., Mitchell, J. W., Saltin, B., and Stolwijk, J. A. J., "Peripheral Modifications to the Central Drive for Sweating," *J. Appl. Physiol.*, Vol. 31, 1971, pp. 828–833.

33 Nadel, E. R., Mitchell, J. W., and Stolwijk, J. A. J., "Control of Local and Total Sweating During Exercise Transients," *Int. J. of Biometeor.*, Vol. 15, 1971, pp. 201–206.

34 Nielsen, Marius, and Pedersen, Lorents, "Studies on the Heat Loss by Radiation and Convection From the Clothed Human Body," *Acta Physiol. Scand.*, Vol. 27, 1952, p. 272.

35 Pennes, H. H., "Analysis of Tissue and Arterial Blood Temperatures in the Resting Human," *J. Appl. Physiol.*, Vol. 1, 1945, pp. 93–122.

36 Perl, W., "Heat and Matter Distribution in Body Tissues and the Determination of Tissue Blood Flow by Local Clearance Methods," *Theoret. Biol.*, Vol. 2, 1962, pp. 201–235.

37 Pirnay, F., Marechal, R., Radermecker, R., and Petit, J. M., "Muscle Blood Flow During Submaximum and Maximum Exercise on a Bicycle Ergometer," *J. Appl. Physiol.*, Vol. 32, 1972, pp. 210–212.

38 Poppendiek, H. F., et al., "Thermal Conductivity Measurements and Predictions for Biological Fluids and Tissues," *Cryobiology*, Vol. 3, 1969, pp. 318–327.

39 Powell, L. B., Brengelmann, G. L., and Murray, J. A., "Cardiovascular Responses to Sustained High Skin Temperature in Man," *J. Appl. Physiol.*, Vol. 27, 1969, p. 673.

40 Powell, L. B., Brengelmann, G. L., Blackmon, J. R., Twiss, R. D., and Kusumi, F., "Splanchnic Blood Flow and Metabolism in Heat Stressed Man," *J. Appl. Physiol.*, Vol. 4, 1968, pp. 475–484.

41 Radigan, I. R., and Robinson, S., "Effect of Environmental Heat Stress and Exercise on Renal Blood Flow and Filtration Rate," *J. Appl. Physiol.*, Vol. 2, 1949, p. 185.

42 Rapp, G. M., "Convective Mass Transfer and the Coefficient of Evaporative Heat Loss From Human Skin," *Physiological and Behavioral Temperature Regulation*, J. D. Hardy, A. P. Gagge, and J. A. J. Stolwijk, eds., Springfield, Ill., Charles C. Thomas, 1970.

43 Redisch, W., et al., "Comparison of Various Vascular Beds in Man—Their Response to a Simple Vasodilator Stimulus," *Circulation*, Vol. 2, 1954, p. 63.

44 Roemer, R. B., and Horvath, S. M., "An Analysis of Human Thermal Response to a Step Change in Environmental Conditions," ASME Paper No. 72-WA/BHF-8, pp. 1–11.

45 Saltin, B., Gagge, A. P., and Stolwijk, J. A. J., "Body Temperatures and Sweating During Thermal Transients Caused by Exercise," *J. Appl. Physiol.*, Vol. 28, 1970, pp. 318–327.

46 Saltin, B., Gagge, A. P., Bergh, U., and Stolwijk, J. A. J., "Body Temperatures and Sweating During Exhaustive Exercise," *J. Appl. Physiol.*, Vol. 32, 1972, pp. 635–643.

47 Stolwijk, J. A. J., "Mathematical Model of Thermoregulation," *Physiological and Behavioral Temperature Regulation*, J. D. Hardy, A. P. Gagge, and J. A. J. Stolwijk, eds., Springfield, Ill., Charles C. Thomas, 1970.

48 Stolwijk, J. A. J., and Hardy, J. D., "Temperature Regulation in Man—A Theoretical Study," *Pflugers Arch. ges. Physiol.*, Vol. 291, 1966, pp. 129–162.

49 Stolwijk, J. A. J., and Hardy, J. D., "Partitional Calorimetric Studies of the Thermoregulatory Responses of Man to Thermal Transients," *J. Appl. Physiol.*, Vol. 21, 1966, pp. 966–977.

50 Stolwijk, J. A. J., Saltin, B., and Gagge, A. P., "Physiological Factors Associated With Sweating During Exercise," *J. Aero. Med.*, Vol. 39, 1967, pp. 1101–1105.

51 Webb, P., "Thermoregulation in Actively Cooled Working Man," *Physiological and Behavioral Temperature Regulation*, J. D. Hardy, A. P. Gagge, and J. A. J. Stolwijk, eds., Springfield, Ill., Charles C. Thomas, 1970.

52 Wyndham, C. H., and Atkins, A. R., "Approach to Solution of Human Biothermal Problem With the Aid of an Analog Computer," Paper No. 27, 3rd Int. Conf. on Med. Electronics, 1960.

53 Winslow, C. E., Gagge, A. P., and Herrington, L. P., "The Influence of Air Movement Upon Heat Losses From the Clothed Human Body," *J. Physiol.*, Vol. 127, 1939, pp. 505–518.

54 Wissler, E. H., "The Use of Finite Difference Techniques in Simulating the Human Thermal System," *Physiological and Behavioral Temperature Regulation*, J. D. Hardy, A. P. Gagge, and J. A. J. Stolwijk, eds., Springfield, Ill., Charles C. Thomas, 1970.

55 Wulff, W., "The Energy Conservation Equation for Living Tissue," *Trans. IEEE*, Vol. BME-21, 1974, pp. 494–495.

56 Wyss, C. R., Brengelmann, G. L., Johnson, J. M., Powell, L. B., and Niederberger, M., "Control of Skin Blood Flow, Sweating, and Heart Rate. Role of Skin Versus Core Temperature," *J. Appl. Physiol.*, Vol. 36, 1974, pp. 726–733.

D. C. Ross
K. R. Diller

Bio-Medical Engineering Program,
The University of Texas at Austin,
Austin, Texas

An Experimental Investigation of Burn Injury in Living Tissue

The effects of thermal insult on living tissue have been studied by direct microscopic observation of the circulatory system's response to a controlled trauma regimen. An experimental apparatus has been developed which utilizes a unique high and low temperature stage in conjunction with a precision thermal control system to examine the injury process in the microcirculation of the golden hamster cheek pouch. Unique features of this experimental apparatus are: (1) continuous monitoring of the injury processes at the cellular level, (2) capability for quantitative assay of thermal injury, (3) precise control over the thermal parameters that govern injury, (4) versatility in isolating the effects of these individual parameters. The important thermal parameters monitored using this experimental procedure are the time rates of change of temperature during burning and cooling, the maximum temperature reached, and the length of time the tissue was held at this temperature. With this type of experimental apparatus any portion of the burn protocol, such as the maximum temperature reached during burning, may be varied while holding all other parameters constant.

It is well documented that the microvascular bed is a primary site for manifestation of burn wound injury. Burn injury occurs as a consequence of rate dependent physiochemical processes, and, therefore, develops over a finite period of time subsequent to trauma. The experimental technique is designed to determine the gross response of the microvascular system to burn trauma.

Initial investigations on burn injury have demonstrated a direct dependency of the extent of damage upon both the maximum temperature attained and the duration of exposure. The minimum temperature required to produce stasis within 20 s after completion of the burn in 95 ± 5 percent of the microcirculation decreased exponentially with burn duration between the extremes of 85°C for 1 s exposure and 60°C for 100 s exposure.

Introduction

The initial microvascular response to burn injury is characterized by complex changes in blood flow, in the coagulation process, and in the permeability of the endothelial barriers. Increased vascular permeability is one of the most important features of this response, since it results in substantial losses of fluid and electrolyte which lead to widespread pathophysiological changes. The physiological response of the microcirculation to elevated temperatures comprises a singularly significant element of the total burn injury which must be completely understood as a basis for rational, optimal therapeutic techniques for the early treatment of burn injury.

The experimental approach employed in this study utilizes a unique technique to directly observe and visually record the microcirculation before, during, and after the thermal injury. It also enables the manipulation of the temperature and duration of the burn which allows direct control of the important thermal parameters in the injury process. The use of high resolution microscopy in the study of the vascular dynamics of the microcirculation during the burn sequence gives an added dimension in the collection of pertinent data.

The response of the microcirculation to thermal injury may be characterized by a slight increase in permeability of the endothelium up to complete stasis and necrosis of tissue in the burned area.

Contributed by the Heat Transfer Division of THE AMERICAN SOCIETY OF MECHANICAL ENGINEERS and presented at the AIChE-ASME National Heat Transfer Conference, San Francisco, Calif., August 9-11, 1975. Revised manuscript received by the Heat Transfer Division February 3, 1976. Paper No. 75-HT-14.

The amount of damage inflicted on the circulation at different temperature levels with varying exposure times was evaluated by direct visual assessment on a Zeiss Universal microscope. This information may help to provide a rational basis for the development of optimal therapeutic techniques for the treatment of burns.

Background

It has been established by past investigators that burns cause a direct impairment of microcirculatory perfusion and that viability of the affected tissue is dependent upon the patency of the microvascular blood vessels [1–12].[1] In general, the extent to which the circulation is altered is a direct function of the severity of the trauma.

In a first-degree burn vasodilatation is the only major change that occurs, resulting in the familiar increased color of the tissue. A second-degree burn is characterized by capillary damage resulting in tissue edema and bleb formation. Increased vascular permeability can occur by the opening of gaps in the endothelium [10, 13, 14] or, in more severe cases, by direct damage to the endothelial cells. The cells may become swollen, with many large vacuoles present or with a loss of internal structure, and project into the lumen partially occluding the vessel. Animal studies have shown an increased permeability of the microcirculation in the burned area to molecules of molecular weight up to 125,000 [15]. Destruction of the capillary wall as a semipermeable membrane allows an overall fluid loss and drop in plasma volume. The decreased plasma volume is a factor of prime importance in the causation of shock in untreated burned patients. This phenomenon (molecular sieving) results in the sequestering of plasma proteins in the extravascular extracellular spaces [16, 17] where they act to osmotically perpetuate the conditions of edema [18]. Concentrations of water and albumin in the affected area reach a peak within 30 min [19, 20, 21] indicating the rapid development of edema following a thermal injury. This vascular response to trauma appears to be a result of both direct thermal injury and of chemical mediators [22–25].

Trauma of even greater severity produces a state of complete arrest of the circulation and eventual necrosis of the tissue. In severe burns which functionally alter the circulation deep into the tissue, a large volume of extravascular fluid may collect beneath the wound before visible swelling occurs at the surface. Thus the extensive fluid loss associated with third degree burns occurs as a consequence of injury to tissue beneath and surrounding the area of full thickness skin destruction.

Changes in blood rheology and coagulation factors are consistently noted during the postburn period [26]. Blood viscosity rises significantly and remains elevated for several days [27]. Platelet adhesiveness is increased in the immediate postburn period and helps to contribute to an abnormal platelet count which remains elevated for three weeks [28]. A marked increase in platelet aggregation occurs immediately in the injured area [29]. Upon microscopic observation these aggregates can be clearly seen adhering to vessel walls, breaking off and flowing with the blood stream and re-adhering further downstream. In some cases the aggregates partially or totally occlude the vessels. This phenomenon explains the slight depression of platelets, fibrinogen, and factor *V* which is observed during the first hour after the burn. Thrombocytopenia, which is observed up to approximately 24 hr after injury, is a result of platelet aggregation, burn wound sequestration and decreased platelet survival. During the following days there is a sustained thrombocytosis resulting from both a synchronous response in bone marrow megakaryocyte production and return of platelet survival to normal. There is also a parallel increase in the plasma fibrinogen and factor *V* levels [30–32].

The production of thermal burns is dependent upon both the elevation of tissue temperature and the duration of exposure to thermal stress. Moritz and Henriques [33] first demonstrated the classical inverse interaction between the temperature and time requisite to produce a graded degree of thermal injury (Fig. 1). Subsequent investigations have corroborated the existence of this phenomenon in other living systems [34, 35]. Thereby, the extent of injury can be predicted as a function of the thermal history of the tissue during trauma.

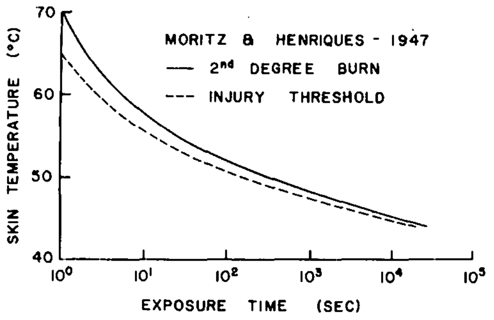

Fig. 1 Moritz and Henriques [33] data for second-degree burn

The objective of the present study is to establish a technique for effecting controlled burn injury via the utilization of a unique experimental apparatus so as to correlate quantitatively the physical parameters of injury. Subsequent application of this apparatus will be to quantify the effectiveness of various therapeutic regimens.

Description of Apparatus

The experimental investigations are performed on a Zeiss Universal microscope that incorporates a unique, controlled temperature stage capable of burning or freezing living tissue. A hamster cheek pouch is placed in contact with the temperature stage allowing a preprogrammed thermal history to be imposed on the tissue (see Fig. 2). The microcirculation may be directly observed through the microscope during the experiment.

The stage consists of two parts as depicted in Figs. 3 and 4. The conductive heating and cooling unit consists of a brass cylinder with outer and inner diameters of 12 and 6 mm, respectively, and a height of 7 mm. The cylinder is divided in two vertically with the two halves of the cylinder electrically insulated from each other by a thin sheet of micarta. The inner chamber is sealed by two 0.33-mm thick sheets of glass, cemented with an epoxy adhesive onto the flat surfaces, with the only access being a 3.175-mm hole drilled transversely through the brass cylinder perpendicular to the micarta sheet and fitted with two lengths of stainless steel tubing. This configuration allows refrigeration fluid to flow into and

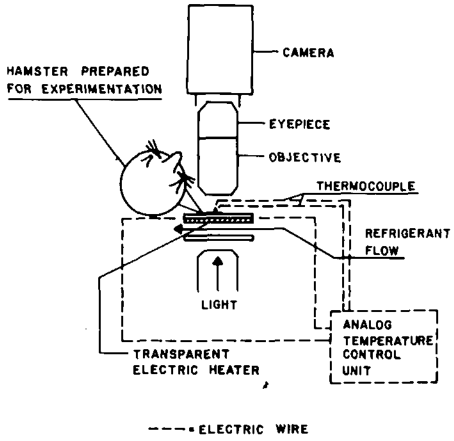

Fig. 2 Schematic of microscope and temperature control system

---

[1] Numbers in brackets designate References at end of paper.

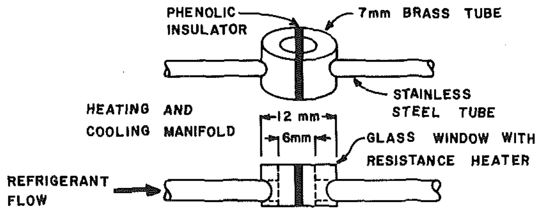

Fig. 3 Conductive heating and cooling unit

out of the internal chamber to provide a cooling effect on the tissue. The brass cylinder and stainless steel tubes are fitted as a unit into the back of a machined phenolic sheet of dimensions 6.35 × 152.4 × 177.8 mm, Fig. 4, which has a cork insert surrounding the chamber to allow easy mounting of the hamster cheek pouch. The temperature stage and hamster are then positioned under the microscope. The microscope is equipped with an optical micrometer eyepiece to measure specimen dimensions. Still and cine cameras and a closed-circuit video taping system are used to record experimental data.

Heat is supplied to the specimen by an electrical resistance heater located on the underneath side of the top glass sheet on the brass conductive heating and cooling unit. A solution of stannic chloride pentadihydrate, antimony trichloride, and acetone is sprayed onto the glass sheet at a temperature of 1100°F (593°C). This procedure deposits a transparent, electrically conductive tin oxide film on the glass which has a resistance of approximately 250 ohms/cm^2. Two small areas of silver epoxy, which are surrounded by nonconductive epoxy, are then used to make electrical connections between the tin oxide coating and the brass cylinder. Copper leads connect the opposing halves of the cylinder to the power output of the temperature control system.

The refrigeration effect is achieved by a steady flow of chilled nitrogen gas through the chamber. A copper tube heat exchanger, filled with liquid nitrogen, has pressurized gas forced through it at a constant flow rate selected according to the cooling capability required to produce a given experimental protocol.

A programable control unit [36], Fig. 5, regulates the tissue temperature and its time rate of change. The control unit is of the analogue feedback type in which an integrator input voltage source, a constant voltage source, an offset voltage source, a command logic signal generator, and an integrator are used to generate a voltage-time profile representative of the desired linear temperature-time profile of the specimen. There is an offset voltage in the voltage-time profile to compensate for the constant refrigeration effect, the voltage being equal to that needed to hold the specimen at initial temperature with the refrigerant flowing. This offset voltage is automatically determined and produced in the integrator at the outset of the operation by increasing the integrator output voltage in relation to the refrigeration capacity being stored in the system. The voltage-time profile is compared continuously in a differential amplifier with the amplified and linearized thermocouple output, which is the electrical analog of the specimen temperature. If the temperature of the specimen is lower than prescribed, the additional positive signal proportional to the temperature difference is fed into the power amplifier, which in turn increases the current to the electric heater which is in thermal communication with the specimen. The resultant effect is that the desired specimen temperature is established. In the reverse case a lower current in the heater allows the refrigerent to cool the specimen to the desired temperature. Under these conditions the thermal history of the system is set by balancing the steady-state cooling effect with the variable heating effect.

This type of feedback system provides precise control over the tissue temperature in the range between −170 and +200°C with thermal transients between ±1 and ±1000°C/min. The accuracy obtained in controlling the thermal history of the tissue provides a unique opportunity to observe the response of the microcirculation under many varied stimuli. Its primary distinguishing features are: (1) versatility in exploring a broad spectrum of thermodnamic states and processes, (2) highly precise measurement and control over the specimen temperature and time rate of change, and (3) capability for isolating independently some of the individual events which occur during thermal stress.

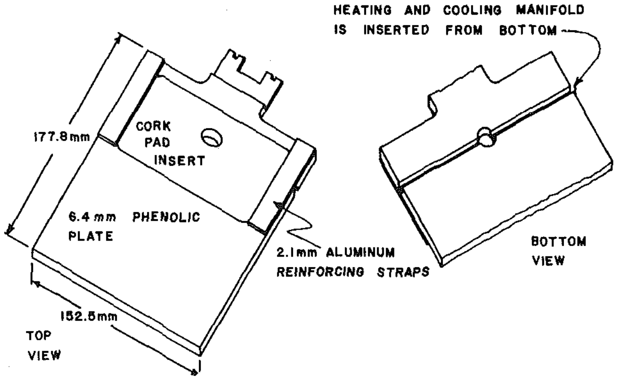

Fig. 4 Phenolic stage for holding the hamster

The temperature of the tissue is measured by a copper-nickel microthermocouple [37] placed onto the tissue by a micromanipulator attached directly to the stage (Fig. 6). The thermocouple substrate is prepared by heating a fused quartz rod 1 mm in diameter and allowing it to extend approximately 0.5 cm. This causes necking down of a small area of the rod which is then reheated to the melting point and pulled apart quickly. A probe is obtained that tapers abruptly from 1 mm to 20–50 microns in diameter. The probe is then placed in a chamber in which the pressure has been reduced to 2×10^{-5} torr. A current is supplied to the nickel source metal until vaporization begins and is continued until the desired film thickness (approximately 2000 Å) on the probe is reached. A lead wire of the same source material is attached to the metal film with conductive epoxy. The tip of the probe is then masked and the substrate is coated with a layer of an insulating material called parylene. Subsequently the mask is removed and the vapor deposition procedure is repeated for copper so that the two metallic films are joined only at the probe tip. A final coat of parylene is applied and the lead wires are sealed with a nonconducting epoxy to yield a microthermocouple with a Seeback coefficient of 22.5 μV/C. The small volume of the metal films (= 0.14 percent of the mass of a 20 micron probe with 0.2 micron films of copper and nickel) with respect to the volume of the quartz substrate provide a sensor with the approximate thermal characteristics of quartz alone.

Experimental Procedure

The hamsters are anesthetized with 3 percent sodium pentobarbital (1 part of 6 percent solution diluted with 1 part 0.9 percent NaCl) given intraperitoneally at a dose of 30 mg/kg and supplemented as needed. The cheek pouch, which extends down to approximately the shoulder, is withdrawn from the animal's mouth and the distal portion, which is semitransparent, is pinned down over the cooling chamber on the stage. The top portion of the pouch is cut and pinned back to reveal the inner surface of the pouch. Care is taken to not sever or occlude the major supply arteries and to insure that neither the skeletal muscle fibers surrounding the proximal portions of the pouch or the thin retractor muscle, which runs longitudinally from the distal portion to the thoracic vertebrae, is included in the preparation area. This three-layered area is composed of dense fibrous connective tissue, a layer of stratified squamous epithelium, and a layer of loose areolar connective tissue. The loose areolar connective tissue is then cut away

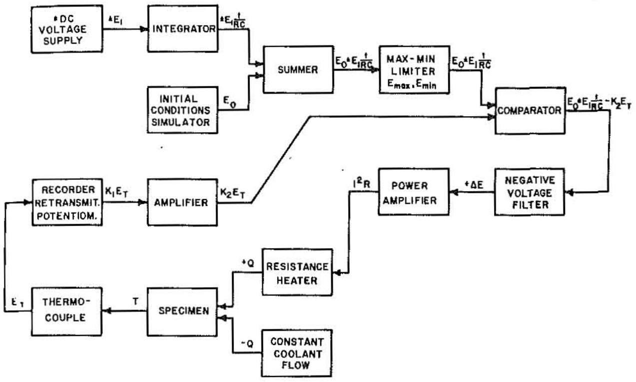

Fig. 5 Block diagram of control unit

Fig. 6 Prepared hamster cheek pouch with thermocouple in place

under a low power dissecting microscope. This procedure results in an extremely clear, highly vascularized field of view which has all classes of microcirculatory vessels represented [38]. The prepared hamster is placed under the microscope and the microthermocouple is positioned onto the tissue by the micromanipulator.

The tissue preparation is quite subject to environmental drying. To counteract this effect, the tissue is moistened frequently with normal saline at physiological temperature. This enables control specimens to be obtained for which observation up to 2 hr indicates no visible dilaterous manifestations occur in the circulatory system.

A thermal protocol is then initiated, such as: (1) the tissue is held at physiological temperature to establish control characteristics of the microcirculation, (2) a constant warming rate is started (e.g., 200°C/min) and is maintained until the desired temperature is reached (e.g., 65°C), (3) the temperature is held constant for a specific length of time (e.g., 15 s), (4) a constant cooling rate is started (e.g., −5°C/min) until the physiological temperature is reached. Thrombotic interference to microcirculatory flow, recorded by use of video tape equipment, is the primary response of the microcirculation to thermal stress. The vessel caliber change and clotting time are two of the major factors contributing to the development of stasis.

Vessel caliber changes are measured directly on the microscope by a calibrated reticule inserted into the optical system. The vessel diameters can also be measured from the television monitor during video tape playback.

The development of stasis is also used to quantify injury. These measurements consist of evaluating the portions of the microcirculation which are static as a function of time following injury. Of necessity the tissue has to be observed for a prolonged postburn period to properly assess the final extent of circulatory stasis.

This type of experimental approach to burn studies is unique in that it allows accurate control of the most important independent variables in burn injury: (1) the rate of temperature change of the tissue during warming, (2) the maximum burning temperature, (3) duration of exposure to the maximum temperature, and (4) the rate of temperature change during cooling to physiological temperature.

The qualitative effects of thermal injury have been defined by past investigators but the specific quantitative correlation between the thermal parameters and the sequence of events in the microcirculation after thermal injury has yet to be adequately determined. The nature of injury to the capillary network is a basic phenomenon that must be characterized and controlled before a completely effective series of treatments for burn injury can be developed.

Results

The initial experiments utilizing this instrument have confirmed the dependency of burn wound severity on temperature and time of exposure. A series of 36 experiments were run to determine the minimum temperature required to produce complete stasis in the microvascular circulation of a hamster cheek pouch within 20 s after the burn. The conditions requisite for this severity of burn are shown in Fig. 7 in comparison with the criteria of Moritz and Henriques for milder first- and second-degree burns. Each data point represents a sequence of iterative experiments designed to establish a temperature at which the circulatory system would repeatedly develop permanent stasis within 20 s after the burn. The tissue was then kept moist at the physiological temperature and continuously observed for 2-hr postburn with no sign of the circulation recovering from the burn injury. The small amount of circulation visible on the periphery of the burn area exhibited minimal effects of the elevated temperature and continued flowing throughout the observation period. The time required to produce stasis in 95 ± 5 percent of the microcirculation decreased exponentially with higher burning temperatures according to the equation

$$t = \mathrm{Exp}\,[0.153(85°\mathrm{C} - T)]$$

where t is the duration of trauma (the time in seconds from when the tissue temperature first started to raise above the physiological temperature until the burn was stopped) and T is the maximum temperature (°C) the tissue reached. This empirical relation holds for the experimentally defined limits of 85°C and 60°C.

The caliber of the arterioles and venules in the viewing area ex-

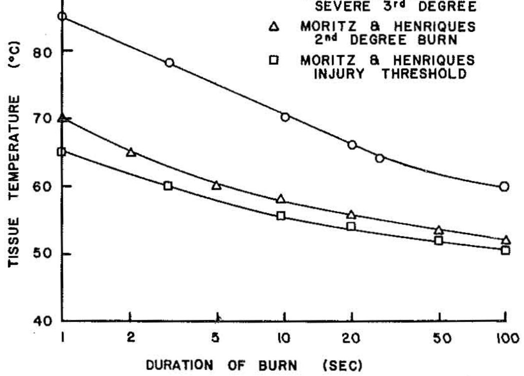

Fig. 7 Duration versus temperature graph for burn injury

hibited little change during the experiment. The larger arteries and veins (approximately 200μ in diameter) did decrease in diameter about 20μ over a 2-hr period with the arteries decreasing slightly more than the veins.

Summary

Utilization of the temperature stage described in this paper has opened up new vistas of experimental exploration in thermal injury at the cellular level which have heretofore been unachievable. The control system, which uses constant cooling along with variable heating, provides extreme accuracy in regulating the thermal history of the cheek pouch. It is now possible to simultaneously observe and photograph the physiological changes in the microcirculation as they occur in response to a burn injury. These initial studies have confirmed that damage to the vascular system is dependent on the maximum temperature of the tissue and also on the duration of the thermal exposure.

Acknowledgments

The authors gratefully acknowledge the support of the National Science Foundation for these studies.

References

1 Cope, O., Moore, F. D., "A Study of Capillary Permeability in Experimental Burns and Burn Shock Using Radioactive Dyes in Blood and Lymph," *J. Clin. Invest.*, Vol. 23, 1944, pp. 241-275.

2 Moritz, A. R., "Studies of Thermal Injury III. The Pathology and Pathogenesis of Cutaneous Burns, an Experimental Study," *Amer. J. of Path.*, Vol. 23, 1947, pp. 915-934.

3 Sevitt, S., "Local Blood-Flow Changes in Experimental Burns," *J. Pathol. Bacteriol.*, Vol. 61, 1949, pp. 427-442.

4 Wells, F. R., and Miles, A. A., "Site of Vascular Response to Thermal Injury," *Nature*, Vol. 200, 1963, pp. 1015-1016.

5 Spector, W. G., Walters, M. N-I., and Willoughby, D. A., "Venular and Capillary Permeability in Thermal Injury," *J. Path. Bact.* Vol. 90, 1965, pp. 635-640.

6 Hardaway, R. M., "Microcoagulation in Shock," *Amer. J. Surgery*, Vol. 110, 1965, pp. 298-301.

7 Order, S. E., et al., "Vascular Destructive Effects of Thermal Injury and Its Relationship to Burn Wound Sepsis," *J. Trauma*, Vol. 5, 1965, p. 62.

8 Robb, H. J., "Dynamics of the Microcirculation During a Burn," *Arch. Surg.*, Vol. 94, 1967, pp. 776-780.

9 Branemark, P. I., et al., "Microvascular Pathophysiology of Burned Tissue," *Ann. N. Y. Acad. Sci.*, Vol. 150, 1968, pp. 474 494.

10 Cotran, R. S., and Remensynder, J. P., "The Structural Basis of Increased Vascular Permeability After Graded Thermal Injury-Light and Electron Microscopic Studies," *Ann. N. Y. Acad. Sci.*, Vol. 150, 1968, pp. 495-509.

11 Schoen, R. E., Wells, C. H., and Kolmen, S. N., "Viscometric and Microcirculatory Observations Following Flame Injury," *J. Trauma*, Vol. 11, 1971, pp. 619-624

12 Shea, S. M., Caufield, J. B., and Burke, J. F., "Microvascular Ultrastructure in Thermal Injury: a Reconsideration of the Role of Mediators," *Microvas. Res.*, Vol. 5, 1973, pp. 87-96.

13 Ham, K. N., and Hurley, J. V., "An Electron-Microscope Study of the Vascular Response to Mild Thermal Injury in the Rate," *J. Path. Bact.*, Vol. 95, 1968, pp. 175-183.

14 Contran, R. X., and Majno, G., "A Light and Electron Microscopic Analysis of Vascular Injury," *Ann. N. Y. Acad. Sci.*, Vol. 116, 1964, pp. 750-764.

15 Arturson, G., "Pathophysiological Aspects of the Burn Syndrome: With Special Reference to Liver Injury and Alterations of Capillary Permeability," *Acta Chir. Scand.* (Suppl), Vol. 274, 1961, pp. 1-35.

16 Courtice, F. C., and Sabine, M. S., "The Effect of Different Degrees of Thermal Injury on the Transfer of Proteins, and Lipoproteins From Plasma to Lymph in the Leg of the Hypercholesterolemic Rabbit," *Aust. J. Exp. Biol. Med. Sci.*, Vol. 44, 1966, pp. 37-44.

17 Courtice, F. E., and Sabine, M. S., "The Effects of Changes in Local Temperature on the Transfer of Proteins and Leproproteins From Plasma to Lymph in the Normal and Injured Paw of the Hyperchol Esterolaemic Rabbit," *Aust. J. Exp. Biol. Med. Sci.*, Vol. 44, 1966, pp. 23-36.

18 Arturson, G., "Patholphysiology of Acute Plasma Loss in Burns," *Bibl. Haem.*, Vol. 23, 1965, pp. 1130-1135.

19 Leape, L. L., "Early Burn Wound Changes," *J. of Pediatric Surgery*, Vol. 3, 1968, pp. 292 299.

20 Leape, L. L., "Kinetics of Burn Edema Formation in Primates," *Ann. Surg.*, Vol. 176, pp. 223 226.

21 Leape, L. L., "Initial Changes in Burns: Tissue Changes in Burned and Unburned Skin of Rhesus Monkeys," *J. Trauma*, Vol. 10, 1972, pp. 488-492.

22 Cotran, R. S., "The Delayed and Prolonged Vascular Leakage in Inflamation II. An Electron Microscopic Study of the Vascular Response After Thermal Injury," *Am. J. Path.*, Vol. 46, 1965, pp. 589-620.

23 Cuppage, F. E., Leape, L. L., and Tate, A., "Morphologic Changes in Rhesus Monkey Skin After Acute Burn," *Arch. Pathol.*, Vol. 95, 1973, pp. 402 406.

24 Shea, S. J., Caufield, J. B., and Burke, J. F., "Microvascular Ultrastructure in Thermal Injury: a Reconsideration of the Role of Mediators," *Microvas. Res.*, Vol. 5, 1973, pp. 87 96.

25 Holder, I. A., and Jogan, M., "Enhanced Survival in Burned Mice Treated With Antiserum Prepared Against Normal and Burned Skin," *J. Trauma*, Vol. 11, 1971, pp. 1041-1046.

26 McMantus, W. F., Eurenium, K., and Pruitt, B. A., "Disseminated Intravascular Coagulation in Burned Patients," *J. Trauma*, Vol. 13, 1973, pp. 416-422.

27 Baxter, C. R., "Crystalloid Resuscitation of Burn Shock," in *Contemporary Burn Management*, Vol. 1, Lihle, Brown and Co., Boston, 1971, pp. 7-32.

28 Curreri, P. W., Eurenius, K., and Pruitt, B. A., Jr., "A Study of Coagulation Factors in the Thermally Injured Patient," *Research in Burns: Transactions of Third International Congress on Research in Burns*, Hans Huber Publisher, Bern, 1971, pp. 594 596.

29 Eurenius, K., and Rothenberg, J., "Platelet Aggregation After Thermal Injury," *J. Lab. Clin. Med.*, Vol. 83, 1974, pp. 344 363.

30 Rammer, L., "Coagulation and Fibrinolysis in Burned Rats," *Scand. J. Haemat.*, Vol. 10, 1973, pp. 244-253.

31 Eurenius, K., Mortensen, R. F., Miserol, P. M., and Curreri, P. W. "Platelet and Megakaryocyte Kinetics Following Thermal Injury," *J. Lab. Clin. Med.* Vol. 79, 1972, pp. 247 257.

32 Encke, A., and Grozinger, K. H., "Studies of Intravascular Coagulation in Experimental Burns of Dogs," *Bulletin de la Societe International de Chirurgie*, Vol. 5, 1972, pp. 445-451.

33 Moritz, A. R., and Henriques, F. C., "Studies of Thermal Injury II. The Relative Importance of Time and Surface Temperature in the Causation of Cutaneous Burns," *Amer. J. Path.*, Vol. 23, 1947, pp. 695-720.

34 Stoll, A. M., and Green, L. C., "Relationship Between Paid and Tissue Damage Due to Thermal Radiation," *J. of Applied Physiology*, Vol. 14, 1959, pp. 373-382.

35 Stoll, A. M., and Chianta, M. A., "Heat Transfer Through Fabrics as Related to Thermal Injury," *Tran. N. Y. Acad. Sci.*, Vol. 33, 1971, pp. 649-670.

36 Ushiyama, M., "Volumetric Changes in Saccharomyces Cerevisiae During Freezing at Constant Cooling Velocities," MS thesis, Massachusetts Institute of Technology, Sept. 1973.

37 Martins, W. D., and Ripperger, E. A., "The Development of a Probe-Type Thin Film Microthermocouple for Biomedical Use," Technical Report No. 120, Electronics Research Center, The University of Texas at Austin, 1972.

38 Duling, B. R., "The Preparation and Case of the Hamster Cheek Pouch for Studies of the Microcirculation," *Microvascular Research*, Vol 5, 1973, pp. 423-429.

K. G. T. Hollands
Assoc. Professor,
Thermal Engineering Group,
Department of Mechanical Engineering,
University of Waterloo,
Waterloo, Ontario, Canada

K. C. Goel
NRC Fellow,
Advanced Engineering Branch,
Atomic Energy of Canada Limited,
Chalk River, Ontario, Canada

Mean Diameters in Parallel-Flow and Counter-Flow Aerosol Systems

The general concept of the mean diameter of the disperse phase of an aerosol system, first introduced by Mugele and Evans in 1951, has proven to be a very useful one. In this concept, the proper mean diameter, $\bar{x}_{p,q}$*, is characterized by a single pair of indices, p and q, which are dependent on the actual type of aerosol system under consideration. This paper re-examines the validity of this concept of mean diameter in heat and mass transfer aerosol systems. The concept is found to be applicable only under a very narrow range of conditions. Attention is then given to a more general definition of a mean diameter, applicable to aerosol heat or mass exchangers. Analyses of these devices shows that the more general mean diameter is a function of the capacity rate ratio, R, and effectiveness of the heat exchanger,* ϵ*. Solutions to the governing equations have permitted the mean diameter to be presented graphically as a function of these variables. These solutions are given for two types of particle size distributions, the Rosin-Rammler and the log-probability, and for both parallel-flow and counter-flow heat exchangers. The solutions are, however, restricted to cases where the resistance to heat or mass transfer lies exclusively in the continuous phase.*

Introduction

The disperse phase of aerosol systems almost invariably consists of particles having a distribution of diameters or sizes. For analysis, it is usually desirable, for the sake of simplicity, to treat the aerosol as if it were monodisperse (i.e., having particles of uniform size) with a particle diameter which is some mean diameter of the actual aerosol. It is generally considered that this proper mean diameter, $\bar{x}$, can be simply expressed in terms of the particle size distribution and a pair of indices which depend on the "field of application" (e.g., evaporation, adsorption, absorption, atomization work, etc.). Thus, Mugele and Evans [1][1] in 1951 defined the mean particle size, $\bar{x}_{p,q}$, given by:

$$\bar{x}_{p,q}{}^{q-p} \int_{x_\ell}^{x_u} x^p \frac{dn}{dx}\, dx = \int_{x_\ell}^{x_u} x^q \frac{dn}{dx}\, dx \qquad (1)$$

and gave an oft-quoted table from which the proper values of p and q can be determined depending on the field of application. For example, for calculations of atomization efficiency, the Sauter mean diameter, $\bar{x}_{3,2}$ is recommended. For any given particle size distribution the integrals in equation (1) can be evaluated and the proper $\bar{x}_{p,q}$ can thereby be expressed in terms of the parameters describing the size distribution.

While the foregoing technique has the advantage of simplicity, its range of application for real systems has never been fully examined. In fact, examination of the literature shows that there are fields of application where this simple concept of mean diameter does not apply. For example, in analyzing the rates of evaporation of sprays, Dickinson and Marshall [2] concluded that "no single mean diameter can properly characterize the evaporation of a spray." Similarly, in analyzing counter-flow spray cooling towers, Hollands [3] found that mean particle sizes of the type defined by equation (1) are inapplicable, and the same conclusion is implicit to the study by Chen, et al. [4] of a cocurrent direct contact heat exchanger.

---

[1] Numbers in brackets designate References at end of paper.

Contributed by the Heat Transfer Division of THE AMERICAN SOCIETY OF MECHANICAL ENGINEERS and presented at the AIChE-ASME National Heat Transfer Conference, San Francisco, Calif., August 10–13, 1975.

Revised manuscript received by the Heat Transfer Division February 18, 1976. Paper No. 75-HT-36.

This paper first discusses in a general way the conditions under which a system is of the $\bar{x}_{p,q}$ type, i.e., has an $\bar{x}$ which satisfies equation (1). It then gives a general analysis of a system not of the $\bar{x}_{p,q}$ type, namely a parallel-flow or counter-flow aerosol heat (or mass) exchanger.

General Considerations

Consider the determination of the rate of heat or mass transfer between the continuous and disperse phases of an aerosol at some local region within an aerosol. The treatment will be equally applicable to heat transfer or mass transfer but we shall couch it in terms of heat transfer relations. The total heat transfer from all particles is readily shown to be:

$$q = \int_{x_\ell}^{x_u} \pi x^2 \frac{dn}{dx} h(x)\,(t_d(x) - t_c)\,dx \tag{2}$$

Defining $\bar{x}$ as the particle size of a monodisperse aerosol having the same number of particles and yielding the same total heat transfer, we obtain:

$$q = \pi \bar{x}^2 \left[\int_{x_\ell}^{x_u} \frac{dn}{dx}\,dx \right] h(\bar{x})\,(t_d(\bar{x}) - t_c) \tag{3}$$

Combining equations (2) and (3):

$$\bar{x}^2 h(\bar{x})\,(t_d(\bar{x}) - t_c) \int_{x_\ell}^{x_u} \frac{dn}{dx}\,dx = \int_{x_\ell}^{x_u} x^2 h(x)\,(t_d(x) - t_c) \frac{dn}{dx}\,dx \tag{4}$$

Comparing equation (4) with equation (1), it is obvious that the system is of $\bar{x}_{p,q}$ type only if it is possible to express $h(x)\cdot(t_d(x) - t_c)$ as some power of x. Usually this is possible for the $h(x)$ part. For example, if the Reynolds number of the particles is so small that they all transfer heat only by conduction, then Nu = 2 and $h(x) \propto x^{-1}$. Assuming that such a procedure is permissible for $h(x)$, i.e., $h(x) = cx^{-m}$, where c is a constant, equation (4) becomes:

$$\bar{x}^{2-m}\,(t_d(\bar{x}) - t_c) \int_{x_\ell}^{x_u} \frac{dn}{dx}\,dx = \int_{x_\ell}^{x_u} x^{2-m}\,(t_d(x) - t_c) \frac{dn}{dx}\,dx \tag{5}$$

If (as in some treatments of this problem [5]), it is *also* assumed that the particles have a uniform external temperature, i.e., $t_d(x)$ is independent of x, one obtains:

$$\bar{x}^{2-m} \int_{x_\ell}^{x_u} \frac{dn}{dx}\,dx = \int_{x_\ell}^{x_u} x^{2-m} \frac{dn}{dx}\,dx \tag{6}$$

which is compatible with equation (1), so that *in this case* the system is then of $\bar{x}_{p,q}$ type, with $p = 0$ and $q = 2 - m$. There are situations where this uniform external temperature assumption is permissible. One example is evaporation from a fine water spray into a massive air stream. Here, as a consequence of an energy and mass balance on the droplets, each droplet very quickly takes up a uniform temperature equal to the wet bulb temperature of the air stream. Another example is the case where the disperse phase is introduced at a uniform temperature and moves through the device in question at a rate so large in comparison to that of the continuous phase, that the particles never change appreciably in temperature.

However, in the vast majority of aerosol heat and mass transfer operations, $(t_d(x) - t_c)$ is not independent of x, nor can it be expressed simply as a power of x, and the system is not of an $\bar{x}_{p,q}$ type. In these operations, although the particles may start at uniform temperature, each particle size, due to its different diameter, transfers heat at a different rate in relation to its internal energy, and hence takes up a different temperature dependence on time. Moreover, each particle size may travel at a different velocity, so that at any local point in the aerosol, each particle size will have been exposed to the continuous phase for a different time.

The question arises: Is it possible to define mean particle diameters for operations which are not of the $\bar{x}_{p,q}$ type? The present paper addresses itself to this question. The system chosen for examination is a general counterflow or parallel flow heat transfer (or

Nomenclature

$A(x, z)$ = function defined in equation (13), $[\mathrm{m}^{-1}]$
$A_z(z)$ = function defined by equation (17), $[\mathrm{m}^{-1-n}]$
c = specific heat at constant pressure, [J/kg K]
C = flow stream capacity rate, = cM, [W/K]
$f_v(x) = f_v(x)\partial x$ is the fraction of the total volume of dispersed phase introduced at $z = 0$ having diameter between x and $x + \partial x$ see equation (14), $[\mathrm{m}^{-1}]$
$F(\xi) = f_v(x_c\xi)x_c$
g = acceleration due to gravity, $[\mathrm{m/s^2}]$
$h(x)$, $(h(x, z))$ = convective heat transfer coefficient between continuous phase and particles of diameter x (at height z)
j = an index which is equal to 1 for parallel flow and 2 for counterflow
k = thermal conductivity of continuous phase, [W/mK]
L = length of exchanger, [m]
M = mass flow, [kg/s]
n = number of particles having diameter between x_ℓ and x, dimensionless; also exponent in equation (19)
q = local heat transfer between phases, $[\mathrm{W/m^3}]$
R = capacity rate ratio of exchanger, = $\dfrac{c_d M_d}{c_c M_c}$
t = temperature, [K]
T = dimensionless temperature, $\dfrac{t_d - t_{d0}}{t_{c0} - t_{d0}}$
$V(x, z)$ = absolute velocity of particles having diameter x, at location z [m/s]
x = particle diameter, [m]
$\bar{x}$ = equivalent mean particle diameter, [m]
x_c = some characteristic particle diameter, [m] (see equation (23))
y = defined by equation (18), $[\mathrm{m}^n]$
z = axial distance coordinate, [m]
δ = characteristic parameter describing size distribution of dispersed phase, see equation (23)
ϵ = heat exchanger effectiveness
η = dimensionless axial coordinate, $y/x_c{}^n$
ξ = dimensionless particle diameter, x/x_c
$\bar{\xi}$ = equivalent mean particle diameter, see equation (22)
ρ = density, [kg/m]
θ = dimensionless temperature: $\theta(\xi, \eta) = T(x, z)$
$\bar{\theta}$ = bulk mean temperature of the dispersed phase, see equation (21), dimensionless
μ = viscosity of continuous phase, $[\mathrm{Ns/M^2}]$

Subscripts

c = of continuous phase (except for x_c, where it indicates characteristic diameter)
d = of dispersed phase
ℓ = lower limit of diameter of particles
0 = at $z = 0$ (except for θ_0, where it represents the equivalent monodisperse phase)
p, q = indices used to identify the type of mean diameter, see equation (1)
u = upper limit on diameter of particles

mass transfer) process of a disperse phase of some known particle size distribution, with a continuous phase. The solution presented accounts for the dependence of $(t_d(x) - t_c)$ on x.

System Model Analysis

Model. The system examined consists of a disperse phase of some known size distribution moving unidirectionally in a duct, in counterflow or parallel flow with a continuous phase, which also moves unidirectionally along the axis of the duct. The continuous phase is assumed to have a uniform velocity and temperature distribution across the duct and the disperse phase is uniformly distributed across any cross section of the duct, so that the flow is completely one-dimensional. The direction of gravity is immaterial to the present treatment. Agglomeration or disintegration of the disperse phase are assumed not to occur, and if mass transfer is taking place, it is assumed not to appreciably affect the diameters of the particles when they move through the device. Hence, the diameter of the particles is assumed to be conserved in the downstream direction. Radiation exchange is assumed to be negligible. Each particle is assumed to be uniform in temperature (or concentration) within itself, i.e., the resistance to heat (or mass) transfer inside the particle is assumed to be negligible compared to that in the continuous phase. This assumption may be lifted in later treatments but is made in the present treatment for the sake of simplicity.

The disperse phase is assumed to be admitted into the duct with a uniform temperature (or concentration) different from that at which the continuous phase is admitted. Either heat or mass transfer is assumed to be occurring *but not both simultaneously* unless Merkel's approximation is known to apply in which case, temperature may be interpreted as enthalpy [3]. The formulation will be couched in terms of heat transfer. The particles are assumed to be spherical; however, extension to nonspherical particles can be readily incorporated by means of a shape parameter.

Analysis. Let the mass flux in the downstream direction of particles having diameter between x and $x + \partial x$ be $dM_d = dM_d/dx \cdot \partial x$. Since the particles do not change in diameter as they proceed downstream, dM_d/dx is invariant with z. Consider an elemental volume of thickness ∂x and unit cross-sectional area normal to the flow in the system described previously. The number of particles contained in this volume and having diameter from x to $x + \partial x$ is readily shown to be:

$$\partial^2 n = \frac{6}{\pi} \cdot \frac{dM_d/dx}{\rho_d x^3 V(x, z)} \cdot \partial x \partial z \tag{7}$$

The heat transfer from these particles to the continuous phase is:

$$\partial^2 q = h(x, z)\,(t_d(x, z) - t_c)\pi x^2\, \partial^2 n \tag{8}$$

An energy balance written on these particles and the elemental volume gives:

$$c_d \frac{dM_d}{dx} \cdot \frac{\partial t_d(x, z)}{\partial z} = -\frac{\partial^2 q}{\partial x \partial z} \tag{9}$$

An energy balance written on the continuous phase yields:

$$c_c M_c \cdot \frac{dt_c(z)}{dz} = (-1)^{j+1} \int_{x_\ell}^{x_u} \frac{\partial^2 q}{\partial x \partial z}\, \partial x \tag{10}$$

where $j = 1$ if the phases are in parallel flow and $j = 2$ if the phases are in counterflow.

Combining equations (7)–(10) so as to eliminate $\partial^2 q$ and $\partial^2 a$ yields:

$$\frac{\partial t_d(x, z)}{\partial z} = -A(x, z)\,(t_d(x, z) - t_c(z)) \tag{11}$$

and

$$\frac{\partial t_c(z)}{\partial z} = (-1)^j R \int_{x_\ell}^{x_u} f_v(x) \frac{\partial t_d(x, z)}{\partial z}\, \partial x \tag{12}$$

where

$$A(x, z) = \frac{h(x, z)}{c_d \rho_d x V(x, z)} \tag{13}$$

and

$$f_v(x) = \frac{1}{M_d} \frac{dM_d}{dx} \tag{14}$$

is the mass (or volume) size distribution of the dispersed phase. Equations (11) and (12) satisfy the boundary conditions: $t_d(x, 0) = t_{d0}$ and $t_c(0) = t_{c0}$.

Equation (12) can be integrated directly to yield:

$$t_c(z) = t_{c0} + (-1)^j R \int_{x_\ell}^{x_u} f_v(x)\,\{t_d(x, z) - t_{d0}\}\partial x \tag{15}$$

and substituting this expression into (11) yields an integro-differential equation for the disperse phase temperature (dedimensionalized):

$$\frac{\partial T}{\partial z} = A(x, z)\left[1 - T + (-1)^j R \int_{x_\ell}^{x_u} f_v(x) T \partial x\right] \tag{16}$$

where $T = T(x, z)$ obeys the boundary condition $T(x, 0) = 0$.

Hydrodynamic Decoupling. Until now the evaluation of $h(x, z)$ and $V(x, z)$ has been left unspecified. Clearly $V(x, z)$ depends on the hydrodynamics of the two-phase flow, including the momentum transfer between the two phases in the duct and the velocity distribution at the start of the duct, $V(x, 0)$. Since $h(x, z)$ depends on $V(x, z)$ the same applies to it. Therefore, as the problem stands, the proper mean particle size will depend on the hydrodynamics of the situation, as well as thermal considerations, thereby making it difficult to evaluate in any general way. However, the prime concern of the present paper is the difficulties associated with the dependence of the driving force temperature difference, (the square bracket part of (16)) on x. The dependence of $A(x, z)$ on x is of secondary difficulty and can largely be overcome by assuming the more usual approach of taking the dependence as being given by a power law; i.e., assuming:

$$A(x, z) = A_z(z)/x^n \tag{17}$$

In this instance, letting

$$y = \int_0^z A_z(z) dz \tag{18}$$

the integro-differential equation (16) becomes:

$$\frac{\partial T}{\partial y} = \frac{1}{x^n}\left[1 - T + (-1)^j R \int_{x_\ell}^{x_u} T f_v(x) \partial x\right] \tag{19}$$

and the total hydrodynamic information is carried in the single quantity, n. A method for evaluating n will be given later.

On introducing dimensionless variables ξ, η, $F(\xi)$, and $\theta(\xi, \eta)$ (defined in the Nomenclature) for x, y, $f(x)$, and $T(x, z)$ respectively, equation (19) becomes:

$$\frac{\partial \theta}{\partial \eta} = \frac{1}{\xi^n}\left[1 - \theta + (-1)^j R \int_{\xi_\ell}^{\xi_u} \theta F(\xi)\, \partial \xi\right] \tag{20}$$

to be solved with boundary conditions: $\theta(\xi, 0) = 0$.

Definition of Mean Diameter. The mean diameter for the system may be defined as that diameter of a monodisperse system which would yield the same outlet temperature of the disperse phase as the bulk mean temperature of the actual disperse phase, all other variables being the same. An expression for the mean diameter, denoted by $\bar{x}$ or $\bar{\xi} = \bar{x}/x_c$, is readily arrived at. Letting θ_0 represent the value of θ in the hypothetical monodisperse system, equation (20) becomes:

$$\frac{d\theta_0}{d\eta} = \frac{1}{\bar{\xi}^n}\,[1 - \theta_0 + (-1)^j R \theta_0]$$

Integrating this equation with boundary condition $\theta_0 = 0$ at $\eta = 0$, equating the resulting θ_0 to the bulk mean temperature of the disperse phase in the actual system, $\bar{\theta}$, given by:

$$\bar{\theta} = \int_{\xi_\ell}^{\xi_u} \theta f(\xi) \partial \xi \tag{21}$$

and solving for $\bar{\xi}$, we get:

$$\bar{\xi}^n = \frac{((-1)^j R - 1)\eta}{\ln\left[1 + ((-1)^j R - 1)\bar{\theta}\right]} \tag{22}$$

The evaluation of the mean diameter requires first solution of equation (20) for θ; substitution of this solution into equation (21) and (22) will then yield $\bar{\xi}$. Clearly $\bar{\xi}$ is a function of at least three variables, R, η, and n. In addition it will depend upon parameters fixing the particle size distribution.

Particle Size Distributions. We examine in this paper two particle size distributions: the log-probability distribution which can be expressed as:

$$F(\xi) = \frac{\delta}{\sqrt{\pi}} \frac{1}{\xi} e^{-\delta^2} (\ln \xi)^2 \tag{23a}$$

and the Rosin-Rammler distribution for which

$$F(\xi) = \delta \xi^{\delta - 1} e^{-\xi^\delta} \tag{23b}$$

both provided x_c is properly chosen. Forcing the actual distribution to fit equation (23a) or (23b) fixes the value of x_c.

Solution

Solution for $R \to \infty$. In the limit $R \to \infty$, the disperse phase moves through the exchanger at such a high rate that the particles do not change appreciably in temperature. Solving equation (20)–(22) in this case gives

$$\bar{\xi}^{-n} = \int_{\xi_\ell}^{\xi_u} \xi^{-n} F(\xi) d\xi \tag{24a}$$

Indicating that the system is of the $\bar{x}_{p,q}$ type with:

$$\bar{\xi} = \bar{\xi}_{3,3-n}, \qquad \text{or } \bar{x} = \bar{x}_{3,3-n} \tag{24b}$$

Equation (24a) may be integrated in closed-form for each of the size distribution functions considered [1]. There results, for the log-probability distribution:

$$\bar{\xi}^{-n} = \bar{\xi}_{3,(3-n)}{}^{-n} = e^{1/4(n/\delta)^2} \tag{25a}$$

and for the Rosin-Rammler distribution:

$$\bar{\xi}^{-n} = \bar{\xi}_{3,(3-n)}{}^{-n} = \Gamma\left(1 - \frac{n}{\delta}\right) \tag{25b}$$

Solution for Finite R. For other values of R, analytical solutions to equation (20) were not possible and it was necessary to integrate the equation numerically. The technique adopted was to substitute a numerical quadrature for the integral in equation (20) and then write this equation for each of the $\theta(\xi_k)$, where ξ_k are the quadrature points. With this equation (20) becomes a set of simultaneous ordinary differential equations:

$$\frac{d\theta(\xi_k)}{d\eta} = \xi_k{}^{-n} \left[1 - \theta(\xi_k) + (-1)^j R \sum_{k=1}^{m} W_k \theta(\xi_k)\right] \tag{26}$$

where m is the total number of quadrature points and W_k are the weighting factors whose values depend upon the function $F(\xi)$ and the type of quadrature used. The set of ordinary differential equations given by equation (26) was then solved by using Runge-Kutta method of fifth order. This method of numerically solving an integro-differential equation is analogous to the method of solving an integral equation as described by Love [6]. Several types of Gaussian quadrature [7] were tried, and that one chosen yielding the best convergence properties. Hermite-Gauss was used for log-probability distribution, and Laguerre-Gauss for the Rosin-Rammler case. Up to 96 quadrature points were required to obtain convergence for the latter, whereas only 9 were required for the former.

Results and Discussion

It can be shown that for the two particle size distributions considered, $\bar{\xi}^n$ is a function of only three variables, namely η, R, and the ratio δ/n. For given values of R and δ/n, η fixes the heat exchanger effectiveness ϵ, or conversely, a specified ϵ fixes the required η. Consequently it is possible to express $\bar{\xi}^n$ as a function of three variables ϵ, R, and δ/n. This functional dependence is shown in Figs. 1 and 2 for the log-probability distribution, and in Figs. 3 and 4 for the Rosin-Rammler distribution, for both parallel-flow and counter-flow arrangements, and for the full range of practical interest of ϵ, R, and δ/n. Presentation of $\bar{\xi}^n$ as a function of ϵ rather than η is preferable for design purposes since ϵ is specified at the beginning of the design procedure. Moreover, the range of ϵ, $(0 < \epsilon < 1)$, is much narrower than that of η, thereby making graphical presentation easier.

The effectiveness ϵ is defined, after Kays and London [8] by:

$$\epsilon = \frac{C_d(t_{d,\text{in}} - t_{d,\text{out}})}{C_{\min}(t_{d,\text{in}} - t_{c,\text{in}})} = \frac{C_c(t_{c,\text{out}} - t_{c,\text{in}})}{C_{\min}(t_{d,\text{in}} - t_{c,\text{in}})} \tag{27}$$

The $\epsilon_{\max}$ in the absissa of the parallel flow charts is defined by:

$$\epsilon_{\max} = \frac{1}{1+R} \qquad R < 1 \tag{28a}$$

$$\epsilon_{\max} = \frac{R}{1+R} \qquad R < 1 \tag{28b}$$

For counterflow, $\epsilon_{\max} = 1$.

The ordinate of Figs. 1–4 is the ratio of $\bar{\xi}^n$ for the value of R considered to that for $R = \infty$, the latter value being given by equations (25a) and (25b). Consequently the ratio equals 1 for $R = \infty$. For other values of R the ratio is seen to be less than unity. The reason for this can be explained as follows. Consider a hypothetical exchanger in which, due to some hypothetical mixing between particles, at any given cross section, all particles have the same temperature, equal to the bulk temperature at the cross section; i.e., $t_d(x, z) = \bar{t}_d(z)$. Now it is readily seen in light of the "General Considerations" given earlier in this paper, that this hypothetical exchanger is of the $\bar{x}_{p,q}$ type. The values of p and q are readily shown to be: $p = 3$ and $q = 3 - n$ so that $\bar{\xi} = \bar{\xi}_{3,3-n}$ and the ordinate in the figures of this exchanger will be unity for all ϵ, R, and δ/n. Now in the ac-

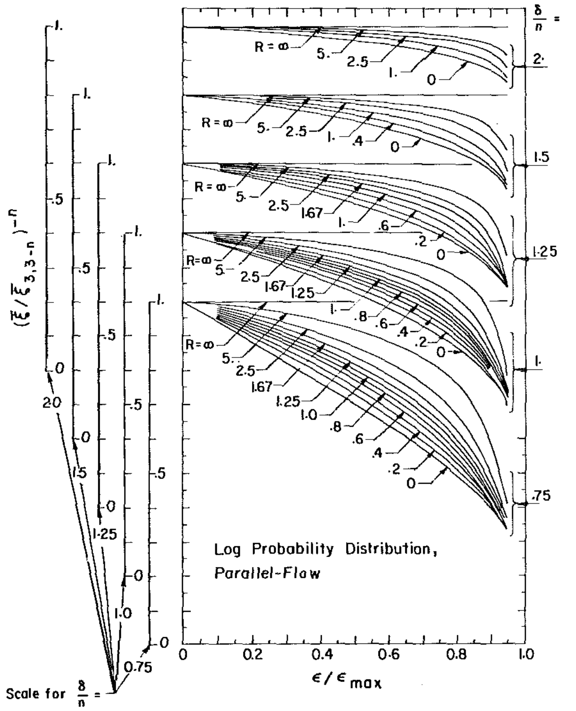

Fig. 1 Plot of mean diameter for a parallel-flow heat exchanger where the disperse phase has a log-probability particle size distribution

tual exchanger the driving force temperature difference, $(t_d(x, z) - t_c(z))$, will be less than the average for the smaller particles, and greater than average for the larger particles. However, since in the hypothetical exchanger the predominate heat transfer is with the smaller particles (due to their greater surface area per unit volume, higher convective coefficient, and lower velocity), the real exchanger exchanges less heat overall than the hypothetical exchanger. The result is that the real exchanger has a larger mean diameter, thereby explaining why the ordinate in the figures is everywhere less than unity.

Application to Design

The design of heat exchangers of the type treated in this paper, using Figs. 1–4, involves a number of steps. Suppose it is required to find the effectiveness of a specified exchanger of specified length, L. The first step is the evaluation of the function $A(x, z)$. The full details of the development of this quantity is beyond the scope of this paper. However, it clearly involves developing an expression for $V(x, z)$ based upon particle dynamics and drag laws. Examples of such calculations are given in [2–4]. The heat transfer coefficient $h(x, z)$ is then determined using the expression for $V(x, z)$, and the Nusselt number-Reynolds number correlation for flow over particles for the appropriate Reynolds number region. The next step is to determine n. The form of the resulting expression for $A(x, z)$ will not generally be explicitly a power law in x, like equation (17). Therefore, it is necessary to calculate an "average" value of n. A good estimate for the proper average is given by:

$$n = \left[\ln \left\{ \frac{\int_0^L A(x_{10}, z)_{dz}}{\int_0^L A(x_{90}, z)dz} \right\} \right] \Bigg/ \ln \left\{ \frac{x_{90}}{x_{10}} \right\} \qquad (29)$$

where x_{10} and x_{90} are the values of x at the 10 and 90 percentiles of the droplet size distribution, $f_v(x)$, as defined in [1]. (Equation (29) was obtained by averaging equation (17) with respect to z over 0 to L, and then making the resulting equation exact for $x = x_{10}$ and for $x = x_{90}$.) This permits the evaluation of $\bar{x}$ from Figs. 1–4 and equation (25). (At this point the value of ϵ must be guessed, to be later revised to the value calculated, by an iterative scheme.) The final step is to find the effectiveness ϵ of a heat exchanger having monodisperse particles of diameter $\bar{x}$. By the definition of $\bar{x}$,

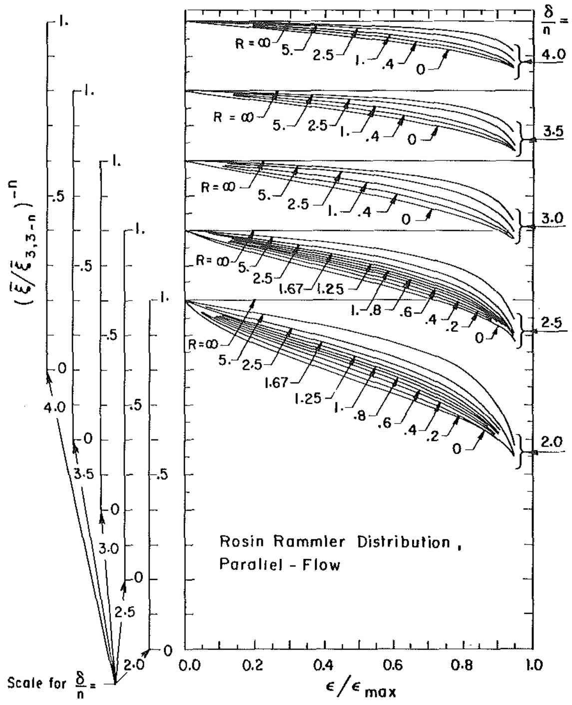

Fig. 3 Plot of mean diameter for a parallel-flow heat exchanger where the disperse phase has a Rosin-Rammler particle size distribution

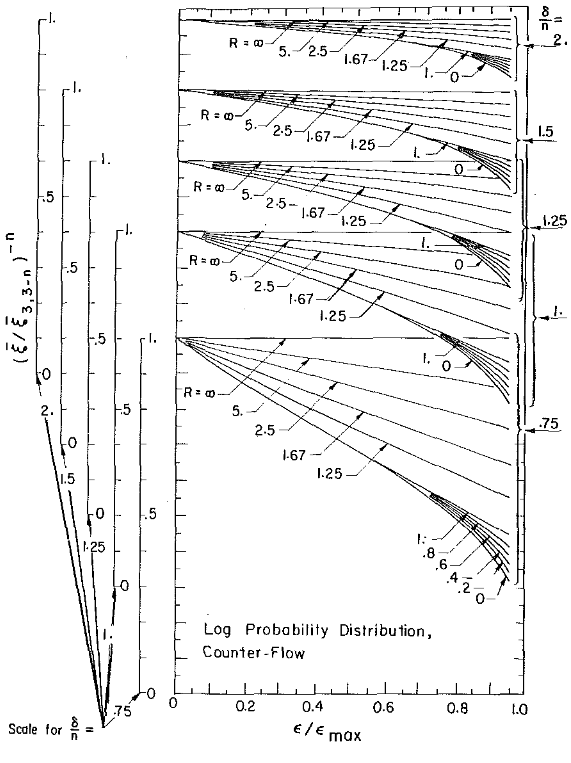

Fig. 2 Plot of mean diameter for a counter-flow heat exchanger where the disperse phase has a log-probability particle size distribution

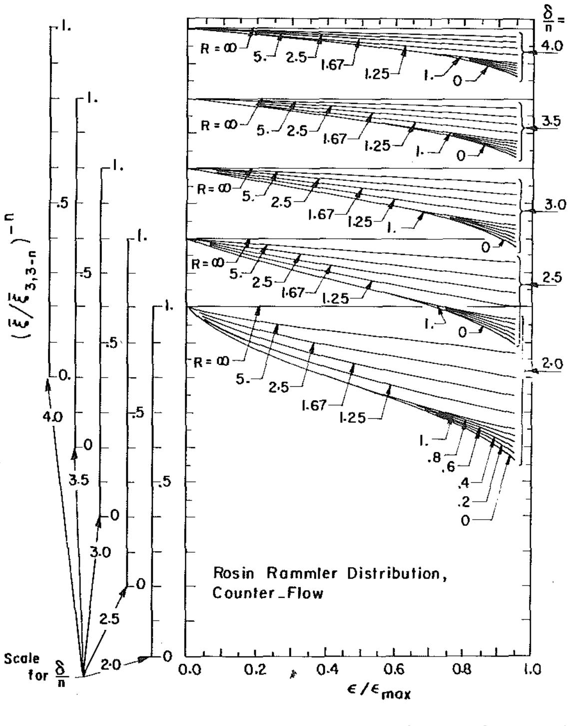

Fig. 4 Plot of mean diameter for a counter-flow heat exchanger where the disperse phase has a Rosin-Rammler particle size distribution

this will also be the effectiveness of the actual exchanger. Expressions for ϵ for such a heat exchanger are readily derived, in terms of an NTU defined by:

$$\mathrm{NTU} = \int_0^L A(\bar{x}, z)dz \tag{30}$$

The expressions are:

For parallel flow		For counterflow	
$\epsilon = \theta_0$	for $R < 1$	$\epsilon = \dfrac{\theta_0}{1 + R\theta_0}$	for $R < 1$
$\epsilon = R\theta_0$	for $R > 1$	$\epsilon = \dfrac{R\theta_0}{1 + R\theta_0}$	for $R > 1$

where θ_0 is given by:

$$\theta_0 = \frac{1 - e^{-(1-(-1)^j R)\mathrm{NTU}}}{1 - (-1)^j R} \tag{31}$$

For $R < 1$ these expressions are identical to the standard ones (see e.g., [8]) for counter flow and parallel flow heat exchangers, provided equation (30) is used to evaluate NTU. The $R > 1$ class has to be introduced since (as opposed to the standard exchanger) the equations are not symmetric with respect to the two streams.

Acknowledgments

The authors acknowledge with thanks financial support for this research from the National Research Council of Canada, both through operating grants and through a Research Fellowship.

References

1 Mugele, R. A., and Evans, H. D., "Droplet Size Distribution in Sprays," *Ind. & Eng. Chem.*, Vol. 43, No. 6, 1951, pp. 1317–1324.

2 Dickinson, D. R., and Marshall, W. R., Jr., "The Rates of Evaporation of Sprays," *AIChE Journal*, Vol. 14, No. 4, 1968, pp. 541–552.

3 Hollands, K. G. T., "An Analysis of a Counterflow Spray Cooling Tower," *International Journal of Heat and Mass Transfer*, Vol. 17, 1974, pp. 1227–1239.

4 Chen, G. T. S., Young, E. H., and York, J. L., "Direct Contact Heat Transfer of a Co-Current Oil-Water System," AIChE, Preprint 2, presented at the 14th National Heat Transfer Conference, Atlanta, Ga., Aug. 5–8, 1973.

5 Yaron, I., and Gal-or, B., "Convective Mass or Heat Transfer from Size Distribution Drops, Bubbles or Solid Particles," *International Journal of Heat and Mass Transfer*, Vol. 14, 1971, pp. 727–737.

6 Love, Tom J., *Radiative Heat Transfer*, Merrill Publishing Co., Columbus, Ohio, 1968, pp. 86–87.

7 Hildebrand, F. B., *Introduction to Numerical Analysis*, McGraw-Hill, New York, 1956.

8 Kays, W., and London, A. L., *Compact Heat Exchangers*, McGraw-Hill, New York, Second ed., 1964.

ERRATA

Erratum: R. N. Smith and R. Greif, "Turbulent Transport to a Rotating Cylinder for Large Prandtl or Schmidt Numbers," published in the Nov. 1975 issue of the JOURNAL OF HEAT TRANSFER, pp. 594–597.

In equations (8) and (9), the velocities U and U^+ should be replaced by $-U$ and $-U^+$, respectively.

P. C. Jain
Professor.

B. S. Goel
Research Scholar.

Department of Mathematics,
Indian Institute of Technology,
Powai, Bombay, India

A Numerical Study of Unsteady Laminar Forced Convection From a Circular Cylinder

A numerical investigation of an unsteady laminar forced convection from a circular cylinder is presented. The Navier-Stokes equations and the energy equation for an unsteady incompressible fluid flow are solved by the finite difference method. The results are obtained at Reynolds numbers 100 and 200. The temperature field around the cylinder is obtained throughout the region of computation and is shown by isotherms at different times. The variations of the local Nusselt number around the cylinder at different times are computed and shown by graphs. The mean Nusselt number and the Strouhal number are also calculated. The computed results are compared with the other available experimental and theoretical results and are found to be in good agreement with them.

Introduction

In a number of engineering applications, such as, in the theory of hot wire anemometer, in the design of heat exchangers, etc., the problem of the heat transfer between a circular cylinder and its surrounding stream of a viscous fluid is of great interest. A large number of experimental papers on this aspect of the problem are available in the literature. The dynamical behavior of the flow close to the surface of a body strongly affects the rate of the heat transfer from a warm rigid surface to the cold fluid flow around it. But this dynamical behavior of the flow, in the region of the separation which occurs at the rear of the body when the flow rate is sufficiently high, is not yet well understood.

It is well known that numerical solutions of the Navier-Stokes equations for fluid flow problems may give reliable information in a case when experimental measurements are difficult. This view is well supported by the numerical studies made by Fromm and Harlow [1],[1] Kawaguti and Jain [2], Thoman and Szewczyk [3], Jain and Rao [4], Son and Hanratty [5], Collins and Dennis [6], and other authors on the problems of the flow of a viscous fluid past a circular cylinder. It is surprising that only a few efforts have been directed at the heat transfer aspects of this problem. Dennis, Hudson, and Smith [7] have reported a theoretical study about a laminar forced convection in an incompressible steady fluid flow past a circular cylinder at low Reynolds numbers. Some other theoretical attempts have been reported in the literature. Harlow and Fromm [8] have presented a numerical study of the heat transfer in an incompressible fluid flow through a channel past a rectangular cylinder. Acrivos, Snowden, Grove, and Peterson [9] have studied this problem on the assumption that the standing vortex region behind a cylinder should elongate with an increase in the Reynolds numbers. The local heat transfer coefficients around a horizontal cylinder in viscous fluid flows at Reynolds numbers 20–500 have been measured by Eckert and Soehngen [10].

The present paper differs from that of Harlow and Fromm [8] mainly in two aspects. The problem of the heat transfer from the rear of a circular cylinderical object to the region of the separated flow has been studied in an infinite region of flow field, so that the blockage correction is not required for modifying the computed results. Second, the proposed numerical method allows the construction of a very fine mesh near the surface of the cylinder and a coarse one far away from the rigid boundary, this scheme is suitable for studying the physical behavior of the fast-changing flow characteristics in the neighborhood of the cylinder and in its wake. It is known that the experimental results at the intermediate

---

[1] Numbers in brackets designate References at end of paper.

Contributed by the Heat Transfer Division for publication in the JOURNAL OF HEAT TRANSFER. Manuscript received by the Heat Transfer Division July 1, 1974. Paper No. 76-HT-FF.

Reynolds numbers 100–300 are not quite satisfactory (cf. Grove, et al. [11] and Roshko [12]); the present paper provides a numerical method for getting results at these intermediate Reynolds numbers. We have reported computational results of the heat transfer aspect of the problem at Re = 100 and 200.

Basic Equations

We consider an unsteady flow of a viscous incompressible fluid past a circular cylinder of radius "a," which starts impulsively at time $t = 0$ with a constant velocity U at infinity in the direction of $\theta = 0$. Using the polar coordinates, the equations of motion of the fluid in dimensionless form are (cf. Jain and Rao [4]),

$$-\frac{\partial \zeta}{\partial t} + \frac{1}{r}\left\{\frac{\partial \Psi}{\partial r}\frac{\partial \zeta}{\partial \theta} - \frac{\partial \Psi}{\partial \theta}\frac{\partial \zeta}{\partial r}\right\} = -\frac{2}{\text{Re}}\nabla^2 \zeta \tag{1}$$

$$\zeta = -\nabla^2 \Psi$$

where

$$\nabla^2 \equiv \frac{\partial^2}{\partial r^2} + \frac{1}{r}\frac{\partial}{\partial r} + \frac{1}{r^2}\frac{\partial^2}{\partial \theta^2}$$

$$\text{Reynolds number Re} = \frac{2aU}{\nu}$$

The initial and boundary conditions for the velocity problem are

$$t < 0, \quad \Psi = \zeta = 0$$

$$t \geq 0, \quad \Psi = \frac{\partial \Psi}{\partial r} = 0 \quad \text{on } r = 1 \tag{2}$$

$$\Psi \to r \sin\theta \quad \text{as } r \to \infty$$

The stream function Ψ is used to get the velocity components as

$$u = \frac{1}{r}\frac{\partial \Psi}{\partial \theta}, \quad v = -\frac{\partial \Psi}{\partial \theta} \tag{3}$$

We have solved this problem for calculating Ψ and ζ (cf. Jain and Goel [13]) by using a modified numerical method as described by Jain and Rao [4]. These values of Ψ have been used as input data for studying the heat transfer aspect of the problem discussed in this paper. By assuming the fluid density ρ, the specific heat c_p, and the thermal conductivity k of the fluid to be constant and by neglecting the internal heat friction, the governing equation in dimensionless form for the unsteady two-dimensional temperature field $T\,(r, \theta, t)$ is given by

$$-\frac{\partial T}{\partial t} + \frac{1}{r}\left\{\frac{\partial \Psi}{\partial r}\frac{\partial T}{\partial \theta} - \frac{\partial \Psi}{\partial \theta}\frac{\partial T}{\partial r}\right\} = -\frac{2}{\text{Re}\cdot\text{Pr}}\nabla^2 T \tag{4}$$

where

$$\text{Prandtl number Pr} = \frac{\rho c_p \nu}{k}$$

It is assumed that the fluid and the cylinder are kept at the same temperature T_0 at $t = 0$. The temperature of the cylinder is raised from T_0 to T_w as soon as the flow starts impulsively.

Transforming the independent variable r by $\xi = \log r$ and the dependent variable Ψ by the relation $\Psi = r \sin\theta + \psi$, equation (4) takes the form

$$-\exp(2\xi)\frac{\partial T}{\partial t} + \left\{\frac{\partial \psi}{\partial \xi}\frac{\partial T}{\partial \theta} - \frac{\partial \psi}{\partial \theta}\frac{\partial T}{\partial \xi}\right\} + \exp(\xi)\left\{\frac{\partial T}{\partial \theta}\sin\theta - \frac{\partial T}{\partial \xi}\cos\theta\right\} + \frac{2}{\text{Re}\cdot\text{Pr}}\Delta T = 0 \tag{5}$$

where

$$\Delta \equiv \frac{\partial^2}{\partial \xi^2} + \frac{\partial^2}{\partial \theta^2}$$

Assuming $\psi\,(\xi, \theta)$ to be known by solving the equations of the motion (cf. Jain and Goel [13]), equation (5) is solved subject to the following boundary conditions:

$$t < 0; \quad \psi = T = 0 \tag{6}$$

$$t \geq 0; \quad \text{on } \xi = 0, \quad \psi = \frac{\partial \psi}{\partial \xi} = -\sin\theta, \quad T = 1 \tag{7}$$

$$\text{on } \xi = \Sigma \quad \psi = T = 0 \tag{8}$$

For computational work, we take a circular domain of radius exp (Σ) in the physical plane. By taking $\Sigma = \pi$, exp $(\pi) = 23.1406226$ which is sufficiently large for assuming ψ and T to be very small on this boundary. Condition (8) has been derived by making use of this assumption.

The Numerical Method

$$T_{i,j}(t + \Delta t) = T_{i,j}(t) + \frac{\Delta t}{4h^2}\Big[e^{-2(i-1)h}\{(\psi_{i+1,j} - \psi_{i-1,j})(T_{i,j+1} - T_{i,j-1}) - (\psi_{i,j+1} - \psi_{i,j-1})(T_{i+1,j} - T_{i-1,j})\} + 2he^{-(i-1)h} \times \{(T_{i,j+1} - T_{i,j-1})\sin(j-1)h - (T_{i+1,j} - T_{i-1,j})\cos(j-1)h\} + \frac{8\cdot e^{-2(i-1)h}}{\text{Re}\cdot\text{Pr}}\{T_{i+1,j} + T_{i-1,j} + T_{i,j+1} + T_{i,j-1} - 4\cdot T_{i,j}\}\Big] \tag{9}$$

In this equation the quantities on the right-hand side are taken at the time t and suffixes (i, j) correspond to the value of the quantity at the mesh point $\xi = (i - 1)h$, $\theta = (j - 1)h$; h is the mesh size. We have used the central differences for the space derivatives and the forward differences for the time derivative in deriving the equation (9).

In the physical plane, we get smaller meshes near the surface of

Nomenclature

a = radius
c_p = specific heat at constant pressure
D = diameter = $2a$
f = shedding frequency
h = local heat-transfer cofficient
k = thermal conductivity
$\bar{r}$ = distance polar coordinate
$\bar{t}$ = time
$\bar{T}$ = temperature
$\bar{T}_0$ = initial temperature
$\bar{T}_w$ = cylinder temperature
U = velocity at infinity
$\bar{u}$ = velocity component in $\bar{r}$-direction
$\bar{v}$ = velocity component in θ-direction
ρ = fluid density
θ = angular velocity
$\bar{\Psi}$ = stream function
$\bar{\zeta}$ = vorticity
ν = kinematic viscosity

Dimensionless Quantities

h = mesh size
Nu = Nusselt number = $2h_\ell a/k$
Pr = Prandtl number = $\rho c_p \nu/k$
r = distance coordinate = $\bar{r}/a$
Re = Reynolds number = $2aU/\nu$
S = Strouhal number = fD/U
t = time = $\bar{t}U/a$
T = temperature = $(\bar{T} - \bar{T}_0)/(\bar{T}_w - \bar{T}_0)$
u = velocity component = $\bar{u}/U$
v = velocity component = $\bar{v}/U$
ξ = log r (transformation)
ζ = vorticity = $\bar{\zeta}a/U$
θ = angular coordinate
ψ = perturbed stream function
Σ = length of rectangular domain
δ = increment
$\Delta \equiv \partial^2/\partial\xi^2 + \partial^2/\partial\theta^2$

Subscripts

i = for ξ-coordinate
j = for θ-coordinate
m = mean value

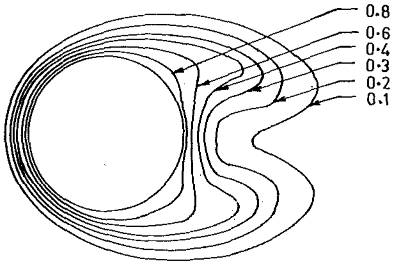

Fig. 1(*a*) **Isotherm pattern at Re = 100, *t* = 3.47**

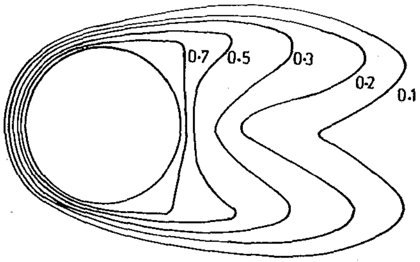

Fig. 1(*b*) **Isotherm pattern at Re = 200, *t* = 6.0**

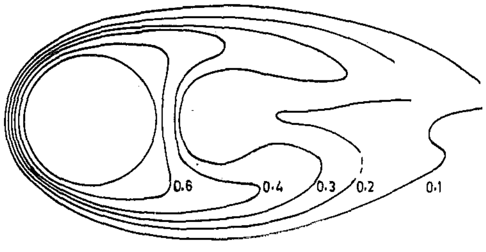

Fig. 3(*a*) **Isotherm pattern at Re = 100, *t* = 9.33**

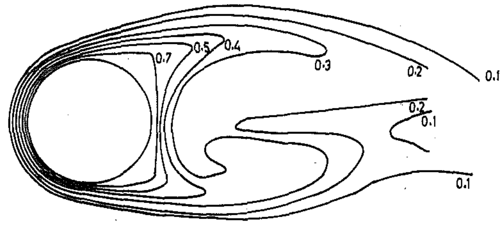

Fig. 3(*b*) **Isotherm pattern at Re = 200, *t* = 13.4**

the cylinder and bigger ones far from the body. In the present study, we have attempted to refine the mesh size considerably in the neighborhood of the cylinder by taking $\delta\xi = \delta\theta = \pi/60$. At a distance away from the cylinder, we have chosen $\delta\xi = \delta\theta = \pi/30$. This seems to be suitable choice of mesh sizes for the study of the fluid flow past a bluff body, as large variations in the stream function ψ, the vorticity ζ, and the temperature T occur near the surface of the cylinder.

The finite difference method for solving the equations has been described by Jain and Rao [4].

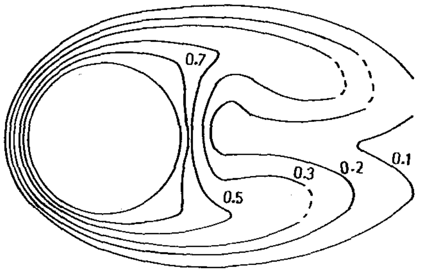

Fig. 2(*a*) **Isotherm pattern at Re = 100, *t* = 6.42**

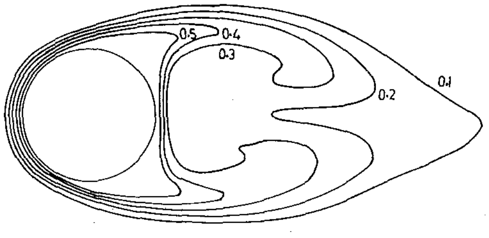

Fig. 2(*b*) **Isotherm pattern at Re = 200, *t* = 9.4**

Nusselt Number

The heat exchange between the cylinder and the fluid is measured by means of the local coefficient of the heat transfer h_ℓ. Once the temperature distribution around the cylinder becomes known, the local heat transfer coefficient can be calculated by the following formula. The Nusselt number

$$\mathrm{Nu}(\theta) = \frac{2h_\ell a}{k} = -2(\partial T/\partial \xi)_{\xi=0} \tag{10}$$

Most of the experimental measurements reported in the literature are confined to the mean Nusselt number, in our case this corresponds to the local coefficient of the heat transfer averaged over the surface of the cylinder

$$\mathrm{Nu}_m = \frac{1}{2\pi}\int_0^{2\pi} \mathrm{Nu}(\theta)\,d\theta \tag{11}$$

In the two-dimensional case, however, the local Nusselt number can be obtained directly from equation (10) using numerical differentiation. The mean Nusselt number Nu_m can be calculated from equation (11) by using Simpson's rule for numerical integration.

Discussion

The development of the vortex shedding behind a circular cylinder has been discussed, along with the results on the flow characteristics, in a separate paper (cf. Jain and Goel [13]). The thermal characteristics of the flow are considered in this paper.

Isotherm maps are presented in Figs. 1(*a*)–4(*a*) for Re = 100 and in Figs. 1(*b*)–4(*b*) for Re = 200. The local Nusselt number distributions for the two Reynolds numbers are given in Figs. 5 and 6. The figures show the time history of the results. In all the cases the Prandtl number has been taken as 0.73.

The process of the vortex shedding is accelerated by introducing a perturbation in the wake of the flow at times $t = 3.47$ (Re = 100) and $t = 6.00$ (Re = 200), the corresponding isotherms are shown in Figs. 1(*a*) and 1(*b*). These isotherms are symmetrical about the line of symmetry. By observing the pattern of the isotherms 2(*a*) ($t = 6.42$, Re = 100) and 2(*b*) ($t = 9.4$, Re = 200), one finds that an unsymmetrical flow in the wake gives rise to an unsymmetrical pattern of the isotherms. As the process of the shedding of vortices sets in, a significant distortion in the symmetry of the isotherms around the cylinder can be observed in Figs. 3(*a*) ($t = 9.33$, Re = 100), 4(*a*) ($t = 12.4$, Re = 100), 3(*b*) ($t = 13.4$, Re = 200), and 4(*b*) ($t = 16.5$, Re = 200).

From these results, one finds that a significant change in the pattern of the isotherms takes place in the region of the wake only.

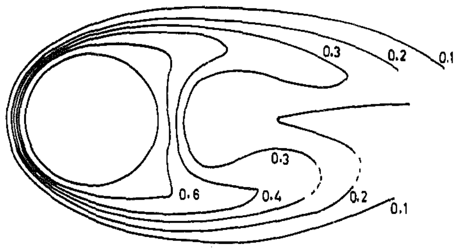

Fig. 4(*a*) Isotherm pattern at Re = 100, *t* = 12.40

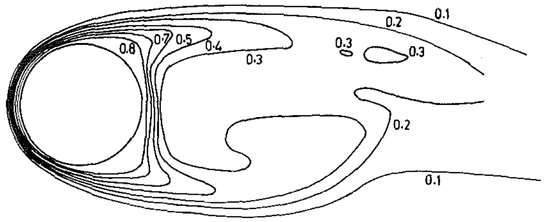

Fig. 4(*b*) Isotherm pattern at Re = 200, *t* = 16.5

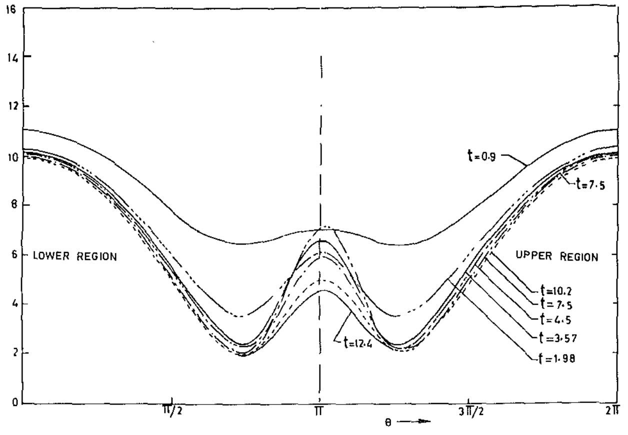

Fig. 5(*a*) Local Nusselt number on the surface of the cylinder at Re = 100

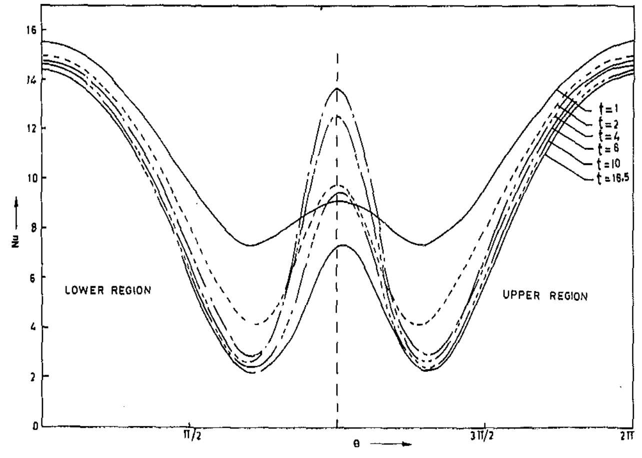

Fig. 5(*b*) Local Nusselt number on the surface of the cylinder at Re = 200

As the wake in the rear stagnation point region gets elongated and increases in breadth, the pattern of the isotherms also gets elongated and becomes broader in the region. Figs. 4(*a*) (t = 12.4, Re = 100) and 4(*b*) (t = 16.5, Re = 200) indicate that the pattern of the isotherms gets distorted as the shedding of the vortices takes place in the flow.

The process of the vortex shedding takes place at a rate which is slower than the rate at which the outer stream lines on the periphery of the wake moves into the main stream. The fluid along stream lines passing in the neighborhood of the cylinder gets heated and these stream lines usually form S-shaped patterns in the wake. Thus, the fluid in the wake region gets more heated than in the outer flow region. The pattern of the isotherms computed at Re = 100 and 200 for the unsteady flow has a similar structure to the pattern of the isotherms around a cylinder given by Eckert and Soehngen [10] and Krall and Eckert [14].

The variations of the local Nusselt number around the surface of the cylinder at different times are presented in Figs. 5(*a*) and 5(*b*) at Re = 100 and 200, respectively. A striking feature of this distribution is the fluctuation on the Nusselt number in the region of rear stagnation point. The Nusselt number in this region decreases from the initial time to the time t = 1.9 (Re = 100) and t = 1 (Re = 200), and then it increases till t = 4.5 (Re = 100) and t = 4 (Re = 200), at which times the Nusselt number near the rear stagnation point attains the peak values. After this, the Nusselt numbers in the wake region again start decreasing and continue to do so for the further times [cf. Figs. 5(*a*), t = 7.5, 12.4 (Re = 100) and 5(*b*), t = 10, 16.5 (Re = 200)]. The Nusselt number distribution on the surface of the cylinder remains almost symmetrical except in the wake region where some asymmetry is found due to the presence of the shedding of vortices. It may be observed that in Eckert and Soehngen's curves at Re = 200 approximately the local Nusselt number is found to be highly nonsymmetric in the wake. Our computational results do not completely confirm the experimental findings of Eckert and Soehngen [10].

Figs. 6(*a*) and 6(*b*) show the behavior of the Nusselt number distribution in the physical plane at different times for Reynolds numbers 100 and 200, respectively. On the surface of the cylinder

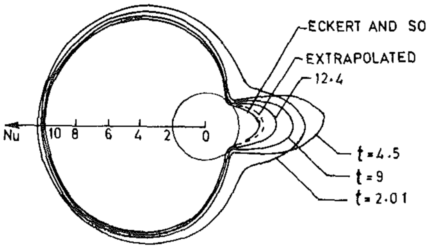

Fig. 6(*a*) Local Nusselt number around the circular cylinder at Re = 100

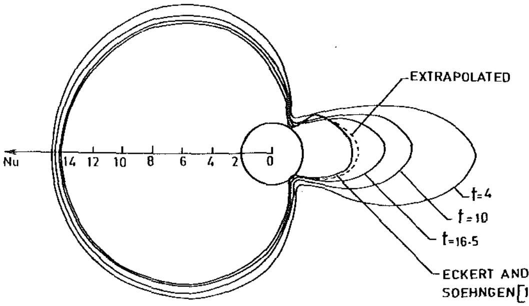

Fig. 6(*b*) Local Nusselt number around the circular cylinder at Re = 200

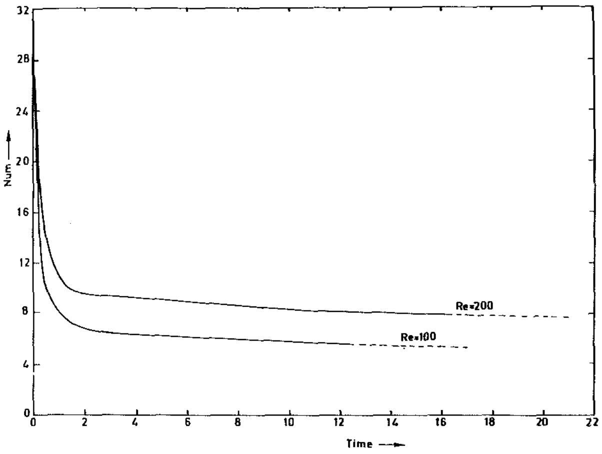

Fig. 7 Mean Nusselt number at Re = 100 and Re = 200

the minimum heat transfer takes place somewhere between the point of the separation and the rear stagnation point. In these figures our results for the Nusselt number have been compared with the experimental results due to Eckert and Soehngen [10] for a fluid flow past a cylinder. We have computed the results for the unsteady case up to $t = 12.4$ (Re = 100) and $t = 16.5$ (Re = 200) and then extrapolated them, the extrapolated results (dotted lines) are found to be quite close to the curves drawn for the experimental results (cf. Figs. 6(*a*) and 6(*b*)). In Fig. 6(*b*), it is found that the nonsymmetry of the Nusselt number is skewed opposite to the nonsymmetry of that presented for the curve by Eckert and Soehngen [10]. This seems to be due to the fact that the nonsymmetry moves from one side of the rear stagnation point to the other as shedding occurs. This view is confirmed by examining Fig. 6(*a*) (Re = 100) where the nonsymmetry of the Nusselt number for the computed results and that for Eckert and Soehngen's results are skewed on the same side of the rear stagnation point.

With these computed results, one would like to find out the total heat transfer from the cylinder to the flow which is equivalent to the heat transfer coefficient averaged over the surface of the cylinder. To achieve it, we have computed the mean Nusselt number Nu_m by using Simpson's rule in equation (11). The computed results are presented in Fig. 7. It is seen that the total heat flowing from the cylinder decreases steeply in the initial stages of the flow. At the later stages, the curves show a gradual variation with time. The extrapolated curves (dotted lines) show the behavior of the total heat transfer from the surface of the cylinder as time becomes very large. Several empirical relations between the Reynolds number and the Nusselt number are available for the steady case in the literature. By taking the Reynolds number as 200 and kinematic viscosity of the air, McAdams [15] has used the empirical expression $\mathrm{Nu}_m = 0.32 + 0.43\,\mathrm{Re}^{0.52}$. The expression has been later modified

$$\mathrm{Nu}_m = 0.43 + 0.48\sqrt{\mathrm{Re}} \tag{12}$$

Kramers [16] has given the formula predicting the trend of the results for Nu_m at large Reynolds numbers. He has claimed that this formula gives results which are consistent with most of the available experimental results in the range $2 < \mathrm{Re} < 200$. H formula for air is given by

$$\mathrm{Nu}_m = 0.39 + 0.51\sqrt{\mathrm{Re}} \tag{13}$$

Expressions (12) and (13) have been used widely by experimenters. Using these expressions, the values of Nu_m turn out to be in good agreement with our computed values as summarized in the following table.

Authors	Nu_m at Re = 100	Nu_m at Re = 200
McAdams [15]	5.23	7.2172
Kramers [16]	5.49	7.6034
Present paper	5.632 ($t = 12.4$) 5.52 (extrapolated)	7.903 ($t = 16.5$) 7.63 (extrapolated)

It may be of interest to give results about the Strouhal number which is defined as $S = f{\cdot}D/U$, where f is the shedding frequency on one side, D is the diameter of the cylinder, and U is the velocity of the upstream. The calculated values of Strouhal numbers are approximately 0.15 and 0.17 for Reynolds numbers 100 and 200, respectively, which are in good agreement with the values calculated by other authors.

Acknowledgments

The authors are thankful to the referees for their suggestions which helped in modifying the manuscript of this paper.

The authors wish to express their gratitude to the Department of Atomic Energy, Government of India, for the support in the preparation of this paper. The computational work was done on CDC 3600 at Tata Institute of Fundamental Research, Bombay.

References

1 Fromm, J. E., and Harlow, P. H., "Numerical Solution of the Problem of Vortex Street Development," *Phys. Fluids*, Vol. 6, 1963, pp. 975–982.

2 Kawaguti, M., and Jain, P. C., "Numerical Study of a Viscous Fluid Flow Past a Circular Cylinder," *J. Phy. Soc. Japan*, Vol. 21, 1966, pp. 2055–2062.

3 Thoman, D. C., and Szewczyk, A. A., "Time Dependent Viscous Flow Over Circular Cylinder," *Phys. Fluids*, Supp. II, Vol. 12, 1969, pp. II-76–II-86.

4 Jain, P. C., and Sankara Rao, K., "Numerical Solution of Unsteady Viscous Incompressible Fluid Flow Past a Circular Cylinder," *Phys. Fluids*, Supp. II, Vol. 12, 1969, pp. II-57–II-64.

5 Son, J. S., and Hanratty, T. J., "Numerical Solution for the Flow Around a Cylinder at Reynolds Numbers of 40, 200 and 500," *J. Fluid Mech.*, Vol. 35, 1969, pp. 369–387.

6 Collins, W. M., and Dennis, S. C. R., "Flow Past an Impulsively Started Circular Cylinder," *J. Fluid Mech.*, Vol. 60, Part 1, 1973, pp. 105–127.

7 Dennis, S. C. R., Hudson, J. D., and Smith N., "Steady Laminar Forced Convection From a Circular Cylinder at Low Reynolds Numbers," *Phys. Fluids*, Vol. 11, 1968, pp. 933–940.

8 Harlow, F. H., and Fromm, J. E., "Dynamics and Heat Transfer in the Von Karman Wake of a Rectangular Cylinder," *Phys. Fluids*, Vol. 7, 1964, pp. 1147–1156.

9 Acrivos, A., Snowden, D. D., Grove, A. S., and Peterson, E. E., "The Steady Separated Flow Past a Circular Cylinder at Large Reynolds Numbers," *J. Fluid Mech.*, Vol. 21, 1965, pp. 737–760.

10 Eckert, E. R. G., and Soehngen, E., "Distribution of Heat Transfer Coefficients Around Circular Cylinder in Cross Flow at Reynolds Numbers 20 to 500," TRANS. ASME, Vol. 74, 1952, pp. 343–347.

11 Grove, A. S., Shair, F. H., Peterson, E. E., and Acrivos, A., "An Experimental Investigation of the Steady Separated Flow Past a Circular Cylinder," *J. Fluid Mech.*, Vol. 19, 1964, pp. 60–80.

12 Roshko, A., "On the Development of Turbulent Wakes From Vortex Streets," NACA, TN-2913, 1953.

13 Jain, P. C., and Goel, B. S., "Shedding of Vortices Behind a Circular Cylinder," (communicated for publication).

14 Krall, K. M., and Eckert, E. R. G., "Heat Transfer to a Transverse Circular Cylinder at Low Reynolds Number Including Rarefaction Effects," Fourth International Heat Transfer Conference, Paris-Versailles, F.C. 7.5, 1970.

15 McAdams, W. H., *Heat Transmission*, McGraw-Hill, New York, 1954.

16 Kramers, H. A., "Heat Transfer From Spheres to Flowing Media," *Physics*, Vol. 12, 1946, pp. 61–80.

journal of heat transfer

technical notes

This section consists of contributions of 1500 words or equivalent. In computing equivalence, a typical one-column figure or table is equal to 250 words. A one-line equation is equal to 30 words. The use of a built-up fraction or an integral sign or summation sign in a sentence will require additional space equal to 10 words. Technical notes will be reviewed and approved by the specific division's reviewing committee prior to publication. After approval such contributions will be published as soon as possible, normally in the next issue of the journal.

Mean Beam Lengths for Spheres and Cylinders

A. T. Wassel[1] **and D. K. Edwards**[1]

Introduction

Mean beam length, introduced by Hottel [1],[2] characterizes the size effect in the radiative heat exchange between a stirred volume of gas and its enclosing wall. Oppenheim and Bevans [2] extended the concept to paired segments of wall and an intervening, participating gas, and Dunkle [3] presented such geometric mean beam lengths for adjacent and opposite rectangles and a sphere and rectangle. The errors in using geometric mean beam length for gas absorption bands with power-law and logarithmic path-length dependencies were discussed there [3, 4]. Tien and Wang [5, 6] extended the analysis using experimentally established expressions for band absorption. Edwards and Balakrishnan [7] derived a transcendental equation fixing mean beam length for the case of exponential-tailed gas bands and the slab geometry. Crosbie and Khalil [8, 9] investigated the mathematical properties of the $K_n(\tau)$ functions which arise in the study of nongray gas radiation transfer in planar and spherical media and obtained closed-form expressions for both triangular and exponential band models. Wassel and Edwards [10] presented mean beam lengths for the cylinder based upon approximate axial band absorption functions. Nelson [11] also studied transmission and absorption functions for planar media.

The purpose of this note is to present new results for the sphere and somewhat more accurate ones for the cylinder enclosing a gas with exponential-tailed narrow absorption bands having overlapped lines. The derivation of appropriate formulas for the sphere and their relation to the $K_n(\tau)$ functions is traced.

Analysis

The solution to the equation of transfer in an isothermal gas at temperature T_g bounded by a black wall at temperature T_w gives the radiant intensity

$$I = I_{bw}e^{-\rho\kappa L} + I_{bg}(1 - e^{-\rho\kappa L}) \tag{1}$$

where ρ is the intensity, κ is spectral absorption coefficient, and L is path length through the gas for the direction along which intensity I is directed. The Planck black body intensity is

$$I_{bg} = \frac{2hc^2\nu^3}{e^{hc\nu/kT_g} - 1} \tag{2}$$

where h is Planck's constant, c is the speed of light, and k Boltzmann's constant. The net radiant heat flux q into the wall is $I - I_{bw}$ integrated over all wavenumbers ν and all directions in the 2π solid angle bounded by the wall,

$$q = \int_0^\infty \int_{2\pi} [I_{bg} - I_{bw}][1 - e^{-\rho\kappa L}] \cos\theta d\Omega d\nu \tag{3}$$

where θ is the angle from the surface normal to L, and Ω is solid angle.

For narrow, nonoverlapped absorption bands the approximation is made that

$$q \doteq \textstyle\sum_i [B_{gi} - B_{wi}] \left[\frac{1}{\pi}\int_0^{2\pi} A_i(L) \cos\theta d\Omega\right] \tag{4}$$

where B_{gi} is black body spectral radiosity πI_b at temperature T_g and wavenumber ν_i, and A_i is the band absorption of the ith band in the gas spectrum,

$$A_i = \int_{\Delta\nu_i} [1 - e^{-\rho\kappa_i L}] d\nu \tag{5}$$

The mean beam length $\bar{L}$ is introduced by engineers to simplify equation (4) as

$$q \doteq \textstyle\sum_i [B_{gi} - B_{wi}] A_i(\bar{L}_i) \tag{6}$$

$$A_i(\bar{L}_i) = \frac{1}{\pi}\int_0^{2\pi} A_i(L) \cos\theta d\Omega \tag{7}$$

A specific band model such as the exponential band model must be introduced to obtain a specific result. For this model, [12], one can write

---

[1] Postdoctoral Fellow and Professor, respectively, School of Engineering, UCLA, Los Angeles, Calif. Mem. ASME.

[2] Numbers in brackets designate References at end of technical note.

Contributed by the Heat Transfer Division of THE AMERICAN SOCIETY OF MECHANICAL ENGINEERS. Manuscript received by the Heat Transfer Division October 17, 1975.

Table 1 Ratio of L_i/R versus $\tau_{R,i}$

$\tau_{R,i}$	$u_i = \bar{L}_i/R$		$\tau_{R,i}$	$u_i = \bar{L}_i/R$	
	Sphere	Cylinder		Sphere	Cylinder
0	1.3333	2.0000	1.0	1.287	1.864
0.01	1.3328	1.9968	2.0	1.258	1.821
0.02	1.3322	1.9938	5.0	1.225	1.792
0.05	1.3306	1.9855	10.0	1.216	1.787
0.10	1.328	1.973	20.0	1.214	1.785
0.20	1.323	1.953	50.0	1.213	1.785
0.50	1.308	1.909	100.0	1.213	1.785

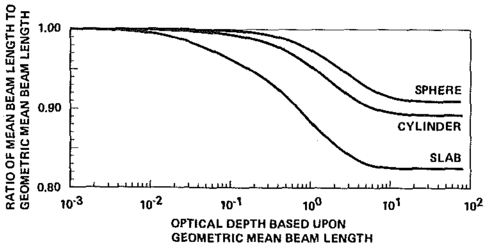

Fig. 1 Ratio of mean beam length to geometric mean beam length

$$\kappa_i = \frac{\alpha_i}{\omega_i} e^{-(\nu_i-\nu)/\omega_i}, \quad \nu < \nu_i \tag{8}$$

$$A_i = \omega_i[\ln (u_i\tau_{R,i}) + E_1(u_i\tau_{R,i}) + \gamma_e] \tag{9}$$

$$\tau_{R,i} = \frac{\alpha_i \rho R}{\omega_i}, u_i = \frac{\bar{L}_i}{R}, E_n(x) = \int_1^\infty e^{-xt}\frac{dt}{t^n}, \gamma_e = 0.5772156\ldots$$

The reference length R is introduced for convenience. For the sphere and cylinder it will be taken to be the radius.

Edwards and Balakrishnan [12] present values of α_i and ω_i for several combustion product gases. Hsieh and Greif [13] and Tiwari [14] discuss the applicability of the exponential-tailed model and line overlapping.

Sphere

In the case of the sphere, polar angular coordinates are natural, and

$$L = 2R \cos \theta, d\Omega = \sin \theta d\theta d\phi$$

Equation (7) indicates

$$A_i(u_i\tau_{R,i}) = \int_0^{\pi/2} A_i(2\tau_{R,i} \cos \theta)2 \cos \theta \sin \theta d\theta \tag{10}$$

Introducing equation (9) and integrating gives

$$\ln (u_i\tau_{R,i}) + E_1(u_i\tau_{R,i}) = \ln (2\tau_{R,i}) - \frac{1}{2} - \frac{1}{\tau_{R,i}} E_2(2\tau_{R,i}) - \frac{2}{(2\tau_{R,i})^2}\left[E_3(2\tau_{R,i}) - \frac{1}{2}\right] \tag{11}$$

In terms of the $K_n(\tau)$ functions [8], equation (11) can be written as

$$-2K_3(u_i\tau_{R,i}) - u_i\tau_{R,i}K_2(u_i\tau_{R,i}) = \ln (2\tau_{R,i}) + \gamma_e - 1/2 + 2K_1(2\tau_{R,i}) \tag{12}$$

Equation (11) or (12) can be solved numerically for u_i as a function of $\tau_{R,i}$.

Cylinder

In the case of the cylinder, a convenient angular coordinate system is shown in reference [10]. For such coordinates

$$\cos \theta = \cos \alpha \cos \gamma, d\Omega = \cos \alpha d\alpha d\gamma, L = 2R \cos \gamma/\cos \alpha$$

Equation (8) then gives

$$A_i(u_i\tau_{R,i}) = \frac{1}{\pi}\int_{-\pi/2}^{+\pi/2}\int_{-\pi/2}^{+\pi/2} A_i\left(2\tau_{R,i}\frac{\cos \gamma}{\cos \alpha}\right) \cos^2 \alpha d\alpha \cos \gamma d\gamma \tag{13}$$

Results

The Newton-Raphson method was used to find the u_i roots of equations (11) and (13). In the case of equation (13), a Tchebycheff numerical quadrature was employed to evaluate the double integral. Table 1 contains the results. In the case of the cylinder the results differ by 1.5 percent at most, in the vicinity of $\tau_{R,i} = 0.2$, from those in reference [10].

The geometric mean beam length $\bar{L}_g$ holds in the limit as $\tau_{R,i}$ goes to zero [1, 3]. It is easily evaluated as four times the volume divided by the surface area for a complete enclosure [1]. Fig. 1 shows a plot of $\bar{L}/\bar{L}_g$ versus optical depth based upon $\bar{L}_g$, i.e., $\tau_{R,i}(\bar{L}_g/R)$. Results for the slab [7] are shown for comparison. Large values of L are given full weight in computing $\bar{L}_g$ but less so in $\bar{L}$. In the slab, the lesser weighting of the large L values has a pronounced effect in lowering $\bar{L}/\bar{L}_g$ from unity, and the reduction starts at a relatively small optical depth. Large values of L have a smaller effect for the cylinder and only at somewhat greater optical depths. For the sphere, where the largest L is the diameter, the deviation of $\bar{L}/\bar{L}_g$ from unity is smallest.

References

1 Hottel, H. C., "Radiant Heat Transmission," Chapter 4 of W. H. McAdams' *Heat Transmission*, McGraw-Hill, New York, 1954; see also *Radiative Transfer* by H. C. Hottel and A. F. Sarofim, McGraw-Hill, New York, 1967.

2 Oppenheim, A. K., and Bevans, J. T., "Geometric Factors for Radiant Heat Transfer Through an Absorbing Medium in Cartesian Coordinates," JOURNAL OF HEAT TRANSFER, TRANS. ASME, Series C, Vol. 82, 1960, pp. 360–368.

3 Dunkle, R. V., "Geometric Mean Beam Lengths for Radiant Heat Transfer Calculations," JOURNAL OF HEAT TRANSFER, TRANS. ASME, Series C, Vol. 86, 1964, pp. 75–80.

4 Edwards, D. K., Discussion of reference [3], loc. cit., p. 80.

5 Tien, C. L., and Wang, L. S., "On the Calculation of Mean Beam Length for a Radiating Gas," *J. Quant. Spectrosc. Radiat. Transfer*, Vol. 5, 1965, pp. 453–456.

6 Tien, C. L., and Wang, L. S., "Band Absorption Laws, Gas Body Geometries, and the Mean Beam Length," *Proceedings 1965 Heat Transfer and Fluid Mechanics Institute*, Stanford University Press, Palo Alto, Calif., pp. 343–357.

7 Edwards, D. K., and Balakrishnan, A., "Slab Band Absorptance for Molecular Gas Radiation," *J. Quant. Spectosc. Radiat. Transfer*, Vol. 12, 1972, pp. 1379–1397.

8 Crosbie, A. L., and Khalil, H. K., "Mathematical Properties of the $K_n(\tau)$ Functions," *J. Quant. Spectrosc. Radiat. Transfer*, Vol. 12, 1972, pp. 1457–1464.

9 Crosbie, A. L., and Khalil, H. K., "Effect of Line or Band Shape on the Radiative Flux of an Isothermal Spherical Layer," *J. Quant. Spectrosc. Radiat. Transfer*, Vol. 13, 1973, pp. 977–993.

10 Wassel, A. T., and Edwards, D. K., "Molecular Gas Band Radiation in Cylinders," JOURNAL OF HEAT TRANSFER, TRANS. ASME, Series C, Vol. 96, 1974, pp. 21–26.

11 Nelson, D. A., "A Study of Band Absorption Equations for Infrared Radiative Transfer in Gases. I. Transmission and Absorption Functions for Planar Media," *J. Quant. Spectrosc. Radiat. Transfer*, Vol. 14, 1974, pp. 69–80.

12 Edwards, D. K., and Balakrishnan, A., "Thermal Radiation by Combustion Gases," *International Journal of Heat and Mass Transfer*, Vol. 16, 1973, pp. 25–40.

13 Hsieh, T. C., and Greif, R., "Theoretical Determination of the Absorption Coefficient and the Total Band Absorptance Including a Specific Application to Carbon Monoxide," *International Journal of Heat and Mass Transfer*, Vol. 15, 1972, pp. 1477–1487.

14 Tiwari, S. N., "Band Models and Correlations for Infrared Radiation," AIAA Paper No. 75-699, AIAA 10th Thermophysics Conference, Denver, Colo., May 27–29, 1975.

Radiation Heat Transfer Through Molecular Gases at Large Optical Depth

D. A. Nelson[1]

An asymptotically exact expression for radiation heat transfer through planar media is obtained at large optical depth for an exponential band model.

Nomenclature

D = band width parameter
E_ν = Planck radiosity at wavenumber ν
h = parallel plate spacing
K_n = dimensionless transmission function for $n = 1, 2$ and absorption function for $n = 3$
Q^r = dimensionless radiation flux

$$Q^r = [q^r - \sigma(T_1{}^4 - T_2{}^4)]/D[E_\nu(T_1) - E_\nu(T_2)]$$

$Q_e{}^r$ = dimensionless gas emission to colder boundary
q^r = total radiation flux
S = integrated band intensity
T_n = boundary temperatures, $n = 1, 2$
y = spatial coordinate
$\gamma = 0.5772\ldots$, Euler-Mascheroni constant
η = dimensionless coordinate, $\eta = y/h$
ν = spectral radiation wavenumber
ρ_a = absorbing gas density
σ = Stefan-Boltzmann constant
$\tau_h = \rho_a Sh/D$, the optical depth
$\phi = [E_\nu(\eta) - E_\nu(T_2)]/[E_\nu(T_1) - E_\nu(T_2)]$, the dimensionless emissive power

Subscripts

i = value for ith band

Introduction

Exact analytical solutions for infrared radiation heat transfer through gases are somewhat of a rarity. Those which exist are limited to small or large optical depth. A solution obtained by Mighdoll and Cess [1][2] for large optical depth was formulated within the framework of the exponential kernel approximation, linearization of the emissive power and with the implicit assumption of thermal continuity at the boundaries. The first two approximations are nonessential and in fact the solution obtained for the emissive power may be regarded as exact for infinite optical depth. This is a consequence of the fact that for band absorption proportional to the logarithm of optical depth, the transmission functions are to first order independent of the kernel substitution constants. This is not so for the expression giving the radiation heat flux and, thus, the result given in reference [1] is an approximate one even at large optical depth. In this note the problem is formulated exactly, linearization is not invoked and a new expression for the radiation heat flux is derived. The latter is compared with exact numerical calculations of Crosbie and Viskanta [2] as well as the result of Mighdoll and Cess. The result is expected to apply for nonisothermal, scaled band parameters [3, 4].

Table 1 A comparison of exact and approximate evaluations of radiation heat transfer at large optical depth

τ_h	Exact Q^r reference [2]	Reference [1] Q^r	Reference [1] Percent error	This note Q^r	This note Percent error
5	−1.6074	−0.6286	−60.89	−1.3004	−19.10
10	−2.1717	−1.3218	−39.14	−1.9935	−8.21
50	−3.6489	−2.9312	−19.67	−3.6029	−1.26
100	−4.3211	−3.6243	−16.13	−4.2961	−0.58
1000	—	−5.9269	−10.18[a]	−6.5987	—

[a] This error is relative to the results of equation (6).

Analysis

In dimensionless form the radiation heat flux and the energy equation for radiative equilibrium of a plane-parallel medium bounded by black, isothermal walls and interacting with thermal radiation in a single narrow band are given by

$$Q^r = 2K_3[\tau_h \eta] + 2\tau_h \int_0^1 \phi(\eta')K_2[\tau_h|\eta - \eta'|] \operatorname{sgn}(\eta - \eta')d\eta' \quad (1)$$

$$2\phi(\eta) = K_2[\tau_h \eta] + \tau_h \int_0^1 \phi(\eta')K_1[\tau_h|\eta - \eta'|]d\eta' \quad (2)$$

The transmission and absorption functions, $K_n(x)$, have been discussed in some detail by Nelson [5] and Crosbie and Khalil [6]. An integration by parts is performed on equation (2) to obtain the alternative expression

$$\int_0^1 \frac{d\phi(\eta')}{d\eta'} K_2[\tau_h|\eta - \eta'|] \operatorname{sgn}(\eta - \eta')d\eta'$$
$$= [1 - \phi(0)]K_2[\tau_h \eta] - \phi(1)K_2[\tau_h(1 - \eta)] \quad (3)$$

If now it is presumed that $\tau_h \rightarrow \infty$, then $\phi(0) \rightarrow 1$, $\phi(1) \rightarrow 0$[2], $K_2(x) \rightarrow 1/2x$ [5] and equation (3) reduces to that given by Mighdoll and Cess [1]. The emissive power distribution given by them is repeated here for convenience

$$\phi(\eta) = \frac{1}{2} + \frac{1}{\pi}\sin^{-1}(1 - 2\eta). \quad (4)$$

Equation (1) may now be rewritten as

$$Q^r = -2\int_0^1 \frac{d\phi(\eta')}{d\eta'} K_3[\tau_h \eta']d\eta' \quad (5)$$

where η has been set to zero since Q^r is a constant. Employing the asymptotic relation for an exponential band [5], $2K_3(x) \sim -\ln x - \gamma - 1/2$, along with equation (4), equation (5) yields,

$$Q^r = -\ln \tau_h - \gamma - 1/2 + 2\ln 2 \quad (6)$$

In this result, the first three factors represent the attenuation of the surface to surface radiative exchange by absorption in the gas. The last term represents emission by the gas absorbed by the cold boundary, thus a nonnegligible gas emission component is given by

$$Q_e{}^r = \ln 4 = 1.386 \quad (7)$$

This value is an upper limit on $Q_e{}^r$ since the asymptotic expression used for $K_3(x)$ is invalid near $x = 0$. It may be noted that other band absorption models with a logarithmic asymptote will also yield this result.

Results

In Table 1 the results of equation (6) are compared with the numerical evaluations of Crosbie and Viskanta [2] as well as with the expression given by Mighdoll and Cess [1] (i.e., $Q^r = -\ln(3\tau_h/2) + 2\ln 2$). The percent error for the present results is quite acceptable for all optical depth greater than about ten while the approximation of reference [1] does not appear to be adequate for any but extremely large values of optical depth. Since equation (6) has a very small error for $\tau_h > 100$ it may be used as an extension of the numerical calculations of reference [2] to arbitrarily larger values.

---

[1] Asst. Professor, Department of Mechanical Engineering, The Pennsylvania State University, University Park, Pa.

[2] Numbers in brackets designate References at end of technical note.

Contributed by the Heat Transfer Division of THE AMERICAN SOCIETY OF MECHANICAL ENGINEERS. Manuscript received by the Heat Transfer Division October 6, 1975.

References

1 Mighdoll, P., and Cess, R. D., "Infrared Radiative Equilibrium Under Large Path Conditions," *AIAA Journal*, Vol. 6, 1968, p. 1778.

2 Crosbie, A. L., and Viskanta, R., "Effects of Band or Line Shape on the Radiative Transfer in a Nongray Planar Medium," *Journal Quant. Spectros. Radiat. Transfer*, Vol. 10, 1970, p. 487.

3 Chan, S. H., and Tien, C. L., "Total Band Absorptance of Nonisothermal Infrared Radiating Gases," *Journal Quant. Spectros. Radiat. Transfer*, Vol. 9, 1969, p. 1261.

4 Edwards, D. K., and Morizumi, S. J., "Scaling of Vibration-Rotation Band Parameters for Nonhomogeneous Gas Radiation," *Journal Quant. Spectros. Radiat. Transfer*, Vol. 10, 1970, p. 175.

5 Nelson, D. A., "A Study of Band Absorption Equations for Infrared Radiative Transfer in Gases—I. Transmission and Absorption Functions for Planar Media," *Journal Quant. Spectros. Radiat. Transfer*, Vol. 14, 1974, p. 69.

6 Crosbie, A. L., and Khalil, H. K., "Mathematical Properties of the $K_n(\tau)$ Functions," *JQSRT*, Vol. 12, 1972, p. 1457.

Determination of Configuration Factors of Irregular Shape

R. Farrell[1]

The computation of configuration factors for irregular shapes, neither available in graphical form nor tabulated, can be a laborious and time-consuming exercise. The device to be explained was evolved to enable configuration factors to be determined and designed on the drawing board. Other devices have been described in references [1–3][2] using mechanical systems, while except for reference [4], the possibilities of projection have been relatively unexplored.

Configuration factors may be calculated for any shape or type of surface where there is adequate time available for this purpose. In practice when time is limited, tables or graphical techniques are frequently adopted. The proposed technique, as will become clear, is a special case of a graphical technique suggested by Zijl[5] with advantages not possessed by the original. These advantages are as follows:

1. It may be used with a drawing or model at any scale.
2. No redrawing is required for the determination of configuration factors at differing positions in space.
3. Surfaces with specific values of configuration factor and of any shape may be drawn directly on the drawing board.
4. Existing orthographic projections may be used irrespective of scale.

Theory

The instrument is based on the unit sphere concept introduced by Herrman around 1900. The configuration factor for a point P with respect to a surface S at a distance d from the surface is given by:

$$F_{P-S} = \int_S \frac{\cos\theta d\omega}{\pi} \tag{1}$$

$$d\omega = \frac{\cos\theta dS}{d^2}$$

$$= \frac{dS'}{r^2} \tag{2}$$

where dS' is the area dS projected onto the surface of a unit hemisphere. dS' projects onto the base of a unit hemisphere as dS'' where,

$$dS'' = dS' \cos\theta$$

Therefore, from (1)

$$F_{P-S} = \frac{dS''}{\pi r^2} \tag{3}$$

From equation (4) the projected area dS'' divided by the area of the circle of radius r is the required configuration factor.

The use of a variety of geometric projections is thus made possible. If the base of the hemisphere is divided into a number of equal areas, for example, 1000, and these areas are reprojected onto the surface of the hemisphere and then to some other convenient projection on which the surface projection of interest dS is also projected, the configuration factor may be obtained by counting the equal areas covering the surface. For convenience it is possible to project the centroids of these areas as dots, each of which in this example would represent a configuration factor value of 0.001. Since the device about to be described uses both the perspective projection and the cylindrical projection, a short description of these projections follows.

Perspective Projection

One advantage of this type of projection is that straight lines remain straight. Three of the terms necessary to an understanding of perspective geometry are, viewpoint, focal length, and picture plane. The focal length is the distance from the viewpoint to the picture plane. The picture plane is that plane in space on which the object being drawn is projected, this projection being the trace on the picture plane of the straight line connecting the viewpoint and the object.

If one were to sit before a window and draw the view outside, the window would be the picture plane, the distance from the eye to the window the focal length, and the eye would be the viewpoint. Should the individual making the sketch move further from the window, the dimensions of the objects being drawn on the picture plane would become smaller. Increasing the focal length reduces the dimensions of the projected objects, as the solid angle subtended by the objects becomes smaller. In the second section of the paper a description will be given of the advantage that is taken of the above principle in the instrument as yet to be described.

A second advantage that the perspective projection has is the relationship that exists between it and the orthographic projection. The orthographic projection is a perspective projection with an infinite focal length, the trace lines being parallel. The orthographic projection is also equal to a perspective projection where the object being drawn is in the picture plane, i.e., the distance from the viewpoint to the object is the focal length of the projection.

Cylindrical Projection

On the projection illustrated in Fig. 1 are placed the dots previously described as being the centroids of equal configuration factor values. This projection has the heights of the constant angles of altitude proportional to the tangents of the angles of altitude, and the angles of azimuth proportional to the angles of azimuth. The lines marking constant altitude are straight lines; therefore, changes in azimuth may be made by lateral displacement of the projection in expanded form or rotation of the barrel.

Description of the Scintilascope

This instrument as shown in Fig. 2 consists of base, stem, arm and barrel. The base leaves a clear space below the arm. The stem is calibrated in centimeters and inches to register the height of the center of the small lamp shown, above the drawing board.

Attached to the end of the arm is a 3V opthalmoscope lamp. This lamp becomes the viewpoint of a perspective projection. The overlay shown in Fig. 3 when positioned around the barrel of the scintilascope, positions each dot in space such that when the lamp is switched on, Fig. 4, the dots are projected in a perspective projection. Each dot having the configuration factor value of 0.001. The overlay as illustrated, Fig. 3, is a cylindrical projection, i.e., the projection on to a cylinder of the angles of azimuth and elevation of those areas of equal value of configuration factor.

---

[1] School of Architecture, University of California, Berkeley, Berkeley, Calif.

[2] Numbers in brackets designate References at end of technical note.

Contributed by the Heat Transfer Division of THE AMERICAN SOCIETY OF MECHANICAL ENGINEERS. Manuscript received by the Heat Transfer Division August 29, 1975.

References

1 Mighdoll, P., and Cess, R. D., "Infrared Radiative Equilibrium Under Large Path Conditions," *AIAA Journal*, Vol. 6, 1968, p. 1778.

2 Crosbie, A. L., and Viskanta, R., "Effects of Band or Line Shape on the Radiative Transfer in a Nongray Planar Medium," *Journal Quant. Spectros. Radiat. Transfer*, Vol. 10, 1970, p. 487.

3 Chan, S. H., and Tien, C. L., "Total Band Absorptance of Nonisothermal Infrared Radiating Gases," *Journal Quant. Spectros. Radiat. Transfer*, Vol. 9, 1969, p. 1261.

4 Edwards, D. K., and Morizumi, S. J., "Scaling of Vibration-Rotation Band Parameters for Nonhomogeneous Gas Radiation," *Journal Quant. Spectros. Radiat. Transfer*, Vol. 10, 1970, p. 175.

5 Nelson, D. A., "A Study of Band Absorption Equations for Infrared Radiative Transfer in Gases—I. Transmission and Absorption Functions for Planar Media," *Journal Quant. Spectros. Radiat. Transfer*, Vol. 14, 1974, p. 69.

6 Crosbie, A. L., and Khalil, H. K., "Mathematical Properties of the $K_n(\tau)$ Functions," *JQSRT*, Vol. 12, 1972, p. 1457.

Determination of Configuration Factors of Irregular Shape

R. Farrell[1]

The computation of configuration factors for irregular shapes, neither available in graphical form nor tabulated, can be a laborious and time-consuming exercise. The device to be explained was evolved to enable configuration factors to be determined and designed on the drawing board. Other devices have been described in references [1–3][2] using mechanical systems, while except for reference [4], the possibilities of projection have been relatively unexplored.

Configuration factors may be calculated for any shape or type of surface where there is adequate time available for this purpose. In practice when time is limited, tables or graphical techniques are frequently adopted. The proposed technique, as will become clear, is a special case of a graphical technique suggested by Zijl[5] with advantages not possessed by the original. These advantages are as follows:

1 It may be used with a drawing or model at any scale.
2 No redrawing is required for the determination of configuration factors at differing positions in space.
3 Surfaces with specific values of configuration factor and of any shape may be drawn directly on the drawing board.
4 Existing orthographic projections may be used irrespective of scale.

Theory

The instrument is based on the unit sphere concept introduced by Herrman around 1900. The configuration factor for a point P with respect to a surface S at a distance d from the surface is given by:

$$F_{P-S} = \int_S \frac{\cos\theta\, d\omega}{\pi} \tag{1}$$

$$d\omega = \frac{\cos\theta\, dS}{d^2}$$

$$= \frac{dS'}{r^2} \tag{2}$$

where dS' is the area dS projected onto the surface of a unit hemisphere. dS' projects onto the base of a unit hemisphere as dS'' where,

$$dS'' = dS' \cos\theta$$

Therefore, from (1)

$$F_{P-S} = \frac{dS''}{\pi r^2} \tag{3}$$

From equation (4) the projected area dS'' divided by the area of the circle of radius r is the required configuration factor.

The use of a variety of geometric projections is thus made possible. If the base of the hemisphere is divided into a number of equal areas, for example, 1000, and these areas are reprojected onto the surface of the hemisphere and then to some other convenient projection on which the surface projection of interest dS is also projected, the configuration factor may be obtained by counting the equal areas covering the surface. For convenience it is possible to project the centroids of these areas as dots, each of which in this example would represent a configuration factor value of 0.001. Since the device about to be described uses both the perspective projection and the cylindrical projection, a short description of these projections follows.

Perspective Projection

One advantage of this type of projection is that straight lines remain straight. Three of the terms necessary to an understanding of perspective geometry are, viewpoint, focal length, and picture plane. The focal length is the distance from the viewpoint to the picture plane. The picture plane is that plane in space on which the object being drawn is projected, this projection being the trace on the picture plane of the straight line connecting the viewpoint and the object.

If one were to sit before a window and draw the view outside, the window would be the picture plane, the distance from the eye to the window the focal length, and the eye would be the viewpoint. Should the individual making the sketch move further from the window, the dimensions of the objects being drawn on the picture plane would become smaller. Increasing the focal length reduces the dimensions of the projected objects, as the solid angle subtended by the objects becomes smaller. In the second section of the paper a description will be given of the advantage that is taken of the above principle in the instrument as yet to be described.

A second advantage that the perspective projection has is the relationship that exists between it and the orthographic projection. The orthographic projection is a perspective projection with an infinite focal length, the trace lines being parallel. The orthographic projection is also equal to a perspective projection where the object being drawn is in the picture plane, i.e., the distance from the viewpoint to the object is the focal length of the projection.

Cylindrical Projection

On the projection illustrated in Fig. 1 are placed the dots previously described as being the centroids of equal configuration factor values. This projection has the heights of the constant angles of altitude proportional to the tangents of the angles of altitude, and the angles of azimuth proportional to the angles of azimuth. The lines marking constant altitude are straight lines; therefore, changes in azimuth may be made by lateral displacement of the projection in expanded form or rotation of the barrel.

Description of the Scintilascope

This instrument as shown in Fig. 2 consists of base, stem, arm and barrel. The base leaves a clear space below the arm. The stem is calibrated in centimeters and inches to register the height of the center of the small lamp shown, above the drawing board.

Attached to the end of the arm is a 3V opthalmoscope lamp. This lamp becomes the viewpoint of a perspective projection. The overlay shown in Fig. 3 when positioned around the barrel of the scintilascope, positions each dot in space such that when the lamp is switched on, Fig. 4, the dots are projected in a perspective projection. Each dot having the configuration factor value of 0.001. The overlay as illustrated, Fig. 3, is a cylindrical projection, i.e., the projection on to a cylinder of the angles of azimuth and elevation of those areas of equal value of configuration factor.

---

[1] School of Architecture, University of California, Berkeley, Berkeley, Calif.

[2] Numbers in brackets designate References at end of technical note.

Contributed by the Heat Transfer Division of THE AMERICAN SOCIETY OF MECHANICAL ENGINEERS. Manuscript received by the Heat Transfer Division August 29, 1975.

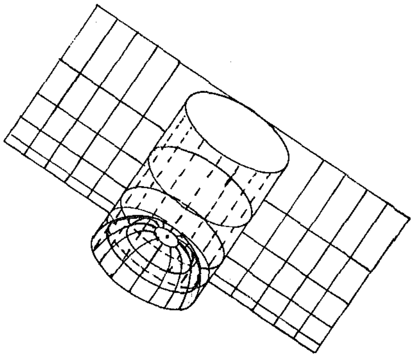

Fig. 1 Cylindrical projection

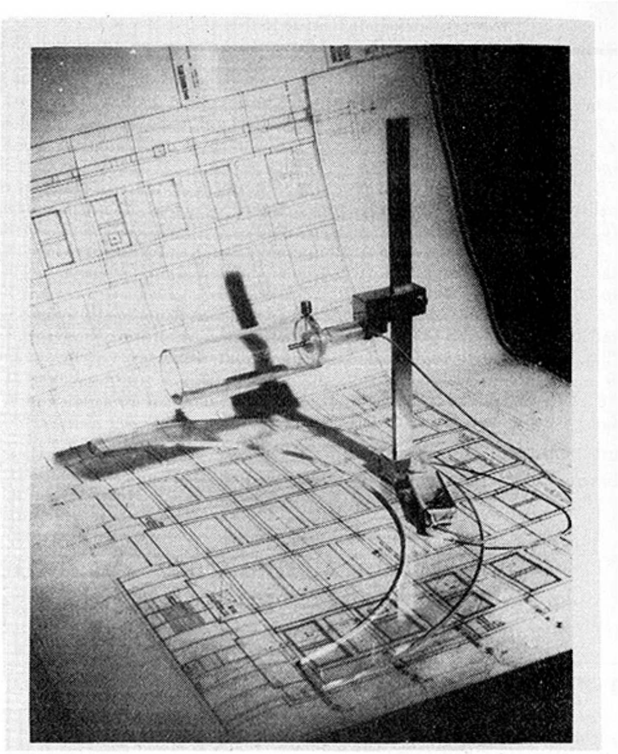

Fig. 3 Configuration factor overlay

Because alterations of the height of the lamp also alter the focal length of the perspective projection of the dots, an infinite number of perspective projections becomes available. Since the usual plans and elevations are orthographic, advantage is taken of the second relationship between orthographic and perspective projection in the following manner. The dimensions of the drawn surface to scale are the real surface dimensions, and the dimensions of a perspective projection of the surface on the picture plane.

The perspective projections of the dots, to the same scale, will enable the plane point configuration factor of the surface to be obtained at the viewpoint of the perspective, or the lamp position. Altering the focal length of the dot projections alters the angular relationships to the surface, and is thus equivalent to redrawing the surface, as one would do on the window previously described, while maintaining a constant focal length.

Obtaining a Configuration Factor in Practice

Assume the surface whose configuration factor is required lies on the X, Y plane of a set of orthogonal axes, the distance from the surface being on the Z axis. To position the lamp correctly in space, the lamp must be switched on, and the projected origin placed correctly with respect to the X, Y plane, e.g. at the bottom right-hand corner of a square. The distance from the square where the configuration factor is required is set on the stem. The number of dots contained within the square is summed, each dot being 0.001, to obtain the value of the configuration factor.

To obtain the configuration factor on the same normal to the X, Y plane, move the barrel towards or away from the surface as required. To obtain a configuration factor on the same parallel plane, reposition the origin by moving the base.

Dimensioning a Surface to Provide a Specific Value of Configuration Factor

It is occasionally necessary, knowing the surface properties and

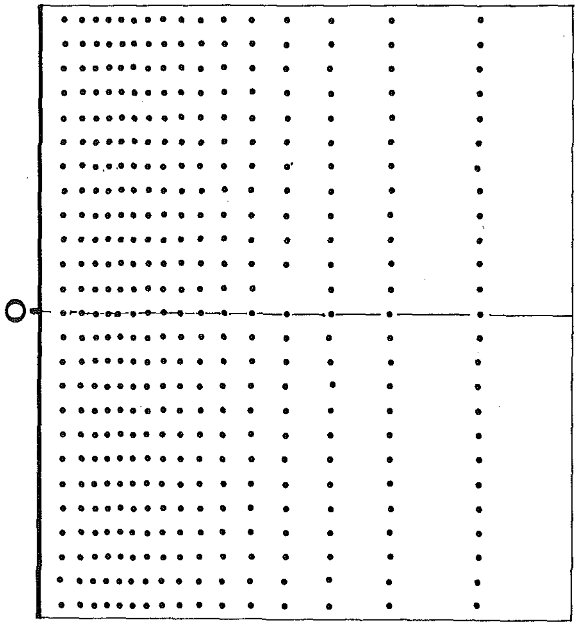

Fig. 2 Scintilascope

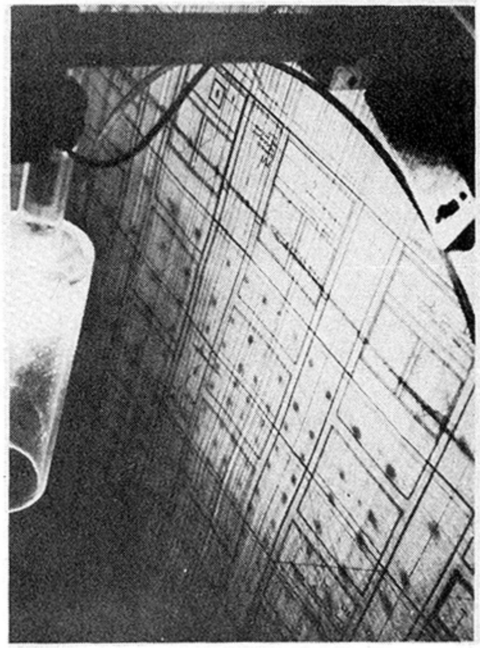

Fig. 4 Configuration factors are determined by summation of contained dots

temperature of a surface, to provide a surface having a certain value of configuration factor at some point in space. With the instrument as described this becomes a simple exercise in graphics. Once more position the opthalmoscope lamp at the point in space where the necessary configuration factor is required. The Z distance is the distance from the surface to some selected scale and also is the distance from the lamp to the drawing board on which the surface will be drawn. Switch on the lamp and draw the surface to contain the required number of dots. This sketch will be the dimensions of the required surface to the same scale as that selected for the Z distance or focal length.

It should be noted that this drawn surface may be as regular or irregular as required. All that is required being that it contains the required number of dots. The sketched surface is also an orthographic projection of the surface to the scale previously described.

Accuracy of Results

Much of the accuracy of the instrument depends on manufacturing details. It is of importance to select a barrel radius which combines compactness with some reasonable degree of accuracy. To obtain some measure of this accuracy the instrument was tested and compared with results obtained by direct integration over the surface. The shapes tested were three squares each of unit side and disposed in an inverted L. The plane point configuration factors were then obtained on the lines normal to the plane of these surfaces, at a variety of distances from these squares.

The greatest percentage error relative to that obtained by surface integration is given by E percent $= 0.314\, x^{-0.8846}$. The error results from graphical errors and the inclusion or exclusion of dots on the periphery of the surfaces over which the computations are being made. A second projection was therefore made with dots of the value of 0.0001. The results of the use of this projection were considerable reduction in relative percentage error, this being given by E percent $= 0.2056\, x^{-0.566}$. It is clear that the relative error is a function of both the configuration factor and the subdivision of the projection.

Discussion

The instrument as described may be used in a variety of problems with the advantages as listed in the introduction. These are most apparent when the surface is irregular, or the problem to be solved three dimensional. When the surfaces are regular, and graphical or tabular solutions are available, the instrument has the advantage of not requiring configuration factor algebra when the surfaces are not disposed about a common side.

The relative percentage error, although not the absolute error, may become large at small values of configuration factor. It may, therefore, become necessary to further subdivide the projection to reduce this error.

References

1 Eckert, E., "Bestimmung des Winkelverhältnisses beim Strahlungsaustausch durch das Lichtbild." Zeit. V. D. I., Bd., 79, No. 50, Dec. 14, 1935, pp. 1495–1496.

2 Hottel, H. C., "Radiant Heat Transmission," *Mech. Eng.*, Vol. 52, No. 7, July, 1930, pp. 699–704.

3 Cherry, V. H., Davis, D. D., and Boelter, L. M. K., "A Mechanical Integrator for Determination of Illumination From Diffuse Surface Sources," *Trans. Illum. Eng. Soc.*, Vol. 34, No. 9, Nov. 1939, pp. 1085–1092.

4 Eckert, E., *Introduction to the Transfer of Heat and Mass*, McGraw-Hill, New York, 1950.

5 Zijl, H., "Large Size Perfect Diffusers," Phillips Technical Library, 1960.

Unsteady and Two-Dimensional Flow of a Condensate Film

S. D. R. Wilson[1]

Nomenclature

a = constant of integration
$A = k\nu(T_1 - T_0)/\rho g\lambda$
$C = -A$
c_p = specific heat of liquid
g; g_1, g_2 = acceleration due to gravity; components in ξ_1, ξ_2 directions
h_1, h_2, h_3 = quantities associated with curvilinear coordinates
k = thermal conductivity of liquid
s, n = arc length and normal distance
R = tube radius
t = time
T; T_0, T_1 = temperature; wall temperature, vapor temperature
u, v, w = velocity components
$\bar{u}$, $\bar{v}$ = mean values of u, v

U = function defined by equation (10)

x, y, z = Cartesian coordinates
r, θ, z = cylindrical polar coordinates
z_0, z_1, z_2 = maximum extent of film (equation (16) et. seq.)
α = inclination of tube to vertical
β = cone semiangle
δ = film-thickness
λ = latent heat of condensation
ν = liquid kinematic viscosity
ρ = liquid density
ξ_1, ξ_2, ξ_3 = curvilinear coordinates

Subscripts

s = evaluation at interface
∞ = steady-state value
0 = evaluation at solid boundary

A well-known field of study in the theory of condensation concerns the situation in which the liquid condensate forms a thin film on the surface of cold solid objects such as tubes, fins, or fan blades. The film moves over the solid wall under the influence of gravity, inertia forces (if the wall is moving) and various forces due to the motion of the vapor. It is of interest to calculate the film thickness and heat transfer coefficient; the details of the velocity field in the liquid phase are of subsidiary importance.

The number and variety of published papers in this area is very large, but almost all the analysis is subject to the restriction of steady flow in two dimensions (which is taken to include axisymmetric flows). The reason is that in order to make mathematical progress the governing equations, which are nonlinear partial differential equations, must be reduced to ordinary differential equations, and this can be done by means of thin-film approximations or similarity transformations in many cases in which the original number of independent variables is two.

The purpose of the present work is to develop a theory in which the thin-film approximation is retained but in which the restriction to steady flow in two dimensions is *not* made, so that two or

---

[1] Department of Mathematics, University of Manchester, Manchester, England.

Contributed by the Heat Transfer Division of THE AMERICAN SOCIETY OF MECHANICAL ENGINEERS. Manuscript received by the Heat Transfer Division May 19, 1975.

temperature of a surface, to provide a surface having a certain value of configuration factor at some point in space. With the instrument as described this becomes a simple exercise in graphics. Once more position the opthalmoscope lamp at the point in space where the necessary configuration factor is required. The Z distance is the distance from the surface to some selected scale and also is the distance from the lamp to the drawing board on which the surface will be drawn. Switch on the lamp and draw the surface to contain the required number of dots. This sketch will be the dimensions of the required surface to the same scale as that selected for the Z distance or focal length.

It should be noted that this drawn surface may be as regular or irregular as required. All that is required being that it contains the required number of dots. The sketched surface is also an orthographic projection of the surface to the scale previously described.

Accuracy of Results

Much of the accuracy of the instrument depends on manufacturing details. It is of importance to select a barrel radius which combines compactness with some reasonable degree of accuracy. To obtain some measure of this accuracy the instrument was tested and compared with results obtained by direct integration over the surface. The shapes tested were three squares each of unit side and disposed in an inverted L. The plane point configuration factors were then obtained on the lines normal to the plane of these surfaces, at a variety of distances from these squares.

The greatest percentage error relative to that obtained by surface integration is given by E percent $= 0.314\, x^{-0.8846}$. The error results from graphical errors and the inclusion or exclusion of dots on the periphery of the surfaces over which the computations are being made. A second projection was therefore made with dots of the value of 0.0001. The results of the use of this projection were considerable reduction in relative percentage error, this being given by E percent $= 0.2056\, x^{-0.566}$. It is clear that the relative error is a function of both the configuration factor and the subdivision of the projection.

Discussion

The instrument as described may be used in a variety of problems with the advantages as listed in the introduction. These are most apparent when the surface is irregular, or the problem to be solved three dimensional. When the surfaces are regular, and graphical or tabular solutions are available, the instrument has the advantage of not requiring configuration factor algebra when the surfaces are not disposed about a common side.

The relative percentage error, although not the absolute error, may become large at small values of configuration factor. It may, therefore, become necessary to further subdivide the projection to reduce this error.

References

1 Eckert, E., "Bestimmung des Winkelverhältnisses beim Strahlungsaustausch durch das Lichtbild." Zeit. V. D. I., Bd., 79, No. 50, Dec. 14, 1935, pp. 1495–1496.

2 Hottel, H. C., "Radiant Heat Transmission," *Mech. Eng.*, Vol. 52, No. 7, July, 1930, pp. 699–704.

3 Cherry, V. H., Davis, D. D., and Boelter, L. M. K., "A Mechanical Integrator for Determination of Illumination From Diffuse Surface Sources," *Trans. Illum. Eng. Soc.*, Vol. 34, No. 9, Nov. 1939, pp. 1085–1092.

4 Eckert, E., *Introduction to the Transfer of Heat and Mass*, McGraw-Hill, New York, 1950.

5 Zijl, H., "Large Size Perfect Diffusers," Phillips Technical Library, 1960.

Unsteady and Two-Dimensional Flow of a Condensate Film

S. D. R. Wilson[1]

Nomenclature

a = constant of integration
$A = k\nu(T_1 - T_0)/\rho g\lambda$
$C = -A$
c_p = specific heat of liquid
g; g_1, g_2 = acceleration due to gravity; components in ξ_1, ξ_2 directions
h_1, h_2, h_3 = quantities associated with curvilinear coordinates
k = thermal conductivity of liquid
s, n = arc length and normal distance
R = tube radius
t = time
T; T_0, T_1 = temperature; wall temperature, vapor temperature
u, v, w = velocity components
$\bar{u}$, $\bar{v}$ = mean values of u, v

U = function defined by equation (10)

x, y, z = Cartesian coordinates
r, θ, z = cylindrical polar coordinates
z_0, z_1, z_2 = maximum extent of film (equation (16) et. seq.)
α = inclination of tube to vertical
β = cone semiangle
δ = film-thickness
λ = latent heat of condensation
ν = liquid kinematic viscosity
ρ = liquid density
ξ_1, ξ_2, ξ_3 = curvilinear coordinates

Subscripts

s = evaluation at interface
∞ = steady-state value
0 = evaluation at solid boundary

A well-known field of study in the theory of condensation concerns the situation in which the liquid condensate forms a thin film on the surface of cold solid objects such as tubes, fins, or fan blades. The film moves over the solid wall under the influence of gravity, inertia forces (if the wall is moving) and various forces due to the motion of the vapor. It is of interest to calculate the film thickness and heat transfer coefficient; the details of the velocity field in the liquid phase are of subsidiary importance.

The number and variety of published papers in this area is very large, but almost all the analysis is subject to the restriction of steady flow in two dimensions (which is taken to include axisymmetric flows). The reason is that in order to make mathematical progress the governing equations, which are nonlinear partial differential equations, must be reduced to ordinary differential equations, and this can be done by means of thin-film approximations or similarity transformations in many cases in which the original number of independent variables is two.

The purpose of the present work is to develop a theory in which the thin-film approximation is retained but in which the restriction to steady flow in two dimensions is *not* made, so that two or

---

[1] Department of Mathematics, University of Manchester, Manchester, England.

Contributed by the Heat Transfer Division of THE AMERICAN SOCIETY OF MECHANICAL ENGINEERS. Manuscript received by the Heat Transfer Division May 19, 1975.

three independent variables may be present. These will be the time and two space coordinates intrinsic to the solid boundary. The equation for the film thickness will, therefore, be a partial differential equation in two or three variables, but (as will be shown) it is of first order and, therefore, amenable to solution by the method of characteristics. Examples will be given in which there are two independent variables and for which analytical solutions in closed form can easily be obtained.

We first obtain the thin film equations in the general case. Let ξ_1, ξ_2 be orthogonal curvilinear coordinates intrinsic to the surface and let ξ_3 be measured normal to the surface. This system may fail to be orthogonal as a whole at general points in space but will be approximately, and sufficiently, so near the surface. These coordinates are related to Cartesian coordinates (x, y, z) by equations of the form $x = x(\xi_1, \xi_2, \xi_3)$ etc.; and the quantities h_i are defined by

$$h_i = \left|\frac{\partial x}{\partial \xi_i}, \frac{\partial y}{\partial \xi_i}, \frac{\partial z}{\partial \xi_i}\right| \quad (i = 1, 2, 3) \tag{1}$$

in the usual way.

The equation of the interface is $\xi_3 = \delta(\xi_1, \xi_2, t)$ and the equation of heat conservation may be written

$$\left(\rho \frac{DF}{DF}\right) \Big/ |\text{grad}\, F| = -\frac{1}{\lambda}\left[k \frac{\partial T}{\partial n}\right] \tag{2}$$

where $F \equiv \xi_3 - \delta$, and square brackets denote the discontinuity in the enclosed quantity at the interface. The velocity components corresponding to ξ_1, ξ_2, ξ_3 are u_1, u_2, u_3 and the average velocity components $\bar{u}_1$, $\bar{u}_2$ are defined by

$$\bar{u}_1 \int_0^\delta h_2 h_3 d\xi_3 = \int_0^\delta u_1 h_2 h_3 d\xi_3;$$

$$\bar{u}_2 \int_0^\delta h_3 h_1 d\xi_3 = \int_0^\delta u_2 h_3 h_1 d\xi_3 \tag{3}$$

The continuity equation for the liquid is

$$\frac{\partial}{\partial \xi_1}(h_2 h_3 u_1) + \frac{\partial}{\partial \xi_2}(h_3 h_1 u_2) + \frac{\partial}{\partial \xi_3}(h_1 h_2 u_3) = 0 \tag{4}$$

Using equations (3) and (4) we find

$$\frac{\partial}{\partial \xi_1}\left\{\bar{u}_1 \int_0^\delta h_2 h_3 d\xi_3\right\} + \frac{\partial}{\partial \xi_2}\left\{\bar{u}_2 \int_0^\delta h_3 h_1 d\xi_3\right\} =$$

$$= -(h_1 h_2 u_3)_s + (u_1 h_2 h_3)_s \frac{\partial \delta}{\partial \xi_1} + (u_2 h_1 h_3)_s \frac{\partial \delta}{\partial \xi_2}$$

$$= (h_1 h_2 h_3)_s \left\{\frac{1}{\rho\lambda}[k\, \text{grad}\, T \cdot \text{grad}\, F] - \frac{\partial \delta}{\partial t}\right\} \tag{5}$$

from equation (2).

The assumption that the film is thin will normally mean that $\int_0^\delta h_2 h_3 d\xi_3 \simeq h_2 h_3 \delta$ etc., that $(h_1 h_2 h_3)_s$ can be evaluated at the known solid surface rather than the unknown interface, and that grad T·grad F is approximately $1/h_3^2\ \partial T/\partial \xi_3$. The approximate form of equation (5) is therefore,

$$\frac{\partial}{\partial \xi_1}(h_2 h_3 \bar{u}_1 \delta) + \frac{\partial}{\partial \xi_2}(h_3 h_1 \bar{u}_2 \delta)$$

$$+ (h_1 h_2 h_3)_0 \frac{\partial \delta}{\partial t} = \frac{h_1}{\rho\lambda} \cdot \frac{h_2}{h_3}\left[k \frac{\partial T}{\partial \xi_3}\right] \tag{6}$$

In this equation h_1, h_2, and h_3 are known. If $\bar{u}_1$, $\bar{u}_2$ and $\partial T/\partial \xi_3$ can be determined, or suitably approximated, in terms of δ, this equation becomes a first-order partial differential equation for δ. In many cases the mechanical forces exerted on the liquid by the vapor can be neglected, in which case $\bar{u}_1$ and $\bar{u}_2$ are determined by a balance between viscosity and the appropriate component of gravity. This gives $\bar{u}_1 = g_1 \delta^2/3\nu$, $\bar{u}_2 = g_2 \delta^2/3\nu$. It is also common to neglect heat conduction in the vapor, so that $[k/h_3\ \partial T/\partial \xi_3]$ is approximately $k\Delta T/\delta$, making also the usual assumption of a linear temperature profile.

As a simple example we have condensation on a vertical semi-infinite plate $x \geqslant 0$, so that $\bar{u}_2 = 0$ and (6) reduces to

$$\delta^2 \frac{\partial \delta}{\partial x} + \frac{\nu}{g}\frac{\partial \delta}{\partial t} = \frac{A}{\delta} \tag{7}$$

a problem solved by Sparrow and Siegel [1].

Somewhat more complicated is the problem of unsteady condensation on a horizontal circular cylinder, of radius R; than with θ measured from the uppermost generator we find

$$\sin\theta\, \delta^2 \frac{\partial \delta}{\partial \theta} + \frac{R\nu}{g}\frac{\partial \delta}{\partial t} = \frac{AR}{\delta} - \frac{1}{3}\delta^3 \cos\theta \tag{8}$$

We note first that the steady-state solution is given by

$$(\sin\theta)^{4/3}\delta^4 = 4ARU(\theta) \tag{9}$$

where

$$U(\theta) = \int_0^\theta (\sin u)^{1/3} du \tag{10}$$

The steady-state thickness at $\theta = 0$ is $(3AR)^{1/4}$ and by setting $\theta = 0$ in (8) the approach to this value may be calculated. We find

$$\frac{\delta^2}{{\delta_\infty}^2} = \frac{\exp\left\{4\frac{g}{\nu}\left(\frac{A}{3R}\right)^{1/2} t\right\} - 1}{\exp\left\{4\frac{g}{\nu}\left(\frac{A}{3R}\right)^{1/2} t\right\} + 1} \tag{11}$$

so that in contrast with the vertical plate, an infinite time is required (in theory) to establish the steady state. However, the steady state is reached effectively when the exponents in (11) are large compared with unity. Thus δ is within 5 percent of δ_∞ when $4g/\nu(A/3R)^{1/2}t = 3$, and for water vapor, with $\Delta T = 50°\text{C}$ and $R = 2$ cm, this gives $t \sim \frac{1}{2}$ s. We conclude that the steady-state theory may be used in cases where fluctuations occur on a time scale long compared with this.

We next consider steady condensation on a circular tube inclined at an angle α to the vertical. We use cylindrical polar coordinates centred on the tube and with θ measured from the uppermost generator. The average velocity components $\bar{u}$, $\bar{v}$ in the z θ-directions, respectively, are given by

$$\bar{u} = \frac{1}{3}\frac{g}{\nu}\cos\alpha\, \delta^2, \ \bar{v} = \frac{1}{3}\frac{g}{\nu}\sin\alpha \sin\theta\, \delta^2 \tag{12}$$

and (6) becomes

$$R\cot\alpha \frac{\partial \delta}{\partial z} + \sin\theta \frac{\partial \delta}{\partial \theta} = \frac{AR}{\delta^3 \sin\alpha} - \frac{1}{3}\delta\cos\theta \tag{13}$$

The general solution of this may be obtained by the method of characteristics and is

$$(\sin\theta)^{4/3}\delta^4 - \frac{4AR}{\sin\alpha}U(\theta) = \Phi\left(\tan\frac{\theta}{2}\exp\left(-\frac{z}{R}\tan\alpha\right)\right) \tag{14}$$

where Φ is an arbitrary function. This function can be identified by using data at $z = 0$, the top end of the tube. Whatever the form of this may be, it is clear that if $\alpha \neq 0$ the solution becomes independent of z as $z \to \infty$ and is in fact very similar to the solution for a horizontal tube (cf. equation (9)). This is in marked contrast to the case $\alpha = 0$, when as is well-known, and follows immediately from (13), $\delta \propto z^{1/4}$. (Note also that there is a singularity in δ at $\theta = \pi$, usually interpreted to mean that condensate is dripping off the tube, as in the case of a horizontal tube.)

It is interesting to continue this investigation somewhat further in the case of an evaporating film, for which the results are more remarkable. The equations can be shown to be the same but with the constant A taking a negative value; accordingly we put $C = -A$, so that $C > 0$.

Sufficient insight can be gained by considering the uppermost and lower-most generators $\theta = 0$ and $\theta = \pi$, reducing (13) to an ordinary differential equation. On $\theta = 0$ we have

$$R \cot \alpha \frac{d\delta}{dz} + \frac{1}{3}\delta = -\frac{CR}{\sin \alpha}\frac{1}{\delta^3} \tag{15}$$

so that

$$\delta^4 = -\frac{3CR}{\sin \alpha} + a \exp\left(-\frac{4}{3}\frac{z}{R}\tan \alpha\right) \tag{16}$$

and we note again that the structure of this solution is completely different from the case $\alpha = 0$.

Let us suppose that the film thickness at $z = 0$ is δ_0. Then if the tube were vertical, the film would disappear at $z = z_0$ where $z_0 = \delta_0{}^4/4C$. When $\alpha \neq 0$ we find that the film disappears at $z = z_1$, which is given by

$$\frac{4}{3}\tan \alpha \frac{z_1}{R} = \log\left(1 + \frac{4}{3}\frac{\sin \alpha}{R} z_0\right) \tag{17}$$

As a numerical example, suppose the data are such that $C = 2 \times 10^{-10}$ cm^3 and $\delta_0 = 2 \times 10^{-2}$ cm. Then $z_0 = 200$ cm. If $R = 1$ cm and α is as small as 0.1 deg, we find $z_1 = 180$ cm, and if $\alpha = 1$ deg, an error which might easily be found in engineering practice, we find $z_1 = 76$ cm. On the lowermost generator a similar calculation gives

$$\delta^4 = \frac{3CR}{\sin \alpha} + \left(\delta_0{}^4 - \frac{3CR}{\sin \alpha}\right)\exp\left(\frac{4}{3}\frac{z}{R}\tan \alpha\right) \tag{18}$$

The film disappears at $z = z_2$ where

$$\frac{4}{3}\tan \alpha \frac{z_2}{R} = -\log\left(1 - \frac{4}{3}\frac{\sin \alpha}{R} z_0\right) \tag{19}$$

and so the film extends to infinity if $4/3 \sin \alpha\, z_0/R \geqslant 1$. In this situation the convergence of liquid round the tube more than offsets the evaporation, and (it may be shown) the wetted region becomes exponentially narrow, surrounding the line $\theta = \pi$.

The sensitivity of film flows to small inclinations of the tube has already been remarked upon (Wilson [2]). (It should be pointed out that this paper contains a numerical error; the factors 3/2 in equation (7) are spurious, and subsequently the factors 2/7 should be replaced by 1/3. It is consoling to note that the conclusions of that paper are marginally enhanced by the correction!) It is clear that the film thickness may be very different from the expected or average (with respect to θ) value, and this has obvious relevance to the problem of film stability and dry-patch formation.

Finally we give an example to indicate that caution may be necessary if the surface is not smooth (that is, contains edges or points). The surface is a cone of semivertical angle β, with axis vertical and point uppermost. Let s denote distance along a generator measured from the vertex, θ the angle measured round the axis, and n the distance measured normally from the surface. Then (6) becomes

$$\frac{\partial}{\partial s}\left\{\bar{u}_1\left(s\delta \sin \beta + \frac{1}{2}\delta^2 \cos \beta\right)\right\} + \frac{\partial}{\partial \theta}(\bar{u}_2\delta) = \frac{k}{\rho\lambda}\left(\frac{\partial T}{\partial n}\right)_s (s \sin \beta + \delta \cos \beta) \tag{20}$$

For simplicity we suppose that all quantities are independent of θ. Then on the reasonable assumption that $\delta \cos \beta \ll s \sin \beta$, we find

$$\frac{d}{ds}\left(\frac{1}{3}s\delta^3\right) = \frac{As}{\delta \cos \beta} \tag{21}$$

with the solution

$$\delta^4 = \frac{12}{7}\frac{As}{\cos \beta} + Ks^{-4/3} \tag{22}$$

The arbitrary constant K is determined from the conditions at $s = 0$ and it is natural to demand $K = 0$ to avoid a singularity. This may or may not be the case; but the argument cannot be sustained because the approximation $\delta \cos \beta \ll s \sin \beta$ fails, as do the other thin film approximations. Nor is it correct to suppose that (22) is the asymptotic solution as $s \rightarrow \infty$, and that K could be determined from a study of the more accurate equation

$$\left(\delta^3 s + \frac{2}{3}\cot \beta\, \delta^4\right)\frac{d\delta}{ds} + \frac{1}{3}\delta^4 = \left(\frac{s}{\cos \beta} + \frac{\delta}{\sin \beta}\right)A \tag{23}$$

It is not possible to solve this in closed form; but whereas (22) would indicate the form $\delta \sim (12/7\, As/\cos \beta)^{1/4} + 0(s^{-25/12})$, in fact a correction term of order $s^{-1/2}$ intervenes, whose coefficient is determinate, giving

$$\delta \sim \left(\frac{12}{7}\frac{As}{\cos \beta}\right)^{1/4} + \frac{5}{19}\cot \beta \left(\frac{12}{7}\frac{A}{\cos \beta}\right)^{1/2} s^{-1/2} \tag{24}$$

The conclusion of all this is that the errors incurred near $s = 0$ persist and affect the solution for large s.

It has been shown that, within the framework of the thin-film approximations, the solution of unsteady and three-dimensional condensation problems can be reduced to the solution of a first-order partial differential equation and, thus, to the solution of a system of ordinary differential equations, thereby adding to the class of problems which can be solved in closed form. Two further points may be made.

(i) The method can easily be extended to include effects due to vapor drag, external pressure gradients, forces due to rotation, and so on, provided that a simple explicit expression for the local average velocity in terms of δ (and possibly the coordinates) can be found. The key approximation is that the flow is locally parallel to the wall, and this is of course the thin-film approximation.

(ii) In cases where the characteristics cannot be found explicitly, the system of ordinary differential equations is readily amenable to numerical solution.

References

1 Sparrow, E. M., and Siegel, R., "Transient Film Condensation," *Journal of Applied Mechanics*, Vol. 26, 1959, p. 120.

2 Wilson, S. D. R., "Flow of a Liquid Down a Slightly Inclined Tube," *AIChE Journal*, Vol. 20, 1974, p. 408.

Evaporation and Heating With Turbulent Falling Liquid Films

R. A. Seban[1] and A. Faghri[2]

Introduction

In 1971, Chun and Seban [1][3] reported experimental results for the evaporation of water from the surface of a falling film flowing turbulently downward on an electrically heated vertical tube. Under these conditions the local heat transfer coefficient at first diminishes in the region of thermal development and then becomes constant as the development is completed and the heat flux through the layer becomes constant, the evaporation at the surface then accounts for all of the heat flux that issues from the wall. The experimental results approximated this kind of variation and it was then concluded that asymptotic conditions had been approached at the end of the heated section.

Subsequently, Mills and Chung [2] showed that excellent predictions of these results could be made as the asymptotic coefficients for a film of uniform thickness incorporating a turbulent transport specified by the usual van Driest model, modified in the

---

[1] Professor, University of California at Berkeley, Calif.

[2] Research Assistant, University of California at Berkeley, Calif.

[3] Numbers in brackets designate References at end of technical note.

Contributed by the Heat Transfer Division of THE AMERICAN SOCIETY OF MECHANICAL ENGINEERS. Manuscript received by the Heat Transfer Division October 6, 1975.

$$R \cot \alpha \frac{d\delta}{dz} + \frac{1}{3}\delta = -\frac{CR}{\sin \alpha}\frac{1}{\delta^3} \tag{15}$$

so that

$$\delta^4 = -\frac{3CR}{\sin \alpha} + a \exp\left(-\frac{4}{3}\frac{z}{R}\tan \alpha\right) \tag{16}$$

and we note again that the structure of this solution is completely different from the case $\alpha = 0$.

Let us suppose that the film thickness at $z = 0$ is δ_0. Then if the tube were vertical, the film would disappear at $z = z_0$ where $z_0 = \delta_0{}^4/4C$. When $\alpha \neq 0$ we find that the film disappears at $z = z_1$, which is given by

$$\frac{4}{3}\tan \alpha \frac{z_1}{R} = \log\left(1 + \frac{4}{3}\frac{\sin \alpha}{R} z_0\right) \tag{17}$$

As a numerical example, suppose the data are such that $C = 2 \times 10^{-10}$ cm^3 and $\delta_0 = 2 \times 10^{-2}$ cm. Then $z_0 = 200$ cm. If $R = 1$ cm and α is as small as 0.1 deg, we find $z_1 = 180$ cm, and if $\alpha = 1$ deg, an error which might easily be found in engineering practice, we find $z_1 = 76$ cm. On the lowermost generator a similar calculation gives

$$\delta^4 = \frac{3CR}{\sin \alpha} + \left(\delta_0{}^4 - \frac{3CR}{\sin \alpha}\right) \exp\left(\frac{4}{3}\frac{z}{R}\tan \alpha\right) \tag{18}$$

The film disappears at $z = z_2$ where

$$\frac{4}{3}\tan \alpha \frac{z_2}{R} = -\log\left(1 - \frac{4}{3}\frac{\sin \alpha}{R} z_0\right) \tag{19}$$

and so the film extends to infinity if $4/3 \sin \alpha \, z_0/R \geqslant 1$. In this situation the convergence of liquid round the tube more than offsets the evaporation, and (it may be shown) the wetted region becomes exponentially narrow, surrounding the line $\theta = \pi$.

The sensitivity of film flows to small inclinations of the tube has already been remarked upon (Wilson [2]). (It should be pointed out that this paper contains a numerical error; the factors 3/2 in equation (7) are spurious, and subsequently the factors 2/7 should be replaced by 1/3. It is consoling to note that the conclusions of that paper are marginally enhanced by the correction!) It is clear that the film thickness may be very different from the expected or average (with respect to θ) value, and this has obvious relevance to the problem of film stability and dry-patch formation.

Finally we give an example to indicate that caution may be necessary if the surface is not smooth (that is, contains edges or points). The surface is a cone of semivertical angle β, with axis vertical and point uppermost. Let s denote distance along a generator measured from the vertex, θ the angle measured round the axis, and n the distance measured normally from the surface. Then (6) becomes

$$\frac{\partial}{\partial s}\left\{\bar{u}_1\left(s\delta \sin \beta + \frac{1}{2}\delta^2 \cos \beta\right)\right\} + \frac{\partial}{\partial \theta}(\bar{u}_2\delta) = \frac{k}{\rho\lambda}\left(\frac{\partial T}{\partial n}\right)_s (s \sin \beta + \delta \cos \beta) \tag{20}$$

For simplicity we suppose that all quantities are independent of θ. Then on the reasonable assumption that $\delta \cos \beta \ll s \sin \beta$, we find

$$\frac{d}{ds}\left(\frac{1}{3}s\delta^3\right) = \frac{As}{\delta \cos \beta} \tag{21}$$

with the solution

$$\delta^4 = \frac{12}{7}\frac{As}{\cos \beta} + Ks^{-4/3} \tag{22}$$

The arbitrary constant K is determined from the conditions at $s = 0$ and it is natural to demand $K = 0$ to avoid a singularity. This may or may not be the case; but the argument cannot be sustained because the approximation $\delta \cos \beta \ll s \sin \beta$ fails, as do the other thin film approximations. Nor is it correct to suppose that (22) is the asymptotic solution as $s \to \infty$, and that K could be determined from a study of the more accurate equation

$$\left(\delta^3 s + \frac{2}{3}\cot \beta \, \delta^4\right)\frac{d\delta}{ds} + \frac{1}{3}\delta^4 = \left(\frac{s}{\cos \beta} + \frac{\delta}{\sin \beta}\right)A \tag{23}$$

It is not possible to solve this in closed form; but whereas (22) would indicate the form $\delta \sim (12/7 \, As/\cos \beta)^{1/4} + 0(s^{-25/12})$, in fact a correction term of order $s^{-1/2}$ intervenes, whose coefficient is determinate, giving

$$\delta \sim \left(\frac{12}{7}\frac{As}{\cos \beta}\right)^{1/4} + \frac{5}{19}\cot \beta \left(\frac{12}{7}\frac{A}{\cos \beta}\right)^{1/2} s^{-1/2} \tag{24}$$

The conclusion of all this is that the errors incurred near $s = 0$ persist and affect the solution for large s.

It has been shown that, within the framework of the thin-film approximations, the solution of unsteady and three-dimensional condensation problems can be reduced to the solution of a first-order partial differential equation and, thus, to the solution of a system of ordinary differential equations, thereby adding to the class of problems which can be solved in closed form. Two further points may be made.

(i) The method can easily be extended to include effects due to vapor drag, external pressure gradients, forces due to rotation, and so on, provided that a simple explicit expression for the local average velocity in terms of δ (and possibly the coordinates) can be found. The key approximation is that the flow is locally parallel to the wall, and this is of course the thin-film approximation.

(ii) In cases where the characteristics cannot be found explicitly, the system of ordinary differential equations is readily amenable to numerical solution.

References

1 Sparrow, E. M., and Siegel, R., "Transient Film Condensation," *Journal of Applied Mechanics*, Vol. 26, 1959, p. 120.

2 Wilson, S. D. R., "Flow of a Liquid Down a Slightly Inclined Tube," *AIChE Journal*, Vol. 20, 1974, p. 408.

Evaporation and Heating With Turbulent Falling Liquid Films

R. A. Seban[1] **and A. Faghri**[2]

Introduction

In 1971, Chun and Seban [1][3] reported experimental results for the evaporation of water from the surface of a falling film flowing turbulently downward on an electrically heated vertical tube. Under these conditions the local heat transfer coefficient at first diminishes in the region of thermal development and then becomes constant as the development is completed and the heat flux through the layer becomes constant, the evaporation at the surface then accounts for all of the heat flux that issues from the wall. The experimental results approximated this kind of variation and it was then concluded that asymptotic conditions had been approached at the end of the heated section.

Subsequently, Mills and Chung [2] showed that excellent predictions of these results could be made as the asymptotic coefficients for a film of uniform thickness incorporating a turbulent transport specified by the usual van Driest model, modified in the

---

[1] Professor, University of California at Berkeley, Calif.

[2] Research Assistant, University of California at Berkeley, Calif.

[3] Numbers in brackets designate References at end of technical note.

Contributed by the Heat Transfer Division of THE AMERICAN SOCIETY OF MECHANICAL ENGINEERS. Manuscript received by the Heat Transfer Division October 6, 1975.

outer portion of the film by a specification of an eddy diffusivity deduced from the one specified by Lamourelle and Sandall [3] from gas absorption experiments. There are, however, defects in this model, for it gives asymptotic heat transfer coefficients which are too high in the case of heating and it also specifies for evaporation a thermal development length far greater than the heated length of the experiment. For this reason, the question of appropriate turbulence models has been examined further, and additional experimental results have been obtained from essentially the same apparatus as that used by Chun. Unfortunately, the revised system retained the same effective heated length, 23.6 cm, as in Chun's system, so that the experimental appraisal of the attainment of asymptotic conditions retains the uncertainty insufficiently appreciated in the initial examination.

Within this limit, it is shown that a turbulence model used by Limberg [4] to predict the coefficients for the heating of a falling film can predict successfully the coefficients for evaporation by a modification of the eddy diffusivity in the outer portion of the film like that of Mills and Chung, but over a reduced extent of the film.

Calculation of the Flow and Heat Transfer

The flow is assumed to be of constant properties, of constant flow rate, of uniform thickness, and to be fully developed. The latter assumption is supported by a numerical calculation for laminar flow using a program of the Genmix [5] type, which indicated, for an initially uniform velocity distribution, an approach of the wall friction to 2 percent of the value for a Nusselt type film at x/δ = 5.8 and 24.2 film thicknesses, for Reynolds numbers of 400 and 1200, respectively. The development of a turbulent flow is expected to require no more than these small distances.

The restriction to constant mass flow was satisfied by the relatively small evaporation that existed in the experiments.

The assumption of a uniform film thickness simplifies the solution of the momentum and energy equations by making the calculation like that used for a pipe or boundary layer flow. But this uniform film thickness is interpreted as the temporal average of the large amplitude waves on the surface of the actual film, and the relatively adequate predictions that are obtained from the uniform film model ultimately may turn out to be coincidental. An indication of this has been given recently by Brumfield, Houze, and Theofanaus [6], who considered the absorption problem in terms of a thin laminar layer surmounted by large amplitude waves.

Within the foregoing restrictions the momentum equation is:

$$\frac{d}{dy}(\nu + \epsilon_M)\frac{du}{dy} + g = 0 \text{ or } \frac{d}{dy^+}\left(\frac{\epsilon_M}{\nu} + 1\right)\frac{du^+}{dy^+} + \frac{g\nu}{u_\tau^3} = 0 \qquad (1)$$

Here, as usual,

$$u_\tau = \sqrt{\tau_0/\rho} \quad \text{and } u^+ = u/u_\tau \quad \text{and } y^+ = yu_\tau/\nu$$

The integration of equation (1) with $u = 0$ at $y = 0$ and $du/dy = 0$ at $y = \delta$, where δ is the film thickness, gives the velocity distribution and the integration of the velocity distribution gives the relation between the Reynolds number and the dimensionless film thickness.

$$u^+ = \int_0^{y^+} \frac{(1 - y^+/\delta^+)}{(1 + \epsilon_M/\nu)} dy^+ \qquad (2)$$

$$\frac{4\Gamma}{\mu} = 4 \int_0^{\delta^+} u^+ dy^+ \qquad (3)$$

The energy equation is, neglecting dissipation:

$$u\frac{\partial T}{\partial x} = \frac{\partial}{\partial y}(\epsilon_H + \alpha)\frac{\partial T}{\partial y} \text{ or } u^+\frac{\partial T}{\partial x^+} = \frac{\partial}{\partial y^+}\left(\frac{\alpha}{\nu} + \frac{\epsilon_H}{\nu}\right)\frac{\partial T^+}{\partial y^+} \qquad (4)$$

where

$$T^+ = T\rho c u_\tau/q_0$$

The initial and boundary conditions are, for heating at a constant rate

	Evaporation	Heating
$x = 0$	$T = T_{\text{sat}}$ (datum)	$T = T_{\text{int}}$ (datum)
$y = 0$	$\dfrac{\partial T}{\partial y} = -\dfrac{q_0}{k}$	$\dfrac{\partial T}{\partial y} = -\dfrac{q_0}{k}$
$y = \delta$	$T = T_{\text{sat}}$	$\dfrac{\partial T}{\partial y} = 0$

If only the asymptotic solutions, applicable for large x, are desired, then for evaporation $\partial T/\partial x = 0$ and for heating $dT_m/dx = q_0/\rho c\Gamma$, so that the temperature profile is obtained from equation (4) by quadratures. This cannot be done, of course, for the case of heating with constant wall temperature, for which the complete thermal development must be calculated in order to obtain the asymptotic values. But for turbulent flow with Prandtl numbers greater than unity there is little difference in the asymptotic values for constant heat rate and constant wall temperatures.

For the complete solution, equation (4) has been solved numerically with the velocity profile given by equation (2), using an implicit scheme similar to that of the Genmix programs [5], with 200–900 increments in δ^+. Such a solution yields the heat transfer coefficients $h = q_0/(T_0 - T_{\text{sat}})$ for evaporation and $h = q_0/(T_0 - T_m)$ for heating.

Turbulence Models

The solution requires the choice of a turbulence model for the specification of ϵ_M/ν and of ϵ_H/ϵ_M. The essential features of the three models used here are given in Table 1. The first is that of Mills and Chung [2], it is the van Driest model, modified in the outer region of the film by the use of an eddy diffusivity deduced by Lamourelle and Sandall [3] from gas absorption measurements made with water at a temperature of 25 °C. Mills modified this by including the surface tension, σ, in a way estimated to be applicable for other water temperatures to give

Table 1 Turbulence models
mixing length $l = \kappa y[1 - \exp(-y\sqrt{\tau/\rho}/\nu A^+)]\ (f)$

Model	κ	Inner region τ	A^+	f	Constant diffusivity region	Interface diffusivity region	Turbulent Prandtl number
1 Mills & Chung	0.4	τ_0	26	1	None	Equation (5)	0.90
2 Limberg	0.41	$\tau_0(1 - y/\delta)$	25.1	$e^{-1.66\frac{y}{\delta}}$	$0.6 \leqslant \frac{y}{\delta} \leqslant 1$ $\epsilon_M = \epsilon_M\vert_{y/\delta = 0.6}$	None	0.89
3 Present	0.40	$\tau_0(1 - y/\delta)$	25.1	$e^{-1.66\frac{y}{\delta}}$	$0.6 \leqslant \frac{y}{\delta} \leqslant 1 - (y/\delta)$ $\epsilon_M = \epsilon_M\vert_{y/\delta = 0.6}$	Equation (5) $y_e < y < \delta$, Table 2	0.90, 3A Equation (6), 3

$$\frac{\epsilon_M}{\nu} = 6.47 \times 10^{-4} \rho \frac{g^{1/3} \nu^{4/3}}{\sigma(\delta^+)^{2/3}} (\delta^+ - y^+)^2 \left(\frac{4\Gamma}{\mu}\right)^{1.678} \tag{5}$$

This is less than the value given by the van Driest model in the outer region of the flow and it supplants this diffusivity when it has a lower value. Fig. 1 illustrates the diffusivity distribution for two typical values of δ^+.

The second model is that used by Limberg [4] in his prediction of the results of Wilke [7] for the case of heating without evaporation. It modifies the van Driest model in a minor way by using slightly different values of the constants, and in a significant way by a reduction factor of $e^{-1.66y/\delta}$, and for $y > 0.60\delta$ taking the diffusivity constant at its value for that position. These latter modifications are almost the same as taking the Nikuradse distribution[4] for the mixing length instead of $l = \kappa y$. Fig. 1 shows the lower diffusivities in the interior of the film that are given by this model which, however, incorporates no reduction in the diffusivity for the outer region of the film.

The third model is the second model with a diffusivity in the outer region given by equation (5) but only over the region $y_e < y < \delta$ necessary to give within 10 percent the absorption coefficient measured by Lamourelle at his lowest Prandtl (Schmidt) number, 140. These values are given in Table 2.

The eddy diffusivity distributions that are shown in Fig. 1 illustrate the much smaller region over which equation (5) is thus applied, compared to Model 1.

In most cases the third model, called 3A when only the foregoing modification is used, is further altered by incorporating a relation like that of Habib and Na [9] for the turbulent Prandtl number near the wall. This specification, with the introduction of a factor 0.90 so that the turbulent Prandtl number becomes 0.90 at large distances from the wall, is:

$$\frac{\epsilon_M}{\epsilon_H} = 0.90 \frac{1 - \exp(-y^+/A^+)}{1 - \exp(-y^+ \sqrt{\nu/\alpha}/B^+)} \tag{6}$$

The values of B^+ are those given by Habib and Na. This form of the third model, used more generally, is called Model 3.

Film Thickness

Limberg [4] has already shown that the film thickness given by Model 2 corresponds to the experimental correlation of Brauer [10] for turbulent flow. Model 3 is equally good in this respect, while Model 1, because of its higher diffusivity, gives values of the film thickness, δ^+, which are 15 percent above the Brauer specification. These comparisons are, however, not decisive because Brauer's values are for an average film thickness, deduced photographically from a magnitude which in turbulent flow has an amplitude of the order of 0.7δ because of the waves on the surface of the film.

Nusselt Number for Evaporation

Fig. 2 shows four examples of the variation of the local Nusselt number with respect to the generalized length, $x^+ = (x/\nu)\sqrt{\delta g}$, as given by the various Models. Data are also shown, the open circles being the original data by Chun [1] and the solid circles the repeated data; for these, the abscissa was evaluated using the value of δ given by the Brauer correlation.

At atmospheric pressure, $\nu/\alpha = 1.77$, at a Reynolds number of 17500, the data agree best with Model 3, and are very considerably below the prediction of Model 1, though the asymptotic values, shown on the right-hand margin of the figure, are about the same for the two models. The length of thermal development is much greater for Model 1 because so much more of its total thermal resistance is situated in the outer part of the liquid film. That length is shortened for Model 3 because the greater part of its thermal resistance is closer to the wall, but at the last data location, at $x = 23.6$ cm, the Nusselt number given by Model 3 is still 6 percent above its asymptotic value.

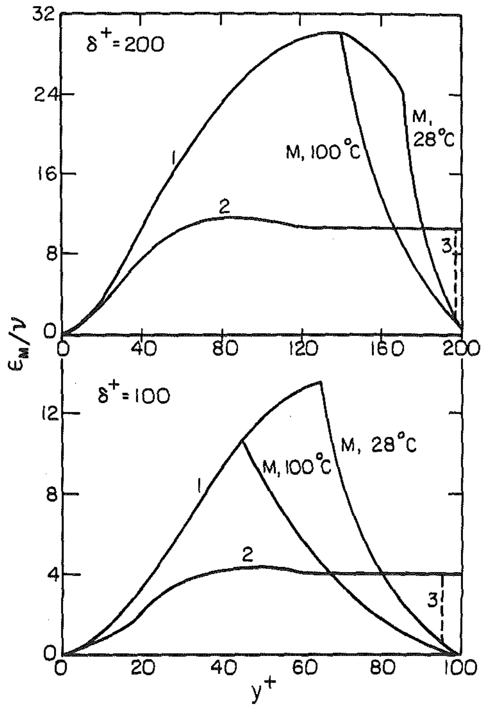

Fig. 1 The eddy diffusivity for momentum curve numbers refer to the model number of Table 1. Curves *M* are equation (5), part of Models 1 and 3.

At the lower Reynolds number, 7600, the data are again in best accord with the prediction of Model 3. At the last data point, $x = 18.4$ cm in this case, the prediction of Model 3 is about 5 percent above the asymptotic value, because of the reduced thermal entry length at the lower Reynolds number.

For the higher Prandtl number of 5.7, obtained by operation at subatmospheric pressure, at a saturation temperature of 28.3°C, the prediction from Model 1 is again high and only the prediction of Model 3 is shown. The data for a Reynolds number of 8100 are slightly below this prediction and they show a tendency toward asymptotic behavior. At a Reynolds number of 4180, two sets of data are available, and together they tend to confirm Model 3, though on the average they are slightly below that prediction. At the last position of measurement, $x = 23.6$ cm, the prediction is 18 percent above its asymptotic value at the Reynolds number of 4180 and it is 20 percent above its asymptotic value at the Reynolds number of 8100.

Asymptotic Nusselt Numbers for Evaporation

Fig. 3 shows the asymptotic values of the Nusselt numbers that are predicted by the various models. The data that are shown there are those for the last location of measurement and, as already indicated, these may be substantially above the asymptotic value.

In this representation, as was shown by Mills and Chung, Model 1 is the best representation of the data, but this correspondence is now regarded as a coincidence because of the very large thermal entry length associated with that Model. The present view is that,

Table 2

δ^+	250	130	115	76
$4\frac{\Gamma}{\mu}$	17363	8106	6999	4190
$(\delta^+ - y_e^+)$	2.16	3.35	3.46	4.89

---

[4] Reference [8, p. 568]

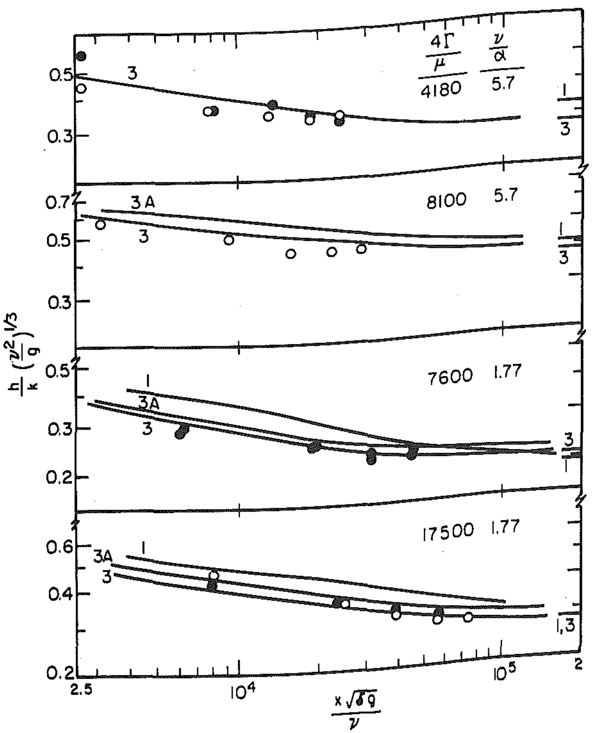

Fig. 2 Nusselt number for evaporation in the thermal development region. Curves: numbers are model numbers. Open circles are Chun [1] results. Solid circles are present results. Indications on right margin are asymptotic values for the numbered models.

had the test section been longer, asymptotic values of the Nusselt number corresponding to Model 3 would have been obtained, particularly at the Prandtl number of 5.7, in conformance with the trends that are shown in Fig. 2.

The predictions for Model 2 show the need for the inclusion of the part of the outer region resistance of equation (5), for without it, the prediction of this Limberg model is far above the data.

Nusselt Numbers for Heating

Limberg [4] compared the asymptotic predictions of Model 2 to the data of Wilke [7] and showed fair correspondence, though the predicted Nusselt numbers were higher. Fig. 2 shows the comparison for a Prandtl number of 5.4, where the curve *W* is obtained from the correlation given by Wilke for all of his data. The prediction of Model 2 is as much as 25 percent above the Wilke correlation. The prediction of Model 3 is better, due to the inclusion of equation (6). For heating the reduced diffusivity near the outside of the layer has no effect because the heat flux is almost zero there, hence Model 3A gives the same prediction as does Model 2. Model 1 is seen to give predictions which are excessively high.

Some data were obtained for the heating of water, without evaporation, at a Prandtl number of 6.35 and these revealed correspondence with Model 3 within 10 percent at all values of x^+ and because of the reduced thermal entry length in the case of heating the last three data locations were essentially in the asymptotic region. Such confirmation was obtained for Reynolds numbers between 3000 and 8000. In this range, Gimbutis [11] gives experimental results which are about 10 percent lower at a Reynolds number of 4000, and less than 3 percent lower at Reynolds numbers greater than 8000. He has offered a model with increased sublayer resistance at lower Reynolds numbers to account for his lower Nusselt numbers in the lower Reynolds number range.

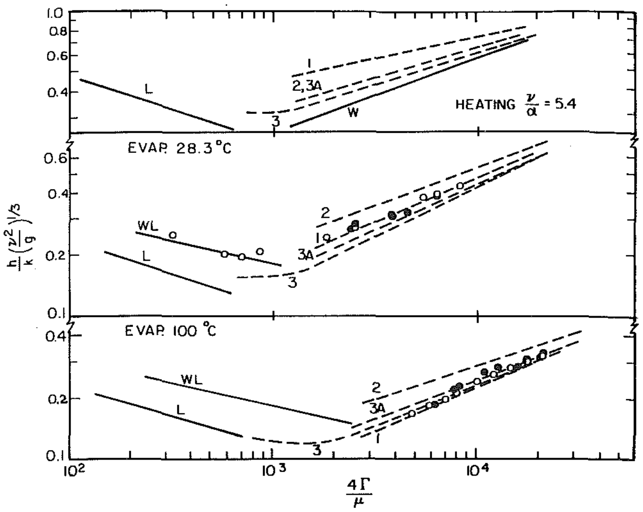

Fig. 3 Asymptotic Nusselt numbers for evaporation. Curves: numbers refer to models: *L*, laminar flow; *WL*, wavy laminar flow Chun [1], *W*, Wilke correlation for heating.

Acknowledgment

This research was accomplished with assistance from the Sea Water Conversion Laboratory, University of California at Berkeley.

References

1 Chun, K. R., and Seban, R. A., "Heat Transfer to Evaporating Liquid Film," JOURNAL OF HEAT TRANSFER, TRANS. ASME, Series C, Vol. 93, 1971, pp. 391–396.

2 Mills, A. F., and Chung, D. K., "Heat Transfer Across Turbulent Falling Films," *International Journal of Heat and Mass Transfer,* Vol. 16, 1973, pp. 694–696.

3 Lamourelle, A. P., and Sandall, O. C., "Gas Absorption Into Turbulent Liquid," *Chem. Engng. Sci.,* Vol. 27, 1972, pp. 1035–1043.

4 Limberg, H., "Warmeubergang an Turbulente und Laminare Rieselfilme," *International Journal of Heat and Mass Transfer,* Vol. 16, 1973, pp. 1691–1702.

5 Patankar, S. V., and Spalding, D. B., *Heat and Mass Transfer in Boundary Layers,* Second ed., Inter-Text Books, London, 1970.

6 Brumfield, L. K., Houze, R. N., and Theofanous, T. G., "Turbulent Mass Transfer at Free, Gas Liquid Interfaces With Application to Film Flows," *International Journal of Heat and Mass Transfer,* Vol. 18, Sept. 1975, pp. 1077–1081.

7 Wilke, W., "Warmeubergang an Rieselfilme," *VDI-Forsch-Heft,* Dusseldorf, Vol. 490, 1962.

8 Schlichting, H., *Boundary Layer Theory,* Sixth ed., McGraw-Hill, New York, 1968.

9 Habib, I. S., and Na, T. P., "Prediction of Heat Transfer in Turbulent Pipe Flow With Constant Wall Temperature," JOURNAL OF HEAT TRANSFER, TRANS. ASME, Series C, Vol. 96, 1974, pp. 253–254.

10 Brauer, H., "Stromung und Warmeubergang an Rieselfilme," *VDI-Forsch-Heft,* Dusseldorf, Vol. 457, 1956.

11 Gimbutis, G., "Heat Transfer of a Turbulent and Vertically Falling Film," *Proceedings of the Fifth International Heat Transfer Conference,* Vol. II, 1974, pp. 85–89.

Heat Transfer Across a Turbulent Falling Film With Cocurrent Vapor Flow[1]

G. L. Hubbard,[2] A. F. Mills,[3] and D. K. Chung[4]

Nomenclature

$Cb = \nu^4\rho^3 g/\sigma^3$, capillary-buoyancy number
C_p = heat capacity
h = heat transfer coefficient
k = thermal conductivity
Pr = Prandtl number
$\mathrm{Re}_L = 4\Gamma/\nu$, film Reynolds number
T = temperature (°C)
$v^* = \sqrt{\tau_w/\rho}$, friction velocity
y = coordinate normal to wall
Γ = volume flow rate per unit wall width
δ = film thickness
ϵ = eddy diffusivity
ν = kinematic viscosity (m²/s)
ρ = density
σ = surface tension (N/m)
τ = shear stress

Subscripts

i = at the interface
t = turbulent
w = at the wall

Superscripts

+, * = dimensionless
0 = zero interfacial shear

In reference [1][5] we presented an analysis of heat transfer across a turbulent falling film, using an eddy diffusivity profile comprised of the conventional van Driest model [2] close to the solid wall, and near the interface the model deduced by Lamourelle and Sandall [3] from their gas absorption experiments. Excellent agreement was obtained with the experimental data of Chun and Seban [4] for evaporation from a freely falling film. Since previous analyses, based on conventional hypotheses about turbulent transport consistent with pipe flow, e.g., [5, 6], were shown by Chun and Seban to be quite inadequate, the analysis of [1] provides the first satisfactory method for making engineering calculations of evaporation from, or condensation on, turbulent falling films. However, the gas absorption data of Lamourelle and Sandall were limited to a freely falling film of water at 25°C only, and hence extrapolation to situations where the fluid properties are different (as was done theoretically in [1]), or where interfacial shear is present, is not justified. Recently [7, 8, 9] we have reported experiments on gas absorption into a turbulent falling film for a wide range of liquid properties for both a freely falling film, and with a cocurrent gas flow giving interfacial shear forces of the same order of magnitude as gravity. Our objective here is to use an eddy diffusivity model based on this new gas absorption data to demonstrate an engineering method for calculating heat transfer across (i) a freely falling turbulent film, and (ii) a turbulent film with interfacial shear due to cocurrent vapor flow.

Our analysis imagines a time-wise steady film thickness, and the Nusselt assumptions of negligible inertia forces and energy convection, appropriate for a slowly growing film, are invoked. There is obtained

$$\mathrm{Re}_L \equiv \frac{4\Gamma}{\nu} = 4\int_0^{\delta^+} \frac{1 - g\nu y^+/v^{*3}}{\epsilon^+}(\delta^+ - y^+)dy^+ \tag{1}$$

$$\frac{h}{k}\left(\frac{\nu^2}{g}\right)^{1/3} = \frac{v^*}{(g\nu)^{1/3}}\left[\int_0^{\delta^+} \frac{dy^+}{1 + \dfrac{\mathrm{Pr}}{\mathrm{Pr}_t}(\epsilon^+ - 1)}\right]^{-1} \tag{2}$$

where $v^{*2} = \tau_w/\rho = g\delta + \tau_i/\rho$. Once an eddy diffusivity profile $\epsilon^+(y^+)$ is specified, equations (1) and (2) can be solved to obtain the dimensionless heat transfer coefficient as a function of film Reynolds number. In developing the eddy diffusivity profile we again use the van Driest model [2] in the near wall region, but now allow for the varying shear stress $\tau = \rho g(\delta - y) + \tau_i$, to obtain

$$\epsilon^+ = \frac{1}{2} + \frac{1}{2}\left[1 + 0.64y^{+2}\frac{\tau}{\tau_w}(1 - \exp(-y^+/26))^2\right]^{1/2} \tag{3}$$

Near the interface we assume a power law variation for the eddy diffusivity and unity turbulent Schmidt number; then the correlations for mass transfer coefficient in [8, 9] give (following [3])

$$\epsilon^+ = 1 + \frac{8.13 \times 10^{-17}(\nu g)^{2/3}}{Cb\, v^{*2}}\mathrm{Re}_L{}^{2n}[1 + b(\tau_i/\tau_w{}^0)]^2(\delta^+ - y^+)^2 \tag{4}$$

where $n = 6.95 \times 10^2\,(\nu m^2/s)^{1/2}$, $b = 0.9 + 1.73 \times 10^{12}\,(\nu m^2/s)^2$, and $\tau_w{}^0$ is calculated using the Brötz equation for film thickness, $\mathrm{Re}_L = 57.2\delta^+$. Equation (4) was established for ν, σ, and Cb in the range 0.66 × 10^{-6}–2.75 × 10^{-6} m²/s, 22.7 × 10^{-3}–73.5 × 10^{-3} N/m, and 5.48 × 10^{-12}–3.44 × 10^{-9}, respectively. The two expressions for ϵ^+ given by equations (3) and (4) are terminated at their intersection. A value of

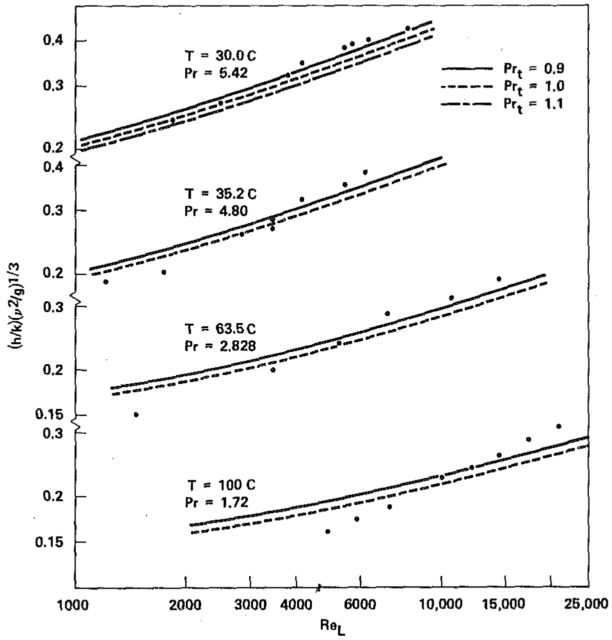

Fig. 1 Comparison of predicted heat transfer with experimental data for evaporation of Chun and Seban [4]; zero interfacial shear

---

[1] This work was sponsored by the University of California Water Resources Center on Project S142, and by the National Science Foundation on Grant GK-40180. Computer time was supplied by the Campus Computing Network of the University of California, Los Angeles.

[2] Research Assistant, University of California, Los Angeles, Calif.

[3] Assoc. Professor, University of California, Los Angeles, Calif. Assoc. Mem. ASME.

[4] Mechanical Engineer, Atomics International, Canoga Park, Calif.

[5] Numbers in brackets designate References at end of technical note.

Contributed by the Heat Transfer Division of THE AMERICAN SOCIETY OF MECHANICAL ENGINEERS. Manuscript received by the Heat Transfer Division January 21, 1975.

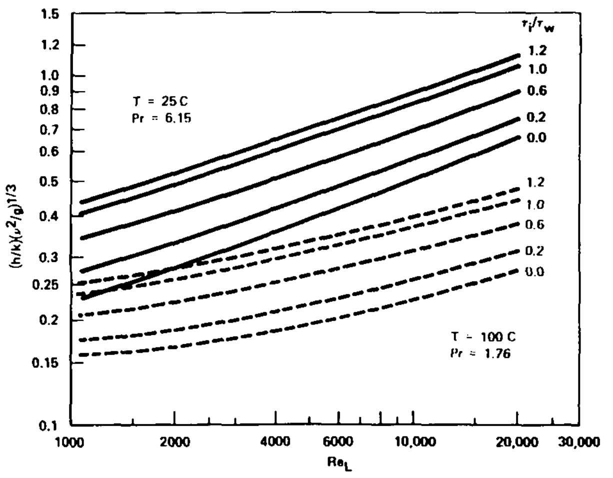

Fig. 2 Effect of interfacial shear on heat transfer: water at 100 and 25°C

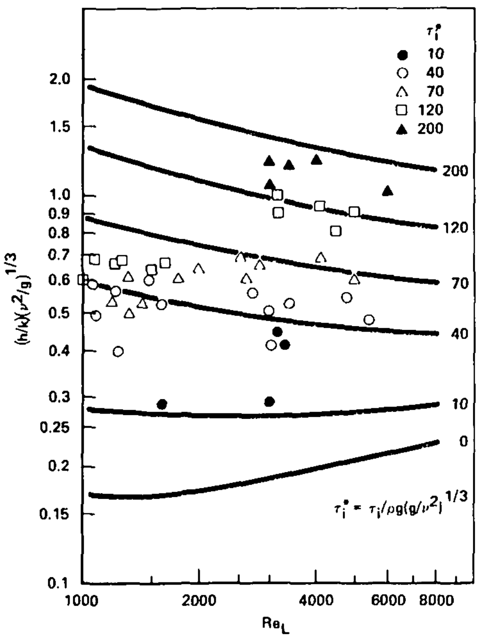

Fig. 3 Comparison of predicted heat transfer with experimental data for condensation with cocurrent vapor flow of Ueda, et al. [13]

Pr_t is required to complete specification of the model; in the absence of information to the contrary, Pr_t was taken to be a constant value to be determined by comparison with experiment.

Fig. 1 shows a comparison of the predictions for a freely falling film with the Chun-Seban data. Thermophysical properties were evaluated at the temperature indicated, and obtained from [10] (k, μ, ρ, C_p) and [11] (σ). The agreement between prediction and experiment is not as good as we previously obtained [1], particularly at the lower Pr values where the Re_L exponent is markedly less than the experimental value of 0.4. Nevertheless, the present model is to be preferred since the liquid properties dependence of ϵ^+ is obtained from experiment rather than the Levich theory [12], as was the case in [1]. (The extrapolation in ν required for water at 100°C, i.e., 0.30×10^{-6}, is modest since the range tested was 0.66×10^{-6}–2.75×10^{-6}.) In addition, we argued in [9] that the Lamourelle and Sandall mass transfer coefficients used to develop the ϵ^+ model in [1] exhibit too high a Reynolds number exponent owing to contamination associated with closed loop operation without adequate water filtration: since the Chun-Seban heat transfer experiments were also operated closed loop without filtration, the precise agreement between prediction and experiment shown in [1] was perhaps more than fortuitous. Fig. 1 also shows that both $Pr_t = 0.9$ and 1.0 give satisfactory agreement with experiment; in the calculations which follow we used $Pr_t = 0.9$. We also note that the increased deviation between prediction and experiment at higher temperatures is possibly due to inaccurate representation of the eddy diffusivity in the midregion of the film. Such an error is expected to become more significant with decrease in Prandtl number.

Fig. 2 shows the effects of interfacial shear for water at two temperatures, 25 and 100°C and a range of interfacial shear stress from $\tau_i/\tau_w{}^0 = 0$ to 1.2. Thus, the interfacial shear forcing ranges up to a value equal to the gravity forcing, which corresponds to the range of shear stress which obtained in the gas absorption experiments. The marked effect of interfacial shear on the heat transfer coefficient can be seen. Very recently Ueda, Kubo, and Inoue [13] experimentally determined condensation heat transfer coefficients for a turbulent falling water film inside a vertical tube with interfacial shear exerted by a high velocity cocurrent vapor flow. The experiments were for $T = 89°\mathrm{C}$ ($Pr = 2.0$); a comparison of theory with experiment is shown in Fig. 3. Given the scatter in the data we conclude that the agreement is satisfactory (we disregard the discrepancy at $\tau_i^* = 10$ because (i) the data are very poor, and (ii) we have already demonstrated the adequacy of the model in the limit of zero shear through the comparisons with the Chun-Seban evaporation data). Note that (i) the calculations for $\tau_i^* > 10$ involve extrapolation to higher shear values than obtained in the gas absorption experiments, and (ii) calculations using the van Driest model, equation (3), without the interface damping of equation (4), gave heat transfer rates which were 54 percent higher at $\tau_i^* = 10$ and 31 percent higher at $\tau_i^* = 200$. In [13] Ueda, et al., compared predictions of the Rohsenow, Webber, and Ling analysis [5] with their data and concluded that the predicted heat transfer coefficients were too high, particularly at the lower values of τ_i^*. Our predictions are lower than those of [5] due to our accounting for damping of turbulence near the interface.

We conclude that our eddy diffusivity model is superior to previous proposals both for freely falling films, and when interfacial shear is present, and recommend its use for engineering calculations.

References

1 Mills, A. F., and Chung, D. K., "Heat Transfer Across Turbulent Falling Films," *International Journal of Heat and Mass Transfer*, Vol. 16, 1973, pp. 694–696.

2 van Driest, E. R., "On Turbulent Flow Near a Wall," *J. Aero. Sci.*, Vol. 23, 1956, pp. 1007–1011.

3 Lamourelle, A. P., and Sandall, O. C., "Gas Absorption Into a Turbulent Liquid," *Chem. Eng. Sci.*, Vol. 27, 1962, pp. 1035–1043.

4 Chun, K. R., and Seban, R. A., "Heat Transfer to Evaporating Liquid Films," JOURNAL OF HEAT TRANSFER, TRANS. ASME, Series C, Vol. 93, No. 4, Nov. 1971, pp. 391–396.

5 Rohsenow, W. M., Webber, J. H., and Ling, A. T., "Effect of Vapor Velocity at Laminar and Turbulent Film Condensation," TRANS. ASME, Vol. 78, 1956, pp. 1637–1644.

6 Dukler, A. E., "Fluid Mechanics and Heat Transfer in Vertical Falling Film Systems," *Chem. Eng. Prog. Symp. Ser.*, Vol. 36, No. 30, 1960, pp. 1–10.

7 Chung, D. K., and Mills, A. F., "Effect of Interfacial Shear on Gas Absorption Into a Turbulent Falling Film With Co-Current Gas Flow," *Letters in Heat and Mass Transfer*, Vol. 1, 1974, pp. 43–48.

8 Chung, D. K., "An Experimental Investigation of Gas Absorption Into a Turbulent Liquid Film With Interfacial Shear," PhD dissertation, University of California, Los Angeles, Sept. 1974.

9 Chung, D. K., and Mills, A. F., "Experimental Study of Gas Absorption Into Turbulent Falling Films of Water and Ethylene Glycol-Water Mixtures," to appear, *International Journal of Heat and Mass Transfer*.

10 Edwards, D. K., Denny, V. E., and Mills, A. F., *Transfer Processes*, Holt, Rinehart and Winston, New York, 1973.

11 Streeter, V. L., *Fluid Mechanics*, Fifth ed., McGraw-Hill, New York, 1971.

12 Levich, V. G., *Physiochemical Hydrodynamics*, Prentice-Hall, Englewood Cliffs, N. J., 1962, p. 691.

13 Ueda, T., Kubo, T., and Inoue, M., "Heat Transfer for Steam Condensing Inside a Vertical Tube," Fifth International Heat Transfer Conference, Tokyo, Vol. III, JSME SCEJ, 1974, pp. 304–308.

Locally Nonsimilar Solution for Laminar Free Convection Adjacent to a Vertical Wall

Tsai-tse Kao[1]

Analysis

With the exception of a few specially prescribed boundary conditions at the wall for laminar free convection adjacent to a vertical wall, the problem is usually nonsimilar. Thus, one often has to solve a set of coupled nonlinear partial differential equations numerically. The locally similar method avoids this by deleting the streamwise derivative terms, thus changing the partial differential equations into nonlinear ordinary differential equations and saving a considerable amount of computer time. However, the error introduced by this technique cannot be easily estimated. Recently, the locally nonsimilar method was introduced by Sparrow, et al. [1, 2][2] to improve this local concept. Like the locally similar method, this technique is locally autonomous. Solutions at any specified streamwise station can be obtained without first obtaining upstream solutions. In this short note, we shall employ this locally nonsimilar method to look at some nonsimilar laminar free convection problems. Only the two equation model will be considered here.

As a starting point, the set of conservation equations governing laminar free convection adjacent to a vertical wall (see Fig. 1) will be transformed into the following:

$$f''' + (3 - 2\tilde{\beta})ff'' - 2f'^2 + \theta = 4\xi(f'\partial f'/\partial\xi - f''\partial f/\partial\xi) \qquad (1)$$

$$1/PR\theta'' + (3 - 2\tilde{\beta})f\theta' - 4\tilde{\beta}f'\theta = 4\xi(f'\partial\theta/\partial\xi - \theta'\partial f/\partial\xi) \qquad (2)$$

$$(3 - 2\tilde{\beta})f(\xi, 0) + 4\xi\partial/\partial\xi f(\xi, 0) = \gamma(x) = \frac{-V_w x}{\nu}\,[4/\mathrm{Gr}_x]^{1/4}\} \qquad (3)$$

$$f'(\xi, 0) = 0, \quad \theta(\xi, 0) = 1$$

$$f'(\xi, \infty) = 0, \quad \theta(\xi, \infty) = 0 \qquad (4)$$

Here primes denote partial derivatives with respect to η. V_w is the transpiration velocity at the wall and Gr_x is the local Grashof number. The transformations used are as given in references [3] and [4]:

$$\xi = \int_0^x \{T_w - T_\infty\}dx \qquad (5)$$

$$\eta = C_1(T_w - T_\infty)^{1/2}y/\xi^{1/4} \qquad (6)$$

$$f(\xi, \eta) = (T_w - T_\infty)^{1/2}\psi/4C_1\nu\xi^{3/4} \qquad (7)$$

$$\theta(\xi, \eta) = T - T_\infty/T_w - T_\infty \qquad (8)$$

$$\tilde{\beta} = \left\{\int_0^x (T_w - T_\infty)dx/(T_w - T_\infty)^2\right\}d(T_w - T_\infty)/dx \qquad (9)$$

Where $C_1 = (g\bar{\beta}/4\nu^2)^{1/4}$. ψ is the usual stream function introduced to satisfy the continuity equation.

In the locally similar method, the right-hand sides of equations (1)–(4) are assumed to be small and thus deleted. The equations that are left are treated as ordinary differential equations and solved with the streamwise variables ($\tilde{\beta}$ and γ) as parameters. According to Sparrow's two-equation locally nonsimilar method, the terms on the right-hand side are all retained. Auxiliarly differential equations are introduced to provide an approximation for them. These auxiliarly equations are obtained simply by differentiating equations (1)–(4) with respect to ξ and defining the new dependent variables:

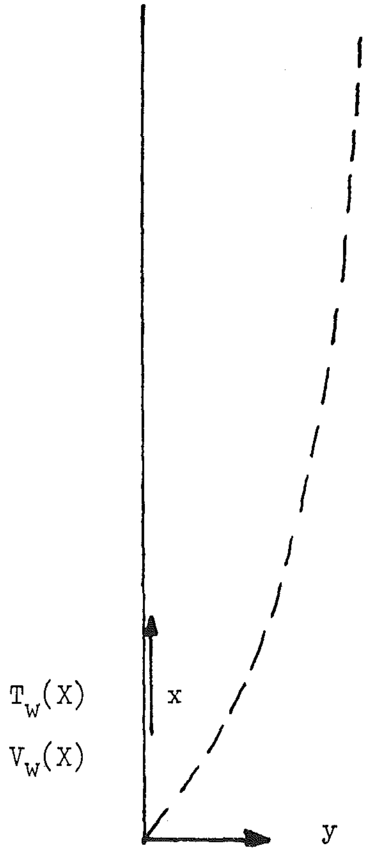

Fig. 1 Physical coordinates

$$g = \partial f/\partial\xi, \quad \varphi = \partial\theta/\partial\xi \qquad (10)$$

to allow the right-hand side of equations (1)–(4) to be retained. Thus:

$$g''' + (3 - 2\tilde{\beta})fg'' - 8f'g' + (7 - 2\tilde{\beta})f''g + \varphi - 2d\tilde{\beta}/d\xi ff'' = 4\xi\partial/\partial\xi(f'g' - f''g) \qquad (11)$$

$$1/PR\varphi'' + (3 - 2\tilde{\beta})f\varphi' - 4(1 + \tilde{\beta})f'\theta + (7 - 2\tilde{\beta})g\theta' - d\tilde{\beta}/d\xi(4\theta f' + 2f\theta') - 4\tilde{\beta}\theta g' = 4\xi\partial/\partial\xi(f'\varphi - \theta'g) \qquad (12)$$

$$(7 - 2\tilde{\beta})g - \partial\gamma/\partial\xi = -4\xi\partial/\partial\xi(g) + 2f(\xi, 0)d\tilde{\beta}/d\xi \qquad (13)$$

$$g'(\xi, 0) = g'(\xi, \infty) = 0$$

$$\varphi(\xi, 0) = \varphi(\xi, \infty) = 0 \qquad (14)$$

To close the system of equations at this second level, $\partial g/\partial\xi$ and $\partial\varphi/\partial\xi$ are deleted from equations (11)–(14). Together with equations (1)–(4), we will have a system of ordinary differential equations. A standard shooting technique, as described by Nachtsheim and Swigert [5] is used to solve this set of equations.

Examples and Discussions

In order to find out how much improvement is obtained by the two equation locally nonsimilar method as applied to free convection problems, two examples will be considered.

In the first example, let us consider the case $T_w - T_\infty = \sin(X)$. The result for the nondimensional temperature gradient at the wall is plotted in Fig. 2. Also shown are the numerical solution from references [3, 4] and the local similarity solution. Near the leading edge, all three solutions show close agreement. However, the local similarity model starts to diverge for $X > 1.0$. The local nonsimilar solution

---

[1] Senior Thermal/Hydraulic Engineer, Nuclear Department, Foster Wheeler Energy Corp., Livingston, N.J. Assoc. Mem. ASME.

[2] Numbers in brackets designate References at end of technical note.

Contributed by the Heat Transfer of THE AMERICAN SOCIETY OF MECHANICAL ENGINEER. Manuscript received by the Heat Transfer Division December 29, 1975.

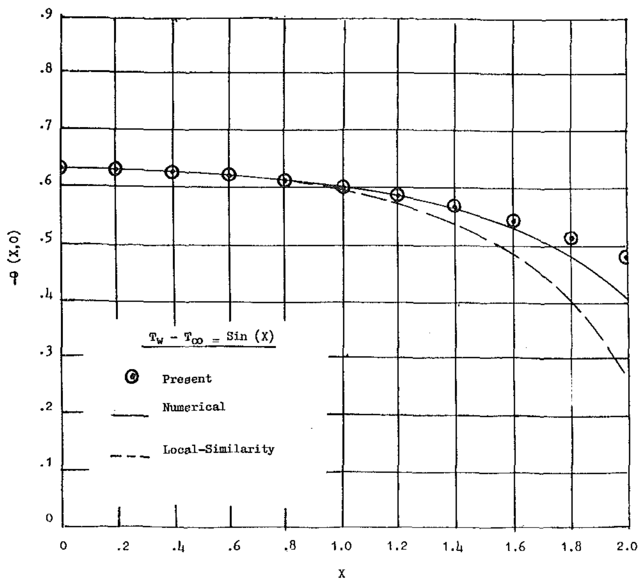

Fig. 2 Comparisons of non-dimensional wall temperature gradient for sinusoidal temperature variation

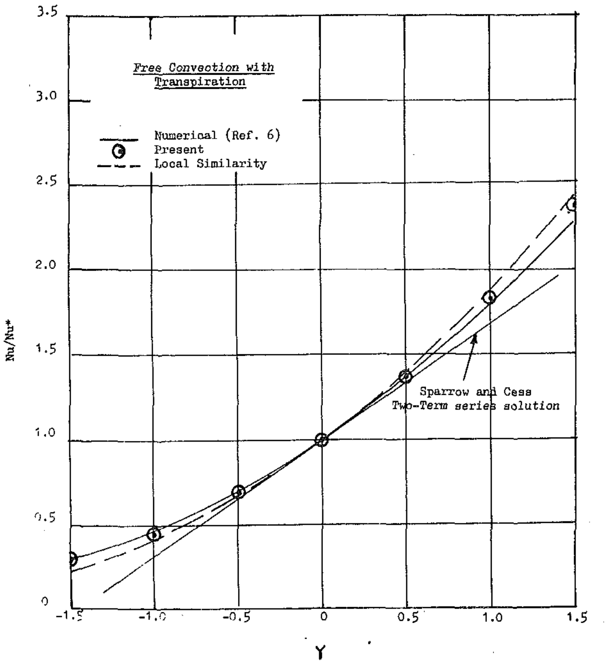

Fig. 3 Comparison of Nu/Nu* for free convection with constant transpiration at the wall

holds up pretty well till $X = 1.6$. At $X = 1.6$ the deviation from numerical solution of the locally nonsimilar model is about 3 percent as compared to 9.4 percent for local similarity model.

As a second example, consider the case of free convection adjacent to an isothermal vertical wall with uniform transpiration. The result for Nu/Nu* for the case of air (Pr = 0.72) is shown in Fig. 3. Here Nu* is the Nusselt number for an impermeable wall. Comparison with the numerical solution of Parikh, et al. [6] shows that the locally nonsimilar method is quite accurate over a fairly large range of γ, as compared to the local similarity solution. Also shown is the two term series solution of Sparrow and Cess [7] which provides a rather good approximation for $\gamma = \pm 0.5$. Thus we see that the locally nonsimilar method can provide a very good approximation to these nonsimilar free convection problems. Its simplicity lends strong support to the use of the method.

References

1 Sparrow, E. M., Quack, H., and Boerner, C. J., "Local Nonsimilar Boundary Layer Solutions," *AIAA Journal*, Vol. 8, No. 11, Nov. 1970, pp. 1936–1942.

2 Sparrow, E. M., and Yu, H. S., "Local Nonsimilar Thermal Boundary Layer Solutions," JOURNAL OF HEAT TRANSFER, TRANS. ASME, Series C, Vol. 94, Nov. 1972, pp. 328–334.

3 Kao, T., Domoto, G. A., and Elrod, H. G., "Free Convection Along a Non-Isothermal Vertical Flat Plate," ASME Paper No. 75-WA/HT-15, 1975.

4 Kao, T., "An Asymptotic Method for the Computation of Laminar Shear Stress and Heat Flux in Forced and Free Convection," PhD dissertation, Department of Mechanical Engineering, Columbia University, N.Y., 1974.

5 Nachtsheim, P. R., and Swigert, P., "Satisfaction of Asymptotic Boundary Conditions in Numerical Solution of Systems of Nonlinear Equations of Boundary Layer Type," NASA TD-D3004, 1965.

6 Parikh, P. G., Moffat, R. J., Kays, W. M., and Bershader, D., "Free Convection Over a Vertical Porous Plate With Transpiration," *International Journal of Heat and Mass Transfer*, Vol. 17, 1974, pp. 1465–1474.

7 Sparrow, E. M., and Cess, R. D., "Free Convection With Blowing or Suction," JOURNAL OF HEAT TRANSFER, TRANS. ASME, Series C, Vol 81, Aug. 1961, pp. 387–389.

Combined Free and Forced Convection in Inclined Circular Tubes

J. A. Sabbagh,[1] A. Aziz,[1] A. S. El-Ariny,[1] and G. Hamad[2]

The problem of combined free and forced convection in an inclined circular tube with uniform peripheral temperature and axial heat flux has been studied experimentally. For fixed Pr and Ra, experimental data showing the effect of tube inclination and Reynolds number on temperature and axial velocity profiles are reported and found to agree qualitatively with the theoretical predictions [7].[3] Also shown is the variation of Nusselt number with inclination angle for Ra Re = 30,000. No optimum angle for maximum Nusselt number was found.

Nomenclature

a = radius of the tube
A = axial pressure gradient = $-(\partial P/\partial Z + \rho_w g \sin \alpha)$
c = specific heat
C = axial temperature gradient = $\partial T/\partial Z$
g = gravitational acceleration
h = heat transfer coefficient
k = thermal conductivity
Nu = Nusselt number = $2ha/k$
P = pressure
Pr = Prandtl number = $\mu c/k$
Ra = Rayleigh number = $\rho c \beta g a^4 C/k\nu$
Re = Reynolds number = $A a^3/4\rho \nu^2$
T = temperature
w = nondimensional axial velocity = $aW/\text{Re}\,\nu$

---

[1] Assoc. Professors, Department of Mechanical Engineering, College of Engineering, University of Riyadh, Riyadh, Saudi Arabia.

[2] Demonstrator, Department of Mechanical Engineering, College of Engineering, University of Riyadh, Riyadh, Saudi Arabia.

[3] Numbers in brackets designate References at end of technical note.

Contributed by the Heat Transfer Division of THE AMERICAN SOCIETY OF MECHANICAL ENGINEERS. Manuscript received by the Heat Transfer Division July 3, 1975.

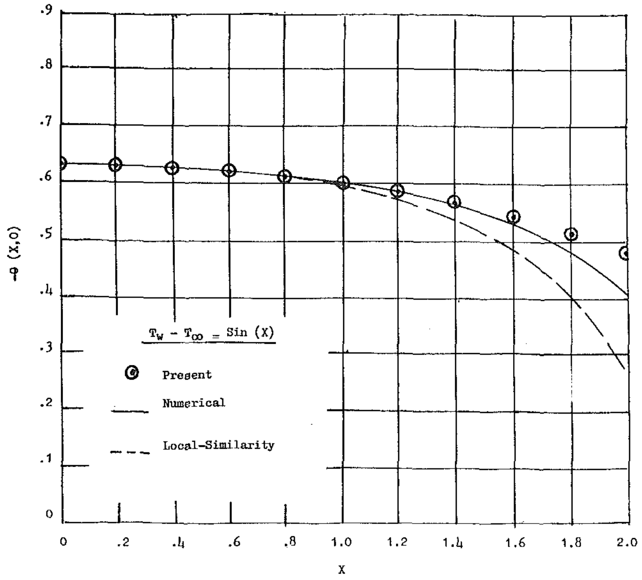

Fig. 2 Comparisons of non-dimensional wall temperature gradient for sinusoidal temperature variation

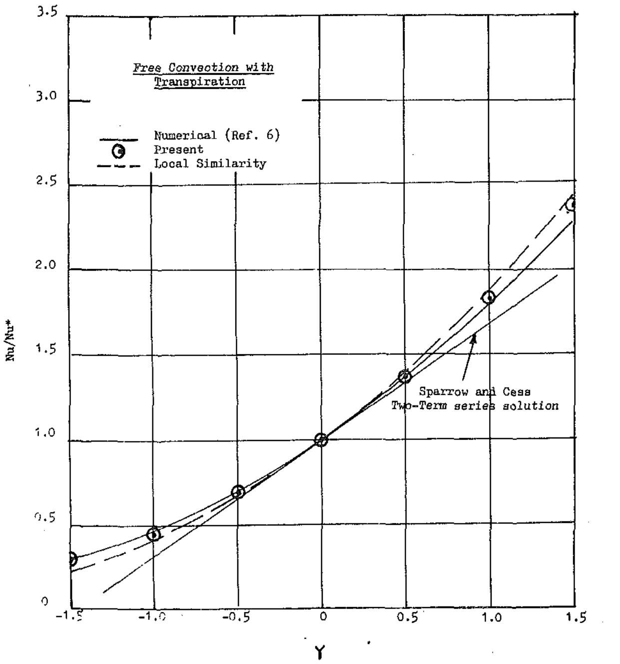

Fig. 3 Comparison of Nu/Nu* for free convection with constant transpiration at the wall

holds up pretty well till $X = 1.6$. At $X = 1.6$ the deviation from numerical solution of the locally nonsimilar model is about 3 percent as compared to 9.4 percent for local similarity model.

As a second example, consider the case of free convection adjacent to an isothermal vertical wall with uniform transpiration. The result for Nu/Nu* for the case of air (Pr = 0.72) is shown in Fig. 3. Here Nu* is the Nusselt number for an impermeable wall. Comparison with the numerical solution of Parikh, et al. [6] shows that the locally nonsimilar method is quite accurate over a fairly large range of γ, as compared to the local similarity solution. Also shown is the two term series solution of Sparrow and Cess [7] which provides a rather good approximation for $\gamma = \pm 0.5$. Thus we see that the locally nonsimilar method can provide a very good approximation to these nonsimilar free convection problems. Its simplicity lends strong support to the use of the method.

References

1 Sparrow, E. M., Quack, H., and Boerner, C. J., "Local Nonsimilar Boundary Layer Solutions," *AIAA Journal*, Vol. 8, No. 11, Nov. 1970, pp. 1936–1942.

2 Sparrow, E. M., and Yu, H. S., "Local Nonsimilar Thermal Boundary Layer Solutions," JOURNAL OF HEAT TRANSFER, TRANS. ASME, Series C, Vol. 94, Nov. 1972, pp. 328–334.

3 Kao, T., Domoto, G. A., and Elrod, H. G., "Free Convection Along a Non-Isothermal Vertical Flat Plate," ASME Paper No. 75-WA/HT-15, 1975.

4 Kao, T., "An Asymptotic Method for the Computation of Laminar Shear Stress and Heat Flux in Forced and Free Convection," PhD dissertation, Department of Mechanical Engineering, Columbia University, N.Y., 1974.

5 Nachtsheim, P. R., and Swigert, P., "Satisfaction of Asymptotic Boundary Conditions in Numerical Solution of Systems of Nonlinear Equations of Boundary Layer Type," NASA TD-D3004, 1965.

6 Parikh, P. G., Moffat, R. J., Kays, W. M., and Bershader, D., "Free Convection Over a Vertical Porous Plate With Transpiration," *International Journal of Heat and Mass Transfer*, Vol. 17, 1974, pp. 1465–1474.

7 Sparrow, E. M., and Cess, R. D., "Free Convection With Blowing or Suction," JOURNAL OF HEAT TRANSFER, TRANS. ASME, Series C, Vol 81, Aug. 1961, pp. 387–389.

Combined Free and Forced Convection in Inclined Circular Tubes

J. A. Sabbagh,[1] A. Aziz,[1] A. S. El-Ariny,[1] and G. Hamad[2]

The problem of combined free and forced convection in an inclined circular tube with uniform peripheral temperature and axial heat flux has been studied experimentally. For fixed Pr and Ra, experimental data showing the effect of tube inclination and Reynolds number on temperature and axial velocity profiles are reported and found to agree qualitatively with the theoretical predictions [7].[3] Also shown is the variation of Nusselt number with inclination angle for Ra Re = 30,000. No optimum angle for maximum Nusselt number was found.

Nomenclature

a = radius of the tube
A = axial pressure gradient = $-(\partial P/\partial Z + \rho_w\, g \sin \alpha)$
c = specific heat
C = axial temperature gradient = $\partial T/\partial Z$
g = gravitational acceleration
h = heat transfer coefficient
k = thermal conductivity
Nu = Nusselt number = $2ha/k$
P = pressure
Pr = Prandtl number = $\mu c/k$
Ra = Rayleigh number = $\rho\, c\, \beta\, g\, a^4\, C/k\nu$
Re = Reynolds number = $A\, a^3/4\rho\, \nu^2$
T = temperature
w = nondimensional axial velocity = $aW/\text{Re}\, \nu$

---

[1] Assoc. Professors, Department of Mechanical Engineering, College of Engineering, University of Riyadh, Riyadh, Saudi Arabia.

[2] Demonstrator, Department of Mechanical Engineering, College of Engineering, University of Riyadh, Riyadh, Saudi Arabia.

[3] Numbers in brackets designate References at end of technical note.

Contributed by the Heat Transfer Division of THE AMERICAN SOCIETY OF MECHANICAL ENGINEERS. Manuscript received by the Heat Transfer Division July 3, 1975.

W = actual axial velocity
Z = axial coordinate
α = tube inclination
β = volumetric coefficient of thermal expansion
ρ = density
μ = dynamic viscosity
ν = kinematic viscosity
θ = nondimensional temperature = $T_w - T/\mathrm{Re}\, C\, a\, \mathrm{Pr}$
ϕ = angular coordinate

Subscripts

w = value at wall

Introduction

The process of combined free and forced convection in circular tubes has been studied both theoretically and experimentally by several workers [1–4]. However, the bulk of the work pertains to the limiting cases of horizontal and vertical tubes. For inclined tubes, the available information appears to be limited to the theoretical contributions of Iqbal and Stachiewicz [5], Futagami and Abe [6], and Cheng and Hong [7]. In [5] the authors adopted a perturbation approach to analyze the effect of tube orientation on heat transfer in uniformly heated circular tubes. The important conclusion was that for any combination of Rayleigh, Reynolds, and Prandtl numbers, there is an optimum inclination angle in the range of 20–60 deg which gives the maximum Nusselt number. A similar conclusion based on perturbation analysis was reached in [6]. In reference [6] experimental data are also reported but no attempt was made to check the effect of inclination angle on Nusselt number. Cheng and Hong [7], on the other hand, employed a combination of the boundary vorticity method and the line iteration method and obtained detailed numerical results illustrating the effect of tube inclination, Rayleigh, Reynolds, and Prandtl numbers on flow and heat transfer characteristics. Their results showed that the perturbation approach [5] was invalid and that there was no optimum inclination angle.

The present experimental work was initiated to supplement and check the aforementioned theoretical works. The parameters selected for this study were tube inclination and Reynolds number. The results described here deal with the effect of these parameters on the velocity and temperature profiles and the Nusselt number. A qualitative comparison is made with the corresponding theoretical predictions [5, 7].

Experimental Setup

Fig. 1 shows the schematic of the rig. It consists of a 3.175 cm ID copper tube mounted inside a 6.350 cm ID steel tube, the tube lengths being 365.7 cm. The inner tube was supplied with air from a centrifugal fan through suitable gauze screens fitted at the tube entrance. The flow was measured by an orifice. The annular space between the tubes was filled with high-tension oil which was heated by six nichrome heating elements, mounted axially and spaced uniformly around the annulus. This arrangement gave constant axial heat flux and uniform peripheral wall temperature. Power was supplied to the heating elements through a variable transformer and measured with an ammeter and a voltmeter. The entire tube assembly was insulated with 5.175 cm thick glasswool which was fixed in wooden supports on a flat table. The table could be inclined to any desired angle from 0 to 90 deg by means of a pulley and rope arrangement.

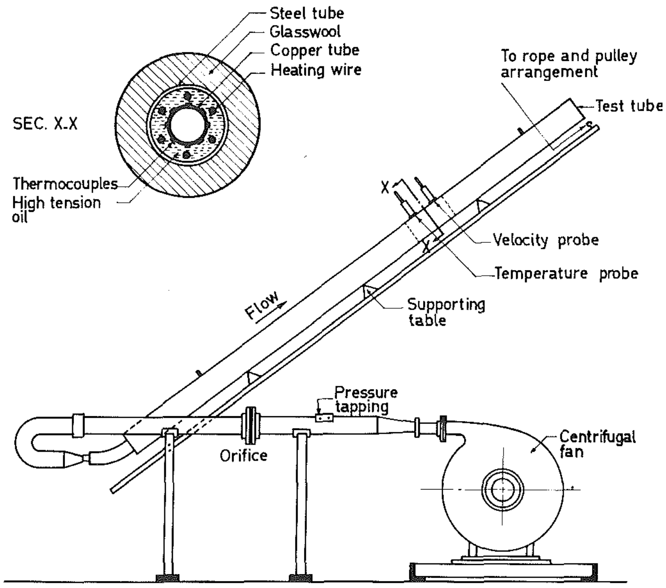

Fig. 1 Sketch of the experimental setup

Chrome-alumel thermocouples were installed at different axial locations to measure the axial temperature gradient and the various heat losses. At the test section, which was located 172.7 cm from the entrance, six thermocouples were uniformly distributed around the periphery. A similar arrangement was employed at a section 45.7 cm upstream from the test station. For both locations, the peripheral temperature variation was found to be uniform to within 1.6 percent. At the test station, the temperature and axial velocity distributions across a diameter were measured. For temperature measurement, a constantan-alumel thermocouple with tip size of about 2 mm was used and was mounted on a traversing mechanism. The axial velocity was measured by a pitot-static tube (2.5 mm tip) with micrometer traverse control. Both the temperature and velocity probes gave steady and reproducible results.

Experiments were conducted to study (i) the effect of tube inclination and (ii) the effect of Reynolds number on the velocity and temperature profiles and the Nusselt number. For (i), the governing flow parameters were fixed at Pr = 0.72, Ra = 40.8, and Re = 746 and tests were carried out at inclination angles of 0, 30, 45, 60, and 90 deg. For (ii), the inclination angle was fixed at 45 deg, and with Pr = 0.72 and Ra = 40.8, test runs were made at Re = 740, 975, and 1204.

Results and Discussion

Following [7], the velocity and temperature are made nondimensional as

$$w = \frac{a}{\mathrm{Re}\,\nu} W, \quad \theta = \frac{T_w - T}{\mathrm{Re}\, C\, a\, \mathrm{Pr}}$$

where the symbols are so defined in the Nomenclature. Fig 2 shows the effect of tube inclination on the axial velocity and temperature distributions along a diameter, $\phi = 0$, $\phi = \pi$. For $\alpha = 0$ (horizontal tube), both the velocity and temperature profiles are distorted, the values in the lower half of the tube being higher than those in the upper half. This appears to be due to the secondary flow resulting from buoyancy effects. As the inclination angle increases, the secondary flow effect diminishes and both the velocity and temperature profiles progress toward symmetry. For the limiting case of α = 90 deg (vertical tube) the profiles are axially symmetric (within experimental accuracy). As the tube inclination increases, the magnitude of the velocity and the temperature difference decreases, the former in accordance with the momentum balance and the latter due to diminution of convective action associated with secondary flow.

It is interesting to note that in the central core region, the velocity appears to vary linearly with radius but this trend is not marked in the temperature profiles. In previous studies on a horizontal tube [4], both the velocity and temperature profiles have been found to exhibit this linear trend.

Numerical results corresponding to the experimental data of Fig. 2 are found in Figs. 2(c) and 3(c) of [7]. Although Pr and Ra are essentially identical in the two cases, the difference in Re (746 as against 100 in [7]) precludes a quantitative comparison. How-

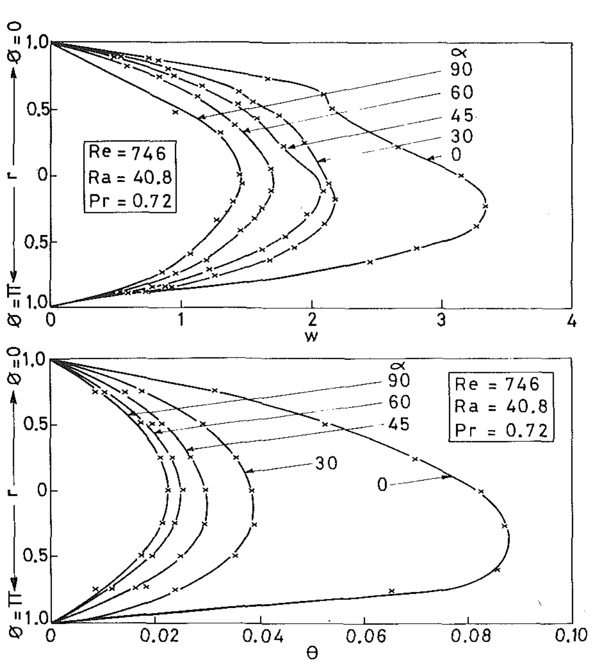

Fig. 2 Effect of tube inclination on axial velocity (upper portion) and temperature (lower portion) profiles along $\phi = 0$, $\phi = \pi$

ever, on a qualitative basis, the two results are seen to be in agreement.

The effect of Re on the velocity and temperature profiles is shown in Fig. 3 for an inclination angle of 45 deg, Pr = 0.72 and Ra = 40.8. As Re increases, the magnitude of the maximum velocity and the maximum temperature decreases and their locations shift toward the lower wall. These findings are consistent with the theoretical results contained in Figs. 2(*b*) and 3(*b*) of [7]. It is worth noting that at Re = 1204, the temperature profile exhibits quite distinctly the linear trend mentioned previously.

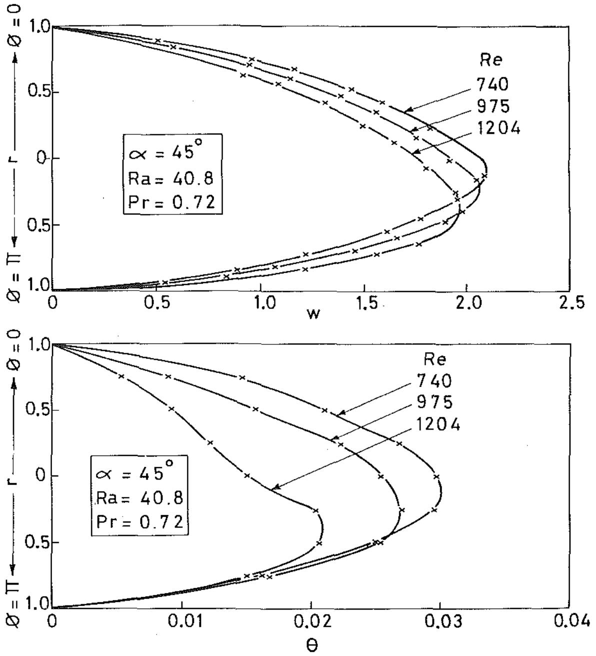

Fig. 3 Effect of Reynolds number on axial velocity (upper portion) and temperature (lower portion) profiles along $\phi = 0$, $\phi = \pi$

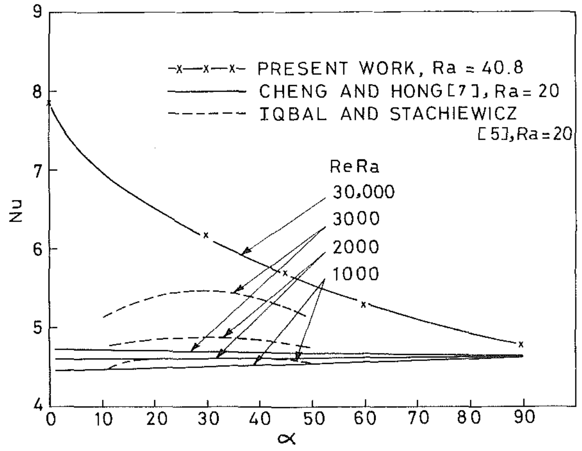

Fig. 4 Variation of Nusselt number with tube inclination

In Fig. 4, the Nusselt number is plotted as a function of the inclination angle. Also shown are some results of Iqbal and Stachiewicz [5] and Cheng and Hong [7]. The curves are characterized by the parameter Re Ra. The results of [7] show that at Re Ra = 1000, the Nusselt number increases slightly with inclination angle. At Re Ra = 3000, the trend is opposite but the dependence on inclination angle is still slight. At Re Ra = 30,000 (present work) the Nusselt number decreases significantly with inclination angle. The present values of Nusselt numbers of 7.85 and 4.76 for the limiting cases of α = 0 deg (horizontal tube) and α = 90 deg (vertical tube), respectively, agree within 6 percent with known numerical results [4, 1]. The fact that no optimum α was found in the present study supports the conclusion in [7] that the perturbation solution [5] is invalid.

References

1 Hallman, T. M., "Combined Forced and Free Convection in a Vertical Tube," PhD thesis, Purdue University, 1958.

2 Morton, B. R., "Laminar Convection in Uniformly Heated Vertical Pipes," *Journal of Fluid Mechanics*, Vol. 8, 1960, pp. 227–240.

3 Mori, Y., and Futagami, K., "Forced Convection Heat Transfer in Uniformly Heated Horizontal Tubes," *International Journal of Heat and Mass Transfer*, Vol. 10, 1967, pp. 1801–1813.

4 Faris, G. N., and Viskanta, R., "An Analysis of Laminar Combined Forced and Free Convection Heat Transfer in a Horizontal Tube," *International Journal of Heat and Mass Transfer*, Vol. 12, 1969, pp. 1295–1309.

5 Iqbal, M., and Stachiewicz, J. W., "Influence of Tube Orientation on Combined Free and Forced Laminar Convection Heat Transfer," JOURNAL OF HEAT TRANSFER, TRANS. ASME, Series C, Vol. 88, 1966, pp. 109–116.

6 Futagami, K., and Abe, F., "Combined Forced and Free Convective Heat Transfer in an Inclined Tube," *Trans. Japan Society of Mechanical Engineers*, Vol. 38, 1972, pp. 1799–1811.

7 Cheng, K. C., and Hong, S. W., "Combined Free and Forced Laminar Convection in Inclined Tubes," *Appl. Sci. Res.*, Vol. 27, Oct. 1972, pp. 19–38.

Transient Response of Straight Fins
Part II

N. V. Suryanarayana[1]

---

[1] Assoc. Professor, Michigan Technological University, Houghton, Mich. Mem. ASME.

Contributed by the Heat Transfer Division of THE AMERICAN SOCIETY OF MECHANICAL ENGINEERS. Manuscript received by the Heat Transfer Division September 29, 1975.

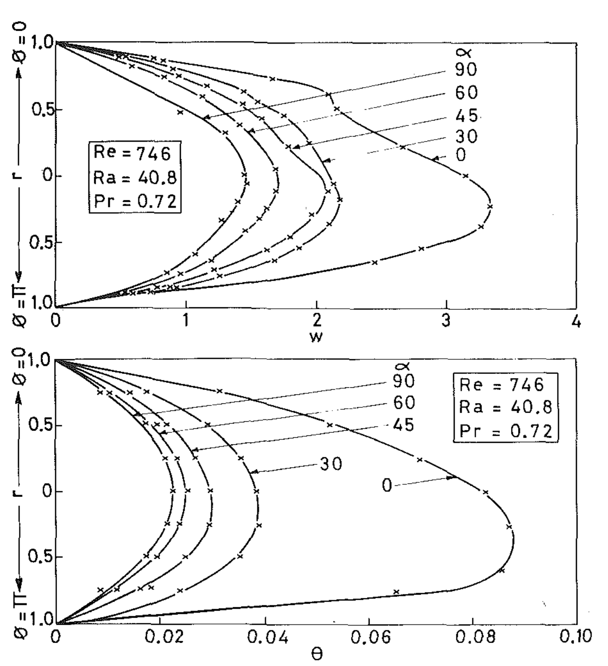

Fig. 2 Effect of tube inclination on axial velocity (upper portion) and temperature (lower portion) profiles along $\phi = 0$, $\phi = \pi$

ever, on a qualitative basis, the two results are seen to be in agreement.

The effect of Re on the velocity and temperature profiles is shown in Fig. 3 for an inclination angle of 45 deg, Pr = 0.72 and Ra = 40.8. As Re increases, the magnitude of the maximum velocity and the maximum temperature decreases and their locations shift toward the lower wall. These findings are consistent with the theoretical results contained in Figs. 2(*b*) and 3(*b*) of [7]. It is worth noting that at Re = 1204, the temperature profile exhibits quite distinctly the linear trend mentioned previously.

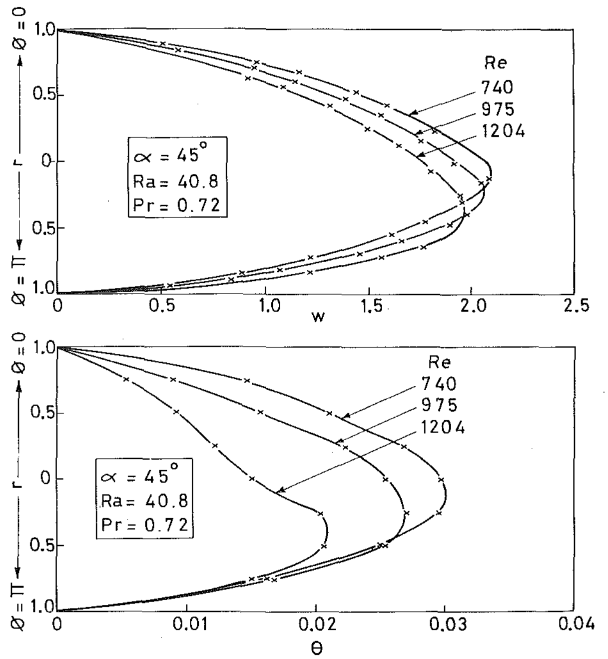

Fig. 3 Effect of Reynolds number on axial velocity (upper portion) and temperature (lower portion) profiles along $\phi = 0$, $\phi = \pi$

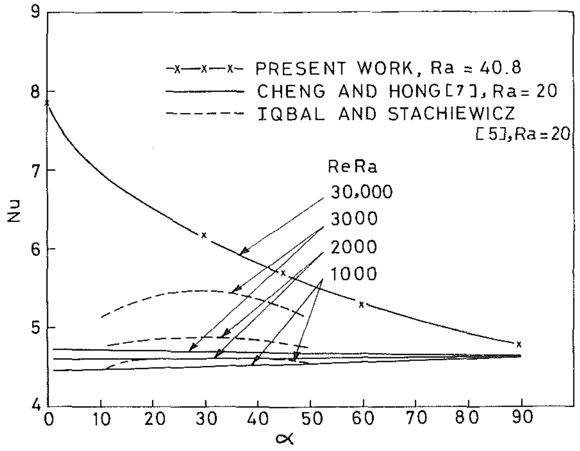

Fig. 4 Variation of Nusselt number with tube inclination

In Fig. 4, the Nusselt number is plotted as a function of the inclination angle. Also shown are some results of Iqbal and Stachiewicz [5] and Cheng and Hong [7]. The curves are characterized by the parameter Re Ra. The results of [7] show that at Re Ra = 1000, the Nusselt number increases slightly with inclination angle. At Re Ra = 3000, the trend is opposite but the dependence on inclination angle is still slight. At Re Ra = 30,000 (present work) the Nusselt number decreases significantly with inclination angle. The present values of Nusselt numbers of 7.85 and 4.76 for the limiting cases of $\alpha = 0$ deg (horizontal tube) and $\alpha = 90$ deg (vertical tube), respectively, agree within 6 percent with known numerical results [4, 1]. The fact that no optimum α was found in the present study supports the conclusion in [7] that the perturbation solution [5] is invalid.

References

1 Hallman, T. M., "Combined Forced and Free Convection in a Vertical Tube," PhD thesis, Purdue University, 1958.

2 Morton, B. R., "Laminar Convection in Uniformly Heated Vertical Pipes," *Journal of Fluid Mechanics*, Vol. 8, 1960, pp. 227–240.

3 Mori, Y., and Futagami, K., "Forced Convection Heat Transfer in Uniformly Heated Horizontal Tubes," *International Journal of Heat and Mass Transfer*, Vol. 10, 1967, pp. 1801–1813.

4 Faris, G. N., and Viskanta, R., "An Analysis of Laminar Combined Forced and Free Convection Heat Transfer in a Horizontal Tube," *International Journal of Heat and Mass Transfer*, Vol. 12, 1969, pp. 1295–1309.

5 Iqbal, M., and Stachiewicz, J. W., "Influence of Tube Orientation on Combined Free and Forced Laminar Convection Heat Transfer," JOURNAL OF HEAT TRANSFER, TRANS. ASME, Series C, Vol. 88, 1966, pp. 109–116.

6 Futagami, K., and Abe, F., "Combined Forced and Free Convective Heat Transfer in an Inclined Tube," *Trans. Japan Society of Mechanical Engineers*, Vol. 38, 1972, pp. 1799–1811.

7 Cheng, K. C., and Hong, S. W., "Combined Free and Forced Laminar Convection in Inclined Tubes," *Appl. Sci. Res.*, Vol. 27, Oct. 1972, pp. 19–38.

Transient Response of Straight Fins Part II

N. V. Suryanarayana[1]

---

[1] Assoc. Professor, Michigan Technological University, Houghton, Mich. Mem. ASME.

Contributed by the Heat Transfer Division of THE AMERICAN SOCIETY OF MECHANICAL ENGINEERS. Manuscript received by the Heat Transfer Division September 29, 1975.

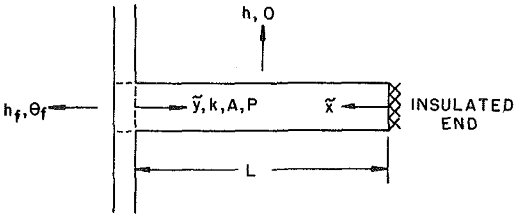

Fig. 1. Model of fin

The transient response of straight fins with the base of the fin subject to changes in temperature or heat flux was analyzed in an earlier paper.[2] There are many situations where heat transfer takes place from one fluid at temperature θ_f to another at temperature 0, separated by a solid boundary with fins on one side as shown. Within the limitations of one-dimensional analysis, a possible approximation to the boundary condition at $x = L$ is the convective boundary condition (ignoring the thermal resistance and capacity of the wall material shown dotted). Using this approximation, two cases will be considered: (a) when there is a step change in θ_f and (b) when θ_f, is a periodic function of time.

(a) **Step Change in Base Fluid Temperature.** Using dimensionless variables $x = \tilde{x}/L$, $t = \alpha\tau/L^2$, $\theta = \bar{\theta}/\theta_f$ and $m^2 = \frac{hP}{kA} L^2$, the differential equation for θ is

$$\frac{\partial^2\theta}{\partial x^2} - m^2\theta - \frac{\partial\theta}{\partial t} = 0 \tag{1}$$

$$t = 0, \theta = 0;\ x = 0, \frac{\partial\theta}{\partial x} = 0;\ x = 1, \frac{\partial\theta}{\partial x} + \text{Bi}\theta = \text{Bi}, \text{Bi} = \frac{h_f L}{K}$$

The solution to the equation, using Laplace transforms, is

$$\theta = \frac{\text{Bi}\cosh mx}{m\sinh m + \text{Bi}\cosh m} - 2\text{Bi}\sum_{n=1}^{\infty}\frac{V_n e^{-(m^2+V_n^2)t}\cos V_n x}{(m^2+V_n^2)[V_n\cos V_n + (1+\text{Bi})\sin V_n]} \tag{2}$$

where V_n's are the roots of $V\tan V = \text{Bi}$.

The base heat flux is given by

$$q''_{x=1} = \left.\frac{\partial\theta}{\partial x}\right|_{x=1} = \frac{m\text{Bi}\sinh m}{m\sinh m + \text{Bi}\cosh m} + 2\text{Bi}\sum_{n=1}^{\infty}\frac{V_n^2 e^{-(m^2+V_n^2)t}\sin V_n}{(m^2+V_n^2)[V_n\cos V_n + (1+\text{Bi})\sin V_n]} \tag{3}$$

For small values of t, a rapidly convergent approximate solution to equation (1) is

$$\theta = \frac{1-e^{-m^2t}}{m^2t}\text{Bi}\sum_{n=1}^{4}\left[2\left(\frac{t}{\pi}\right)^{1/2} e^{-f_n^2(x)4t} - f_n(x)\,\text{erfc}\,\frac{f_n(x)}{2\sqrt{t}}\right] - \frac{\text{Bi}^2}{m^4t}[1-(1+m^2t)e^{-m^2t}]\sum_{n=1}^{6} a_n\,\text{erfc}\,\frac{f_n(x)}{2\sqrt{t}} \tag{4}$$

where $f_n(x) = (1-x), (1+x), (3-x), (3+x), (5-x), (5+x)$ and $a_n = 1, 1, 3, 3, 2, 2$.

The base heat flux for small values of time is then given by

$$q''_{x=1} = \left.\frac{\partial\theta}{\partial x}\right|_{x=1} = \frac{1-e^{-m^2t}}{m^2t}\text{Bi}\left(1 - \text{erfc}\frac{2}{\sqrt{t}}\right) - \frac{\text{Bi}^2}{m^4t\sqrt{\pi t}}[1-(1+m^2t)e^{-m^2t}](1+2e^{-1/t}-e^{-4/t}-2e^{-9/t}) \tag{5}$$

From equation (2), it can be shown that the time required for the fin temperature at any point to reach values within 1 percent of the steady-state value at that point is given by

$$t_{st} = \frac{1}{m^2+V_1^2}\ln\left[\frac{200V_1(m\sinh m + \text{Bi}\cosh m)}{(m^2+V_1^2)[V_1\cos V_1 + (1+\text{Bi})\sin V_1]}\right] \tag{6}$$

(where V_1 is the first root of $V\tan V = \text{Bi}$).

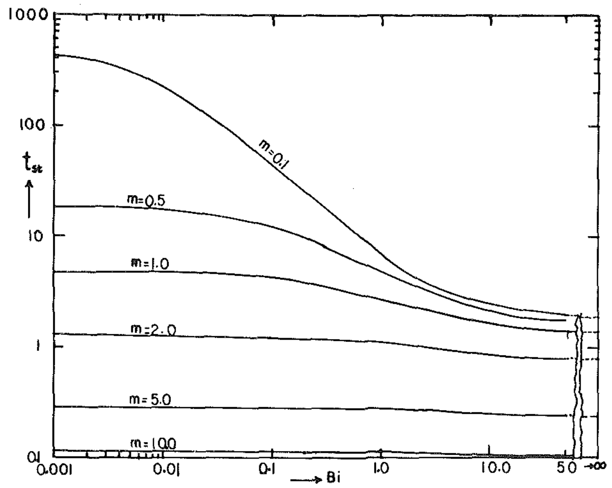

Fig. 2. Time to reach steady state

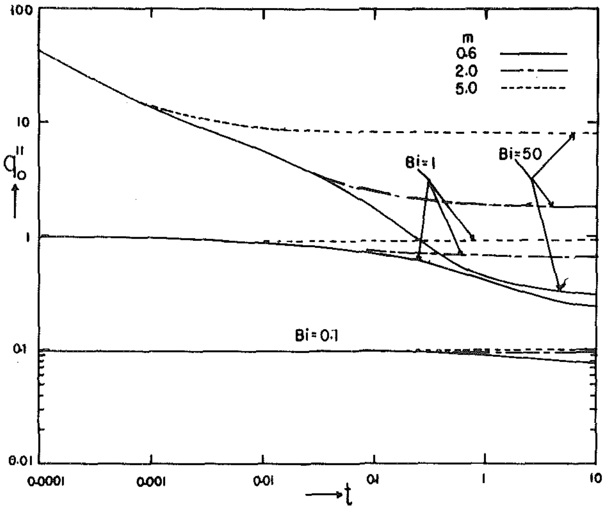

Fig. 3. Base heat flux

Fig. 2 is a plot of t_{st} for different values of Bi and m. For a given value of m, the dimensionless time decreases with an increase in Bi, as with an increase in Bi, the base heat flux is larger. Values of t_{st} for Bi → ∞ (corresponding to step change in base temperature, taken from reference [1]) are also indicated in the figure. From these values, and values of base temperatures from equation (2), it can be seen that where the ratio of Bi/m > 50, it can be regarded as a step change in base temperature.

Base heat flux values from equations (3) and (5) are shown in Fig. 3 for several values of Bi and m. For small values of time, the base heat flux is essentially constant for different values of m. For a given length of fin, an increase in the value of m, may be taken as indicating an increase in the value of the convective heat transfer coefficient h; thus, initially, the base heat flux is relatively insensitive to changes in values of h, indicating that most of the energy transfer from the base fluid goes to increase the internal energy of the fin. This trend is similar to that observed in the case of a step change in the base temperature [1]. From the boundary condition at $x = 1$, $\partial\theta/\partial x = \text{Bi}(1-\theta)$, one may expect that initially when $\theta_{x=1}$

---

[2] Suryanarayana, N. V., "Transient Response of Straight Fins," JOURNAL OF HEAT TRANSFER, TRANS. ASME.

is small, the heat flux $\partial\theta/\partial x \approx \text{Bi}$. This is confirmed in Fig. 3. From a comparison of values of base heat flux for Bi = 50, with those for a step change in base heat flux, it can be seen that even at such a high value of Bi as 50, the heat flux is approaching those values for a step change in temperature but is somewhat lower because of the convective resistance to heat transfer at the base.

(*b*) **Oscillating Base Fluid Temperature.** If the base fluid temperature is represented by $T_f = T_0 + T_A \sin \tilde{\omega}\tilde{t}$, equation (1) is to be solved subject to the boundary condition

$$x = 1, \frac{\partial\theta}{\partial x} + \text{Bi}\theta = \text{Bi}\theta_0 + \text{Bi}\sin\omega t$$

where

$$\theta = \frac{T - T_\infty}{T_A}, \theta_0 = \frac{T_0 - T_\infty}{T_A}, \omega = \frac{\tilde{\omega}L^2}{\alpha}$$

Because of the linearity of equation (1), it is sufficient to solve the equation with the boundary condition $x = 1$, $\partial\theta/\partial x + \text{Bi}\theta = \text{Bi}\sin\omega t$. The solution, using Laplace transforms, is given by:

$$\theta = \theta_A \sin(\omega t - \phi) + \sum_{n=1}^{\infty} \frac{2\omega\text{Bi}V_n e^{-(m^2+V_n{}^2)t}\cos V_n x}{[\omega^2 + (m^2 + V_n{}^2)^2][V_n \cos V_n + (1 + \text{Bi})\sin V_n]} \quad (7)$$

where

$$\theta_A = \text{temperature amplitude} = \frac{\text{Bi}\sqrt{(CF_1 + SF_2)^2 + (CF_2 - SF_1)^2}}{F_1{}^2 + F_2{}^2}$$

$$C = \cosh ax \cos bx;\ S = \sinh ax \sin bx$$

$$F_1 = a \sinh a \cos b - b \cosh a \sin b + \text{Bi} \cosh a \cos b$$

$$F_2 = a \cosh a \sin b + b \sinh a \cos b + \text{Bi} \sinh a \sin b$$

$$\phi = \tan^{-1}\frac{CF_2 - SF_1}{CF_1 + SF_2}$$

$a = \sqrt{r}\cos(\beta/2)$; $b = \sqrt{r}\sin(\beta/2)$; $r = \sqrt{m^4 + \omega^2}$, $\beta = \tan^{-1}(\omega/m^2)$ and V_n's are the roots of $V \tan V = \text{Bi}$. The base heat flux is given by

$$q''_{x=1} = q''_{0A}\sin(\omega t - \phi') - \sum_{n=1}^{\infty}\frac{2\omega\text{Bi}V_n{}^2 e^{-(m^2+V_n{}^2)t}\sin V_n}{[\omega^2 + (m^2 + V_n{}^2)^2][V_n \cos V_n + (1 + \text{Bi})\sin V_n]} \quad (8)$$

where q''_{0A} = Base heat flux amplitude under steady-state conditions

$$= \frac{\text{Bi}}{F_1{}^2 + F_2{}^2}[(F_1F_3 + F_2F_4)^2 + (F_1F_4 - F_2F_3)^2]^{1/2}$$

$$\phi' = \tan^{-1}\left(\frac{F_1F_4 - F_2F_3}{F_1F_3 + F_2F_4}\right)$$

$$F_3 = a \sinh a \cos b - b \cosh a \sin b$$

$$F_4 = a \cosh a \sin b + b \sinh a \cos b$$

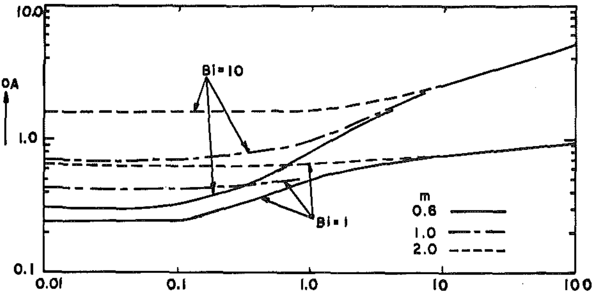

Fig. 4. Heat flux amplitude

Table 1 Time required to attain steady state

Biot No.	ω ↓ m→	0.6	1.0	2.0	5.0
1.0	0.1	2.15	1.15	0.296	0.0667
	1.0	3.98	2.4	0.777	0.156
	10.0	4.60	2.94	1.13	0.245
	100.0	7.79	4.94	0.999	0.367
10.0	0.1	0.707	0.503	0.191	0.051
	1.0	1.63	1.24	0.57	0.136
	10.0	2.08	1.66	0.863	0.22
	100.0	3.31	2.62	1.34	0.327

In equations (7) and (8) the first terms represent the steady periodic response to the oscillating base fluid temperature, and the other terms, the initial transient response.

If we define the time required to attain steady state t_{st} as that required for the temperature at any point to be within 1 percent of the amplitude of temperature oscillation at that point, then

$$t_{st} = \frac{1}{m^2 + V_1{}^2}\ln\left[\frac{200\omega\text{Bi}V_1}{[\omega^2 + (m^2 + V_1{}^2)^2][V_1\cos V_1 + (1 + \text{Bi})\sin V_1]}\right] \quad (9)$$

A few values of t_{st} computed from equation (9) are given in Table 1.

In general, the time to attain steady state increases with an increase in the frequency of oscillation and corresponding to $\omega = 100$, the time to attain steady state is approximately the same as that for a step change in the base fluid temperature. From an examination of the values of temperature amplitude, it is seen that for the range of values of Bi (0.1–50) and m (0.1–10) considered, the temperature amplitude is the same as the steady temperature response for a step change in the base fluid temperature, at low frequencies corresponding to $\omega \leq 0.1$. For higher values of ω, the temperature oscillation is attenuated and for $\omega = 100$, for the major part of the fin (except very close to the base at $x = 1$), the temperature amplitude is considerably attenuated. This indicates that if the base fluid temperature is expressed as a Fourier series (as a function of time), neglecting terms corresponding to $\omega > 100$, will not introduce any appreciable error.

A plot of base heat flux amplitude for different values of ω, Bi and m is shown in Fig. 4. The base heat flux amplitude increases with ω, m, and Bi but for $\omega > 10$, the base heat flux amplitude for a given Bi, is relatively insensitive to changes in m.

Thermal Analysis of a Fast-Moving Slab in Two Adjacent Temperature Chambers

L. S. Yao,[1] C. L. Tien[2] and S. A. Berger[2]

---

[1] The Rand Corp., Santa Monica, Calif.

[2] Department of Mechanical Engineering, University of California, Berkeley, Calif.

Contributed by the Heat Transfer Division of THE AMERICAN SOCIETY OF MECHANICAL ENGINEER. Manuscript received by the Heat Transfer Division December 1, 1975.

is small, the heat flux $\partial\theta/\partial x \approx \mathrm{Bi}$. This is confirmed in Fig. 3. From a comparison of values of base heat flux for Bi = 50, with those for a step change in base heat flux, it can be seen that even at such a high value of Bi as 50, the heat flux is approaching those values for a step change in temperature but is somewhat lower because of the convective resistance to heat transfer at the base.

(*b*) **Oscillating Base Fluid Temperature.** If the base fluid temperature is represented by $T_f = T_0 + T_A \sin \tilde{\omega}\tilde{t}$, equation (1) is to be solved subject to the boundary condition

$$x = 1, \frac{\partial\theta}{\partial x} + \mathrm{Bi}\theta = \mathrm{Bi}\theta_0 + \mathrm{Bi}\sin\omega t$$

where

$$\theta = \frac{T - T_\infty}{T_A}, \theta_0 = \frac{T_0 - T_\infty}{T_A}, \omega = \frac{\tilde{\omega}L^2}{\alpha}$$

Because of the linearity of equation (1), it is sufficient to solve the equation with the boundary condition $x = 1$, $\partial\theta/\partial x + \mathrm{Bi}\theta = \mathrm{Bi}\sin\omega t$. The solution, using Laplace transforms, is given by:

$$\theta = \theta_A \sin(\omega t - \phi) + \sum_{n=1}^{\infty} \frac{2\omega \mathrm{Bi} V_n e^{-(m^2+V_n{}^2)t} \cos V_n x}{[\omega^2 + (m^2 + V_n{}^2)^2][V_n \cos V_n + (1 + \mathrm{Bi}) \sin V_n]} \qquad (7)$$

where

$$\theta_A = \text{temperature amplitude} = \frac{\mathrm{Bi}\sqrt{(CF_1 + SF_2)^2 + (CF_2 - SF_1)^2}}{F_1{}^2 + F_2{}^2}$$

$$C = \cosh ax \cos bx; S = \sinh ax \sin bx$$

$$F_1 = a \sinh a \cos b - b \cosh a \sin b + \mathrm{Bi} \cosh a \cos b$$

$$F_2 = a \cosh a \sin b + b \sinh a \cos b + \mathrm{Bi} \sinh a \sin b$$

$$\phi = \tan^{-1} \frac{CF_2 - SF_1}{CF_1 + SF_2}$$

$a = \sqrt{r}\cos(\beta/2)$; $b = \sqrt{r}\sin(\beta/2)$; $r = \sqrt{m^4 + \omega^2}$, $\beta = \tan^{-1}(\omega/m^2)$ and V_n's are the roots of $V \tan V = \mathrm{Bi}$. The base heat flux is given by

$$q''_{x=1} = q''_{0A} \sin(\omega t - \phi') - \sum_{n=1}^{\infty} \frac{2\omega \mathrm{Bi} V_n{}^2 e^{-(m^2+V_n{}^2)t} \sin V_n}{[\omega^2 + (m^2 + V_n{}^2)^2][V_n \cos V_n + (1 + \mathrm{Bi}) \sin V_n]} \qquad (8)$$

where q''_{0A} = Base heat flux amplitude under steady-state conditions

$$= \frac{\mathrm{Bi}}{F_1{}^2 + F_2{}^2}[(F_1F_3 + F_2F_4)^2 + (F_1F_4 - F_2F_3)^2]^{1/2}$$

$$\phi' = \tan^{-1}\left(\frac{F_1F_4 - F_2F_3}{F_1F_3 + F_2F_4}\right)$$

$$F_3 = a \sinh a \cos b - b \cosh a \sin b$$

$$F_4 = a \cosh a \sin b + b \sinh a \cos b$$

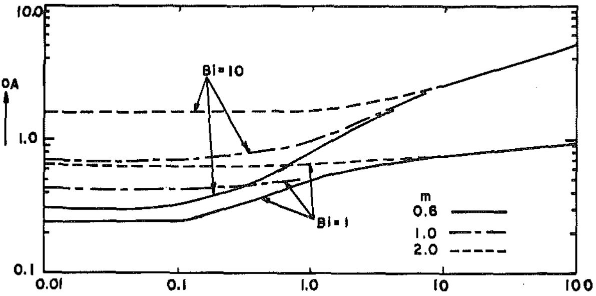

Fig. 4. Heat flux amplitude

Table 1 Time required to attain steady state

Biot No.	ω ↓ m →	0.6	1.0	2.0	5.0
1.0	0.1	2.15	1.15	0.296	0.0667
	1.0	3.98	2.4	0.777	0.156
	10.0	4.60	2.94	1.13	0.245
	100.0	7.79	4.94	0.999	0.367
10.0	0.1	0.707	0.503	0.191	0.051
	1.0	1.63	1.24	0.57	0.136
	10.0	2.08	1.66	0.863	0.22
	100.0	3.31	2.62	1.34	0.327

In equations (7) and (8) the first terms represent the steady periodic response to the oscillating base fluid temperature, and the other terms, the initial transient response.

If we define the time required to attain steady state t_{st} as that required for the temperature at any point to be within 1 percent of the amplitude of temperature oscillation at that point, then

$$t_{st} = \frac{1}{m^2 + V_1{}^2} \ln \left[\frac{200\omega \mathrm{Bi} V_1}{[\omega^2 + (m^2 + V_1{}^2)^2][V_1 \cos V_1 + (1 + \mathrm{Bi}) \sin V_1]}\right] \qquad (9)$$

A few values of t_{st} computed from equation (9) are given in Table 1.

In general, the time to attain steady state increases with an increase in the frequency of oscillation and corresponding to $\omega = 100$, the time to attain steady state is approximately the same as that for a step change in the base fluid temperature. From an examination of the values of temperature amplitude, it is seen that for the range of values of Bi (0.1–50) and m (0.1–10) considered, the temperature amplitude is the same as the steady temperature response for a step change in the base fluid temperature, at low frequencies corresponding to $\omega \leq 0.1$. For higher values of ω, the temperature oscillation is attenuated and for $\omega = 100$, for the major part of the fin (except very close to the base at $x = 1$), the temperature amplitude is considerably attenuated. This indicates that if the base fluid temperature is expressed as a Fourier series (as a function of time), neglecting terms corresponding to $\omega > 100$, will not introduce any appreciable error.

A plot of base heat flux amplitude for different values of ω, Bi and m is shown in Fig. 4. The base heat flux amplitude increases with ω, m, and Bi but for $\omega > 10$, the base heat flux amplitude for a given Bi, is relatively insensitive to changes in m.

Thermal Analysis of a Fast-Moving Slab in Two Adjacent Temperature Chambers

L. S. Yao,[1] C. L. Tien[2] and S. A. Berger[2]

---

[1] The Rand Corp., Santa Monica, Calif.

[2] Department of Mechanical Engineering, University of California, Berkeley, Calif.

Contributed by the Heat Transfer Division of THE AMERICAN SOCIETY OF MECHANICAL ENGINEER. Manuscript received by the Heat Transfer Division December 1, 1975.

Nomenclature

c = specific heat
d = half-width of the slab, Fig. 1
k = thermal conductivity
Nu = Nusselt number, equations (6), (10), and (15)
P = Peclet number, $\rho cud/k$
T = temperature
T_0 = initial temperature, Fig. 1
T_w = wall temperature, Fig. 1
u = slab moving speed, Fig. 1
x, y = coordinates, Fig. 1
θ = dimensionless temperature, $(T - T_0)/(T_w - T_0)$
η = similarity variable, equation (5)
ρ = density

Subscripts

1, 2, 3, 4 = regions I, II, III, IV, Fig. 1

Introduction

Thermal analysis of a moving slab has been a subject of great importance in many manufacturing processes, such as hot-rolling, continuous casting, dip-forming and quenching [1–4],[3] as well as in emergency core cooling of water reactors [5]. The temperature distribution and the heat loss associated with a moving slab between two adjacent chambers have been analyzed by Horvay [1, 2] by use of the Wiener-Hopf technique. His analysis, however, is restricted to a slowly-moving slab. For a fast-moving slab the heat transfer mechanism is somewhat different than for a slowly-moving one. Some processes, such as the dip-forming process of producing a continuous copper rod [3, 4], can be shown to involve fast-moving slabs. It is the purpose of this note to present the thermal analysis of a fast-moving slab. Since the mathematical formulation for the moving slab problem is identical to that for the thermal entrance problem with slug flow, the terminology associated with the Graetz problem is used to describe the physics of a fast-moving slab.

Analysis

The idealized physical model under consideration is an infinitely extended slab moving at a constant speed, u, from the left chamber at temperature T_0 to the right chamber at temperature T_w. The thermal field can be divided into four regions in the slab, see Tien and Yao [5], as shown in Fig. 1.

The transient two-dimensional conduction equation in the coordinate system moving with a constant velocity, u, can be written as [1, 5]

$$\rho cu \frac{\partial T}{\partial x} = k\left(\frac{\partial^2 T}{\partial x^2} + \frac{\partial^2 T}{\partial y^2}\right) \tag{1}$$

Equation (1) can be expressed in the following nondimensional form

$$\theta_{x_1} - \frac{1}{P}(\theta_{x_1x_1} + \theta_{y_1y_1}) = 0 \tag{2}$$

where $\theta = (T - T_0)/(T_w - T_0)$ is the nondimensional temperature; $x_1 = x/d$; $y_1 = y/d$; P = $\rho cud/k$, Peclet number; ρ, the density; c, the specific heat; k, the thermal conductivity; d, the half-width of the slab and the characteristic length in region I. Subscripts denote derivatives. The associated boundary conditions are

$$\begin{gathered} x_1 \to -\infty \;:\; \theta = 0 \\ x_1 \to \infty \;:\; \theta = 1 \\ y_1 = \pm 1, x_1 \geq 0 \;:\; \theta = 1 \\ y_1 = \pm 1, x_1 < 0 \;:\; \theta_{y_1} = 0 \end{gathered} \tag{3}$$

For large values of P corresponding to the case of a fast-moving slab, the conduction is negligible in region I compared with convection. Equation (2) thus becomes

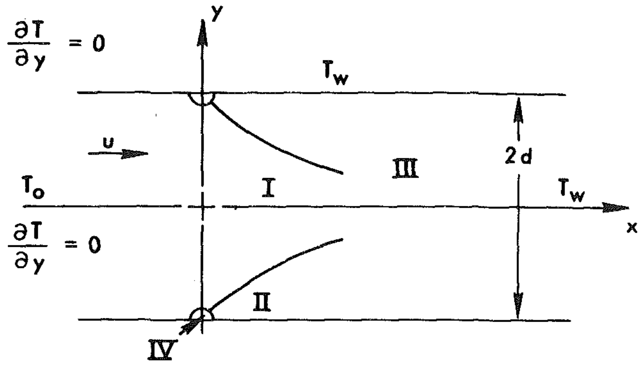

Fig. 1 Physical model and coordinates

$$\theta_{x_1} = 0 \tag{4}$$

with the appropriate boundary condition from equation (3) is

$$x_1 \to \infty \;:\; \theta = 0 \tag{5}$$

The solution is readily seen as

$$\theta = 0 \tag{6}$$

which indicates that region I is undisturbed.

Region II is the thermal boundary layer where heat conduction normal to the wall is of the same order as the convection term. A sketched normal coordinate in this region along the upper surface is introduced, defined as $y_2 = \sqrt{P}\,(1 - y_1)$, reflecting the fact that the thickness of the thermal boundary layer is proportional to $P^{-1/2}$. The conduction equation, after neglecting smaller order terms becomes,

$$\theta_{x_1} = \theta_{y_2y_2} \tag{7}$$

The solution for equation (7) is the classic Graetz solution, and is the complementary error function

$$\theta(\eta) = \operatorname{erfc}(\eta) \tag{8}$$

satisfying the boundary conditions:

$$\left.\begin{array}{l} x_1 = 0, |y_1| \leq 1 \;:\; \theta = 0, \\ x_1 \geq 0, y_2 \to \infty \;:\; \theta \to 0, \end{array}\right\} \begin{array}{l}\text{(matching conditions} \\ \text{between regions I} \\ \text{and II)}\end{array}$$
$$x_1 \geq 0, y_2 = 0 \;:\; \theta = 1, \tag{9}$$

where $\eta = y_2/(2\sqrt{x_1})$ is the similarity variable. The Nusselt number with respect to d and $(T_0 - T_w)$ can be easily derived from equation (8) and can be written as

$$(\mathrm{Nu}_x)_2 = \frac{\sqrt{P}}{\sqrt{\pi x_1}} \tag{10}$$

In region III, two thermal boundary layers merge at $x_3 = x_1/P$, and their thickness is bounded by the half-width of the slab. The conduction equation in this region can be written as

$$\theta_{x_3} = \theta_{y_1y_1} \tag{11}$$

with the boundary conditions

$$\begin{gathered} x_3 \to 0 \;:\; \theta \to 0, \quad \text{(matching condition between regions I and III)} \\ y_1 = \pm 1, x_3 > 0 \;:\; \theta = 1, \\ y_1 = 0, x_3 > 0 \;:\; \theta_{y_3} = 0, \quad \text{(symmetry condition)} \end{gathered} \tag{12}$$

---

[3] Numbers in brackets designate References at end of technical note.

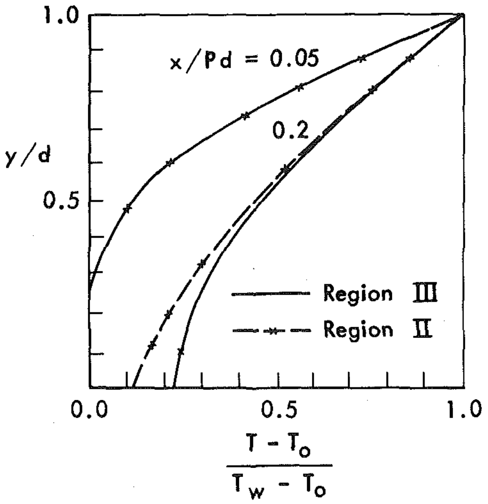

Fig. 2 Temperature distribution in regions II and III

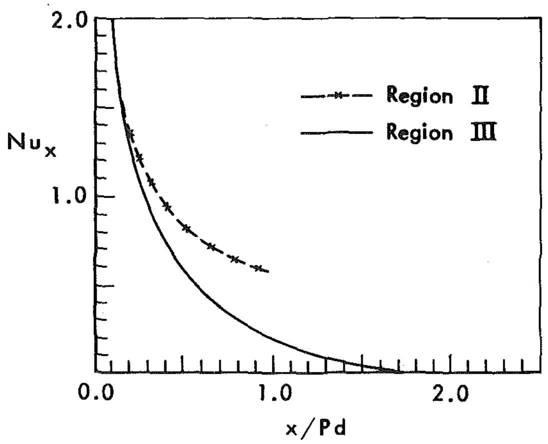

Fig. 3 Nondimensional heat flux distribution in regions II and III

The solution of (11) and (12) can be expressed as the following convergent infinite series:

$$\theta = 1 - \sum_{n=0}^{\infty} \frac{4\cdot(-1)^n}{(2n+1)\pi}\cos\left(n\pi+\frac{\pi}{2}\right)y_1 e^{-(n\pi+\pi/2)^2 x_3} \tag{13}$$

The Nusselt number is found to be

$$(\mathrm{Nu}_x)_3 = 2\cdot\sum_{n=0}^{\infty} e^{-(n\pi+\pi/2)^2 x_3} \tag{14}$$

Both axial and normal heat conduction are important in the neighborhood of the interface of the two chambers. This is region IV, where $x_4 = \mathrm{P}x_1$, and $y_4 = \mathrm{P}(1 + y_1)$ are appropriate nondimensional coordinates. The size of region IV is inversely proportional to the Peclet number. Therefore, it is very small for large P; however, the steep temperature gradient in this region plays an important role in the moving-slab problem. It is worthwhile to point out that region IV occupies the whole slab when P is small (slowly-moving slab), which is the case to which Horvay's analysis applies. The conduction equation in this region is

$$\theta_{x_4} = \theta_{x_4x_4} + \theta_{y_4y_4} \tag{15}$$

The associated boundary conditions are

$$y_4 = 0, x_4 \geq 0 \;:\; \theta = 1,$$

$$x_4 < 0 \;:\; \theta_{y_4} = 0,$$

$$\left.\begin{array}{l} x_4 \to -\infty \;:\; \theta \to 0, \\ y_4 \to \infty \;:\; \theta \to 0, \end{array}\right. \quad \text{(matching conditions between Regions I and IV)}$$

$$x_4 \to \infty \;:\; \theta \text{ is bounded} \tag{16}$$

Carrier, Krook, and Pearson [6] solved the equation (15) with conditions (16) by the Wiener-Hopf techniques. The solution is

$$\theta = 1 - \mathrm{erf}\left[\sqrt{\frac{-x_4 + \sqrt{x_4{}^2 + y_4{}^2}}{2}}\right] \tag{17}$$

for $x_4 \geq 0$. They do not give the solution for $x_4 < 0$, explicitly. However, it can be easily obtained, and is

$$\theta = \mathrm{erfc}\sqrt{|x_4|} - \mathrm{erf}\left[\sqrt{\frac{-x_4 + \sqrt{x_4{}^2 + y_4{}^2}}{2}}\right] (x_4 < 0) \tag{18}$$

The corresponding Nusselt number is

$$(\mathrm{Nu}_x)_4 = -\frac{\sqrt{\mathrm{P}}}{\sqrt{\pi x_1}} \tag{19}$$

Results and Discussion

Comparison of the temperature distributions and Nusselt numbers in regions II and III, in Fig. 2 and 3, respectively, indicates that the domain of region II is $x/\mathrm{P}d \leq 0.13$, and the solution of region II is included in region III. This may be a consequence of the zero displacement effect of the thermal boundary layer. The infinite series solution of region III can be taken as the solution for the entire thermal entrance problem, at least under the slug flow assumption. However, the series diverges at $x = 0$, where the solution of region IV applies.

The temperature distribution in region IV is presented in Fig. 4. The temperature approaches a uniformly distributed profile as one moves away from the interface along the negative x-axis. The shape of region IV for $x_4 \geq 0$ can be obtained from equation (17) at the location where its temperature matches with the temperature of region I within 0.05 percent. This gives

$$(1 - y_1)^2 = \frac{(2\times1.99)^2}{\mathrm{P}}\left(x_1 + \frac{1.99^2}{\mathrm{P}}\right), x_1 \geq 0 \tag{20}$$

which is a parabola intersecting the y-axis at $(1 - y_1) = 2 \times 1.99^2/\mathrm{P}$. For $\mathrm{P} = 7.92$, $y_1 = 1$. Thus, for $\mathrm{P} > 8$, region IV occupies the whole slab, for which Horvay's solution applies. For $\mathrm{P} > 8$, Horvay's series solution diverges. This is obvious because the size of region IV is not large enough to cover the whole slab, and has to be considered independently, as in this note.

The shape of region II, from equation (8) is

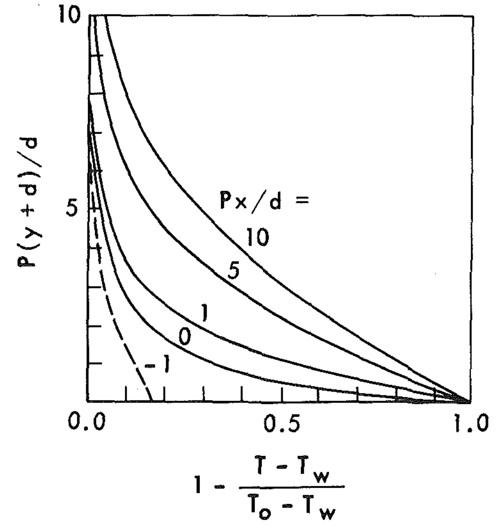

Fig. 4 Temperature distribution in region IV

$$(1 - y_1)^2 = \frac{(2 \times 1.99)^2}{P} x_1 \tag{21}$$

Equations (20) and (21) differ only by terms of order $1/P^2$ and, therefore, to lowest order in P the solution for region II is included in the solution for region IV.

It is of interest to note that although region II was introduced on physical grounds (that is, where conduction and convection are of equal importance) the results indicate that the solution for regions IV and III, in fact, covers the entire physical domain so that the separate solution for region II is not really required.

The thermal behavior of the moving rod is essentially similar to that of the moving slab. In particular, the curvature effect is negligible in regions II and IV due to their small size; therefore, the solutions for these two regions can be applied directly to the case of the moving rod.

References

1 Horvay, G., "Temperature Distribution in a Slab Moving From a Chamber at One Temperature to a Chamber at Another Temperature," JOURNAL OF HEAT TRANSFER, TRANS. ASME, Series C, Vol. 83, 1961, pp. 391–402.

2 Horvay, G., "The Dip-Forming Process," JOURNAL OF HEAT TRANSFER, TRANS. ASME, Series C, Vol. 87, 1965, pp. 1–16.

3 Carreker, R. P., Jr., "Dip-Forming—A Continuous Casting Process," *J. Metals*, Vol. 15, 1963, pp. 774–780.

4 Carreker, R. P., Jr., and Hurst, R., "Dip-Formed Copper Rod—Pilot to Production," *Wire and Wire Products*, Vol. 39, 1964, pp. 1161–3, 1165–7, 1233.

5 Tien, C. L., and Yao, L. S. "Analysis of Conduction-Controlled Rewetting of a Vertical Surface," JOURNAL OF HEAT TRANSFER, TRANS. ASME, Series C, Vol. 97, 1975, pp. 161–165.

6 Carrier, G. G., Krook, M., and Pearson, G. E., *Functions of a Complex Variable*, McGraw-Hill, New York, 1966.

Transient Temperature Rise in Layered Media

H. Domingos[1] and D. Voelker[1]

An analytic expression for the temperature rise produced by a heat-generating layer in contact with a large body is obtained by the Laplace transform method. The solution is used to study the temperature distribution in thin film nichrome resistors under transient conditions.

Nomenclature

x = distance
t = time
θ = temperature
D = thermal diffusivity
Q = power density
ρ = mass density
c = specific heat at constant pressure
L = thickness of heat producing layer
Θ = Laplace transform of temperature
s = Laplace transform variable
A,B = constants of integration
λ = defined by equation (9)
F_{n1}, F_{n2}, G_n = defined by equations (12)–(14)

Subscripts

1,2 = refer to regions 1 and 2, respectively, indicated in equations (1) and (2)
n = index of summation

1 Introduction

The problem of one-dimensional transient heat flow in composite slabs has been treated by many authors over the years. Several examples, as well as an outline of the Laplace transform method, are given in Carslaw and Jaeger [1].[2] The problem has been solved more recently by Giere for the case of a slab of two materials of finite thickness with constant flux and zero flux at the external boundaries [2]. The solution has also been published for the general case of composite sections with internal heat generation, discrete sources or sinks at the interface, and heat transfer at the external boundaries [3]. A review of the literature on this topic is contained in a book by Ozisik [4].

One problem of considerable importance in modern technology occurs when a layer of heat producing material is in intimate contact with a much larger body which acts as a heat sink. This problem has been investigated in the study of thin film resistors subjected to single, large power pulses [5] but is applicable to a wide range of situations, such as the temperature distribution in thin and thick film hybrid circuits, second breakdown in silicon monolithic integrated circuits, dielectric heating in cables, etc. The problem has been addressed, but not solved, for linear heat conduction [6]. The present paper presents an analytic solution obtained by the Laplace transform method.

2 Solution

Consider a semi-infinite body composed of two materials, one of which extends from $x = 0$ to $x = L$. This layer begins to generate heat at a uniform rate Q beginning at $t = 0$. The remaining material contacts this layer perfectly, with no thermal interface resistance. The boundary of the heat producing layer at $x = 0$ is insulated. Prior to the generation of heat the entire body is at zero temperature.

The temperature distribution is given by the solution to the heat diffusion equation in each region

$$\frac{\partial\theta_1(x,t)}{\partial t} = \frac{D_1\partial^2\theta_1(x,t)}{\partial x^2} + \frac{Q}{\rho_1 c_1} \quad 0 \le x < L \tag{1}$$

$$\frac{\partial\theta_2(x,t)}{\partial t} = \frac{D_2\partial^2\theta_2(x,t)}{\partial x^2} \quad L \le x < \infty \tag{2}$$

where $\theta(x,t)$ is the temperature, D is the diffusivity, Q is the power density, ρ is the density, and c is the specific heat. The subscripts refer to region 1 or region 2.

The following initial and boundary conditions hold.

$$\theta_1(x,0) = 0, \quad \theta_2(x,0) = 0, \quad \frac{\partial\theta_1}{\partial x}(0,t) = 0 \tag{3}$$

In addition, the temperature goes to zero at infinity. At the interface continuity of temperature and flux requires that

$$\theta_1(L,t) = \theta_2(L,t), \quad k_1\frac{\partial\theta_1(L,t)}{\partial x} = k_2\frac{\partial\theta_2(L,t)}{\partial x} \tag{4}$$

where k is the thermal conductivity.

After Laplace transformation, the solutions of equations (1) and (2) are

$$\Theta_1(x,s) = A_1 \exp\,(x\sqrt{s/D_1}) + A_2 \exp\,(-x\sqrt{s/D_1}) + \frac{Q}{\rho_1 c_1 s^2} \tag{5}$$

---

[1] Clarkson College, Potsdam, N.Y.

Contributed by the Heat Transfer Division of THE AMERICAN SOCIETY OF MECHANICAL ENGINEERS. Manuscript received by the Heat Transfer Division September 22, 1975.

[2] Number in brackets designate References at end of technical note.

$$(1-y_1)^2 = \frac{(2 \times 1.99)^2}{P} x_1 \tag{21}$$

Equations (20) and (21) differ only by terms of order $1/P^2$ and, therefore, to lowest order in P the solution for region II is included in the solution for region IV.

It is of interest to note that although region II was introduced on physical grounds (that is, where conduction and convection are of equal importance) the results indicate that the solution for regions IV and III, in fact, covers the entire physical domain so that the separate solution for region II is not really required.

The thermal behavior of the moving rod is essentially similar to that of the moving slab. In particular, the curvature effect is negligible in regions II and IV due to their small size; therefore, the solutions for these two regions can be applied directly to the case of the moving rod.

References

1 Horvay, G., "Temperature Distribution in a Slab Moving From a Chamber at One Temperature to a Chamber at Another Temperature," JOURNAL OF HEAT TRANSFER, TRANS. ASME, Series C, Vol. 83, 1961, pp. 391-402.

2 Horvay, G., "The Dip-Forming Process," JOURNAL OF HEAT TRANSFER, TRANS. ASME, Series C, Vol. 87, 1965, pp. 1-16.

3 Carreker, R. P., Jr., "Dip-Forming—A Continuous Casting Process," *J. Metals*, Vol. 15, 1963, pp. 774-780.

4 Carreker, R. P., Jr., and Hurst, R., "Dip-Formed Copper Rod—Pilot to Production," *Wire and Wire Products*, Vol. 39, 1964, pp. 1161-3, 1165-7, 1233.

5 Tien, C. L., and Yao, L. S. "Analysis of Conduction-Controlled Rewetting of a Vertical Surface," JOURNAL OF HEAT TRANSFER, TRANS. ASME, Series C, Vol. 97, 1975, pp. 161-165.

6 Carrier, G. G., Krook, M., and Pearson, G. E., *Functions of a Complex Variable*, McGraw-Hill, New York, 1966.

Transient Temperature Rise in Layered Media

H. Domingos[1] and D. Voelker[1]

An analytic expression for the temperature rise produced by a heat-generating layer in contact with a large body is obtained by the Laplace transform method. The solution is used to study the temperature distribution in thin film nichrome resistors under transient conditions.

Nomenclature

x = distance
t = time
θ = temperature
D = thermal diffusivity
Q = power density
ρ = mass density
c = specific heat at constant pressure
L = thickness of heat producing layer
Θ = Laplace transform of temperature
s = Laplace transform variable
A,B = constants of integration
λ = defined by equation (9)
F_{n1}, F_{n2}, G_n = defined by equations (12)-(14)

Subscripts

1,2 = refer to regions 1 and 2, respectively, indicated in equations (1) and (2)
n = index of summation

1 Introduction

The problem of one-dimensional transient heat flow in composite slabs has been treated by many authors over the years. Several examples, as well as an outline of the Laplace transform method, are given in Carslaw and Jaeger [1].[2] The problem has been solved more recently by Giere for the case of a slab of two materials of finite thickness with constant flux and zero flux at the external boundaries [2]. The solution has also been published for the general case of composite sections with internal heat generation, discrete sources or sinks at the interface, and heat transfer at the external boundaries [3]. A review of the literature on this topic is contained in a book by Ozisik [4].

One problem of considerable importance in modern technology occurs when a layer of heat producing material is in intimate contact with a much larger body which acts as a heat sink. This problem has been investigated in the study of thin film resistors subjected to single, large power pulses [5] but is applicable to a wide range of situations, such as the temperature distribution in thin and thick film hybrid circuits, second breakdown in silicon monolithic integrated circuits, dielectric heating in cables, etc. The problem has been addressed, but not solved, for linear heat conduction [6]. The present paper presents an analytic solution obtained by the Laplace transform method.

2 Solution

Consider a semi-infinite body composed of two materials, one of which extends from $x = 0$ to $x = L$. This layer begins to generate heat at a uniform rate Q beginning at $t = 0$. The remaining material contacts this layer perfectly, with no thermal interface resistance. The boundary of the heat producing layer at $x = 0$ is insulated. Prior to the generation of heat the entire body is at zero temperature.

The temperature distribution is given by the solution to the heat diffusion equation in each region

$$\frac{\partial \theta_1(x,t)}{\partial t} = \frac{D_1 \partial^2 \theta_1(x,t)}{\partial x^2} + \frac{Q}{\rho_1 c_1} \quad 0 \le x < L \tag{1}$$

$$\frac{\partial \theta_2(x,t)}{\partial t} = \frac{D_2 \partial^2 \theta_2(x,t)}{\partial x^2} \quad L \le x < \infty \tag{2}$$

where $\theta(x,t)$ is the temperature, D is the diffusivity, Q is the power density, ρ is the density, and c is the specific heat. The subscripts refer to region 1 or region 2.

The following initial and boundary conditions hold.

$$\theta_1(x,0) = 0, \quad \theta_2(x,0) = 0, \quad \frac{\partial \theta_1}{\partial x}(0,t) = 0 \tag{3}$$

In addition, the temperature goes to zero at infinity. At the interface continuity of temperature and flux requires that

$$\theta_1(L,t) = \theta_2(L,t), \quad k_1 \frac{\partial \theta_1(L,t)}{\partial x} = k_2 \frac{\partial \theta_2(L,t)}{\partial x} \tag{4}$$

where k is the thermal conductivity.

After Laplace transformation, the solutions of equations (1) and (2) are

$$\Theta_1(x,s) = A_1 \exp(x\sqrt{s/D_1}) + A_2 \exp(-x\sqrt{s/D_1}) + \frac{Q}{\rho_1 c_1 s^2} \tag{5}$$

---

[1] Clarkson College, Potsdam, N.Y.

Contributed by the Heat Transfer Division of THE AMERICAN SOCIETY OF MECHANICAL ENGINEERS. Manuscript received by the Heat Transfer Division September 22, 1975.

[2] Number in brackets designate References at end of technical note.

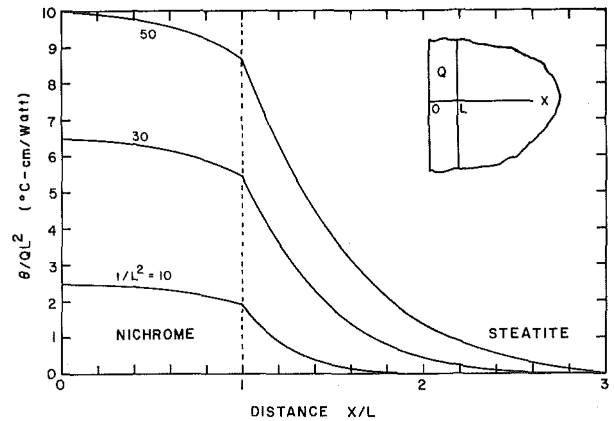

Fig. 1 Normalized temperature distribution—the heat is generated in a nichrome layer in perfect thermal contact with a steatite substrate

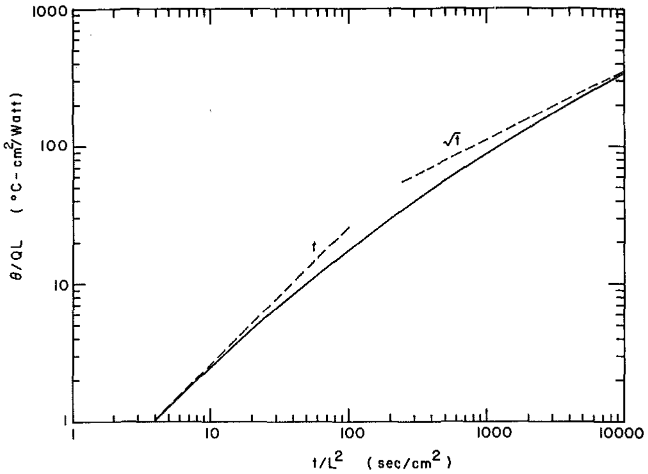

Fig. 2 Normalized peak temperature rise (at $x = 0$)—dotted lines show the asymptotic limits

$$\Theta_2(x,s) = B_1 \exp(x\sqrt{s/D_2}) + B_2 \exp(-x\sqrt{s/D_2}) \quad (6)$$

The constants can be evaluated by employing the transformed counterparts of equations (3) and (4). Once this has been accomplished, it is possible to expand the transformed temperatures in an infinite series such that

$$\Theta_1(x,s) = \frac{Q}{\rho_1 c_1 s^2} - \frac{k_2 Q}{\rho_1 c_1 (k_1\sqrt{D_2/D_1} + k_2)} \sum_{n=0}^{\infty} \frac{\lambda^n}{s^2} \times [\exp(-[(2n+1)L - x]\sqrt{s/D_1}) + \exp(-[(2n+1)L + x]\sqrt{s/D_1})] \quad (7)$$

$$\Theta_2(x,s) = \frac{k_1 Q}{\rho_1 c_1 (k_1 + k_2\sqrt{D_1/D_2})} \sum_{n=0}^{\infty} \frac{\lambda^n}{s^2} \times [\exp(-[2nL/\sqrt{D_1} + (x-L)/\sqrt{D_2}]\sqrt{s}) - \exp(-[2(n+1)L/\sqrt{D_1} + (x-L)/\sqrt{D_2}]\sqrt{s})] \quad (8)$$

where

$$\lambda = \left\{\frac{k_1}{\sqrt{D_1}} - \frac{k_2}{\sqrt{D_2}}\right\} \Big/ \left\{\frac{k_1}{\sqrt{D_1}} + \frac{k_2}{\sqrt{D_2}}\right\} \quad (9)$$

These equations can be transformed back to the time domain to give

$$\theta_1(x,t) = \frac{Q}{\rho_1 c_1} t + \frac{k_2 Q}{\rho_1 c_1 (k_1\sqrt{D_2/D_1} + k_2)} \times \sum_{n=0}^{\infty} \lambda^n [F_{n1}(x,t) + F_{n1}(-x,t) - F_{n2}(x,t) - F_{n2}(-x,t)] \quad (10)$$

$$\theta_2(x,t) = \frac{k_1 Q}{\rho_1 c_1 (k_1 + k_2\sqrt{D_1/D_2})} \sum_{n=0}^{\infty} \lambda^n [G_n(x,t) - G_{n+1}(x,t)] \quad (11)$$

where

$$F_{n1}(x,t) = \frac{[(2n+1)L + x]\sqrt{t}}{\sqrt{\pi D_1}} \exp\left[\frac{-[(2\mathrm{n}+1)\mathrm{L} + \mathrm{x}]^2}{4D_1\mathrm{t}}\right] \quad (12)$$

$$F_{n2}(x,t) = \left\{t + \frac{[(2n+1)L + x]^2}{2D_1}\right\} \operatorname{erfc}\left[\frac{(2n+1)L + x}{2\sqrt{D_1 t}}\right] \quad (13)$$

$$G_n(x,t) = \left\{t + \frac{\left[\frac{2nL}{\sqrt{D_1}} + \frac{x-L}{\sqrt{D_2}}\right]^2}{2}\right\} \operatorname{erfc}\left[\frac{\frac{2nL}{\sqrt{D_1}} + \frac{x-L}{\sqrt{D_2}}}{2\sqrt{t}}\right]$$

$$- \left\{\frac{2nL}{\sqrt{\pi D_1}} + \frac{x-L}{\sqrt{\pi D_2}}\right\} \sqrt{t} \exp\left\{\frac{-[2nL/\sqrt{D_1} + (x-L)/\sqrt{D_2}]^2}{4t}\right\} \quad (14)$$

Table 1 Thermal properties of thin film resistor materials

	k, W/cm °C	D, cm²/s	ρc, J/cm³/°C
nichrome	0.15	0.04	3.75
steatite	0.03	0.01	3.0

3 Application

Equations (10) and (11) can be applied to find the temperature distribution in thin film resistors. As an illustrative example a nichrome thin film resistor on a steatite ceramic substrate will be analyzed. The thermal properties of the film and substrate are listed in Table 1.

The normalized temperature distribution for several intervals of time is shown in Fig. 1. In the heat generating region the curves are concave downward, whereas outside the resistive layer they are concave upward. For very short time intervals, where the heat diffusing out of the active layer is small compared to the total energy input, the temperature rise is nearly adiabatic and is proportional to t. After long time intervals the heat flow is approximately that due to a flux of heat at the surface, producing a peak temperature rise proportional to $t^{1/2}$.

This is shown more clearly in Fig. 2, where the normalized temperature rise at $x = 0$ is plotted together with the two asymptotic limits.

References

1 Carslaw, H. S., and Jaeger, J. C., *Conduction of Heat in Solids*, Second ed., Oxford University Press, London, 1959.

2 Giere, A. C., "Transient Heat Flow in a Composite Slab—Constant Flux, Zero Flux Boundary Conditions," *App. Sci. Res.*, A14, 1964–1965, pp. 191–198.

3 Mulholland, G. P., and Cobble, M. H., "Diffusion Through Composite Media," *International Journal of Heat and Mass Transfer*, Vol. 15, 1972, pp. 147–160.

4 Ozisik, M. N., *Boundary Value Problems of Heat Conduction*, International Textbook Co., Scranton, Pa., 1968.

5 Domingos, H., "Transient Temperature Rise in Film Resistors," Rome Air Development Center Technical Report RADC-TR-74-92, Apr. 1974.

6 Engelmaier, W., "Thermal Behavior and Aging of Tantalum Nitride Thin Film Resistors Under Pulsed Operation," *Proceedings 21st Electronic Components Conference*, 1971, pp. 210–220.

Thermal Contact Conductance of Lead Ferrite and Boron Nitride

L. S. Fletcher[1] **and W. R. Ott**[2]

Introduction

There are many instances in which significant heat transfer takes place in electrical systems where different material interfaces exist. One such case involves the use of permanent magnets with high electrical resistivity for large electrical systems. Another such case deals with dielectric insulators requiring good thermal conductivity. In both of these cases, extreme thermal gradients may be imposed in a junction between the two materials.

The phenomenon occurring at the junction, or the thermal contact conductance, provides one of the more promising techniques for thermal control in electrical systems. This technique involves the use of suitable materials inserted in the junctions associated with the various electrical components. Although thermal contact conductance data have been reported for many different materials, such data are available for only a few ceramic materials [1].[3] This note presents the results of an experimental investigation of the thermal contact conductance of lead ferrite and boron nitride.

Ceramic Materials

Ceramics are used in electrical systems primarily because of their dielectric and magnetic properties. Lead ferrite and boron nitride were selected for investigation in order to establish some general characteristics for a dielectric and a magnetic material for use in appropriate electrical systems.

Permanent magnets with a high coercive force and high electrical resistivity generally have been developed from ceramic oxides, particularly barium ferrites. Recently, lead ferrites have been developed with properties equivalent to barium ferrites [2, 3]. The ferrite studied in the present investigation was composed of $PbO\ 4.5Fe_2O_3$ with 0.27 percent B_2O_3 and 0.50 percent SiO_2 added to improve the properties. The samples were prepared by ball milling calcined (1000°C) powder, of the composition noted, for 144 hr. The resulting milled material was pressed at 3.4×10^7 N/cm^2 and fired to 1150°C for 1 hr. The sintered bulk density of the sample was 5.27 gm/cc. Abrams [3] has reported other material properties for the lead ferrite investigated.

There are many electrical systems, such as radar and other microwave units, which require high dielectric strength. Hot pressed boron nitride (HBR) is one of the more suitable materials for such applications. In addition to having a high dielectric strength, good thermal conductivity, high heat capacity, and good mechanical strength, it is readily available and can be fabricated easily. The boron nitride samples were prepared by hot pressing to 2000°C at pressures to 6.9×10^6 N/m^2. The strength, thermal expansion, and thermal conductivity are all greater perpendicular to the direction of pressing [4].

Experimental Program

The experimental facility used in this investigation was composed of a vertical aluminum 2024-T4 column, 2.54 cm in diameter, which was axially loaded, with contacting surfaces located at approximately one-third and two-thirds of the column height [5]. The flatness deviation of the test specimens was 0.508 μm for all surfaces, and the roughness deviation ranged from 0.220 to 0.406 μm. The ceramic test samples were kept in an airtight container to minimize water absorption and oxidation. For experimental tests, the samples were inserted in the aluminum junctions, the test chamber was evacuated, and appropriate load and temperature conditions were established. Data were taken when the temperatures did not vary more than 1°C over a 30-min period.

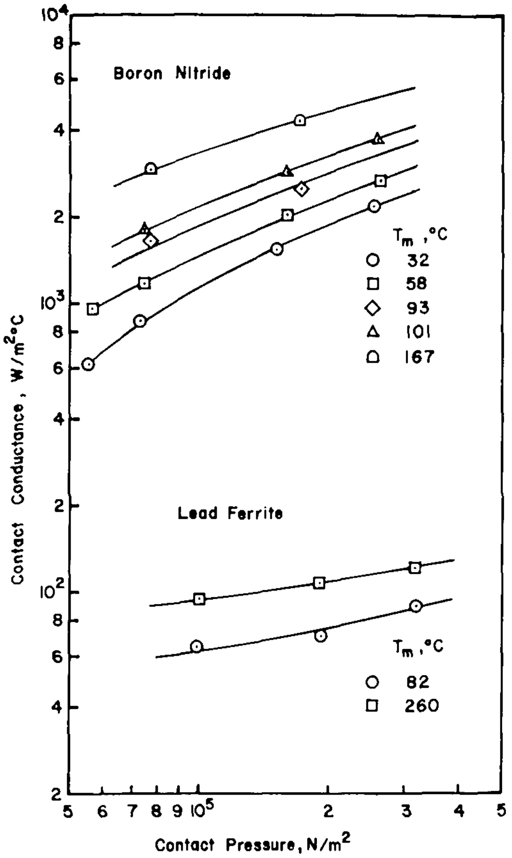

Fig. 1 Variation of thermal contact conductance with apparent load pressure and temperature for lead ferrite and boron nitride

Results and Discussion

Thermal contact conductance data were obtained for the ceramic materials over an apparent contact pressure range of 3.4×10^5 N/m^2 at mean junction temperatures ranging from 24 to 163°C. The thermal contact conductance values for lead ferrite are shown in Fig. 1 as a function of apparent contact pressure. The conductance values increased slightly as apparent contact pressure was increased. For samples of the same thickness (0.318 cm), a higher temperature at the same heat flux resulted in a higher contact conductance.

The effect of apparent contact pressure on the thermal conductance of boron nitride is also shown in Fig. 1. The boron nitride samples (0.318 cm thick) were inserted in the test facility such that the heat flux was parallel to the direction of hot pressing. It is interesting to note that contact conductance increases slightly with increase in apparent contact pressure.

The thermal contact conductance of the boron nitride sample is over an order of magnitude greater than that for lead ferrite. This is consistent with the relation between the thermal conductivity of the two samples. Kingery [6] has noted that oxides, carbides, and nitrides with low atomic weight cations have higher conductivities than those with higher atomic weight cations. Further, complex crystals such as lead ferrite have a greater tendency toward thermal scattering of waves, and consequently a lower thermal conductivity.

The thermal contact conductance of boron nitride increased significantly with temperature, as shown in Fig. 2. In contrast, the thermal conductivity of boron nitride decreases with temperature [3,

---

[1] Professor, Department of Mechanical Engineering, University of Virginia, Charlottesville, Va. Mem. ASME.

[2] Assoc. Professor, Department of Ceramics, Rutgers University, New Brunswick, N. J.

[3] Numbers in brackets designate References at end of technical note.

Contributed by the Heat Transfer Division of THE AMERICAN SOCIETY OF MECHANICAL ENGINEERS. Manuscript received by the Heat Transfer Division January 9, 1976.

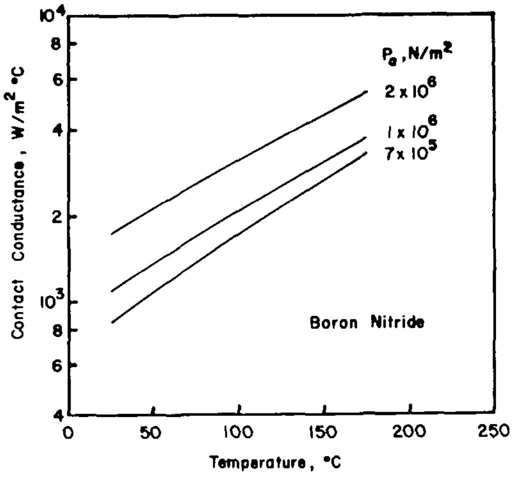

Fig. 2 Variation of thermal contact conductance with mean junction temperature for boron nitride

7]. In fact, the thermal conductivity of ceramic materials decreases as temperature is increased above room temperature [6]. This temperature dependence is largest for materials of high conductivity. If the thermal conductivity of the sample were the principal variable which caused the temperature dependence of the thermal contact conductance, then a trend in the opposite direction would be expected. Since the contact conductance increases with temperature, the effect is not caused by thermal conductivity changes.

One possible reason for the increase in thermal contact conductance of the material with temperature would be a change in the sample. If the sample is densified by the heat treatment (with pressure) the conductivity might increase. The elimination of pores will increase the conductivity of the sample [6]. Since the boron nitride samples were fabricated at 2000°C and 6.9×10^6 N/m^2, there is little likelihood that any substantial densification would have occurred, much less an amount sufficient to create the trend observed. For the same reason, there is little reason to expect any alteration in the surface texture.

Both the boron nitride and lead ferrite samples were seen to increase in contact conductance with pressure. Such an increase could be due to pressure sintering. While one lead ferrite sample did show some signs of sintering (a circumferential crack), the boron nitride samples were completely unaffected by the heat treatment.

Examination of the thermal contact conductance of a variety of materials [1] shows a similar temperature and pressure effect for most materials. The thermal conductivity of the alumium test specimens increases with temperature. It appears that creep is possible in the aluminum test specimens for the temperature and pressure range of the present tests. Calculations by Murray, et al. [8], which are supported by experimental data for copper obtained by Goetzel [9], show that metals can readily sinter at low temperature with pressure. The yield stress of copper can be reduced by a factor of 100 with a pressure of 1.38×10^7 N/m^2. Aluminum has a much lower melting temperature than copper. It is likely, then, that an increase in temperature and pressure can effect the characteristics of the ceramic-aluminum interface, resulting in a decrease in the resistance to heat transfer. This change at the interface may result from plastic deformation of the surface of the aluminum test specimen as well as possible surface oxidation.

Conclusions

The contact conductances of both ceramic materials exhibit a significant dependence on temperature and pressure, and increase as temperature and pressure increase. It appears that the primary factor which influences the thermal contact conductance of the ceramic materials is the change in resistance resulting from the change of the metallic surface as the temperature and pressure are increased. The thermal analysis and design of electrical systems incorporating ceramic materials could be substantially improved by selection of appropriate metal-ceramic junction materials.

References

1 Fletcher, L. S., "A Review of Thermal Control Materials for Metallic Junctions," *Journal of Spacecraft and Rockets,* Vol. 9, No. 12, Dec. 1972, pp. 849–850.

2 Tokar, Michael, "Microstructure and Magnetic Properties of Lead Ferrites," *Journal American Ceram. Society,* Vol. 52, No. 6, June 1969, pp. 302–306.

3 Abrams, Hohn, "Oriented High Lead Ferrites," PhD thesis, Rutgers University, 1972.

4 Union Carbide, Technical Information Bulletin No. 442-205G1.

5 Miller, R. G., and Fletcher, L. S., "A Facility for the Measurement of Thermal Contact Conductance," *Proceedings of the Tenth Southeastern Seminar on Thermal Sciences,* New Orleans, La., Apr. 1974, pp. 263–285.

6 Kingery, W. W., *Introduction to Ceramics,* Wiley, New York, 1960, pp. 448–450.

7 Hove, J. E., and Riley, W. C., *Modern Ceramics—Some Principles and Concepts,* Wiley, New York, 1965, p. 248.

8 Murray, P., Livey, D. T., and Williams, J., "The Hot Pressing of Ceramics," *Ceramic Fabrication Processes,* W. D. Kingery, ed., MIT Press, Cambridge, Mass., 1963, pp. 147–171.

9 Goetzel, C. G., *Trans. Amer. Soc. Metals,* Vol. 28, 1940, p. 909.

A Correction to Noncircular Duct Hot Patch Data

C. C. Maneri[1] and R. E. Schneider[1]

Noncircular duct hot patch data, extensively referred to in the literature, have been found to be in error. When these data are corrected and compared with predictions of hot patch dryout using the most recent form of the Tong F factor, it is found that physically unintelligible results are obtained. It is not clear whether the Tong F factor, the method of predicting the equivalent uniform dryout flux, or the method of reducing the hot patch dryout data is at fault.

A recent evaluation of the hot patch data of [1][2] disclosed that an unrealistic assumption had been made in the data reduction process which significantly affects the final results. Since these data have been extensively referred to in the literature [2, 3, 4] and texts [5, 6] and represent a significant fraction of the data used to justify the well-used Tong *F* factor [2], it was felt that the corrected data should be published and the *F* factor reevaluated with respect to them.

The hot patch data were obtained on a 27-in. long electrically heated test section having a 0.097- × 1-in. flow area. A hot patch having an axial length of 1.35 inches was located 0.4 in. from the exit. Cross sectional views of the normal (uniform) and hot patch segments have been reproduced from [7] and are presented in Fig. 1. As seen from Fig. 1, the ratio of hot patch-to-normal metal thickness is ½. If, as assumed in [7], the current were confined to the central region, the flux ratio would be 2. This is a poor assumption, however, since the wall thickness in the edge region is 0.016 in. as compared with a hot patch thickness of 0.025 in.

A more realistic assumption is that the current redistributes transversely such that the voltage gradients in the meat and edge regions of the test section are equal both in the hot patch and normal sections. With this assumption and that of constant electrical con-

---

[1] General Electric Company, Knolls Atomic Power Laboratory, Schenectady, N. Y.

[2] Numbers in brackets designate References at end of technical note.

Contributed by the Heat Transfer Division of THE AMERICAN SOCIETY OF MECHANICAL ENGINEERS. Manuscript received by the Heat Transfer Division September 5, 1975.

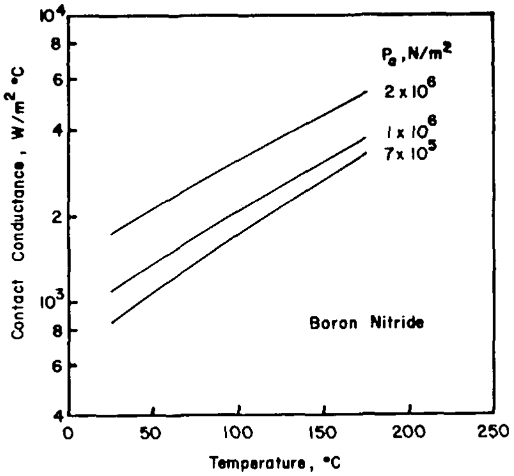

Fig. 2 Variation of thermal contact conductance with mean junction temperature for boron nitride

7]. In fact, the thermal conductivity of ceramic materials decreases as temperature is increased above room temperature [6]. This temperature dependence is largest for materials of high conductivity. If the thermal conductivity of the sample were the principal variable which caused the temperature dependence of the thermal contact conductance, then a trend in the opposite direction would be expected. Since the contact conductance increases with temperature, the effect is not caused by thermal conductivity changes.

One possible reason for the increase in thermal contact conductance of the material with temperature would be a change in the sample. If the sample is densified by the heat treatment (with pressure) the conductivity might increase. The elimination of pores will increase the conductivity of the sample [6]. Since the boron nitride samples were fabricated at 2000°C and 6.9×10^6 N/m^2, there is little likelihood that any substantial densification would have occurred, much less an amount sufficient to create the trend observed. For the same reason, there is little reason to expect any alteration in the surface texture.

Both the boron nitride and lead ferrite samples were seen to increase in contact conductance with pressure. Such an increase could be due to pressure sintering. While one lead ferrite sample did show some signs of sintering (a circumferential crack), the boron nitride samples were completely unaffected by the heat treatment.

Examination of the thermal contact conductance of a variety of materials [1] shows a similar temperature and pressure effect for most materials. The thermal conductivity of the alumium test specimens increases with temperature. It appears that creep is possible in the aluminum test specimens for the temperature and pressure range of the present tests. Calculations by Murray, et al. [8], which are supported by experimental data for copper obtained by Goetzel [9], show that metals can readily sinter at low temperature with pressure. The yield stress of copper can be reduced by a factor of 100 with a pressure of 1.38×10^7 N/m^2. Aluminum has a much lower melting temperature than copper. It is likely, then, that an increase in temperature and pressure can effect the characteristics of the ceramic-aluminum interface, resulting in a decrease in the resistance to heat transfer. This change at the interface may result from plastic deformation of the surface of the aluminum test specimen as well as possible surface oxidation.

Conclusions

The contact conductances of both ceramic materials exhibit a significant dependence on temperature and pressure, and increase as temperature and pressure increase. It appears that the primary factor which influences the thermal contact conductance of the ceramic materials is the change in resistance resulting from the change of the metallic surface as the temperature and pressure are increased. The thermal analysis and design of electrical systems incorporating ceramic materials could be substantially improved by selection of appropriate metal-ceramic junction materials.

References

1 Fletcher, L. S., "A Review of Thermal Control Materials for Metallic Junctions," *Journal of Spacecraft and Rockets*, Vol. 9, No. 12, Dec. 1972, pp. 849–850.

2 Tokar, Michael, "Microstructure and Magnetic Properties of Lead Ferrites," *Journal American Ceram. Society*, Vol. 52, No. 6, June 1969, pp. 302–306.

3 Abrams, Hohn, "Oriented High Lead Ferrites," PhD thesis, Rutgers University, 1972.

4 Union Carbide, Technical Information Bulletin No. 442-205G1.

5 Miller, R. G., and Fletcher, L. S., "A Facility for the Measurement of Thermal Contact Conductance," *Proceedings of the Tenth Southeastern Seminar on Thermal Sciences*, New Orleans, La., Apr. 1974, pp. 263–285.

6 Kingery, W. W., *Introduction to Ceramics*, Wiley, New York, 1960, pp. 448–450.

7 Hove, J. E., and Riley, W. C., *Modern Ceramics—Some Principles and Concepts*, Wiley, New York, 1965, p. 248.

8 Murray, P., Livey, D. T., and Williams, J., "The Hot Pressing of Ceramics," *Ceramic Fabrication Processes*, W. D. Kingery, ed., MIT Press, Cambridge, Mass., 1963, pp. 147–171.

9 Goetzel, C. G., *Trans. Amer. Soc. Metals*, Vol. 28, 1940, p. 909.

A Correction to Noncircular Duct Hot Patch Data

C. C. Maneri[1] and R. E. Schneider[1]

Noncircular duct hot patch data, extensively referred to in the literature, have been found to be in error. When these data are corrected and compared with predictions of hot patch dryout using the most recent form of the Tong F factor, it is found that physically unintelligible results are obtained. It is not clear whether the Tong F factor, the method of predicting the equivalent uniform dryout flux, or the method of reducing the hot patch dryout data is at fault.

A recent evaluation of the hot patch data of [1][2] disclosed that an unrealistic assumption had been made in the data reduction process which significantly affects the final results. Since these data have been extensively referred to in the literature [2, 3, 4] and texts [5, 6] and represent a significant fraction of the data used to justify the well-used Tong F factor [2], it was felt that the corrected data should be published and the F factor reevaluated with respect to them.

The hot patch data were obtained on a 27-in. long electrically heated test section having a 0.097- × 1-in. flow area. A hot patch having an axial length of 1.35 inches was located 0.4 in. from the exit. Cross sectional views of the normal (uniform) and hot patch segments have been reproduced from [7] and are presented in Fig. 1. As seen from Fig. 1, the ratio of hot patch-to-normal metal thickness is ½. If, as assumed in [7], the current were confined to the central region, the flux ratio would be 2. This is a poor assumption, however, since the wall thickness in the edge region is 0.016 in. as compared with a hot patch thickness of 0.025 in.

A more realistic assumption is that the current redistributes transversely such that the voltage gradients in the meat and edge regions of the test section are equal both in the hot patch and normal sections. With this assumption and that of constant electrical con-

---

[1] General Electric Company, Knolls Atomic Power Laboratory, Schenectady, N. Y.

[2] Numbers in brackets designate References at end of technical note.

Contributed by the Heat Transfer Division of THE AMERICAN SOCIETY OF MECHANICAL ENGINEERS. Manuscript received by the Heat Transfer Division September 5, 1975.

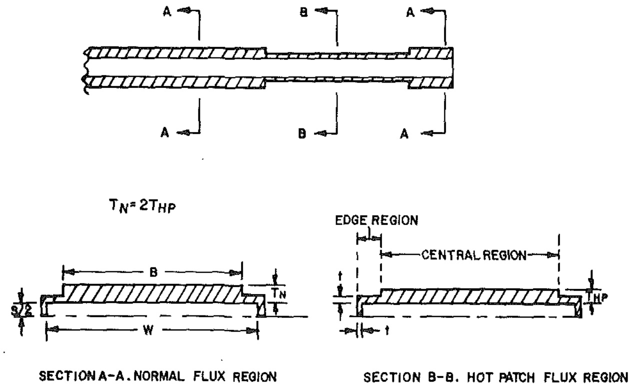

Fig. 1 Cross-sectional views of hot patch test section

ductivity,[3] Ohm's law gives for the normal and hot patch heat fluxes

$$\phi_N = \frac{Q_T}{P_C L}\left[\frac{L A_{HP}}{\ell_N A_{HP} + \ell_{HP} A_N}\right]\frac{A_{NM}}{A_N} = 0.88\frac{Q_T}{P_C L}$$

$$\phi_{HP} = \frac{Q_T}{P_C L}\left[\frac{L A_N}{\ell_N A_{HP} + \ell_{HP} A_N}\right]\frac{A_{HPM}}{A_{HP}} = 1.5\frac{Q_T}{P_C L} \qquad (1)$$

where P_C is the heated perimeter of the central region, L the length of the test section, and Q_T the total power which is obtained from the given information in [1] or [7] and the relation

$$Q_T = G A_f (h_{\text{Exit}} - h_{\text{Inlet}}) \qquad (2)$$

Here G is the mass flux, A_f the flow area, and h the enthalpy. It should be pointed out that the given dryout enthalpy value was used for the exit enthalpy since actual exit enthalpies were not given and the enthalpy rise over the remaining 0.4 in. of the test section is negligible.

The corrected data are given in Table 1 and are seen to substantially differ from the original values which have been included for comparison. Furthermore, the flux ratio $\phi_{HP}/\phi_N = 1.71$, which is 13.5 percent lower than the value of 1.98 quoted in the literature [1, 2, 5, 7].

Before the Tong F factor is reevaluated, it will be instructive to briefly review its form for the hot patch test section considered. By definition, the F factor is given in general by the equation

$$F = \frac{\phi_{DU}}{\phi_{DNU}} = \frac{C}{\phi_{DNU}(1 - e^{-C\ell_D})}\int_0^{\ell_D} \phi(z) e^{-C(\ell_D - z)} dz \qquad (3)$$

where ϕ_{DU} and ϕ_{DNU} are the local dryout fluxes in corresponding uniformly and nonuniformly heated ducts respectively, $\phi(z)$ is the flux distribution in the nonuniform duct and ℓ_D is the location of dryout measured from the inception of local boiling. The parameter C was empirically determined by Tong, et al. [2] and found to be

$$C = 0.44\frac{(1 - X_D)^{7.9}}{[G/(10^6 \text{ lbm/hr ft}^2)]^{1.72}} \text{ in.}^{-1} \qquad (4)$$

where X_D is the bulk fluid equilibrium quality at the dryout location. A more recent correlation of C was given by Tong [3] and has the form

$$C = 0.15\frac{(1 - X_D)^{4.31}}{[G/(10^6 \text{ lbm/hr ft}^2)]^{0.478}} \text{ in.}^{-1} \qquad (5)$$

The hot patch test section considered has the flux distribution

$$\phi(z) = \begin{cases} \phi_N & 0 \le z \le \ell_D - 1.35 \\ \phi_{HP} & \ell_D - 1.35 \le z \le \ell_D \end{cases} \qquad (6)$$

where ℓ_D is measured to the end of the hot patch step. Substitution of equation (6) into equation (3) leads to the relation

$$F = \frac{\phi_N}{\phi_{HP}} + \left[1 - \frac{\phi_N}{\phi_{HP}}\right]\frac{(1 - e^{-1.35C})}{(1 - e^{-\ell_D C})} \qquad (7)$$

which is plotted in Fig. 2 for the range of hot patch data with $\ell_D = 26.6$ in. as suggested in [2] and C from equation (5).

The experimental F factor values (closed symbols) shown in Fig. 2 were obtained by dividing the corrected hot patch fluxes ϕ_{HP} into the corresponding uniform values. The latter were extracted from the eight uncorrected values given in [8] which are also shown (open symbols) in Fig. 2 for comparative purposes. Tong [8] did not plot all the data so that a complete set of uniform values could not be obtained.

Initial attempts by the present authors to obtain corresponding uniform values quickly revealed that a good degree of subjectivity was

---

[3] Second order errors still exist in the corrected data due to this assumption; however, a discussion of these errors is beyond the scope of this technical brief.

Table 1 Summary of hot patch data obtained at 2000 psia

Inlet Temp., F	Mass Flux, lbm/hr-ft^2/10^6	Dryout Enthalpy, Btu/lb	Dryout Quality	Normal Flux at Dryout Conditions, Btu/hr-ft^2/10^6		Hot Patch Flux at Dryout Conditions, Btu/hr-ft^2/10^6	
				Ref. [1]	Corrected	Ref. [1]	Corrected
103	0.374	839	0.359	0.556	0.512	1.100	0.872
104	0.512	755	0.179	0.640	0.623	1.267	1.063
106	0.753	594	-0.166	0.792	0.698	1.568	1.190
106	0.993	549	-0.263	0.933	0.840	1.847	1.432
303	0.503	804	0.281	0.528	0.474	1.045	0.808
302	0.750	741	0.151	0.665	0.629	1.317	1.072
302	1.010	630	-0.091	0.767	0.644	1.520	1.098
303	1.503	593	-0.166	0.942	0.858	1.864	1.463
302	1.992	555	-0.253	1.112	1.002	2.215	1.708
502	.490	918	0.531	0.397	0.377	0.787	0.642
503	.765	823	0.324	0.485	0.455	0.961	0.775
503	1.006	777	0.222	0.553	0.513	1.095	0.875
502	1.507	716	0.099	0.640	0.617	1.287	1.052
502	2.005	699	0.056	0.801	0.749	1.586	1.277

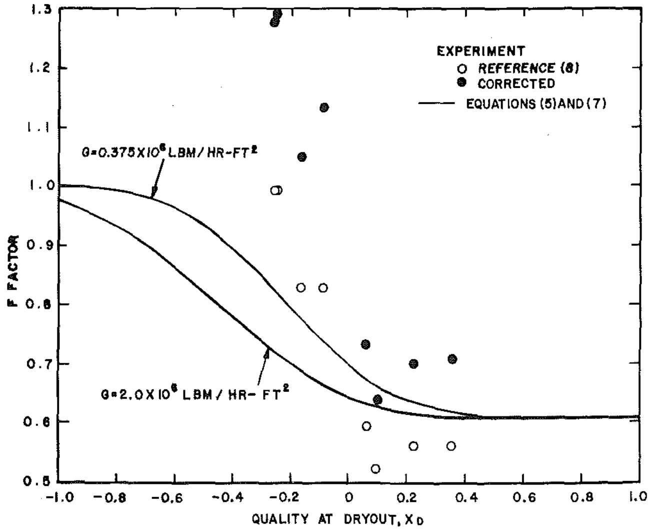

Fig. 2 Comparison of the *F* factor with hot patch data

involved, since, except for mass flux, none of the uniform data in [1] were taken at the dryout conditions of the hot patch data. By using Tong's uniform values, which differ from those that would have been obtained in the present evaluation, the authors preserve the same basis for comparing the corrected *F* factor values with Tong's original values.

In regard to the corrected values, it is interesting to note that all the subcooled points are greater than unity, a situation which defies interpretation by accepted dryout mechanisms. This is most probably a combined result of experimental errors in the hot patch data and interpolative/extrapolative errors in the uniform flux estimates. In any event, even if these four values are placed at unity, it is evident that the Tong *F* factor in its present form does not represent an adequate fit of the hot patch data. In light of this, additional evaluations may be required to qualify the form of the *F* factor as given by equation (5) and its use in ensuring adequate thermal margins during reactor operation.

Acknowledgment

The authors would like to acknowledge the assistance of A. Weiss and B. W. Le Tourneau of Westinghouse in confirming the correction.

References

1 De Bortoli, R. A., et al., "Forced-Convection Heat Transfer Burnout Studies For Water in Rectangular Channels and Round Tubes at Pressures Above 500 Psia," WAPD-188, Oct. 1958.

2 Tong, L. S., et al., "Influence of Axially Non-Uniform Heat Flux on DNB," AIChE Preprint 17, Eighth National Heat Transfer Conference, Aug. 8–11, 1965.

3 Tong, L. S., "Boiling Crisis and Critical Heat Flux," TID-25887, 1972.

4 Tong, L. S., and Hewitt, G. F., "Overall Viewpoint of Flow Boiling CHF Mechanisms," ASME Paper No. 72-HT-54, 1972.

5 Tong, L. S., *Boiling Heat Transfer and Two Phase Flow,* Wiley, New York, 1965.

6 Collier, J. G., *Convective Boiling and Condensation,* McGraw-Hill, London, 1972.

7 Weiss, A., "Hot Patch Tests in .097 in. × 1 in. × 27 in. Long Rectangular Channels at 2000 Psia," WAPD-TH-338, Aug. 1957.

8 Tong, L. S., "Two Phase Flow in Nuclear Reactors," Notes from a short course in Boiling Heat Transfer and Multiphase Flow taught at the University of Michigan 7/21/69–8/1/69.

A Theoretical Study of Thermally Developing Fully Turbulent Boundary Layer Flow

L. C. Thomas[1]

Introduction

Several analyses have been presented for heat transfer through a turbulent boundary layer with an unheated starting length ζ and uniform wall temperature for $x \geq \zeta$ [1, 2].[2] These analyses were based on the Reynolds analogy such that application has been restricted to $\mathrm{Pr} \simeq 1$. Further, these analyses are suspect in the vicinity of the step where the thermal boundary layer is very small.

The development of a solution for this problem that is viable within the close vicinity of ζ, and that provides information pertaining to the effect of Pr on the thermal development, requires the use of a turbulent transport model that more faithfully characterizes the actual mechanism. In this regard, a new approach to the analysis of turbulent transport processes recently has been developed which is based on physically meaningful and measureable modeling parameters. This surface renewal approach involves the hypothesis that an intermittent exchange of fluid occurs between the turbulent core and wall regions. Until recently, this principle has been coupled with the assumption that unsteady molecular transport is predominant within individual elements of fluid during their residency at the surface. The use of this assumption has lead to surface renewal based analyses for a fairly broad range of turbulent transport processes associated with fully developed channel flow [3, 4, 5] and high Re_x boundary layer flow [6–8]. More recently the surface renewal principle has been adapted to momentum transfer associated with transitional turbulent boundary layer flow [9] and heat transfer associated with low Peclet number turbulent tube flow of liquid metals [10], which have required the inclusion of the effects of axial convection as well as unsteady molecular transport. This more general surface renewal modeling concept now will be utilized in the formulation of a solution for the thermal boundary layer problem surveyed in the foregoing.

Analysis

In this study, emphasis will be placed upon thermally developing boundary layer flow with constant wall temperature heating maintained for $\mathrm{Re}_\zeta = 10^6$, which is in the fully turbulent region. Attention is focused upon an individual element of fluid that has moved from the turbulent core to the wall region.

For these high Re_x conditions, the convective effects on momentum transfer have been found to be secondary such that the standard surface renewal based analysis [3–8] can be utilized. This approach previously has led to the development of expressions for the mean velocity profile, $\bar{u}$, and mean residence time (τ_x for boundary layer flow or τ for tube flow) [4, 5], which have been found to be in good agreement with experimental data.

Whereas the convective terms are not significant for high Re_x momentum transfer, the thermal convective terms $u\partial T/\partial x$ and $v\partial T/dy$ must be included in the energy equation for the present application. Consequently, the energy equation for the instantaneous transport within fluid elements at the wall is

$$\frac{\partial T}{\partial \theta} + u\frac{\partial T}{\partial x} + v\frac{\partial T}{\partial y} = \alpha\frac{\partial^2 T}{\partial y^2} \qquad (1)$$

---

[1] Mechanical Engineering Department, The University of Akron.

[2] Numbers in brackets designate References at end of technical note.

Contributed by the Heat Transfer Division of THE AMERICAN SOCIETY OF MECHANICAL ENGINEER. Manuscript received by the Heat Transfer Division July 31, 1975.

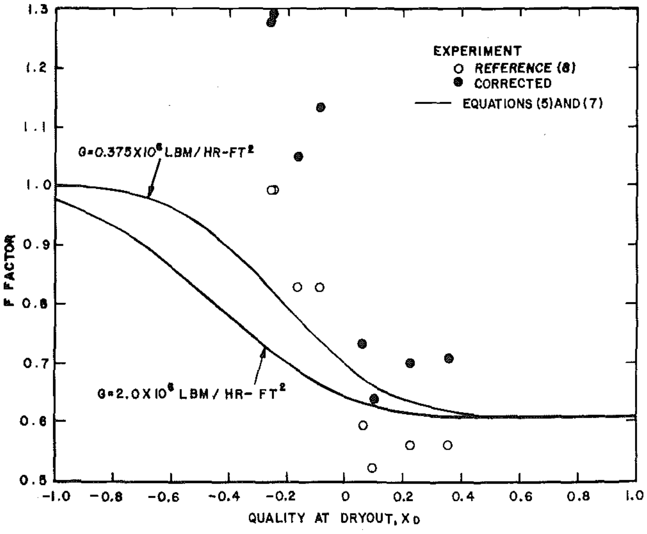

Fig. 2 Comparison of the *F* factor with hot patch data

involved, since, except for mass flux, none of the uniform data in [1] were taken at the dryout conditions of the hot patch data. By using Tong's uniform values, which differ from those that would have been obtained in the present evaluation, the authors preserve the same basis for comparing the corrected F factor values with Tong's original values.

In regard to the corrected values, it is interesting to note that all the subcooled points are greater than unity, a situation which defies interpretation by accepted dryout mechanisms. This is most probably a combined result of experimental errors in the hot patch data and interpolative/extrapolative errors in the uniform flux estimates. In any event, even if these four values are placed at unity, it is evident that the Tong F factor in its present form does not represent an adequate fit of the hot patch data. In light of this, additional evaluations may be required to qualify the form of the F factor as given by equation (5) and its use in ensuring adequate thermal margins during reactor operation.

Acknowledgment

The authors would like to acknowledge the assistance of A. Weiss and B. W. Le Tourneau of Westinghouse in confirming the correction.

References

1 De Bortoli, R. A., et al., "Forced-Convection Heat Transfer Burnout Studies For Water in Rectangular Channels and Round Tubes at Pressures Above 500 Psia," WAPD-188, Oct. 1958.
2 Tong, L. S., et al., "Influence of Axially Non-Uniform Heat Flux on DNB," AIChE Preprint 17, Eighth National Heat Transfer Conference, Aug. 8–11, 1965.
3 Tong, L. S., "Boiling Crisis and Critical Heat Flux," TID-25887, 1972.
4 Tong, L. S., and Hewitt, G. F., "Overall Viewpoint of Flow Boiling CHF Mechanisms," ASME Paper No. 72-HT-54, 1972.
5 Tong, L. S., *Boiling Heat Transfer and Two Phase Flow*, Wiley, New York, 1965.
6 Collier, J. G., *Convective Boiling and Condensation*, McGraw-Hill, London, 1972.
7 Weiss, A., "Hot Patch Tests in .097 in. × 1 in. × 27 in. Long Rectangular Channels at 2000 Psia," WAPD-TH-338, Aug. 1957.
8 Tong, L. S., "Two Phase Flow in Nuclear Reactors," Notes from a short course in Boiling Heat Transfer and Multiphase Flow taught at the University of Michigan 7/21/69–8/1/69.

A Theoretical Study of Thermally Developing Fully Turbulent Boundary Layer Flow

L. C. Thomas[1]

Introduction

Several analyses have been presented for heat transfer through a turbulent boundary layer with an unheated starting length ζ and uniform wall temperature for $x \geq \zeta$ [1, 2].[2] These analyses were based on the Reynolds analogy such that application has been restricted to $\Pr \simeq 1$. Further, these analyses are suspect in the vicinity of the step where the thermal boundary layer is very small.

The development of a solution for this problem that is viable within the close vicinity of ζ, and that provides information pertaining to the effect of Pr on the thermal development, requires the use of a turbulent transport model that more faithfully characterizes the actual mechanism. In this regard, a new approach to the analysis of turbulent transport processes recently has been developed which is based on physically meaningful and measureable modeling parameters. This surface renewal approach involves the hypothesis that an intermittent exchange of fluid occurs between the turbulent core and wall regions. Until recently, this principle has been coupled with the assumption that unsteady molecular transport is predominant within individual elements of fluid during their residency at the surface. The use of this assumption has lead to surface renewal based analyses for a fairly broad range of turbulent transport processes associated with fully developed channel flow [3, 4, 5] and high Re_x boundary layer flow [6–8]. More recently the surface renewal principle has been adapted to momentum transfer associated with transitional turbulent boundary layer flow [9] and heat transfer associated with low Peclet number turbulent tube flow of liquid metals [10], which have required the inclusion of the effects of axial convection as well as unsteady molecular transport. This more general surface renewal modeling concept now will be utilized in the formulation of a solution for the thermal boundary layer problem surveyed in the foregoing.

Analysis

In this study, emphasis will be placed upon thermally developing boundary layer flow with constant wall temperature heating maintained for $\mathrm{Re}_\zeta = 10^6$, which is in the fully turbulent region. Attention is focused upon an individual element of fluid that has moved from the turbulent core to the wall region.

For these high Re_x conditions, the convective effects on momentum transfer have been found to be secondary such that the standard surface renewal based analysis [3–8] can be utilized. This approach previously has led to the development of expressions for the mean velocity profile, $\bar{u}$, and mean residence time (τ_x for boundary layer flow or τ for tube flow) [4, 5], which have been found to be in good agreement with experimental data.

Whereas the convective terms are not significant for high Re_x momentum transfer, the thermal convective terms $u\partial T/\partial x$ and $v\partial T/\partial y$ must be included in the energy equation for the present application. Consequently, the energy equation for the instantaneous transport within fluid elements at the wall is

$$\frac{\partial T}{\partial \theta} + u\frac{\partial T}{\partial x} + v\frac{\partial T}{\partial y} = \alpha\frac{\partial^2 T}{\partial y^2} \qquad (1)$$

---

[1] Mechanical Engineering Department, The University of Akron.

[2] Numbers in brackets designate References at end of technical note.

Contributed by the Heat Transfer Division of THE AMERICAN SOCIETY OF MECHANICAL ENGINEER. Manuscript received by the Heat Transfer Division July 31, 1975.

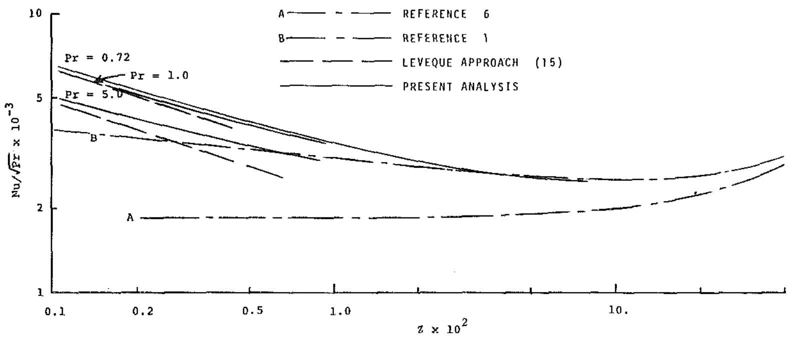

Fig. 1 Predictions for Nusselt number

with initial-boundary conditions $T(x, 0, \theta) = T_0$, $T(x, \infty, \theta) = T_i$ and $T(x, y, 0) = T_i$; the x-boundary condition will be written momentarily in the context of the spatial mean domain.

In the previous analysis for heat transfer to liquid metals in the low Peclet number region mentioned in the introduction [10], the simplifying assumption $u \simeq \bar{u}$ was found to be reasonable. The introduction of this type of assumption into the present analysis and the use of the random contact time distribution [11] leads to an equation in terms of the spatial mean transport properties of the form

$$\frac{\bar{T} - T_i}{\tau_x} + \bar{u}\frac{\partial \bar{T}}{\partial x} + \bar{v}\frac{\partial \bar{T}}{\partial y} = \alpha \frac{\partial^2 \bar{T}}{\partial y^2} \qquad (2)$$

The y-boundary conditions are written as $\bar{T}(x, 0) = T_0$ and $\bar{T}(x, \infty) = T_i$. Because this equation for $\bar{T}$ applies to the entire axial domain, the x-boundary condition can be written as $\bar{T}(\zeta, y) = T_\infty$. It is clear that T_i can be approximated by T_∞ in the region for which the thermal boundary layer, Δ, is small. However, as x-increases, the energy transport to eddies passing through the thermal boundary layer brings about a change in T_i for low to moderate Prandtl number fluids, such that this assumption becomes inappropriate.

With T_i approximated by T_∞, the energy equation takes the form

$$\frac{\bar{\psi} - 1}{\tau^+} + \frac{\bar{u}}{U_\infty}\frac{\partial \bar{\psi}}{\partial X} + \frac{\bar{v}}{U_\infty}\frac{\partial \bar{\psi}}{\partial Y} = \frac{1}{\mathrm{Pr}}\frac{\partial^2 \bar{\psi}}{\partial Y^2} \qquad (3)$$

where $\bar{\psi}(0, Y) = 1$, $\bar{\psi}(X, 0) = 0$, $\bar{\psi} = (\bar{T} - T_w)(T_\infty - T_w)$, $X = xU_\infty/\nu$ and $\tau^+ = \tau_x U_\infty{}^2/\nu$. τ_x, $\bar{u}$ and $\bar{v}$ are obtained from the momentum analysis and a numerical approach has been utilized to obtain a solution to this equation with the understanding that the assumptions for T_i, $\bar{u}$, and $\bar{v}$ restrict its applicability to small values of x-ζ. Reference [12] may be consulted for details.

Results and Discussion

Calculations have been obtained for $\bar{\psi}_{k+1,j}$ and Nu_x for $\mathrm{Re}_\zeta = 10^6$ and $\mathrm{Pr} = 0.72$, 1.0 and 5.0. Because the expressions utilized for $\bar{u}$ and $\bar{v}$ can only be assumed to be appropriate for the region $y^+ \lesssim 30$ and because the assumption $T_i = T_\infty$ becomes inappropriate for thermal molecular penetration much beyond this region, this analysis can be assumed to be applicable for values of X for which $\bar{T}$ approaches T_∞ for $y^+ \lesssim 30$.

Calculations for $\bar{T}$ obtained on the basis of this analysis are presented in reference [12] in terms of $\bar{\psi}$ versus y^+ for several values of $Z(\equiv 1 - (\zeta/X)^{0.9})$. The thermal penetration depth has been found to reach the critical depth $30 \lesssim y^+ \lesssim 35$ for $0.0133 \lesssim Z \lesssim 0.03$. Consequently, the present analysis for thermal developing boundary layer flow appears to be viable for $0 < Z \lesssim 0.01$ to 0.03.

The predictions for Nusselt numbers resulting from this analysis are shown in Fig. 1 in terms of $\mathrm{Nu}_x/\sqrt{\mathrm{Pr}}$ versus Z for several values of Pr. Predictions for assumed negligible convective effects [6] are also shown. The predictions of the present analysis are seen to approach the predictions of reference [6] as Z increases. This result indicates that the simple numerical approach utilized in this study converges appropriately for large Z. Consequently, the predictions for $\bar{T}$ and Nu_x for smaller values of Z can be assumed to be reasonable.

An important limitation of the previous analysis by Reynolds, et al. [1] is the restriction to Prandtl numbers very near unity. The assumptions utilized in Reynolds' analysis which brings about this restriction also inappropriately lead to predictions for $\mathrm{Nu}_x/\mathrm{Nu}_{\zeta=0}$ that are independent of Prandtl number. The effect of Pr on the heat transfer in the thermal developing region obtained on the basis of the present analysis is illustrated by Fig. 1. As is the case for tube flow [14] the longitudinal extent of the thermal developing region is seen to decrease with increasing Pr. Further, predictions for Nu_x based on this study lie well above the predictions of reference [1] for $\mathrm{Pr} \simeq 1$ for small values of Z, which is the region in which the analysis by Reynolds, et al., is least appropriate.

The predictions for Nusselt number resulting from this analysis are compared in reference [12] with the predictions of Reynolds, et al. [1] and experimental data for air in terms of $\mathrm{Nu}_x/\mathrm{Nu}_{\zeta=0}$ versus Z. The predictions for $\mathrm{Nu}_x/\mathrm{Nu}_{\zeta=0}$ are in good agreement with the data in the region of applicability of the model. As indicated earlier, the simpler surface renewal based analysis can be relied upon for large values of Z ($\gtrsim 0.3$) where the convective effects are small and T_i can be approximated with reasonable accuracy.

References

1 Reynolds, W. C., Kays, W. M., and Kline, S. J., "Heat Transfer in the Turbulent Incompressible Boundary Layer, II—The Step Wall Temperature Distribution," *NASA Memo 12-2-58 W*, Washington, D. C., 1958.

2 Spalding, D. B., "Heat Transfer to a Turbulent Stream From a Surface With a Step Wise Discontinuity in Wall Temperature," International Mechanical Engineering Joint Heat Transfer Conference, Boulder, Colo., 1961.

3 Thomas, L. C., "Temperature Profiles for Liquid Metals and Moderate-Prandtl Number Fluids," JOURNAL OF HEAT TRANSFER, TRANS. ASME, Series C, Vol. 92, 1970, p. 562.

4 Meek, R. L., and Baer, A. D., "The Periodic Viscous Sublayer in Turbulent Flow," *AIChE Journal*, Vol. 16, 1970, p. 841.

5 Thomas, L. C., and Kakarala, C. R., "A Unified Model For Turbulent and Laminar Momentum Transfer: Channel Flow," *Journal of Applied Mechanics*, TRANS. ASME, Series E, Vol. 93, 1976, p. 8.

6 Thomas, L. C., and Fan, L. T., "Heat and Momentum Transfer Analogy for Incompressible Turbulent Boundary Layer Flow," *International Journal of Heat and Mass Transfer*, Vol. 14, 1971, p. 715.

7 Gerhart, P. M., and Thomas, L. C., "Predictions of Heat Transfer for Turbulent Boundary Layer With Pressure Gradient," *AIAA Journal*, Vol. 11, 1973, p. 552.

8 Einstein, H. A., and Li, H., "The Viscous Sublayer Along a Smooth Boundary," *ASCE, J. Eng. Mech. Div.*, Vol. 82, No. 293, 1956.

9 Thomas, L. C., "Surface Renewal Based Formulation for Turbulent Boundary Layer Flow," *AIAA Journal*, Vol. 13, 1975, p. 32.

10 Kakarala, C. R., and Thomas L. C., "An Analysis of Liquid Metal Heat Transfer for Turbulent Tube Flow and Moderate to Low Peclet Numbers," National Heat Transfer Conference, San Francisco, Calif., 1975, ASME Paper No. 75-HT-33.

11 Danckwerts, P. V., "Significance of Liquid-Film Coefficients in Gas Absorption," *I & EC*, Vol. 43, 1951, p. 1460.

12 Thomas, L. C., "A Theoretical Study of Thermally Developing Fully Turbulent Boundary Layer Flow," Report 76-1, College of Engineering, The University of Akron, 1976.

13 Thomas, L. C., and Greene, H. L., "An Experimental and Theoretical Study of the Viscous Sublayer for Turbulent Tube Flow," Symposium on Turbulence in Liquids, The University of Missouri, Rolla, 1973.

14 Kays, W. M., *Convection Heat and Mass Transfer*, McGraw-Hill, New York, 1966.

15 Kestin, J., and Person, L. N., "The Transfer of Heat Across a Turbulent Boundary Layer at Very High Prandtl Numbers," *International Journal of Heat and Mass Transfer*, Vol. 5, 1962, p. 355.

Packed Bed Thermal Storage Models for Solar Air Heating and Cooling Systems

P. J. Hughes,[1] S. A. Klein,[2] and D. J. Close[3]

Nomenclature

A = cross-sectional area of packed bed [m^2]
D = diameter of the packing material [m]
h_v = volumetric heat transfer coefficient [kJ hr^{-1} °C^{-1} m^{-3}]
L = length of the packed bed (in the flow direction) [m]
$\dot{m}$ = mass flow rate of fluid [kg hr^{-1}]
NTU = $h_v AL/\dot{m}C_f$ [dimensionless]
P = perimeter of the packed bed [m]
U = energy loss coefficient from the packed bed to the surroundings [kJ hr^{-1} m^{-2} °C^{-1}]
x = position along the bed in the flow direction [m]
ϵ = void fraction of the packing [dimensionless]
$\tau = \rho_b C_b(1-\epsilon)AL/\dot{m}C_f$ [hr]

Subscripts

b = packing (or bed) material
env = environment
f = fluid

Introduction

In order to simulate solar heating systems where air is the transfer fluid, an adequate model of the packed gravel bed energy store is required. One model of a packed bed thermal store can be obtained by solving the partial differential equations of the Schumann Model as described by Jakob [1].[4] However, when these equations are solved as part of a long term simulation, the computing costs become unacceptably high. This paper describes the development of a simple model, whose validity is demonstrated by comparing the long term behavior of a system incorporating both the complex and simplified packed bed models.

System Description

The system chosen for the investigation is similar to that proposed by Balcomb [2]. It has three modes of operation. Mode 1 occurs when solar energy is available for collection and there is a space heating load. Then room temperature air is drawn through the solar collectors, heated, and returned to the building. Mode 2 occurs when solar energy is available for collection at times when there is no space heating demand. Air from the bottom of the packed bed is drawn through the solar collectors, heated, and returned to the top of the storage unit. The hot air moving down through the bed heats the gravel resulting in sensible heat storage. Mode 3 occurs when no solar energy can be collected but there is a space heating load. Hot air is drawn from the top of the packed bed into the house, and room temperature air is returned to the bottom of the bed. In Modes 1 and 3, auxiliary energy from a conventional furnace may supplement the solar contribution.

The Schumann Model

The partial differential equations which describe the thermal performance of a packed bed with forced fluid flow are given in the following together with the assumptions required to derive them. Heat transport axially down the bed with no forced flow is an unimportant mechanism unless the bed is heated from below as in Katto, et al. [3]. Since flow through the bed is arranged so that generally higher temperature gravel is at the top of the bed, this situation will not be considered. If it is assumed that:

1. the bed material has infinite conductivity in the radial direction and the fluid is in plug flow;
2. the bed material has zero conductivity in the axial direction;
3. no fluid phase axial dispersion, or conduction takes place;
4. the system has constant properties;
5. no mass transfer occurs;
6. no heat losses to the environment occur.

Then the equations describing the system can be written,

$$A\rho_f C_f \epsilon \frac{\partial T}{\partial \theta} = -\dot{m} C_f \frac{\partial T}{\partial x} + h_v A(T_b - T);$$

$$A\rho_b C_b(1-\epsilon)\frac{\partial T_b}{\partial \theta} = h_v A(T - T_b) \qquad (1)$$

An additional assumption, justified for the air-gravel packed beds normally used in solar air systems, is that of zero thermal capacitance of the fluid. Equations (1) can then be simplified to

$$\frac{\partial T}{\partial (x/L)} = \mathrm{NTU}(T_b - T); \qquad \frac{\partial T_b}{\partial(\theta/\tau)} = \mathrm{NTU}(T - T_b) \qquad (2)$$

Applicability of the Schumann Model to Air-Gravel Packed Beds

The first three assumptions listed previously can be modified by using the approach suggested by Jeffreson [4]. A modified NTU, or NTU$_c$ can be defined, which includes effects due to large Biot numbers (accounting for temperature gradients in the gravel) and large Peclet numbers (accounting for axial conduction and dispersion). The value of NTU$_c$ can be estimated using the relation proposed by Jeffreson;

$$\frac{1}{\mathrm{NTU}_c} = \frac{D}{L(\mathrm{Pe})} + \frac{(1 + \mathrm{Bi}/5)}{\mathrm{NTU}} \qquad (3)$$

NTU can be estimated using either the correlation for h_v reported by Löf and Hawley [5], or the correlation from Dunkle and Ellul [6]. When used in the Schumann model equations, Jeffreson shows by comparing predictions of packed bed behavior with experimental results, that the modified NTU or NTU$_c$ adequately accounts for these additional effects.

Concerning assumption 4, it is reasonable to assume that material properties are constant over the range of temperatures encountered in most solar energy thermal systems. The assumption of no mass transfer is correct for beds of nonadsorbing solids such as glass spheres, but gravel will experience a combined heat and vapor transfer process when exposed to air-water vapor mixtures. Close, et al. [7] have observed experimentally the increased storage capacity effect which mass transfer causes in air-gravel systems. In most well-designed solar heating and cooling systems, increased storage capacity can only improve system performance. Since the saturation water content of gravel is only approximately 0.03 kg/kg, it was considered justifiable to avoid the added complication required to consider this mechanism, especially since ignoring the mass transfer effect yields conservative estimates of system performance.

---

[1] Research Assistant, Solar Energy Laboratory, University of Wisconsin-Madison.

[2] Research Assistant, Solar Energy Laboratory, University of Wisconsin-Madison.

[3] Presently Senior Lecturer, Dept. of Engineering, James Cook University, Townsville, Queensland, Australia.

[4] Numbers in brackets designate References at end of technical note.

Contributed by The Heat Transfer Division of THE AMERICAN SOCIETY OF MECHANICAL ENGINEER. Manuscript received by the Heat Transfer Division

13 Thomas, L. C., and Greene, H. L., "An Experimental and Theoretical Study of the Viscous Sublayer for Turbulent Tube Flow," Symposium on Turbulence in Liquids, The University of Missouri, Rolla, 1973.

14 Kays, W. M., *Convection Heat and Mass Transfer*, McGraw-Hill, New York, 1966.

15 Kestin, J., and Person, L. N., "The Transfer of Heat Across a Turbulent Boundary Layer at Very High Prandtl Numbers," *International Journal of Heat and Mass Transfer*, Vol. 5, 1962, p. 355.

Packed Bed Thermal Storage Models for Solar Air Heating and Cooling Systems

---

P. J. Hughes,[1] S. A. Klein,[2] and D. J. Close[3]

Nomenclature

A = cross-sectional area of packed bed [m^2]
D = diameter of the packing material [m]
h_v = volumetric heat transfer coefficient [kJ hr^{-1} °C^{-1} m^{-3}]
L = length of the packed bed (in the flow direction) [m]
$\dot{m}$ = mass flow rate of fluid [kg hr^{-1}]
NTU = $h_v AL/\dot{m}C_f$ [dimensionless]
P = perimeter of the packed bed [m]
U = energy loss coefficient from the packed bed to the surroundings [kJ hr^{-1} m^{-2} °C^{-1}]
x = position along the bed in the flow direction [m]
ϵ = void fraction of the packing [dimensionless]
$\tau = \rho_b C_b(1-\epsilon)AL/\dot{m}C_f$ [hr]

Subscripts

b = packing (or bed) material
env = environment
f = fluid

Introduction

In order to simulate solar heating systems where air is the transfer fluid, an adequate model of the packed gravel bed energy store is required. One model of a packed bed thermal store can be obtained by solving the partial differential equations of the Schumann Model as described by Jakob [1].[4] However, when these equations are solved as part of a long term simulation, the computing costs become unacceptably high. This paper describes the development of a simple model, whose validity is demonstrated by comparing the long term behavior of a system incorporating both the complex and simplified packed bed models.

System Description

The system chosen for the investigation is similar to that proposed by Balcomb [2]. It has three modes of operation. Mode 1 occurs when solar energy is available for collection and there is a space heating load. Then room temperature air is drawn through the solar collectors, heated, and returned to the building. Mode 2 occurs when solar energy is available for collection at times when there is no space heating demand. Air from the bottom of the packed bed is drawn through the solar collectors, heated, and returned to the top of the storage unit. The hot air moving down through the bed heats the gravel resulting in sensible heat storage. Mode 3 occurs when no solar energy can be collected but there is a space heating load. Hot air is drawn from the top of the packed bed into the house, and room temperature air is returned to the bottom of the bed. In Modes 1 and 3, auxiliary energy from a conventional furnace may supplement the solar contribution.

The Schumann Model

The partial differential equations which describe the thermal performance of a packed bed with forced fluid flow are given in the following together with the assumptions required to derive them. Heat transport axially down the bed with no forced flow is an unimportant mechanism unless the bed is heated from below as in Katto, et al. [3]. Since flow through the bed is arranged so that generally higher temperature gravel is at the top of the bed, this situation will not be considered. If it is assumed that:

1 the bed material has infinite conductivity in the radial direction and the fluid is in plug flow;
2 the bed material has zero conductivity in the axial direction;
3 no fluid phase axial dispersion, or conduction takes place;
4 the system has constant properties;
5 no mass transfer occurs;
6 no heat losses to the environment occur.

Then the equations describing the system can be written,

$$A\rho_f C_f \epsilon \frac{\partial T}{\partial \theta} = -\dot{m}C_f \frac{\partial T}{\partial x} + h_v A(T_b - T);$$

$$A\rho_b C_b(1-\epsilon)\frac{\partial T_b}{\partial \theta} = h_v A(T - T_b) \qquad (1)$$

An additional assumption, justified for the air-gravel packed beds normally used in solar air systems, is that of zero thermal capacitance of the fluid. Equations (1) can then be simplified to

$$\frac{\partial T}{\partial (x/L)} = \mathrm{NTU}(T_b - T); \qquad \frac{\partial T_b}{\partial (\theta/\tau)} = \mathrm{NTU}(T - T_b) \qquad (2)$$

Applicability of the Schumann Model to Air-Gravel Packed Beds

The first three assumptions listed previously can be modified by using the approach suggested by Jeffreson [4]. A modified NTU, or NTU$_c$ can be defined, which includes effects due to large Biot numbers (accounting for temperature gradients in the gravel) and large Peclet numbers (accounting for axial conduction and dispersion). The value of NTU$_c$ can be estimated using the relation proposed by Jeffreson;

$$\frac{1}{\mathrm{NTU}_c} = \frac{D}{L(\mathrm{Pe})} + \frac{(1 + \mathrm{Bi}/5)}{\mathrm{NTU}} \qquad (3)$$

NTU can be estimated using either the correlation for h_v reported by Löf and Hawley [5], or the correlation from Dunkle and Ellul [6]. When used in the Schumann model equations, Jeffreson shows by comparing predictions of packed bed behavior with experimental results, that the modified NTU or NTU$_c$ adequately accounts for these additional effects.

Concerning assumption 4, it is reasonable to assume that material properties are constant over the range of temperatures encountered in most solar energy thermal systems. The assumption of no mass transfer is correct for beds of nonadsorbing solids such as glass spheres, but gravel will experience a combined heat and vapor transfer process when exposed to air-water vapor mixtures. Close, et al. [7] have observed experimentally the increased storage capacity effect which mass transfer causes in air-gravel systems. In most well-designed solar heating and cooling systems, increased storage capacity can only improve system performance. Since the saturation water content of gravel is only approximately 0.03 kg/kg, it was considered justifiable to avoid the added complication required to consider this mechanism, especially since ignoring the mass transfer effect yields conservative estimates of system performance.

---

[1] Research Assistant, Solar Energy Laboratory, University of Wisconsin-Madison.

[2] Research Assistant, Solar Energy Laboratory, University of Wisconsin-Madison.

[3] Presently Senior Lecturer, Dept. of Engineering, James Cook University, Townsville, Queensland, Australia.

[4] Numbers in brackets designate References at end of technical note.

Contributed by The Heat Transfer Division of THE AMERICAN SOCIETY OF MECHANICAL ENGINEER. Manuscript received by the Heat Transfer Division

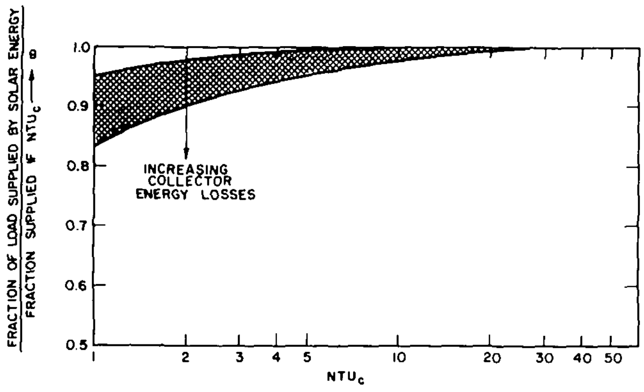

Fig. 1 Sensitivity of system performance to NTU$_c$

The assumption of zero thermal losses to the environment can be relaxed by including an energy loss term in the equations. With this addition, equations (2) become

$$\frac{\partial T}{\partial(x/L)} = \mathrm{NTU}_c(T_b - T) + \frac{\mathrm{UPL}}{\dot{m}C_f}(T_{\mathrm{env}} - T);$$

$$\frac{\partial T_b}{\partial(\theta/\tau)} = \mathrm{NTU}_c(T - T_b) \qquad (4)$$

Equations (4) can be solved using a standard finite difference approximation suggested by Hausen [1] and used by Balcomb [2].

The Simulation Model

A simulation model of the solar air heating system was formulated using equations (4) for the thermal storage component, and relations describing the collector and load as given in reference [8]. The simulation model has been used to estimate the long-term thermal performance of the solar air heating system. Each simulation was supplied with hour by hour meterological data for an average year in Madison, chosen in the manner described in [8].

Sensitivity of System Performance to NTU$_c$

The sensitivity of the long-term performance of solar air heating systems to the parameter NTU$_c$, has been investigated using system simulations for the average Madison year. The results, presented as the ratio of the fraction of the yearly heating load supplied by solar energy to that supplied if NTU$_c$ becomes infinitely large, appear in Fig. 1. The cross-hatched area in Fig. 1 indicates that, at low values of NTU$_c$, the correlation presented is a function of other system design parameters such as the air flow rate, the volume of the packed bed, the collector parameters, and the ratio of the collector to load size. In particular, a change in any system parameter which increases the energy losses from the collector, either by increasing the average collector temperature or the collector overall loss coefficient, will tend to reduce the ordinate in Fig. 1 at low values of NTU$_c$. A range of practical values of the system parameters were used in the construction of Fig. 1. Air flow rates per unit collector area were varied between 22 and 88 kg hr^{-1} m^{-2}. The packed bed volumes per unit collector area ranged between 0.125 and 0.5 m^3 m^{-2}. Air heaters having one, two, and three glass covers and with both selective and nonselective absorber plate surfaces were considered. Ratios of the collector to load size were selected so that the air heating system supplied from 25 to 75 percent of the yearly space heating load. As a result, it is expected that the crosshatched area in Fig. 1 includes most practical system designs.

The significance of the asymptotic behavior illustrated in Fig. 1 becomes apparent when it is recognized that the value of NTU$_c$ for many practical system designs is much greater than ten. For these systems, an accurate value of the volumetric heat transfer coefficient, h_v, is not required in order to estimate the long-term system performance. Considering the uncertainty in heat transfer coefficient data discussed by Barker [9], this is indeed fortunate.

In order to investigate the location dependence of the conclusion represented in Fig. 1, the same sensitivity study has been repeated using one year of hour by hour weather data for each of the following locations: Boulder, Colorado; Blue Hill, Massachusetts; Albuquerque, New Mexico; and Charleston, South Carolina. The insensitivity of long-term solar air heating system performance to the parameter NTU$_c$ (shown in Fig. 1) has been found to be location independent.

Development of the Infinite NTU Model

The asymptotic dependence of system performance upon NTU$_c$ suggests that the Schumann model equations are needlessly complex if NTU$_c$ is sufficiently large. In fact, a model in which NTU$_c$ is assumed to be infinitely large will provide an accurate estimate of long-term thermal performance of the packed bed for most practical systems. Using the same assumptions employed in the development of the Schumann model, a packed bed model for infinite NTU$_c$ can be developed from an energy balance on a differential element of the bed in the flow direction. The result is

$$\frac{\partial T}{\partial(\theta/\tau)} = -L\frac{\partial T}{\partial x} + \frac{\mathrm{UPL}}{\dot{m}C_f}(T_{\mathrm{env}} - T) \qquad (5)$$

Instead of two coupled partial differential equations as required by the Schumann model, the packed bed model for infinite NTU$_c$ is a single partial differential equation, since as NTU$_c$ becomes infinitely large, the packing material and air temperatures at any point in the bed become identical. Equation (5) can be solved approximately using finite difference methods.

It should be noted that an infinite NTU$_c$ model for a system with constant properties, will always retain complete separation between temperature fronts passing through the bed. In the single blow case a front is sharp or square with $\partial T/\partial x$ either zero or infinity. The finite difference approximation to the infinite NTU$_c$ model reintroduces smearing of temperature fronts, hence the term infinite NTU$_c$ refers to the source of the model rather than its behavior.

The accuracy of this finite difference method depends upon the choice of N, the number of isothermal segments in the bed. As N is increased, the accuracy of the solution method improves, but at the expense of additional calculation effort. In order to determine a practical value of N, the results of simulations of many system designs for various values of N have been compared with the results obtained using the Schumann model with NTU$_c$ = 25. It has been found that the infinite NTU$_c$ model with $N = 5$ presents a reasonable compromise between accuracy and calculation effort.

Conclusions

By examining the long-term performance of a number of systems with various collector and store sizes and collector mass flow rates, system performance is shown to be insensitive to values of NTU$_c$ greater than ten. This is an important conclusion since most practical stores have properties corresponding to an NTU$_c$ which is much greater than ten. Consequently the simple model of a gravel bed based on an infinite NTU$_c$, is adequate for reasonable gravel bed designs. As a result, the high computing costs associated with the solution of the Schumann model equations can be avoided.

Acknowledgments

The authors express their gratitude to J. A. Duffie and W. A. Beckman of the Solar Energy Laboratory, University of Wisconsin, for their help in formulating the problem. This research has been supported by ERDA grant E(11-1) 2588 to the University of Wisconsin-Madison.

References

1 Jakob, Max, *Heat Transfer Volume II*, Chapter 35, Wiley, New York, 1957.

2 Balcomb, J. D., Hedstrom, J. D., Roger, B. T., "Design Considerations of Air Cooled Collector/Rock-Bin Storage Solar Heating Systems," Los Alamos Scientific Lab Report LA-UR-75-1334; submitted for publication in *Solar Energy*.

3 Katto, Y., Masuoka, T., "Criterion for the Onset of Convective Flow in a Fluid in a Porous Medium," *International Journal of Heat and Mass Transfer*, Vol. 10, 1967, pp. 297–309.

4 Jeffreson, C. P., "Prediction of Breakthrough Curves in Packed Beds," *AIChE Journal*, Vol. 18, No. 2, Mar. 1972, p. 409.

5 Löf, G. O. G., Hawley, R. W., "Unsteady State Heat Transfer Between Air and Loose Solids," *Ind. and Engr. Chem.*, Vol. 40, June 1948, p. 1061.

6 Dunkle, R. V., Ellul, W. M. J., "Randomly Packed Particulate Bed Regenerators and Evaporative Coolers," *Mech. and Chem. Engr. Trans. I. E. Australia*, Vol. MC8, No. 2, Nov. 1972, pp. 117–121.

7 Close, D. J., et al., "Design and Performance of a Thermal Storage Air Conditioning System," *Mech. and Chem. Engr. Trans. I. E. Australia*, Vol. MC4, no. 1, May 1968, p. 45.

8 Klein, S. A., Beckman, W. A., Duffie, J. A., "A Design Procedure for Solar Heating Systems," submitted for publication in *Solar Energy*.

9 Barker, J. J., "Heat Transfer in Packed Beds," *Ind. and Engr. Chem.*, Vol. 57, No. 4, 1965, p. 43

journal of heat transfer

discussion

Heat and Mass Transfer From Freely Falling Drops[1]

R. Porter.[2] Authors employ the analogy between heat and mass transfer in order to relate the mass-transfer coefficient h_D to the sensible-heat-transfer coefficient h. They are then able to determine h in the dimensionless form of the Nusselt number by measuring the combined heat transfer due to sensible and evaporative modes. This may lead to error because the evaporative-transfer mode usually dominates and the relation between heat and mass transfer is not exactly known for the present case.

Indeed, the specific form of the analogy employed by the authors in their dimensionless groups following equation (6) and in equation (8) does not appear to be appropriate for the present case. The form used is based on

$$\frac{h_D}{h} = \frac{h_D d}{D}\frac{k_c}{hd}\frac{D}{k_c} = \frac{\text{Sh}}{\text{Nu}}\frac{D}{\alpha\rho c_p}$$

$$\frac{h_D}{h} = \frac{\text{Sh}}{\text{Nu}}\frac{\text{Le}}{\rho c_p}$$

being taken as

$$\frac{h_D}{h}\,(\text{authors}) = \frac{\text{Le}}{\rho c_p}$$

which requires

$$\frac{\text{Sh}}{\text{Nu}}\,(\text{authors}) = 1$$

This form of the analogy applies where Nusselt and Sherwood numbers are independent of Prandtl and Schmidt numbers, respectively, such as for pure diffusion where Nu = Sh = 2. Note that this is the leading term in the Ranz-Marshall correlation (5*a*) and (5*b*). However, in the present case convection dominates, and it is more appropriate to utilize the well-known empirical relation for laminar and turbulent flows over a wide range of geometries[3]

$$\frac{\text{Nu}}{\text{Sh}} = \left(\frac{\text{Pr}}{\text{Sc}}\right)^{1/3} = \text{Le}^{1/3}$$

which corresponds to the second terms in the Ranz-Marshall equations. In this case

$$\frac{h_D}{h} = \frac{\text{Le}^{2/3}}{\rho c_p}$$

as compared with $\text{Le}/(\rho c_p)$ used by the authors in their equation (8).

In the present case Le > 1, and so the heat exchange due to mass transfer is over predicted and the calculated Nusselt number is under predicted. Because of the dominance of the evaporative mode, Nusselt number is effectively divided by $\text{Le}^{1/3}$. Fortunately, Le = 0(1), and so the error is not large. Nevertheless, we estimate a reduction by about 7 percent. This may explain part of the correction factor g applied to the Ranz-Marshall relation for $x/d \gtrsim 150$.

Actually, in most cooling-tower work the assumption of psychrometric ratio $h/(\rho c_p h_D) \equiv 1$ (Le = 1) is made, and combined heat and mass transfer is determined solely from the total heat (Carrier's sigma function) which is a function only of the adiabatic-saturation temperature. However, some recent work is directed toward separate computations on both modes.[4]

It may be desirable to perform experiments such as those of the present authors where the drops would be collected and weighed in addition to temperature measurement. This may allow measurement of both sensible and evaporative transport and evaluation of the appropriate analogy.

W. E. Dunn.[5] I found the paper by Yao and Schrock quite interesting. However, my analysis suggests an alternative and equally plausible explanation of the apparent discrepancy between the authors' data and the Ranz-Marshall correlation.

I have plotted their data for 3-mm drops versus time in Fig. 1. The error bars shown are based on the authors' estimate that the data are accurate to ±0.1°C. There are several key features of this plot that warrant comment.

First, to emphasize that the drop spends roughly the same time inside the thermal cavity as it does falling, I have taken the origin of the time axis as the instant at which the drop begins to form and not the instant at which it begins to fall. The time spent inside the cavity is calculated from the frequency of drop production ($2\ \text{s}^{-1}$ from Yao [21]) and the time (0.09 s) required for a 3-mm drop to fall through the 4-cm height of the thermal cavity. Unfortunately, the first data point was not taken until roughly 0.7 s after formation began (outside the thermal cavity).

Second, the solid lines in Fig. 1 show calculations based on the Ranz-Marshall correlation but matched with the temperature measured at the first data point. The agreement here is quite good. Therefore, I conclude that the Ranz-Marshall correlation is adequate after the first 0.6 s of a drop's life. In their analysis Yao and Schrock assume that the drop loses no heat in the thermal cavity and suggest that it follows a temperature history like that shown by the dotted line of Fig. 1. This reasoning leads to the conclusion that the Nusselt number is initially very large (as indicated by the large slope of the dotted curve). Yao and Schrock further state that this enhanced cooling is due to oscillation and other dynamic effects not accounted for by the Ranz-Marshall correlation. Although I acknowledge that

---

[1] By S. C. Yao and V. E. Schrock, published in the Feb. 1976 issue of the JOURNAL OF HEAT TRANSFER, TRANS. ASME, Series C, Vol. 98, pp. 120–126.

[2] Assoc. Professor, Illinois Institute of Technology, Chicago, Ill. Mem. ASME.

[3] Sherwood, T. K., Pigford, R. L., and Wilke, C. R., *Mass Transfer*, McGraw-Hill, New York, Section 5.3, 1975.

[4] Yadigaroglu, G., and Pastor, E. J., "An Investigation of the Accuracy of the Merkel Equation for Evaporative Cooling Tower Calculations," AIAA Paper No. 74-765, ASME Paper No. 74-HT-59, July, 1974.

[5] Department of Mechanical and Industrial Engineering, University of Illinois at Urbane-Champaign, Urbane, Ill. Assoc. Mem. ASME.

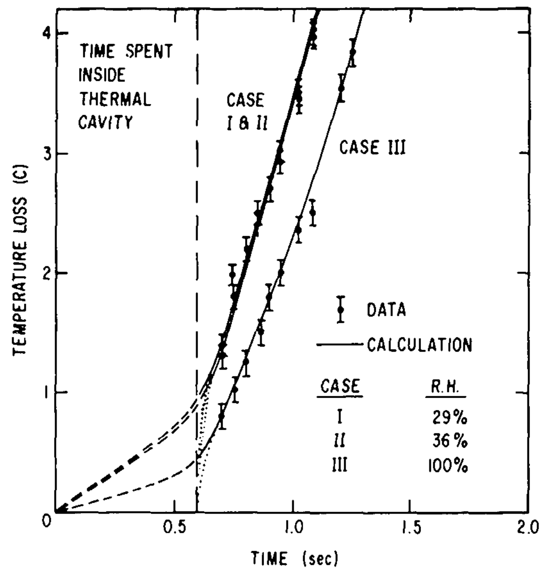

Fig. 1

such enhancement is indeed possible, I would submit that the drop could equally well follow a temperature history like that shown by the dashed line, cooling at a somewhat slower, but still nonzero, rate within the thermal cavity. I would argue further that it is impossible to determine from these data alone what factors in what proportions are responsible for the observed increase in cooling over the Ranz-Marshall correlation. Moreover, due to very complex nature of the processes involved, theoretical analysis is of little value here. The only way to satisfactorily determine the role of dynamic effects is through a very precise experimental study of the cooling that takes place in the first few centimeters of fall. This is, of course, a very difficult experiment. Finally, I would suggest that a falling distance of 3 m is probably too small to determine whether an increase in internal resistance can significantly reduce cooling during the late stages of the life of the drop.

In summary, I would conclude from these observations that the Ranz-Marshall correlation well represents the trend of the data in the range of 0.2–3 m, and that the data are insufficient to draw hard-and-fast conclusions concerning either the very early or the very late stages of a drop's life.

Authors' Closure

The authors are grateful to Porter and Dunn for their discussions which contribute to the understanding of this problem. In most cooling-tower work the analogy between heat and mass transfer is employed. Porter estimated the error as 7 percent. Yadigaroglu and Pastor[6] conducted systematic study of the comparison of results based upon the Merkel equation and the exact formulation for a cooling tower heat exchanger problem. As to their finding, the error depends on operation conditions and is about 4–7 percent with the Merkel equation giving larger cooling range. But this error will not affect the evaluation of the correction factor g. The g factor, which is less than 1 for $x/d > 100$, fits the data adequately. This does not imply that the transfer coefficient from the drop is less than predicted by Ranz-Marshall correlation. The g factor compensates for the overprediction by the complete mixing model while actually internal circulation is developing within the drop at $x/d > 100$.

Porter suggests to relate the mass transfer to the mass change in the drop. It will be a very hard task to measure the change of weight of 3–6-mm dia drops which undergo temperature change no larger than 3°C, even by assuming that all the cooling is due to evaporation.

In response to Dunn, in the present experiment the temperature at the drop generator needle was seen to be within 0.03°C of the thermal cavity temperature. Also the drop temperature measured in a small cup at the mount of the cavity (while it partially blocks the opening of the cavity) is in good agreement with the needle temperature. The water temperature in the calorimeter was maintained at about 0.11°C higher than the drop temperature measured in the dewar to compensate for the evaporative cooling of the water in the dewar. The differential was chosen on the basis of a simple analysis which assumed that the drops entering the calorimeter entrain about six times their own volume of air. Thus the cooling of crops in the cavity and in the dewar was prevented approximately.

The first location for measurement of the drop temperature is 17.7 cm from the needle, which is about 44 dia for 4-mm drops. In this falling range strong oscillations of large drops were observed. The augmentation of heat transfer estimated by using the formulas of Scanlan [24] gave reasonable comparisons as suggested by the proposed correction factor g in this falling range. Nevertheless, as suggested in the present paper, further investigation on the augmentation of heat transfer by large oscillations in drop shape is needed.

In the range $60 \leq x/d \leq 600$ the internal circulation of large drops is developing. The proposed correction factor gives 1.5–0.3 times the Ranz-Marshall transfer coefficient in the falling range investigated in our experiment. The procedure chosen to explain this behavior and the empirical fit of experimental data is of course not the only possible one as shown by Dunn. However, it provides a systematic approach for further understanding of the transient internal circulation upon drop heat transfer.

Nucleation Site Activation in Saturated Boiling[1]

J. J. Lorenz,[2] B. B. Mikic,[3] and W. M. Rohsenow.[3] In nucleation experiments with individual cavities, the authors found that the photographically measured cavity radii were equal to those determined from the following well-known nucleation criteria:

$$\rho = \frac{2\sigma T_s V_{fg}}{h_{fg}\,\Delta T} \tag{1}$$

where ρ is the effective radius of nucleation. Experiments were performed with water only. The authors then suggested that a unique description of the cumulative nucleation site distribution for a given surface could be given by N/A versus equation (1).

In an earlier study of the effects of surface conditions on boiling characteristics, we performed nucleation experiments with both water and organics [4, 5, 6].[4] In our nucleation experiments with water, we obtained results similar to those of the authors', i.e., that the photo-

---

[6] Yadigaroglu, G., and E. Pastor, "An Investigation of the Accuracy of the Merkel Equation for Evaporative Cooling Tower Calculations," ASME Paper No. 74-HT-59.

[1] By M. Shoukri and R. L. Judd, published in the Feb. 1975 issue of the JOURNAL OF HEAT TRANSFER, TRANS. asme, Series C, Vol. 97, pp. 93–98.

[2] Argonne National Laboratory, Argonne, Ill.

[3] Massachusetts Institute of Technology, Cambridge, Mass.

[4] Numbers in brackets designate Additional References at end of discussion.

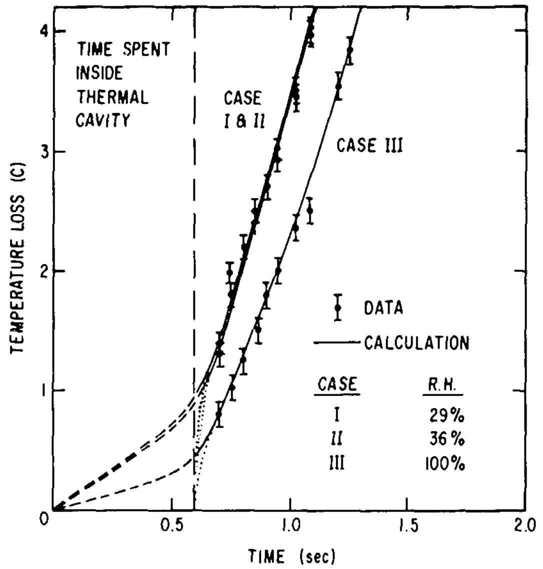

Fig. 1

such enhancement is indeed possible, I would submit that the drop could equally well follow a temperature history like that shown by the dashed line, cooling at a somewhat slower, but still nonzero, rate within the thermal cavity. I would argue further that it is impossible to determine from these data alone what factors in what proportions are responsible for the observed increase in cooling over the Ranz-Marshall correlation. Moreover, due to very complex nature of the processes involved, theoretical analysis is of little value here. The only way to satisfactorily determine the role of dynamic effects is through a very precise experimental study of the cooling that takes place in the first few centimeters of fall. This is, of course, a very difficult experiment. Finally, I would suggest that a falling distance of 3 m is probably too small to determine whether an increase in internal resistance can significantly reduce cooling during the late stages of the life of the drop.

In summary, I would conclude from these observations that the Ranz-Marshall correlation well represents the trend of the data in the range of 0.2–3 m, and that the data are insufficient to draw hard-and-fast conclusions concerning either the very early or the very late stages of a drop's life.

Authors' Closure

The authors are grateful to Porter and Dunn for their discussions which contribute to the understanding of this problem. In most cooling-tower work the analogy between heat and mass transfer is employed. Porter estimated the error as 7 percent. Yadigaroglu and Pastor[6] conducted systematic study of the comparison of results based upon the Merkel equation and the exact formulation for a cooling tower heat exchanger problem. As to their finding, the error depends on operation conditions and is about 4–7 percent with the Merkel equation giving larger cooling range. But this error will not affect the evaluation of the correction factor g. The g factor, which is less than 1 for $x/d > 100$, fits the data adequately. This does not imply that the transfer coefficient from the drop is less than predicted by Ranz-Marshall correlation. The g factor compensates for the overprediction by the complete mixing model while actually internal circulation is developing within the drop at $x/d > 100$.

Porter suggests to relate the mass transfer to the mass change in the drop. It will be a very hard task to measure the change of weight of 3–6-mm dia drops which undergo temperature change no larger than 3°C, even by assuming that all the cooling is due to evaporation.

In response to Dunn, in the present experiment the temperature at the drop generator needle was seen to be within 0.03°C of the thermal cavity temperature. Also the drop temperature measured in a small cup at the mount of the cavity (while it partially blocks the opening of the cavity) is in good agreement with the needle temperature. The water temperature in the calorimeter was maintained at about 0.11°C higher than the drop temperature measured in the dewar to compensate for the evaporative cooling of the water in the dewar. The differential was chosen on the basis of a simple analysis which assumed that the drops entering the calorimeter entrain about six times their own volume of air. Thus the cooling of crops in the cavity and in the dewar was prevented approximately.

The first location for measurement of the drop temperature is 17.7 cm from the needle, which is about 44 dia for 4-mm drops. In this falling range strong oscillations of large drops were observed. The augmentation of heat transfer estimated by using the formulas of Scanlan [24] gave reasonable comparisons as suggested by the proposed correction factor g in this falling range. Nevertheless, as suggested in the present paper, further investigation on the augmentation of heat transfer by large oscillations in drop shape is needed.

In the range $60 \leq x/d \leq 600$ the internal circulation of large drops is developing. The proposed correction factor gives 1.5–0.3 times the Ranz-Marshall transfer coefficient in the falling range investigated in our experiment. The procedure chosen to explain this behavior and the empirical fit of experimental data is of course not the only possible one as shown by Dunn. However, it provides a systematic approach for further understanding of the transient internal circulation upon drop heat transfer.

Nucleation Site Activation in Saturated Boiling[1]

J. J. Lorenz,[2] B. B. Mikic,[3] and W. M. Rohsenow.[3] In nucleation experiments with individual cavities, the authors found that the photographically measured cavity radii were equal to those determined from the following well-known nucleation criteria:

$$\rho = \frac{2\sigma T_s V_{fg}}{h_{fg}\, \Delta T} \tag{1}$$

where ρ is the effective radius of nucleation. Experiments were performed with water only. The authors then suggested that a unique description of the cumulative nucleation site distribution for a given surface could be given by N/A versus equation (1).

In an earlier study of the effects of surface conditions on boiling characteristics, we performed nucleation experiments with both water and organics [4, 5, 6].[4] In our nucleation experiments with water, we obtained results similar to those of the authors', i.e., that the photo-

---

[6] Yadigaroglu, G., and E. Pastor, "An Investigation of the Accuracy of the Merkel Equation for Evaporative Cooling Tower Calculations," ASME Paper No. 74-HT-59.

[1] By M. Shoukri and R. L. Judd, published in the Feb. 1975 issue of the JOURNAL OF HEAT TRANSFER, TRANS. asme, Series C, Vol. 97, pp. 93–98.

[2] Argonne National Laboratory, Argonne, Ill.

[3] Massachusetts Institute of Technology, Cambridge, Mass.

[4] Numbers in brackets designate Additional References at end of discussion.

graphically measured cavity radii were equal to those calculated from equation (1). However, our nucleation results with organics were quite different than those with water. It was found that for the same set of cavities employed in the water nucleation experiments, the effective radii of nucleation as calculated from equation (1) were considerably less than previously calculated for water. Thus, for a given cavity the value of ρ as determined from equation (1) is not unique but depends upon the particular fluid.[5] Using a model incorporating Bankoff's vapor trapping hypothesis, this difference in nucleation behavior was attributed to fluid-surface contact angle differences between water and organics. For certain cavities dynamic effects also play an important role. Only for very deep cylindrical cavities, which are generally not produced on real surfaces by common finishing procedures, are the influence of contact angle and dynamic effects insignificant, and hence the effective radii the same for water and organics.

Our data for the cumulative nucleation site density on a given surface were consistent with our studies of individual cavities. Fig. 1 clearly shows that equation (1) does not correlate the data for water and organics. By extending our model for individual nucleation sites, this behavior was also explained in references [4, 5] as a contact angle effect. All three organics have nearly the same fluid-surface contact angles and consequently fall on a single curve. Water has a relatively large contact angle and at a given ρ value more sites are active.

Thus, the author's conclusions concerning the nucleation behavior of a particular surface must be restricted to water only. No generalizations can be made to arbitrary fluids.

Additional References

4 Lorenz, J. J., "The Effects of Surface Conditions on Boiling Characteristics," PhD thesis, Department of Mechanical Engineering, MIT, Dec. 1971.

5 Lorenz, J. J., Mikic, B. B., and Rohsenow, W. M., "The Effect of Surface Conditions on Boiling Characteristics," *Heat Transfer 1974*, Vol. IV, *Proceedings of the 5th International Heat Transfer Conference*, Tokyo, Japan.

6 Lorenz, J. J., Mikic, B. B., and Rohsenow, W. M., "A Gas Diffusion Technique for Determining Pool Boiling Nucleation Sites," JOURNAL OF HEAT TRANSFER, TRANS. ASME, Series C, Vol. 97, No. 2, May 1975, pp. 317–319.

7 Griffith, P., and Wallis, J. D., "The Role of Surface Conditions in Nucleate Boiling," *Chem. Eng. Progress Symp. Series*, Vol. 56, No. 30, pp. 49–63.

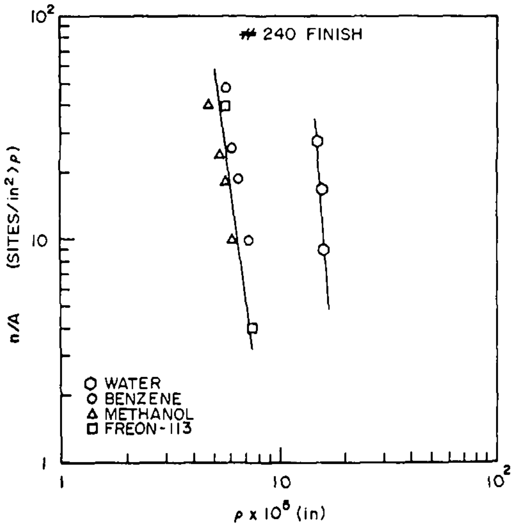

Fig. 1 Cumulative nucleation site densities, reference [5]

Authors' Closure

The authors wish to express their thanks to Lorenz, Mikic, and Rohsenow for their relevant comments. The authors agree that the parameter group $[2\sigma T_s v_{fg}/h_{fg}\Delta T]$ represents the effective radius of nucleation ρ rather than the cavity mouth radius r_c. The agreement obtained between the cavity radius and those predicted by the parameter group in the case of water is due to the large contact angle of water which caused the ratio (ρ/r_c) to approach unity.

This fact has been recognized and accounted for in a recently published paper by the authors,[6] in which (ρ/r_c) was assumed to be function of both the contact angle θ and the cavity conical angle ψ, i.e., $(\rho/r_c) = f(\theta, \psi)$. In this paper the data for boiling of five different organic fluids on a glass surface were used to assess the Mikic and Rohsenow model.[7] Only the slope of boiling characteristic curve as predicted by the model was found to agree with the experimental data. However, upon introducing the function $(\rho/r_c) = f(\theta, \psi)$, good agreement was obtained when this function was set equal to 0.83 to account for the small contact angle of the organic fluids.

---

[5] This directly contradicts the results of Griffith and Wallis [7] who claimed that a single dimension is sufficient to characterize a cavity. Employing equation (1) their data for water and organics fell on a single curve. In reference [4] it was shown that the data of Griffith and Wallis is suspect because in performing the experiments, a subcooled bulk temperature was maintained in order to facilitate bubble counting. As a result of the subcooling, air was able to diffuse into the system at the upper surface. It is expected that the presence of this dissolved gas altered the nucleation process in such a way as to fortuitously indicate a unique effective radius of nucleation. In our nucleation experiments a saturated bulk temperature was maintained in order to eliminate this problem.

[6] Judd, R. L., and Shoukri, M., "Nucleate Boiling on an Oxide Coated Glass Surface," JOURNAL OF HEAT TRANSFER, TRANS. ASME, Series C, Vol. 97, Aug. 1975, p. 494.

[7] Mikic, B. B., and Rohsenow, W. H., "A Correlation of Pool Boiling Data Including the Effect of Heating Surface Characteristics," JOURNAL OF HEAT TRANSFER, TRANS. ASME, Series C, Vol. 91, May 1969, p. 245.

Addendum

"Laminar Free Convection Over Two-Dimensional and Axisymmetric Bodies of Arbitrary Contour," by F. N. Lin and B. T. Chao, JOURNAL OF HEAT TRANSFER, TRANS. ASME, Series C, Vol. 96, 1974, pp. 435–442.

In the above referenced paper, we made a comparison of the local heat transfer results calculated by our procedure for isothermal, horizontal circular cylinders in air with those obtained by the Görtler-type series developed by Saville and Churchill.[1] The comparison was not as satisfactory as that obtained for the Blasius-type series. Recently, we re-examined the analysis of Saville and Churchill and discovered two sources of errors that could be held responsible for the discrepancy. It is the purpose of this letter to make these errors known to our readers.

(*a*) Equation (17) of the Saville-Churchill paper should read:

$$K(\xi) = \frac{3}{4} - 2\sqrt{2}\left(\frac{3}{40}\right)\left(\frac{64}{27}\right)^{1/2} \xi^{3/2} + \ldots$$

The factor $2\sqrt{2}$ was inadvertently left out.

(*b*) The expression for $T'(o)$ given on p. 397 should read:

$$T_1'(o) = +0.03226\, K_1$$

instead of

$$T_1'(o) = -0.03226\, K_1.$$

When these errors are corrected, the numerical data listed in Table 1 and under the heading "Görtler-type Series" of our paper become:

ϕ, deg.	1st Term	2nd Term	Sum ($Nu/Gr^{1/4}$)
0	0.4402	0.0000	0.4402
10	0.4396	0.0001	0.4397
20	0.4376	0.0004	0.4380
30	0.4343	0.0008	0.4351
40	0.4295	0.0013	0.4308
50	0.4234	0.0020	0.4254
60	0.4158	0.0029	0.4187
70	0.4068	0.0037	0.4105
80	0.3963	0.0047	0.4010
90	0.3842	0.0056	0.3898
100	0.3703	0.0066	0.3769
110	0.3546	0.0074	0.3620
120	0.3367	0.0082	0.3449
130	0.3163	0.0088	0.3251
140	0.2928	0.0091	0.3019
150	0.2649	0.0091	0.2740

The "2nd Term" results differ from those originally listed not only in magnitude but, more importantly, also in sign. The corrected sum ($Nu/Gr^{1/4}$) now compares more favorably with our result.

---

[1] Saville, D. A., and Churchill, S. W., "Laminar Free Convection in Boundary Layers Near Horizontal Cylinders and Vertical Axisymmetric Bodies," *Journal of Fluid Mechanics*, Vol. 29, 1967, pp. 391–399.